ISSN 1580-2949
UDK 669+666+678+53 MTAEC9, 49(5)663–844(2015)

MATER. TEHNOL.	LETNIK VOLUME 49	ŠTEV. NO. 5	STR. P. 663–844	LJUBLJANA SLOVENIJA	SEP.–OCT. 2015

VSEBINA – CONTENTS

PREGLEDNI ČLANKI – REVIEW ARTICLES

IZVIRNI ZNANSTVENI ČLANKI – ORIGINAL SCIENTIFIC ARTICLES

STROKOVNI ČLANKI – PROFESSIONAL ARTICLES

UDK 669.058:669.781:544.034
Review article/Pregledni članek

ISSN 1580-2949
MTAEC9, 49(5)665(2015)

KINETIC STUDY AND CHARACTERIZATION OF BORIDED AISI 4140 STEEL

ŠTUDIJ KINETIKE IN KARAKTERIZACIJA BORIRANEGA JEKLA AISI 4140

Mourad Keddam[1], Martín Ortiz-Domínguez[2], Oscar Armando Gómez-Vargas[3], Alberto Arenas-Flores[4], Miguel Ángel Flores-Rentería[2], Milton Elias-Espinosa[5], Abel García-Barrientos[6]

[1]Département de Sciences des Matériaux, Faculté de Génie Mécanique et Génie des Procédés, USTHB, B.P. No. 32, 16111 El-Alia, Bab-Ezzouar, Algiers, Algeria
[2]Universidad Autónoma del Estado de Hidalgo, Escuela Superior de Ciudad Sahagún-Ingeniería Mecánica, Carretera Cd. Sahagún-Otumba s/n, Zona Industrial CP. 43990 Hidalgo, México
[3]Instituto Tecnológico de Tlalnepantla-ITTLA. Av., Instituto Tecnológico, S/N. Col. La Comunidad, Tlalnepantla de Baz. CP. 54070 Estado de México, México
[4]Universidad Autónoma del Estado de Hidalgo-AACTyM, Carretera Pachuca Tulancingo Km. 4.5, Mineral de la Reforma, CP. 42184 Hidalgo, México
[5]Instituto Tecnológico y de Estudios Superiores de Monterrey-ITESM Campus Santa Fe, Av. Carlos Lazo No. 100, Del. Álvaro Obregón, CP. 01389 D. F., México
[6]Universidad Autónoma del Estado de Hidalgo-CITIS, Carretera Pachuca Tulancingo Km. 4.5, Mineral de la Reforma, CP. 42184 Hidalgo, México
keddam@yahoo.fr

Prejem rokopisa – received: 2014-02-11; sprejem za objavo – accepted for publication: 2014-10-08

doi:10.17222/mit.2014.034

In the present study, an alternative diffusion model was proposed for analyzing the growth of Fe_2B layers formed on the AISI 4140 steel during the pack-boriding process. This model was based on solving the mass-balance equations for the Fe_2B/Fe interface to evaluate boron diffusion coefficients through the Fe_2B layers in a temperature range of 1123–1273 K. The boride incubation time for the Fe_2B phase was included in the present model. The suggested model was validated experimentally at a temperature of 1253 K for a treatment time of 5 h.
Furthermore, the generated boride layers were analyzed with light microscopy, scanning electron microscopy (SEM), energy dispersive X-ray spectroscopy (EDS) and X-ray diffraction analysis (XRD). In addition, a contour diagram was also proposed as a function of treatment time and temperature. On the basis of our experimental results, the boron activation energy for the AISI 4140 steel was found to be 189.24 kJ mol^{-1}.

Keywords: boriding, incubation time, diffusion model, growth kinetics, activation energy, adherence

V tej študiji je predlagan alternativni model difuzije za analiziranje rasti Fe_2B-plasti, ki nastane na jeklu AISI 4140 pri boriranju v škatli. Ta model temelji na rešitvi enačbe ravnotežja mas na stiku (Fe_2B/Fe) pri oceni koeficienta difuzije bora skozi Fe_2B-sloje v temperaturnem območju 1123–1273 K. Inkubacijski čas borida za Fe_2B-fazo je bil vključen v predstavljeni model. Predlagani model je bil eksperimentalno ocenjen pri temperaturi 1253 K in času obdelave 5 h.
Poleg tega so bili izdelani sloji analizirani na svetlobnem mikroskopu, z vrstičnim elektronskim mikroskopom (SEM), energijsko disperzijsko rentgensko spektroskopijo (EDS) in z rentgensko difrakcijsko analizo (XRD). Dodatno je bil predlagan še konturni diagram kot funkcija časa obdelave in temperature. Na podlagi eksperimentalnih rezultatov je bilo ugotovljeno, da je aktivacijska energija bora pri jeklu AISI 4140 189,24 kJ mol^{-1}.

Ključne besede: boriranje, čas inkubacije, model difuzije, kinetika rasti, aktivacijska energija, adherenca

1 INTRODUCTION

Boriding is a well-known thermochemical treatment in which boron (because of its relatively small size) diffuses into the metal substrate to form hard borides. As a result of boriding, properties such as wear resistance, surface hardness and corrosion resistance are improved.[1] Boriding can be carried out with boron in different states such as solid powder, paste, liquid, gas and plasma. The most frequently used method is pack boriding owing to its technical advantages.[2] Generally, the commercial boriding mixture is composed of boron carbide (B_4C) as a donor, KBF_4 as an activator and silicon carbide (SiC) as a diluent to control the boriding potential of the medium. The boriding treatment requires temperatures ranging from 800 °C to 1000 °C. Usually the treatment time varies between 0.5 h and 12 h producing a boride layer whose thickness depends on the boriding parameters (time and temperature). The morphology of the boride layer is affected by the presence of alloying elements in the matrix. Saw-tooth-shaped layers are obtained in low-alloy steels or Armco iron whereas in high-alloy steels, the interfaces are smooth. According to the Fe-B phase diagram,[3] two iron borides can be formed (FeB and Fe_2B).

A monophase Fe_2B layer with a tooth-shaped morphology is generally suitable for industrial applications because of the difference between the specific volume and the coefficients of the thermal expansion of iron

boride and the substrate.[4,5] The boron-rich phase FeB is not preferred since FeB is more brittle and less tough than Fe_2B.[4,5] Furthermore, the brittleness of FeB layers causes a spalling when a high normal or tangential load is applied.

The modeling of the boriding kinetics is considered as a suitable tool to select the optimized parameters for obtaining a desired boride layer of the treated material for its practical use in the industry. In particular, many models reported in the literature were used for analyzing the kinetics of the Fe_2B layers grown on different substrates[6–16], with and without the boride incubation times.

In the current work, an alternative diffusion model, based on solving the mass-balance equation for the Fe_2B/substrate interface, was proposed to simulate the kinetics of the Fe_2B layers grown on the AISI 4140 steel. In the present model, the boride incubation time was independent of the temperature. The pack-borided AISI 4140 steel was characterized by means of the following techniques: light microscopy, scanning electron microscopy and XRD. Based on the experimental data, the boron activation energy was also evaluated when pack boriding the AISI 4140 steel in a temperature range of 1123–1273 K.

2 KINETIC MODEL

The model considers the growth of the Fe_2B layer on a substrate saturated with boron atoms as illustrated in **Figure 1.** The $f(x,t)$ function represents the boron distribution in the iron matrix before the nucleation of the Fe_2B phase. $t_0^{Fe_2B}$ corresponds to the incubation time required to form the Fe_2B phase when the matrix reaches the state of being saturated with boron atoms. $C_{up}^{Fe_2B}$ represents the upper limit of the boron content in Fe_2B ($60 \cdot 10^3$ mol m^{-3}), $C_{low}^{Fe_2B}$ is the lower limit of the boron content in Fe_2B ($59.8 \cdot 10^3$ mol m^{-3}) and the point $x(t = t) = v$ represents the Fe_2B layer thickness.[17,18]

The term C_{ads}^{B} represents the effective adsorbed boron concentration during the boriding process.[19] In **Figure 1**, $a_1 = C_{up}^{Fe_2B} - C_{low}^{Fe_2B}$ defines the homogeneity range of the Fe_2B layer, $a_2 = C_{low}^{Fe_2B} - C_0$ is the miscibility gap[15,16] and C_0 is the boron solubility in the matrix considered as zero.[3] The following assumptions are considered for the diffusion model:

– The growth kinetics is controlled by the boron diffusion in the Fe_2B layer.
– The Fe_2B iron boride nucleates after a specific incubation time.
– The boride layer grows because of the boron diffusion perpendicular to the specimen surface.
– Boron concentrations remain constant in the boride layer during the treatment.
– The influence of the alloying elements on the growth kinetics of the layer is not taken into account.
– The boride layer is thin compared to the sample thickness.
– A uniform temperature is assumed throughout the sample.
– A planar morphology is assumed for the phase interface.

The initial and boundary conditions for the diffusion problem are represented as:

$$t = 0,\ x > 0,\ \text{with: } C_{Fe2B}\ [x(t),\ t = 0]\ = C_0 \approx 0 \quad (1)$$

Boundary conditions:

$$C_{Fe_2B}\left[x(t = t_0^{Fe_2B}) = v_0, t = t_0^{Fe_2B}\right] = C_{up}^{Fe_2B} \quad (2)$$

(the upper boron concentration is kept constant) for $C_{ads}^{B} > 60 \cdot 10^3$ mol m^{-3}:

$$C_{Fe_2B}\left[x(t = t) = v, t = t\right] = C_{low}^{Fe_2B} \quad (3)$$

(the upper boron concentration is kept constant) for $C_{ads}^{B} < 59.8 \cdot 10^3$ mol m^{-3}

v_0 is a thin layer with a thickness of ≈ 5 nm that formed during the nucleation stage,[20] thus v_0 (≈ 0) is used when compared to the thickness of the Fe_2B layer (v). The mass-balance equation at the Fe_2B/substrate interface can be formulated with Equation (4) as follows:

$$\left(\frac{C_{up}^{Fe_2B} + C_{low}^{Fe_2B} - 2C_0}{2}\right)(A \cdot dv) = \quad (4)$$

$$= J_{Fe_2B}(x = v, t = t)(A \cdot dt) - J_{Fe}(x = v + dv, t = t)(A \cdot dt)$$

where A(=1.1) is defined as the unit area and C_0 represents the boron concentration in the matrix. The fluxes J_{Fe2B} and J_{Fe} are obtained from the Fick's first law as:

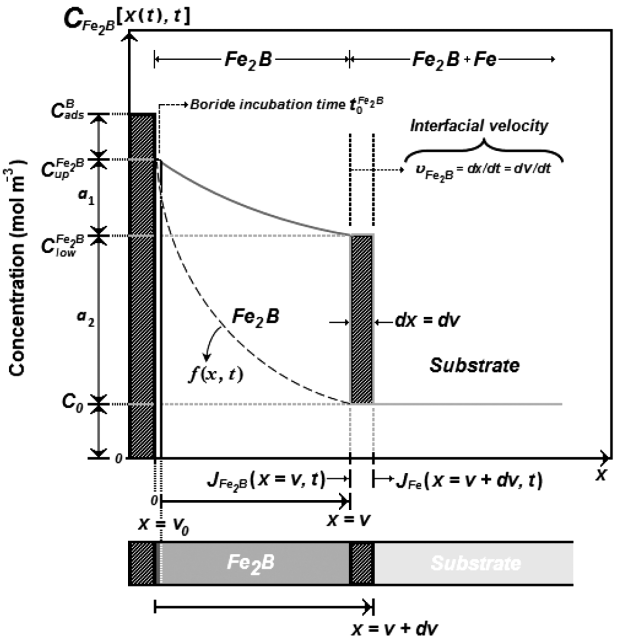

Figure 1: Schematic boron-concentration profile through the Fe_2B layer

Slika 1: Shematski prikaz profila koncentracije bora skozi Fe_2B-plast

$$J_{Fe_2B}[x(t=t)=v,t=t)]= =-\left\{\frac{D_{Fe_2B}\partial C_{Fe_2B}[x(t=t)=v,t=t)]}{\partial x}\right\}_{x=v} \quad (5)$$

and:

$$J_{Fe}[x(t=t)=v+dv,t=t)]= =-\left\{\frac{D_{Fe}\partial C_{Fe}[x(t=t)=v+dv,t=t)]}{\partial x}\right\}_{x=v+dv} \quad (6)$$

The term J_{Fe} is zero since the boron solubility in the matrix is very low (≈ 0 mol m^{-3}).[3]

Thus, Equation (4) can be written as:

$$\left(\frac{C_{up}^{Fe_2B}+C_{low}^{Fe_2B}-2C_0}{2}\right)\frac{dx(t)}{dt}\bigg|_{x(t)=v} = =-D_{Fe_2B}\frac{\partial C_{Fe_2B}[x(t=t),t=t]}{\partial x}\bigg|_{x(t)=v} \quad (7)$$

The Fick's second law of diffusion relating to the change in the boron concentration through the Fe_2B layer with the time t and the distance $x(t)$ is given with Equation (8) :

$$\frac{\partial C_{Fe_2B}[x(t),t]}{\partial t}=D_{Fe_2B}\frac{\partial^2 C_{Fe_2B}[x(t),t]}{\partial x^2} \quad (8)$$

When applying the boundary conditions proposed in Equations (2) and (3), the solution of Equation (8) takes the following form:

$$C_{Fe_2B}[x(t),t]=C_{up}^{Fe_2B}+\frac{C_{low}^{Fe_2B}-C_{up}^{Fe_2B}}{\operatorname{erf}\left(\frac{v}{2\sqrt{D_{Fe_2B}t}}\right)}\cdot\operatorname{erf}\left(\frac{x}{2\sqrt{D_{Fe_2B}t}}\right) \quad (9)$$

By substituting the derivative of Equation (9) with respect to the distance $x(t)$ in Equation (7), Equation (10) is obtained:

$$\left(\frac{C_{up}^{Fe_2B}+C_{low}^{Fe_2B}-2C_0}{2}\right)\frac{dv}{dt}= =\sqrt{\frac{D_{Fe_2B}}{\pi t}}\cdot\frac{\left(C_{up}^{Fe_2B}-C_{low}^{Fe_2B}\right)}{\operatorname{erf}\left(\frac{v}{2\sqrt{D_{Fe_2B}t}}\right)}\cdot\exp\left(-\frac{v^2}{4D_{Fe_2B}t}\right) \quad (10)$$

for $0 \le x \le v$.

Substituting the expression of the parabolic growth law ($v=2\varepsilon\sqrt{D_{Fe_2B}t}$) in Equation (10), Equation (11) is deduced:

$$\left(\frac{C_{up}^{Fe_2B}+C_{low}^{Fe_2B}-2C_0}{2}\right)\varepsilon= =\sqrt{\frac{1}{\pi}}\left(\frac{C_{up}^{Fe_2B}-C_{low}^{Fe_2B}}{\operatorname{erf}(\varepsilon)}\right)\exp(-\varepsilon^2) \quad (11)$$

The normalized growth parameter (ε) for the Fe_2B/substrate interface can be estimated numerically using the Newton-Raphson method. It is assumed that expressions $C_{up}^{Fe_2B}$, $C_{low}^{Fe_2B}$ and C_0 do not depend significantly on the temperature (in the considered temperature range).[18]

A schematic representation of the square of the layer thickness against the linear time ($v^2 = 4\varepsilon^2 D_{Fe_2B}t = 4\varepsilon^2 D_{Fe_2B}[t_v + t_0^{Fe_2B}(T)]$) is depicted in **Figure 2**. $t_v(= t - t_0^{Fe_2B})$ is the effective growth time of the Fe_2B layer and t is the treatment time.

3 EXPERIMENTAL PROCEDURE

3.1 Boriding process

The AISI 4140 steel was used in this experimental study. It had a nominal chemical composition of 0.38–0.43 % C, 0.75–1.00 % Mn, 0.80–1.10 % Cr, 0.15–0.30 % Si, 0.040 % S, and 0.035 % P. Samples had a cubic shape with dimensions of 10 mm × 10 mm × 10 mm. Prior to the boriding process, the specimens were polished, ultrasonically cleaned in an alcohol solution and deionized water for 15 min at room temperature, dried and stored under clean-room conditions. The samples were packed along with a Durborid fresh powder mixture in a closed cylindrical case (AISI 304L). The used powder mixture had an average size of 30 μm. The powder-pack boriding process was carried out in a conventional furnace under a pure argon atmosphere in the temperature range of 1123–1273 K. Four treatment times ((2, 4, 6 and 8) h) were selected for each temperature. After the completion of the boriding treatment, the container was removed from the furnace and slowly cooled to room temperature.

3.2 Microscopical observations of boride layers

The borided samples were cross-sectioned for metallographic examinations using a LECO VC-50 precision cutting machine. The cross-sectional morphology of the boride layers was observed with an Olympus GX51 light microscope in a clear field. **Figure 3** shows cross-sectional views of light images of the Fe_2B layers of the AISI 4140 steel formed at a temperature of 1223 K over different process durations.

The resultant microstructures of the Fe_2B layers appear to be very dense and homogenous, exhibiting saw-tooth morphologies. Since the growth of a saw-tooth boride layer is a controlled diffusion process with a highly anisotropic nature, higher temperatures and/or

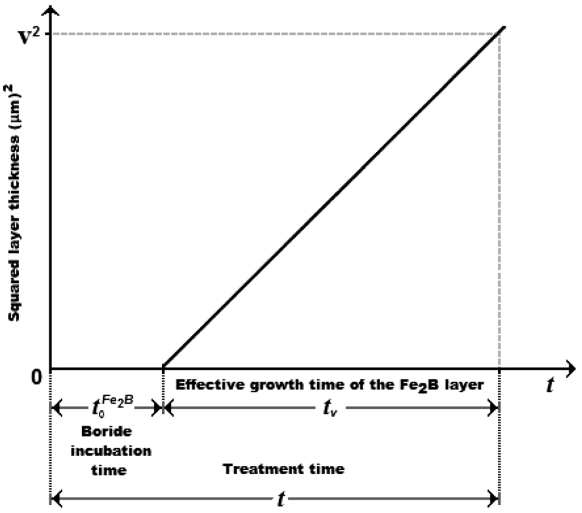

Figure 2: Schematic representation of the square of the layer thickness against the treatment time

Slika 2: Shematski prikaz kvadrata debeline plasti, odvisno od časa obdelave

longer times stimulated the Fe_2B crystals to make contact with the adjacent crystals and forced them to retain an acicular shape.[21] It is seen that the thickness of the Fe_2B layer increased with an increase in the boriding time (**Figure 3**) because the boriding kinetics is influenced by the treatment time. For the kinetic study, the boride-layer thickness was automatically measured with the aid of the MSQ PLUS software. To ensure the reproducibility of the measured layer thicknesses, fifty measurements were collected in different sections of the samples of the borided AISI 4140 steel to estimate the Fe_2B layer thickness, defined as the average value of the long boride teeth.[22–24] All the thickness measurements were taken from a fixed reference on the surface of the borided AISI 4140 steel, as illustrated in **Figure 4.**

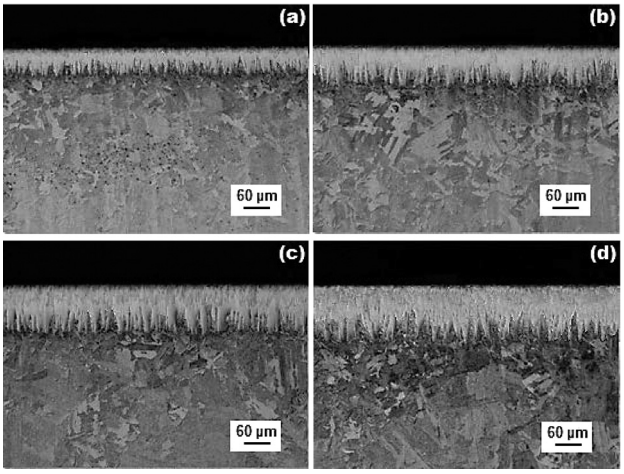

Figure 3: Light micrographs of the boride layers formed on the surface of AISI 4140 steel treated at 1223 K for variable times: a) 2 h, b) 4 h, c) 6 h and d) 8 h

Slika 3: Svetlobni posnetki boriranih plasti, nastalih na površini jekla AISI 4140 pri temperaturi 1223 K in različnem trajanju: a) 2 h, b) 4 h, c) 6 h in d) 8 h

The phases of the boride layers were investigated with X-ray diffraction (XRD) equipment (Equinox 2000) using Co-K_α radiation with a wavelength of 0.179 nm. The elemental distribution within the cross-section of a boride layer was determined with electron dispersive spectroscopy (EDS) equipment (JEOL JSM 6300 LV), from the surface.

4 RESULTS AND DISCUSSIONS

4.1 SEM observations and EDS analyses

A cross-sectional view of the SEM micrograph of the AISI 4140 steel borided at 1273 K for 6 h is shown in **Figure 5a**. The boride layer grown on the substrate has a saw-tooth morphology. The needles of Fe_2B, with different lengths, are visible on the SEM micrograph, penetrating into the substrate. This typical morphology is responsible for a good adhesion to the substrate. EDS results obtained with SEM are shown in **Figures 5b** and **5c.** These results indicate the presence of two elements at the surface: Fe and Cr (**Figure 5a**). The results also show the possible dissolution of chromium in Fe_2B. In fact, the atomic radius of Cr (= 0.166 nm) is about the same and larger than that of Fe (= 0.155 nm), and it can then be expected that Cr dissolved in the Fe sublattice of Fe_2B. The obtained result in **Figure 5c** indicates the presence of the following elements: Fe, C, Cr, Si and Mn in the vicinity of the Fe_2B/substrate interface. It is seen that two elements (carbon and silicon) are not dissolved in Fe_2B, being displaced towards the substrate. Silicon and boron may form complex phases such as $FeSi_{0.4}B_{0.6}$, FeSiB and boron cementite ($Fe_3B_{0.67}C_{0.33}$).[25]

4.2 X-ray diffraction analysis

Figure 6 displays the XRD pattern recorded on the surface of the AISI 4140 steel borided at a temperature of 1273 K for a treatment time of 8 h. The diffraction peaks relative to the Fe_2B phase are easily identified. Peaks with very small intensities are also observed for

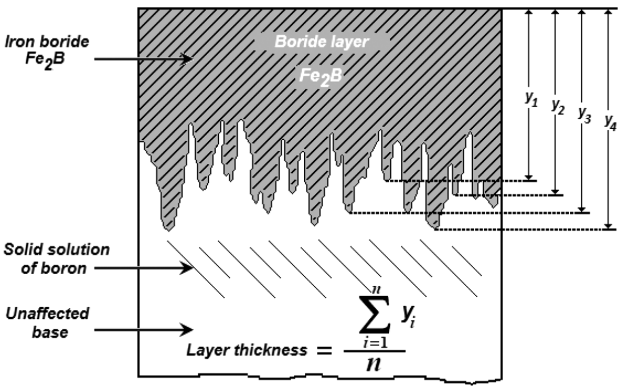

Figure 4: Schematic diagram illustrating the procedure for estimating the boride-layer thickness on the AISI 4140 steel

Slika 4: Shematski diagram, ki prikazuje postopek za ugotavljanje debeline borirane plasti na jeklu AISI 4140

the FeB phase but the Fe_2B phase is dominant with high-peak intensities. The CrB phase is also visible in the XRD pattern recorded at the surface of the borided AISI 4140 steel. In the experimental study about the boriding of the AISI 4140 steel in molten borax, boric acid and a ferro-silicon bath performed by Sen et al.[26], the XRD study showed the presence of FeB, Fe_2B and CrB at the surface of a sample borided at 1223 K for 6 h. In addition, Ulutan et al.[27] also identified, with an XRD analysis, the same phases at the surface of the AISI 4140 steel (at 1000 °C for 6 h) after the powder-pack boriding.

Crystals of the Fe_2B type orientate themselves with the *z*-axis perpendicular to the surface. Consequently, the peaks of the Fe_2B phase belonging to the crystallographic planes and having a deviation from zero of the *l* index, showed increased intensities in the X-ray diffraction spectra.[28]

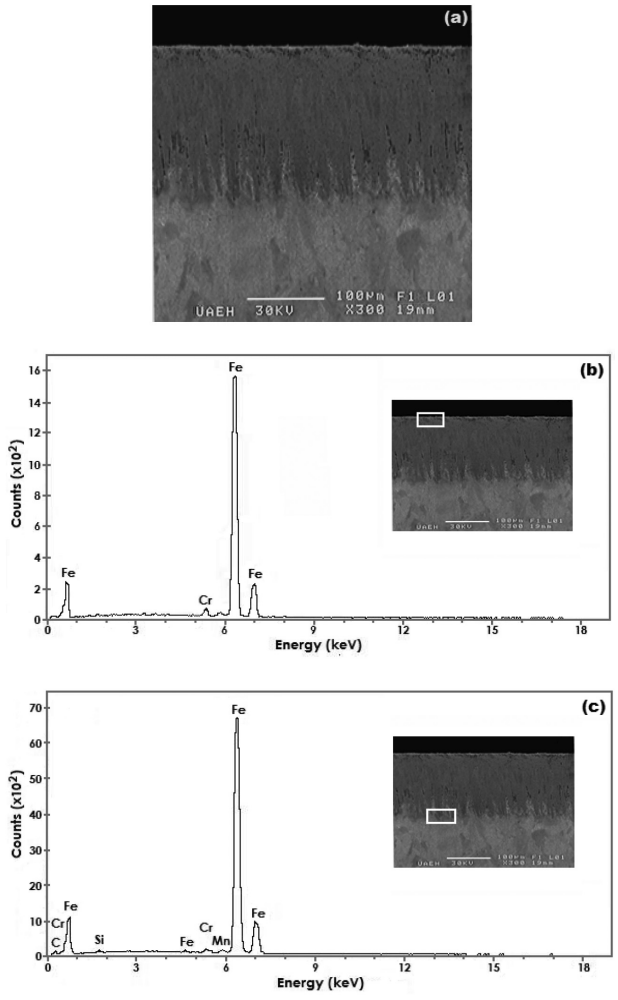

Figure 5: a) SEM micrograph of the cross-section of the AISI 4140 steel borided at 1273 K for 6 h, b) EDS spectrum of the surface of a borided sample and c) EDS spectrum of the interface of a borided sample

Slika 5: a) SEM-posnetek prereza boriranega jekla AISI 4140 po 6 h na 1273 K, b) EDS-spekter boriranega vzorca na površini in c) EDS-spekter boriranega vzorca na stiku z osnovo

The growth of boride layers is a controlled diffusion process with a highly anisotropic nature. In the case of the Fe_2B phase, the [001] crystallographic direction is the easiest path for the boron diffusion in Fe_2B because of the tendency of the boride crystals to grow along the direction of minimum resistance, perpendicular to the external surface. As the metal surface is covered, an increasing number of the Fe_2B crystals come in contact with the adjacent crystals, being forced to grow inside the metal and retaining the acicular shape.[21] In the powder-pack boriding, the active boron is supplied by the powder mixture. To form a Fe_2B phase on any borided steel, a low boron potential is required as reported in the reference works[4,29], while a high amount of active boron in a powder mixture gives rise to a bilayer configuration consisting of FeB and Fe_2B.

4.3 Estimation of the boron activation energy

The growth kinetics of the Fe_2B layers formed on the AISI 4140 steel was used to estimate the boron diffusion coefficient through the Fe_2B layers by applying the suggested diffusion model. The ε parameter is then determined by solving the mass-balance equation for the Fe_2B/substrate interface (Equation (11)) using the Newton-Raphson method. **Table 1** lists the estimated value of boron diffusion coefficient in Fe_2B at each temperature along with the squared value of normalized growth parameter ε determined from Equation (11). **Figure 7** depicts the time dependence of the squared value of the Fe_2B layer thickness. The slopes of the straight lines in this figure provide the values of the growth constants ($= 4\varepsilon^2 D_{Fe_2B}$) for each boriding temperature. The values of the boron diffusion coefficients in the Fe_2B layers can be determined by knowing the value of the ε parameter. The boride incubation times for Fe_2B can also be deduced from the straight lines displayed in **Figure 7** by extrapolating them to the boride-layer thickness of zero.

To estimate the boron activation energy for the AISI 4140 steel, it is necessary to plot the natural logarithm of

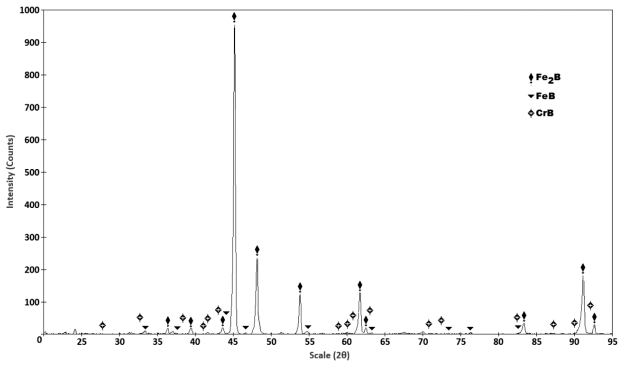

Figure 6: XRD pattern obtained at the surface of the borided AISI 4140 steel treated at 1273 K for 8 h

Slika 6: Rentgenogram, dobljen na površini boriranega jekla AISI 4140 po 8 h na 1273 K

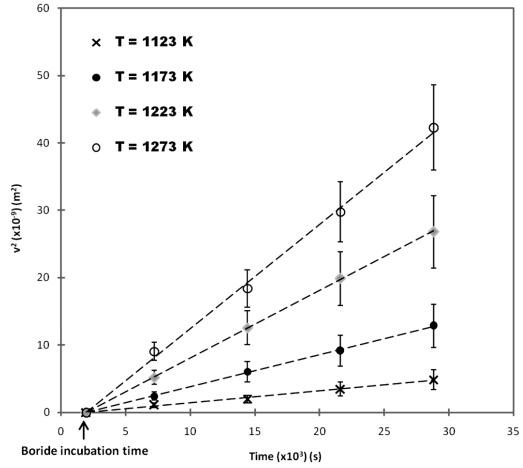

Figure 7: Evolution of the squared value of Fe_2B layer thickness as a function of boriding time

Slika 7: Razvoj vrednosti kvadrata debeline plasti Fe_2B v odvisnosti od časa boriranja

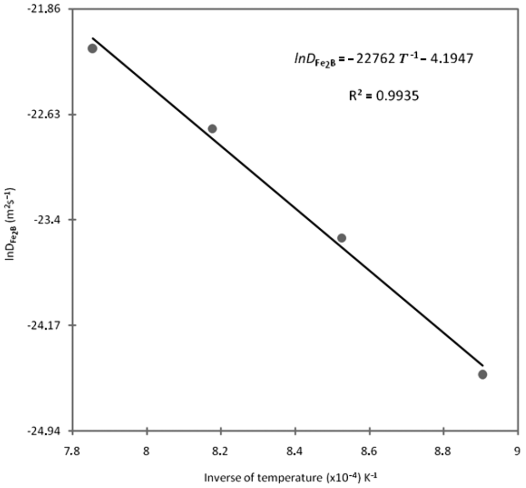

Figure 8: Temperature dependence of the boron diffusion coefficient for Fe_2B

Slika 8: Temperaturna odvisnost koeficienta difuzije v Fe_2B

Table 1: Squared value of normalized growth parameter and boron diffusion coefficients for Fe_2B as a function of boriding temperature

Tabela 1: Kvadratna vrednost normaliziranih parametrov rasti in koeficientov difuzije bora v Fe_2B v odvisnosti od temperature boriranja

Temperature (K)	Type of layer	ε^2 (Dimensionless)	$4\varepsilon^2 D_{Fe_2B}$ ($\mu m^2\ s^{-1}$)
1123	Fe_2B	1.7×10^{-3}	1.51×10^{-1}
1173			4.11×10^{-1}
1223			9.12×10^{-1}
1273			16.3×10^{-1}

Table 2: Comparison of the boron activation energies for some borided steels

Tabela 2: Primerjava aktivacijskih energij bora pri nekaterih boriranih jeklih

Material	Boron activation energy (kJ mol^{-1})	References
AISI 5140	223	30
AISI 4340	324	30
AISI 1040	118.8	31
AISI 51100	106.0	32
AISI 4140	215	26
AISI 4140	189.24	Present study

the boron diffusion coefficient for Fe_2B versus the reciprocal temperature following the Arrhenius equation (**Figure 8**). A linear fitting was assumed to obtain the temperature dependence of the boron diffusion coefficient for Fe_2B with a correlation factor of 0.9935:

$$D_{Fe_2B} = 1.51\times10^{-2}\ \exp\left(\frac{-189.24\ \text{kJ mol}^{-1}}{RT}\right) \quad (12)$$

where R = 8.3144621 J mol^{-1} K^{-1} and T is the absolute temperature in Kelvin.

Table 2 shows a comparison of the boron activation energies for some borided steels.[26,30–32] The found value of the boron activation energy (= 189.24 kJ mol^{-1}) for the AISI 4140 steel is slightly different from the value reported in[26] due to the boriding conditions (using the liquid-boriding method).

4.4 Validation of the diffusion model

The present model was validated by comparing the experimental value of the Fe_2B layer thickness with the predicted result at a temperature of 1253 K for a treatment time of 5 h using Equation (13):

$$v = \frac{4}{\sqrt{\pi}}\left(\frac{C_{up}^{Fe_2B} - C_{low}^{Fe_2B}}{C_{up}^{Fe_2B} + C_{low}^{Fe_2B}}\right)\cdot\frac{\exp(-\varepsilon^2)}{erf(\varepsilon)}\sqrt{D_{Fe_2B}t} \quad (13)$$

Figure 9 shows the optical image of the boride layer formed at 1253 K after 5 h of treatment.

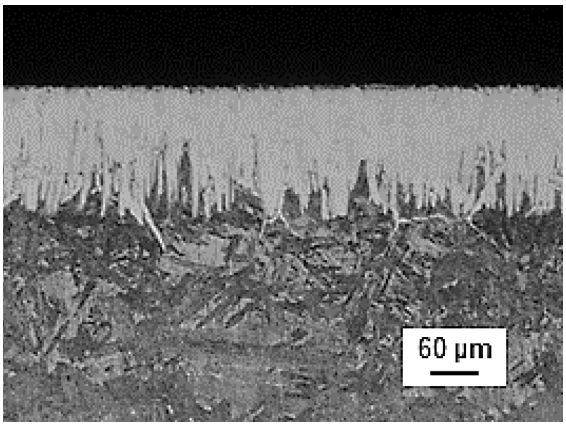

Figure 9: Light micrograph of the cross-section of the borided AISI 4140 treated at 1253 K for 5 h

Slika 9: Svetlobni posnetek prereza boriranega jekla AISI 4140 po 5 h na 1253 K

Table 3 gives a comparison between the experimental value of the Fe_2B layer thickness and the one predicted on the basis of Equation (13). A good agreement was obtained between the experimental value of the Fe_2B layer thickness and the predicted one for the AISI 4140 steel borided at 1253 K for 5 h.

Table 3: Predicted and estimated values of the Fe_2B layer thickness obtained at 1253 K for a treatment time of 5 h

Tabela 3: Predvidene in dobljene vrednosti za debelino plasti Fe_2B po 5 h na 1253 K

Temperature (K)	Type of layer	Boride-layer thickness (μm) estimated by Eq. (13)	Experimental boride-layer thickness (μm)
1253	Fe_2B	154.48	158.12±10.43

4.5 Future exploitation of the simulation results

This kinetic approach can be used as a tool to determine the Fe_2B layer thickness as a function of boriding parameters (time and temperature) for the AISI 4140 steel. Equation (13) predicts the Fe_2B layer thickness for any temperature and boriding time. An iso-thickness diagram was plotted as a function of the temperature and exposure time as shown in **Figure 10**.

The results of **Figure 10** can serve as a powerful tool to select the optimum value of the Fe_2B layer thickness in relation with the potential applications of the borided AISI 4140 steel at industrial scale.

As a rule, thin layers (e.g., 15–20 μm) are used to protect against adhesive wear (in the cases of chipless-shaping and metal-stamping dies and tools), whereas thick layers are recommended for combating abrasive wear (extrusion tooling for plastics with abrasive fillers and pressing tools for the ceramic industry). In the case of low-carbon steels and low-alloy steels, the optimum boride-layer thicknesses range from 50 μm to 250 μm. Finally, this model can be extended to predict the growth kinetics of a bilayer configuration (FeB + Fe_2B) grown on any boride steel.

5 CONCLUSIONS

The AISI 4140 steel was pack borided in the temperature range of 1123–1273 K over the treatment times varying from 2 h to 8 h. The Fe_2B layers were formed on the AISI 4140 steel substrate. A mathematical model was suggested to estimate the boron diffusion coefficients for the Fe_2B layers. The boron activation energy for the AISI 4140 steel was found to be 189.24 kJ mol^{-1}. This value was compared with the data reported in the literature.

The validity of the diffusion model was examined by comparing the experimental value of the Fe_2B layer thickness obtained at 1253 K after 5 h of treatment with that predicted by the model.

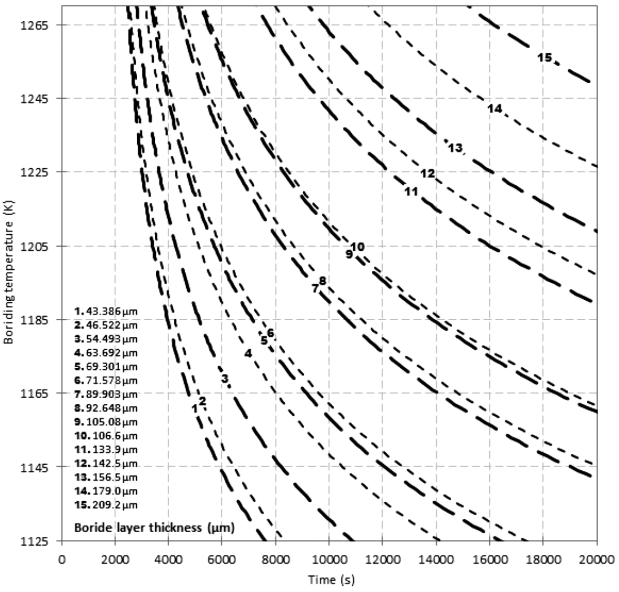

Figure 10: Iso-thickness diagram describing the evolution of Fe_2B layer as a function of boriding parameters

Slika 10: Diagram enakih debelin, ki opisuje nastanek Fe_2B-plasti v odvisnosti od parametrov boriranja

Finally, an iso-thickness diagram was proposed to be used as a tool to select the optimum boride layer thickness in relation with the industrial use of this steel grade.

NOMENCLATURE

v is the boride-layer thickness (m)

t_v is the effective growth time of the Fe_2B layer (s)

t is the treatment time (s)

$t_0^{Fe_2B}$ is the boride incubation time (s)

$C_{up}^{Fe_2B}$ represents the upper limit of the boron content in Fe_2B ($60 \cdot 10^3$ mol m^{-3})

$C_{low}^{Fe_2B}$ is the lower limit of the boron content in Fe_2B ($59.8 \cdot 10^3$ mol m^{-3})

C_{ads}^{B} is the adsorbed boron concentration in the boride layer (mol m^{-3})

$a_1 = C_{up}^{Fe_2B} - C_{low}^{Fe_2B}$ defines the homogeneity range of the Fe_2B layer (mol m^{-3})

$a_2 = C_{low}^{Fe_2B} - C_0$ is the miscibility gap (mol m^{-3})

C_0 is the terminal solubility of the interstitial solute ($\approx$ 0 mol m^{-3})

C_{Fe_2B} [$x(t)$] is the boron concentration profile in the Fe_2B layer (mol m^{-3})

v_0 indicates the initial Fe_2B layer (m)

ε is the normalized growth parameter for the Fe_2B/substrate interface (it has no physical dimensions)

D_{Fe_2B} denotes the diffusion coefficient of boron in the Fe_2B phase (m^2 s^{-1})

J_i [$x(t)$], (with i = Fe_2B and Fe) are the fluxes of boron atoms at the Fe_2B/substrate interface boundary (mol m^{-2} s^{-1})

Acknowledgements

The work described in this paper was supported by a grant of CONACyT and PROMEP, México. Also, the authors wish to thank Ing. Martín Ortiz Granillo, the Director of Escuela Superior de Ciudad Sahagún which is part of Universidad Autónoma del Estado de Hidalgo, México, for providing all the facilities necessary to accomplish this research work.

6 REFERENCES

[1] A. K. Sinha, Boriding (Boronizing) of Steels, ASM Handbook, vol. 4, ASM International, 1991, 437-447

[2] C. Meric, S. Sahin, S. S. Yilmaz, Mater. Res. Bull., 35 (**2000**) 13, 2165–2172, doi:10.1016/S0025-5408(00)00427-X

[3] H. Okamoto, J. Phase Equilib. Diff., 25 (**2004**) 3, 297–298, doi:10.1007/s11669-004-0128-3

[4] J. Vipin, G. Sundararajan, Surf. Coat. Technol., 149 (**2002**), 21–26, doi:10.1016/S0257-8972(01)01385-8

[5] A. Pertek, M. Kulka, Appl. Surf. Sci., 202 (**2002**), 252–260, doi:10.1016/S0169-4332(02)00940-6

[6] I. Campos, J. Oseguera, U. Figueroa, J. A. Garcia, O. Bautista, G. Keleminis, Mater. Sci. Eng. A, 352 (**2003**) 1–2, 261–265, doi:10.1016/S0921-5093(02)00910-3

[7] M. Keddam, Appl. Surf. Sci., 236 (**2004**) 1, 451–455, doi:10.1016/j.apsusc.2004.05.141

[8] R. D. Ramdan, T. Takaki, Y. Tomita, Mater. Trans., 49 (**2008**) 11, 2625–2631

[9] D. S. Kukharev, S. P. Fizenko, S. I. Shabunya, J. Eng. Phys. Therm., 69 (**1996**) 2, 187–193, doi:10.1007/BF02607937

[10] M. Keddam, M. Ortiz-Domínguez, I. Campos-Silva, J. Martinez-Trinídad, Appl. Surf. Sci., 256 (**2010**) 10, 3128–3132, doi:10.1016/j.apsusc.2009.11.085

[11] I. Campos-Silva, M. Ortiz-Domínguez, H. Cimenoglu, R. Escobar-Galindo, M. Keddam, M. Elías-Espinosa, N. López-Perrusquia, Surf. Eng., 27 (**2011**) 3, 189–195, doi:10.1179/026708410X12550773057820

[12] M. Ortiz-Domínguez, E. Hernandez-Sanchez, J. Martinez-Trinídad, M. Keddam, I. Campos-Silva, Kovove Mater., 48 (**2010**) 5, 285–290

[13] I. Campos-Silva, N. López-Perrusquia, M. Ortiz-Domínguez, U. Figueroa-López, O. A. Gómez-Vargas, A. Meneses-Amador, G. Rodríguez-Castro, Kovove Mater., 47 (**2009**) 2, 75–81

[14] M. Keddam, R. Chegroune, Appl. Surf. Sci., 256 (**2010**) 16, 5025–5030, doi:10.1016/j.apsusc.2010.03.048

[15] M. Ortiz-Domínguez, M. Keddam, M. Elias-Espinosa, O. Damián-Mejía, M. A. Flores-Rentería, A. Arenas-Flores, J. Hernández-Ávila, Surf. Eng., 30 (**2014**), 490–497, doi:10.1179/1743294414Y.0000000273

[16] M. Elias-Espinosa, M. Ortiz-Domínguez, M. Keddam, M. A. Flores-Rentería, O. Damián-Mejía, J. Zuno-Silva, J. Hernández-Ávila, E. Cardoso-Legorreta, A. Arenas-Flores, J. Mater. Eng. Perform., 23 (**2014**), 2943–2952, doi:10.1007/s11665-014-1052-2

[17] M. Kulka, N. Makuch, A. Pertek, L. Maldzinski, J. Solid State Chem., 199 (**2013**), 196–203, doi:10.1016/j.jssc.2012.12.029

[18] C. M. Brakman, A. W. J. Gommers, E. J. Mittemeijer, J. Mater. Res., 4 (**1989**), 1354–1370, doi:10.1557/JMR.1989.1354

[19] L. G. Yu, X. J. Chen, K. A. Khor, G. Sundararajan, Acta Mater., 53 (**2005**), 2361–2368, doi:10.1016/j.actamat.2005.01.043

[20] V. I. Dybkov, Reaction Diffusion and Solid State Chemical Kinetics, Trans Tech Publications, Switzerland-UK-USA 2010, 7

[21] G. Palombarini, M. Carbucicchio, J. Mater. Sci. Lett., 6 (**1987**), 415–416, doi:10.1007/BF01756781

[22] I. Campos-Silva, D. Bravo-Bárcenas, A. Meneses-Amador, M. Ortiz-Dominguez, H. Cimenoglu, U. Figueroa-López, J. Andraca-Adame, Surf. Coat. Technol., 237 (**2013**), 402–414, doi:10.1016/j.surfcoat.2013.06.083

[23] H. Kunst, O. Schaaber, Härterei-Tech. Mitt., 22 (**1967**), 275

[24] I. Campos-Silva, M. Ortiz-Domínguez, O. Bravo-Bárcenas, M. A. Doñu-Ruiz, D. Bravo-Bárcenas, C. Tapia-Quintero, M. Y. Jiménez-Reyes, Surf. Coat. Technol., 205 (**2010**), 403–412, doi:10.1016/j.surfcoat.2010.06.068

[25] I. S. Dukarevich, M. V. Mozharov, A. S. Shigarev, Metallovedenie Termicheskaya i Obrabotka Metallov, 2 (**1973**), 64–66, doi:10.1007/BF00679753

[26] S. Sen, U. Sen, C. Bindal, Vacuum, 77 (**2005**), 195–202, doi:10.1016/j.vacuum.2004.09.005

[27] M. Ulutan, M. M. Yildirim, O. N. Celik, S. Buytoz, Tribol. Lett., 38 (**2010**), 231–239, doi:10.1007/s11249-010-9597-1

[28] C. Badini, D. Mazza, J. Mater. Sci. Lett., 23 (**1988**), 661–665

[29] C. Bindal, A. H. Ucisik, Surf. Coat. Technol., 122 (**1999**), 208–213, doi:10.1016/S0257-8972(99)00294-7

[30] S. Sen, U. Sen, C. Bindal, Surf. Coat. Technol., 191 (**2005**) 2–3, 274–285, doi:10.1016/j.surfcoat.2004.03.040

[31] O. N. Celik, N. Aydinbeyli, H. Gasan, Prakt. Metallogr., 45 (**2008**) 7, 334–347, doi:10.3139/147.100390

[32] M. Ipek, G. Celebi Efe, I. Ozbek, S. Zeytin, C. Bindal, J. Mater. Eng. Perform., 21 (**2012**) 5, 733–738, doi:10.1007/s11665-012-0192-5

UDK 669.14:669.112.227.1:539.37
Review article/Pregledni članek

ISSN 1580-2949
MTAEC9, 49(5)673(2015)

KINETICS OF THE PRECIPITATION IN AUSTENITE HSLA STEELS

KINETIKA IZLOČANJA V AVSTENITNIH HSLA-JEKLIH

Elżbieta Kalinowska-Ozgowicz[1], Roman Kuziak[2], Wojciech Ozgowicz[3], Klaudiusz Lenik[1]

[1]Lublin University of Technology, Fundamentals of Technology, Nadbystrzycka Str 38, 20-618 Lublin, Poland
[2]Institute for Ferrous Metallurgy, K. Miarki Str 12-14, 44-100 Gliwice, Poland
[3]Silesian University of Technology, Mechanical Engineering Faculty, Konarskiego Str 18a, 44-100 Gliwice, Poland
kalinowska-ozgowicz@tlen.pl

Prejem rokopisa – received: 2014-07-30; sprejem za objavo – accepted for publication: 2014-11-06

doi:10.17222/mit.2014.139

Presented are the results of an investigation of the kinetics of the static precipitation in HSLA steels with microalloying additions of Nb, V, Ti and high N between the consecutive hot plastic-deformation cycles. The hot plastic deformation was carried out using a torsional plastometer and a Gleeble thermomechanical simulator. The kinetics curves of the precipitation process in the examined steels were determined based on the changes in the values of strain ε_m in the flow curves during continuous and interrupted deformations. The precipitation process in the austenite of the examined steels was investigated using transmission electron microscopy of the test specimens quenched immediately after hot deformation and held isothermally for various times. The precipitation effects inherited in the martensite were analysed with electron diffraction and X-ray microanalysis.

Keywords: hot plastic deformation, kinetics of precipitation, HSLA steels, structure, Gleeble simulator

Predstavljeni so rezultati preiskave kinetike statičnega izločanja v HSLA-jeklih, mikrolegiranih z Nb, V, Ti in visokim N med zaporednimi cikli vroče plastične deformacije. Vroča plastična deformacija je bila izvršena s torzijskim plastometrom in z Gleeble-jevim termomehanskim simulatorjem. Krivulje kinetike procesa izločanja v preiskovanih jeklih so bile ugotovljene na podlagi sprememb vrednosti napetosti ε_m in krivulj tečenja med kontinuirnimi in prekinjenimi deformacijami. Proces izločanja v avstenitu preiskovanih jekel je bil preiskovan s presevno elektronsko mikroskopijo preizkusnih vzorcev, kaljenih takoj po vroči deformaciji in različno dolgem izotermnem zadrževanju. Podedovani učinki izločanja v martenzitu so bili analizirani z difrakcijo elektronov in rentgensko mikroanalizo.

Ključne besede: vroča plastična deformacija, kinetika izločanja, HSLA-jekla, struktura, Gleeble-jev simulator

1 INTRODUCTION

Chemical compositions and structural changes of HSLA steels during a hot plastic deformation are the basic sources of the diversity of the mechanical properties of finished products. Shaping the mechanical properties of this group of steels takes place by inducing the relevant strengthening mechanisms and by developing proper phase compositions of steels.[1–3] A decisive role in shaping the mechanical properties of microalloyed steels is played by the precipitates of secondary interstitial phases (MX-type carbo-nitrides formed as a result of alloying the microalloying elements of Nb, Ti, V and N into steel, i.e., carbides and nitrides as well as the products of their intersolubility – carbonitrides. The stability of these phases depends mainly on their chemical compositions and solution temperatures.[4–8] The knowledge of the basic thermodynamic data of the analysed compounds makes it possible to use them in hot-working processes such as: controlled rolling, rolling with controlled recrystallisation, finish rolling and thermomechanical treatments.[9–11] HSLA microalloyed steels with ferritic-pearlitic structures obtain relatively high mechanical properties due to the grain refinement and precipitation hardening.

2 EXPERIMENTAL PROCEDURE

The studies of the kinetics of the precipitation were carried out on HSLA microalloyed constructional steels with ferritic-pearlitic structures obtained from industrial

Table 1: Chemical compositions of investigated steels in mass fractions, *w*/%
Tabela 1: Kemijska sestava preiskovanih jekel v masnih deležih, *w*/%

Steel type	Concentration of the elements in *w*/%										
	C	Mn	Si	P	S	Nb	V	Ti	N	Al	Cu
B2	0.15	1.03	0.25	0.018	0.009	0.017	0.050	–	0.0070	0.004	–
G1	0.16	1.48	0.29	0.030	0.017	0.037	0.002	0.004	0.0098	0.010	0.049

heats. The chemical compositions of the examined steels are given in **Table 1**.

For steels B2 and G1 the studies of the kinetics of the precipitation of carbides and carbonitrides were carried out and PTT (precipitation-temperature-time) diagrams were developed for various austenite deformation conditions and isothermal holding times of the following deformation sequences.

A static precipitation in the non-deformed austenite of the B2 steel was performed in a torsional plastometer and test specimens of 6 mm in diameter and 10 mm in gauge length were used. The specimens were heated at 3 °C/s to the austenitizing temperature of 1150 °C, held for 360 s, cooled to a deformation temperature of 900 °C at approximately 10 °C/s and held isothermally for 6 s to 10800 s, then deformed at a rate of 4.4 s^{-1} until a failure (torsion) took place. The heating was performed in the plastometer's resistance-heat furnace, in an argon atmosphere. The austenitizing and deformation temperatures were measured with a radiation pyrometer with an accuracy of ± 1 °. The cooling of the test specimens to room temperature, immediately after the hot deformation, was performed with a water jet from the plastometer's hydraulic system. An analysis of the value of deformation corresponding to the maximum stress on the $\sigma - \varepsilon$ curves as a function of the isothermal holding time, enabled us to determine[3] the characteristic times of the beginning (P_s) and the end (P_f) of the precipitation process in the non-deformed austenite of the B2 steel.

For the G1 steel, the precipitation process was investigated in the non-deformed state and after a high-temperature deformation of the austenite using the cyclic axisymmetric-upsetting and stress-relaxation methods. The investigations were performed on a Gleeble 3800 simulator using cylindrical test specimens of 7 mm in diameter and 8.4 mm in length. The specimens were heated at 3 °C/s to an austenitizing temperature of 1200 °C, held for 3 s, cooled to a deformation temperature of 1100 °C at approximately 1.0 °C/s and held isothermally for 2 s to 1800 s, then deformed at 1.0 s^{-1} to $\varepsilon = 1$. In the stress-relaxation method, the precipitation process was investigated in the austenite deformed to $\varepsilon = 0.2$ at 800 °C to 1100 °C after an austenitization at 1200 °C, keeping the same strain parameters as for the cyclic compression test. The heating of the test specimens in the simulator was performed with the resistance method and in an argon atmosphere. To reduce the coefficient of friction, the faces of the test specimens were coated with a graphite-and-tantalum foil.

The microstructures of the G1 steel after the selected hot deformation and precipitation stages were determined with transmission electron microscopy (TEM) using the selective electron diffraction and energy-dispersive X-ray spectroscopy (EDX) methods. In the investigations, an S/TEM Titan 80-300 scanning electron microscope by FEI, fitted with a field electron gun (XFEG), an energy-dispersion spectrometer (EDS), an external energy filter for imaging (EFTEM) and for spectroscopy (EELS) as well as a system of BF/ADF/HAADF detectors for the operations of the scanning system were used. Observations were performed within the scope of 245–300 kV, in a classic TEM system with a spatial resolution of the network image below 0.10 μm and using the microscope's field emission gun to allow the electron beam to be focused up to 0.3 nm during the observation of high-resolution images (HRTEM). Microstructures were observed on the foils and small lamellas. The foils were obtained by mechanical thinning and ion polishing using a Gatan PIPS polishing machine, while the lamella-formed preparations of 20 μm × 8 μm were cut out with a gallium-focused ion beam from a specific cross-sectional area of the test specimen and then thinned with this ion beam to a thickness of approximately 50–70 nm using a FEI FIB Quanta 3D200 machine. The lamella-preparation process was observed in situ using the scanning electron microscope.

The procedure of a phase identification based on electron diffraction was supported with the ELDYF software for indexing and simulating electron diffraction patterns.

3 RESULTS AND DISCUSSION

The results of the kinetics of the static precipitation in the microalloyed constructional steels (B2 and G1) are shown in **Figures 1** to **6**. In particular, for the B2 steel, the kinetics of the static precipitation in the austenite not deformed by the hot torsion was determined (**Figure 1**), while, for the G1 steel, the precipitation process was determined for the austenite in the non-deformed state and after a high-temperature deformation (**Figures 2** to **5**). It was found that an increase in the holding time before the deformation resulted in a distinct reduction in the values of ε_m and the corresponding maximum stresses. This effect is equivalent to the reduction in the degree of strain hardening of the austenite and results from the growing share of the static precipitation during

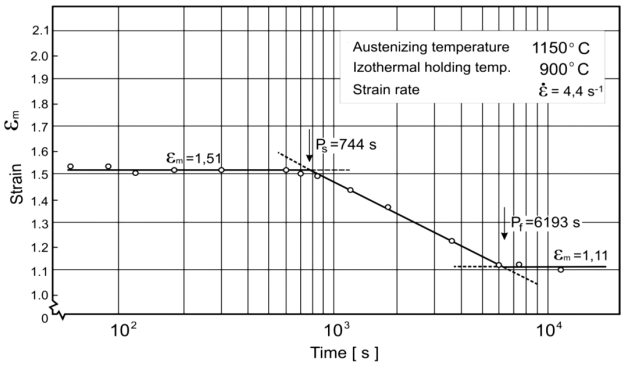

Figure 1: Kinetics of the static precipitation in non-deformed austenite of microalloyed steel B2, determined with a hot-deformation test

Slika 1: Kinetika statičnega izločanja v nedeformiranem avstenitu mikrolegiranega jekla B2, določena s preizkusom vroče deformacije

the isothermal holding. Thereby, the potential for dynamic precipitation at the stage of hardening is decreasing, which, in turn, results in a reduced degree of inhibition of dynamic recrystallization and the observed changes in ε_m for the values of σ_{max}. Therefore, in the absence of precipitation before the deformation, the constant and maximum value of ε_m is obtained (**Figures 1** and **2**). It is connected with the maximum solubility of Nb in the austenite, potentially inhibiting the nucleation process of dynamic recrystallisation so that the precipitation process leads to a stabilisation of the ε_m values at the minimum level, observed at the stage of the stress increase in the flow curves. The end of the first plateau and the beginning of the next one on the kinetic curves were adopted as the times of the beginning (P_s) and the end (P_f) of the static precipitation in the examined microalloyed steels.

The static precipitation process in the B2 steel after the austenitization at 1150 °C and isothermal holding at 900 °C starts after approximately 740 s and ends after approximately 6200 s (**Figure 1**). Before the start of the precipitation in the B2 steel, the value of ε_m is 1.51 and after its completion it is ε_m = 1.11. During the precipitation the relationship between strain ε_m and the isothermal holding time can be described with a linear function ($\varepsilon_m = -0.43 \cdot \lg \tau + 2.67$) whose intersection points determine the times of the beginning and the end of the precipitation process.

In the case of the isothermal holding of microalloyed steel G1 at 1100 °C after the austenitization at 1200 °C, the relationship between ε_m and the time is described in a similar way. The first stage, the period of up to 47 s, is described as ε_m = 0.53, while the second stage (to approximately 1380 s) is described with the linear function $\varepsilon_m = -0.1 \lg \tau + 0.7$. When the isothermal holding $\tau >$ 1380 s, the third section with a stabilised value is described with the formula ε_m = 0.37. The inflexion points of the function determine the times of the beginning (P_s = 47 s) and the end (P_f = 1380 s) of the static precipitation in the non-deformed austenite of the examined microalloyed steel at the holding temperature of 1100 °C (**Figure 2**).

The static precipitation process was also analysed in the microalloyed steel G1 using the two-stage compression method after the austenitization at 1200 °C and the pre-strain of the test specimens (ε = 0.2) before the isothermal holding at 1100 °C. The diagram of the changes in ε_m during the isothermal holding is also characterised by three stages (**Figure 3**). In the initial stage, there is a constant value, ε_m = 0.42, then this value changes linearly to settle again at a strain level of ε_m = 0.62 for a longer holding time. The characteristic inflexion points of the diagram determine similarly the time of the beginning and the end of the static precipitation in the non-deformed austenite. The process takes place during the isothermal holding after the plastic deformation from approximately 13 s to approximately 28 min.

For comparison, the static precipitation in the microalloyed steel G1 was also investigated, with the stress-relaxation method, after the austenitization at 1200 °C and the preliminary compression of the test specimens within a temperature range of 800–1100 °C, using the Gleeble thermodynamic simulator. The times of the beginning and the end of the static-precipitation process were determined analytically and shown graphically in diagrams (**Figures 4** to **6**). The values of the pre-strain (ε = 0.2 and 0.4) were found to have a slight impact on the time to the initiation of the precipitation (P_s was approximately 17 s) at 900 °C, while for the maximum value of the strain (ε = 0.6) the corresponding time was twice as high. The static precipitation at this temperature ends, regardless of the size of the pre-strain, after approximately 3 min (**Figure 5**). The precipitation at a lower deformation temperature (800 °C) is evident in the distinct plateau on the stress-relaxation curve and it takes place within the period from P_s of approximately 30 s to P_f of approximately 600 s (**Figure 5**). The studies imply that for the austenite deformed before the isothermal

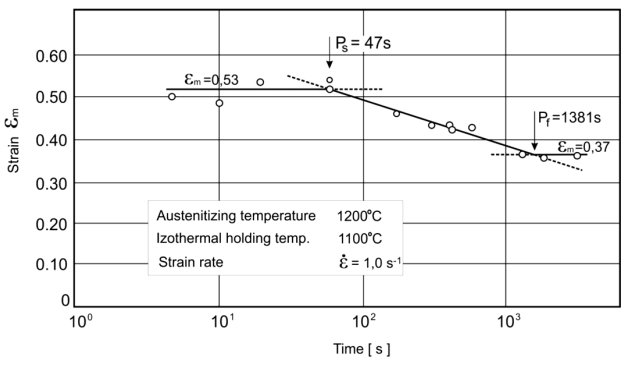

Figure 2: Kinetics of the static precipitation in non-deformed austenite of microalloyed steel G1, determined with a hot-compression test

Slika 2: Kinetika statičnega izločanja v nedeformiranem avstenitu mikrolegiranega jekla G1, določena z vročim tlačnim preizkusom

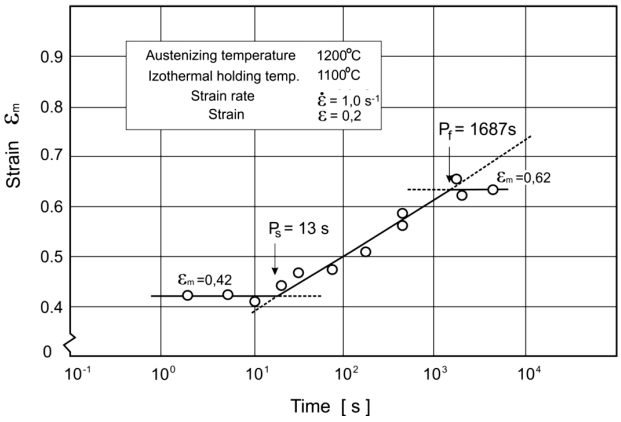

Figure 3: Kinetics of the static precipitation in deformed austenite of microalloyed steel G1, determined with a hot-compression test

Slika 3: Kinetika statičnega izločanja v deformiranem avstenitu mikrolegiranega jekla G1, določena z vročim tlačnim preizkusom

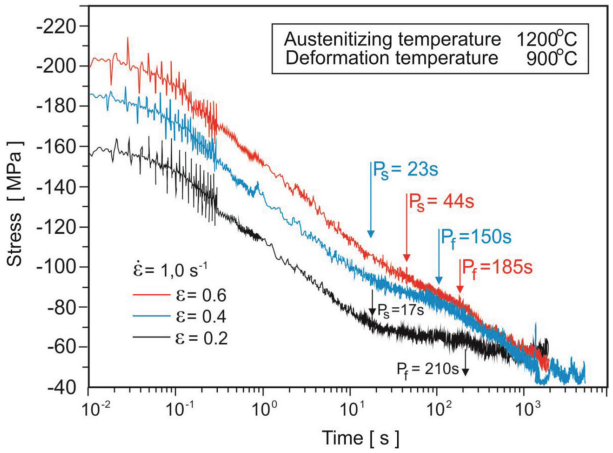

Figure 4: Stress-relaxation curves for microalloyed steel G1 subject to a hot-compression test at 900 °C; $P_{s,f}$ – times of the beginning and end of the static precipitation process

Slika 4: Krivulje zmanjševanja napetosti pri mikrolegiranem jeklu G1 pri vročem tlačnem preizkusu na 900 °C; $P_{s,f}$ – časi do začetka in konca statičnega procesa izločanja

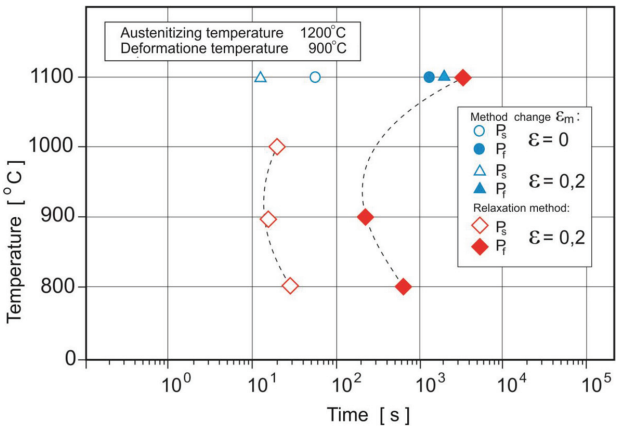

Figure 6: Results of the studies of the kinetics of the static precipitation (PTT) for microalloyed steel G1 subject to plastic deformation with the hot-compression method

Slika 6: Rezultati študija kinetike statičnega izločanja (PTT) za mikrolegirano jeklo G1 po plastični deformaciji z metodo vročega stiskanja

holding of the G1 steel, the time to the beginning of the static precipitation is clearly shorter than the corresponding time for the non-deformed austenite. The kinetic analysis also revealed that the times of the end of the static-precipitation process in both cases (non-deformed austenite and the austenite deformed before the isothermal holding) are comparable.

The analysis of the results of the kinetics obtained for the examined microalloyed steel G1, considering the austenite before the isothermal holding as well as the conditions of the high-temperature deformation, allowed PTT curves to be determined (**Figure 6**). The static-precipitation curves obtained for the austenite of the G1 steel in the investigated conditions of hot deformation indicate that the precipitation process is the fastest at the isothermal-holding temperature of 900 °C. The times of the initiation and the end of the precipitation are 17 s and 210 s, respectively. The times of the initiation of the precipitation at both higher (1000 °C) and lower (800 °C) temperatures are longer, 22 s and 30 s, respectively. The end of the precipitation process at 800 °C takes place after approximately 10 min.

The precipitation process in the G1 steel was investigated on the test specimens quenched in water immediately after the hot deformation and isothermal holding for various periods. The phase-precipitation effects

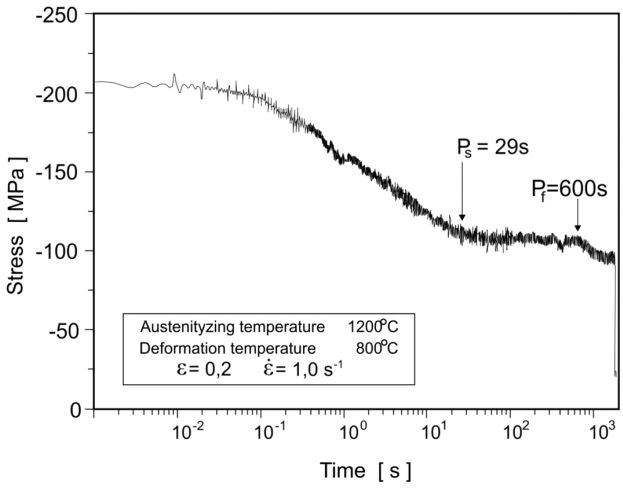

Figure 5: Stress-relaxation curve for microalloyed steel G1 subject to a hot-compression test at 800 °C

Slika 5: Krivulja zmanjševanja napetosti pri mikrolegiranem jeklu G1 po vročem tlačnem preizkusu pri 800 °C

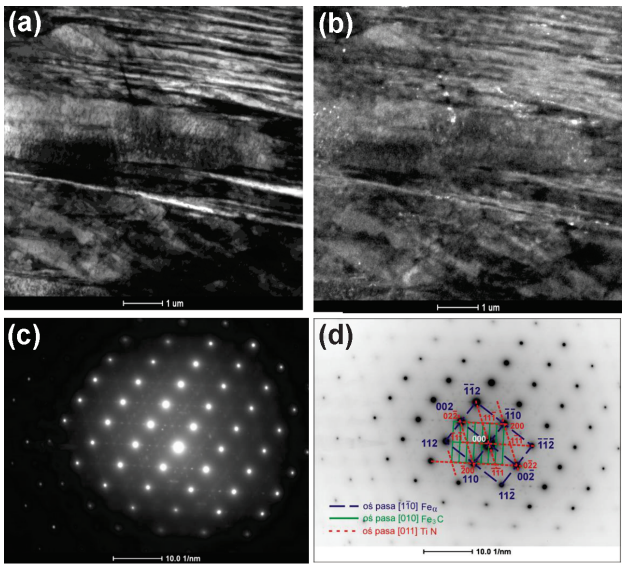

Figure 7: a) Microstructure of martensite lath with Fe_3C and TiN precipitates, b) image in the dark field, c) diffraction, d) diffraction solution; G1 steel, T_A = 1200 °C, T_{def} = 1100 °C, $\dot{\varepsilon}$ = 1.0 s^{-1}, ε = 0.2, τ_w (water) = 30 s

Slika 7: a) Mikrostruktura latastega martenzita z Fe_3C in izločki TiN, b) posnetek v temnem polju, c) difrakcija, d) difrakcija indeksirana; jeklo G1, T_A = 1200 °C, T_{def} = 1100 °C, $\dot{\varepsilon}$ = 1,0 s^{-1}, ε = 0,2, τ_w (voda) = 30 s

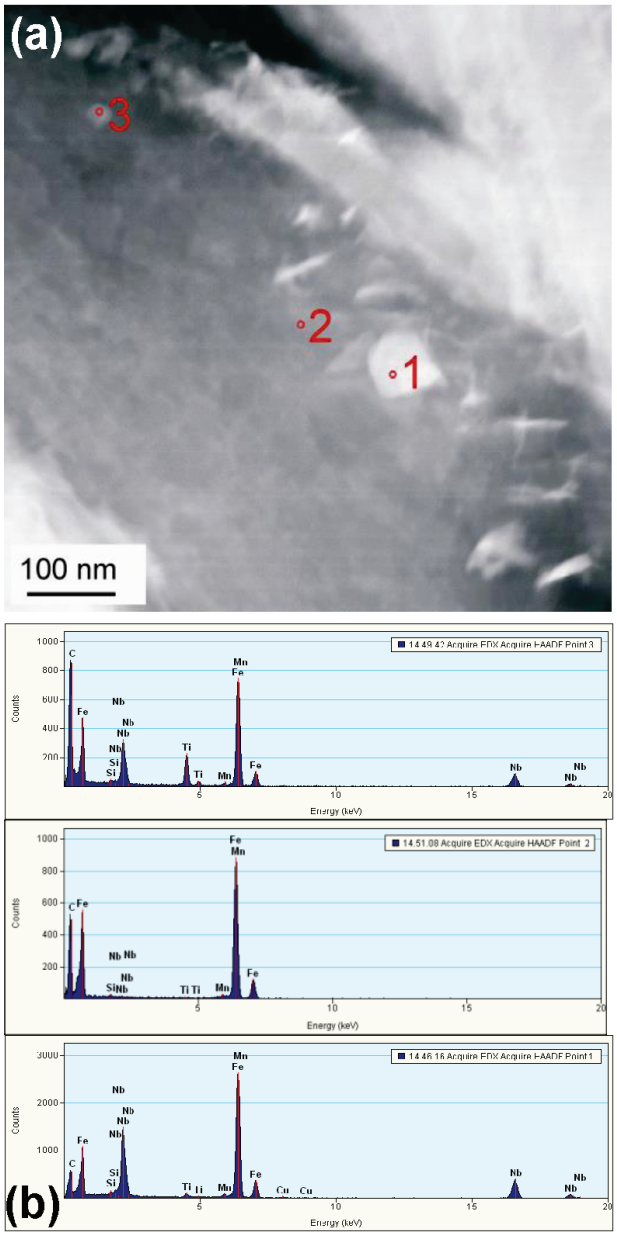

Figure 8: a) Microstructure of martensite lath with (Ti,Nb)C precipitates, b) microanalysis of micro-areas (1, 2, 3); G1 steel, T_A = 1200 °C, T_{def} = 1100 °C, $\dot{\varepsilon}$ = 1.0 s^{-1}, ε = 0.2, τ_w (water) = 10800 s

Slika 8: a) Mikrostruktura martenzitne late s (Ti,Nb)C-izločki, b) mikroanaliza mikropodročij (1, 2, 3); jeklo G1, T_A = 1200 °C, T_{def} = 1100 °C, $\dot{\varepsilon}$ = 1,0 s^{-1}, ε = 0,2, τ_w (voda) = 10800 s

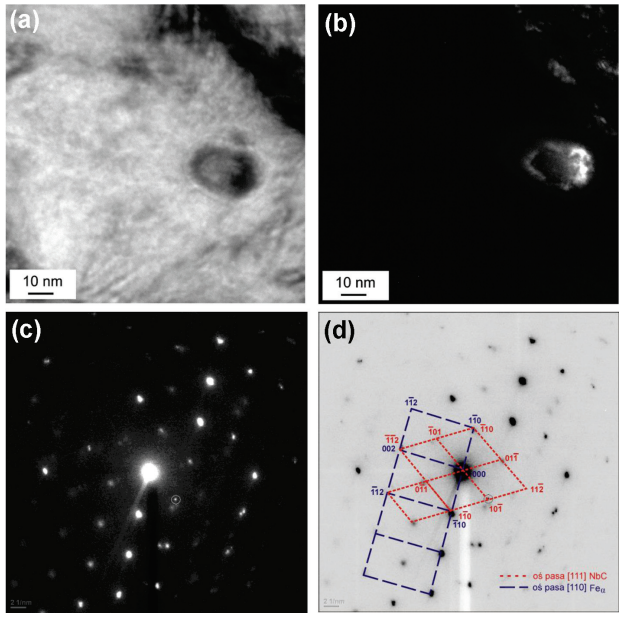

Figure 9: a) NbC spherical precipitate in martensite lath, b) image in the dark field, c) diffraction, d) diffraction solution; G1 steel, T_A = 1200 °C, T_{def} = 900 °C, $\dot{\varepsilon}$ = 1.0 s^{-1}, ε = 0.6, τ_w(water) = 10800 s

Slika 9: a) Okrogli izloček NbC v martenzitni lati, b) posnetek v temnem polju, c) difrakcija, d) difrakcija indeksirana; jeklo G1, T_A = 1200 °C, T_{def} = 900 °C, $\dot{\varepsilon}$ = 1,0 s^{-1}, ε = 0,6, τ_w(voda) = 10800 s

inherited in the martensite were analysed with electron diffraction and X-ray microanalysis.

The isothermal holding of the examined steel after the hot deformation results in static-precipitation processes. After a deformation at 1100 °C and an isothermal holding for 30 s, dispersive precipitates with varied sizes and morphologies were revealed in the martensite-lath matrix with a high dislocation density (**Figure 7**).

In the martensite laths a TiN precipitation was revealed in the dark field (**Figure 7b**) of the reflection from plane $(1\bar{1}1)_{TiN}$. There are also reflections from Fe_3C in the diffraction pattern, indicating the likelihood of a formation of lower bainite bands formed due to cooling. The NbC particles with a spherical form and a size of approximately 60 nm were also revealed in the martensite laths and at the former austenite-grain boundaries. In addition, at the martensite-lath boundaries, the traces of the retained austenite were revealed too. Similar results of the phase identification for microalloyed steels are also quoted in[12–15].

An increase in the isothermal-holding time after the plastic deformation of the examined steel up to approximately 3 h results in a formation of complex titanium and niobium carbides with diverse morphologies and different chemical compositions on the bainite and martensite laths (**Figure 8**). A microanalysis of the polygon-shaped (Ti, Nb)C particle area of approximately 120 nm revealed a high concentration of Nb (**Figure 8b**, point 1), whereas in the precipitates of 30 nm (**Figure 8b**, point 3), comparable niobium and titanium contents were found.

The HRTEM investigations of the precipitation in the martensitic matrix of the G1 steel austenitized at 1200 °C and deformed at 900 °C, with a comparable strain rate (1.0 s^{-1}) and similar isothermal-holding times, but with higher pre-strains (ε = 0.6), allowed a determination of the morphology of the observed particles and their probable identification with the electron-diffraction method.

In the test specimens held for 44 s and cooled in water, there are titanium-containing nanometric precipitates of approximately 7 nm in the martensite-lath

matrix. Using diffraction analysis and following the air cooling of the specimens in ferrite, precipitates of a similar size were observed and identified as TiC. After the hot deformation at 1100 °C and the same holding time (44 s) and air cooling, spheroidal precipitates (Ti, Nb) of approximately 15 nm were found in the examined steel. The electron microphotographs showed that the precipitates in the martensitic matrix, especially after the deformation at 900 °C, are not evenly distributed and that in many micro-areas the spacing of the particles was less than 100 nm.

An increase in the holding time up to 185 s following the deformation at 900 °C results in a formation of NbC precipitates with a size between 20 nm and approximately 30 nm in the recrystallised austenite matrix (**Figure 9**). Niobium carbide precipitates were identified with electron diffraction. Their shape and distribution were revealed in the dark field of the reflection of $(10\bar{1})$NbC (**Figures 9b** to **9d**). These observations indicate that the precipitation-hardening process is not uniformly distributed within the entire volume of a test specimen. It can also be assumed that the distribution of the precipitates in the solution matrix – α' – reflexes the distribution of the preferred nucleation sites in the hot-deformed austenite substructure. However, the confirmation of this effect is difficult as the austenite substructure is subject to degradation during the phase transformation that takes place due to quench hardening. Micro-bands of twins in the martensitic matrix and precipitates in the form of discrete particles at the boundaries between these bands were identified. The chemical composition of these precipitates does not differ from that of the precipitates in the matrix.

It needs to be emphasised that Nb forms carbides and nitrides with equal lattices (NaCl type) that are completely intersoluble. The similarity of the lattices of NbC and NbN formed in the examined steel makes their precise identification difficult. As NbC and NbN form isomorphous phases in the solid solution, these precipitates can be regarded as carbonitrides. Such suggestions are made frequently.[16] In addition, the results of the chemical analyses of the Nb(C, N) precipitates extracted from the deformed austenite in the steels with microalloying elements confirmed that Nb carbonitride is rich in carbon. Compared with a stoichiometric composition, it is similar to that of NbC.[17]

4 CONCLUSIONS

The results obtained with the investigations and the analysis support the following conclusions:

1. In the examined HSLA steels microalloyed with Nb, Ti, V and N, the precipitation of carbonitrides in both deformed and non-deformed austenite after the isothermal holding corresponds to PTT (precipitation-temperature-time) curves.
2. The precipitation of NbC, TiN and (Ti, Nb)C during a plastic deformation of microalloyed steels (B2, G1) with torsion and compression in a temperature range of 800–1100 °C takes place in the torsion test for up to about 5 s.
3. The static-precipitation process in microalloyed steel B2, determined by means of hot-torsion tests after an austenitization at a temperature of 1150 °C and isothermal holding at 900 °C, starts after about 740 s and finishes after about 6200 s. A similar process of the precipitation of steel G1, hot compressed after an austenitization at 1200 °C and isothermal holding at 1100 °C takes place in the course of holding from about 50 s to about 1400 s.
4. The static precipitation of the G1 steel examined with the compression and stress-relaxation method within the temperature range of 800–1100 °C depends mainly on the pre-strain temperature and size. In the investigated deformation conditions the maximum isothermal rate of this process was found at the temperature of 900 °C. The times of the beginning and the end of the static-precipitation process were about 17 s and about 210 s, respectively.
5. The microstructure of the α' solution matrix is formed by a partially twined martensite lath with a high dislocation density, while the precipitates with equal frequencies of the particles of single NbC and TiC carbides, NbN and TiN nitrides and also of complex (Ti, Nb)C carbides were identified with electron diffraction and energy-dispersive X-ray spectrometry (EDX).
6. The diameters of the precipitates revealed in the G1 steel range between approximately 7 nm and approximately 120 nm, and their growth is proportional to the isothermal holding time after the hot deformation.

5 REFERENCES

[1] B. Dutta, C. M. Sellars, Effect of composition and process variables on Nb(C, N) precipitation in niobium microalloyed austenite, Materials Science and Technology, 3 (**1987**) 3, 197–206, doi:10.1179/026708387790122846

[2] R. Kuziak, T. Bold, Y. W. Cheng, Microstructure control of ferrite–pearlite high strength low alloy steels utilizing microalloying additions, Journal of Materials Processing Technology, 53 (**1995**) 1–2, 255–262, doi:10.1016/0924-0136(95)01983-L

[3] E. Kalinowska-Ozgowicz, Structural and mechanical factors of the strengthening and recrystallization of hot plastic deformation of steels with microadditives, Open Access Library, 20 (**2013**) 2, 1–246 (in Polish)

[4] H. Adrian, In: Numerical Modeling of Heat Treatment Processes, AGH University of Science and Technology Publishers, Kraków 2011 (in Polish)

[5] M. Opiela, A. Grajcar, Elaboration of forging conditions on the basis of the precipitation analysis of MX-type phase in microalloyed steels, Archives of Civil and Mechanical Engineering, 12 (**2012**) 4, 427–435, doi:10.1016/j.acme.2012.06.013

[6] A. Grajcar, Thermodynamic analysis of precipitation processes in Nb-Ti-microalloyed Si-Al TRIP steel, J. Therm. Anal. Calorim., 118 (**2014**) 2, 1011–1020, doi:10.1007/s10973-014-3801-8

[7] B. Dutta, E. J. Palmiere, C. M. Sellars, Modelling the kinetics of strain induced precipitation in Nb microalloyed steels, Acta Mater., 49 (**2006**) 5, 785–794, doi:10.1016/S1359-6454(00)00389-X

[8] W. J. Liu, J. J. Jonas, Nucleation kinetics of Ti carbonitride in microalloyed austenite, Metallurgical Transactions A, 20 (**1989**) 4, 689–697, doi:10.1007/BF02667586

[9] J. Adamczyk, E. Kalinowska-Ozgowicz, W. Ozgowicz, R. Wusatowski, Interaction of carbonitrides V(C, N) undissolved in austenite on the structure and mechanical properties of microalloyed V–N steels, Journal of Materials Processing Technology, 53 (**1995**) 1–2, 23–32, doi:10.1016/0924-0136(95)01958-H

[10] M. Opiela, The influence of heat treatment on microstructure and crack resistance of boron microalloyed steel plates, Journal of Achievements in Materials and Manufacturing Engineering, 43 (**2010**) 1, 117–124

[11] J. Adamczyk, Engineering of Metallic Materials, The Silesian University of Technology Publishers, Gliwice 2004 (in Polish)

[12] G. K. Tirumalasetty, M. A. van Huis, C. M. Fang, Q. Xu, F. D. Tichelaar, D. N. Hanlon, J. Sietsma, H. W. Zandbergen, Characterization of NbC and (Nb, Ti)N nanoprecipitates in TRIP assisted multiphase steels, Acta Materialia, 59 (**2011**) 19, 7406–7415, doi:10.1016/j.actamat.2011.08.012

[13] G. K. Tirumalasetty, C. M. Fang, Q. Xu, J. Jansen, J. Sietsma, M. A. van Huis, H. W. Zandbergen, Novel ultrafine Fe(C) precipitates strengthen transformation-induced-plasticity steel, Acta Materialia, 60 (**2012**) 20, 7160–7168, doi:10.1016/j.actamat.2012.09.025

[14] S. H. Mousavi Anijdan, D. Sediako, S. Yue, Optimization of flow stress in cool deformed Nb-microalloyed steel by combining strain inducted transformation of retained austenite, cooling rate and heat treatment, Acta Materialia, 60 (**2012**) 3, 1221–1229, doi:10.1016/j.actamat.2011.11.019

[15] H. J. Jun, K. B. Kang, C. G. Park, Effects of cooling rate and isothermal holding on the precipitation behavior during continuous casting of Nb-Ti bearing HSLA steels, Scripta Materialia, 49 (**2003**) 11, 1081–1086, doi:10.1016/j.scriptamat.2003.08.013

[16] N. Shams, Carbonitride precipitates in HSLA, Journal of Metals, 38 (**1986**) 5, 31–33, doi:10.1007/BF03257840

[17] M. J. Crooks, A. J. Garratt-Reed, J. B. Vander Sande, Precipitation and recrystallization in some Vanadium and Vanadium-Niobium Microalloyed Steels, Metallurgical and Materials Transactions A, 12 (**1981**) 12, 1999–2013, doi:10.1007/BF02644169

UDK 669.715:621.74.046:66.046.51
Review article/Pregledni članek

ISSN 1580-2949
MTAEC9, 49(5)681(2015)

COMBINED INFLUENCE OF V AND Cr ON THE AlSi10MgMn ALLOY WITH A HIGH Fe LEVEL

VZAJEMNI VPLIV V IN Cr NA ZLITINO AlSi10MgMn Z VISOKO VSEBNOSTJO Fe

Dana Bolibruchová, Mária Žihalová

Department of Technological Engineering, Faculty of Mechanical Engineering, University of Žilina, Univerzitná 8215/1, 010 26 Žilina, Slovakia
maria.zihalova@fstroj.uniza.sk

Prejem rokopisa – received: 2014-07-31; sprejem za objavo – accepted for publication: 2014-10-09

doi:10.17222/mit.2014.146

Removing impurities from aluminium alloys increases the final cost of castings. The most common impurity in Al-Si based alloys is iron, whose removal is the main problem for secondary Al-Si alloys. Several techniques of eliminating iron effects have been introduced, but the most common one is the use of iron "correctors" that change the morphology of iron-based intermetallic phases. The use of the correctors like Co and Mn is well described but other elements such Ni, Cr and V need to be studied more extensively. In the present paper, the influence of V and the combined influence of V and Cr are analysed. The aim of the article is to determine the microstructure, the mechanical properties and the solidification behaviour of the AlSi10MgMn cast alloy with a high iron level treated with V and Cr.

Keywords: AlSi10MgMn, iron correctors, combined effect, vanadium, chromium

Odstranjevanje nečistoč iz aluminijevih zlitin povečuje končne stroške pri ulitkih. Najbolj pogosta nečistoča v zlitinah na osnovi Al-Si je železo. Uvedenih je bilo več tehnik za odstranitev vpliva železa, vendar je najpogostejša uporaba "korektorjev" železa, ki spremenijo morfologijo intermetalnih faz na osnovi železa. Uporaba korektorjev, kot sta Co in Mn, je dobro opisana, pri drugih elementih, kot na primer Ni, Cr in V, pa so potrebne še dodatne raziskave. V članku je analiziran vpliv V in vzajemni vpliv V in Cr. Namen članka je določiti mikrostrukturo, mehanske lastnosti in vedenje pri strjevanju livarske zlitine AlSi10MgMn z visoko vsebnostjo železa in te zlitine, obdelane z V in Cr.

Ključne besede: AlSi10MgMn, korektorji železa, vzajemni vpliv, vanadij, krom

1 INTRODUCTION

Aluminium has been acquiring increasing significance over the past few decades due to its excellent properties and a diversified range of applications.[1] Over the years, aluminium alloys have been specially developed to meet the increasing demands of today's industry. This development has resulted in the production of smaller and light-weight components that comply with property, environmental and other specifications. Recently, the appeal for recycling the resources has become more intensive with the increasing public awareness of the need to preserve the materials and energy and to protect the environment. However, the increasing use of recycled aluminium casting alloys requires a strict procedure of removing the harmful effects of impurity elements.[2]

The most common impurity in aluminium Al-Si alloys is iron. Iron is highly soluble in liquid aluminium and its alloys, but it has a very low solubility in the solid state and so it tends to combine with other elements to form intermetallic-phase particles of various types.[3–5] The morphologies of iron-containing intermetallics are often found to cause negative effects, where the plate-like phases, such as β-Al_5FeSi, are considered to be more harmful than the script-type phases, such as α-$Al_{15}(FeMn)_3Si_2$.[5]

When Fe is present in excess of specified levels, various methods are available to reduce its harmful influence. The conventional method is to add some chemical "correctors" to change the morphology from the platelet β-Al_5FeSi (a brittle form) to the globular or script forms (less brittle forms). The globular or script Fe-rich phases are considered not to lead to brittleness. Alternative methods of iron reduction are described in various references.[6,7] Manganese is the most commonly used and the least expensive element for Fe neutralisation in Al-Si alloys.[2] If an iron amount exceeds a value of the mass fraction w = 0.45 %, the recommended addition of Mn should not be lower than half of the iron amount;[7] however, script-like particles containing Mn are still observed at the Mn-to-Fe ratio of 0.17.[8] Other iron correctors also include Co, Cr, Mo, Ni, V and Be.[3,4,6,7] Cr improves the strength at indoor and higher temperatures and mildly deteriorates the elongation. The presence of Cr phases $(CrFe)_4Si_4Al_{13}$ and $(CrFe)_5Si_8Al_2$ can increases the brittleness.[9,10] Vanadium refines the grains of aluminium alloys. Together with Ti and Mo, it increases the hot-cracking resistance and decreases the porosity.[9] The influence of V occurs with an amount of 0.05–0.15

Table 1: Chemical composition of AlSi10MgMn alloy
Tabela 1: Kemijska sestava zlitine AlSi10MgMn

Element	Si	Mg	Mn	Fe	Ti	Zn	Cu	V	Cr	Al
Amount (*w*/%)	10.220	0.277	0.108	0.448	0.046	0.029	0.047	0.010	0.006	balance

% of the melt mass. V reduces the length of β-phase platelets Al_5FeSi and, together with Ni and T, it has a significant influence on improving the mechanical properties (R_m and A_5). Similarly to Fe and Co, vanadium has a negative influence on the fluidity of Al-Si alloys.[9] There is also a significant beneficial influence of vanadium on the hardness.[10]

Until now a large number of experiments focusing on the influence of individual iron correctors have been performed[9,10] but few papers about a combined influence of iron correctors have been published. Petrík et al.[11] evaluated the properties of an Al-Si alloy containing Fe, Ni and Mn. Kumari et al.[2] investigated the effects of individual and combined additions of Be, Mn, Ca and Sr on the solidification behaviour of the structure and mechanical properties of the AlSi7Mg0.3Fe0.8 alloy. These papers refer to the beneficial influences of the combined additions of the selected iron correctors; however, there is very little evidence of an influence of combined vanadium-and-chromium additions on Al-Si alloys.

In this paper the influences of vanadium and of an addition combining V and Cr are analysed in the AlSi10MgMn alloy with an elevated iron amount.

2 MATERIALS AND METHODOLOGY

Aluminium alloy AlSi10MgMn was used as the experimental material. The chemical composition of the used alloy is presented in **Table 1**. In the first stage of the experiments, the commercial AlSi10MgMn alloy was alloyed with iron. Iron was added in the amount of 40000 µg/g using the AlFe10 master alloy. After obtaining the alloy with a high Fe mass content (1 % of Fe), V and Cr were added. Vanadium was added in the mass fraction of 0.2 % and the combined addition of V and Cr included 0.2 % of V and 0.5 and 1 % of Cr. The required amounts of V and Cr were added as the AlV10 and AlCr20 master alloys. For each experiment, the alloy was melted in a graphite crucible using an electric-resistance furnace. The melts were not further modified, grain refined or purified. The melts were poured into perma-

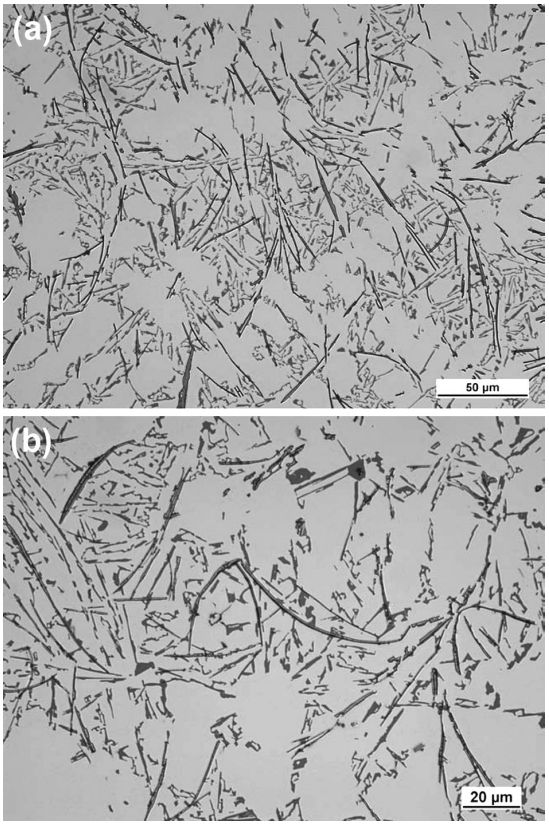

Figure 1: a) AlSi10MgMn + *w*(Fe) 1 %, b) detail of Fe phases, etched in 20 mL H_2SO_4 + 100 mL H_2O
Slika 1: a) AlSi10MgMn + *w*(Fe) 1 %, b) detajl Fe-faz, jedkano v 20 mL H_2SO_4 + 100 mL H_2O

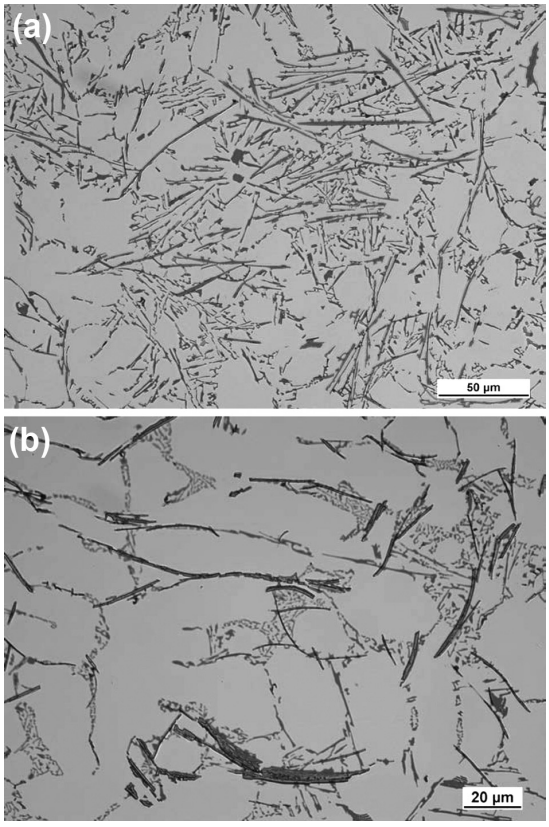

Figure 2: a) AlSi10MgMnFe + *w*(V) 0.2 %, b) detail of Fe phases, etched in 20 mL H_2SO_4 + 100 mL H_2O
Slika 2: a) AlSi10MgMnFe + *w*(V) 0,2 %, b) detajl Fe-faz, jedkano v 20 mL H_2SO_4 + 100 mL H_2O

nent moulds preheated to 200 °C after reaching a temperature of (760 ± 5) °C. From the poured castings, specimens for the tensile testing, hardness testing and microstructure evaluation were prepared. The solidification behaviour of the melts was analysed with the measuring equipment containing NiCr-Ni thermocouples.

3 RESULTS

3.1 Microstructure

Figure 1 shows the typical microstructure of the AlSi10MgMn alloy with an addition of a mass fraction 1 % of Fe. It can be seen that platelets of the β-Al_5FeSi phases are present in the interdendritic regions as well as precipitated along with the eutectic Si. The needles of the β-Al_5FeSi phase are evenly dispersed in the alloy and only small amounts of script-like particles are present.

The microstructure of the alloy with the V addition is shown in **Figure 2**. The needle-like phases present in the microstructure were of a different colour after the etching compared to alloy containing 1 % of Fe. The distribution and dimensions of the needles are similar to those of the alloy without the vanadium addition.

The combined addition of V and Cr caused the occurrence of sludge phases in the alloys' microstructures (**Figures 3** and **4**). In the alloy with a higher Cr level, a higher amount of sludge phases is present as the sludge-phase formation is mostly influenced by the Cr level in the alloy.[7] Iron-based intermetallic phases are smaller after both additions of Cr (w = 0.5 % and 1.0 %).

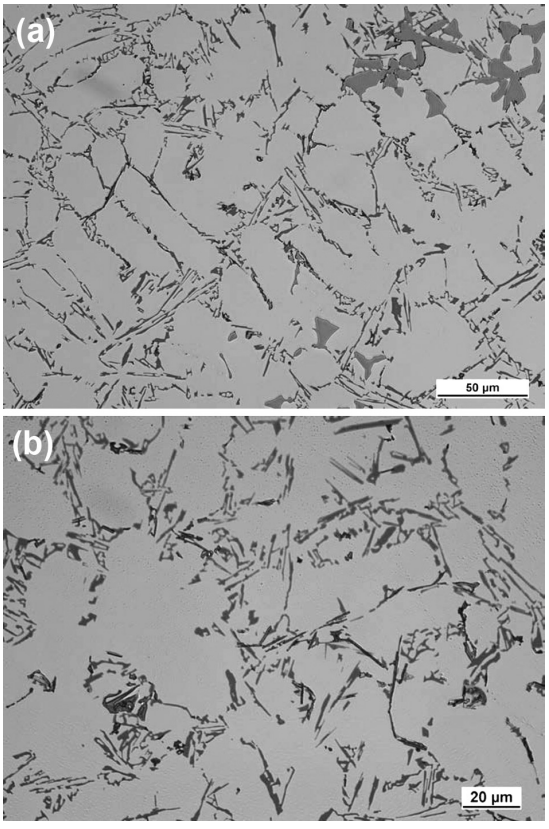

Figure 3: a) AlSi10MgMnFe + w(V) 0.2 % + w(Cr) 0.5 %, b) detail of Fe phases, etched in 20 mL H_2SO_4 + 100 mL H_2O
Slika 3: a) AlSi10MgMnFe + w(V) 0,2 % + w(Cr) 0,5 %, b) detajl Fe-faz, jedkano v 20 mL H_2SO_4 + 100 mL H_2O

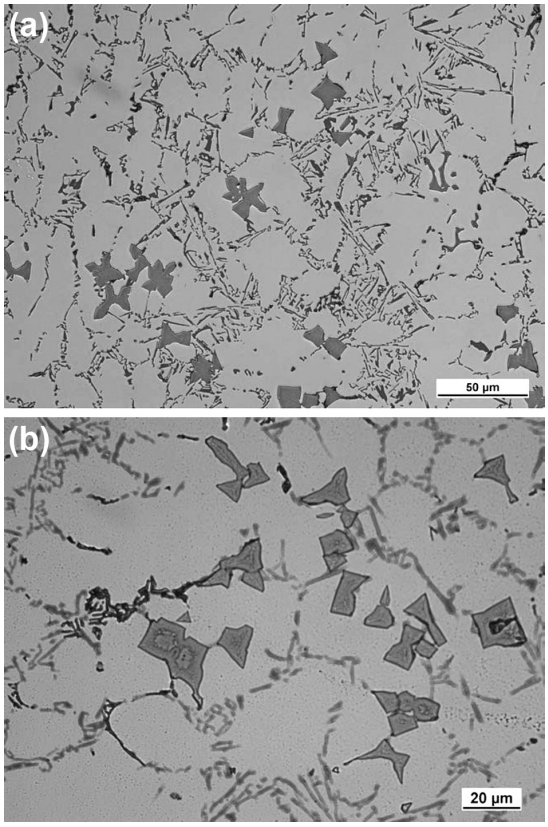

Figure 4: a) AlSi10MgMnFe + w(V) 0.2 % + w(Cr) 1.0 %, b) detail of Fe phases, etched in 20 mL H_2SO_4 + 100 mL H_2O
Slika 4: a) AlSi10MgMnFe + w(V) 0,2 % + w(Cr) 1,0 %, b) detajl Fe-faz, jedkano v 20 mL H_2SO_4 + 100 mL H_2O

3.2 Mechanical properties

An examination of the ultimate tensile strength (*UTS*) and elongation of the alloys was performed in line with the EN ISO 6892-1 standard. The ultimate tensile strength and elongation of the alloys are shown in **Figure 5**. The addition of Fe to the commercial AlSi10MgMn alloy caused a decrease in the *UTS* and elongation (sample No. 2). The highest improvement in both *UTS* and elongation was observed after the vanadium addition (w = 0.2 %). The combined addition of V and Cr decreased the alloy's tensile properties. The tensile strength of the alloy with the combined addition is even lower than that of the alloy containing a high iron amount. The same is true of the elongation in the case of the addition of V and Cr in the mass fractions of 0.2 % and 0.5 %. The hardness of the alloys was evaluated with the Brinell hardness-measuring method in line with the EN ISO 6506-1 standard. In **Figure 6** it can be seen that after the additions of all the investigated elements, Brinell hardness increased. The most significant increase

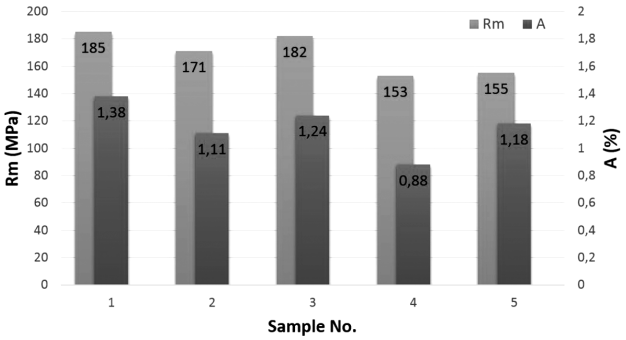

Figure 5: Tensile strength and elongation of AlSi10MgMn alloy: sample No. 1 – commercial AlSi10MgMn alloy, sample No. 2 – AlSi10MgMn + *w*(Fe) 1 %, sample No. 3 – AlSi10MgMnFe + *w*(V) 0.2 %, sample No. 4 – AlSi10MgMnFe + *w*(V) 0.2 % + *w*(Cr) 0.5 % and sample No. 5 – AlSi10MgMnFe + *w*(V) 0.2 % + *w*(Cr) 1.0 %

Slika 5: Natezna trdnost in raztezek zlitine AlSi10MgMn: vzorec št. 1 – komercialna zlitina AlSi10MgMn, vzorec št. 2 – AlSi10MgMn + *w*(Fe) 1 %, vzorec št. 3 – AlSi10MgMnFe + *w*(V) 0,2 %, vzorec št. 4 - AlSi10MgMnFe + *w*(V) 0,2 % + *w*(Cr) 0,5 % in vzorec št. 5 – AlSi10MgMnFe + *w*(V) 0,2 % + *w*(Cr) 1,0 %

(42 %) in the alloy's hardness occurred for the V-alloyed sample.

3.3 Thermal analysis

A cylindrical sample with a thermocouple placed in the middle of the casting was used for obtaining the thermal curve. **Figures 7** to **10** show the cooling curves and their first derivatives and **Table 2** lists the alloys, thermal arrests and phases formed in the analysed alloys. The first derivative is a measure of the instantaneous cooling rate along the cooling curve and is used to indicate the presence of minor slope changes on the curves.[2] **Figure 7** shows the first thermal-arrest point of the AlSi10MgMn alloy with the mass fraction 1.0 % of Fe at 591.2 °C, where the formation and growth of Al nuclei occur. After this arrest, the temperature of the solidifying alloy continues to decrease. The second thermal arrest occurs at 575 °C. This is caused by the latent heat of fusion of the iron intermetallic phases. The last thermal-arrest point occurs at 566.7 °C, corresponding to the eutectic-Si formation and growth. The cooling curve does not indicate the thermal arrest at the temperature corresponding with the formation of the Mg_2Si phase. It might have been caused by a very low Mg level in the measuring place and solidification conditions that do not result in the formation of the Mg_2Si phase. The thermal arrests corresponding with the primary α-Al after the additions of V and also V with Cr occur at higher temperatures. The eutectic temperature after the combined addition of V and Cr decreased compared to that of the

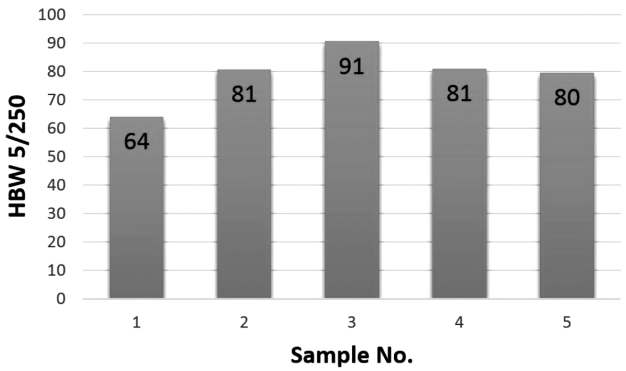

Figure 6: Brinell hardness of AlSi10MgMn alloy: sample No. 1 – commercial AlSi10MgMn alloy, sample No. 2 – AlSi10MgMn + *w*(Fe) 1 %, sample No. 3 – AlSi10MgMnFe + *w*(V) 0.2 %, sample No. 4 – AlSi10MgMnFe + *w*(V) 0.2 % + *w*(Cr) 0.5 % and sample No. 5 – AlSi10MgMnFe + *w*(V) 0.2 % + *w*(Cr) 1.0 %

Slika 6: Brinellova trdota zlitine AlSi10MgMn: vzorec št. 1 – komercialna zlitina AlSi10MgMn, vzorec št. 2 – AlSi10MgMn + *w*(Fe) 1 %, vzorec št. 3 – AlSi10MgMnFe + *w*(V) 0,2 %, vzorec št. 4 – AlSi10MgMnFe + *w*(V) 0,2 % + *w*(Cr) 0,5 % in vzorec št. 5 – AlSi10MgMnFe + *w*(V) 0,2 % + *w*(Cr) 1,0 %

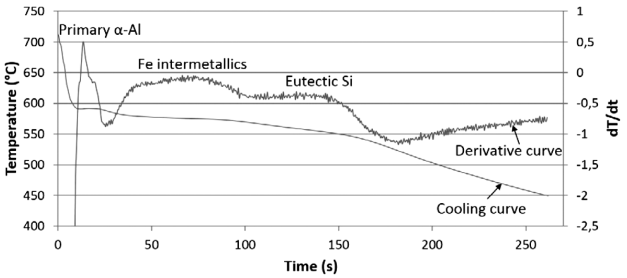

Figure 7: Cooling curve and its first derivative of AlSi10MgMn alloy with *w*(Fe) 1.0 %

Slika 7: Ohlajevalna krivulja in njen prvi odvod zlitine AlSi10MgMn z *w*(Fe) 1,0 %

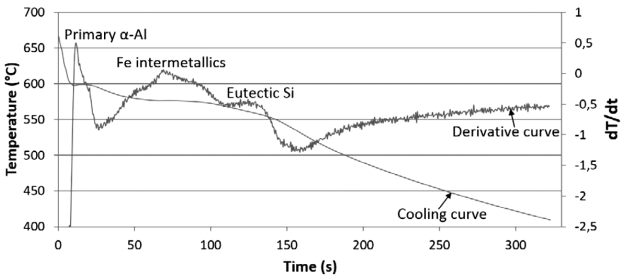

Figure 8: Cooling curve and its first derivative of AlSi10MgMnFe alloy with *w*(V) 0.2 %

Slika 8: Ohlajevalna krivulja in njen prvi odvod zlitine AlSi10MgMnFe z *w*(V) 0,2 %

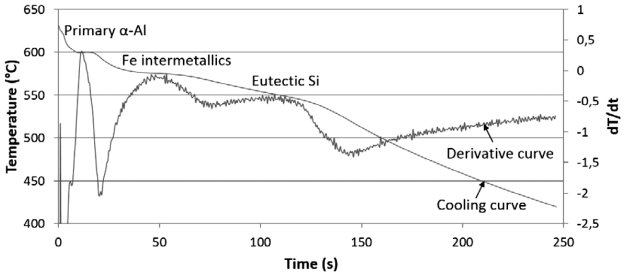

Figure 9: Cooling curve and its first derivative of AlSi10MgMnFe alloy with *w*(V) 0.2 % and *w*(Cr) 0.5 %

Slika 9: Ohlajevalna krivulja in njen prvi odvod zlitine AlSi10MgMnFe z *w*(V) 0,2 % in *w*(Cr) 0,5 %

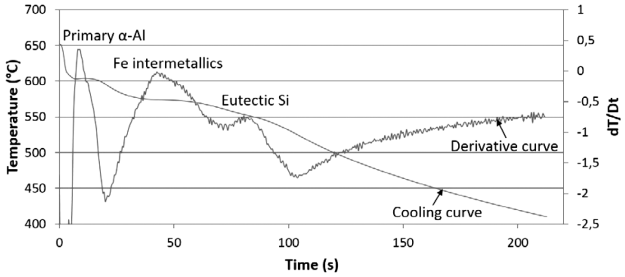

Figure 10: Cooling curve and its first derivative of AlSi10MgMnFe alloy with *w*(V) 0.2 % and *w*(Cr) 1.0 %

Slika 10: Ohlajevalna krivulja in njen prvi odvod zlitine AlSi10MgMnFe z *w*(V) 0,2 % in *w*(Cr) 1,0 %

alloy with the Fe addition and the difference between the eutectic temperatures of the alloy containing mass fractions 0.5 % and 1.0 % of Cr and the alloy without V and Cr is 17.9 °C and 14 °C, respectively. This leads to the formation of a finer eutectic Si compared to the alloy with the iron addition.

Table 2: Thermal arrests and phases formed in AlSi10MgMn alloy with a high iron level without and with V and Cr additions

Tabela 2: Toplotni zastoji in faze, ki nastajajo v AlSi10MgMn zlitini z visoko vsebnostjo železa ter brez dodatka V in Cr ali z njima

Alloy	Thermal arrest (Temperature (°C))	Phases formed
AlSi10MgMn + *w*(Fe) 1.0 %	591.2 575.0 566.7	Primary α-Al Iron intermetallics Eutectic Si
AlSi10MgMnFe + *w*(V) 0.2 %	597.7 576.0 563.2	Primary α-Al Iron intermetallics Eutectic Si
AlSi10MgMnFe + *w*(V) 0.2 % + *w*(Cr) 0.5 %	599.4 575.5 548.8	Primary α-Al Iron intermetallics Eutectic Si
AlSi10MgMnFe + *w*(V) 0.2 % + *w*(Cr) 1.0 %	603.4 574.1 552.7	Primary α-Al Iron intermetallics Eutectic Si

4 DISCUSSIONS

The microstructure of the AlSi10MgMn alloy after the iron addition in the mass fractions of 1.0 % contains a large amount of iron-based intermetallic phases, mostly in the form of platelets. After the addition of *w*(V) = 0.2 %, the platelet-like particles were still present but after the same etching technique as used with the iron-treated alloy, the needles obtained a different colour. This might have been due to a different chemical composition of the iron-based platelets. The combined addition of V and Cr caused the formation of sludge phases in the alloy. As the size and amount of the sludge phases are mostly influenced by Cr, more of them were observed after the addition of V and Cr in the mass fractions of 0.2 % and 1.0 %, respectively.

The formations of different intermetallic phases were reflected on the alloy's mechanical properties. The *UTS* of the alloy after the Fe addition decreased compared to the commercial AlSi10MgMn alloy. The decrease in the *UTS* is connected with a higher number of the brittle needle-like intermetallics in the iron-treated alloy. The addition of V (*w* = 0.2 %) improved the tensile strength of the iron-polluted alloy, but its value was still lower than for the commercial alloy. Vanadium is known as a grain-refining element and this characteristic might have been one of the reasons for the tensile-strength improvement. Also, it is possible that the chemical interaction between the iron-based phases and vanadium caused the change in the phase colour after the etching, leading to a decrease in the deleterious effect of such phases on the *UTS*. The combined addition of V and Cr in both mass fractions (0.2 % V + 0.5 % Cr and 0.2 % V + 1.0 % Cr) leads to a significant decrease in the alloy's *UTS*. The reason for the decreased tensile properties is the formation of hard and brittle sludge phases. These phases are brittle and cannot withstand the same stress as the ductile aluminium matrix.

The elongation of the alloys was influenced similarly by the analysed elements. The highest elongation was found for the commercial alloy (1.38 %), followed by the alloy treated with iron and vanadium (1.24 %). Brinell hardness was positively influenced by every used element. The highest Brinell hardness was found for the alloy containing Fe (*w* = 1.0 %) and V (*w* = 0.2 %). The reason for the increase in the hardness value after the addition of iron is probably a higher amount of iron intermetallic phases with a high value of microhardness. The same effect on Brinell hardness might have occurred due to the presence of sludge phases after the combined addition of V and Cr. The microhardness of the sludge phases can reach 800–1000 HV [7] while the aluminium-matrix microhardness is only 60–100 HV. The increase in the hardness after the V addition might have been caused by a high number of iron intermetallics and also by the strengthening of the aluminium matrix due to dissolved vanadium.

The thermal analysis of the alloys did not show any significant differences between the analysed alloys. It was found that the thermal arrest of the primary Al formation occurs at higher temperatures after the addition of V and Cr compared to the alloy containing the mass fraction 1.0 % of Fe.

5 CONCLUSION

Several conclusions can be drawn from the obtained results of the individual and combined effects of V and Cr on the AlSi10MgMn alloy with a high iron level:

- The iron addition (*w* = 1.0 %) to the commercial AlSi10MgMn alloy caused the formation of a high amount of iron-based platelet particles. The tensile properties (*UTS* and elongation) were decreased but the hardness increased.

- The addition of V (w = 0.2 %) to the iron-containing alloy led to changes in the mechanical properties. The *UTS* and elongation were positively affected and the measured values almost reached the values of the commercial alloy. V also caused Brinell hardness to increase to the highest value (91 HBW) compared to the other analysed alloys.
- The combined influence of V and Cr led to the formation of sludge phases. These phases decreased the mechanical properties compared to the vanadium-treated alloy. The *UTS* and Brinell hardness were almost the same at the chromium levels of w = (0.5 and 1.0) %. The elongation of the samples was the lowest with the combined V and Cr addition of the mass fractions 0.2 % and 0.5 %, respectively.
- The thermal analysis showed that alloying elements V and Cr do not have a significant influence on the solidification behaviour of the AlSi10MgMn alloy with a high iron level.
- The best combination of the mechanical and foundry properties was obtained with the vanadium addition in the mass fraction of 0.2 %.

6 REFERENCES

[1] E. Tillová, M. Chalupová, L. Hurtalová, Evolution of Phases in a Recycled Al-Si Cast Alloy During Solution Treatment, In: V. Kazmiruk (ed.), Scanning Electron Microscopy, chapter 21, Intech, 2012, 411–438, doi:10.5772/1973

[2] S. S. S. Kumari, R. M. Pillai, T. P. D. Rajan, B. C. Pai, Materials Science and Engineering A, 460–461 (**2007**), 561–573, doi:10.1016/j.msea.2007.01.082

[3] J. A. Taylor, The Effect of Iron in Al-Si Casting Alloys, 35th Australian Foundry Institute National Conference, Adelaide, South Australia, 2004, 148–157

[4] J. A. Taylor, Procedia Materials Science, 1 (**2012**), 19–33, doi:10.1016/j.mspro.2012.06.004

[5] C. M. Dinnis, J. A. Taylor, A. K. Dahle, Scripta Materialia, 53 (**2005**), 955–958, doi:10.1016/j.scriptamat.2005.06.028

[6] X. Cao, J. Campbell, Materials Transactions, 47 (**2006**) 5, 1303–1312, doi:10.2320/matertrans.47.1303

[7] E. Tillová, M. Chalupová, Structural analysis of Al-Si cast alloys, 1st ed., EDIS, Žilina 2009, 191 (in Slovak)

[8] X. Cao, J. Campbell, Metallurgical and Materials Transactions A, 35 (**2004**), 1425–1435, doi:10.1007/s11661-004-0251-0

[9] J. Petrík, M. Horvath, Annals of Faculty Engineering Hunedoara – International Journal of Engineering, (**2011**), 401–405

[10] P. Szarvasy, J. Petrík, V. Špeťuch, Slévarenství, 53 (**2005**) 11–12, 521–524 (in Slovak)

[11] J. Petrík, P. Szarvasy, V. Špeťuch, Acta Metallurgica Slovaca, 10 (**2004**), 73–79

UDK 532.6:669.782:620.186
Original scientific article/Izvirni znanstveni članek

ISSN 1580-2949
MTAEC9, 49(5)687(2015)

A RELIABLE APPROACH TO A RAPID CALCULATION OF THE GRAIN SIZE OF POLYCRYSTALLINE THIN FILMS AFTER EXCIMER LASER CRYSTALLIZATION

ZANESLJIV NAČIN HITREGA IZRAČUNA VELIKOSTI ZRN V POLIKRISTALNI TANKI PLASTI PO UV-LASERSKI KRISTALIZACIJI

Chil-Chyuan Kuo

Department of Mechanical Engineering, Ming Chi University of Technology, No. 84, Gungjuan Road, Taishan Taipei Hsien 243, Taiwan
jacksonk@mail.mcut.edu.tw

Prejem rokopisa – received: 2013-10-08; sprejem za objavo – accepted for publication: 2014-11-27

doi:10.17222/mit.2013.237

Excimer laser crystallization (ELC) is the most commonly employed technology for fabricating low-temperature polycrystalline silicon (LTPS) thin films. The grain size of polycrystalline thin films after ELC is usually determined with a manual calculation, which includes certain disadvantages, i.e., human error and is time-consuming and exhausting. To mitigate these disadvantages, a high-efficiency approach to calculating the grain size of polycrystalline thin films automatically is proposed. It was found that the selected-boundary-definition approach is a promising candidate for calculating the grain size of polycrystalline thin films. The savings in the analysis time is up to 75 %. The average error rate of the measurement can be controlled within 8.33 %.

Keywords: low-temperature polycrystalline silicon, automatic grain-size analysis, excimer laser crystallization

UV-laserska kristalizacija (ELC) je najbolj pogosto uporabljena tehnologija za izdelavo nizkotemperaturne polikristalne tanke plasti silicija (LTPS). Velikost zrn v polikristalni tanki plasti po ELC se navadno določa z ročnim izračunom, ki pa ima nekatere pomanjkljivosti, kot je človeška napaka, in je časovno potratna in utrujajoča. Za ublažitev teh pomanjkljivosti je predlagan zelo učinkovit, avtomatičen način za izračun velikosti zrn v polikristalni tanki plasti. Ugotovljeno je, da je približek k selektivnemu določanju meje obetajoč način za izračun velikosti zrn polikristalnih tankih plasti. Prihranek časa za analizo je do 75 %. Povprečni odmik napake pri meritvah je okrog 8,33 %.

Ključne besede: nizkotemperaturni polikristalni silicij, avtomatska analiza velikosti zrn, UV-laserska kristalizacija

1 INTRODUCTION

High-performance complementary metal-oxide-semiconductor (CMOS) circuits on glass are essential for the system-on panel (SOP) technology, which has potential applications in various information devices including cell-phones, laptop computers and large-size flat panel television sets. Polycrystalline silicon (poly-Si) thin films have been widely used as CMOS gates, thin-film transistors (TFTs), solar cells and various other applications in semiconductor-device technology. Excimer laser crystallization (ELC) is an industrial technique used for preparing poly-Si thin films on commercially available, inexpensive glass substrates for the development of high-performance TFTs in active-matrix flat panel displays.[1–6] A rapid deposition of the laser-energy density, on a nanosecond time scale, onto the surface region of the an amorphous-silicon (a-Si) thin film leads to its melting and recrystallisation into a poly-Si thin film, while keeping the glass substrate at a low temperature. The final quality of the device depends significantly on the phase-transformation mechanisms which need to be manipulated precisely for obtaining poly-Si thin films with a large grain size and a good uniformity. The phase-transformation mechanisms of a-Si thin films have been extensively investigated using an in-situ optical diagnostic technique during ELC in the previous studies.[7–17] Numerous researches have been done for fabricating large-grained poly-Si thin films because the performance of TFTs is significantly affected by the size of the poly-Si thin films after ELC.[18–23] Until now, however, the grain size of the poly-Si thin films after ELC has usually been determined with a manual calculation. This approach included certain disadvantages such as human error and was time-consuming and exhausting. Therefore, a high-efficiency approach is proposed in this work for calculating the grain size of polycrystalline thin films efficiently and accurately using the Image-Pro software.[24,25]

2 EXPERIMENT

Figure 1 shows a schematic illustration of the experimental set-up for ELC. The sample has a stacked structure consisting of a thick 300 nm SiO_2 capping layer and a thick 90 nm a-Si layer formed on a thick 0.7 mm non-alkali glass substrate (Corning 1737). All the films were prepared with plasma-enhanced chemical vapor deposition (PECVD). These samples were then dehydroge-

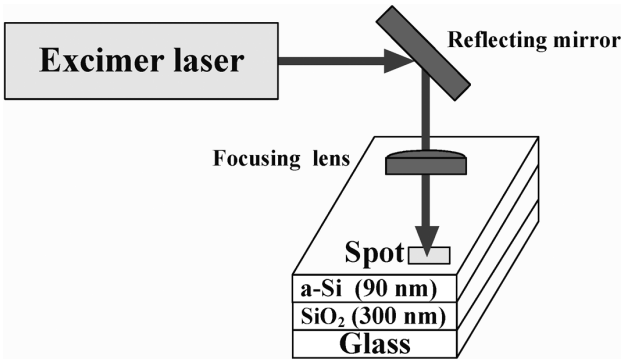

Figure 1: Schematic illustration of the experimental set-up for ELC
Slika 1: Shematski prikaz eksperimentalnega sestava za ELC

nated with a thermal treatment at 500 °C for 2 h to reduce the hydrogen content in order to prevent the ablation caused by a sudden hydrogen eruption during ELC.[26] The samples were then held by self-closing tweezers at the end of a cantilever beam fixed to an $x - y$ precision translation stage. The x- and y-axis displacements of the two stages can be accurately manipulated (resolution = 0.625 μm). The movement of the focusing lens mounted onto a z-axis stage was precisely controlled to adjust the desired excimer laser fluences for crystallization. The pulsed excimer laser-energy levels were monitored using a laser power meter (Vector H410 SCIENTECH). The variation in the pulse-to-pulse excimer laser energy was found to be less than 5 %. The a-Si thin films were irradiated with an excimer laser beam (λ = 351 nm, repetition rate = 1 Hz, LAMBDA PHYSIK COMPex 102) with laser fluences ranging from 100 mJ/cm^2 to 500 mJ/cm^2. A stainless-steel slit (2 mm × 15 mm) located in the optical path of the excimer laser was employed to transform the incident Gaussian beam into a rectangular beam spot with a better than ± 10 % energy variation. All the experiments were performed at ambient temperature and pressure.

After ELC, the microstructural analyses of the annealed poly-Si thin films were carried out using field emission scanning electron microscopy (FE-SEM) with JEOL JSM-6500F. Before the FE-SEM observation, the crystallized silicon films were Secco-etched in order to highlight the grain boundaries (GBs) and intra-grain defects.[27] The acceleration electron beam energy for FE-SEM was 15 kV (a resolution of 1.5 nm). Six approaches (count, auto-split, watershed split, limited watershed split, boundary definition and selected-boundary definition) were employed for calculating the grain size of the poly-Si thin films.

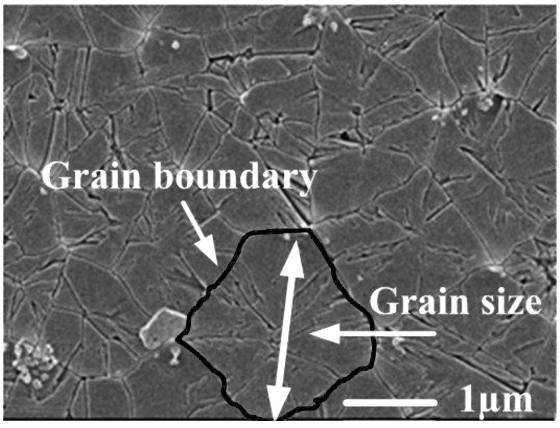

Figure 2: SEM micrograph of poly-Si thin films after ELC
Slika 2: SEM-posnetek poli-Si tanke plasti po ELC

3 RESULTS AND DISCUSSION

Figure 2 shows a typical SEM micrograph of the poly-Si thin films after ELC. The grain size can be determined from the longest length inside the grain boundary. To determine the best approach to replace the tradition manual-calculation method, a test SEM micrograph was selected to be investigated. **Figure 3** shows the grain-size calculation result using the manual-calculation approach. The total number of the grain size of poly-Si was 24. The largest grain size, the smallest grain size and the average grain size were (333.3, 26.6 and 152.2) mm, respectively. **Figure 4** shows the grain-size calculation result using six different approaches. **Figure 5** shows the variation in the counts of the grain size for seven different calculation approaches. The average error rate for the approaches of count, auto-split, watershed split, limited watershed split, boundary definition and selected-boundary definition was (21.32, 19.33, 20.76, 20.76, 16.29 and 8.33) %, respectively. As one can see, the selected-boundary-definition approach provides the lowest average error rate in the grain-size calculation compared with the tradition manual-calculation approach in this case. The average error rates for the approaches of count, auto-split, watershed split and limited watershed split were higher than those of the approaches of boundary definition and selected-boundary definition because the Image-Pro software cannot precisely evaluate the

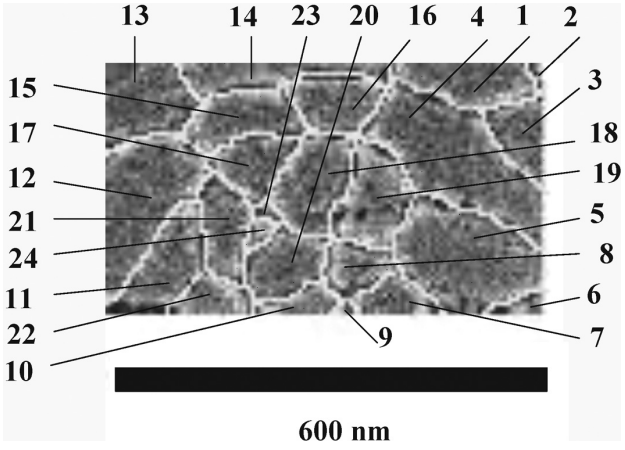

Figure 3: Grain-size calculation result using manual-calculation approach
Slika 3: Izračun velikosti zrn z ročnim štetjem

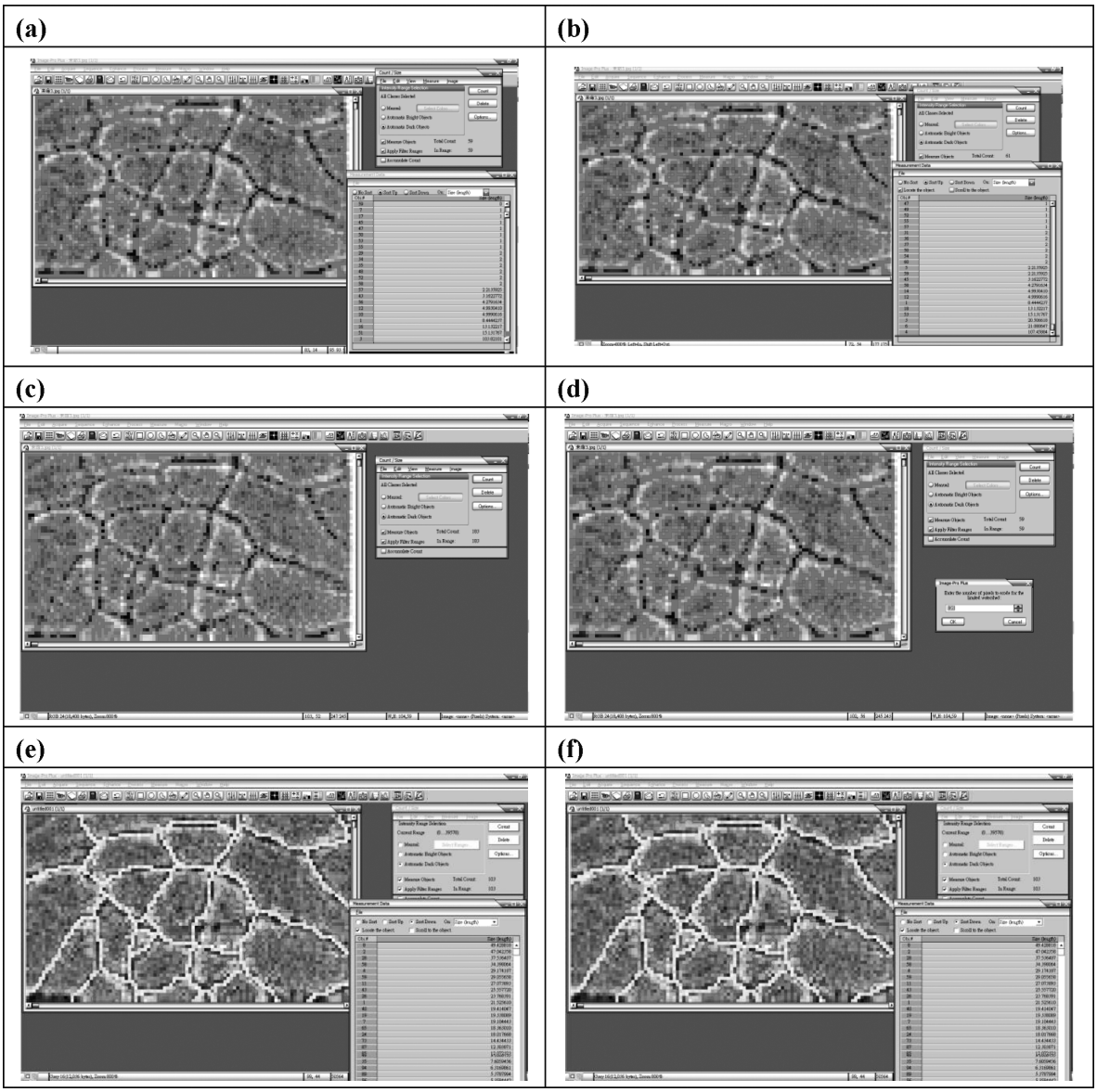

Figure 4: Grain-size calculation result using six different approaches of: a) count, b) auto-split, c) watershed split, d) limited watershed split, e) boundary definition and f) selected-boundary definition

Slika 4: Rezultat izračuna velikosti zrn s šestimi različnimi načini: a) štetje, b) avtomatska razdelitev, c) razdelitev po razvodnicah, d) omejena razdelitev po razvodnicah, e) definicija mej in f) selektivna definicija mej

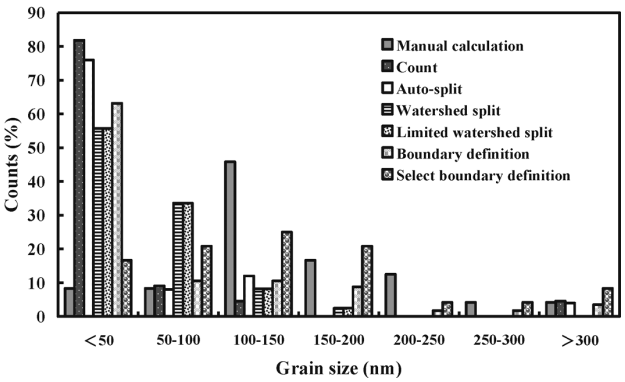

Figure 5: Variation in the counts of the grain size for seven different calculation approaches

Slika 5: Razlike v izračunu velikosti zrn pri sedmih različnih načinih izračuna

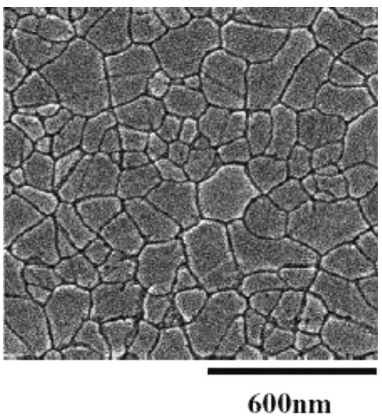

Figure 6: SEM micrograph of poly-Si thin film of case study 1 [28]

Slika 6: SEM-posnetek poli-Si tanke plasti pri študiju primera 1 [28]

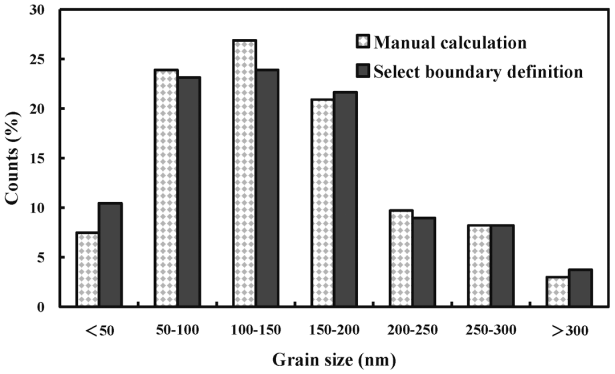

Figure 7: Variation in the counts of the grain size for two different calculation approaches in case study 1

Slika 7: Razlike v izračunu velikosti zrn pri dveh različnih načinih izračuna za primer 1

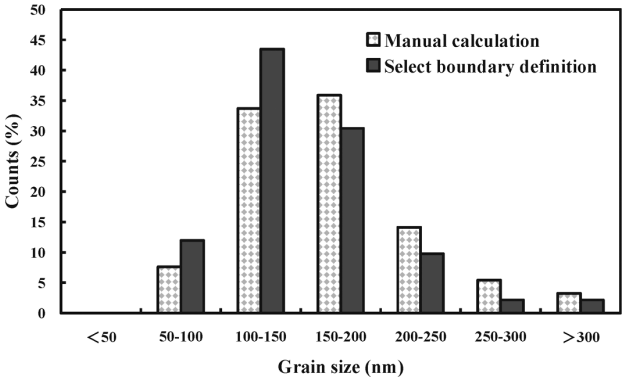

Figure 9: Variation in the counts of the grain size for two different calculation approaches in case study 2

Slika 9: Razlike v izračunu velikosti zrn pri dveh različnih načinih izračuna, za primer 2

grain boundary of a SEM micrograph. To reduce the average error rate of the measurement, the two approaches of boundary definition and selected-boundary definition were further applied. The average error rate of the measurement was still not acceptable, though the boundary-definition approach can reduce the average error rate of the measurement. Finally, the selected-boundary-definition approach was applied. The selected-boundary-definition approach provides the best accuracy of the grain-size calculation because the grain boundary of the SEM micrograph was traced first and then calculated using the Image-Pro software.

To evaluate the accuracy of the selected-boundary-definition approach, two case studies were applied to investigate the average error rate. **Figure 6** shows a SEM micrograph of the poly-Si thin film of case study 1.[28] **Figure 7** shows the variation in the counts of the grain size for two different calculation approaches in case study 1. The average error rate of the measurement was only 1.28 %. In this case, the total time for calculating the grain size with the manual calculation was approximately 16 h. However, the total calculating time was drastically reduced to approximately 4 h using the selected-boundary-definition approach. The saving in the analysis time was up to 75 %. **Figure 8** shows a SEM micrograph of the poly-Si thin film of case study 2. **Figure 9** shows the variation in the counts of the grain size for two different calculation approaches in case study 2.[28] The average error rate of the measurement was only 4.03 %. In this case, the total time for calculating the grain size with the manual calculation was approximately 12 h. However, the total calculating time was drastically reduced to approximately 3 h using the selected-boundary-definition approach. The saving in the analysis time was up to 75 %. It is worth noting that the average error rate of the measurement was obviously smaller than for the test sample because the grain boundary was clear for the two SEM micrographs. Thus, a SEM micrograph with a clear grain boundary is critical for calculating the grain size with the Image-Pro software when the Secco etching is employed[29–31].

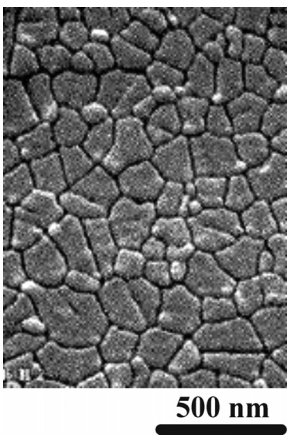

Figure 8: SEM micrograph of poly-Si thin film of case study 2 [28]

Slika 8: SEM-posnetek poli-Si tankih plasti pri študiju primera 2 [28]

As discussed above, the Image-Pro software is a powerful tool for analyzing the grain size of the poly-Si thin films after ELC. The saving in the analysis time is up to 75 % and the average error rate of the measurement can be controlled within 8.33 % when using the computer-calculation approach compared with the manual-calculation approach.

4 CONCLUSIONS

A simple and highly efficient approach for calculating the grain size of the poly-Si thin films after ELC was successfully demonstrated. A SEM micrograph with a clear grain boundary is critical for calculating the grain size with the Image-Pro software. The selected-boundary-definition approach was proved to be a promising candidate for calculating the grain size of the poly-Si thin films efficiently and accurately. The saving in the analysis time was up to 75 % and the average error rate of the measurement can be controlled within 8.33 % when compared with the manual-calculation approach.

Acknowledgements

This work was financially supported by the National Science Council of Taiwan under contract nos. NSC 102-2221-E-131-012 and NSC 101-221-E-131-007. The skillful technical assistance of Mr. Kun-Wei Wu of the Ming Chi University of Technology is gratefully acknowledged.

5 REFERENCES

[1] J. S. Im, R. S. Sposili, M. A. Crowder, Single-crystal Si films for thin-film transistor devices, Applied Physics Letters, 70 (**1997**) 19, 3434–3436, doi:10.1063/1.119194

[2] L. Mariucci, R. Carluccio, A. Pecora, V. Foglietti, G. Fortunato, P. Legagneux, D. Pribat, D. Della Sala, J. Stoemenos, Lateral growth control in excimer laser crystallized polysilicon, Thin Solid Films, 337 (**1999**) 1–2, 137–142, doi:10.1016/S0040-6090(98)01174-2

[3] C. C. Kuo, P. J. Huang, Rapid surface roughness measurements of silicone thin films with different thicknesses, Optik – International Journal for Light and Electron Optics, 123 (**2012**) 19, 1755–1760, doi:10.1016/j.ijleo.2011.11.048

[4] C. C. Kuo, Effects of angle of probe laser and pinhole diameter on the time-resolved optical inspection system, Optik – International Journal for Light and Electron Optics, 122 (**2011**) 20, 1799–1803, doi:10.1016/j.ijleo.2010.09.045

[5] C. C. Kuo, P. J. Huang, A low-cost and reliable optical inspection system for rapid surface roughness measurements of polycrystalline thin films, Materialwissenschaft und Werkstofftechnik, 43 (**2012**) 10, 878–885, doi:10.1002/mawe.201200876

[6] C. C. Kuo, C. S. Chao, Rapid optical measurement of surface roughness of polycrystalline thin films, Optics and Lasers in Engineering, 48 (**2010**) 12, 1166–1169, doi:10.1016/j.optlaseng.2010.07.007

[7] C. C. Kuo, Characterization of in-situ time-resolved optical spectra during excimer laser crystallization, Journal of Russian Laser Research, 30 (**2009**) 1, 12–20, doi:10.1007/s10946-009-9057-2

[8] C. C. Kuo, Characterization of Polycrystalline Ge Thin Films Fabricated by Excimer Laser Crystallization, Journal of Russian Laser Research, 29 (**2008**) 2, 167–175, doi:10.1007/s10946-008-9008-3

[9] C. C. Kuo, Characterization of Polycrystalline Silicon Thin Films Fabricated by Excimer Laser Crystallization, Journal of Russian Laser Research, 28 (**2007**) 4, 383–392, doi:10.1007/s10946-007-0027-2

[10] C. C. Kuo, A novel optical diagnostic technique for analyzing the recrystallization characteristics of polycrystalline silicone thin films following frontside and backside excimer laser irradiation, Optics and Lasers in Engineering, 49 (**2011**) 11, 1281–1288, doi:10.1016/j.optlaseng.2011.06.008

[11] C. C. Kuo, C. S. Chao, A simple and cost-effective system for measuring the recrystallization characterization of polycrystalline silicon following excimer laser crystallization, Lasers in Engineering, 21 (**2011**) 5–6, 353–364

[12] C. C. Kuo, Non-destructive measurements on recrystallization and grain size characterization of polycrystalline silicon, Journal of Russian Laser Research, 32 (**2011**) 2, 130–138, doi:10.1007/s10946-011-9198-y

[13] C. C. Kuo, Dynamical resolidification behavior of silicon thin films during frontside and backside excimer laser annealing, Optics and Lasers in Engineering, 49 (**2011**) 7, 804–810, doi:10.1016/j.optlaseng.2011.03.006

[14] C. C. Kuo, In situ time-resolved optical measurements of a-Si thin films during excimer laser crystallization, Optik – International Journal for Light and Electron Optics, 122 (**2011**) 8, 655–659, doi:10.1016/j.ijleo.2010.04.023

[15] C. C. Kuo, On-line determination of average grain size of polycrystalline silicon from melt duration of molten silicon, Journal of Russian Laser Research, 32 (**2011**) 1, 12–18, doi:10.1007/s10946-011-9185-3

[16] C. C. Kuo, A non-destructive optical diagnostic technique for measuring the grain size of polycrystalline silicon produced by excimer laser crystallization, Laser Physics, 20 (**2010**) 6, 1525–1531, doi:10.1134/S1054660X10110113

[17] C. C. Kuo, Phase Transformation Mechanism in Pulsed Excimer Laser Crystallization of Amorphous Silicon Thin Films, Lasers in Engineering, 19 (**2010**) 3–4, 225–238

[18] J. S. Im, H. J. Kim, M. O. Thompson, Phase transformation mechanisms involved in excimer laser crystallization of amorphous silicon films, Applied Physics Letters, 63 (**1993**) 14, 1969–1971, doi:10.1063/1.110617

[19] J. S. Im, H. J. Kim, On the super lateral growth phenomenon observed in excimer laser-induced crystallization of thin Si film, Applied Physics Letters, 64 (**1994**) 17, 2303–2305, doi:10.1063/1.111651

[20] T. Sameshima, H. Watakabe, N. Andoh, S. Higashi, Pulsed Laser Annealing of Thin Silicon Films, Japanese Journal of Applied Physics, 45 (**2006**), 2437–2440, doi:10.1143/JJAP.45.2437

[21] M. Tsubuku, K. S. Seol, I. H. Choi, Y. Ohki, Enhanced Crystallization of Strontium Bismuth Tantalate Thin Films by Irradiation of Elongated Pulses of KrF Excimer Laser, Japanese Journal of Applied Physics, 45 (**2006**), 1689–1693, doi:10.1143/JJAP.45.1689

[22] L. Mariucci, A. Pecora, G. Fortunato, C. Spinella, C. Bongiorno, Crystallization mechanisms in laser irradiated thin amorphous silicon films, Thin Solid Films, 427 (**2003**) 1–2, 91–95, doi:10.1016/S0040-6090(02)01254-3

[23] D. H. Choi, E. Sadayuki, O. Sugiura, M. Matsumura, Lateral Growth of Poly-Si Film by Excimer Laser and Its Thin Film Transistor Application, Japanese Journal of Applied Physics, 33 (**1994**), 70–74, doi:10.1143/JJAP.33.70

[24] A. Rawlinson, C. Elcock, A. Cheung, A. Al-Buhairi, S. Khanna, T. F. Walsh, R. P. Ellwood, An in-vitro and in-vivo methodology study of alveolar bone measurement using extra-oral radiographic alignment apparatus, Image Pro-Plus® software and a subtraction programme, Journal of Dentistry, 33 (**2005**) 9, 781–788, doi:10.1016/j.jdent.2005.01.013

[25] R. J. Blatt, A. N. Clark, J. Courtney, C. Tully, A. L. Tucker, Automated quantitative analysis of angiogenesis in the rat aorta model using Image-Pro Plus 4.1, Computer Methods and Programs in Biomedicine, 75 (**2004**) 1, 75–79, doi:10.1016/j.cmpb.2003.11.001

[26] C. C. Kuo, Solidification velocity in liquid silicon during excimer laser crystallization, Applied Physics A: Materials Science and Processing, 95 (**2009**) 2, 573–578, doi:10.1007/s00339-008-4953-9

[27] B. Rezek, C. E. Nebel, M. Stutzmann, Polycrystalline Silicon Thin Films Produced by Interference Laser Crystallization of Amorphous Silicon, Japanese Journal of Applied Physics, 38 (**1999**), L1083–L1084, doi:10.1143/JJAP.38.L1083

[28] G. Fortunato, L. Mariucci, R. Carluccio, A. Pecora, V. Foglietti, Excimer laser crystallization techniques for polysilicon TFTs, Applied Surface Science, 154–155 (**2000**), 95–104, doi:10.1016/S0169-4332(99)00475-4

[29] D. Bouhafs, M. Fathi, L. Guerbous, Photoluminescence activity of Yang and Secco etched multicrystalline silicon material, Applied Surface Science, 252 (**2006**) 23, 8337–8340, doi:10.1016/j.apsusc.2005.11.046

[30] J. Mahlib, A. Abbadie, B. O. Kolbesen, A comparison of the etching behaviour of the FS Cr-free SOI with that of the Secco etching solution on silicon-on-insulator substrates, Materials Science and Engineering B, 159–160 (**2009**), 309–313, doi:10.1016/j.mseb.2008.09.008

[31] J. Zhang, C. Liu, Q. Zhou, J. Wang, Q. Hao, H. Zhang, Y. Li, Evolution of flow pattern defects in boron-doped (1 0 0) Czochralski silicon crystals during secco etching procedure, Journal of Crystal Growth, 269 (**2004**) 2–4, 310–316, doi:10.1016/j.jcrysgro.2004.05.095

UDK 621.791/.792:669.715
Original scientific article/Izvirni znanstveni članek

ISSN 1580-2949
MTAEC9, 49(5)693(2015)

EFFECTS OF DIFFERENT STIRRER-PIN FORMS ON THE JOINING QUALITY OBTAINED WITH FRICTION-STIR WELDING

VPLIV RAZLIČNIH OBLIK VRTILNIH KONIC NA KVALITETO SPOJA PRI TORNEM VRTILNEM VARJENJU

Hudayim Basak[1], Kadir Kaptan[2]

[1]Gazi University, Technology Faculty, Department of Industrial Design Engineering, Ankara, Turkey
[2]Gazi University, Technical Education Faculty, Department of Mechanical Education, Ankara, Turkey
hbasak@gazi.edu.tr

Prejem rokopisa – received: 2014-04-02; sprejem za objavo – accepted for publication: 2014-10-15

doi:10.17222/mit.2014.062

In this study, 20 different pins that could be employed in friction-stir welding were manufactured. These pins and the Al7075 T6 material were joined with the friction-stir-welding technique. Tensile tests, microstructure and microhardness measurements, scanning-electron-microscopy (SEM) and energy-dispersion-spectrometry (EDS) analyses were conducted on the components joint by friction-stir welding. Designs of the weld and the tip that achieve the best performance were determined.

Keywords: friction-stir welding, stirrer-pin forms

V tej študiji je bila napravljena primerjava 20 različnih konic, ki se uporabljajo pri tornem vrtilnem varjenju. Konice in Al7075 T6 material so bili spojeni s tornim vrtilnim varjenjem. Pri komponentah, spojenih z vrtilno tornim varjenjem, so bili izvršeni natezni preizkusi, pregledana mikrostruktura in izmerjena mikrotrdota. Uporabljena je bila vrstična elektronska mikroskopija (SEM) in energijsko disperzijska rentgenska spektroskopija (EDS). Določena je bila tudi oblika zvara in konice, kjer so bile dosežene najboljše lastnosti.

Ključne besede: torno vrtilno varjenje, oblika konic

1 INTRODUCTION

Friction-stir welding (FSW) is a welding method undergoing continuous development that was originally introduced in England (Cambridge) in 1991,[1,2] and went through a major development in the 1990s.[3,4] Newly developed materials generally require modern joining techniques. With the development of new alloys in the past twenty years, major advances were also made regarding the welding of these materials. Friction-stir welding (FSW) was successfully employed in the welding of aluminum alloys that are difficult to weld with the traditional melt-welding methods, especially those that are subjected to age hardening.[5,6]

The problems arising from joining aluminum and Al-alloys with the traditional melt-welding methods stimulated the researchers to develop new joining methods. When joining aluminum alloys (especially those subjected to age hardening) with the melt-welding methods, a high heat input may culminate in these materials leading to a high thermal expansion and crack formation in the welding seam due to wide solidification intervals.[7] In addition, it is known that the high heat input in arc welding leads to the formation of low melting-point phases at the grain boundaries in the region under the effect of the heat in aluminum alloys and, therefore, cracks at the grain boundaries of the region during the solidification. Another problem encountered when joining aluminum alloys subjected to age hardening with the melt-welding methods is a reduction in the hardness and strength due to the solution of hardening precipitates in the welding seam and an excessive aging of the heat-effected zone.[8–10] This situation results in mechanical disconformities in the welding zone. Due to these specific reasons, solid-state welding methods (diffusion, friction and friction-stir welding) provide huge advantages for the welding of these materials.

Friction-stir welding, which is a solid-state welding method, is an appropriate alternative welding method for joining the materials whose welding construction is difficult, due to its unique advantages like a brief welding duration, minimum surface preparation and ease of automation.[11] With this method, no protective gas, additional welding metal or opening of the welding grooves on the components to be welded are necessary. The welding quality of the welded joints obtained with friction-stir welding does not show variation with respect to the type of material.[10] Even though the method is suitable for several materials, its most significant area of application is the welding of aluminum and aluminum alloys. Aluminum alloys joined with this method exhibit decent mechanical properties.[12] The FSW method can be comfortably applied in all positions.[13,14] In the studies conducted for aluminum materials, it was found that appropriate joining can be performed for plate thicknesses between 1–75 mm.[15]

The tool-pin profile and welding parameters play major roles in achieving the quality of friction-stir weld-

ing. Friction-stir-welding studies used different parameters and stirrer pins made for these studies. The effect of the tool-pin profile on mechanical properties was the subject of a few studies.[16–18] The effect of the tool-pin profile on the bonding and mechanical properties was investigated together with certain parameters such as the rotational speed,[16] welding speed[19] shoulder diameter[20,21] and axial force.[22] Also, in recent years, some studies have been made on the optimization of the tool geometry using statistical analyses and finite-element methods.[23,24]

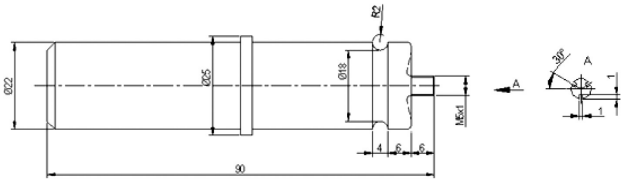

Figure 1: Drawing of a manufactured stirrer pin
Slika 1: Risba izdelane konice

2 EXPERIMENTS AND MATERIAL

The Al7075 material was chosen to be employed in this study. For the FSW method, this material was chosen due to its superior hardness, tensile strength, joining capability and resistance properties. In addition, the Al7075 material is used in many industrial areas (especially in the space and aeronautical industry) thanks to its mechanical properties. Stirrer-pin profiles were formed by taking screw-thread types (metric (triangular), trapezoidal, circular, square and saw-shaped) into consideration. Along with that, in the case when no screw thread is cut, triangular, cylindrical, conical

 1. Square screwed stirrer pin	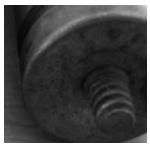 2. Circular screwed stirrer pin	 3. Trapezoidal screwed stirrer pin	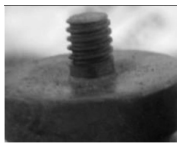 4. Triangular screwed stirrer pin	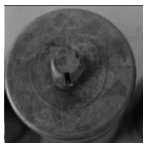 5. Saw-type screwed stirrer pin	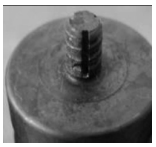 6. 3-groove square screwed stirrer pin
 7. 3-groove circular screwed stirrer pin)	 8. 3-groove triangular (metric) screwed stirrer pin	 9. 3-groove trapezoidal screwed stirrer pin	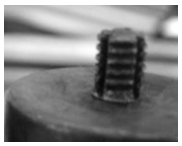 10. 3-groove saw-type screwed stirrer pin 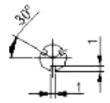	 11. 4-groove square screwed stirrer pin	 12. 4-groove circular screwed stirrer pin 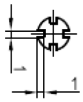
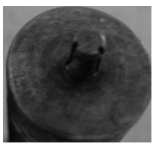 13. 4-groove triangular (metric) screwed stirrer pin	 14. 4-groove trapezoidal screwed stirrer pin	 15. 4-groove saw-type screwed stirrer pin	 16. Unscrewed conical profiled stirrer pin	 17. Unscrewed 3-groove circular profiled stirrer pin	 18. Unscrewed 4-groove circular profiled stirrer pin
		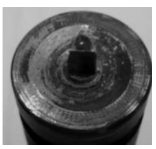 19. Unscrewed triangular profiled stirrer pin 	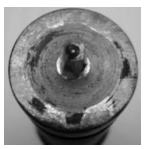 20. Unscrewed square profiled stirrer pin 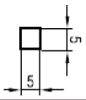		

Figure 2: Manufactured stirrer pins
Slika 2: Izdelane vrste konic

and square pin profiles were created in order to compare the joining qualities of the pin profiles. Stirrer pins were manufactured on the basis of the drawing given in **Figure 1**. The manufacturing principle for all the stirrer pins was taken into account in accordance with this drawing. As it is theoretically known, screw types are divided into two groups: connection and movement types. The triangular screw type is the most frequently used connection bolt. Since the profile gradient in triangular profile screws increases the frictional resistance ($\mu' = \tan \rho' = \mu/(\cos(\beta/2))$), the friction per unit area for triangular threads is at the highest level. As for the movement bolts, the friction per unit area is very low.[25] For the profiles designed on the basis of this theoretical information, we can predict that, of all the pin designs, the highest joining-strength quality is achieved with the triangular screw. We can also state that low joining strengths are achieved with the movement-type screws (circular and square). The AISI/SAE 4340 (DIN 1.6582, EN 34CrNiMo6) material was selected as the stirrer-pin material and it was subjected to a heat treatment for a hardness of 50–52 HRC. The stirrer pins were made ready for use with the FSW method. The manufactured stirrer pins are presented in **Figure 2**.

2.1 Friction-stir-welding method

The friction-stir welding process is shown in **Figure 3**. The FSW method is a type of welding that was developed using the friction-stir-welding technique. This welding method consists of moving an immersed shoulder pin (probe) revolving at a high speed over two plates butted to each other at a particular speed.[26] Even though aluminum alloys are usually difficult to weld, this method can be used for enhancing the welding performance. Researchers are focused on joining aluminum alloys. This welding method was applied on aluminum materials thinner than 1 mm and thicker than 35 mm and it was found that very good mechanical properties were achieved.[27–31]

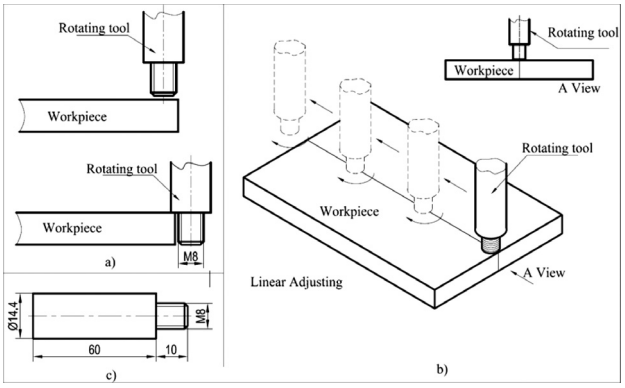

Figure 3: a) Tool approaching the workpiece, b) adjusting the tool before the welding, c) drawing of the tool[30,31]
Slika 3: a) Orodje se približuje obdelovancu, b) prilagoditev orodja pred varjenjem, c) risba orodja[30,31]

The parameters used in the tests are given in **Table 1**.

Table 1: Test parameters
Tabela 1: Parametri preizkusa

Material	Aluminum alloy (Al7075 T6), a (80 × 120) mm prismatic component
Stirrer pins	20 stirrer pins created on the basis of screw types
Feed rate	28–40 mm/min
Number of revolutions	710–1200 r/min
Bench used for burnishing process	Taksan 40T1500, a CNC milling bench with a vertical processing center

During the construction stage of friction-stir welding, the values of the movement rate and rotational speed were determined separately for different stirrer pins. The reason for this is the fact that a rotational speed yielding very good results for one pin does not provide for an efficient joining for another pin. Therefore, the values that yield good welding results were determined in terms of increasing or decreasing the movement and rotational speeds. In this way, the welding operation was carried out (**Figure 4**).

The friction-stir welding was started with ungrooved stirrer pins and the welding was performed with square, circular, saw-type, trapezoidal and triangular screwed

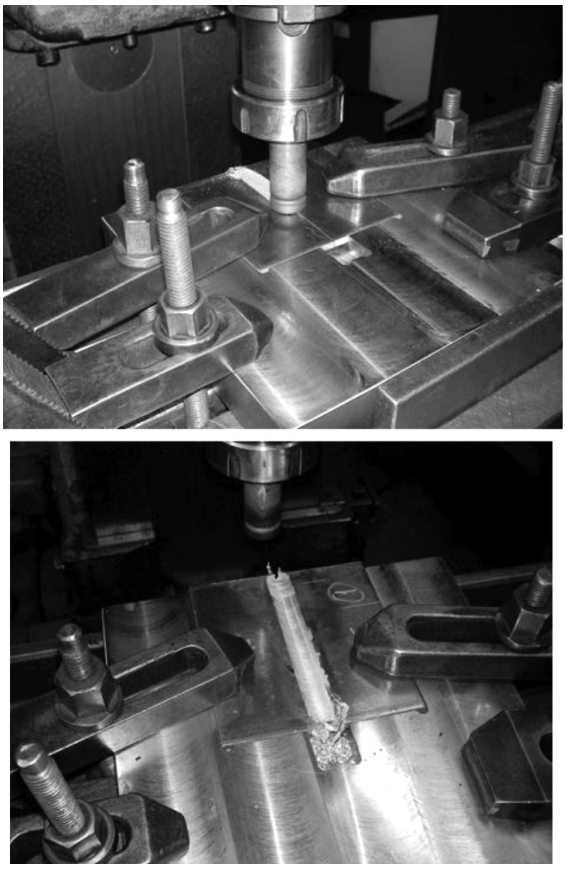

Figure 4: Performing the welding operation
Slika 4: Izvedba varjenja

stirrer pins. In the welding operations involving the circular, trapezoidal and triangular screwed 3-groove pins, the components were welded at a rotational speed of 1200 r/min and a movement rate of 28 mm/min. In the cases of the 4-groove pins, fractures occurred in the triangular and saw-type screwed pins. A good joint was achieved at the rotational rate of 1200 r/min and the movement rate of 28 mm/min.

Lastly, the joining operation was conducted with untapped stirrer pins. The joining could not be achieved with these pins when carried out on the basis of standard workpiece values. In order to ensure the joining, the movement rate was reduced to 28 mm/min and the rotation was increased to 1200 r/min according to our previous experiences and the joint was achieved in this manner. Afterwards, the process was finalized by performing joining operations with the 4-groove stirrer pins.

Since the triangular and saw-type threaded stirrer pins fractured at the selected standard rotational speed and movement rate, the stirrer-pin rotational speed was reduced to 710 r/min and the movement rate to 28 mm/min and the joining was performed in this manner; lastly, the untapped stirrer pins were used for the joining operation. When the joining operation with these pins was conducted at the standard workpiece values, the joining did not take place. In order to ensure the joining, the movement rate was 28 mm/min and the rotational speed was 1200 r/min.[32]

2.2 Tensile test

For the entire FSW using different stirrer pins, three tensile-test samples were extracted from the welding samples joined with the FSW method. The samples were cut to the desired dimensions with the erosion machine and prepared for testing. The tensile-test samples were prepared according to standards TSE 138 (EN 10002-1).[33] They were milled in a ZWICK tensile-testing device. During the test, the pulling speed was determined as 5 mm/min and the frontload as 10 N.

2.3 Microstructure, scanning electron microscopy (SEM) and energy dispersion spectrometry (EDS)

For the purpose of conducting a microstructural analysis, the welding samples joined with the screwed stirrer pins that display the highest and the lowest tensile strengths (triangular and circular screwed pins: samples 2, 4, 7, 8, 13) were selected. The samples were prepared with the standard metallographic sample-preparation method. At the end of this procedure, the samples were seared with a macro-searing machine.

A Prior light microscope was employed for scanning the microstructures and its images were transferred into a computer environment. In order to obtain the profiles of the microhardness distributions from the welded regions towards the main metal in the samples, loads of 100 g were applied on the samples with adjusted microstructures, and their Vickers ($HV_{0.1}$) microhardness levels were measured with a Shimadzu microhardness device. The measurements were repeated at least three times, within certain intervals, and the graphs were obtained after taking the arithmetic averages and standard deviations. In addition, in order to determine the coating status of the stirrer-pin samples according to the pin geometry, a scanning electron microscope was employed. For this purpose, a Jeol 6060 LV SEM device was used. To prove that the coated material was welded, an EDS analysis was conducted using the IXRF (X-ray fluorescence) system.

3 RESULTS AND DISCUSSION

3.1 Tensile-rest results and discussion

Duplicates of the tensile-test samples prepared according to the standards were created. After this stage, the sample components were ready for the tensile test. Significant variations in the tensile-stress values of the used stirrer pins depending on their geometries were observed. The samples were usually ruptured from the welded zone to the main metal. The rupture points of samples 2, 4 and 13 are shown in **Figure 5**.

The welded connections created with the FSW operations using the screwed pins exhibit higher tensile strengths compared to those of the unscrewed pins.

The obtained tensile values are displayed as a graph in **Figure 6**. In this figure, stirrer pin "0" indicates the unwelded Al7075 material.

The samples formed with the screwed stirrer pins exhibited tensile-strength values close to that of the main component. The highest tensile strength was achieved by the sample component formed with the triangular (metric) screwed stirrer pin. The lowest tensile strength was exhibited by the unscrewed conical profiled stirrer pin. Among the sample components made with the unscrewed stirrer pins, the highest tensile strength was achieved with the square profile stirrer pin. The tensile strengths of the samples acquired with the unthreaded

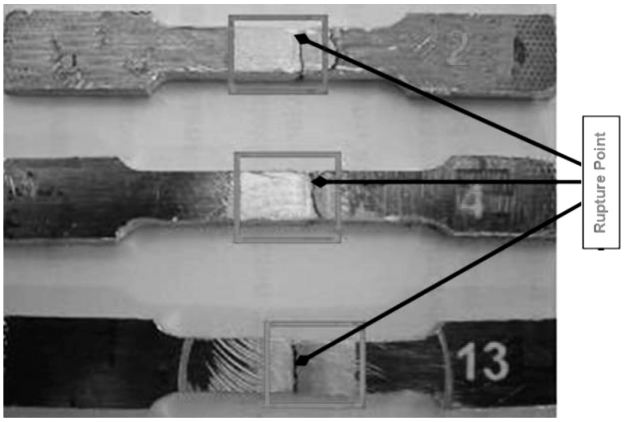

Figure 5: Rupture points on the samples used in the tensile test
Slika 5: Mesto porušitve pri nateznem preizkusu vzorcev

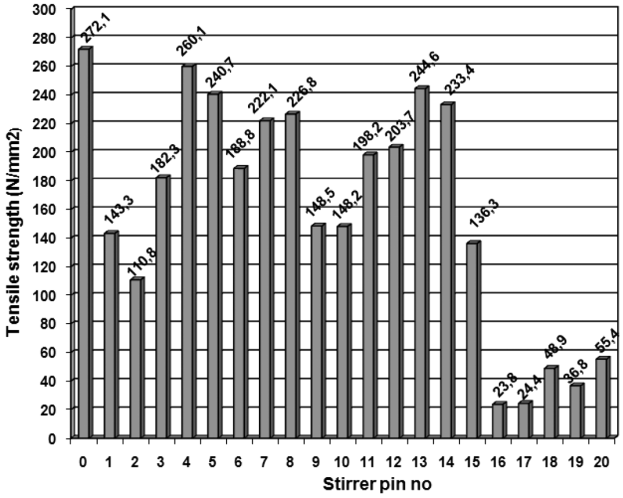

Figure 6: Tensile-test values of the welding samples created with FSW

Slika 6: Vrednosti, dobljene pri nateznem preizkusu vzorcev, zvarjenih s FSW

stirrer pins were well below the desired level. Therefore, the unthreaded pins were not used in the other analysis. The lowest tensile strength among the sample components made with the screwed stirrer pins was achieved with the circular screwed stirrer pin. On average, the lowest tensile strength among the sample components made with both the grooved and ungrooved screwed stirrer pins was achieved with the square screwed stirrer pin. In general, better tensile strengths were achieved when grooves in the screwed stirrer pins were opened. Only with the triangular screw does the ungrooved screwed stirrer pin provide an exception.

In order for an FSW operation to be effective, the surface of the stirrer pin needs to be large. For this reason, it is believed that the parameter of the surface area, which depends on the stirrer pin's geometry, directly affects the FSW operation. If the surface area increases, the emerging quantity of heat is higher as friction is more dominant. Thus, it can be stated that a smoother stir can be obtained when joining two components. However, for some samples of this study, possibly due to the stirring geometry, the stir at the welding root was not homogeneous. In such cases, a microstructure-characterization study was also performed.

3.2 Microstructure and characterization of the welding interface

The interface microstructures of the samples used in the FSW process are shown in **Figures 7a** to **7f**. In sample 2 (the circular screwed stirrer pin), microfractures were found at the root of the weld. These fractures probably caused the mixture not to be effective. Hence, the tensile strengths of these samples turned out to be low (**Figure 7a**). It is seen that the FSW operations involving samples 4, 7 and 8 (triangular (metric) screwed stirrer pin, 3-groove circular screwed stirrer pin and 3-groove triangular (metric) screwed stirrer pin, respectively) were more successful. No problems such as disintegration or cracking between the weld and the main metal were observed (**Figures 7b** to **7d**). However, the formation of thin cracks seen on sample 13 (the 4-groove triangular (metric) screwed stirrer pin) is thought to be resulting from the thermal expansion (**Figure 7f**).

The samples prepared for the microstructural analysis were used for microhardness measurements. During these measurements, a 100 g (0.1 HV) pressure in terms of HV (Vickers) was applied for 5 s. The hardness was measured at 3 different zones, starting at the weld zone,

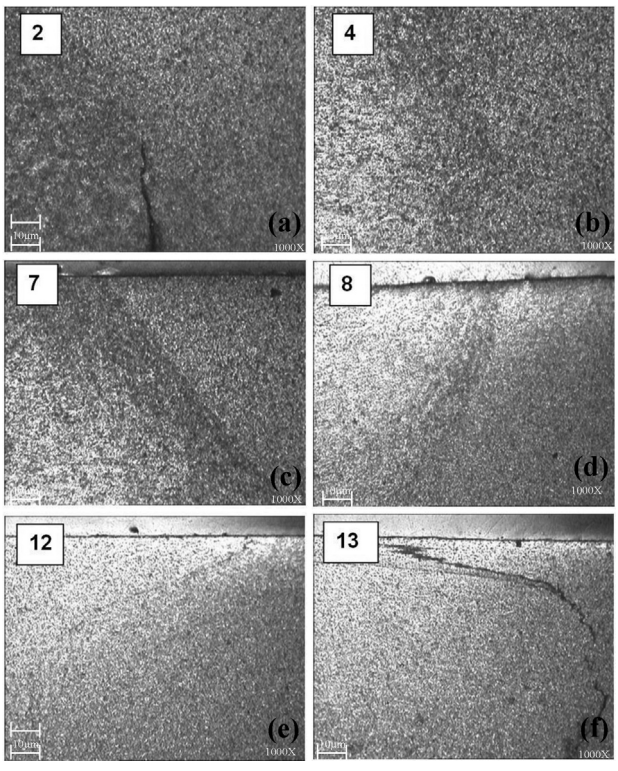

Figure 7: Microstructure images of samples joined with stirrer pins nos. 2, 4, 7, 8, 12 and 13

Slika 7: Posnetki mikrostrukture vzorcev, spojenih z vrtilno konico št. 2, 4, 7, 8, 12 in 13

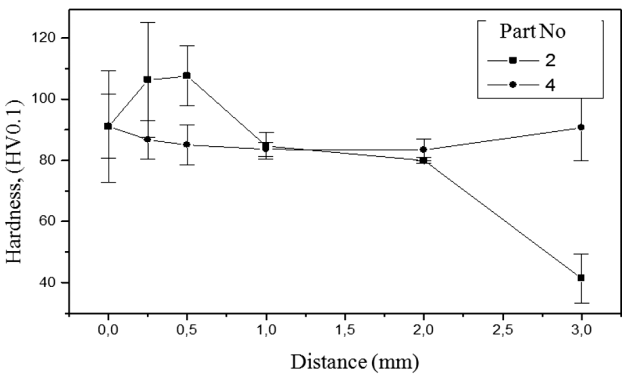

Figure 8: Comparison of microhardness values for samples nos. 2 and 4

Slika 8: Primerjava vrednosti mikrotrdote vzorcev št. 2 in 4

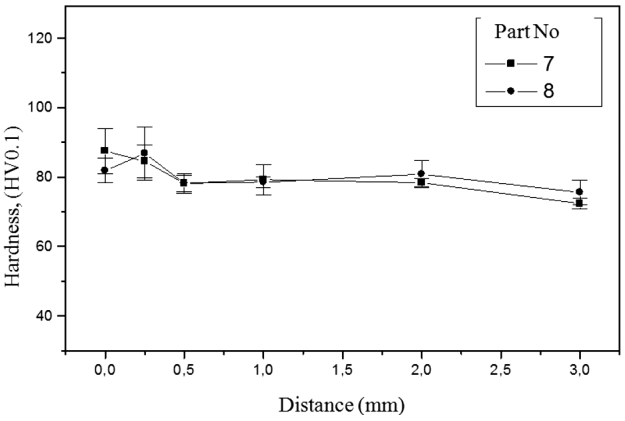

Figure 9: Comparison of microhardness values for samples nos. 7 and 8

Slika 9: Primerjava vrednosti mikrotrdote vzorcev št. 7 in 8

at distances of (0.25, 0.5, 1, 2 and 3) mm. The determined microhardness average and the standard deviation were calculated. Graphs of the determined values were prepared for comparison.

In **Figures 8** to **10** the graphs displaying the microstructure profiles of the samples subjected to the FSW operation, measured at specific intervals from the weld zone towards the main metal are given. These graphs provide significant information about whether the FSW operations were conducted correctly or not. In **Figure 9**, the hardness profiles belonging to samples 7 and 8 relate to the FSW operation conducted with the 3-groove circular screwed stirrer pin and 3-groove triangular (metric) screwed stirrer pin. It is observed that the hardness profiles of the samples exhibit similar tendencies after both situations. No significant variation is observed in the hardness tendencies from the weld zone towards the main metal. This situation explicitly demonstrates that the other mechanical properties of these samples may also be superior. However, it is seen that the hardness relatively increased in sample 8, made with the 3-groove triangular (metric) screwed stirrer pin, at about a distance of 0.25 mm from the weld zone. The potential reason behind this situation may be the thinning of crystallized grains as a consequence of excessive heat and sudden cooling taking place at this region. As it is known, a deformation of crystal grains of a material whose recrystallization mechanism was deformed, takes place as a result of the formation of subgrain boundaries at the end of dynamic recovery that occurs due to a polygonization of dislocations when the material's temperature reaches between 1/3–2/3 of its melting temperature. Probably, this mechanism took place in sample 8. At the same time, the tensile values of samples 7 and 8 can be explained with their hardness profiles and they turn out to be similar. In general, it is observed that the average hardness tendencies of these samples are relatively lower compared to the other samples. This may be considered to be leading to the relatively lower tensile strengths of these samples. The fact that the average hardness of these samples turned out to be low can be attributed to a larger temperature increase in these samples during the FSW operation. It can be shown that the higher friction provided by the stirrer pins used for these samples causes the temperature of the samples to become higher.

Figure 8 shows the hardness profiles for samples 2 and 4 after the FSW operation was conducted with the circular screwed stirrer pin and triangular (metric) screwed stirrer pin, respectively. It was observed that the distribution of the hardness for sample 4, the material with which the triangular (metric) screwed stirrer pin was used and which yielded the best result in the study, is more homogenous compared to all the other samples. This demonstrates that both the weld zone and the main metal were more modified in terms of the microstructure and chemical composition. This situation can also be seen clearly in **Figure 7b**. When the hardness profile for sample 2, whose FSW operation was done with the circular screwed stirrer pin, is examined, it is deduced from the increasing hardness that in this sample, deformation hardening might have occurred in the region near the joining area (at the 0–0.5 mm interval). However, extreme deformation hardening may lead to microfractures like the ones that occurred in this sample due to an excessively increased density of dislocations. These microfractures, in turn, led to the sample's low tensile strength. It is likely that the decreasing effectiveness of the FSW was due to inadequate heat. Along with the inadequate level of the heat, an excessive plastic deformation might have lead to deformation hardening.

In **Figure 10**, the hardness profiles for samples 12 and 13, whose FSW operations were conducted with the 4-groove circular screwed stirrer pin and 4-groove triangular (metric) screwed stirrer pin, respectively, are demonstrated. Significant drops and rises in sample 13, in the regions near the joining area, stand out, while the hardness profile of sample 12 is smoother compared to sample 13. A possible reason behind this is thought to be the capillary fractures arising from the thermal expansion as seen from **Figure 7f** as well. For welded joints, this is

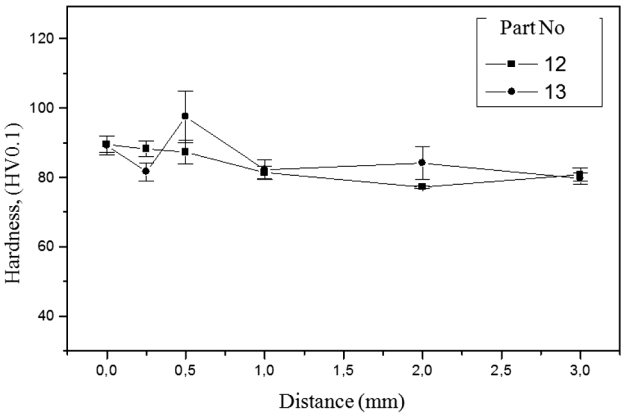

Figure 10: Comparison of microhardness values for samples nos. 12 and 13

Slika 10: Primerjava vrednosti mikrotrdote vzorcev št. 12 in 13

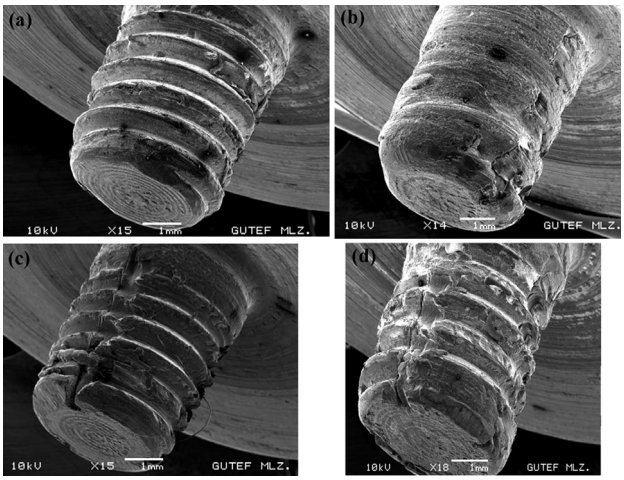

Figure 11: SEM images of stirrer pin: a) no. 4 (triangular screwed), b) 2 (circular screwed), c) 8 (3-groove triangular screwed) and d) 13 (4-groove triangular screwed)

Slika 11: SEM-posnetki vrtilnih konic: a) št. 4 (trikotni vijak), b) 2 (krožni navoj), c) 8 (trikotni vijak s tremi zarezami) in d) 13 (trikotni vijak s štirimi zarezami)

perceived to be a critical problem. However, if no such problem occurred in this sample, we could expect its hardness profile to be higher and smoother and, correspondingly, we could expect it to exhibit the highest tensile strength.

In order to see the changes in the physical structures of the stirrer pins after a welding operation, SEM images of some stirrer pins (triangular and circular screwed) were taken. The stirrer-pin images taken with SEM are given in **Figure 11**.

When the SEM images were analyzed, as seen at the first sight, a higher amount of the joining material was found to be covering the circular screwed stirrer pin compared to the triangular screwed stirrer pin. It was also observed that the circular screwed stirrer pin demonstrated the lowest strength among the screwed types during the tensile test and the highest joining strength

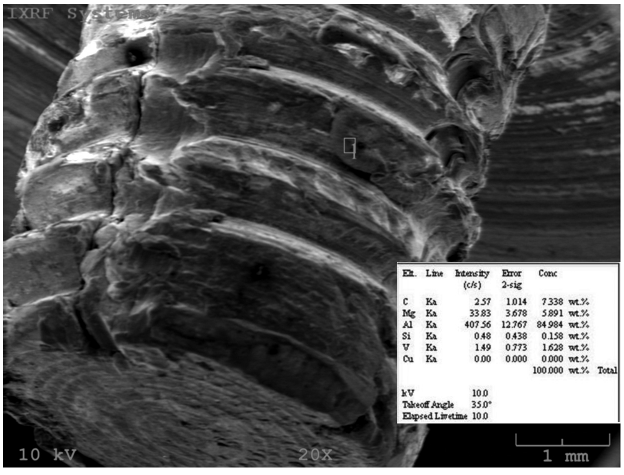

Figure 12: Stirrer pin on which EDS analysis was conducted

Slika 12: Vrtilna konica z označenim mestom EDS-analize

was obtained with the triangular screwed stirrer pin. On the basis of this observation, we can state that one reason why the joining performed with the circular screwed stirrer pin failed to display an adequate strength is the fact that a portion of the material was being deposited on the stirrer pin. In addition, it can be asserted that the grooves employed on the stirrer pins yield higher joining strengths than the ungrooved stirrer pins.

3.3 EDS analysis of a stirrer pin

For the purpose of making a partial estimation of the stirrer-pin lifetime, an EDS analysis of a stirrer pin was carried out (**Figure 12**). The EDS analysis was conducted in the marked zone on the stirrer pin and the materials found in it were determined.

After the analysis, no fragment was found to be broken from the stirrer pin's material. According to this result, we can assume that the stirrer pin can have a long lifetime. Also, we can presume that since the Al-alloy that collects over the stirrer-pin cavities and grooves due to the heat at each joining, a decrease in the performance of the stirrer pin will not take place.

4 DISCUSSION

The internal structure formed at the weld zone after the friction-stir welding consists of three different regions: the recrystallized region (RCR), the thermo-mechanically affected region (TAR) and the region under the influence of heat.

It was observed that the hardness increased in the weld zone of sample 2 (the circular screwed stirrer pin) and the hardness distribution from the weld zone towards the main metal decreased. However, there was no noteworthy variation in the hardness distribution between the weld zone and the main metal in sample 4 (the triangular screwed stirrer pin). Homogenous distributions of the microstructure and the hardness are essential for achieving the superior mechanical properties expected from the welded joints. On the other hand, the yield and tensile strength are proportional to the hardness. It is believed that even though the hardness level at the weld zone for sample 4 turned out to be lower than that of sample 2, the fact that its microstructure and hardness distributions are more homogenous leads to an increase in the sample's tensile strength. The microfractures seen at the welding root of sample 2 indicate that an effective stir did not take place and it is thought that this caused the tensile strength to be low.

Even though the hardness values for samples 7 and 8 were relatively a bit higher at the weld zones than at the main metal, it can be stated that they exhibited homogenous hardness distributions. Moreover, the hardness levels of both samples are similar in all the regions. Therefore, it is understood that both pins yield results similar to these properties.

Even though the hardness distribution in sample 13 (the triangular screw stirrer pin) was expected to be homogenous, or just slightly higher at the midpoint of the weld zone, it was found to be higher in the region close to the main metal. The probable reason for this is an excessive increase in the temperature in the unmelted region close to the main metal because the friction stirring of the pin with this geometry is more dominant and, along with that, the grain structure becomes finer due to the influence of fast cooling. As for the hardness distribution in sample 12 (the circular screw stirrer pin) it is much more homogenous.

In general, it was observed that an increase in the hardness in the weld zones or regions close to the joining areas of the analyzed and discussed samples leads to an increase in their tensile strengths.

It was observed that the tensile values for the samples whose microstructures and microhardnesses demonstrate homogenous distributions are similar to those of the main metal. It was seen that the size and shape of the regions formed as a result of joining depend on the geometry of the stirrer pin. Hence, it can be concluded that the geometry of the stirrer pin has a significant effect on the mechanical behavior.

5 CONCLUSIONS

In this study, joining operations were carried out by employing the friction-stir welding technique. On the basis of the samples joined in this way, the stirrer pin providing the best performance was determined with tensile tests, microstructure characterizations, SEM and EDS.

As a result of the conducted studies, the results given below were obtained:

- It was observed that the welding seam made with the FSW is smoother than the seams obtained with the other methods.
- Among the stirrer pins, the best performance and highest joining strength were achieved with the triangular thread. It is suggested that this type is preferred in stirrer-pin designs.
- Neither the joining surface nor the tensile strength turned out to be at the desired level in the welds performed with the unscrewed stirrer pins.
- Among the joints made with the screwed stirrer pins, the poorest results were obtained with the circular threaded stirrer pins.
- As we had theoretically predicted, the lowest strengths were achieved with the conductive screws.
- Using the FSW method, a tensile-strength value close to the one of the main metal can be achieved.
- In the stirrer-pin designs, screwed types should be preferred as they facilitate the flow of the welding seam.
- The pins with large friction surfaces facilitate more homogenous and better joints.
- An increase in the hardness in the regions of the weld zone or close to the joining area increases the tensile-strength values.
- A larger friction surface of a stirrer pin increases the tensile strength of the welded joint.

6 REFERENCES

[1] G. Cam, Friction Stir Welding and Applications, 9th Materials Symposium Proceedings, Pamukkale University, Denizli, 2002, 450–458

[2] M. W. Mahoney, C. G. Rhodes, J. G. Flintoff, W. H. Bingel, R. A. Spurling, Properties of friction-stir-welded 7075 T651 aluminum, Metallurgical and Materials Transactions A, 29 (**1998**) 7, 1955–1964, doi:10.1007/s11661-998-0021-5

[3] D. P. Field, T. W. Nelson, Y. Hovanski, K. V. Jata, Heterogeneity of crystallographic texture in friction stir welds of aluminum, Metallurgical and Materials Transactions A, 32 (**2001**) 11, 2869–2877, doi:10.1007/s11661-001-1037-2

[4] T. U. Seidel, A. P. Reynolds, Visualization of the material flow in AA2195 friction-stir welds using a marker insert technique, Metallurgical and Materials Transactions A, 32 (**2001**) 11, 2879–2884, doi:10.1007/s11661-001-1038-1

[5] W. M. Thomas, E. D. Nicholas, J. C. Needham, M. G. Murch, P. Templesmith, C. J. Dawes, Improvements to Friction Welding, GB Patent Application No.9125978.8, 1991

[6] C. Dawes, W. Thomas, Friction Stir Joining of Aluminium Alloys, TWI Bulletin, 6 (**1995**), 124

[7] G. Çam, Improved New welding Technology for Al-Alloys, Engineers and Machinery, 46 (**2005**), 30–39

[8] G. Çam, Developments in Friction Stir Welding, Part 1, Machine Technology, 80 (**2004**), 44–49

[9] G. Çam, Developments in Friction Stir Welding, Part 2, Machine Technology, 81 (**2004**), 100–104

[10] M. K. Külekçi, A. Şık, Sürtünme Karıştırma Kaynağı İle Alüminyum Alaşımı Levhaların Birleştirilmesi Ve Elde Edilen Kaynaklı Bağlantıların Mekanik Özellikleri, Süleyman Demirel Üniversitesi Fen Bilimleri Enstitüsü Dergisi, 2003, 70–75

[11] G. Çam, Developments in the Tool Used in Friction Stir Welding, TMMOB Chamber of Mechanical Engineers, Welding Technology, IV. National Convention And Exhibition, Kocaeli, 2003, 47–62

[12] M. Boz, A. Kurt, The influence of stirrer geometry on bonding and mechanical properties in friction stir welding process, Materials and Design, 25 (**2004**) 4, 343–347, doi:10.1016/j.matdes.2003.11.005

[13] K. Kolligan, Material Flow Behavior during Friction Stir Welding of Aluminum, Weld Res. Supply, (**1999**), 229-237

[14] K. V. Jata, S. L. Semiatin, Continious Dynamic Recristalization During Friction Stir Welding of High Strength Aluminum Alloys, Scripta Materialia, 43 (**2000**), 743–749, doi:10.1016/s1359-6462(00)00480-2

[15] W. M. Thomas, E. D. Nicholas, Friction stir welding for the transportation industries, Materials and Design, 18 (**1997**) 4, 269–273, doi:10.1016/s0261-3069(97)00062-9

[16] K. Elangovan, V. Balasubramanian, M. Valliappan, Effect of Tool Pin Profile and Tool Rotational Speed on Mechanical Properties of Friction Stir Welded AA6061 Aluminium Alloy, Materials and Manufacturing Processes, 23 (**2008**) 3, 251–260, doi:10.1080/10426910701860723

[17] H. Fujii, L. Cui, M. Maeda, K. Nogi, Effect of tool shape on mechanical properties and microstructure of friction stir welded aluminum alloys, Materials Science and Engineering A, 419 (**2006**) 1, 25–31, doi:10.1016/j.msea.2005.11.045

[18] S. J. Vijay, N. Murugan, Influence of tool pin profile on the metallurgical and mechanical properties of friction stir welded Al–10 wt.% TiB_2 metal matrix composite, Materials and Design, 31 (**2010**) 7, 3585–3589, doi:10.1016/j.matdes.2010.01.018

[19] K. Elangovan, V. Balasubramanian, Influences of tool pin profile and welding speed on the formation of friction stir processing zone in AA2219 aluminium alloy, Journal of Materials Processing Technology, 200 (**2008**) 1, 163–175, doi:10.1016/j.jmatprotec.2007.09.019

[20] M. Mehta, A. Arora, A. De, T. Debroy, Tool Geometry for Friction Stir Welding – Optimum Shoulder Diameter, Metallurgical and Materials Transactions A, 42 (**2011**) 9, 2716–2722, doi:10.1007/s11661-011-0672-5

[21] K. Elangovan, V. Balasubramanian, Influences of tool pin profile and tool shoulder diameter on the formation of friction stir processing zone in AA6061 aluminium alloy, Materials and Design, 29 (**2008**) 2, 362–373, doi:10.1016/j.matdes.2007.01.030

[22] K. Elangovan, V. Balasubramanian, M. Valliappan, Influences of tool pin profile and axial force on the formation of friction stir processing zone in AA6061 aluminium alloy, The International Journal of Advanced Manufacturing Technology, 38 (**2011**), 285–295, doi:10.1007/s00170-007-1100-2

[23] C. Blignault, D. G. Hattingh, M. N. James, Optimizing Friction Stir Welding via Statistical Design of Tool Geometry and Process Parameters, Journal of Materials Engineering and Performance, 21 (**2012**) 6, 927–935, doi:10.1007/s11665-011-9984-2

[24] H. Li, D. Mackenzie, R. Hamilton, Parametric finite-element studies on the effect of tool shape in friction stir welding, Proceedings of the Institution of Mechanical Engineers, Part B: Journal of Engineering Manufacture, 224 (**2010**) B8, 1161–1173, doi:10.1243/09544054jem1810

[25] M. Akkurt, Makina Elemanlari Problemleri, Birsen Yayinevi, 1994

[26] B. London, M. Mahoney, B. Bingel, M. Calabrese, D. Waldron, Experimental Methods for Determining Material Flow in Friction Stir Welds, Proceedings of the Third International Symposium on Friction Stir Welding, Kobe, Japan, 2001

[27] C. G. Rhodes, M. W. Mahoney, W. H. Bingel, R. A. Spurling, C. C. Bampton, Effects of FSW on Microstructure of 7075 Aluminum, Scripta Materialia, 36 (**1997**), 69–75, doi:10.1016/s1359-6462(96)00344-2

[28] G. Liu, L. E. Murr, C. S. Niou, J. C. McClure, F. R. Vega, Micro Structural Aspects of the Friction Stir Welding of 6061-T6 Aluminum, Scripta Materialia, 37 (**1997**), 355–361, doi:10.1016/s1359-6462(97)00093-6

[29] S. Benavides, Y. Li, L. E. Murr, D. Brown, J. C. McClure, Low Temperature Friction Stir Welding of 2024 Aluminum, Scripta Materialia, 41 (**1999**), 809–815, doi:10.1016/s1359-6462(99)00226-2

[30] S. Özkan, H. Basak (Supervisor), Sürtünme Karıştırma Kaynağı İle Birleştirilen Parçalarda Haddeleme (Burnishing) İle Yüzeylerin İşlenmesi, Haddelemenin Yüzey Pürüzlülüğü Ve Sertleşmeye Etkisinin İncelenmesi, Gazi Üniveristesi Fen Bilimleri Enstitüsü, Yüksek Lisans Tezi, 2006

[31] H. Basak, S. Ozkan, A. Taskesen, Application of burnishing process on friction stir welding and investigation of the effect of burnishing process on the surface roughness, hardness and strength, Experimental Techniques, 35 (**2011**) 1, 8–16, doi:10.1111/j.1747-1567.2009.00555.x

[32] K. Kaptan, H. Basak (Supervisor), Sürtünme karıştırma kaynağı birleştirmelerinde farklı karıştırıcı uç formlarının birleştirme kalitesine etkilerinin incelenmesi, Gazi Üniveristesi Fen Bilimleri Enstitüsü, Yüksek Lisans Tezi, 2009

[33] Turkish Standards Institution, TS 138 EN 10002-1:1996, Metallic materials – Tensile testing, Part 1: Method of test at ambient temperature, 1996

UDK 691:620.1:691.3:620.179.1
Original scientific article/Izvirni znanstveni članek

ISSN 1580-2949
MTAEC9, 49(5)703(2015)

MONITORING EARLY-AGE CONCRETE WITH THE ACOUSTIC-EMISSION METHOD AND DETERMINING THE CHANGE IN THE ELECTRICAL PROPERTIES

PREGLED SVEŽEGA BETONA Z METODO AKUSTIČNE EMISIJE IN DOLOČANJEM SPREMEMB ELEKTRIČNIH LASTNOSTI

Lubos Pazdera[1], Libor Topolar[1], Marta Korenska[1], Tomas Vymazal[1], Jaroslav Smutny[1], Vlastimil Bilek[2]

[1]Brno University of Technology, Faculty of Civil Engineering, Veveri 331/95, 602 00 Brno, Czech Republic
[2]ZPSV a.s., Uhersky Ostroh, Czech Republic
pazdera.l@fce.vutbr.cz

Prejem rokopisa – received: 2014-07-18; sprejem za objavo – accepted for publication: 2014-11-05

doi:10.17222/mit.2014.112

Concrete is the most popular building composite material (CM). Its long-term aging properties depend on the mixture, the setting and the curing. When concrete is produced and used in the place where we want it to be for the whole of its life, it is very sensitive and easily ruined. Curing is one of the things that we do to keep concrete protected during the first week or so of its life: we maintain proper temperature (neither too hot nor too cold) and dampness. The acoustic-emission method and the electrical-property measurement technique are applied to monitor early-age concrete. The relationships between the acoustic-emission activity, the temperature and the electrical properties, e.g., the resistivity and the capacity of concrete at an early age were studied in this research. W. Chen et al. studied the microstructure development of hydrating cement pastes during early ages using non-destructive methods including the ultrasound P-wave propagation-velocity measurement and non-contact electrical-resistivity tests. Nevertheless, there are not many references about the continuous study of the properties of concrete during an early age. A long-time monitoring of concrete properties is necessary to determine its lifetime and quality. The acoustic-emission method was proven to be a very advantageous tool for a non-destructive monitoring of structural micro-changes during the lifetime of concrete. The differences between hardened concrete mixtures detected with acoustic emission can partly determine their properties at the age of 28 d. The basic concrete property is its compressive strength after 28 d; nevertheless, this can change over a long time period, thus a continuous measuring needs to be applied.

Keywords: concrete, acoustic emission, electrical properties, early age, lifetime, curing

Beton je najbolj priljubljen gradbeni kompozitni material (CM). Njegove dolgoletne lastnosti so odvisne od mešanice, položitve in strjevanja. Ko je beton izdelan in ko ga položimo na mesto, kjer naj bi bil do konca trajnostne dobe, je zelo občutljiv in se lahko poškoduje. Strjevanje je ena od stvari, ki zahteva zaščito betona v prvih tednih njegovega trajanja s pravilno temperaturo (niti pretoplo niti prehladno) in vlažnostjo. Metoda akustične emisije in meritve električnih lastnosti so bile uporabljene za kontrolo mladega betona. Preiskovana je bila odvisnost med aktivnostjo akustične emisije in temperaturo, električnimi lastnostmi, kot sta upornost in kapacitivnost mladega betona. W. Chen s sodelavci je študiral razvoj mikrostrukture mlade hidratantne cementne zmesi z neporušnimi metodami, vključno z merjenjem hitrosti napredovanja ultrazvočnih P-valov, in naredil preizkuse brezkontaktne električne upornosti. Vseeno ni veliko literaturnih virov o kontinuirnem spremljanju lastnosti mladega betona. Za določitev zdržljivosti in kvalitete betona je potrebna dolgotrajna kontrola. Metoda akustične emisije se je izkazala kot napredno orodje za neporušno kontrolo mikrospremememb zgradbe med trajnostno dobo betona. Razlike, ugotovljene z akustično emisijo med mešanicami betona pri strjevanju, so delno določile njihove lastnosti po 28 d. Osnovna lastnost betona je 28-dnevna tlačna trdnost; vendar se ta lahko spreminja v daljšem časovnem obdobju, zato se uporabljajo kontinuirne meritve.

Ključne besede: beton, akustična emisija, električne lastnosti, zgodnja starost, trajnostna doba, strjevanje

1 INTRODUCTION

Cement hydration plays a critical role in the temperature development of early-age concrete due to the heat generation[1–4]. It also has significant effects on the material properties and performances at an early age, including material strengths[5], critical stresses[6] and distresses like cracking[7]. Therefore, it is essential to capture the hydration property and temperature development of concrete at an early age to prevent premature failures. It is known that the durability of cement-based products and concrete structures is highly influenced by the early stages of hydration[8]. A precise knowledge of the micro-mechanical properties during the successive phases of the hydration process provides information on the concrete resistance and allows an assessment of its durability[9]. Several non-destructive techniques have been developed and applied in that respect, most of them based on ultrasonic-wave measurements[10]. The recording of passive energy using acoustic-emission techniques was used to evaluate the structural activity in concrete during the early ages, showing periods of intense micro-structural changes during the curing process[11].

Microstructural changes occurring in freshly poured concrete during the curing were monitored on a laboratory scale using a combination of the acoustic-emission technique and the monitoring of electrical properties[12]. The acoustic-emission method is a passive-ultrasonic-

signal recording technique allowing an online monitoring of the internal microstructural activity of young concrete during the hydration process[8]. The acoustic-emission technique, which is one of the non-destructive evaluation techniques, is a useful method for investigating local damage in concrete during its lifetime[13]. The micro-changes in concrete structures can be easily estimated, taking account of the number of acoustic-emission hits and counts of the acoustic-emission signal[14]. Acoustic-emission signals are detected, due to microcracks (i.e., structural changes in the material) by the acoustic-emission sensors attached to the surface of a concrete specimen. The acoustic-emission parameters such as the number of hits, counts, duration time, amplitude, energy and rise time are recorded by the acoustic-emission measurement system[15].

Impedance spectroscopy, called also dielectric spectroscopy, the monitoring of electrical properties and nuclear-magnetic-resonance spectroscopy have become promising techniques for probing cements and concretes[16]. Cement paste is electrically conductive due to its interconnected pore network filled with an aqueous phase containing mobile ions such as Na^+, K^+ and OH^-.[17] Electrical conductivity and resistivity are effective parameters used to monitor the microstructural features of cement-based materials. The electrical conductivity of cement-based materials is dependent on the porosity, the pore connectivity and the conductivity of the pore solution, all of which are significant for the durability of the material[18]. The impedance characteristics and spectra recorded over a wide range of frequencies (if possible from 100 mHz to 10 MHz or higher) provide new information and an insight into the concrete microstructure and hydration[19]. Electrical resistivity is related to the reinforcement corrosion, moisture and heat transfer in concrete[20].

2 EXPERIMENTAL SET-UP

An acoustic-emission measuring system called LOCation ANalyser (LOCAN) 320 made by PAC (France) was used for the measurements. Wide-band sensors (made by the 3S Sedlak Company) were used. The sensor output was connected to pre-amplifiers (the PAC Company) with a 2 kHz high-pass filter. The proprietary PAC program package was used to record the acoustic-emission parameters. The acoustic-emission signals were taken by a LOCAN 320 acoustic-emission localizer. The LOCAN 320 system was fine-tuned at a well site and with a sonic-logging tool in the wellbore, with the acoustic threshold set slightly above the background-noise level as measured by LOCAN 320 and the internal gain set according to the manufacturer's recommendations. This device was designed to record and evaluate ultrasonic signals. It was used to analyze and store the acoustic-emission parameters. It can process signals coming from four measuring points. Each recorded event can be characterized with the following acoustic-emission parameters: recording date and time, (maximum) amplitude, acoustic-emission energy, count, rise time and mean frequency[21].

The impedance of the material under investigation changes in accordance with the structural changes, particularly the water absorption and evaporation. A change in the resistance is obvious. The capacity C of a parallel-plate capacitor is computed with:

$$C(f) = \varepsilon_r \cdot \varepsilon_0 \cdot \frac{S}{d} \tag{1}$$

where ε_r is the relative permittivity, ε_0 is the vacuum permittivity ($8.854 \cdot 10^{-12}$ F/m), S is the measuring-electrode area, d is the distance and f is the frequency. The resistance, R, of the electrodes is given by:

$$R(f) = \rho \cdot \frac{d}{S} \tag{2}$$

where ρ is the resistivity. Microstructural changes in a material make the material's permittivity change. The permittivity value can also be affected by macrocracks, depending on the frequency[22].

Two cylindrical steel electrodes of a diameter of 6 mm, buried 65 mm under the specimen surface, were used for measuring the resistance. To measure the capacitance, two rectangular metal-plate electrodes with dimensions of 25 mm × 45 mm were applied. All the electrodes were fixed to a plastic slab so that their constant configuration was guaranteed. The electrodes and the temperature-sensor outputs were connected to an automated measuring device. The measurements of the capacitance, the temperature and the impedance were started within 15 min after the mixture preparation. This phase of the experiment was carried out using a TESLA BM 595 RLCG bridge and a selector switch. The measurement was carried out at selected points with frequencies in the range from 100 Hz to 20 kHz. Each of the electrical quantities (resistance, capacitance, temperature, etc.) was measured separately[23].

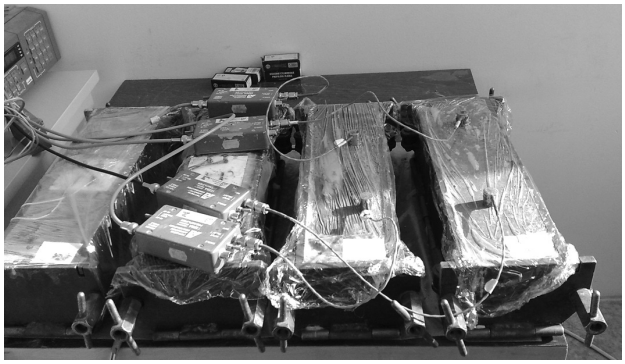

Figure 1: Experimental set-up before unmoulding, (samples S1, S2 tested with the acoustic-emission method and S3, S4 with impedance spectroscopy)
Slika 1: Eksperimentalni sestav pred razdrtjem (vzorca S1, S2 preizkušena z metodo akustične emisije in S3, S4 z impedančno spektroskopijo)

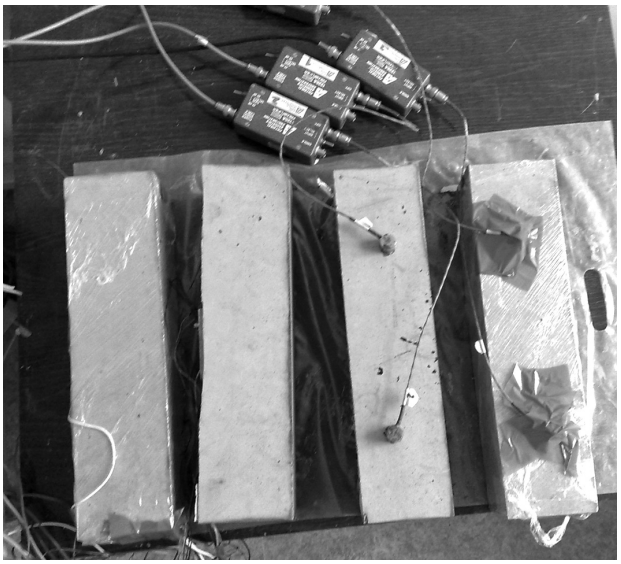

Figure 2: Experimental set-up after unmoulding (sample S1 and S4 are covered, S2 and S3 are uncovered)
Slika 2: Eksperimentalni sestav po razdrtju (vzorca S1 in S4 sta pokrita in S2 ter S3 nepokrita)

Sleeper concrete with a 32 mm crushed aggregate attained a compression strength of 107 MPa. Two of the specimens with dimensions of 100 mm × 100 mm × 400 mm were mould cast. Steel-mould upper sides were covered with PE foil (**Figure 1**). The components of the mixture are shown in **Table 1**. The mechanical properties of the monitored samples are statistically processed in **Table 2**. When the specimens were unmoulded, 24 h after the mixing, one specimen was covered with foil and the other one was not (**Figure 2**). In **Figures 1** and **2**, samples S1 and S2 are tested with the acoustic-emission method and samples S3 and S4 with impedance spectroscopy; samples S1 and S4 are covered.

Table 1: Concrete mixture
Tabela 1: Mešanica betona

Composition	Mass, *m*/kg
Cement CEM I 42.5R	390
Water	125
Plasticizer Stachement 2060	4
Sand 0/4	700
Coarse aggregate 16/32	1275

3 RESULTS

The acoustic-emission activities of both samples during hydration, hardening and setting are shown in **Figures 3** and **4**. After the unmoulding, i.e., at the age of 24 h, when one sample was wrapped and the other one was left without any protection, the acoustic-emission activities were different. The increase in the cumulative acoustic-emission-count curve of the protected sample is lower than that of the sample without protection during the whole 120 d period, as shown in **Figure 4**. It should

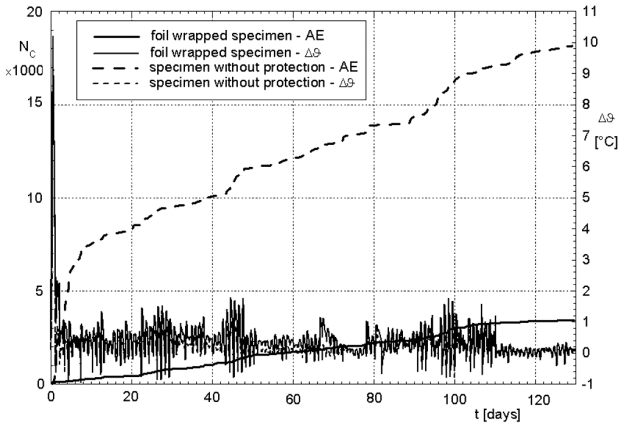

Figure 3: Dependence of cumulative acoustic emission (N_C) and temperature difference ($\Delta\vartheta$) on time (t)
Slika 3: Odvisnost kumulativne akustične emisije (N_C) in temperaturne razlike ($\Delta\vartheta$) od časa (t)

be noted that the acoustic-emission signals were picked up six hours after the mixtures were made.

The temperature of the samples after the unmoulding was kept close to the ambient temperature (**Figure 3**). The basic changes in the concrete structure during the hydration relate to the temperature peak, in this case after 12 h, as shown in **Figure 4**.[24] The temperature curves for both samples are the same as before the unmoulding, i.e., slightly different[25].

Electrical measurements show a higher resistivity and a lower capacity, i.e., a higher capacitance of the specimen without protection after the unmoulding (**Figure 5**).

Different changes of both samples are also shown in **Figure 6**. On the first day the frequency characteristics of resistance (R) and capacitance (X_C) are the same, but thereafter they are different. There are three types of curves described in the legend in **Figure 6**. Each curve, as described on the curve at the 6th h, consists of eight points whose frequencies from the left-hand side of the horizontal axis are 100 Hz, 200 Hz, 400 Hz, 1 kHz,

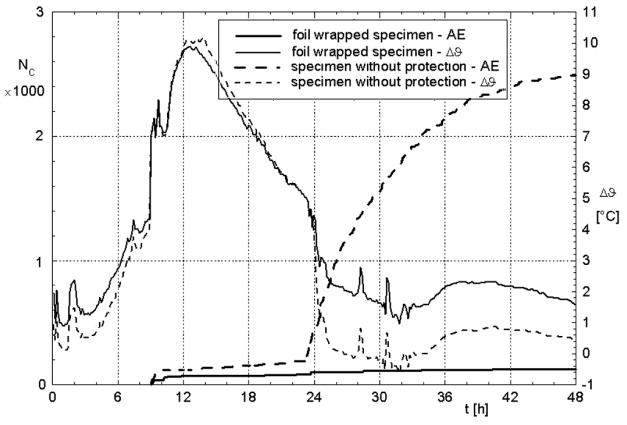

Figure 4: Details of the curves plotted in **Figure 3** for the first two days
Slika 4: Detajl krivulje s **slike 3** za prva dva dneva

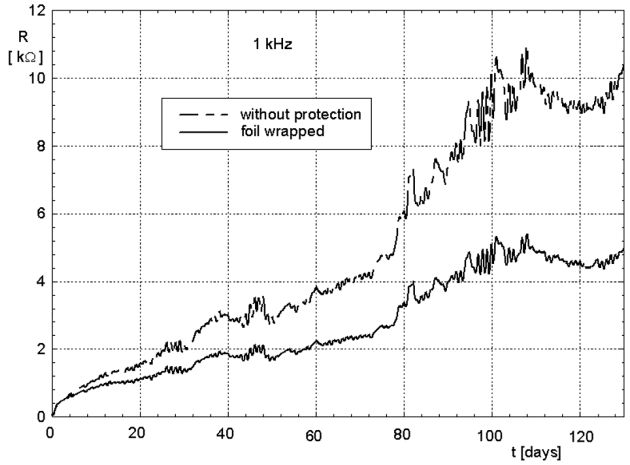

Figure 5: Dependence of electrical resistance (*R*) and capacity (*C*) on time (*t*)
Slika 5: Odvisnost električne upornosti (*R*) in kapacitete (*C*) od časa (*t*)

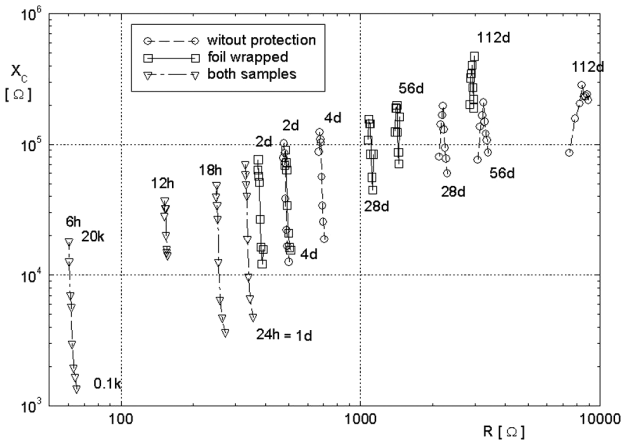

Figure 6: Dependence of capacitance (X_C) on resistance (*R*)
Slika 6: Odvisnost kapacitivnosti (X_C) od upornosti (*R*)

2 kHz, 4 kHz, 10 kHz and 20 kHz [26]. It is clear that the shapes of the curves are different after the unmoulding, therefore, the curves of both samples are the same on the first day (in **Figure 6** marked with downward-pointing triangles).

Table 2: Main parameters of samples
Tabela 2: Glavni parametri vzorcev

	Units	Mean	Deviation
Compressive strength	MPa	107	5
Flexural strength	MPa	10.0	0.2
Modulus of elasticity (bending)	GPa	37	3
Fracture toughness	MPa $m^{1/2}$	1.8	0.4
Fracture energy	J/m^2	200	10

4 CONCLUSION

The acoustic-emission method and impedance spectroscopy are powerful tools for determining the development of microcracks during the hardening and setting of concrete. It can be assumed that higher numbers of microcracks cause higher numbers of acoustic-emission events. The dependence of a cumulative acoustic-emission activity on the time shows the necessity of curing the concrete during its whole lifetime, especially during intense hydration and hardening. The big differences between the acoustic-emission activities of wrapped and unprotected samples clearly indicate the essentiality of the high moistness of hardened concrete. The number of microcracks in cement mortar affects the resulting mechanical properties of concrete.

Impedance, or dielectric, spectroscopy together with acoustic emission can also help with the monitoring and a detailed description of lifetime behaviours of concrete specimens during hydration.

As the acoustic emission (**Figure 3**) and the impedance (**Figure 5**) history of both samples are similar, the number of microcracks is higher in the samples without foil, which means that the curing of concrete during an early age is necessary.

Acknowledgement

This paper has been worked out under the project No. LO1408 "AdMaS UP – Advanced Materials, Structures and Technologies", supported by Ministry of Education, Youth and Sports under the "National Sustainability Programme I" and under the project No. 13-18870S "Assessment and Prediction of the Concrete Cover Layers Durability" supported by Czech Science Foundation.

5 REFERENCES

[1] G. Venkiteela, Z. H. Sun, H. Najm, Journal of Materials in Civil Engineering, 25 (**2013**) 2, 30–38, doi:10.1061/(ASCE)MT.1943-5533.0000528
[2] W. Chen, Y. Li, P. L. Shen, Z. H. Shui, Journal of Nondestructive Evaluation, 32 (**2013**) 3, 228–237, doi:10.1007/s10921-013-0175-y
[3] I. M. Nikbin, M. Dehestani, M. H. A. Beygi, M. Rezvani, Construction and Building Materials, 59 (**2014**), 144–150, doi:10.1016/j.conbuildmat.2014.02.008
[4] Q. Xua, J. M. Ruiza, J. Hub, K. Wangc, R. O. Rasmussena, Thermochimica Acta, 512 (**2011**), 76–85, doi:10.1016/j.tca.2010.09.003
[5] W. M. Hale, T. D. Bush, B. W. Russell, S. F. Freyne, Journal of the Transportation Research Board, 1914 (**2005**), 97–104
[6] T. Nishizawa, T. Fukuda, S. Matsuno, K. Himeno, Transportation Research Record, 1525 (**1996**), 35–43, doi:10.3141/1525-05
[7] M. Gawlicki, W. Nocun-Wczelik, L. Bak, Journal of Thermal Analysis and Calorimetry, 100 (**2010**), 571–576, doi:10.1007/s10973-009-0158-5
[8] K. V. D. Abeele, W. Desadeleer, G. D. Schutter, M. Wevers, Cement and Concrete Research, 39 (**2009**), 426–432, doi:10.1016/j.cemconres.2009.01.016
[9] H. W. Reinhardt, C. U. Grosse, A. T. Herb, Materials and Structures, 33 (**2000**) 233, 581–583, doi:10.1007/BF02480539
[10] V. A. Aleshin, K. V. D. Abeele, Journal of the Mechanics and Physics of Solids, 55 (**2007**) 2, 366–390, doi:10.1016/j.jmps.2006.07.002

[11] S. F. Huang, M. M. Li, D. Y. Xu, M. J. Zhou, S. H. Xie, X. Cheng, Research in Nondestructive Evaluation, 24 (**2013**) 4, 202–210, doi:10.1080/09349847.2013.789949

[12] I. Gabrijel, D. Mikulic, N. Bijelic, Tehnicki Vjesnik-Technical Gazette, 17 (**2010**) 4, 493–497

[13] K. Ohno, M. Ohtsu, Construction and Building Materials, 24 (**2010**), 2339–2346, doi:10.1016/j.conbuildmat.2010.05.004

[14] P. Lura, J. Couch, O. M. Jensen, J. Weiss, Cement and Concrete Research, 39 (**2009**) 10, 861–867, doi:10.1016/j.cemconres.2009.06.015

[15] M. Tasic, Z. Andic, A. Vujovic, P. Jovanic, Mater. Tehnol., 44 (**2010**) 6, 397–401

[16] M. Marinsek, Mater. Tehnol., 43 (**2009**) 2, 79–84

[17] Y. M. Kim, J. H. Lee, S. H. Hong, Cement and Concrete Research, 33 (**2003**) 3, 299–304, doi:10.1016/S0008-8846(02)00944-4

[18] K. B. Sanish, N. Neithalath, M. Santhanam, Construction and Building Materials, 49 (**2013**), 288–297, doi:10.1016/j.conbuildmat.2013.08.038

[19] J. M. Cruz, I. C. Fita, L. Soriano, J. Paya, M. V. Borrachero, Cement and Concrete Research, 50 (**2013**), 51–61, doi:10.1016/j.cemconres.2013.03.019

[20] R. Ranade, J. Zhang, J. P. Lynch, V. C. Li, Cement and Concrete Research, 58 (**2014**), 1–12, doi:10.1016/j.cemconres.2014.01.002

[21] C. Jomdecha, A. Prateepasen, P. Kaewtrakulpong, NDT & E International, 40 (**2007**) 8, 584–593, doi:10.1016/j.ndteint.2007.05.003

[22] S. R. Mahapatra, V. Sridhar, D. K. Tripathy, Polymer Composites, 29 (**2008**) 5, 465–472, doi:10.1002/pc.20421

[23] M. Lunak, I. Kusak, L. Pazdera, L. Topolar, V. Bilek, Proc. of the 48th International Scientific Conference on Experimental Stress Analysis EAN 2010, Velke Losiny, Czech Republic, 2010, 233–240, Code 106809

[24] A. Feylessoufi, F. C. Tenoudji, V. Morin, P. Richard, Cement and Concrete Research, 31 (**2001**) 11, 1573–1579, doi:10.1016/S0008-8846(01)00602-0

[25] M. H. Cornejo, J. Elsen, H. Baykara, C. Paredes, European Journal of Environmental and Civil Engineering, 18 (**2014**) 6, 629–651, doi:10.1080/19648189.2014.897005

[26] J. M. Deus, B. Diaz, L. Freire, X. R. Novoa, Electrochimica Acta, 131 (**2014**), 106–115, doi:10.1016/j.electacta.2013.12.012

UDK 691:620.1
Original scientific article/Izvirni znanstveni članek

ISSN 1580-2949
MTAEC9, 49(5)709(2015)

EFFECT OF THE AGGREGATE TYPE ON THE PROPERTIES OF ALKALI-ACTIVATED SLAG SUBJECTED TO HIGH TEMPERATURES

VPLIV VRSTE AGREGATA NA LASTNOSTI Z ALKALIJO AKTIVIRANE ŽLINDRE, IZPOSTAVLJENE VISOKIM TEMPERATURAM

Pavel Rovnaník, Ámos Dufka

Faculty of Civil Engineering, Brno University of Technology, Veveří 95, 602 00 Brno, Czech Republic
rovnanik.p@fce.vutbr.cz

Prejem rokopisa – received: 2014-07-24; sprejem za objavo – accepted for publication: 2014-12-08

doi:10.17222/mit.2014.116

High temperatures present a risk of destruction for most silicate-based construction materials. Although these materials are not flammable, they lose their properties due to a thermal decomposition. In contrast to ordinary Portland-cement-based materials, alkali-activated slag exhibits a better thermal stability when exposed to temperatures up to 1200 °C. Due to its different porosity it is less susceptible to spalling. However, the properties of the composites after a high-temperature treatment depend also on the stability of the aggregates. The effects of two different types of the aggregate (quartz and chamotte) on the residual mechanical properties and microstructure of the alkali-activated slag mortars exposed to 200–1200 °C is presented in this study. The results showed an improved mechanical performance of the thermally stable chamotte aggregate at temperatures above 600 °C. α-quartz is transformed to β-quartz at 573 °C, causing a volume instability and, consequently, a strength deterioration. Although chamotte also contains some quartz phase, the reaction of mullite with the alkalis from the matrix leads to the formation of albite and anorthite, making the material tougher and, thus, compensating the negative effect of quartz.

Keywords: alkali-activated slag, high temperatures, chamotte, quartz, strength, microstructure

Visoke temperature so tveganje za razpad večine gradbenih materialov, ki temeljijo na silikatih. Čeprav ti materiali niso vnetljivi, izgubijo svoje lastnosti zaradi termične razgradnje. Nasprotno od materialov, ki temeljijo na portland cementu, z alkalijo aktivirane žlindre izkazujejo boljšo temperaturno obstojnost, če so izpostavljene temperaturam do 1200 °C. Zaradi različne poroznosti so manj občutljive za pojav luščenja. Vendar pa so lastnosti kompozita po visokotemperaturni obdelavi odvisne tudi od stabilnosti agregatov. V študiji so predstavljeni vplivi dveh različnih vrst agregatov (kremen in šamota) na preostale mehanske lastnosti in mikrostrukturo malte iz z alkalijo aktivirane žlindre, izpostavljene temperaturam 200–1200 °C. Rezultati so pokazali izboljšane mehanske lastnosti toplotno stabilnega šamotnega agregata pri temperaturah nad 600 °C. α-kremen se transformira pri 573 °C v β-kremen, kar povzroči volumensko nestabilnost in posledično poslabšanje trdnosti. Čeprav šamot vsebuje nekaj kremenove faze, reagiranje mulita z alkalijami iz osnove povzroči nastanek albita in anortita, ki povzročita, da material postane bolj žilav in s tem kompenzira negativni vpliv kremena.

Ključne besede: z alkalijo aktivirana žlindra, visoke temperature, šamot, kremen, trdnost, mikrostruktura

1 INTRODUCTION

Portland cement is today's most commonly used construction material. It owes its widespread utilization to its good mechanical properties, a low cost and a generally good performance. Nonetheless, Portland-cement concrete is not an eternal material and its performance can be affected by several degradation processes, one of which involves high temperatures. Although concrete is not flammable, when exposed to elevated temperatures it partially decomposes and loses its mechanical properties.[1–3] The second mostly discussed problem about Portland-cement concrete is spalling. This effect is mainly related to the build-up of the pore pressure in consequence of the vaporization of the physically/chemically bound water which results in tensile loading of the microstructure of heated concrete.[4–6] These two phenomena can be partially eliminated by utilizing alkali-activated slag as a binder instead of ordinary Portland cement.

Alkali-activated slag (AAS) is a hydraulic binder based on finely ground, granulated blast-furnace slag. Since the slag itself has no hydraulic properties it must be activated with strong alkaline solutions, among which hydroxides, carbonates and especially silicates play the main roles. In contrast to the composites based on Portland cement, alkali-activated slag shows a much better performance when exposed to very high temperatures.[7–9] Similar to the case of Portland cement, a partial dehydration and decomposition of the binder can be observed up to 600 °C. The principle changes in the microstructure of alkali-activated slag occur between 600 °C and 800 °C, when the dehydration of the C-A-S-H phase is complete and new phases start to crystallize, among which akermanite is dominant. Such a significant phase transformation is reflected in the morphology, pore distribution and, especially, in the improvement of the mechanical properties of the alkali-activated slag.[8] However, the properties of the composite materials with an

AAS matrix after a high-temperature treatment also depend on the stability of the aggregates. The effects of two different types of the aggregate (quartz and chamotte) on the residual mechanical properties and microstructure of the alkali-activated slag mortars exposed to 200–1200 °C is presented are this study.

2 EXPERIMENTAL PART

2.1 Materials

The tested material was prepared with the alkali activation of granulated blast-furnace slag. The slag supplied by Kotouč, s. r. o. (CZ) was ground to a fineness of about 380 m^2/kg (Blaine). It was a neutral slag with the basicity coefficient $M_b = (CaO + MgO)/(SiO_2 + Al_2O_3)$ equal to 1.08, and its chemical composition in mass fractions (w/%) was: SiO_2 39.75, Al_2O_3 6.61, Fe_2O_3 0.46, CaO 39.03, MgO 10.45, Na_2O 0.38, K_2O 0.63, MnO 0.37, SO_3 0.71. A small amount of merwinite and a trace of quartz were present as the only crystalline phases. Solid sodium water glass having a SiO_2/Na_2O ratio of 1.95 was used as an alkaline activator. Its chemical composition in mass fractions (w/%) was: SiO_2 50.75, Na_2O 26.78, H_2O 22.47.

To assess the influence of the aggregate on the stability of the AAS mortar at very high temperatures two types of the aggregate were used. One of them was quartz sand as a type of the commonly used standard materials and the second one was burnt clay, chamotte. The main mineralogical phases found in the chamotte aggregate with an XRD analysis were quartz, cristobalite and mullite.

2.2 Sample preparation and heat treatment

Sodium silicate activator was suspended and partially dissolved in water. Then, slag was added and the mixture was stirred in a planetary mixer for about 3 min to prepare homogeneous slurry. Finally, the aggregate was added into the slurry and stirred to prepare fresh mortar. The amount of the activator added was 20 % of the mass of the slag, the aggregate/slag ratio was 3.0 and a water/slag ratio of 0.4 was used to achieve an accurate consistency.

The mixes were cast into prismatic moulds of the size of 40 mm × 40 mm × 160 mm. After 24 h the hardened specimens were immersed into a water bath at 20 °C for another 27 d. After this period, they were allowed to air dry for another 5 d before undergoing a high-temperature treatment. The hardened mortars were heated in a Muffle furnace to temperatures of (200, 400, 600, 800, 1000, and 1200) °C at a constant heating rate of 5 °C min^{-1}. The specimens were kept at the given temperature for 1 h and then allowed to cool down slowly to room temperature.

The heat-treated specimens were tested for their residual mechanical properties, which were compared with those obtained for the unheated AAS mortar at the age of 28 d. Flexural strengths were determined using the standard three-point-bending test and compressive strengths were measured on the far edge of each of the two residual pieces obtained from the flexural test according to the EN 196-1 standard.

The pore distribution was evaluated by means of a mercury intrusion porosimetry analysis, conducted on the samples using a Micromeritics Poresizer 9300 porosimeter that can generate the maximum pressure of 207 MPa and can evaluate a theoretical pore diameter of 0.006 μm. Micrographs of the alkali-activated slag mortars were taken with a TESCAN MIRA3 XMU scanning electron microscope in the SE mode. The experiments were carried out on dry samples that were sputtered with gold and an acceleration voltage of 25 kV was used. X-ray diffraction analyses were carried out using a Bruker D8 advance system equipped with a Cu tube ($\lambda(K_\alpha)$ = 0.154184 nm). The instrument is also equipped with an Anton Paar HTK 16 temperature attachment facilitating the measurements at up to 1600 °C.

3 RESULTS AND DISCUSSION

The mechanical properties and microstructures of the AAS mortars subjected to high temperatures were compared with the samples, treated only at ambient temperature, marked as 'Ref' (**Table 1**). The compressive

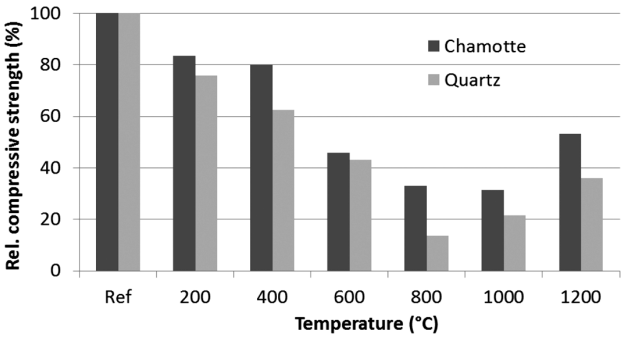

Figure 1: Comparison of the relative residual compressive strengths of AAS mortars after high-temperature treatment
Slika 1: Primerjava relativnih preostalih tlačnih trdnosti AAS-malt po obdelavi na visoki temperaturi

Table 1: Compressive and flexural strengths of AAS mortars with different aggregate types after exposure to high temperatures
Tabela 1: Tlačna in upogibna trdnost AAS-malt z različno vrsto agregata po izpostavitvi visokim temperaturam

Temperature (°C)	Compressive strength (MPa)		Flexural Strength (MPa)	
	Quartz	Chamotte	Quartz	Chamotte
Ref	73	92	9.6	10.4
200	55	77	4.4	7.5
400	46	74	3.8	6.2
600	31	42	2.6	4.8
800	10	31	1.7	4.2
1000	16	29	1.0	5.0
1200	26	49	2.9	12.5

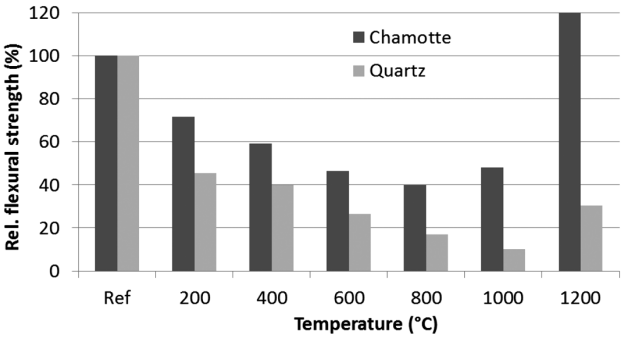

Figure 2: Comparison of the relative residual flexural strengths of AAS mortars after high temperature treatment

Slika 2: Primerjava relativne preostale upogibne trdnosti AAS-žlinder po obdelavi na visoki temperaturi

strengths of the AAS mortars with chamotte reached 92 MPa which is very close to the value for the AAS matrix itself;[8] therefore, the aggregate seems not to be a limiting factor for the mechanical properties of such composites. On the contrary, quartz sand caused a strength decrease by 19 MPa. This might be explained with weaker contacts between the AAS matrix and the aggregate. After the exposure to an elevated temperature, the compressive strengths gradually decreased (**Figure 1**). The trend, however, appeared to be the same for both composites; therefore, it can be attributed to the dehydration and decomposition of the AAS matrix. The strength decrease of the AAS composite with quartz above 600 °C was partly caused by the phase transition of quartz at 573 °C (β-quartz $\rightarrow$ α-quartz), accompanied by a change in the volume. The exposure of the AAS material to temperatures above 800 °C caused an increase in the strength that reached 53 % of the original strength for the AAS with the chamotte aggregate and 36 % of that obtained for the AAS with quartz.

The flexural strengths of both AAS composites treated at an ambient temperature were quite similar. After a high-temperature treatment the strengths decreased due to the decomposition processes in the matrix; however, in the case of the quartz aggregate the strength deterioration was more pronounced (**Figure 2**). The minimum value for the chamotte composite was achieved at 800 °C when the strength dropped to 40 % of the reference value, while the mortar with quartz exhibited the minimum strength at 1000 °C reaching only 10 % of the original value. An enormous difference in the mechanical performance was observed after the exposure to 1200 °C. The flexural strength of the chamotte composite exceeded the reference value by 20 %, while the strength achieved for the quartz sample remained very low.

The pore distribution obtained by means of mercury intrusion porosimetry up to 400 °C resembled the porosity of the matrix itself.[8] The main difference in the pore distribution appeared after the exposure to 600 °C (**Figure 3**). There was an increase in the pore volume in the range of large capillary pores (1–10 μm) for the quartz composite, which can be clearly attributed to the reversible phase transition to high quartz, followed by an increase in the aggregate volume by approximately 4.5 %.[10] After the exposure to 1200 °C, the major part of the porosity can be attributed to the pores > 10 μm. This is mainly caused by the shrinkage of the matrix during the crystallization of the new phases. However, the total porosity of the chamotte composite was much lower and it also corresponded to the differences in the achieved mechanical parameters.

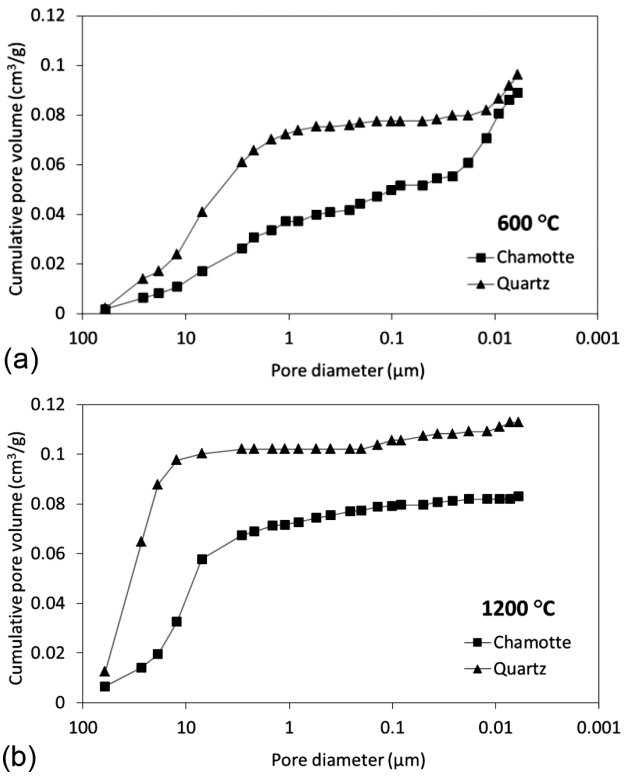

Figure 3: Differences in pore distribution for AAS mortars with quartz and chamotte after exposure to 600 °C and 1200 °C, respectively

Slika 3: Razlike v razporeditvi por v AAS-žlindrah s kremenom in šamotom po izpostavitvi na temperaturo 600 °C in 1200 °C

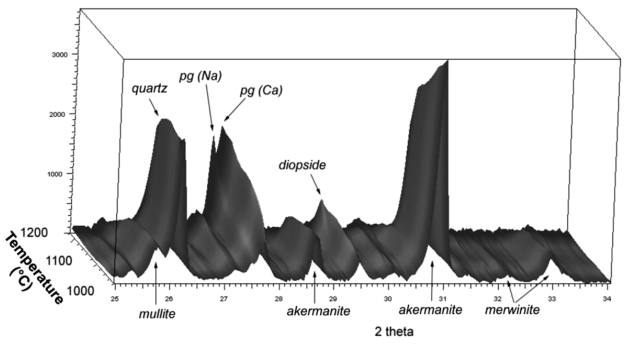

Figure 4: High temperature XRD of AAS mortar with chamotte aggregate (pg – plagioclase)

Slika 4: Visokotemperaturna XRD in AAS-malta s šamotnim agregatom (pg – plagioklas)

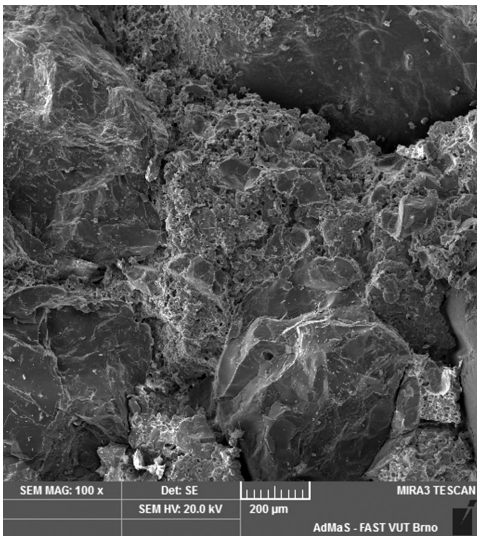

Figure 5: Microstructure of AAS mortar with quartz aggregate after exposure to 1200 °C (SEM)
Slika 5: Mikrostruktura AAS-malt s kremenovim agregatom po izpostavitvi na 1200 °C (SEM)

The changes in the mineralogical phases of the AAS mortars were observed by means of a high-temperature XRD analysis. Since quartz is quite an inert phase that does not react with the AAS matrix even at a very high temperature, there was practically no difference between the XRD patterns of the quartz composite and the AAS matrix itself.[8] On the other hand, chamotte contains two main crystalline phases, quartz and mullite. The latter is not stable when such a high concentration of alkalis is present in the material and reacts with the AAS matrix to form two plagioclase phases, albite and anothite, at temperatures exceeding 1000 °C (**Figure 4**). These two phases were not observed in the XRD pattern of the pure AAS matrix giving the proof of such an explanation.

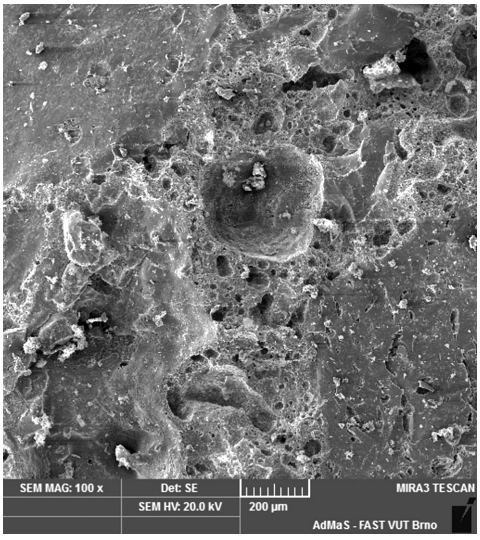

Figure 6: Microstructure of AAS mortar with chamotte aggregate after exposure to 1200 °C (SEM)
Slika 6: Mikrostruktura AAS-malt s šamotnim agregatom po izpostavitvi na 1200 °C (SEM)

Since the melting point of albite is in the range of 1100–1120 °C,[11] it caused a partial fusing of the contact zone between the aggregate grains and the matrix during the heating to 1200 °C.

The microstructure and morphology of the AAS mortars were investigated with scanning electron microscopy. To explain the difference in the mechanical behaviour of various AAS composites we focused on the interstitial zone between the aggregate grains and the matrix. **Figure 5** shows the microstructure of the AAS mortar with the quartz aggregate. The connection between the quartz grains and the AAS matrix is very weak and it is clearly evident that a small gap is present between both phases as a result of the volume changes in quartz at 573 °C. Therefore, the quartz grains can be easily pulled out of the matrix, which predominantly causes a deterioration of the flexural strength. Contrary to quartz, the surfaces of the chamotte grains were sintered with the matrix after the exposure to very high temperatures (**Figure 6**). This finally resulted in the formation of ceramic bonds which were so strong that a fracture of the aggregate grains occurred during the mechanical testing.

4 CONCLUSIONS

This study aimed to estimate the influence of the aggregate type on the behaviour of the alkali-activated slag mortars subjected to very high temperatures. The alkali-activated slag materials exhibit a much better performance compared to the concrete made from ordinary Portland cement when subjected to very high temperatures or fire. A utilization of chamotte as an aggregate in the AAS composites brought several benefits compared to quartz sand. Chamotte is a material that is produced from natural clay at 1350 °C and, therefore, it is more thermally stable than pure quartz that undergoes a phase transition at 573 °C. From the viewpoint of the mechanical properties, the chamotte aggregate did not limit the mechanical parameters of the AAS paste at temperatures of up to 1000 °C and it even considerably improved the flexural strength of the composite at 1200 °C due to the sintering of the aggregate surface layer with the AAS matrix. Although a degradation of the material occurred upon heating, the compressive strength of the chamotte composite was higher by 15 % and the flexural strength was even four times higher compared to the quartz composite after the exposure to 1200 °C. Therefore, the properties of the chamotte aggregate predestine its application in the alkali-activated slag composites with an improved high-temperature resistance.

Acknowledgement

This outcome was achieved with the financial support of the Czech Science Foundation, project GA CR 14-25504S and the Ministry of Education, Youth and

Sports of the Czech Republic under the "National Sustainability Programme I" (project No. LO1408 AdMaS UP), as an activity of the regional Centre AdMaS, "Advanced Materials, Structures and Technologies". The authors would like to thank Dr Patrik Bayer for measuring some of the microstructural data.

5 REFERENCES

[1] A. F. Bingöl, R. Gül, Fire Mater., 33 (**2009**), 79–88, doi:10.1002/fam.987

[2] G. F. Peng, Z. S. Huang, Constr. Build. Mater., 22 (**2008**) 4, 593–599, doi:10.1016/j.conbuildmat.2006.11.002

[3] K. Y. Kim, T. S. Zun, K. P. Park, Cem. Concr. Res., 50 (**2013**), 34–40, doi:10.1016/j.cemconres.2013.03.020

[4] P. Kalifa, F. D. Menneteau, D. Quenard, Cem. Concr. Res., 30 (**2000**), 1915–1927, doi:10.1016/S0008-8846(00)00384-7

[5] K. D. Hertz, Fire Safety J., 38 (**2003**) 2, 103–116, doi:10.1016/S0379-7112(02)00051-6

[6] M. Zeiml, D. Leithner, M. Lackner, H. A. Mang, Cem. Concr. Res., 36 (**2006**) 5, 929–942, doi:10.1016/j.cemconres.2005.12.018

[7] M. Guerrieri, J. G. Sanjayan, F. Collins, Fire Mater., 33 (**2009**) 1, 51–62, doi:10.1002/fam.983

[8] P. Rovnaník, P. Bayer, P. Rovnaníková, Constr. Build. Mater., 47 (**2013**), 1479–1487, doi:10.1016/j.conbuildmat.2013.06.070

[9] R. Zhao, J. G. Sanjayan, Mag. Concr. Res., 63 (**2011**) 3, 163–173, doi:10.1680/macr.9.00110

[10] U. Raz, S. Girsperger, A. B. Thompson, Schweiz. Mineral. Petrogr. Mitt., 82 (**2002**), 561–574

[11] J. P. Greenwood, P. C. Hess, J. Geophys. Res., 103 (**1998**) B12, 29815–29828, doi:10.1029/98JB02300

UDK 669.15-194.591:621.77:620.187
Original scientific article/Izvirni znanstveni članek

ISSN 1580-2949
MTAEC9, 49(5)715(2015)

MICROSTRUCTURE EVOLUTION OF ADVANCED HIGH-STRENGTH TRIP-AIDED BAINITIC STEEL

RAZVOJ MIKROSTRUKTURE NAPREDNEGA VISOKOTRDNOSTNEGA BAINITNEGA JEKLA Z UPORABO TRIP

Adam Grajcar

Silesian University of Technology, Institute of Engineering Materials and Biomaterials, Konarskiego Street 18a, 44-100 Gliwice, Poland
adam.grajcar@polsl.pl

Prejem rokopisa – received: 2014-08-01; sprejem za objavo – accepted for publication: 2014-10-08

doi:10.17222/mit.2014.154

The present work is focused on monitoring the microstructure evolution of the thermomechanically rolled medium-C steel containing Si and Al to prevent the precipitation of carbides. The initial microstructure consists of carbide-free bainite, polygonal ferrite and blocky-type and interlath retained austenite. To monitor the transformation behaviour of the retained austenite transforming into strain-induced martensite, tensile tests were interrupted at particular strains (5 %, 10 %, 15 %, 18.4 %). The amount of the retained austenite determined with XRD and EBSD techniques decreased from 17 % to 6.8 % upon straining, which was related to the transformation-induced plasticity effect. The identification of the retained austenite and strain-induced martensite was carried out using an electron scanning microscope equipped with EBSD (electron backscatter diffraction). It was found that sheet samples are strongly strengthened by the transformation of the blocky retained austenite, whereas the layers and films of the γ phase are over-stabilized and they do not transform into martensite.

Keywords: AHSS, bainitic steel, retained austenite, thermomechanical treatment, TRIP effect, strain-induced martensite

Delo obravnava pregled razvoja mikrostrukture pri termomehanskem valjanju srednje ogljičnega jekla s Si in Al, ki preprečita izločanje karbidov. Začetna mikrostruktura je bila iz bainita brez karbidov, poligonalnega ferita ter zaostalega avstenita kockaste oblike in zaostalega avstenita med lamelami. Za spremljanje vedenja zaostalega avstenita pri pretvorbi v deformacijsko induciran martenzit so bili natezni preizkusi prekinjeni pri posameznih raztezkih (5 %, 10 %, 15 %, 18,4 %). Delež zaostalega avstenita, določen z XRD in EBSD, se je zmanjšal po natezni deformaciji iz 17 % na 6,8 %, kar je posledica vpliva z deformacijo povzročene pretvorbe na plastičnost. Identifikacija zaostalega avstenita in napetostno induciranega martenzita je bila izvršena z vrstičnim elektronskim mikroskopom, opremljenim z EBSD (difrakcija odbitih elektronov). Ugotovljeno je, da se vzorci pločevine bolj utrjujejo s pretvorbo kockastega zaostalega avstenita, medtem ko so plasti in sloji γ-faze bolj stabilizirani in se ne pretvorijo v martenzit.

Ključne besede: AHSS, bainitno jeklo, zaostali avstenit, termomehanska obdelava, učinek TRIP, napetostno induciran martenzit

1 INTRODUCTION

Advanced high-strength steels (AHSS) for the automotive industry cover a wide group of multiphase steels showing a superior balance between the strength and plasticity. Dual-phase (DP), complex-phase (CP) and transformation-induced plasticity (TRIP) steels are representatives of the AHSSs containing ferrite as the main structural constituent.[1–3] The strain-induced martensitic transformation of retained austenite during cold forming, resulting in additional plasticity, stimulated increased research activities to assess the microstructure-property relationships in TRIP-aided steels.[2–4] The demand for ultra-high-strength steels can be satisfied when a soft ferritic matrix is replaced by harder bainite. Hence, a growing importance of the AHSSs containing increased bainite amounts can be observed in[4–9]. The desired ductility can be only obtained in advanced carbide-free bainitic steels, achieved with Si, Al, or Si-Al alloying. Unfortunately, Al-alloyed steels have a lower solid-solution strengthening effect. Thus, increased carbon contents are used or microalloying is employed to improve the strength levels with grain refinement and precipitation strengthening, in a similar way as in the HSLA steels.[9–12] Recently, medium-Mn bainitic-austenitic steels have also been developed.[8,13] Medium-C or medium-alloyed sheet steels are used for the products capable of mechanical binding and chemical adhesion[14] or they can be also used for forgings and wires.[4,6]

Bainite-based steels containing large volume fractions of retained austenite can be produced with cold rolling or hot rolling. The knowledge concerning the relationships between the manufacturing conditions, the microstructure and the mechanical properties of cold-rolled and annealed products is sufficiently documented in literature studies.[5,6,10,14] However, there are only few reports on the microstructure-property relationships in hot-rolled medium-C, carbide-free bainitic steels.[4,7] It is known that thermomechanical processing requires a detailed time-temperature regime during a sheet's cooling.[13,15] It is especially important for multiphase steels because austenite retention requires one or two isothermal holding steps upon cooling. Isothermal holding of steel at a bainitic transformation temperature is obligatory for the enrichment of austenite in carbon from bainitic ferrite. This schedule is used for bainitic-austenitic

alloys.[9] An additional enrichment of austenite in C can be provided with an isothermal holding step at the intercritical region[5,15] or using low finishing rolling temperatures.[7]

Mechanical properties of multiphase steels are dependent on the volume fractions and properties of bainite and retained austenite. The final fraction of retained austenite that can be stabilized depends, in turn, on the chemical composition of steel and heat-treatment conditions. However, the most important is the mechanical stability of retained austenite, dependent on its carbon content, size, dislocation density, morphology (blocky, interlath), etc.[3–5,10] An efficient monitoring of the evolution of retained austenite and strain-induced martensite as a function of strain is crucial for understanding microstructure-property relationships. This approach can be used with typical TRIP-aided ferrite-based steels.[1–3,16] The aim of the present study is to monitor the evolution of the microstructure of TRIP-aided medium-C bainitic steel.

2 EXPERIMENTAL PROCEDURE

The work was focused on monitoring the microstructure evolution of the Si-Al type TRIP-aided steel containing 0.43 % C, 1.45 % Mn, 0.98 % Si, 1.0 % Al, 0.033 % Nb, 0.01 % Ti, 0.004 % S, 0.01 % P and 0.0028 % N. The steel was produced with vacuum-induction melting followed by casting under an Ar atmosphere, hot forging and rough rolling to a thickness of 4.5 mm. The chemical composition was designed to obtain a large fraction of retained austenite and carbide-free bainite using the complex Si+Al approach.[2,3] Nb and Ti microadditions were used to increase the strength level through grain refinement and precipitation strengthening.

The thermomechanical rolling was conducted in 3 passes between 1100 °C and 750 °C to the final thickness of about 2 mm. The cooling schedule consisted of the finishing rolling at 750 °C followed by slow cooling of the sheet samples to a temperature of 600 °C within 25 s. Immerse cooling of the specimens at a rate of about 50 °C/s to an isothermal holding temperature of 450 °C was the next step. The isothermal holding time was 600 s. Finally, the samples were cooled at a rate of about 0.5 °C/s to room temperature. Then, the samples with a gauge length of 50 mm and a width of 12.5 mm were prepared for the tensile tests carried out at a strain rate of 5×10^{-3} s^{-1}. To monitor the transformation of the retained austenite into martensite as a function of the strain, interrupted tensile tests were carried out. The tensile tests were interrupted at different tensile strains in steps of 5 % followed by EBSD investigations to determine the volume fraction of the remaining austenite at a particular strain.

Metallographic specimens were taken along the rolling and tensile directions. Scanning electron microscopy (SEM) and transmission electron microscopy (TEM) were used to reveal morphological details of the microstructure. Additionally, orientation imaging microscopy (OIM) using SEM was applied. Metallographic observations were carried out with the SUPRA 25 SEM using BSE electrons. Observations were performed on nital-etched samples at an accelerating voltage of 20 kV. The EBSD technique was carried out using the Inspect F SEM equipped with Schottky field emission. After classical grinding and polishing, the specimens were polished with Al_2O_3 with a granularity of 0.1 μm. The final step of the sample preparation was their ion polishing using the GATAN 682 PECS system. Thin-foil investigations were carried out with JEOL JEM 3010 at an accelerating voltage of 200 kV using a mixture of 490 mL H_3PO_4 + 7 mL H_2SO_4 + 50 g CrO_3 as the electrolyte for the sample preparation.

A determination of the retained austenite fraction and its carbon content after the thermomechanical rolling was performed using the X-ray phase analysis based on the Rietveld method. X-ray tests were done using a Philips PW 1140 diffractometer with Co radiation. The positions of the maxima of the diffraction lines of the austenitic phase were used to determine the lattice constant of austenite (a_γ). This parameter is necessary to calculate the carbon content in the retained austenite (C_γ) using the following formula: $a_\gamma = 0.3578 + 0.0033C_\gamma$.[17] The fraction of the retained austenite at a particular strain ((5, 10, 15, 18.4) %) was determined with EBSD as the average value of three measurements. A magnification lower than 3000-times was applied to obtain reliable quantitative results.

3 RESULTS AND DISCUSSION

The initial microstructure of the steel after the thermomechanical rolling and isothermal holding at a temperature of 450 °C is presented in **Figure 1**. It consists of bainite, fine-grained ferrite (F) and retained austenite (RA). The structural constituents are characterized by a significant refinement related to a large population of nucleation sites in the $\gamma \rightarrow \alpha$ transformation after the finishing rolling at a temperature of 750 °C. The largest amount of retained austenite occurs between the laths of bainitic ferrite (BF), while blocky grains of the γ phase, of up to about 4 μm, are located in the boundary regions of the bainitic-austenitic (BA) islands. The interlath retained austenite takes the form of continuous or interrupted laths or small regions located in the bainitic islands (**Figure 1b**). The average size of ferrite grains is approximately 5 μm.

The amount of the retained austenite in the initial state determined with an X-ray examination is 17.6 %. This result is in good agreement with the EBSD measurements, showing that the retained-austenite fraction reaches 17.1 % (**Table 1**). The stabilization of the large fraction of the retained austenite is due to its high carbon content $w(C_\gamma = 1.64$ %). The enrichment of austenite in

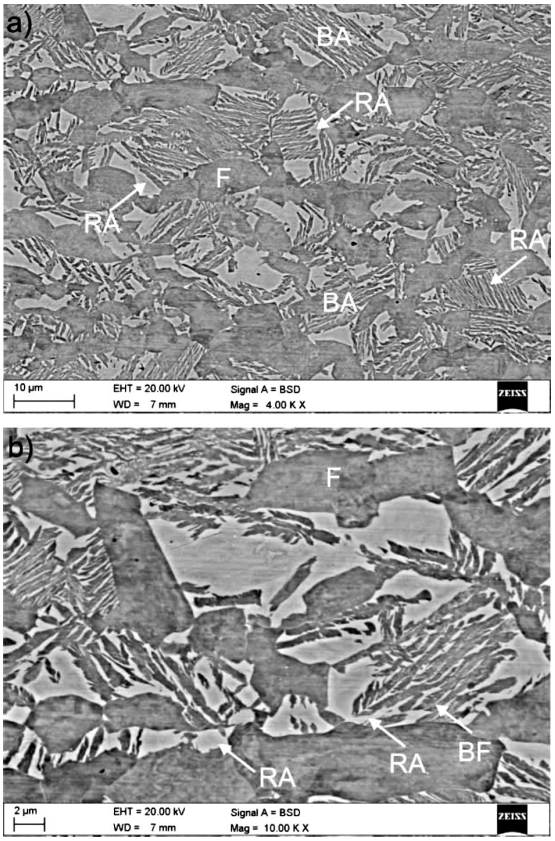

Figure 1: SEM micrographs of the: a) bainitic-ferritic steel containing blocky and interlath retained austenite after thermomechanical rolling, b) morphological details of the bainitic-austenitic (BA) islands; F – ferrite, BA – bainitic-austenitic islands, RA – retained austenite, BF – bainitic ferrite

Slika 1: SEM-posnetka bainitno-feritnega jekla, ki vsebuje: a) kockast in medlamelni zaostali avstenit, po termomehanskem valjanju, b) detajli morfologije bainitno-avstenitnih (BA) otočkov; F – ferit, BA – bainitno-avstenitni otočki, RA – zaostali avstenit, BF – bainitni ferit

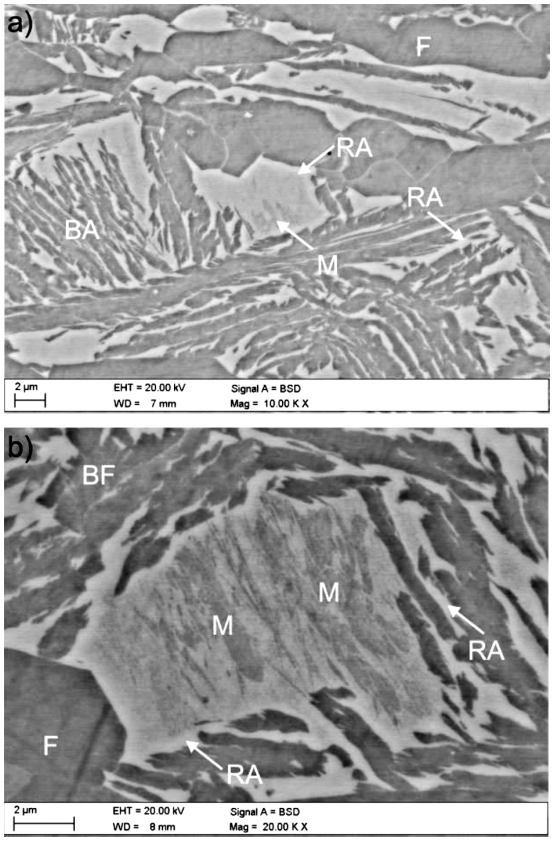

Figure 2: SEM micrographs showing strain-induced martensite in blocky grains of retained austenite at 5 % strain; magnifications of: a) 10000-times and b) 20000-times; F – ferrite, BA – bainitic-austenitic islands, RA – retained austenite, BF – bainitic ferrite, M – strain-induced martensite

Slika 2: SEM-posnetka, ki prikazujeta napetostno induciran martenzit v kockastih zrnih zaostalega avstenita pri raztezku 5 %; povečava: a) 10000-kratna in b) 20000-kratna; F – ferit, BA – bainitno-avstenitni otočki, RA – zaostali avstenit, BF – bainitni ferit, M – deformacijsko induciran martenzit

carbon was possible due to its partitioning from polygonal and bainitic ferrite during the slow cooling of the sheet samples during the $\gamma \rightarrow \alpha$ transformation and subsequent isothermal holding at 450 °C for 600 s. This C content is higher when compared to the other TRIP-aided ferrite-based steels $w(C_\gamma \approx 1.0–1.4\ \%)$.[2,3,7,16,17] Due to the very low finishing rolling temperature (750 °C) almost all the austenite grains are pancaked (not recrystallized) during the bainitic transformation. Thus, both the blocky grains and the layers of the retained austenite remain heavily deformed and exhibit a high dislocation density.

At a strain of 5 % the amount of the retained austenite decreases to about 13.1 % (**Table 1**), which corresponds to 23 % of the initial amount of the γ phase transformed into martensite. The evidence of the strain-induced martensitic transformation at the strain of 5 % is found on the micrographs in **Figure 2**. It can be seen that the strain-induced martensite forms in the largest grains of the retained austenite, usually located on the boundaries of the bainitic-austenitic islands. On the other hand, the laths of the retained austenite located between the bainitic-ferrite laths are mechanically stable.

Table 1: Retained-austenite fractions after thermomechanical rolling (0 % strain) and at particular strains determined with the EBSD technique

Tabela 1: Delež zaostalega avstenita, določenega z EBSD-tehniko, po termomehanskem valjanju (0 % raztezka) in pri določenih raztezkih

0 %	5 %	10 %	15 %	18.4 %
17.1 ± 1.2	13.1 ± 1.4	11.2 ± 1.3	9.0 ± 1.0	6.8 ± 1.1

Figure 3 shows EBSD maps registered at a strain of 10 %. Comparing the image quality (IQ) map (**Figure 3a**) and phase map (**Figure 3b**) it is possible to identify particular structural constituents. In the grey-scale IQ map the retained austenite regions correspond to the dark areas of a poor diffraction quality. The IQ factor represents a quantitative description of the sharpness of the EBSD pattern. A lattice distorted by crystalline defects such as dislocations and grain/subgrain boundaries has a distorted Kikuchi pattern, leading to lower IQ values.[1,2]

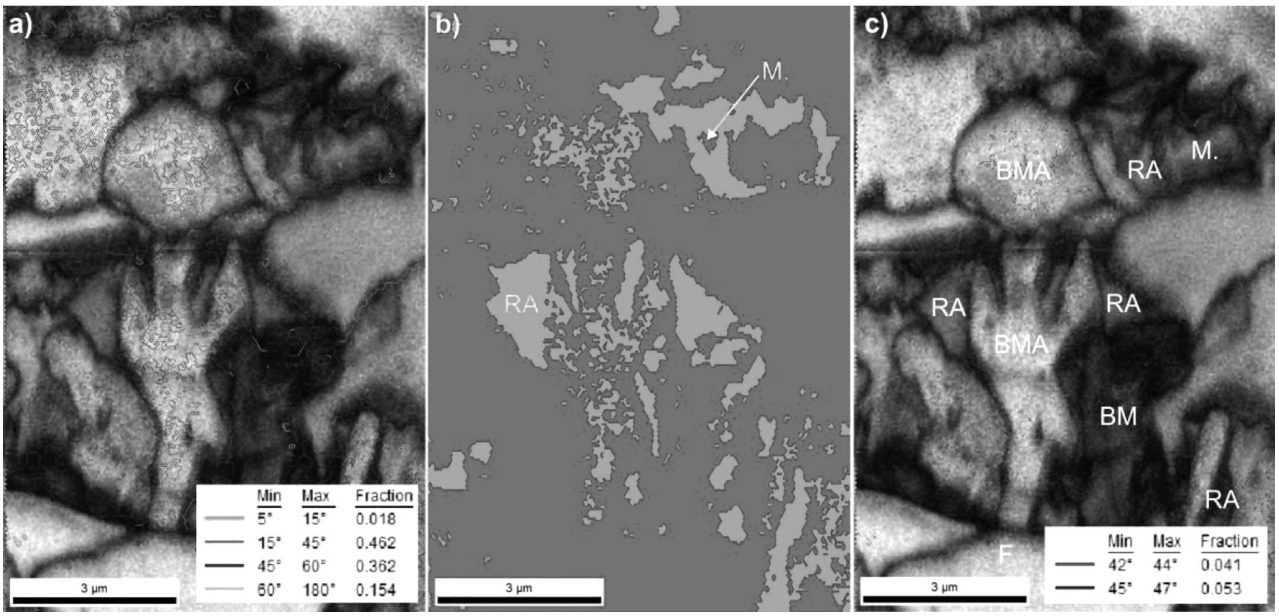

Figure 3: a) Image quality (IQ) map with misorientation angles, b) phase map showing retained austenite – RA regions, and c) IQ map with misorientation angles corresponding to the Kurdjumov-Sachs (42–44 °) and Nishiyama-Wasserman (45–47 °) relationships at 10 % strain; F – ferrite, BMA – bainitic-martensitic-austenitic constituents, RA – retained austenite, BM – bainitic-martensitic constituents, M – strain-induced martensite

Slika 3: a) Posnetek področja kvalitete (IQ) z razporeditvijo slabo orientiranih zrn, b) načrt faz prikazuje zaostali avstenit – RA področja in c) načrt slabo orientiranih zrn po odvisnostih Kurdjumov-Sachs (42–44 °) in Nishiyama-Wasserman (45–47 °) pri raztezku 10 %; F – ferit, BMA – bainitno-martenzitno-avstenitne sestavine, RA – zaostali avstenit, BM – bainitno-martenzitne sestavine, M – deformacijsko induciran martenzit

Hence, the strain-induced martensite can be distinguished from the other BCC phases (bainitic ferrite and polygonal ferrite) because it has the most defected structure and, thus, it is characterized by the poorest diffraction quality. Additionally, Wasilkowska et al.[2], Zaefferer el al.[3] and Petrov et al.[16] reported that bainitic ferrite and martensite can be indentified if we know special crystallographic orientations between these BCC phases and retained austenite. It is known that the Kurdjumov-Sachs (KS) orientation shows a misorientation angle of 43 °, whereas the Nishiyama-Wasserman (NW) orientation shows a 46 ° angle. During deformation they are mixed with each other. The way to distinguish them is to analyse the rotation-axis distributions. They are around <0.18 0.18 0.97> and <0.2 0.08 0.98> for the KS and NW, respectively.

Fortunately, the characteristic misorientation angles fulfilling the Kurdjumov-Sachs and Nishiyama-Wasserman relationships are sufficiently different to be distinguished using the EBSD mapping. Hence, **Figure 3c** shows the IQ map with the angles corresponding to the KS and NW relationships with a deviation of ± 1 °. It is clear that these special angles are mainly located between the retained austenite (RA) and strain-induced martensite (M). The strongly defected strain-induced martensite occurs as dark regions in the phase map. The transformation causes a gradual fragmentation of the retained-austenite regions. Thus, bainitic-martensitic-austenitic constituents (BMA) are formed.

A further increase in the strain to 15 % causes the amount of the retained austenite to decrease to about 9 % (**Table 1**). The martensitic transformation takes place in large blocky grains of the retained austenite. The initiation of the transformation at smaller blocky grains located in the BA regions can be also observed (**Figure 4**). However, a high content of C in the retained austenite results in the lack of transformation of the γ phase layers. According to the literature data[2,3,7,9] the carbon content in the blocky grains is smaller when compared to retained-austenite films. The reason is a longer diffusion path of carbon in the relatively large blocky grains. Thus, the center of a grain has a smaller amount of carbon compared to the external regions of the grain. The same applies to the films of the retained austenite. The diffusion path of C from the bainitic-ferrite laths into the retained-austenite films is much shorter. Hence, these are mechanically stable upon the straining. Their stability is additionally increased by hard laths of bainitic ferrite, which form a protecting barrier against strain distribution into the retained austenite.[4,9]

The strengthening caused by the complex effects of the thermomechanical processing, strongly defected ferrite and bainite, strain-induced martensite and over-stabilized films of the retained austenite, lead to a premature breaking of the samples at an elongation of 18.4 % and *UTS* of 930 MPa. The volume fraction of the retained austenite present after the sample breaking is about 6.8 %. It means that about 40 % of the initial amount of the retained austenite is untransformed. This

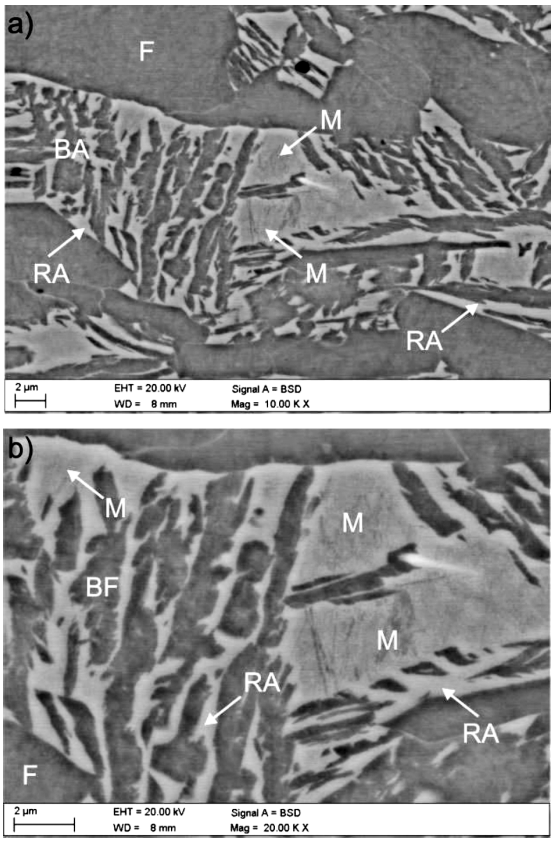

Figure 4: SEM micrographs showing strain-induced martensite in small blocky grains of retained austenite located in BA regions at 15 % strain: a) magnifications of 10000-times and b) 20000-times; F – ferrite, BA – bainitic-austenitic islands, RA – retained austenite, BF – bainitic ferrite, M – strain-induced martensite

Slika 4: SEM-posnetka deformacijsko induciranega martenzita v kockastih zrnih zaostalega avstenita v območjih BA pri raztezku 15 %: a) povečava 10000-kratna in b) 20000-kratna; F – ferit, BA – bainitno-avstenitni otočki, RA – zaostali avstenit, BF – bainitni ferit, M – deformacijsko induciran martenzit

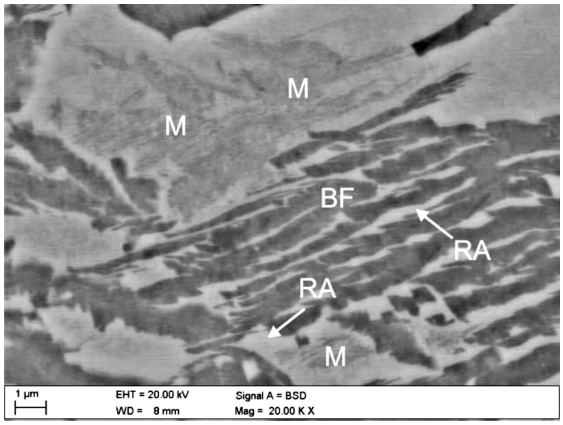

Figure 5: SEM micrograph showing strain-induced martensite in blocky grains of retained austenite and stable interlath retained austenite at rupture strain of 18.4 %; RA – retained austenite, BF – bainitic ferrite, M – strain-induced martensite

Slika 5: SEM-posnetek deformacijsko induciranega martenzita v kockastih zrnih zaostalega avstenita in stabilen zaostali avstenit med lamelami pri raztezku 18,4 % ob porušitvi; RA – zaostali avstenit, BF – bainitni ferit, M – deformacijsko induciran martenzit

phase remains mainly in the form of thin layers and films located between the hard laths of bainitic ferrite (**Figure 5**). Firstly, the high mechanical stability of the retained austenite results from its high C concentration of 1.64 %. Secondly, it is due to the fragmentation of the γ-phase particles and the compressive stresses caused by the hard

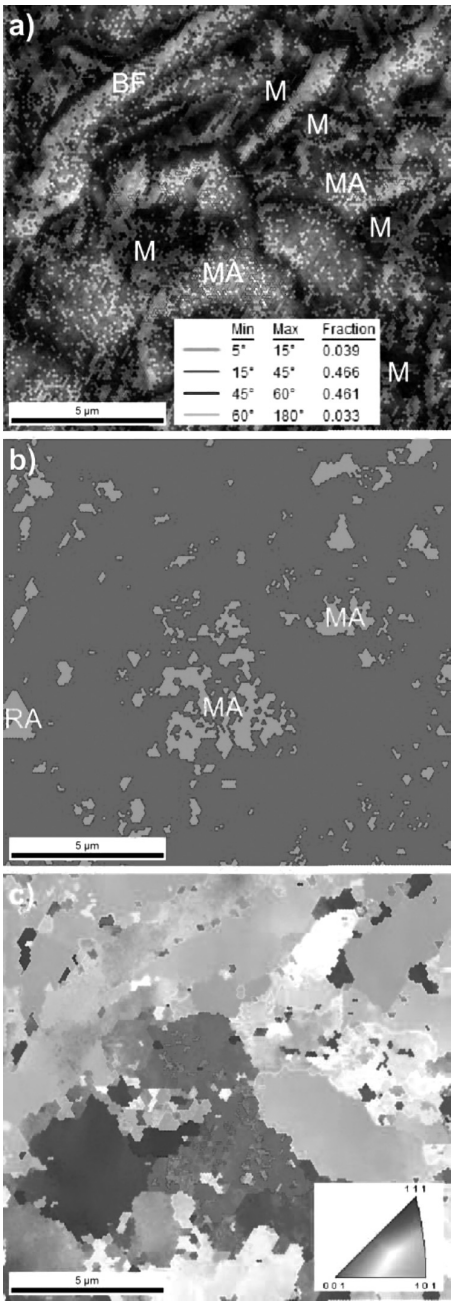

Figure 6: a) Image quality (IQ) map with misorientation angles, b) phase map showing retained austenite – RA regions, and c) inverse pole-figure map at rupture strain of 18.4 %; BF – bainitic ferrite, RA – retained austenite, MA – martensitic-austenitic constituents, M – martensite

Slika 6: a) Posnetek razporeditve kvalitete (IQ) s področij slabo orientiranih zrn, b) razporeditev faz prikazuje zaostali avstenit – RA področja in c) razporeditev inverznih polovih figur pri raztezku 18,4 % ob porušitvi; BF – bainitni ferit, RA – zaostali avstenit, MA – martenzitno-avstenitne sstavine, M – martenzit

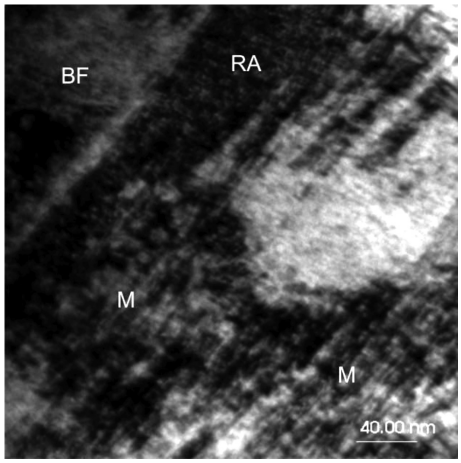

Figure 7: TEM micrograph showing the plate morphology of strain-induced martensite at 18.4 % strain; BF – bainitic ferrite, RA – retained austenite, M – strain-induced martensite

Slika 7: TEM-posnetek prikazuje morfologijo plošč deformacijsko induciranega martenzita pri raztezku 18,4 %; BF – bainitni ferit, RA – zaostali avstenit, M – deformacijsko induciran martenzit

laths of bainitic ferrite. Finally, the stabilization of the γ phase is favoured due to a high density of the dislocations in this phase remaining after the thermomechanical processing.[7]

At the fracture strain, the IQ map (**Figure 6a**) no longer coincides exactly with the inverse pole-figure map (**Figure 6c**) showing the orientations of individual grains. It is a result of a strongly defected multiphase microstructure. The brightest areas in **Figure 6** correspond to the occurrence of defected ferrite and bainitic ferrite, while dark areas of a poor diffraction quality can be identified as the retained austenite and martensite. The particles of the strain-induced martensite are the reason of a substantial fragmentation of the retained-austenite regions. Thus, martensitic-austenitic (MA) regions are formed (**Figure 6b**). A transmission electron micrograph reveals that the strain-induced martensite has a fine-plate morphology (**Figure 7**). It is formed from the retained austenite containing about the mass fraction $w(C) = 1.64$ %. This high carbon concentration determines the plate morphology of the stain-induced martensite.

4 CONCLUSIONS

The thermomechanically processed, medium-C bainitic steel contains a large volume fraction of retained austenite (about 17 %), appearing as layers between the bainitic-ferrite laths and blocky grains located in the boundary regions of bainitic-austenitic islands. The morphology of the retained austenite affects the transformation behaviour of this phase into martensite. The blocky grains of the retained austenite gradually transform into strain-induced martensite as a function of the increasing strain. On the other hand, the interlath retained austenite, more enriched in carbon than the blocky grains, is stable upon the straining not providing a TRIP effect. The mechanical stability of the retained austenite is too high especially due to its high average carbon content ($w(C_\gamma = 1.64$ %). The high dislocation density, the progressive fragmentation of the retained austenite (its size) and the compressive stresses caused by the bainitic-ferrite laths and strain-induced martensite are equally important for the mechanical stabilization of the retained austenite. It can be concluded that polygonal ferrite and the subsequent partitioning of C during the $\gamma \rightarrow \alpha$ transformation are not necessary for fine-grained, thermomechanically processed, medium-C steel. Over-stabilization of the retained-austenite layers should be avoided by producing homogeneous bainitic-austenitic microstructures with a lower C content in the γ phase.

5 REFERENCES

[1] A. J. DeArdo, C. I. Garcia, K. Cho, M. Hua, Mater. Manuf. Proc., 25 (**2010**), 33–40, doi:10.1080/10426910903143415

[2] A. Wasilkowska, R. Petrov, L. Kestens, E. A. Werner, C. Krempaszky, S. Traint, A. Pichler, ISIJ Int., 46 (**2006**), 302–309, doi:10.2355/isijinternational.46.302

[3] S. Zaefferer, J. Ohlert, W. Bleck, Acta Mater., 52 (**2004**), 2765–2778, doi:10.1016/j.actamat.2004.02.044

[4] K. I. Sugimoto, S. Sato, G. Arai, Mater. Sci. Forum, 638–642 (**2010**), 3074–3079, doi:10.4028/www.scientific.net/MSF.638-642.3074

[5] A. Kokosza, J. Pacyna, Arch. Metall. Mater., 59 (**2014**), 1017–1022, doi:10.2478/amm-2014-0170

[6] S. Wiewiorowska, Arch. Metall. Mater., 58 (**2013**), 573–576, doi:10.2478/amm-2013-0040

[7] A. Basuki, E. Aernoudt, J. Mater. Proc. Tech., 89–90 (**1999**), 37–43, doi:10.1016/S0924-0136(99)00037-0

[8] A. Grajcar, R. Kuziak, Adv. Mater. Res., 314–316 (**2011**), 119–122, doi:10.4028/www.scientific.net/AMR.314-316.119

[9] J. Adamczyk, A. Grajcar, J. Micro. Mater. Prop., 2 (**2007**), 112–122, doi:10.1504/IJMMP.2007.014305

[10] F. G. Caballero, C. Garcia-Mateo, J. Chao, M. J. Santofimia, C. Capdevila, C. G. de Andres, ISIJ Int., 48 (**2008**), 1256–1262, doi:10.2355/isijinternational.48.1256

[11] D. A. Skobir, M. Godec, M. Balcar, M. Jenko, Mater. Tehnol., 44 (**2010**) 6, 343–347

[12] M. Opiela, A. Grajcar, Arch. Civ. Mech. Eng., 12 (**2012**), 427–435, doi:10.1016/j.acme.2012.06.013

[13] A. Grajcar, S. Lesz, Mater. Sci. Forum, 706–709 (**2012**), 2124–2129, doi:10.4028/www.scientific.net/MSF.706-709.2124

[14] O. Matsumura, Y. Sakuma, H. Takechi, Scripta Metall., 21 (**1987**), 1301–1306, doi:10.1016/0036-9748(87)90103-7

[15] B. Barucija, M. Oruc, O. Beganovic, M. Rimac, S. Muhamedagic, Mater. Tehnol., 47 (**2013**) 5, 665–668

[16] R. Petrov, L. Kestens, Y. Houbaert, Mater. Sci. Forum, 550 (**2007**), 1–6, doi:10.4028/www.scientific.net/MSF.550.1

[17] Z. C. Wang, S. J. Kim, C. G. Lee, T. H. Lee, J. Mater. Proc. Tech., 151 (**2004**), 141–145, doi:10.1016/j.jmatprotec.2004.04.029

UDK 621.762:621.762.5:669.018.29
Original scientific article/Izvirni znanstveni članek

ISSN 1580-2949
MTAEC9, 49(5)721(2015)

EFFECT OF ELECTRIC CURRENT ON THE PRODUCTION OF NiTi INTERMETALLICS VIA ELECTRIC-CURRENT-ACTIVATED SINTERING

VPLIV ELEKTRIČNEGA TOKA PRI IZDELAVI INTERMETALNE ZLITINE NiTi S SINTRANJEM, AKTIVIRANIM Z ELEKTRIČNIM TOKOM

Tuba Yener[1], Shafaqat Siddique[2], Frank Walther[2], Sakin Zeytin[1]

[1]Sakarya University, Engineering Faculty, Department of Metallurgy and Materials Engineering, Esentepe Campus, 54187 Adapazari, Sakarya, Turkey

[2]TU Dortmund University, Faculty of Mechanical Engineering, Department of Materials Test Engineering (WPT), Baroper Str. 303, 44227 Dortmund, Germany

tcerezci@sakarya.edu.tr

Prejem rokopisa – received: 2014-08-01; sprejem za objavo – accepted for publication: 2014-10-09

doi:10.17222/mit.2014.161

This study focuses on investigating the fabrication of in-situ intermetallic NiTi composites from a powder mixture containing the mass fractions 50 % nickel powder and 50 % titanium powder. The elemental powders were mixed in the stoichiometric ratio corresponding to the NiTi intermetallic molar proportion of 1 : 1, ball-milled and uniaxially compressed under a pressure of 170 MPa. Sintering was then carried out for 15 min in a steel mold using the electric-current-activated sintering method. Electric-current values of 1000 A, 1300 A and 2000 A were used for the sintering while keeping the voltage in the range of 0.9 V to 1.2 V. The phases in the samples were analyzed with XRD and their Vickers hardness was measured as (701 ± 166) $HV_{0.05}$. Energy dispersive X-ray spectroscopy carried out with a scanning electron microscope (SEM-EDS) showed that the microstructures of the samples consist of different phases such as Ti, Ni_2Ti_3, $NiTi_2$, Ni_3Ti and TiO_2 as a function of electric current. The XRD analysis also supported the SEM-EDS results. The nano-indentation technique was used to determine the elastic modulus of different phases.

Keywords: NiTi intermetallics, electric-current-activated sintering (ECAS), nano-indentation

Ta študija je usmerjena v preiskavo in situ izdelave intermetalnega NiTi-kompozita iz mešanice prahov z masnima deležema 50 % niklja v prahu in 50 % titana v prahu. Obe vrsti prahu sta bili zmešani v stehiometričnem razmerju, ki ustreza molskemu razmerju NiTi 1 : 1, zmleti v kroglastem mlinu in enoosno stisnjeni pri tlaku 170 MPa. Petnajstminutno sintranje je bilo izvršeno v jeklenem kalupu s sintranjem, aktiviranim z električnim tokom. Pri sintranju so bili uporabljeni električni tokovi 1000 A, 1300 A in 2000 A, medtem ko je bila napetost v območju med 0,9 V in 1,2 V. Faze v vzorcih so bile določene z rentgenom (XRD) in izmerjena je bila trdota po Vickersu (701 ± 166) $HV_{0,05}$. Energijska disperzijska rentgenska spektroskopija (EDS), izvršena na vrstičnem elektronskem mikroskopu (SEM-EDS), je pokazala, da je mikrostruktura vzorcev sestavljena iz različnih faz, kot so Ti, Ni_2Ti_3, $NiTi_2$, Ni_3Ti in TiO_2, odvisno od električnega toka. XRD-analiza je podprla rezultate, dobljene s SEM-EDS. Elastični modul različnih faz je bil določen z nanovtiski.

Ključne besede: intermetalna zlitina NiTi, sintranje, aktivirano z električnim tokom (ECAS), nanovtiski

1 INTRODUCTION

To meet the increasing demand of the aerospace and automobile industries for lightweight structural materials suitable for high-temperature applications, researchers focus on lightweight and high-strength intermetallics.[1] Intermetallic compounds are promising materials for structural and non-structural high-temperature applications (heat resistance, corrosion resistance, electronic devices, magnets, super conductors).[2,3] Especially NiTi alloys are some of the most technologically important shape-memory alloys[4,5] which find extensive applications in the mechanical, medical, electronic, chemical and aerospace industries due to their excellent shape-memory effect, high erosion resistance, high damping capacity and biocompatibility. These properties make them suitable candidates for various engineering applications.[2–7] Nickel titanium is a near-equiatomic intermetallic exhibiting distinctive and desirable thermo-mechanical properties, namely, the thermal shape-memory effect and super elasticity.[8] Up to now, a number of processes including self-propagating high-temperature synthesis (SHS), thermal explosion, laser-melting deposition, casting and mechanical alloying techniques[2,5,9,10] have been used for manufacturing ıntermetallics. In the electric-current-activated/assisted sintering (ECAS) technique, a cold-formed compact obtained with uniaxial compression is inserted into a container heated by the passing electrical current. A sintering pressure of 50 MPa is applied and maintained throughout the sintering.[11] The present study aimed to determine the effect of the current on the production of a NiTi intermetallic from the Ni and Ti elemental powders.

2 EXPERIMENTAL PROCEDURE

2.1 Materials and methods

Powder materials from titanium (99.5 % purity, 35–44 μm) and nickel (99.8 % purity, 3–7 μm) were used as the starting materials to manufacture a NiTi intermetallic compound. The Ni and Ti powders were mixed in the stoichiometric ratio corresponding to the Ni-Ti phase diagram (**Figure 1**), in a molar proportion of 1 : 1.

The powder mixture was cold-pressed before the sintering to form a cylindrical compact in a metallic die under a uniaxial pressure of 170 MPa. Dimensions of a compact were 15 mm in diameter and 5 mm in thickness. The production of the NiTi intermetallic compounds was performed with the electric-current-activated sintering technique in an open atmosphere at 1000–2000 A for 15 min as shown in **Figure 2**. The process parameters are listed in **Table 1**.

Table 1: Process parameters for the samples
Tabela 1: Procesni parametri pri vzorcih

Sample code	*x*/%	Current (A)	Voltage (V)
NT1	50Ti-50Ni	1.000	0.9–1.2
NT2	50Ti-50Ni	1.300	0.9–1.2
NT3	50Ti-50Ni	2.000	0.9–1.2

After the sintering, the specimens were unloaded and air-cooled to room temperature. After metallographic preparations, the resulting microstructures and phase constitutions were characterized.

2.2 Characterization

The morphologies of the samples were examined with scanning electron microscopy (SEM-EDS) in terms of the resulting phases. An X-ray diffraction (XRD) analysis was carried out using Cu-K_α radiation with a wavelength of 0.15418 nm over a 2θ range of 10–80 °. The micro-hardness of the investigated samples was measured employing the Vickers-indentation technique with a load of 50 g using a Struers Duramin hardness instrument. For determining the elastic modulus of the samples, nano-indentation device DUH-211S by Shimadzu was used at a load of 98 mN and a dwell time of 10 s. The ImageJ programme was also used to determine the porosity of fractions of the samples.

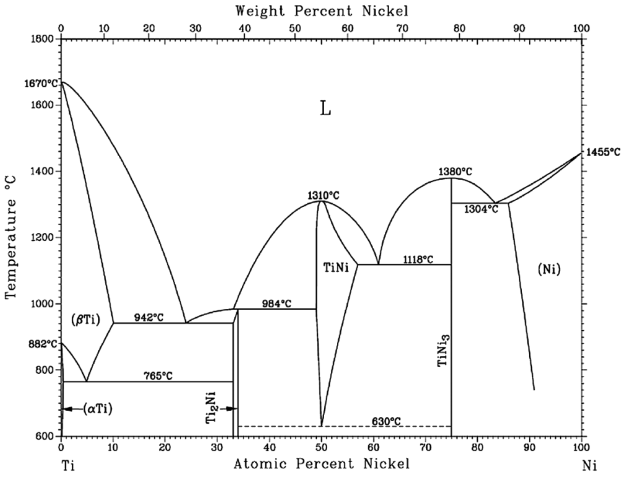

Figure 1: Ni-Ti phase diagram[3]
Slika 1: Fazni diagram Ni-Ti [3]

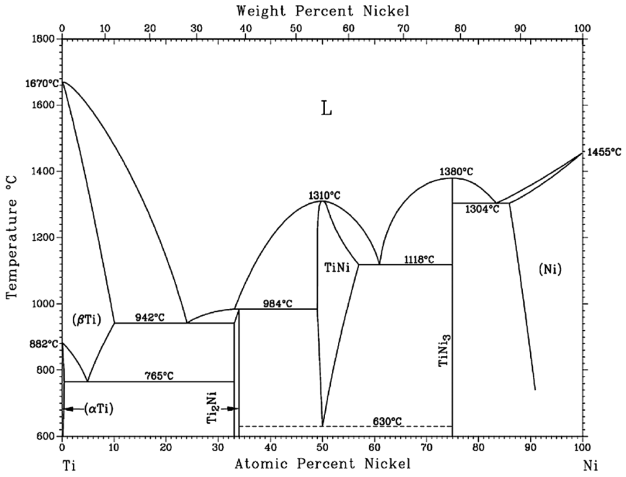

Figure 2: Schematic of electric-current-assisted sintering (ECAS) process
Slika 2: Shematski prikaz sintranja z električnim tokom (ECAS)

3 RESULTS AND DISCUSSION

3.1 SEM-EDS analysis

The morphologies of the as-received Ni and Ti powders are shown in **Figure 3**. The metallic Ni-powder

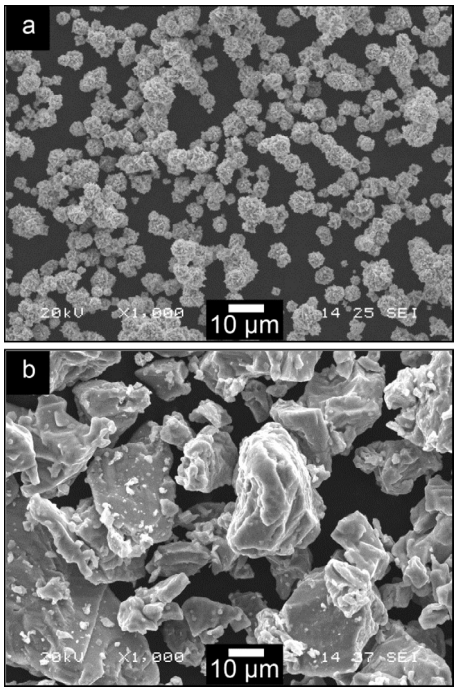

Figure 3: SEM micrographs of: a) Ni powder, b) Ti powder
Slika 3: SEM-posnetka prahov: a) Ni, b) Ti

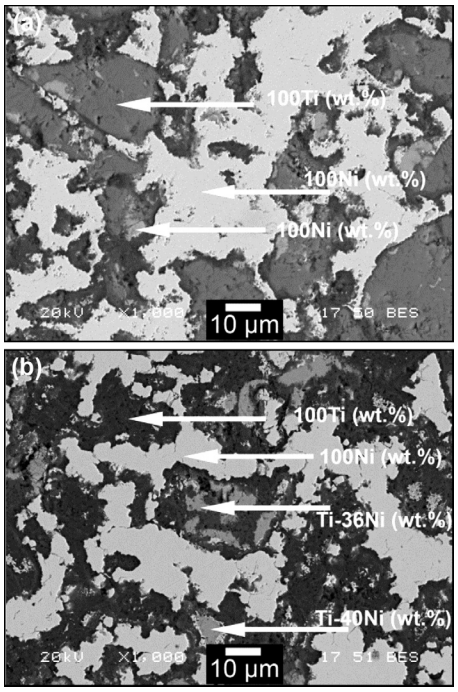

Figure 4: SEM-EDS analyses of: a) NT1, b) NT2 composites
Slika 4: SEM-EDS-analizi kompozitov: a) NT1, b) NT2

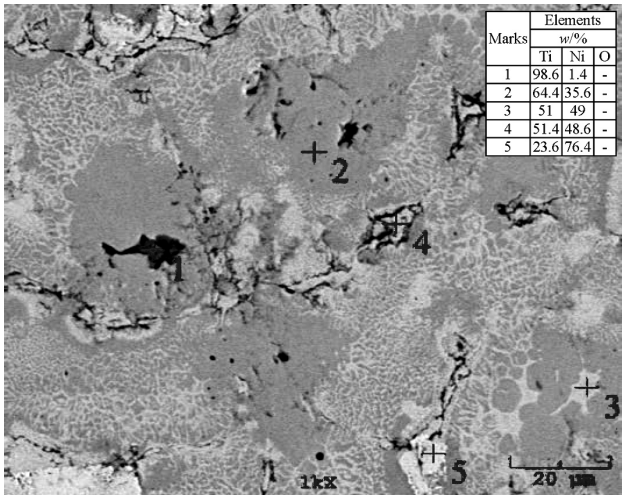

Figure 6: SEM-EDS analyses of NT3 composite
Slika 6: SEM-EDS-analize kompozita NT3

particles were generally spherical with a diameter of 4–7 μm. The Ti-powder particles had sharp corners and were less than 40 μm in size.

SEM-EDS analyses of the NT1 and NT2 intermetallic compounds are shown in **Figure 4**. The microstructure in **Figure 4a** shows that a low current intensity results in separately formed Ni and Ti areas. When increasing the values of the current for NT2 (**Figure 4b**), new phases like $NiTi_2$ (**Figure 1**) start to form, but these microstructures are still far from the stoichiometric composition of the main NiTi phase.

When increasing the current to 2000 A for the NT3 sample (**Figure 5**), the main phases in the microstructure such as NiTi, $NiTi_2$, Ni_3Ti are evident. Besides, there are also a small amount of the residual Ti phase and a small oxidation problem due to the open atmosphere. It can be inferred that a high current intensity leads to a high amount of intermetallic phases. According to the ImageJ image-analysis programme, a porosity of 0.2 % can be found in the microstructures.

As can be seen from the SEM and EDS analyses presented in **Figure 6**, the reaction of the NiTi-compound synthesis was not completed. It is assumed that the applied voltage was insufficient for a complete transformation of the NiTi phases during the sintering.

3.2 XRD analysis

The XRD analysis (**Figure 7**) shows that the main phase of the composite is $NiTi_2$. The NiTi phase is also seen as a small peak. Additionally, Ni_3Ti, Ti and TiO are the other phases existing in the NT3 composite. These results support the observations from the SEM-EDS analysis.

3.3 Hardness and the elastic modulus

The measured $HV_{0.05}$ hardness values for the NT1, NT2 and NT3 samples are (250 ± 27), (405 ± 71) and

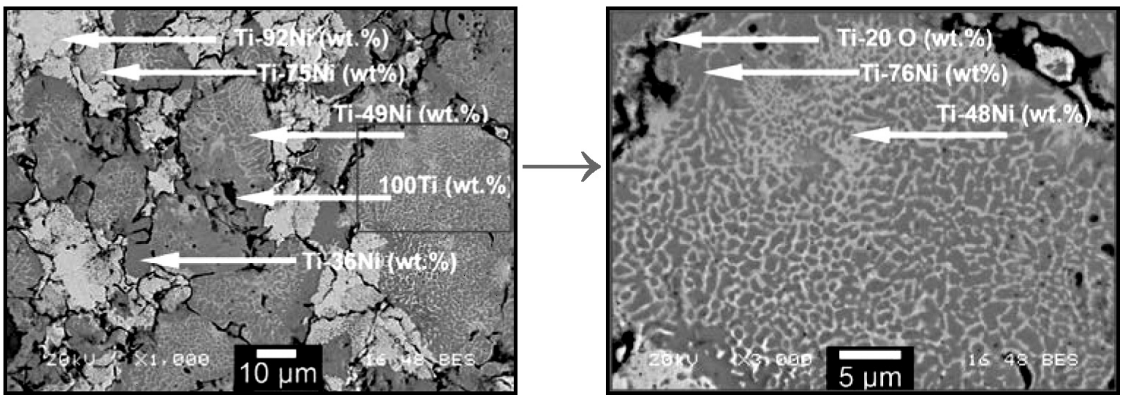

Figure 5: SEM-EDS analyses of NT3 composite
Slika 5: SEM-EDS-analizi kompozita NT3

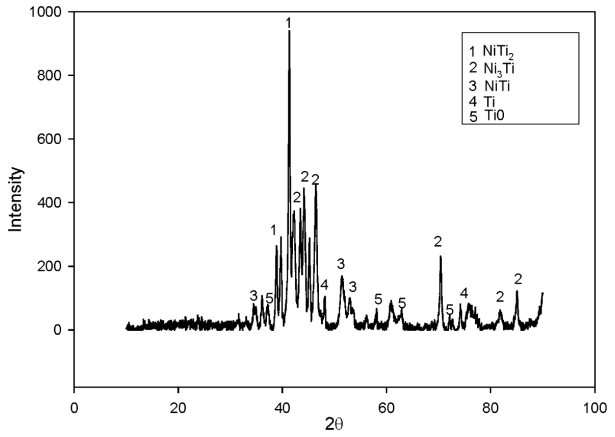

Figure 7: XRD analysis of NT3 sample
Slika 7: Rentgenogram vzorca NT3

(701.6 ± 166), respectively. The hardness values are in good agreement with the literature.[1,12] The elastic-modulus values for the NT1, NT2 and NT3 samples determined with the nano-indentation technique are (98.3 ± 9) GPa, (120 ± 23) GPa and (132 ± 25) GPa, respectively. Nano-indentation is an important technique for probing the mechanical behavior of materials at small-length scales.[13] The results for the elastic modulus cannot be compared to the literature because of the contrasting reported values.[14] However, the obtained value of 135 GPa is between the elastic-modulus values for the Ni and Ti materials.

4 CONCLUSIONS

The reaction of the NiTi-compound synthesis was not completed. It is inferred that the applied voltage was insufficient for a complete transformation of the NiTi phases. When increasing the current intensity from 1000 A to 2000 A, the fractions of intermetallic phases NiTi, $NiTi_2$ and Ni_3Ti increased as well. There was also a small amount of retained metallic Ti in the microstructure. The hardness of the intermetallic composites was increased from 250 HV to 701 HV by increasing the current intensity, due to the formation of higher amounts of the intermetallic phases. The elastic modulus of the composites was between the elastic-modulus values for the Ni and Ti materials.

Acknowledgements

This paper was completed within the framework of the PhD work of Mrs. Tuba YENER during a research visit at the TU Dortmund University, the Department of Materials Test Engineering (WPT) between 06–09/2014. The host institution and the home institution, the Sakarya University, the Department of Metallurgy and Materials Engineering, gratefully acknowledge the excellent scientific exchange and the financial support of the PhD student exchange.

5 REFERENCES

[1] X. Songa et al., Microstructure and mechanical properties of Nb- and Mo-modified NiTi-Al-based intermetallics processed by isothermal forging, Materials Science & Engineering A, 594 (**2014**), 229–234, doi:10.1016/j.msea.2013.11.070

[2] N. Ergin et al., An investigation on TiNi intermetallic produced by electric current activated sintering, Acta Physica Polonica A, 123 (**2013**), 248–249, doi:10.12693/APhysPolA.123.248

[3] M. Farvizi et al., Microstructural characterization of HIP consolidated NiTi-nano Al_2O_3 composites, Journal of Alloys and Compounds, 606 (**2014**), 21–26, doi:10.1016/j.jallcom.2014.03.184

[4] F. Neves et al., Mechanically activated reactive forging synthesis (MARFOS) of NiTi, Intermetallics, 16 (**2008**), 889–895, doi:10.1016/j.intermet.2008.04.002

[5] P. Novak et al., Effect of SHS conditions on microstructure of NiTi shape memory alloy, Intermetallics, 42 (**2013**), 85–91, doi:10.1016/j.intermet.2013.05.015

[6] T. Yener et al., Synthesis and characterization of metallic-intermetallic Ti-$TiAl_3$, Nb-Ti-$TiAl_3$ composite produced by electric current activated sintering (ECAS), Mater. Tehnol., 48 (**2014**) 6, 847–850

[7] G. Chan et al., In-situ observation and neutron diffraction of NiTi powder sintering, Acta Materialia, 67 (**2014**), 32–44, doi:10.1016/j.actamat.2013.12.013

[8] Z. Huan et al., Porous NiTi surfaces for biomedical applications, Applied Surface Science, 258 (**2012**), 5244–5249, doi:10.1016/j.apsusc.2012.02.002

[9] M. Krasnowski et al., Al_3Ni_2-Al composites with nanocrystalline intermetallic matrix produced by consolidation of milled powders, Advanced Powder Technology, 25 (**2014**), 1362–1368, doi:10.1016/j.apt.2014.03.018

[10] A. Molladavoudi et al., The production of nanocrystalline cobalt titanide intermetallic compound via mechanical alloying, Intermetallics, 29 (**2012**), 104–109, doi:10.1016/j.intermet.2012.05.012

[11] R. Orrù et al., Consolidation/synthesis of materials by electric current activated/assisted sintering, Materials Science and Engineering R: Reports, 63 (**2009**), 127–287, doi:10.1016/j.mser.2008.09.003

[12] F. Gao et al., Abrasive wear property of laser melting/deposited Ti_2Ni/TiNi intermetallic alloy, Transactions of Nonferrous Metals Society of China, 17 (**2007**), 1358–1362, doi:10.1016/S1003-6326(07)60277-5

[13] X. Deng et al., Deformation behavior of (Cu, Ag)-Sn intermetallics by nanoindentation, Acta Materialia, 52 (**2004**), 4291–4303, doi:10.1016/j.actamat.2004.05.046

[14] Y. Liu et al., Apparent modulus of elasticity of near-equiatomic NiTi, Journal of Alloys and Compounds, 270 (**1998**), 154–159, doi:10.1016/S0925-8388(98)00500-3

UDK 519.61/.64:621.74.047
Original scientific article/Izvirni znanstveni članek

ISSN 1580-2949
MTAEC9, 49(5)725(2015)

CONTROL OF SOFT REDUCTION OF CONTINUOUS SLAB CASTING WITH A THERMAL MODEL

KONTROLA MEHKE REDUKCIJE PRI KONTINUIRNEM LITJU SLABOV S TERMIČNIM MODELOM

Josef Stetina, Pavel Ramik, Jaroslav Katolicky

Brno University of Technology, Technicka 2, 616 69 Brno, Czech Republic
stetina@fme.vutbr.cz

Prejem rokopisa – received: 2014-08-09; sprejem za objavo – accepted for publication: 2014-10-17

doi:10.17222/mit.2014.189

The internal quality of cast steel slabs during the radial continuous casting is significantly affected by the setting of support rollers. During the passes through the support rolls the steel cools from 1400 °C to 600 °C, therefore the shrinkage of the material must be controlled with the setting of the reduction profile. The setting of the reduction profile with fixed rollers is a compromise used for all the cast steel. During the continuous casting the wear of the rolls occurs and this must also be considered when setting the profile with rollers. A 3D thermal model is used for the optimum setting. As the reduction setting cannot be optimized for older casters, internal defects are often present. New machines for continuous casting of steel are fitted with soft reduction, i.e., the system for controlling the roller position and setting the reduction profile for any type of steel. The control system is connected on-line with the 3D thermal model.

Keywords: concast slab, numerical models, contraction, soft reduction

Notranja kakovost ulitih jeklenih slabov pri radialnem kontinuirnem litju je odvisna od nastavitev podpornih valjev. Ko jeklo prehaja preko podpornih valjev, se ohlaja iz 1400 °C na 600 °C. Pri tem nastaja krčenje materiala, kar je treba upoštevati pri nastavitvi profila. Nastavitev profila redukcije z valji je kompromis za vse ulito jeklo. Med kontinuirnim litjem nastaja tudi obraba valjev, ki jo je treba upoštevati pri nastavitvi profila z valji. Za optimalno nastavitev podpornih valjev je uporabljen 3D termični model. Nastavitve redukcije ni mogoče optimirati pri starih livnih napravah, zato so pogoste notranje napake. Nove naprave za kontinuirno litje jekla so opremljene z mehko redukcijo, to je s sistemom upravljanja kontrole pozicije valjev, ki omogoča nastavitev profila redukcije za vsako jeklo. Ta sistem kontrole je on-line povezan s 3D termičnim modelom.

Ključne besede: concast slab, numerični modeli, krčenje, mehka redukcija

1 INTRODUCTION

Materials with high utility parameters are increasingly in demand and the traditional production is being replaced with higher-quality steels. More and more sophisticated aggregates using more sophisticated technological procedures are being implemented. To maintain the competitiveness and diversification of the production and to expand to the other markets, it is necessary to monitor the technological development.

In the case of concasting, it is not possible to fulfil these requirements without the application of the models of caster processes depending on thermo-mechanical relationships. These models can be applied both off-line and on-line. For an off-line model the calculation time is longer than the actual casting process. An on-line model runs in real time and uses the data directly from the operation – and the time used for the calculation is equal or shorter than the time of the actual process.

These models support the designs of new machines and the redesigns of old machines. They facilitate the identification and quantification of any potential defect and the optimization of various operational conditions with the aim to increase the productivity and minimize the occurrence of defects[1].

Due to the complexity of the investigations of the influences of all the involved factors, it is not possible to develop a mathematical model that would cover all of them. It is better to group the influences according to the three main parameters, the heat and the mass transfer and the mechanical behaviour.

The influences of the heat and the mass transfer are the greatest because the temperature field gives rise to mechanical and structural effects. The development of a model of the temperature field (of a slab) with an interface providing the data for the mechanical stress and strain models is therefore the top-priority task.

The new caster for casting steel must be designed to cast different types of steel, including special types, with the maximum quality. **Figure 1** shows a diagram of a modern caster with a straight first section, followed by a curvature. In segments 1 to 12 the displacement of the whole structure and of individual rollers with a small radius can be controlled hydraulically. Another trend in the modern caster is a split of the secondary-cooling area into several zones, in this case up to 17 individually controlled cooling zones equipped with air-mist nozzles. More information about the optimization of the secondary cooling is found in[2,3].

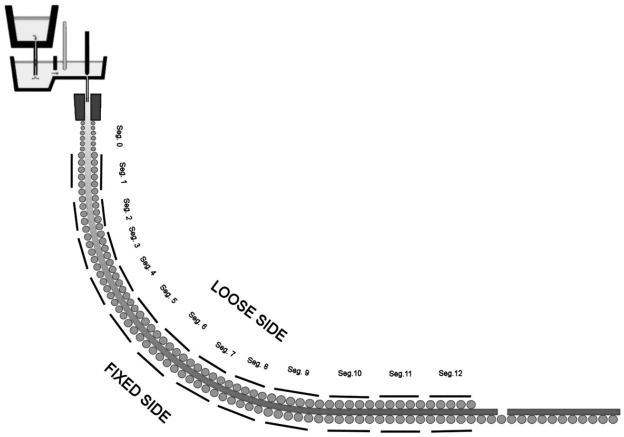

Figure 1: Slab caster
Slika 1: Naprava za ulivanje slabov

In continuous casting of steel there are two problems that affect the quality of the resulting slabs. The first is the contraction of steel during its cooling in the caster; to prevent internal shrinkage the rollers that are in contact with the blank must be set to reduce the profiles of individual segments. A fixed reduction is optimal only for one temperature profile of one blank, but a change in the casting speed makes the reduction larger or smaller. The second problem is bulging, i.e., the bulge of a solidified shell due to the hydrostatic pressure of the steel. This bulge requires additional rollers and thus leads to the alternating stress, decreasing the possibility of cracking. The solution of both problems is soft reduction (**Figure 2**). On one side of the roller track, the caster from **Figure 1** usually has a small radius with options in real time to adjust the positions of the rollers and, thereby, control the reduction profile. The reduction can be carried out only in the place where the centre of the slab is still stiff and the optimum point is the end of the solidification (the metallurgical length). This paper aims to find out when it is necessary to use soft reduction during steel casting and when it is desirable to have linear or other profiles. To answer these questions a model of the temperature field[4] is applied.

2 MODEL OF THE SLAB TEMPERATURE FIELD

The 3D model was first designed as an off-line version and later as an on-line version so that it worked in real time. After being corrected and tested and thanks to the universal nature of the code, it is possible to implement it on any caster. The numerical model takes into account the temperature field of the entire slab (from the meniscus of the level of the melt in the mould to the cutting torch) using a 3D mesh containing more than a million nodal points.

The solidification and cooling of a concast slab are global problems of the 3D transient-heat and mass transfer. If the heat conduction within the heat transfer in this

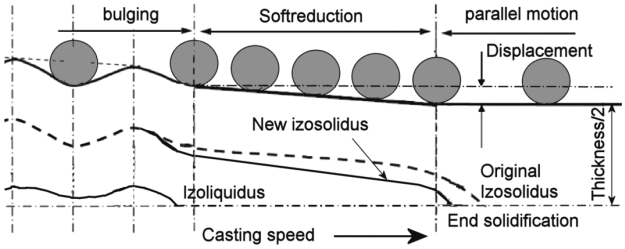

Figure 2: Diagram of soft reduction
Slika 2: Shematski prikaz mehke redukcije

system is decisive, the process is described with the Fourier-Kirchhoff equation. It describes the temperature field of a solidifying slab in all three states: at the temperatures above the liquidus (i.e., the melt), within the interval between the liquidus and solidus (i.e., in the mushy zone) and at the temperatures below the solidus (i.e., the solid state). For reliable solutions it is appropriate to use the explicit numerical method of control volumes. A numerical simulation of the release of the latent heats of the phase or structural changes is carried out by introducing the enthalpy function dependent on temperature T, preferably in the form of the enthalpy related to unit volume H_v, containing the latent heats. After an automated generation of the mesh (pre-processing), the model uses the thermophysical material properties of the investigated system, including their dependence on the temperature – in the form of tables or using polynomials: heat conductivity k, specific heat capacity c and density ρ of the cast metal. The temperature distribution in the slabs is described with the enthalpy balance equation.

A simplified Equation (1), suitable for application on radial casters with a large radius, where only the speed

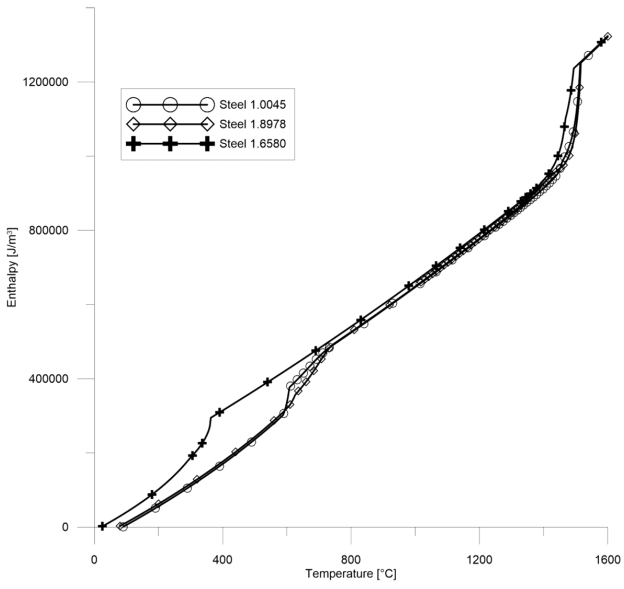

Figure 3: Enthalpy functions of steels
Slika 3: Funkcija entalpij jekel

Table 1: Selected types of steel with their compositions used for the calculation
Tabela 1: Kemijska sestava izbranih jekel, uporabljenih pri izračunu

Class	Mark	Group	C	Mn	Si	P	S	Cu	Ni	Cr	Mo	V	Ti	Al	Nb	$T_{solidus}$	$T_{liquidus}$
1.0045	S355G8	1	0.011	1.550	0.450	0.075	0.025	0.000	0.000	0.000	0.00	0.000	0.000	0.375	0.020	1443.6	1514.1
1.8978	L555MB	2	0.050	1.600	0.300	0.150	0.010	0.250	0.150	0.250	0.000	0.000	0.015	0.350	0.055	1466.0	1516.4
1.6580	30CRNIMO	3	0.280	0.450	0.250	0.125	0.025	0.100	1.900	1.900	0.350	0.000	0.000	0.300	0.000	1371.5	1493.8

(of the movement of the slab) component w in the z-direction is considered, is:

$$\frac{\partial H_v}{\partial t}+\frac{\partial}{\partial z}(\rho w_z H_v)=k\left(\frac{\partial^2 T}{\partial x^2}+\frac{\partial^2 T}{\partial y^2}+\frac{\partial^2 T}{\partial z^2}\right) \quad (1)$$

Volume enthalpy H_v as a thermodynamic function of the temperature must be known for each specific steel. It depends on the steel composition and the cooling rate. The dependence of function H_v for three different steels is shown in **Figure 3**.

The unknown enthalpy of the general nodal point of the slab in the next time step ($\tau + \Delta\tau$) is expressed with the following explicit formula:

$$H_{v_{i,j,k}}^{(\tau+\Delta\tau)}=H_{v_{i,j,k}}^{(\tau)}+(Qz1_{i,j}+Qz_{i,j}+Qy1_i+Qy_i+Qx1+Qx)\cdot\frac{\Delta\tau}{\Delta x\cdot\Delta y\cdot\Delta z} \quad (2)$$

The heat flow through the general nodal point *(i, j, k)* in the z-direction is described with Equation (3):

$$Qz_{i,j}=k\frac{A_z}{\Delta z}(T_{i,j,k+1}^{(\tau)}-T_{i,j,k}^{(\tau)})-A_z w_z H_{v_{i,j,k}}^{(\tau)} \quad (3)$$

The initial condition for the solution is the setting of the initial temperature in individual points of the mesh. The appropriate value is the highest possible temperature, i.e., the casting temperature. The boundary conditions in different places and different systems are described with Equations (4a) to (4e):

1. $T = T_{cast}$ at the meniscus (4a)

2. $-k\frac{\partial T}{\partial n}=0$ at the plane of symmetry (4b)

3. $-k\frac{\partial T}{\partial n}=a-b\sqrt{\frac{L_{mould}}{w_z}}$ in the mould (4c)

4. $-k\frac{\partial T}{\partial n}=\left[h_{tc}+\sigma_0\varepsilon(T_{surface}^2+T_{amb}^2)(T_{surface}+T_{amb})\right]\cdot(T_{surface}-T_{amb})$ in the secondary- and tertiary-cooling zones (4d)

5. $-k\frac{\partial T}{\partial n}=11513.7T_{surface}^{0.76}w_z^{-0.2}(2\theta)^{-0.16}$ beneath the support rollers[5]. (4e)

3 PARAMETRIC STUDY OF SLAB CASTING

For this parametric study we selected three steels with different chemical compositions, where the problems of internal defects[4] were solved. The chemical compositions are shown in **Table 1**, which also shows the liquidus and solidus temperatures.

Solidification-analysis package IDS using the chemical compositions for calculating the thermophysical properties is used to model the temperature field.[6] As can be seen from **Figure 4** the density in the temperature range between the liquidus temperature and 800 °C is almost identical for all three investigated steel grades.

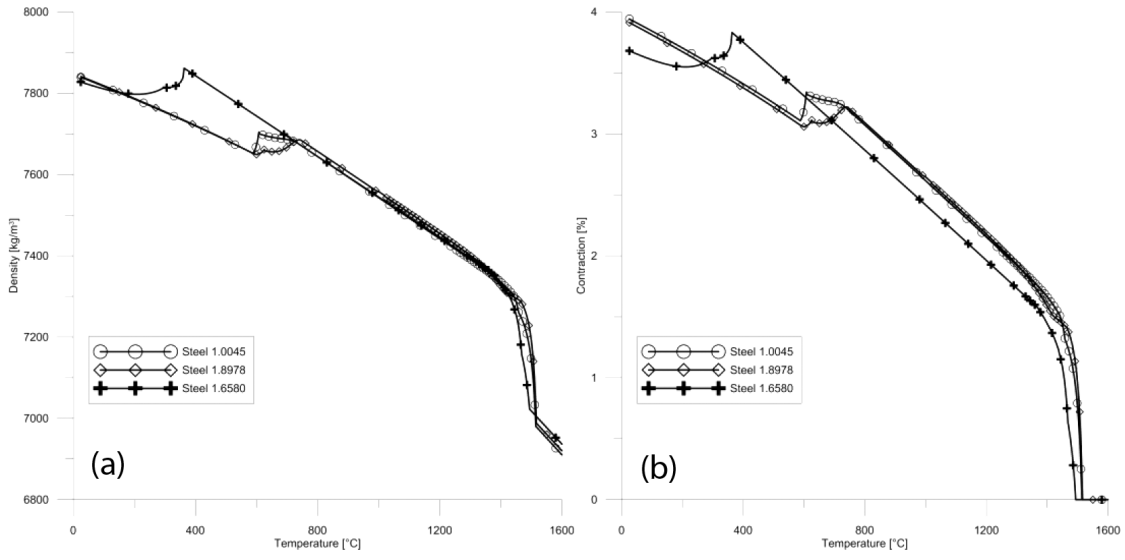

Figure 4: a) Density and b) contraction of the selected steels
Slika 4: a) Gostota in b) krčenje izbranih jekel

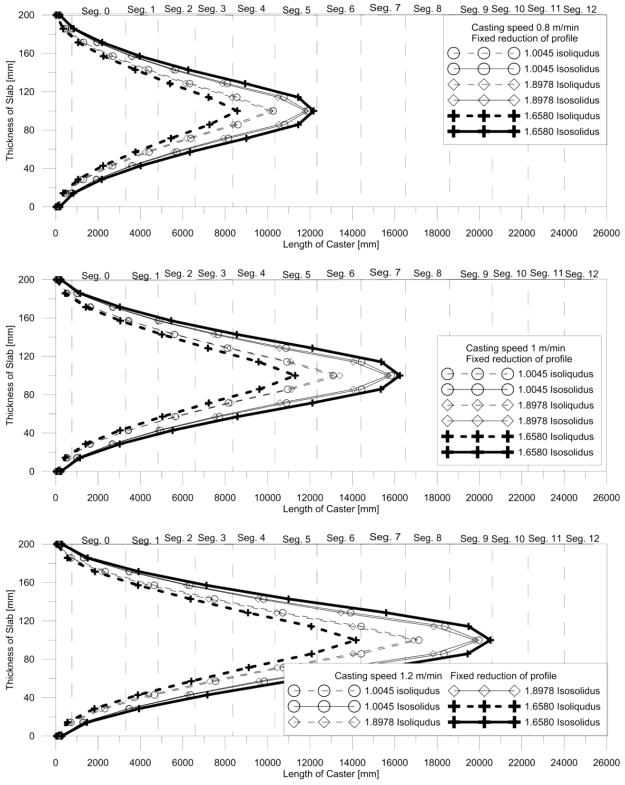

Figure 5: Liquidus and solidus temperatures for casting speeds of (0.8, 1.0 and 1.2) m/min

Slika 5: Likvidusna in solidusna temperatura za hitrosti ulivanja (0,8, 1,0 in 1,2) m/min

An analogous conclusion can be made for the contraction (**Figure 4**). However, the cross-sectional reduction of a cast blank has to be considered for the temperatures lower than 800 °C, together with the influence of the structural-phase changes in the solid state. In such cases, the casting control has to take into account the cross-sectional reduction due to the phase changes, or the secondary-cooling requirements, to be properly updated to keep the temperature of the blank above 800 °C.

The next step is a parametric study of the simulations of casting the three steel classes and three casting speeds ((0.8, 1.0 and 1.2) m/min), representing the expected caster operating range. The calculated waveforms of the isolines of the liquidus and solidus are shown in **Figure 5**.

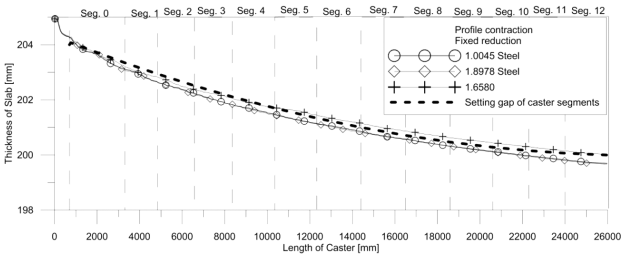

Figure 6: Contraction due to the thickness and slab-temperature decreases and the setting of the roll gap

Slika 6: Profil krčenja zaradi zmanjšanja debeline in temperature slaba ter nastavitev reže med valji

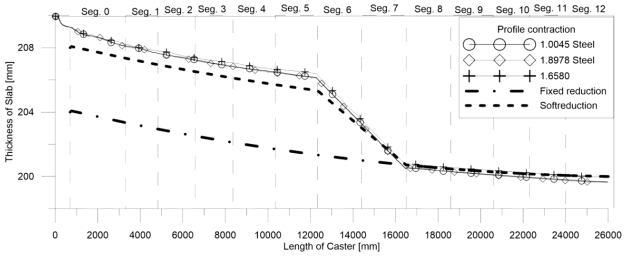

Figure 7: Contraction profile that uses soft reduction in segments 6 and 7

Slika 7: Profil krčenja pri uporabi mehke redukcije v segmentih 6 in 7

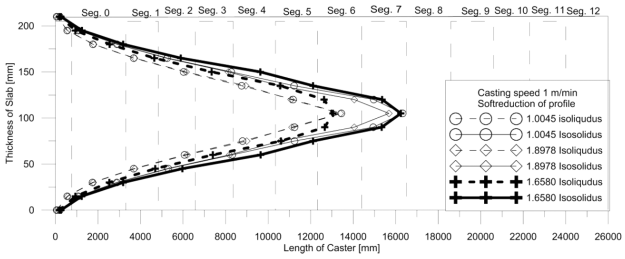

Figure 8: Course liquidus and solidus isolines when applying soft reduction in segments 6 and 7

Slika 8: Likvidusne in solidusne izolinije pri uporabi mehke redukcije v segmentih 6 in 7

These calculations and other parameters, such as the temperature superheat, the primary and secondary cooling, are set in equal forms. A constant reduction of the profile is considered, so the resulting slab thickness is 200 mm (**Figure 6**).

Figures 6 and **7** show the calculated contraction profiles for the selected classes of steel. In both cases the calculation considered is calculated for a casting speed of 1 m/min and the conditions corresponding to **Figure 5** as the basic requirements for the output profile on the machine and a slab thickness of about 200 mm. The thick dashed line marks the roller positions obtained with the narrowing of the machine profile. To allow the use of soft reduction the input size of a blank must be larger. The difference in the size of the mould is 205 mm for the caster without soft reduction and 210 mm for the caster with soft reduction.

The temperature field in the form of mileage isocurves of the liquidus and solidus considering soft reduction is shown in **Figure 8**. With respect to the position of the isolines of the solidus and liquidus temperature, the temperature field is virtually the same, as shown in the middle of **Figure 5**. However, it should be understood that the initial thickness of the slab is larger by 5 mm because soft reduction shortens the metallurgy length.

4 CONCLUSION

This paper presents a 3D numerical model of a temperature field (for concasting steel) using the in-house software and its applications for the initial study that compares the waveforms of liquidus and solidus isolines

and strand shrinkage. Furthermore, we compared a caster with a constant constriction, i.e., with a fixed adjustment between the roller gap and the caster with adjustable rollers used for controlling the narrowing, i.e., soft reduction. The results of this analysis will be used in a mathematical model designed for the management of soft reduction. The mathematical model will be integrated in the control systems at all the levels within the automation pyramid that is being developed in the ASM Automation Company (www.asmautomation.com). One of the future tasks is a study of the stochastic behaviour of the continuous casting process[7].

Acknowledgments

This work is a result of the research and scientific activities of the NETME Centre, the regional R&D centre built with the financial support from the Operational Programme Research and Development for Innovations within a NETME Centre project (New Technologies for Mechanical Engineering), Reg. No. CZ.1.05/2.1.00/01. 002 and, in the follow-up sustainability stage, supported through NETME CENTRE PLUS (LO1202) with the financial means from the Ministry of Education, Youth and Sports of the Czech Republic under the National Sustainability Programme I.

Nomenclature

a constant of the mold (W/m^2)
A area (m^2)
b constant of the mold (W/(m^2 s$^{0.5}$))
c specific heat capacity (J/(kg K))
h_{tc} heat-transfer coefficient (W/(m^2 K))
H_v volume enthalpy (J/m^3)
k heat conductivity (W/(m K))
L_{mould} length of the mould (m)
T temperature (K)
T_{amb} ambient temperature (°C, K)
T_{cast} casting temperature (°C, K)
$T_{surface}$ temperature of the surface (°C, K)
q density of the heat flow (W/m^2)
Qx, Qy, Qz heat flows (W)
x, y, z axes in a given direction (m)
w_z casting speed in a given direction (m/s)
ρ density (kg/m^3)
σ_o Stefan-Bolzmann constant (W/(m^2 K^4))
ε emissivity (–)
Θ angle of the contact (°)
τ time (s)

5 REFERENCES

[1] A. W. Cramb (Ed.), The Making, Shaping and Treating of Steel: Casting Volume, 11th edition, The AISE Steel Foundation, Pittsburgh, PA, USA 2003, 1000

[2] T. Mauder, C. Sandera, J. Stetina, Mater. Tehnol., 46 (**2012**) 4, 325–328

[3] J. Stetina, T. Mauder, L. Klimes, F. Kavicka, Mater. Tehnol., 47 (**2013**) 3, 311–316

[4] J. K. Brimacombe, The Challenge of Quality in Continuous Casting Process, Metallurgical and Materials Trans. B, 30 (**1999**), 553–566, doi:10.1007/s11663-999-0016-7

[5] J. Zhang, D. Chen, S. Wang, M. Long, Compensation control model of superheat and cooling temperature for secondary cooling of continuous casting, Steel Research Int., 82 (**2011**) 3, 213–221 doi:10.1002/srin.201000148

[6] J. Miettinen, S. Louhenkilpi, J. Laine, Solidification analysis package IDS, Proceeding of General COST 512 Workshop on Modelling in Materials Science and Processing, ECSC-EC-EAEC, Brussels, Luxembourg, 1996

[7] E. Zampachova, P. Popela, M. Mrazek, Optimum beam design via stochastic programming, Kybernetika, 46 (**2010**) 3, 571–582

UDK 621.35/.36:621.352.6
Original scientific article/Izvirni znanstveni članek

ISSN 1580-2949
MTAEC9, 49(5)731(2015)

OPTIMIZATION OF OPERATING CONDITIONS IN A LABORATORY SOFC TESTING DEVICE

OPTIMIZACIJA OBRATOVALNIH RAZMER LABORATORIJSKE GORIVNE CELICE SOFC

Tina Skalar, Martin Lubej, Marjan Marinšek

University of Ljubljana, Faculty of Chemistry and Chemical Technology, Večna pot 113, 1000 Ljubljana, Slovenia
marjan.marinsek@fkkt.uni-lj.si

Prejem rokopisa – received: 2014-08-22; sprejem za objavo – accepted for publication: 2014-12-01

doi:10.17222/mit.2014.209

Solid-oxide fuel cells (SOFCs) are devices that convert chemical energy into electrical energy. They are assembled from three solid components, which, in principle, differ in their thermal expansion coefficients. These differences may cause residual stresses during an operation and consequently lead to physical damage of a cell. From this perspective, the reliability of an operating SOFC is seriously dependent on the thermal stress built inside the multi-layer structure. In this work, some operating conditions in the SOFCs based on an SDC electrolyte, an LSM cathode and a Ni-SDC anode were investigated both experimentally and theoretically. Within the theoretical analysis, the residual stresses and temperature profiles inside an operating cell were modelled with the finite-element method. The results of the mathematical modelling of the warm-up, steady-state or cool-down periods were used to optimize the cell geometry and the thickness of individual cell layers, and to determine the most appropriate operating cell conditions. In order to experimentally confirm some theoretical calculations, a new SOFC testing system was developed, which enabled relatively easy assembling and dismantling as well as quick changes in the operating conditions (temperature, atmospheres). Based on the modelling results, optimization of the operating conditions was proposed in order to reduce the thermal stresses built in the materials.

Keywords: SOFC, modelling, temperature gradient, thermal stress, optimization

Visokotemperaturne gorivne celice pretvarjajo kemično energijo preko katalitskih reakcij v električno energijo. Sestavljene so iz treh trdnih (keramičnih) materialov, ki imajo različne temperaturne razteznostne koeficiente. Različni raztezki materialov povzročajo mehanske napetosti, kar ima lahko za posledico degradacijo (razpad) strukture večslojnega sistema. Zanesljivost gorivne celice je tako odvisna od ustvarjenih mehanskih napetosti v materialih. V tem delu smo raziskovali razmere pri obratovanju tako eksperimentalno kot teoretično za večplastno preizkusno tableto. Zapisali smo matematični model za opis generiranih mehanskih napetosti med segrevanjem, v stacionarnem stanju in med ohlajanjem ter z metodo končnih elementov prišli do numerične rešitve modela. Dobljene rezultate smo uporabili pri optimizaciji geometrije celice in debeline posameznih plasti v večplastni tableti. Za eksperimentalno preverjanje dobljenih rezultatov modeliranja smo razvili nov preizkusni sistem, ki omogoča relativno hitro sestavljanje in razstavljanje ter hitro spremembo obratovalnih razmer (temperature, atmosfere). Na osnovi dobljenih rezultatov je bila predlagana optimizacija preizkusnega sistema za zmanjšanje mehanskih napetosti v materialih.

Ključne besede: SOFC, modeliranje, temperaturni gradienti, termične napetosti, optimizacija

1 INTRODUCTION

Solid-oxide fuel cells (SOFCs) are highly promising and environmentally friendly energy converters with a high energy-conversion efficiency, converting chemical energy of reactants into electrical energy.[1–4]

SOFCs, as any other batteries, consist of three different layers, called SOFC membranes, i.e., an electrolyte, an anode and a cathode, and operate at temperatures between 600 °C and 1000 °C. As an electrolyte, samaria-doped ceria (SDC), a well-known advanced ceramic material, was recently proposed to reduce the SOFC operating temperatures due to its high oxygen-ion conductivity.[5–9]

A cermet of metallic nickel and ceramic, i.e., SDC (Ni-SDC), is most commonly used as the anode material in a SOFC. The main reasons for the selection of Ni-SDC are its thermal-expansion coefficient that is comparable with the SDC electrolyte, a relatively good ionic and electronic conductivity and a catalytic activity acceptable for hydrogen or hydro-carbon electro-oxidation. On the cathode side, doped lanthanum manganite (i.e., lanthanum strontium manganite, LSM) is most commonly used.[10–13]

Since SOFC membranes, in principle, are composed of various materials, their thermal-expansion coefficients (TEC) may differ. For instance, the TEC of an anode cermet is normally somewhat higher than those of the electrolyte and cathode. These differences in the TECs may build stresses in the SOFC membrane during a temperature alteration and, consequently, lead to a SOFC-membrane delamination. From this perspective, the reliability of an SOFC membrane is seriously dependent on the SOFC operating conditions, especially during its heating to the operating steady-state conditions or cooling down to room temperature.[14–18]

One way to approach the problem of determining the optimum operating conditions of an SOFC system is to

employ mathematical modelling. In this way, several parameters, i.e., temperature profiles and stress fields, can be followed without performing complicated and lengthy SOFC experimental tests. The finite-element-method (FEM) modelling was already successfully used by several authors to address similar engineering problems.[19–22]

With the FEM, a continuous problem can be transformed into a discrete problem with a finite number of degrees of freedom.[23–25]

In this paper, the optimum operating parameters in which an SOFC multilayer membrane is not exposed to a critical thermal stress caused by temperature gradients are determined. Additionally, the problem of the optimum cell geometry and the thicknesses of individual cell layers during the warm-up or steady-state periods is addressed.

2 EXPERIMENTAL PROCEDURE

2.1 Material and membrane preparation

An electrolyte made of samarium-doped ceria (SDC) or an anode made of nickel oxide samarium-doped ceria (NiO-SDC) and a lanthanum manganite (LSM) cathode were synthesized using the modified Pechini method and carbonate precipitation, respectively. The exact synthesis procedures are described in[26,27]. Before a multi-layer membrane was prepared, a supporting layer (electrolyte or anode) was pressed into a tablet and pre-sintered at 1000 °C in air in order to ensure the mechanical strength for the screen printing of other layers. The thickness of the screen-printed layers was 20 μm. If an anode-supported system was prepared, an SCD electrolyte was first screen-printed on a NiO-SDC pre-sintered anode. Such a multi-layer system was co-sintered at 1250 °C in order to form a good contact between the layers. The same procedure was used for electrolyte-supported systems with an exception, in which an SDC was first pre-sintered and a NiO-SDC was then screen printed and co-sintered. After the co-sintering, an LSM cathode was screen printed on the electrolyte, opposite to the anode side. Such a multi-layer system was again co-sintered at 1200 °C.

2.2 Testing-system assembly

The testing system (**Figure 1**) was composed of a multilayer tablet (anode/electrolyte/cathode), which was sealed in steatite ceramics. The steatite ceramics was placed between two quartz tubes to prevent the mixing of the inner and outer atmospheres, or the mixing of the cathode oxidative and anode reductive atmospheres (Viton o-rings were used for sealing). The whole system was then placed into another protective quartz tube. Heaters were mounted outside the protective quartz tube. The inner and outer quartz tubes were embedded into a stainless-steel (1.4404) case and fixed to the construction with four screws. The testing system was isolated with a α-alumina insulation 2 cm. The NiCr-Ni thermocouple was pushed through a small hole in the stainless-steel case and coupled with the display.

2.3 Used model

The gas flow and temperature distribution were simulated using numerical methods. The transport of mass and energy was calculated using the continuum theory.[28] The heat was introduced as a homogeneous-volume heat source at the heating element. The heat was dissipated at the outer boundaries with a heat flux corresponding to the wall temperature and the heat-transfer coefficient obtained with the Churchill and Chu correlation.[29] The system of differential equations was solved utilizing the finite-elements method in a 2D axisymmetric geometry, and the stationary state was achieved at the 35th iteration.

The mechanical stress inside the tested membrane was calculated using a linear elastic material model[30] in combination with the thermal expansion. The reference temperature was defined as the temperature, at which there is no stress in the material. The mechanical model was solved utilizing the finite elements in a 2D axisymmetric geometry.

For all the materials, the average emissivity (ε) of 0.8 was used. Young's modulus (E), Poisson's ratio (ν), the density (ρ), the thermal-expansion coefficient (α) were $200 \cdot 10^9$ Pa,[23] 0.32,[23] 7600 kg/m^3, $11.5 \cdot 10^{-6}$ K^{-1},[31] $55 \cdot 10^9$ Pa,[23] 0.17,[27] 8900 kg/m^3, $13 \cdot 10^{-6}$ K^{-1} [23] and $40 \cdot 10^9$ Pa,[31] 0.25,[31] 6500 kg/m^3,[31] $11.4 \cdot 10^{-6}$ K^{-1} [31] for the SDC, NiO-SDC and the LSM cathode, respectively. The densities for the anode and electrolyte materials were calculated as Archimedes' densities from the dimensions of the sintered bodies.

3 RESULTS AND DISCUSSION

Finding the optimum design and operating conditions makes the SOFC testing rather time-consuming. Moreover, in order to track various parameters during an SOFC continuous run, the testing systems are usually rather complicated and difficult to assemble, making visual observing of a tested multilayer SOFC membrane practically impossible. For this reason, a new SOFC testing system was developed, in which a multilayer tablet (anode/electrolyte/cathode) is sealed in a steatite-ceramics holder and embedded into a double quartz-glass tube, which is then put into a tube oven (as presented in the experimental work, **Figure 1**).

Such a system has a rather simple design, is easy to assemble/dismantle or manipulate, and enables quick changes in the operating conditions (temperature, atmospheres). The true advantage of the simplified SOFC design, however, is the fact that it enables the start of new experiments in short cycles, thereby overcoming the time-consuming difficulty of more complex testing

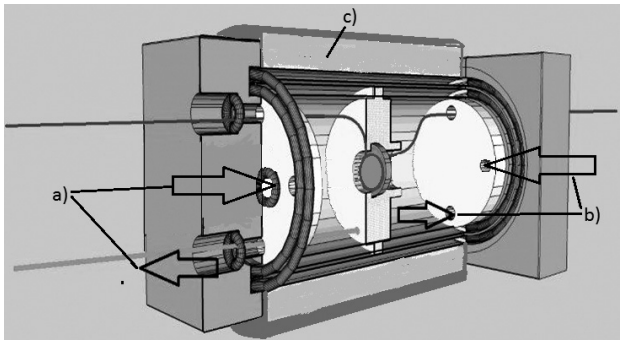

Figure 1: Scheme of a test cell: a) anode inlet/outlet atmosphere, b) cathode inlet/outlet atmosphere and c) tube oven
Slika 1: Shema preizkusne celice: a) vpih in izpih anodnega plina, b) vpih in izpih katodnega plina in c) obodni grelnik

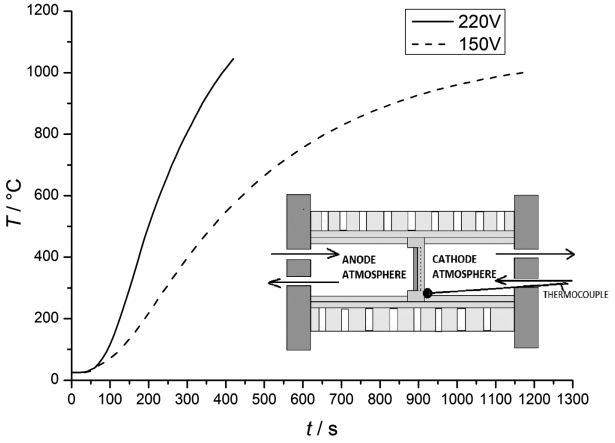

Figure 2: *T* versus *t* relationship measured at the inner side of the quartz tube during the SOFC testing-system start-up; the small insert represents the measuring point
Slika 2: Odvisnost *T* od *t*, merjena na notranji strani kremenove cevi pri zagonu sistema SOFC; izrez prikazuje točko merjenja temperature

systems. However, short testing cycles are always related to rapid temperature changes inside the testing system. It is well known that the temperature increases or decreases in a ceramic multilayer system with different temperature-expansion coefficients, thereby building stresses that may initiate crack formation, which eventually leads to a complete system delamination. In order to avoid such an undesirable multilayer degradation, two approaches are possible: i) numerous tests to determine the temperature regime during a testing cycle, or ii) employing a mathematical simulation model and predicting the temperature gradients as well as the built stress fields in the tested membrane, as was the case in this work.

The first addressed question is the position of the heating elements in the testing system as the heating elements may be placed inside or outside the tested SOFC cell. Positioning the heating elements inside each of the SOFC chambers (the cathode and anode sides) has the advantage of a very fast temperature change, as shown in our previous work.[24] However, the heating of the individual chambers and the tested membrane positioned between both chambers with two point sources placed above and below the membrane also causes some undesired temperature gradients in the membrane, where the center of the membrane is always hotter than its outer regions. These temperature gradients are the greatest during the membrane's rapid heating but cannot be eliminated completely even in the steady operating state due to the heat exchange between the SOFC testing cell and its surroundings. For this reason, the heating elements were placed around the double quartz tube. In such a modification, additional heat-insulating layers between the heater and the membrane are introduced (the quartz tube itself). However, due to the powerful heating elements, rapid temperature changes are still possible (**Figure 2**) even with the heaters placed outside the quartz tubes.

The newly developed SOFC testing design enables the work with multi-layer membrane systems of various shapes, e.g., a cube or a cylinder. Altering the shape of a multi-layer system also causes some changes in the temperature distribution in the heated membrane. The temperature gradients are much more pronounced alongside the radius of the membrane due to the relative position of the heating elements and practically negligible alongside the *z*-axis. Furthermore, the heating mode of the multi-layer membrane suggests that the biggest temperature gradients appear during the membrane heating (shortly after the heaters start to heat up the outer quartz tube) and gradually declines when the temperature of the inner chambers of the SOFC testing system approaches its final value. According to the results of the mathematical modelling, the maximum temperature gradients from the membrane center to its edge ΔT_1 are ≈ 90 °C or ≈ 75 °C for cube or cylinder membranes, respectively (**Figure 3**). This rather noticeable difference in the maximum temperature gradients is introduced by the design of the SOFC testing system itself. Since the heating elements are positioned cylindrically around the quartz tubes, the outer positions of the cube membrane are unevenly distant from the heaters and thus exposed to various heat fluxes. At the same time, due to the relatively thin multi-layer membrane (≈ 3 mm), the temperature gradient alongside the *z*-axis, ΔT_2, is only 2.2 °C for both membrane designs. Since the temperature gradients inside the

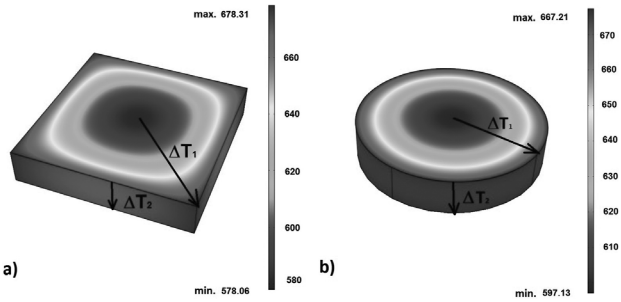

Figure 3: Temperature distribution in the tested membranes: a) cubic membrane and b) cylindrical membrane
Slika 3: Porazdelitev temperature v preizkusni membrani: a) v obliki kvadra in b) v obliki valja

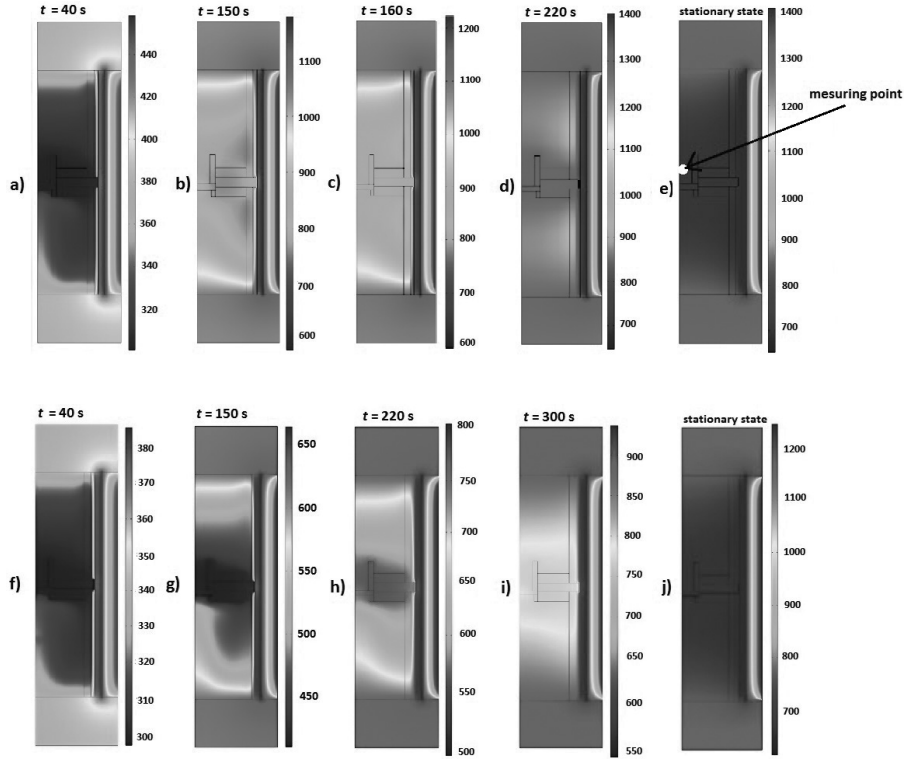

Figure 4: Temperature distributions in both inner chambers of the SOFC testing system and throughout the membrane at various times presented in a vertical plane: a) to e) the heating element is powered with 220 V, f) to j) the heating element is powered with 150 V

Slika 4: Porazdelitev temperature, prikazana v vertikalni ravnini v preizkusni celici po različnih časih segrevanja: a) do e) pri nazivni napetosti grelnika 220 V, f) do j) pri nazivni napetosti grelnika 150 V

tested membrane are one of the prime causes for the induced thermal stresses (as discussed later) a cubic membrane is much more susceptible to potential cracking. For this reason, such membranes are omitted from further modelling.

Starting a new testing cycle and heating up the membrane is a critical point that decisively influences the survival chances of a multi-layer membrane. In order to obtain a greater insight into the circumstances during the system heating, the temperature distribution inside the testing system (including the tested membrane) is mathematically modelled at several pre-chosen times and presented in **Figure 4**. For mathematical modelling, a multilayer electrolyte-supported membrane with thicknesses of the individual layers (anode/electrolyte/cathode) being 20 μm/2000 μm/20 μm, respectively, is assumed. From the sequence of the pictures showing the temperature distribution, it is evident that the temperature inside the testing system starts to rise due to the hot quartz tube that heats the adjacent gas and causes its circulation. The system design, where a stainless-steel case is used to cover the quartz tubes at both ends, is the reason for further temperature increases. More precisely, stainless steel heats up relatively quickly, serving as an additional heat source for the gases inside individual chambers causing their increased circulation. The vertical position of the testing system forces the hot gases to flow alongside the z-axis. Due to this vertical flow of the hot gas inside the bottom chamber, the bottom plane of the membrane heats up more quickly than its top plane, causing temperature gradients in the vertical cross-section throughout the membrane (the temperature distributions at various times throughout the membrane are presented in **Figure 4**). At some critical point, the temperature gradient ΔT_2 in the membrane is maximal (**Figures 4c** and **4h**). This critical time was determined as 160 s or 300 s if the heating element worked with its maximum power (powered with 220 V) or with just 46 % of its maximum power (powered with 150 V), respectively. In the latter case, the temperature inside the SOFC testing system typically rises more slowly, also reducing the built temperature gradients ΔT_1 and ΔT_2 (**Figure 5**). Since the membrane is a multilayer system in which individual layers exhibit different temperature-expansion coefficients, temperature gradient ΔT_2 is particularly important. Dissimilar temperature-expansion coefficients, together with temperature gradient ΔT_2, may introduce a situation in which the expansion of an individual layer during the membrane heating differs from the expansion of the adjacent layer to a degree that causes a membrane delamination. After the critical time, temperature gradient ΔT_2 slowly diminishes and becomes negligible in the steady operating state (**Figures 4e** and **4j**).

A verification of the modelled temperature fields was conducted via additional temperature measurements

using NiCr-Ni thermocouples. The measuring points at each specific time are marked in **Figure 4**. It is evident that the mathematical model used describes the temperature field in the tested system rather well (**Table 1**). Temperature mismatches between the modelled and measured temperatures in either point and at each specific time do not exceed 8 °C. These slight mismatches are ascribed to a somewhat difficult positioning of the thermocouple at the predetermined point and in the dynamic temperature field (the response time of the NiCr-Ni thermocouple is ≈ 2 s).

Table 1: Comparison between modelled and measured temperatures (marked point in **Figure 4**) in the tested system at various heating times

Tabela 1: Primerjava modelirane in merjene temperature (točka merjenja je označena na **sliki 4**) v preizkusnem sistemu pri različnih časih segrevanja

220 V			150 V		
$t_{heating}$ /s	$T_{modelled}$ /K	$T_{measured}$ /K	$t_{heating}$ /s	$T_{modelled}$ /K	$T_{measured}$ /K
40	306	304	40	304	303
160	882	877	300	756	750
7200	1379	1371	7200	1233	1227

Another important issue addressed by mathematical modelling is the fluid-velocity simulation inside both SOFC chambers (**Figure 6**). According to the simulation, the causes of the gas turbulence in the SOFC chambers are the fresh-gas inlet and the created temperature gradients. The cylindrical design of the SOFC testing system causes the gas velocity to be the highest close to the chamber center (≈ $2.2 \cdot 10^{-3}$ m s^{-1}) and relatively low near the surface of the tested membrane. The complex movement path of gas molecules is indicated by their trajectories. The fluid-velocity pictures inside the anode and cathode chambers, however, are not mirror-inverted. Due to the vertical rise of the hot gases, the region of high-gas velocity in the bottom chamber is closer to the membrane relative to the top chamber. Despite the lowest gas velocity of ≈ 3 μm s^{-1} near the membrane surface (10 μm from the surface), no gas pockets with a stationary atmosphere could be observed, which is important from the practical viewpoint of an operating SOFC. Only dynamic atmosphere conditions at the membrane surface may deliver fresh reactants to the diffusion layer of the porous-membrane catalyst and remove gaseous products. Additionally, it can be presented with the mathematical modelling that the introduction of fresh cold gases negligibly influences the temperature fields inside both of the SOFC chambers. The gases entering the anode or cathode chambers are practically instantly heated up to the temperature of the chambers operating at a steady state. This fact is not surprising since the gas inlets are relatively low (≈ 15 mL min^{-1}) while the chambers are relatively large and only ≈ 72 W is needed to heat a gas flow of 15 mL min^{-1} from room temperature to the chamber temperature.

In an SOFC multi-layer system, in principle, three different materials are combined in a single membrane. Since the temperature-expansion coefficients of individual layers are not identical, any temperature alteration may build a stress alongside a phase border and, consequently, cause a delamination of the multi-layer membrane. The first critical point in the lifecycle of a multi-layer membrane arises during its preparation. Specifically, the membrane is prepared by co-sintering all three layers and, subsequently, reducing NiO to Ni in the anode composite. During the sintering, a plastic deformation of the material is allowed. From this perspective, it can be assumed that the system is stress-free at the sintering temperature. In the testing system, the stress-free state is adopted at 1250 °C, at which the NiO/SDC

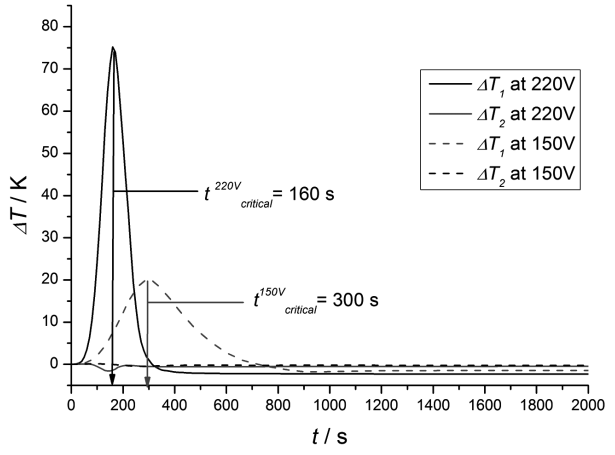

Figure 5: Relationships of induced temperature gradients ΔT_1 and ΔT_2 with t, presented in a vertical plane through the multi-layer membrane

Slika 5: Inducirani temperaturni gradienti ΔT_1 in ΔT_2 v odvisnosti od časa t, prikazani v vertikalni ravnini skozi večplastno membrano

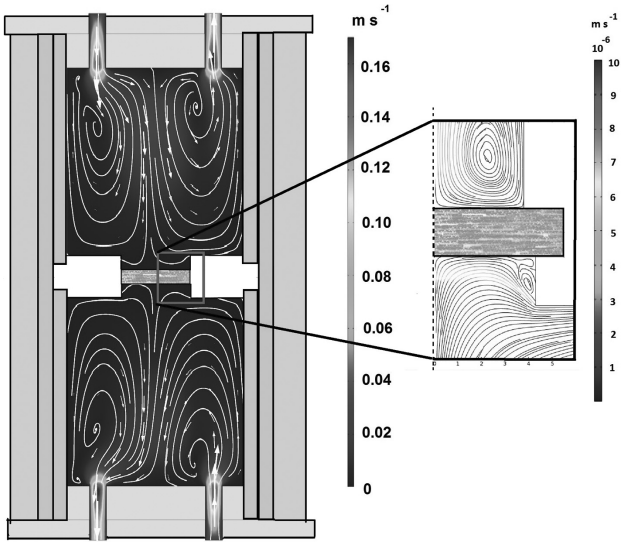

Figure 6: Fluid-velocity simulation together with gas trajectories in both inner chambers

Slika 6: Simulacija gibanja plinov skupaj s trajektorijami plina v notranjih prostorih preizkusnega sistema

anode, the SDC electrolyte, and the LSM cathode are co-sintered. The subsequent reduction of NiO to Ni should not induce any additional stress since Ni may undergo a plastic deformation. Thermal stresses in the multilayer system start to build up below the plastic-deformation temperature, reaching their peak at room temperature.[32] Depending on the temperature-expansion coefficients of the adjacent layers ($13 \cdot 10^{-6}$ K^{-1}, $11.5 \cdot 10^{-6}$ K^{-1} and $11.4 \cdot 10^{-6}$ K^{-1} for Ni/SDC, SDC and LSM, respectively) these built-up stresses may be as high as several hundred MPa and may cause cracks to form.

The residual stresses after the membrane preparation are practically impossible to measure directly; however, by adopting an appropriate mathematical model, they can be calculated rather easily. Thus, if Ni/SDC-SDC-LSM (20 μm-3000 μm-20 μm) is cooled down to room temperature (after the reduction of NiO to Ni) the residual thermal stresses are calculated as ≈ 130 MPa for Ni/SDC of the anode layer, close to the anode-electrolyte phase boundary, ≈ 9 MPa for the electrolyte adjacent to the anode layer, and the lowest stress for LSM (< 1 MPa), at the SDC-LSM phase boundary. Together with the calculated number, the nature of the built stresses must also be taken into consideration. Due to a higher thermal-expansion coefficient, the Ni/SDC layer tends to shrink more than the SDC electrolyte, while LSM shrinks to approximately the same degree as SDC. In a hypothetical situation in which two layers subjected to uneven material shrinkage have approximately the same thickness, the induced stress should bend the bilayer system where the layer with the smaller shrinkage forms a concave surface at the phase boundary. In view of the chosen set of materials and the actual membrane design, the degree of shrinkage suggests that the stress in the anode layer in the cooled-down state is always tensile, while the electrolyte layer is under compression. Therefore, at room temperature, the anode appears to be the potential weak point of the multi-layer system. However, the maximum calculated tensile stress in the anode layer does not exceed the Ni/SDC tensile strength, which is ≈ 150 MPa.[33] As the final result, the calculated values suggest that the multi-layer system should survive the first thermal cycle (sintering and reduction), which is also in accordance with practical observations.

During the repeated heating from room temperature to operating temperatures (700–800 °C) it would be expected that the stresses in the multi-layer membrane slowly diminish since the increasing temperature brings the system closer to a stress-free state. However, it turns out that the picture of the stresses built during the heating is far more complex. As mentioned previously, the membrane is not heated up evenly. Instead, the outer layers of the membrane are heated up faster than the inner layers due to the circulating hot gases in the top (anode) and bottom (cathode) chambers. Due to these temperature gradients and the fact that the layers have different temperature-expansion coefficients, it appears that the center of the membrane (relative to the membrane outskirts) is always at higher loads regarding the built stresses (**Figure 7**). The adopted mathematical model predicts that the maximum stress is created at the critical time when the temperature gradient ΔT_2 is maximal. In a situation in which the stress in the membrane (a thickness of 20 μm Ni/SDC, 2000 μm SDC, 20 μm LSM, a diameter ø = 11 mm, the critical time t = 160 s) is modelled, it can be calculated that any given temperature above the cooled-down state causes some relaxation and reduces the tensile stress in the anode layer. In contrast, the relatively thick electrolyte adjacent to the anode stretches unevenly in accordance with the created temperature gradient. In addition, the stress in the electrolyte layer near the anode/electrolyte phase boundary is also built up due to anode stretching, meaning that the electrolyte is under the tensile stress at critical times. The absolute value of the induced tensile stress in the electrolyte layer after ≈ 160 s of the heating at the maximum power (220 V) is ≈ 70 MPa (**Figure 7a**). This value exceeds the tensile strength of SDC, which is 53 MPa.[34] When the maximum tensile strength is surpassed, the material is prone to cracking. If the heating power is reduced (46 % of the heater's maximum power; the heaters are powered with 150 V), the induced tensile stress in the electrolyte at the critical time (≈ 300 s) decreases to 27 MPa, which is acceptably low and demonstrates that a somewhat slower heating rate significantly reduces the stress load in the membrane.

Another interesting situation is demonstrated in **Figure 7b**, in which the membrane diameter is increased to ø = 18 mm. According to the mathematical modelling, membranes with larger diameters will build higher stresses under the same heating conditions. The absolute value of the induced tensile stress in the electrolyte layer at the critical time (≈ 160 s) thus increases to ≈ 83 MPa

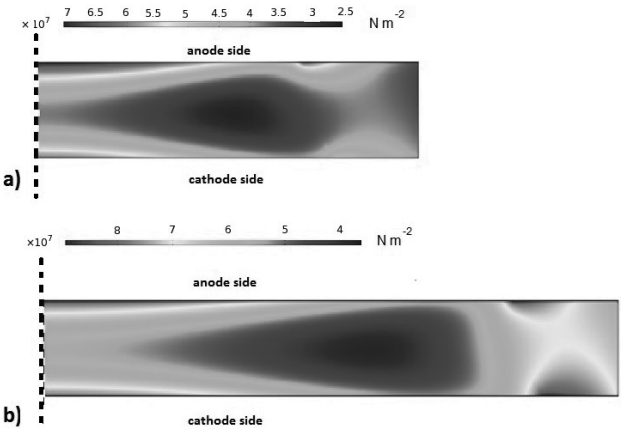

Figure 7: Induced stresses in the membrane (20 μm–2000 μm-20 μm, t = 160 s) presented in a vertical plane: a) ø = 11 mm, b) ø = 18 mm
Slika 7: Inducirane napetosti v membrani (20 μm–2000 μm-20 μm, t = 160 s), predstavljene v vertikalni ravnini: a) ø = 11 mm, b) ø = 18 mm

(the heaters powered with 220 V) or ≈ 30 MPa (the heaters powered with 150 V).

Since membranes in modern SOFC systems may be designed as anode- or electrolyte-supported, the next logical task addresses the thicknesses of individual layers and the associated stress load in the membrane during the heating. This question was approached by conducting a series of mathematical modelling tasks, in which the built stresses versus the thicknesses of individual layers were calculated (**Figure 8**). The investigated scenario includes the membrane discs (ø = 11 mm) in which the thicknesses of the Ni/SDC anode or SDC electrolyte layers vary from 20 µm to 3000 µm (the thickness of the LSM cathode layer is constant, being 20 µm). Since the most challenging conditions, with respect to the built-up stress, occur at the critical time of the heating when the temperature gradients are the highest (160 s or 300 s if the heaters are powered with 220 V or 150 V, respectively), only the maximum stresses built in the individual layers are presented. According to the results, several distinct features can be easily identified. Firstly, during the heating, the stress in the anode is always compressive, while the stresses in the electrolyte and cathode are tensile. Secondly, the stress in one component decreases with an increase in its thickness, when the thicknesses of the other two components are fixed. In addition, decreases in the compressive stress in the anode layer cause increases in the tensile stress in both the electrolyte and the cathode and vice versa. Thirdly, the thicknesses of the anode and the electrolyte have a pronounced influence on the stresses in the adjacent layers. Fourthly, due to very similar temperature-expansion coefficients of SDC and LSM, the tensile stress in the cathode layer never exceeds its tensile strength, which is assumed as 138 MPa.[34]

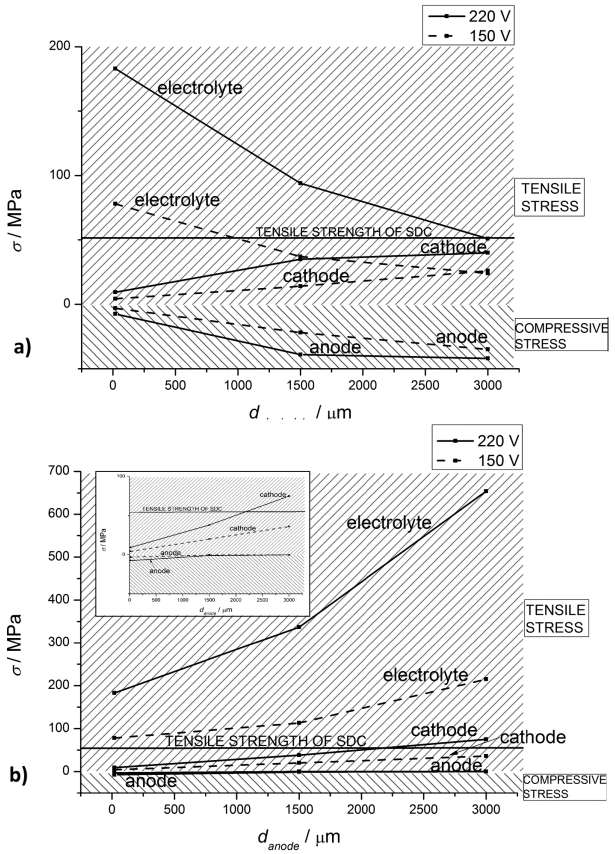

Figure 8: Maximum stresses in the multi-layer SOFC membrane as a function of: a) electrolyte thickness (d_{anode} = $d_{cathode}$ = 20 µm, $ø_{membrane}$ = 11 mm, $t_{heating}$ = 160 s at 220 V or $t_{heating}$ = 300 s at 150 V) and b) anode thickness ($d_{electrolyte}$ = $d_{cathode}$ = 20 µm, $ø_{membrane}$ = 11 mm, $t_{heating}$ = 160 s at 220 V or $t_{heating}$ = 300 s at 150 V)

Slika 8: Maksimalna napetost v večslojni SOFC-membrani kot funkcija: a) debeline elektrolita (d_{anoda} = d_{katoda} = 20 µm, $ø_{membrana}$ = 11 mm, $t_{segr.}$ = 160 s pri 220 V oz. $t_{segr.}$ = 300 s pri 150 V), b) debeline anode ($d_{elektrolit}$ = d_{katoda} = 20 µm, $ø_{membrana}$ = 11 mm, $t_{segr.}$ = 160 s pri 220 V oz. $t_{segr.}$ = 300 s pri 150 V)

The absolute values of the calculated stress also reveal that the electrolyte layer is most likely to crack. The maximum tensile stress in the electrolyte (adjacent to the anode) reaches ≈ 180 MPa if the membrane is composed of three 20 µm layers and heated with the maximum heating power (**Figure 8a**). Even if the electrolyte layer is broadened to 3000 µm, the maximum tensile stress is still ≈ 50 MPa, which is very close to the tensile strength of SDC. Under the same conditions, the tensile stress in the cathode and the compressive stress in the anode change from ≈ 40 MPa to less than 10 MPa and, therefore, never reach the tensile or compressive strength of LSC and Ni/SDC, respectively. In order to improve the survival chances of the electrolyte, the heating rate has to be reduced. If the heaters are powered with 150 V, an electrolyte thickness of ≈ 2 mm or more is enough to avoid the exceeding overcritical tensile stress. Powering the heaters with 150 V indeed results in a reduced heating rate. However, even with the reduced heating rate, the SOFC operating temperature of 700 °C is reached in 540 s, which favours the developed SOFC testing system for quick test cycles.

If the thicknesses of the electrolyte and cathode layers are kept constant, and the anode layer is broadened from 20 µm to 3000 µm, the built maximum tensile stresses in the electrolyte are rather high (**Figure 8b**). In all the investigated membrane designs, they exceed the tensile strength of SDC. It appears that the relatively large difference in the thermal-expansion coefficients between Ni/SDC and SDC and the thick anode layer substantially reduce the chances of the multi-layer system to survive the heating. In order to reduce the probability of failure in the anode-supported membrane, the design heating rate must be further decreased.

4 CONCLUSIONS

A new SOFC system enabling quick testing cycles was developed and successfully described using the finite-element modelling. It was shown that Ni/SDC-SDC-LSM membranes were subjected to temperature gradients during the heating. These gradients were pri-

marily caused by the heating mode in the testing system, where hot gases circulated inside the anode and cathode compartments and caused non-uniform membrane heating. The critical point with respect to a membrane failure was recognized during the early stage of the system heating when the temperature gradients in the membrane were the largest. During the heating, the electrolyte and cathode were always under a tensile stress, while the anode was under a compressive stress. The maximum thermally induced stress during the heating was observed in the electrolyte layer adjacent to the anode/electrolyte phase boundary. The absolute values of the induced maximum stress increased with the increasing diameter of the membrane. Additionally, the electrolyte-supported membranes had greater chances of surviving rapid temperature increases. In an electrolyte layer of $\approx$ 2 mm or more, the SDC tensile stress was never exceeded even if the system was heated with the maximum power. The anode-supported membranes, in contrast, were much more prone to cracking due to a relatively large difference between the thermal-expansion coefficients of the Ni/SDC anode and SDC electrolyte. Even a somewhat reduced heating rate still induced the occurrence of over-critical tensile stresses in the electrolyte. To reduce the probability of an anode-supported membrane failure, the heating power in the testing system should be further lowered, at least during the early stage of the membrane heating.

5 REFERENCES

[1] S. M. Haile, Acta Mater., 51 (**2003**) 19, 5981–6000, doi:10.1016/j.actamat.2003.08.004

[2] F. Tietz, I. Arul Raj, W. Jungen, D. Stöver, Acta Mater., 49 (**2001**) 5, 803–810, doi:10.1016/S1359-6454(00)00385-2

[3] T. Suzuki, Z. Hasan, Y. Funahashi, T. Yamaguchi, Y. Fujishiro, M. Awano, Sci. Mag., 325 (**2009**) 5942, 852–855

[4] Y. Yin, S. Li, C. Xia, G. Meng, Electrochim. Acta, 51 (**2006**), 2594–2598, doi:10.1016/j.electacta.2005.07.046

[5] J. Li, T. Ikegami, T. Mori, Acta Mater., 52 (**2004**), 2221–2228, doi:10.1016/j.actamat.2004.01.014

[6] J. Wright, A. Virkar, J. Power Sources, 196 (**2011**), 6118–6124, doi:10.1016/j.jpowsour.2011.03.043

[7] J. Cheng, L. Deng, B. Zhang, P. Shi, G. Meng, Rare Metals, 26 (**2007**), 110–117, doi:10.1016/S1001-0521(07)60169-7

[8] M. Chen, B. H. Kim, Q. Xu, B. K. Ahn, W. J. Kang, D. P. Huang, Ceram. Int., 35 (**2009**), 1335–1343, doi:10.1016/j.ceramint.2008.06.014

[9] Q. Liu, X. Dong, C. Yang, S. Ma, F. Chen, J. Power Sources, 195 (**2010**), 1543–1550, doi:10.1016/j.jpowsour.2009.09.071

[10] M. Chen, B. H. Kim, Q. Xu, O. J. Nam, J. H. Ko, J. Eur. Ceram. Soc., 28 (**2008**), 2947–2953, doi:10.1016/j.jeurceramsoc.2008.05.009

[11] X. Fang, G. Zhu, C. Xia, X. Liu, G. Meng, Solid State Ionics, 168 (**2004**), 31–36, doi:10.1016/j.ssi.2004.02.010

[12] Y. Yin, W. Zhu, C. Xia, G. Meng, J. Power Sources, 132 (**2004**), 36–41, doi:10.1016/j.jpowsour.2004.01.017

[13] C. M. Grgicak, R. G. Green, W. F. Du, J. B. Giorgi, J. Am. Ceram. Soc., 88 (**2005**), 3081–3087, doi:10.1111/j.1551-2916.2005.00544.x

[14] W. Fischer, J. Malzbender, G. Blass, R. W. Steinbrech, J. Power Sources, 150 (**2005**), 73–77, doi:10.1016/j.jpowsour.2005.02.014

[15] C. R. He, W. G. Wang, J. Wang, Y. Xue, J. Power Sources, 196 (**2011**), 7639–7644, doi:10.1016/j.jpowsour.2011.05.025

[16] K. P. Recknagle, R. E. Williford, L. A. Chick, D. R. Rector, M. A. Khaleel, J. Power Sources, 113 (**2003**), 109–114, doi:10.1016/S0378-7753(02)00487-1

[17] L. Petruzzi, S. Cocchi, F. Fineschi, J. Power Sources, 118 (**2003**), 96–107, doi:10.1016/S0378-7753(03)00067-3

[18] M. Ambrožič, K. Vidovič, Mater. Tehnol., 41 (**2007**) 4, 179–184

[19] O. C. Zienkiewicz, R. Taylor, The Finite Element Method: Volumes 1, 2 & 3, 5th ed., Elsevier, Butterworth-Heinemann, 2000

[20] J. N. Reddy, An Introduction to the Finite Element Method, McGraw-Hill, 1993

[21] K. J. Bathe, Finite Element Procedures, Prentice Hall, Englewood Cliffs, New Jersey 1996

[22] A. Selimovic, M. Kemm, T. Torisson, M. Assadi, J. Power Sources, 145 (**2005**), 463–469, doi:10.1016/j.jpowsour.2004.11.073

[23] C. K. Lin, T. T. Chen, Y. P. Chyou, L. K. Chiang, J. Power Sources, 164 (**2007**) 4, 238–251, doi:10.1016/j.jpowsour.2006.10.089

[24] T. Skalar, M. Marinšek, M. Lubej, T. Skalar, M. Lukežič, J. Maček, Mater. Tehnol., 48 (**2014**) 6, 861–867

[25] T. Skalar, A. Golobič, M. Marinšek, J. Maček, Mater. Tehnol., 47 (**2013**) 4, 423–429

[26] T. Skalar, J. Maček, A. Golobič, J. Eur. Ceram. Soc., 32 (**2012**), 2333–2339, doi:10.1016/j.jeurceramsoc.2012.02.008

[27] M. Marinšek, Mater. Tehnol., 43 (**2009**) 2, 79–84

[28] I. S. Liu, Continuum Mechanics, Springer, 2002, doi:10.1007/978-3-662-05056-9

[29] S. W. Churchill, H. H. S. Chu, Int. J. Heat Mass Transfer, 18 (**1975**), 1323, doi:10.1016/0017-9310(75)90243-4

[30] G. K. Batchelor, An Introduction to Fluid Dynamics, Cambridge University Press, 1967

[31] S. Sameshima, T. Ichikawa, M. Kawaminami, Y. Hirata, Mater. Chem. Phys., 61 (**1999**), 31–35, doi:10.1016/S0254-0584(99)00109-1

[32] X. B. Li, H. Y. Wang, H. X. Gu, J. Wang, W. J. Zhang, T. G. Wang, Sci. Sinter., 42 (**2010**), 153–159, doi:10.2298/SOS1002153L

[33] Y. X. Gan (Ed.), Continuum mechanics – Progress in fundamentals and engineering applications, InTech, Rijeka, Croatia 2012, doi:10.5772/2103

[34] R. Cutler, D. Meixner, Solid State Ionics, 159 (**2003**), 9–19, doi:10.1016/S0167-2738(03)00006-7

UDK 621.77:621.777.2
Original scientific article/Izvirni znanstveni članek

ISSN 1580-2949
MTAEC9, 49(5)739(2015)

PRODUCTION OF SHAPED SEMI-PRODUCTS FROM AHS STEELS BY INTERNAL PRESSURE

IZDELAVA POLPROIZVODOV IZ AHS-JEKEL, OBLIKOVANIH Z NOTRANJIM TLAKOM

Ivan Vorel[1], Hana Jirková[1], Bohuslav Mašek[1], Petr Kurka[2]

[1]University of West Bohemia in Pilsen, Research Centre of Forming Technology, Univerzitni 22, 306 14 Pilsen, Czech Republic
[2]Fraunhofer Institute for Machine Tools and Forming Technology IWU, Reichenhainer Straße 88, 09126 Chemnitz, Germany
frost@vctt.zcu.cz

Prejem rokopisa – received: 2014-09-04; sprejem za objavo – accepted for publication: 2014-11-05

doi:10.17222/mit.2014.218

The constant evolution of industry brings demands for components of ever-higher quality, complex shapes and excellent mechanical properties, with reduced operating costs and with improved reliability in service. Such demands can be met by processing high-strength, low-alloyed steels using novel heat-treatment methods. One of such methods is the quenching and partitioning (Q&P) process, which can lead to high strengths of about 2000 MPa at elongation levels of more than 10 %. The Q&P process can be combined with unconventional procedures for making complex-shaped parts to manufacture components with excellent mechanical properties and an intricate shape. This paper describes the sequence of internal high-pressure forming, hot stamping and the Q&P process used for making a functional product with good mechanical properties and a complex shape. The purpose of the experimental programme was to employ a production chain for processing hollow, thin-walled stock. Using a step-by-step optimization, commercially usable products were obtained. The microstructure of the products consisted primarily of martensite and a small fraction of bainite. Such a microstructure guarantees a high ultimate strength. The strength level throughout the part was not less than 1950 MPa, combined with an excellent elongation of approximately 15 %.

Keywords: Q&P process, hot stamping, internal high pressure forming

Stalen razvoj industrije zahteva komponente vedno boljših kvalitet, kompleksnih oblik, odličnih mehanskih lastnosti pri nižjih proizvodnih stroških in z večjo zanesljivostjo obratovanja. Take zahteve se lahko dosežejo z izdelavo visokotrdnostnih malolegiranih jekel z uporabo novih metod toplotne obdelave. Ena od takih metod je postopek kaljenja in delitve (Q&P), ki omogoča velike trdnosti okrog 2000 MPa pri več kot 10-odstotnem raztezku. Postopek Q&P se lahko kombinira z nekonvencionalnimi metodami izdelave delov s kompleksno obliko in za izdelavo komponent z odličnimi mehanskimi lastnostmi in komplicirano obliko. Predstavljeni članek obravnava zaporedne operacije notranjega visokotlačnega preoblikovanja, vročega stiskanja in Q&P-postopka za izdelavo funkcionalnih proizvodov z dobrimi mehanskimi lastnostmi in zapleteno obliko. Namen eksperimentalnega dela je bil postaviti proizvodno verigo za izdelavo votlih tankostenskih kosov. Z optimizacijo korak za korakom so bili izdelani komercialno uporabni proizvodi. Mikrostruktura proizvodov je bila sestavljena predvsem iz martenzita in majhnega deleža bainita. Taka mikrostruktura zagotavlja veliko natezno trdnost. Nivo trdnosti po vsem kosu ni bil manjši od 1950 MPa v kombinaciji z odličnim raztezkom okrog 15 %.

Ključne besede: Q&P-proces, vroče stiskanje, preoblikovanje z velikim notranjim tlakom

1 INTRODUCTION

Advanced high-strength steels (AHSS) find an ever-increasing number of uses in a wide range of industrial sectors. Thanks to their excellent mechanical properties, they become the materials of choice for structural parts, which can thus be more lightweight than, but equally reliable and safe as, those made of conventional steels. Due to the continuously evolving needs of industry, new processing methods must always be sought to be combined in a comprehensive production chain.

2 Q&P PROCESSING

The Q&P process is an advanced method of heat treatment for high-strength steels.[1] It relies on the processes that take place in the steel between the M_s and M_f temperatures and are related to carbon diffusion. Carbon migrates from the super-saturated martensite to the retained austenite, making the latter more stable. The Q&P process comprises heating to the austenitizing temperature and quenching to the quenching temperature (QT), which lies between the M_s and M_f temperatures. This produces a mixture of martensite and retained austenite.[2,3] The workpiece is then heated to, and held at, the partitioning temperature (PT).[4]

With regard to the austenite stabilization, carbon must not precipitate in the form of carbides at the PT. To ensure this, aluminium, silicon or phosphorus should be used as alloying additions. In order to strengthen the solid solution, the steel can be alloyed with manganese and chromium. These elements shift the pearlitic and bainitic transformation curves in the transformation diagrams towards longer times, thus reducing the critical cooling rate. As silicon is present in the steel in order to retard carbide precipitation, the optimum level of chromium must be controlled, as chromium in the presence

Table 1: Chemical composition of steel 42SiCr, *w*/%
Tabela 1: Kemijska sestava jekla 42SiCr, *w*/%

C	Si	Mn	Cr	Mo	Nb	P	S	M_s/°C	M_f/°C
0.42	2.6	0.59	1.33	0.03	0.03	0.01	0.01	289	178

of carbon acts as a carbide-former. The addition of manganese as an austenite-forming element effectively prevents any free ferrite from forming. Free ferrite can impair the mechanical properties of the steel.[5–7]

2.1 Internal High Pressure Forming

This method can be used for manufacturing complex-shaped, hollow products. It is based on forming a hollow feedstock in a closed die using pressurized gas. The final temperature of the product can be controlled by changing the die-opening time. At the end of this die-opening time, the product is removed from the die and cooled in air or heat treated further.

3 EXPERIMENTAL PROGRAMME

The goal of the experimental programme was to form hollow feedstock using internal, high-pressure gas and then apply the Q&P process. The experimental material was high-strength 42SiCr steel (**Table 1**). The initial microstructure of this steel consisted of ferrite and pearlite. The ultimate strength was 981 MPa, the elongation reached 30 % and the hardness was 295 HV10. Using the JMatPro software, the important M_s and M_f temperatures were found: 289 °C and 178 °C, respectively (**Figure 1**).

3.1 Experimental Production of Shaped Products

The hollow feedstock used for making the shaped products was 380 mm in length and 48 mm in diameter. Its wall thickness was 4 mm (**Figure 2**).

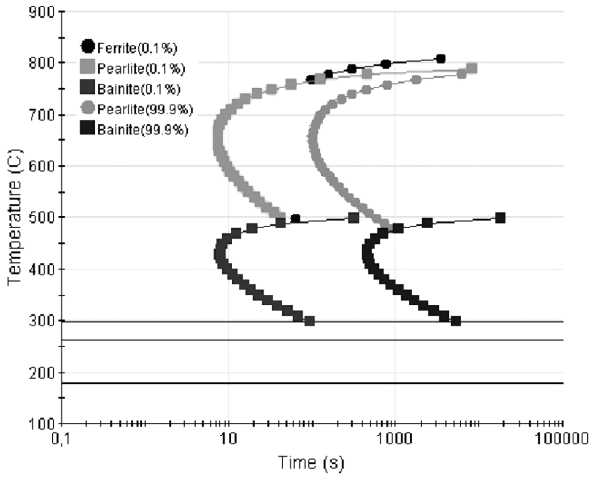

Figure 1: TTT diagram of 42SiCr steel calculated using JMatPro software
Slika 1: TTT-diagram jekla 42SiCr, izračunan s programsko opremo JMatPro

Figure 2: Experimental stock and the resulting shape after hot stamping
Slika 2: Preizkusni kos in dobljena oblika po vročem stiskanju

The sequence comprised heating to 915 °C and holding for 25 min to guarantee full austenitizing. Then the feedstock was transferred to a die at the ambient temperature. After the die was closed, the feedstock was formed by pressurized gas at an overpressure of 700 bar. The working gas was nitrogen. The contact between the workpiece and the die wall caused the workpiece to cool down rapidly to a pre-defined temperature. The die wall was at room temperature and was cooled by water. This was achieved by selecting the appropriate die-opening time between 5 s and 20 s. After the die-opening time, the workpiece is removed. In order to explore the effect of Q&P processing, the final step of the proposed sequence, on the microstructure evolution and the related mechanical properties, the workpieces were further processed in three different ways (**Figure 3**). Some workpieces were cooled in air after hot stamping in the

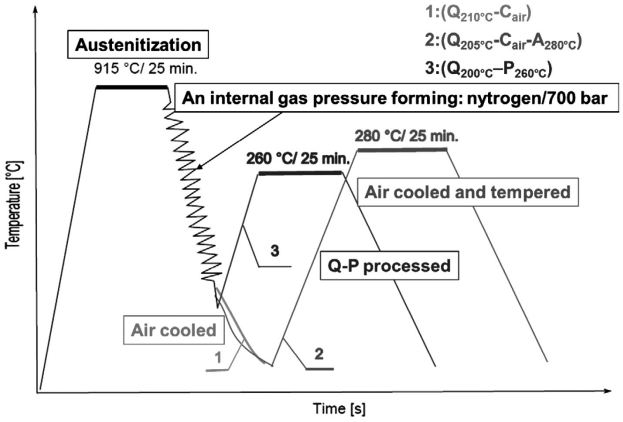

Figure 3: Experimental modes of heat treatment
Slika 3: Eksperimentalni načini toplotne obdelave

die. The product from this group was hot stamped in the die for 15 s and was then removed and cooled in air ($Q_{210\ °C} - C_{air}$). The temperature at the moment of removal from the die was 210 °C. Another group comprised workpieces that were cooled in the die, then cooled in air to the ambient temperature and were then reheated in a furnace to 280 °C, where they were held for 25 min, and then removed and cooled in air. The product from the second group was cooled in the die for 15 s to a temperature of 205 °C ($Q_{150\ °C} - C_{air} - A_{280\ °C}$). Yet another group included workpieces that were removed from the die and immediately placed in a furnace. The significant product from this third group was cooled in the die for 15 s as well. Then it was placed in a furnace and annealed at 260 °C for a time of 25 min ($Q_{200\ °C} - P_{200\ °C}$). The temperature after removal from the die reached 200 °C (**Table 2**). They were therefore treated using the Q&P process.

Table 2: Parameters of the experimental heat treatment
Tabela 2: Parametri eksperimentalne toplotne obdelave

	Austenitizing °C	QT-temperature °C	PT-temperature °C	Tempering time min
($Q_{210\ °C} - C_{air}$)	915	210	–	–
($Q_{205\ °C} - C_{air} - A_{280\ °C}$)	915	205	280	25
($Q_{200\ °C} - P_{260\ °C}$)	915	200	260	25

4 RESULTS AND DISCUSSION

Representative products were selected from these groups of workpieces for metallographic examination and for mechanical property measurements. The specimens for the mechanical property measurement were taken from the products representing the different processing sequences. The specimen locations were chosen to allow an evaluation of the effects of the production sequence and of the position within the die upon the resulting product properties. Representative specimens were taken from the parts with which the workpiece was held in the die, from the area of the steepest change in cross-section, which is the point of the largest plastic strain, and from the transitions between the different diameters. A total of 14 test specimens were taken from each product (**Figure 4**)

Due to the shape of the workpieces, miniature tension test specimens with a gauge length of 5 mm and a cross-section of 2 mm × 1.5 mm were used for measuring the mechanical properties (**Figure 5**).

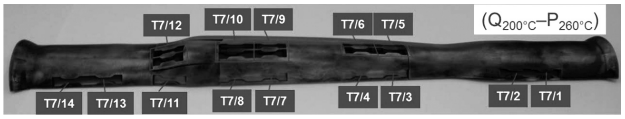

Figure 4: Selected locations of the T7 ($Q_{200\ °C} - P_{260\ °C}$) workpiece, upon the Q&P process
Slika 4: Izbrana področja kosa T7 ($Q_{200\ °C} - P_{260\ °C}$) pri Q&P-procesu

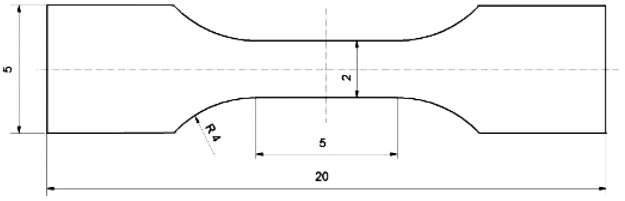

Figure 5: Shape of specimen for mechanical testing
Slika 5: Oblika vzorca za mehanske preizkuse

4.1 Mechanical Properties

The product that was only cooled in air after removal from the die ($Q_{210\ °C} - C_{air}$) showed a very high ultimate strength (**Table 3**). None of the 14 specimens exhibited ultimate strengths of less than 2260 MPa. The elongation level was higher than 10 % in all cases. The specimen with the lowest ultimate strength, 2263 MPa, and an elongation of 12 %, was T3/5, which had been taken from the transition to the largest diameter. It also showed the lowest hardness of all the specimens: 667 HV10. It is likely that this part of the workpiece was not in full contact with the die wall. No similar effect of the specimen position was found in any other specimen from this product.

Table 3: Results of tensile testing (proof stress $R_{p0.2}$, ultimate tensile strength R_m and elongation $A_{5\ mm}$) and hardness testing (HV10) of the semi-product ($Q_{210\ °C} - C_{air}$) upon air cooling
Tabela 3: Rezultati nateznih preizkusov (meja tečenja $R_{p0,2}$, natezna trdnost R_m in raztezek $A_{5\ mm}$) in merjenja trdote (HV10) polproizvodov ($Q_{210\ °C} - C_{zrak}$) po ohlajanju na zraku

	$R_{p0.2}$/MPa	R_m/MPa	$A_{5\ mm}$/%	HV10
T3/2	1550	2324	14	709
T3/3	1534	2314	11	685
T3/5	1518	2263	12	667
T3/8	1641	2333	10	701
T3/12	1681	2345	10	738
T3/14	1652	2310	16	705

All the specimens from the product ($Q_{205\ °C} - C_{air} - A_{280\ °C}$) exhibited ultimate strengths of more than 2110 MPa and $A_{5\ mm}$ elongation levels of more than 14 % (**Table 4**). A low ultimate strength was found in the T6/5 specimen: 2133 MPa. The T6/5 specimen also showed $A_{5\ mm}$ elongation of 18 %. This situation is similar to that in the product that was removed from the die and cooled

Table 4: Results of tensile testing of the semi-product ($Q_{150\ °C} - C_{air} - A_{280\ °C}$)
Tabela 4: Rezultati nateznih preizkusov polproizvodov ($Q_{150\ °C} - C_{zrak} - A_{280\ °C}$)

	$R_{p0.2}$/MPa	R_m/MPa	$A_{5\ mm}$/%	HV10
T6/2	1822	2117	18	656
T6/3	1862	2160	17	653
T6/5	1838	2133	18	672
T6/8	1886	2189	18	637
T6/12	1771	2144	14	623
T6/14	1818	2196	19	671

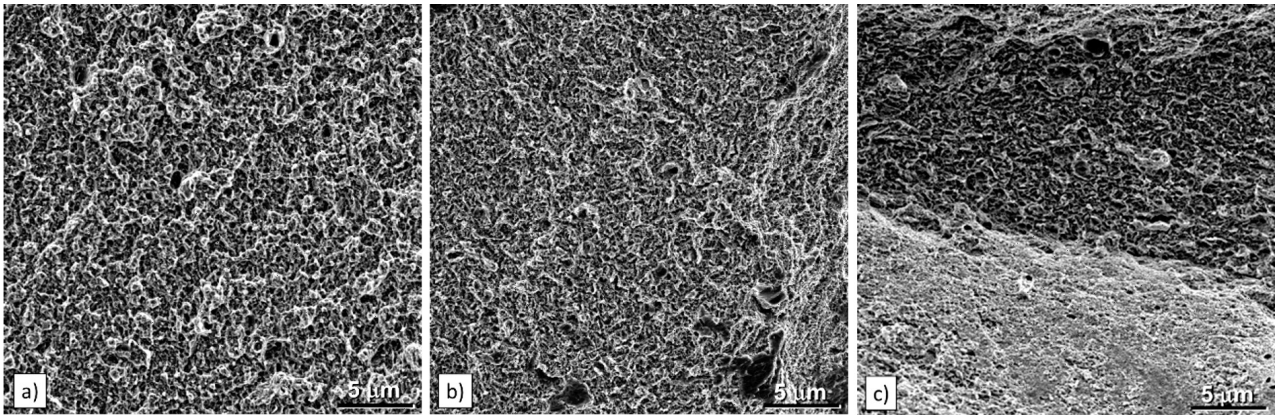

Figure 6: Fracture surfaces: a) T3 ($Q_{200\ °C} - C_{air}$) product that was cooled in air (T3/3), b) T6 ($Q_{205\ °C} - C_{air} - A_{280\ °C}$) that was cooled in air and then annealed in a furnace (T6/3), c) T7 ($Q_{200\ °C} - P_{260\ °C}$) product after Q&P process (T7/3)

Slika 6: Površine prelomov: a) T3 ($Q_{200\ °C} - C_{zrak}$)-proizvod, ohlajen na zraku (T3/3), b) T6 ($Q_{205\ °C} - C_{zrak} - A_{280\ °C}$), ohlajen na zraku in potem žarjen v peči (T6/3), c) T7 ($Q_{200\ °C} - P_{260\ °C}$) proizvod po Q&P-postopku (T7/3)

in air. By contrast, the hardness in the corresponding location of the latter product was the highest of all the locations tested: 672 HV10.

The ultimate strength of the product ($Q_{200\ °C} - P_{260\ °C}$) was approximately 250 MPa to 300 MPa lower than that of the product that had been removed from the die and merely cooled in air (**Table 5**). In addition, it is approximately 150 MPa to 200 MPa lower than in the product that was removed from the die, cooled in air and then reheated to 280 °C and held for 25 min. As in the previous cases, the lowest ultimate strength was found in the T7/5 location. It was 1914 MPa. The corresponding $A_{5\ mm}$ elongation was 20 % and the hardness reached 600 HV10. The specimens in the remaining locations exhibited strengths of approximately 2000 MPa. The Q&P processing of the product improved its elongation. It was between 17 % and 21 %.

Table 5: Results of tensile testing of the product ($Q_{200\ °C} - P_{260\ °C}$) prepared using the Q&P process

Tabela 5: Rezultati nateznih preizkusov proizvodov ($Q_{200\ °C} - P_{260\ °C}$), izdelanih po Q&P-postopku

	$R_{p0.2}$/MPa	R_m/MPa	$A_{5\ mm}$/%	HV10
T7/2	1576	1978	17	623
T7/3	1490	1956	21	615
T7/5	1379	1914	20	600
T7/8	1600	2006	18	596
T7/12	1584	1952	18	597
T7/14	1626	1978	17	608

4.2 Metallographic and Fractographic Characterization

With reference to the results of the tension test, the fracture surfaces were examined. In all cases, ductile fractures with dimples were found (**Figure 6**). No signs of brittle fracture were detected, even in the product that was cooled in air after quenching in the die.

The microstructure was examined in locations corresponding to those of the samples taken for mechanical testing. In almost all the specimens taken from the product ($Q_{200\ °C} - C_{air}$) the microstructure consisted of martensite and a small proportion of bainite (**Figure 7**). Only those areas where the workpiece was not in full

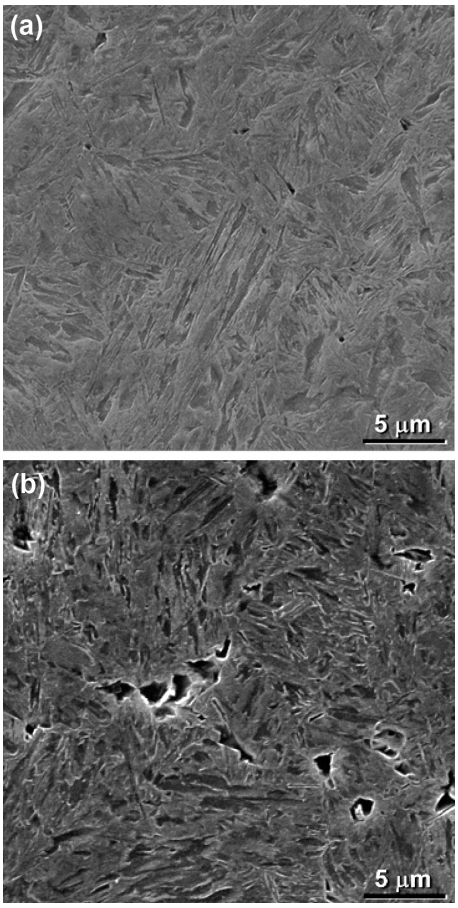

Figure 7: T3 ($Q_{200\ °C} - C_{air}$) product upon air cooling: a) martensite-bainite microstructure (point T3/2), b) martesite-bainite with a small fraction of ferrite (point T3/12)

Slika 7: T3 ($Q_{200\ °C} - C_{zrak}$)-proizvod po ohlajanju na zraku: a) martenzitno-bainitna mikrostruktura (točka T3/2), b) martenzit-bainit z majhnim deležem ferita (točka T3/12)

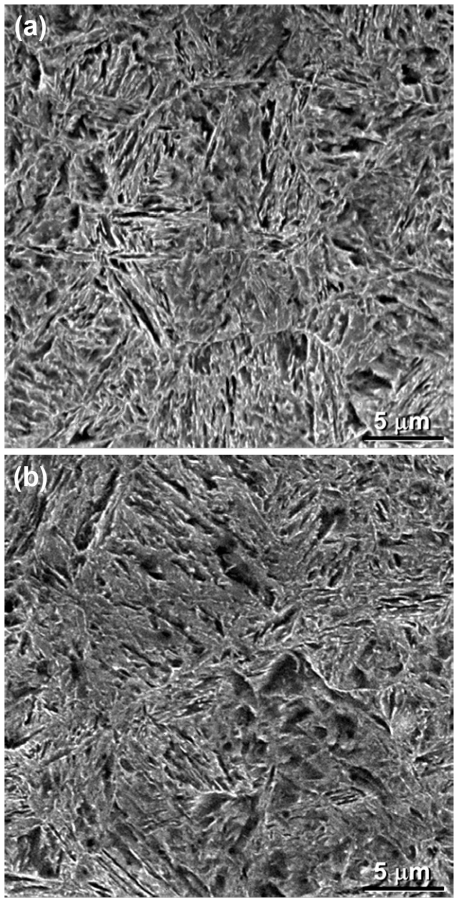

Figure 8: T6 ($Q_{205\ °C} - C_{air} - A_{280\ °C}$) product upon air cooling and annealing: a) tempered martensite-bainite microstructure (point T6/2), b) tempered martensite-bainite microstructure (point T6/12)

Slika 8: T6 ($Q_{205\ °C} - C_{zrak} - A_{280\ °C}$)-proizvod po ohlajanju na zraku in popuščanju: mikrostruktura: a) popuščeni martenzit-bainit (točka T6/2), b) mikrostruktura: popuščeni martenzit-bainit (točka T6/12)

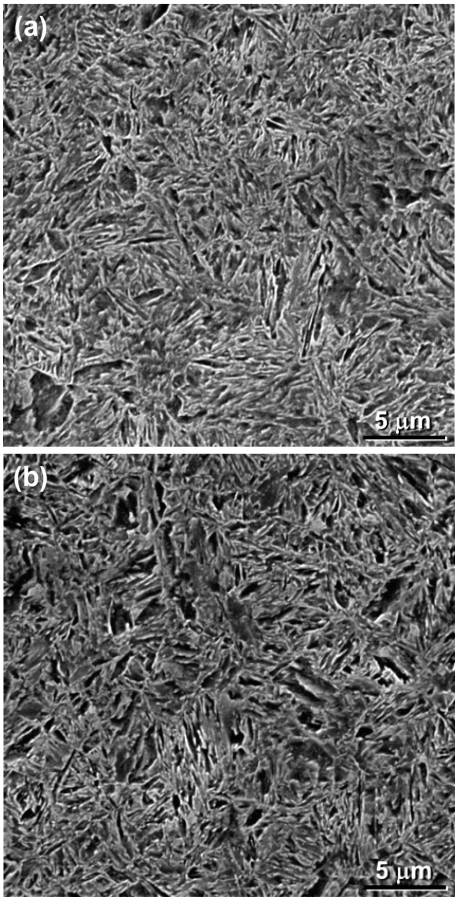

Figure 9: T7 ($Q_{200\ °C} - P_{260\ °C}$) product upon Q&P process: a) martensite-bainite microstructure with a small fraction of ferrite (point T7/2), b) martensite-bainite with a small fraction of ferrite (point T7/12)

Slika 9: T7 ($Q_{200\ °C} - P_{260\ °C}$) proizvod po Q&P postopku: a) martenzitno-bainitna mikrostruktura z majhnim deležem ferita (točka T7/2), b) martenzit-bainit z majhnim deležem ferita (točka T7/12)

contact with the die wall contain some free ferrite, which is probably due to the resulting insufficient cooling rate

An examination of the microstructure of the product ($Q_{205\ °C} - C_{air} - A_{280\ °C}$) revealed tempered martensite and bainite (**Figure 8**). The locations where the workpiece was not in full contact with the die wall contained a small amount of free ferrite.

The Q&P-processed product ($Q_{200\ °C} - P_{260\ °C}$) contained a mixture of martensite and bainite (**Figure 9**). As in the products mentioned above, the locations of partial contact between the workpiece and the die wall contained a small amount of free ferrite.

5 CONCLUSION

Using internal high-pressure forming, products with complex shapes were obtained. A detailed inspection of their surfaces revealed no distinct discontinuities. In the product that was cooled in air after removal from the die, the 15 s in the die caused quenching to 210 °C. Its microstructure was a mixture of martensite, bainite and a small proportion of free ferrite. No location of the product showed an ultimate strength of less than 2260 MPa. The elongation was more than 10 %.

The product that was cooled in air after removal from the die and then annealed in a furnace had a temperature of 205 °C after the 15 s die-opening time. The annealing of the product at 280 °C for 25 min produced a microstructure of tempered martensite, bainite and a small amount of free ferrite. No location of the product, where the mechanical properties were measured, showed an ultimate strength of less than 2110 MPa. Annealing after removal of the product from the die and subsequent cooling in air caused the elongation level to increase from 10 % to 14 %.

Cooling in the die for 15 s, which is used as part of the Q&P process, led to the quenching of the product to 200 °C. The subsequent reheating to the carbon-partitioning temperature of 260 °C and holding for 25 min resulted in a microstructure that consisted of tempered martensite, bainite and free ferrite. The ultimate strength of the product did not decrease below 1900 MPa at any

location. The Q&P processing led to an increase in the elongation from 10 % to 18 %.

The measurement of mechanical properties by means of tension testing did not identify any substantial effect of the location, and thus no substantial effect of the strain magnitude on the ultimate strength.

Acknowledgment

This paper includes results achieved in the project CZ.1.05/3.1.00/14.0297 Technological Verification of R&D Results II, individual activity Hollow Shafts for Passenger Cars Produced by Heat Treatment with the Integration of Q-P Process and the project GAČR P107/12/P960 Influence of a Structure Modification on Mechanical Properties of AHS Steel. The paper also includes results from the project SGS-2013-028 Support of Students Research Activities in Materials Engineering Field.

6 REFERENCES

[1] L. Kucerova et al., Comparison of Microstructures and Properties Obtained After Different Heat Treatment Strategies of High Strength Low Alloyed Steel, Journal of Iron and Steel Research International, 18 (**2011**), 427–431

[2] J. Speer et al., Carbon Partitioning into Austenite after Martensite Transformation, Acta Materialia, 51 (**2003**), 2611–2622, doi:10.1016/S1359-6454(03)00059-4

[3] J. Speer et al., The Quenching and Partitioning Process: Background and Recent Progress, Materials Research, 8 (**2005**) 4, 417–423, doi:10.1590/S1516-14392005000400010

[4] T. Tsuchiyma et al., Quenching and partitioning treatment of a low-carbon martensitic stainless steel, Materials Science and Engineering A, 532 (**2012**), 585–592, doi:10.1016/j.msea.2011.10.125

[5] H. Jirkova, L. Kucerova, B. Masek, Effect of Quenching and Partitioning Temperatures in the Q-P Process on the Properties of AHSS with Various Amounts of Manganese and Silicon, Materials Science Forum, 706–709 (**2012**), 2734–2739, doi:10.4028/www.scientific.net/MSF.706-709.2734

[6] L. Kucerova et al., Optimization of Q-P Process Parameters with Regard to Final Microstructures and Properties, Annals of Daaam For 2009 & Proceedings of the 20th International Daaam Symposium, 20 (**2009**), 1035–1036

[7] B. Masek et al., Improvement of Mechanical Properties of automotive Components Using Hot Stamping with Integrated Q-P Process, Journal of Iron and Steel Research International, 18 (**2011**) 1–2, 730–734

UDK 669.018.95:621.396.67
Original scientific article/Izvirni znanstveni članek

ISSN 1580-2949
MTAEC9, 49(5)745(2015)

COMPOSITE-MATERIAL PRINTED ANTENNA FOR A MULTI-STANDARD WIRELESS APPLICATION

TISKANA ANTENA IZ KOMPOZITNEGA MATERIALA ZA VEČSTANDARDNO BREZŽIČNO UPORABO

Touhidul Alam[1], Mohammad Rashed Iqbal Faruque[1], Mohammad Tariqul Islam[2], Norbahiah Misran[2]

[1]Space Science Center (ANGKASA), Universiti Kebangsaan Malaysia, 43600UKM Bangi, Selangor, Malaysia
[2]Department of Electrical, Electronic and Systems Engineering, Universiti Kebangsan Malaysia, 43600UKM Bangi, Selangor, Malaysia
touhid13@yahoo.com

Prejem rokopisa – received: 2014-09-14; sprejem za objavo – accepted for publication: 2014-10-08

doi:10.17222/mit.2014.232

This paper presents a printed multi-standard wireless antenna fabricated from a cost effective composite material to cover GPS (1575 MHz), GSM 1800, GSM 1900, WLAN (2400 MHz), LTE band 40 (2.3–2.4 GHz), WiMAX (3600 MHz) and WLAN (5.1–5.35 GHz) frequency bands. The reported antenna is incorporated with two distinct monopole radiators with a meander-line-type ground plane. The wireless mobile antenna can be conveniently simulated with the commercially available EM simulation software (CST Microwave Studio) using the finite-difference time-domain (FDTD) method. A parametric analysis of the antenna geometry is demonstrated and the specific absorption rate (SAR) is also analyzed with a human-head model.

Keywords: antenna, material, multiband, meander line, wireless communication, SAR

Ta članek predstavlja tiskano večstandardno brezžično anteno, izdelano iz cenovno ugodnega kompozitnega materiala, ki obsega frekvenčne pasove GPS (1575 MHz), GSM 1800, GSM 1900, WLAN (2400 MHz), LTE pas 40 (2,3–2,4 GHz), WiMAX (3600 MHz) in WLAN (5,1–5,35 GHz). V predstavljeno anteno sta vgrajena dva različna monopolna sevalnika v obliki zanke na osnovni ravnini. Brezžično mobilno anteno se lahko prikladno simulira s komercialno razpoložljivo EM simulacijsko programsko opremo (CST Microwave Studio) z uporabo metode domene s končno diferenco časa (FDTD). Prikazana je parametrična analiza geometrije antene in analizirana je bila hitrost specifične absorpcije (SAR) na modelu človeške glave.

Ključne besede: antena, material, večpasovno, linija zanke, brezžična komunikacija, SAR

1 INTRODUCTION

Multiband antenna design with a low-profile and stable performance has recently been a significant issue to the researchers. Therefore, research has been focused on minimizing the physical size of individual parts of a modern wireless system. In the most recent years, printed planar antennas have been thought to be most suitable for multiband wireless applications in view of their unique features, for example, light weight, low costs, simple fabrication, multi-frequency mode and stable performances.[1,2] Several types of multiband antenna have been studied for GPS, GSM, WLAN, LTE band 40, WiMAX and WLAN applications.

A compact dual-arm-structure mobile handset antenna was designed for a multi-band wireless mobile operation, covering DCS, PCS, UMTS and WLAN (2.4 GHz) frequency bands.[3] The dimensions of the antenna were 119 mm × 50 mm. An inverted L-shaped antenna was presented for wireless communication, covering DCS, PCS and IMT tri-bands.[4] Chen et al.[5] introduced a modified T-shaped planar monopole antenna for DCS 1800, PCS 1900, UMTS and WLAN applications. However, its dimensions were 65 mm × 40 mm.

This paper presents a multiband printed monopole antenna for wireless communication, which can operate within the existing wireless standards: GPS (1.565–1.585 GHz), GSM (1800, 1900), WiMAX (3.6 GHz), WLAN, LTE band 40 (2.3–2.4 GHz) and WLAN (5.47–5.9 GHz). The overall volume of the proposed antenna is 30 mm × 60 mm, which is at least 26.5 % less than[4], 50 % less than[3] and 40 % less than[5], considering its length and width. However, according to the IEEE and ICNIRP guidelines the specific absorption rate of the proposed antenna must be confirmed and the value should be less than 1.6 W/kg in a 1 g averaging mass and 2 W/kg in a 10 g averaging mass of biological tissues.[6,7] To comply with this requirement, the SAR value of the proposed antenna was analyzed and compared.

2 PROPOSED ANTENNA CONFIGURATION

The geometric configuration and the physical dimensions of the proposed antenna are illustrated in **Figure 1**. The proposed antenna consists of a meander-line radiator with a defected ground plane. The antenna is printed on an FR4-material (a relative permittivity of 4.6, a loss tangent of 0.02) substrate with dimension of 30 mm × 60 mm × 1.6 mm. A 50 Ω microstrip feeding line is connected with an inverted S-shaped radiator. The specifications of the proposed antenna are listed in **Table 1**.

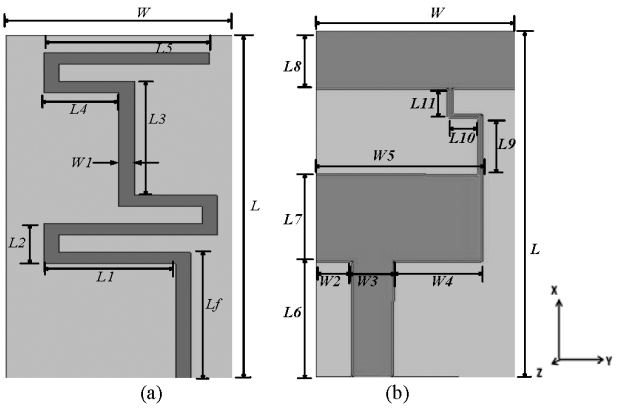

Figure 1: Geometry of the proposed antenna: a) top view, b) bottom view

Slika 1: Geometrija predlagane antene: a) pogled od zgoraj, b) pogled od spodaj

Table 1: Antenna-design specifications

Tabela 1: Specifikacije antene

Parameter code	Value (mm)	Parameter code	Value (mm)
L	60	*L9*	10
W	30	*L10*	4.5
L1	17.5	*L11*	5
L2	7	*Lf*	22
L3	20	*W1*	2
L4	10	*W2*	5.87
L5	22	*W3*	6
L6	20	*W4*	13.125
L7	15	*W5*	25
L8	10		

3 ANTENNA PERFORMANCE WITH AN EPOXY-RESIN-POLYMER SUBSTRATE

The proposed planar microstrip patch antenna was designed and analyzed using a finite-difference time domain (FDTD) based CST Microwave Studio. The designed antenna was fabricated on a recently available 1.6 mm thick, low-cost, durable, polymer-resin substrate using an in-house printed-circuit-board (PCB) prototyping machine. The substrate material consists of an epoxy matrix reinforced with woven glass. The composition of epoxy resin and fiber glass varies in the thickness and is direction dependent. One of the attractive properties of polymer-resin composites is that they can be shaped and reshaped repeatedly without losing their material properties.[8] Due to the lower manufacturing cost, ease of fabrication, design flexibility and market availability of the proposed material, it has become popular for its use as the substrate in patch-antenna designs. The material is composed of 60 % of fiber glass and 40 % of epoxy resin. **Figure 2** shows the steps needed to construct an epoxy-resin-polymer substrate (FR4).[9]

Moreover, a parametric study was performed for several substrate materials, illustrated in **Figure 3**. The

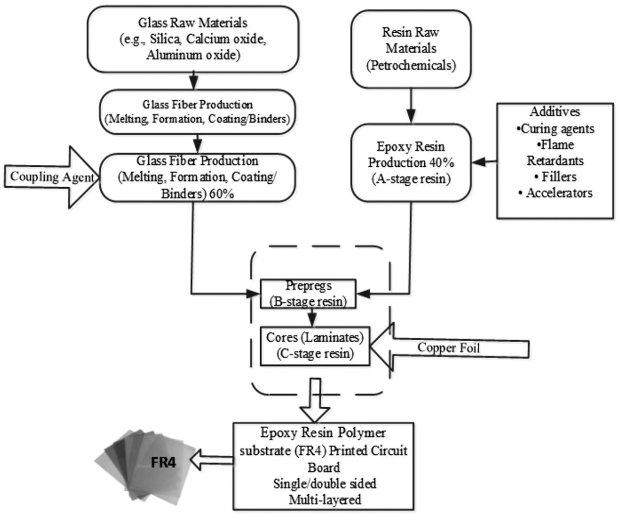

Figure 2: Flow chart of FR4-material construction[9]

Slika 2: Shema poteka priprave FR4-materiala[9]

dielectric properties of these materials are listed in **Table 2**. It is seen from **Figure 3** that the FR4 substrate material shows a better performance in terms of reflection coefficient than the other materials listed in **Table 2**.

Table 2: Dielectric properties of substrate materials

Tabela 2: Dielektrične lastnosti materiala podlage

Substrate material	Relative permittivity (ε_r)	Dielectric loss tangent
Glass (Pyrex)	4.82	0.0012
FR4	4.60	0.02
Taconic CER-10	10.00	0.0023
Teflon (PTFE)	2.10	0.01

4 RESULTS AND DISCUSSION

The prototype of the proposed antenna was fabricated using the FR4 substrate material with a relative permittivity of 4.4 and a loss tangent of 0.02. The simulated and measured reflection coefficients of the proposed

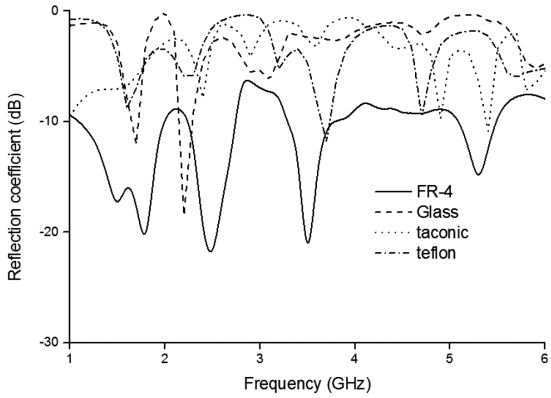

Figure 3: Reflection coefficient of the proposed antenna for the materials listed in **Table 2**

Slika 3: Koeficient refleksije predlagane antene pri materialih iz **tabele 2**

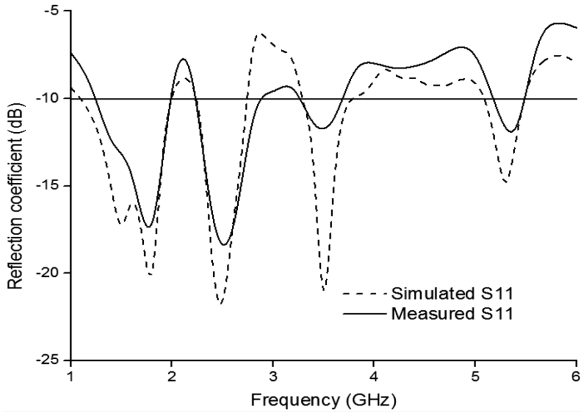

Figure 4: Simulated and measured reflection coefficients of the proposed antenna
Slika 4: Simuliran in izmerjen koeficient refleksije predlagane antene

antenna are presented in **Figure 4**. The measured and simulated reflection coefficients are identical. It is clearly seen that four operating bandwidths for the multi-band operation are obtained. The measured bandwidths, determined with the reflection coefficient –10 dB, are 755 MHz (1.255–1.98 GHz), 674 MHz (2.16–2.89 GHz), 44 MHz (3.26–3.7 GHz) and 34 MHz (5.14–5.48 GHz) which cover GPS (1575 MHz), GSM 1800, GSM 1900, WLAN (2400 MHz), LTE band 40 (2.3–2.4 GHz), WiMAX (3600 MHz) and WLAN (5.1–5.35 GHz).

The surface-current distributions at 1.8 GHz, 2.4 GHz and 3.6 GHz are demonstrated in **Figure 5**. From this figure, it is seen that with the increasing frequency the current flow increased in the S-shaped region. The radiation patterns at 1.8 GHz, 2.4 GHz and 3.6 GHz are shown in **Figure 6**. It is clear from this figure that the radiation patterns for both the E-plane and H-plane are omnidirectional at 3.6 GHz. But some directivity was

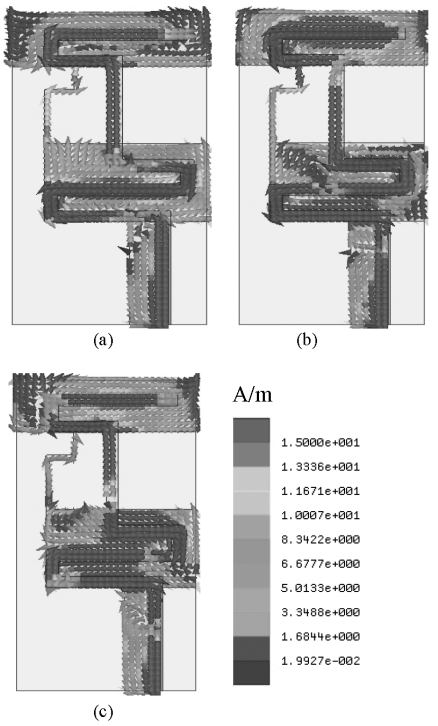

Figure 5: Surface-current distribution of the proposed antenna: a) 1.8 GHz, b) 2.4 GHz and c) 3.6 GHz
Slika 5: Razporeditev tokov na površini predlagane antene: a) 1,8 GHz, b) 2,4 GHz in c) 3,6 GHz

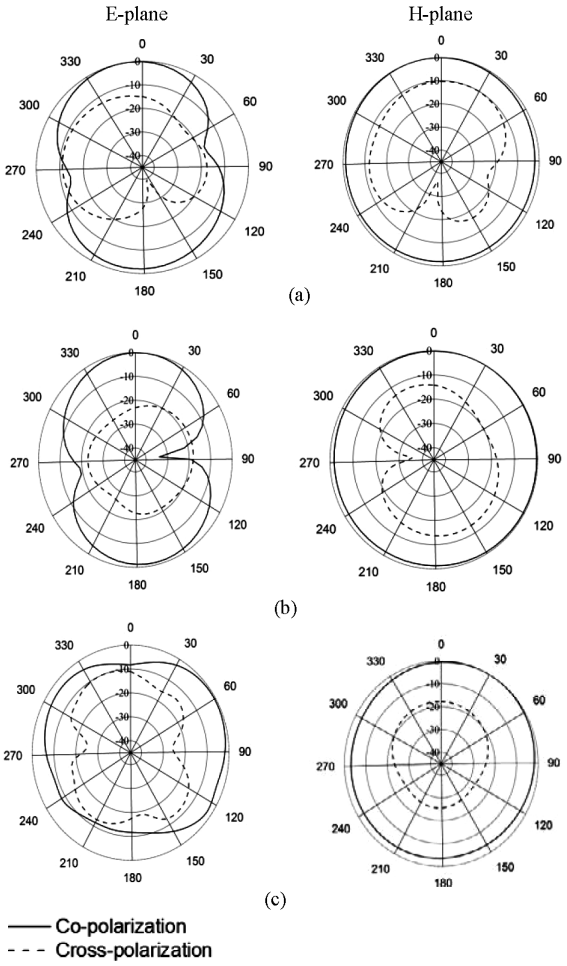

Figure 6: Radiation patterns of the proposed antenna for the frequencies of: a) 1.8 GHz, b) 2.4 GHz, c) 3.6 GHz
Slika 6: Vzorec sevanja predlagane antene pri frekvencah: a) 1,8 GHz, b) 2,4 GHz in c) 3,6 GHz

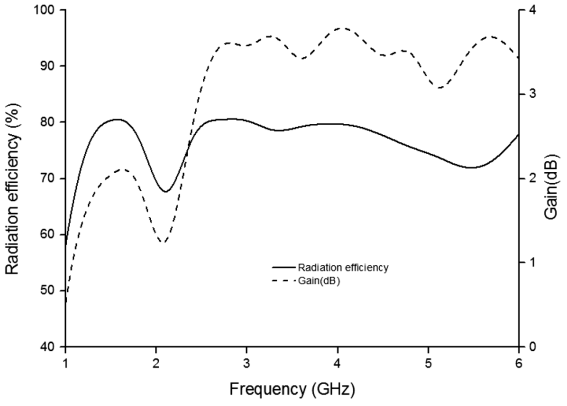

Figure 7: Radiation efficiency and gain of the proposed antenna
Slika 7: Učinkovitost sevanja in pridobitev predlagane antene

shown for the E-plane at 1.8 GHz and 3.6 GHz. Moreover, the simulated radiation efficiency and peak gain of the proposed antenna are presented in **Figure 7**. This figure shows that the maximum radiation efficiency of 81.25 % and the minimum of 67.5 % were achieved. In addition, the maximum peak gain of 3.72 dB was also obtained with the proposed antenna. A brief comparison of antenna performances is presented in **Table 3**.

Table 3: Comparison of antenna performances
Tabela 3: Primerjava zmogljivosti antene

Antenna	Dimensions (mm × mm)	Resonances (GHz)	Bandwidth (MHz)	Max. gain (dB)
[3]	119 × 50	1.71–2.48	770	5.4 at 2.15 GHz
[5]	65 × 40	1.66–2.59, 4.48–5.89	930, 1410	Not given
Proposed antenna	60 × 30	1.255–1.98, 2.16–2.89, 3.26–3.7, 5.14–5.48	755, 674, 44, 34	3.72 at 4.10 GHz

5 SPECIFIC ABSORPTION RATE (SAR)

The analysis of the health risk of the electromagnetic radiation of wireless devices is extensively in progress. These devices paved the way for an extensive utilization of mobile phones in modern society resulting in increased concerns about the inimical radiation.[10–12] There are several factors that affect the electromagnetic interaction; a close proximity between the human head and a wireless device is one of them. The specific absorption rate is defined with the power absorbed per mass of biological tissue and it is expressed with the units of watts per kilogram (W/kg). Currently, two international bodies have developed guidelines for limiting the effects of the electromagnetic radiation on human health. The EM absorption limit specified in IEEE C95.1:2005[6] is 1.6 W/kg in a 1 g averaging mass and 2 W/kg in a 10 g averaging mass of tissue, which is similar to the limit stated in the International Commission on Non-Ionizing Radiation Protection (ICNIRP) guideline.

Table 4: SAR values of the proposed antenna
Tabela 4: Vrednosti SAR za predlagano anteno

Frequency (GHz)	SAR for 1 g (W/kg)	SAR for 10 g (W/kg)	Absorbed power (rms) W	S_{11} with human head model (dB)
1.8	1.10	0.763	0.1179	–10.5
2.4	1.04	0.715	0.0957	–12.76

In designing antennas for wireless communication, it is very important to analyze the SAR values of the proposed antenna. In this research, a SAR analysis was performed, with the reference power of the wireless device set to 500 mW. The distance between the head and the handset was 4.5 mm. Moreover, the commercially available CST Microwave Studio software head-phantom model was adopted for this study. The head phantom is made of two layers, one is the shell and the other is fluid. The shell material specifications are: $\varepsilon = 5$, $\mu = 1$, $\tan\delta = 0.05$; and the specifications of the fluid inside the shell are: $\varepsilon = 42$, $\mu = 1$, el. conductivity of 0.99 S/m, fluid density of 1000 kg/m^3. In addition, the SAR values at 1.8 GHz and 2.4 GHz are presented in **Figure 8** and listed in **Table 4**. The obtained 1 g SAR for the proposed antenna at 1.8 GHz is 1.10 W/kg, which is about 27 % less than the reference value.[3]

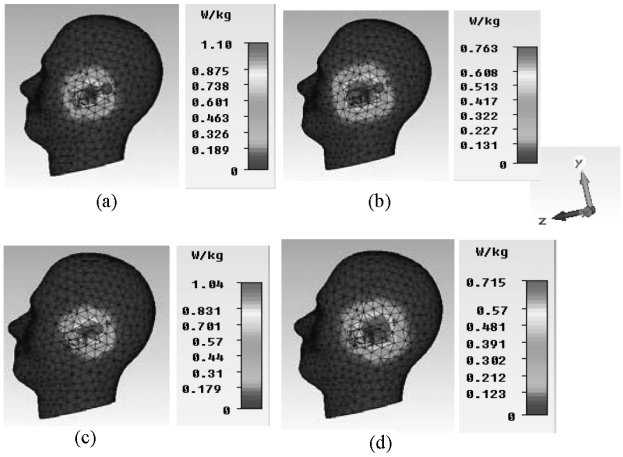

Figure 8: a) 1 g SAR at 1.8 GHz, b) 10 g SAR at 1.8 GHz, c) 1 g SAR at 2.4 GHz and d) 10 g SAR at 2.4 GHz
Slika 8: a) 1 g SAR pri 1,8 GHz, b) 10 g SAR pri 1,8 GHz, c) 1 g SAR pri 2,4 GHz in d) 10 g SAR pri 2,4 GHz

6 CONCLUSION

This paper presents a new printed planar antenna for GPS, GSM, WLAN, LTE band 40, WiMAX and WLAN wireless applications with a better antenna performance, including impedance bandwidth, antenna gain, radiation pattern and radiation efficiency obtained over operating bands. The experimental results validated the simulated ones. Moreover, the proposed antenna satisfies the requirements relating to the specific absorption rate. Therefore, the overall performance of the proposed antenna makes it suitable for the wireless mobile application.

7 REFERENCES

[1] W. C. Liu, C. M. Wu, Y. Dai, Design of triple-frequency microstrip-fed monopole antenna using defected ground structure, IEEE Transactions on Antennas and Propagation, 59 (**2011**), 2457–2463, doi:10.1109/TAP.2011.2152315

[2] T. Alam, M. R. I. Faruque, M. T. Islam, Printed Circular Patch Wideband Antenna for Wireless Communication, Informacije MIDEM, 44 (**2014**), 212–217

[3] D. Zhou, R. A. Abd-Alhameed, C. H. See, A. G. Alhaddad, P. S. Excell, Compact wideband balanced antenna for mobile handsets, IET Microwaves, Antennas & Propagation, 4 (**2010**), 600–608, doi:10.1049/iet-map.2009.0153

[4] Q. Rao, T. A. Denidni, New broadband dual-printed inverted L-shaped monopole antenna for tri-band wireless applications, Microwave and optical technology letters, 49 (**2007**), 278–280, doi:10.1002/mop.22107

[5] S. B. Chen, Y. C. Jiao, W. Wang, F. S. Zhang, Modified T-shaped planar monopole antennas for multiband operation, IEEE Transactions on Microwave Theory and Techniques, 54 (**2006**), 3267–3270, doi:10.1109/TMTT.2006.877811

[6] IEEE Standard for Safety Levels with Respect to Human Exposure to Radio Frequency Electromagnetic Fields, 3 kHz to 300 GHz, IEEE Std C95.1-2005 (Revision of IEEE Std C95.1-1991), 2006, pp. 0_1-238, doi:10.1109/IEEESTD.2006.99501

[7] International Non-Ionizing Radiation Committee of the International Radiation Protection Association, Guidelines on limits on exposure to radio frequency electromagnetic fields in the frequency range from 100 kHz to 300 GHz, Health Physics, 54 (**1988**), 9

[8] I. Yarovsky, E. Evans, Computer simulation of structure and properties of crosslinked polymers: application to epoxy resins, Polymer, 43 (**2002**), 963–969, doi:10.1016/S0032-3861(01)00634-6

[9] M. Samsuzzaman, M. Islam, J. Mandeep, N. Misran, Printed wide-slot antenna design with bandwidth and gain enhancement on low-cost substrate, The Scientific World Journal, 2014 (**2014**), article ID 804068, doi:10.1155/2014/804068

[10] M. R. I. Faruque, M. T. Islam, N. Misran, Evaluation of specific absorption rate (SAR) reduction for PIFA antenna using metamaterials, Frequenz, 64 (**2010**), 144–149, doi:10.1515/FREQ.2010.64.7-8.144

[11] M. R. I. Faruque, M. T. Islam, N. Misran, Influence of SAR Reduction in Muscle Cube with Metamaterial Attachment, Informacije Midem-Journal of Microelectronics, Electronic Components and Materials, 41 (**2011**), 233–237

[12] M. R. I. Faruque, M. T. Islam, Novel Triangular Metamaterial Design for Electromagnetic Absorption Reduction in Human Head, Progress in Electromagnetics Research, 141 (**2013**), 463–478, doi:10.2528/PIER13050603

UDK 539.92:531.43
Original scientific article/Izvirni znanstveni članek

ISSN 1580-2949
MTAEC9, 49(5)751(2015)

FRICTION AND WEAR BEHAVIOUR OF ULEXITE AND CASHEW IN AUTOMOTIVE BRAKE PADS

ODPORNOST PROTI TRENJU IN OBRABI AVTOMOBILSKIH ZAVORNIH OBLOG Z ULEKSITOM IN PRAHOM IZ INDIJSKEGA OREHA

İlker Sugözü[1], İbrahim Mutlu[2], Ahmet Keskin[3]

[1]Mersin University, Tarsus Technology Faculty, Mersin, Turkey
[2]Afyon Kocatepe University, Technology Faculty, Afyonkarahisar, Turkey
[3]Abant Izzet Baysal University, Bolu Vocational School, Bolu, Turkey
ibrahimmutlu@aku.edu.tr

Prejem rokopisa – received: 2014-09-14; sprejem za objavo – accepted for publication: 2014-10-15

doi:10.17222/mit.2014.228

In the experimental studies, ulexite and cashew were investigated as new materials in brake pads. A newly formulated brake-pad material with five different ingredients was produced using ulexite. Tribological properties of the friction materials were obtained using the brake-test equipment. The friction and wear characteristics of the samples in contact with a disk made of cast iron were studied. The change in the friction coefficient, the temperature of the friction surface and the amount of the wear were examined to assess the performance of these samples. In addition, microstructural characterizations of the braking pads were carried out using scanning electron microscopy (SEM). The results showed that the friction materials containing ulexite and cashew have an important effect on the friction stability and fade resistance. The strategy proposed in this paper can be considered for the alternative friction materials where ulexite and cashew can be used as friction materials in the brake pads.

Keywords: brake pad, composite materials, friction coefficient, ulexite, cashew

Preiskovan je bil vpliv uleksita in prahu iz indijskega oreha kot novega materiala v zavornih oblogah. Novo zasnovani material za zavorne obloge iz petih sestavin je bil izdelan z uporabo uleksita. Tribološke lastnosti tornega materiala so bile preizkušene na napravi za preizkus zavor. Preučevano je bilo trenje in značilnosti obrabe vzorcev v stiku z diskom iz sive litine. Za oceno zmogljivosti vzorcev so bile preiskane spremembe koeficienta trenja, izmerjena temperatura na površini stika in količina obrabe. Z vrstičnim elektronskim mikroskopom (SEM) so bile dodatno preiskane mikrostrukturne značilnosti zavornih oblog. Rezultati so pokazali, da imajo torni materiali, ki vsebujejo uleksit in prah indijskega oreha, pomemben vpliv na stabilnost trenja in odpornost proti odpovedi zavor pri višjih temperaturah. V tem članku predlagana usmeritev se lahko upošteva kot nadomestni torni material za zavorne obloge na osnovi uleksita in prahu iz indijskega oreha.

Ključne besede: zavorne obloge, kompozitni material, koeficient trenja, uleksit, prah iz indijskega oreha

1 INTRODUCTION

The friction element of an automotive brake system is one of the most important composite materials and generally consists of more than ten ingredients. This is because the friction materials have to provide a steady friction force, a reliable strength, and a good wear resistance in a broad range of braking circumstances.[1] Recently, some studies have shown that the most fatal accidents on the roads happen because of failed brake systems.[2,3] The performance of a brake system in a vehicle is mainly determined by the tribological characteristics of the friction couple, composed of a gray-iron disk (or drum) and friction materials.[1,4]

The most important property of the friction materials is a high friction coefficient so that they remain stable under high forces and, especially, at high temperatures.[2,3] The function of the brakes is to change the kinetic energy into the heat energy by absorbing it and releasing it into the atmosphere. If the generated heat exceeds the capacity of a brake, there is a decrease in the friction coefficient of the brake pads. When brake pads are exposed to high temperatures for long time, they are damaged. This damage results in a decrease in the brake performance, a high brake-pad wear or noise.[3,5] A great deal of effort has been made to develop friction materials with optimized tribological characteristics regardless of the type of braking conditions.[3,4]

Currently, more than 800 raw materials cited in the literature are used to produce friction materials for the commercial brakes.[6,7] Most automotive friction materials contain a phenolic-resin binder with additions of mineral fibers, fillers, friction-modifying compounds, abrasives and metallic particles to modify the heat-flow characteristics.[8,9] In a simplistic sense, fibers are included for their friction properties, heat resistance and thermal conductivity. The physical and chemical properties of a resin affect the wear process and friction characteristics of the friction material. In addition, a straight phenolic resin was used for brake friction materials and various modified resins are available to improve the compressibility, thermal stability, damping capacity and mechanical strength.[10] They play an important function of

toughening and strengthening the binder, which is quite brittle in its pure form.[11] Numerous compositions of friction materials have been developed, largely by empirical testing.[8,9] Several projects were conducted to investigate the friction materials that could improve the braking effectiveness, while also contributing to the energy efficiency.[12] In the literature, there are a lot of studies about using new materials for the brake pads in order to increase the braking performance.[13–18]

Raw and refined borates are used in ceramic glazes; thin coatings are applied onto ceramics. Borates are consumed mostly in the glass and fiberglass industry. Borates help the glass formation, reduce the thermal expansion and give resistance and durability to the ceramics. An addition of borates reduces the material stresses caused by the temperature gradients, thus making it more resistant to breaking. Borates are also used in borosilicate glasses. Borosilicate glass is not only highly resistant to a chemical attack, but it also has a very low coefficient of thermal expansion and, as a result, a high resistance to thermal shock. This thermal-shock resistance exceeds that of the ordinary glass by a factor of three.[19]

Ulexite is a mineral that combines calcium, sodium, water molecules and boron in a complicated arrangement with the following formula: $NaCaB_5O_9{\cdot}8H_2O$. It consists of thin crystals that act like optical fibers. On the surface, ulexite takes the shape of soft-looking masses and is often called "cotton ball". This form also occurs beneath the surface in veins similar to chrysotile, in which the crystal fibers run across the width of the veins.[20]

Cashew friction dust is made of CNSL (cashew nut-shell liquid). Due to its friction particles it is used as a stability agent in brake products; it has a resilient nature, acting as a cushioning agent of the engaging property of the lining. Further, it is easily decomposed on the surface of a brake lining at various elevated temperatures controlling the wear and acting as a protective element by prohibiting the generation of excessive temperature. It also easily absorbs the heat and disperses it accross the whole area of the friction material. It is mainly used as one of the prime raw materials for heavy-automobile non-asbestos and asbestos brake linings. It is also used for clutch facings and disc pads.[21,22]

In order to test the performance of ulexite in automotive friction materials, ulexite is sifted after grinding to obtain dust as raw boron products. In the case of ulexite and cashew being used together, when the amount of ulexite is increased, the amount of cashew is decreased. Five kinds of samples with different ingredients were designed. The tribological properties of these samples were determined using brake-test equipment. The friction tests were performed up to 400 °C. The change in the friction coefficient, the temperature of friction surface and the amount of wear were examined to identify the performance of these samples. In addition, microstructural characterizations of the braking pads were carried out using scanning electron microscopy (SEM). The results showed that the friction materials containing ulexite have an important effect on the friction stability and fade resistance. Due to the heat and abrasion resistance and the ability to reduce the thermal expansion of ulexite, the use of this material in brake pads can be attractive.

2 MATERIALS AND METHODS

In this study, a new automotive-brake friction material was developed using an addition of ulexite. The influence of ulexite on the brake's friction characteristics was especially examined. The friction materials investigated in this study were variations of a NAO (non-asbestos organic)-type material containing different ingredients including ulexite. Ulexite was obtained from Balikesir, the Bigadiç mine of Etibank in Turkey. The composition of the ulexite studied in this work is shown in **Table 1**.

Table 1: Composition of ulexite studied in this work[19]
Tabela 1: Sestava uleksita, uporabljenega v tej študiji[19]

Element	B_2O_3	CaO	Na_2O	SiO_2
w/%	24–38	18–24	2–7	4–13

Five different samples were produced. These samples contained ulexite, phenolic resin, steel fiber, copper, aluminium oxide, graphite, brass particles, cashew and barite. The friction-coefficient and temperature values were stored in a databank. Friction coefficient/temperature/time graphs and the mean coefficients of friction were obtained to identify the friction characteristics. An analytical balance was used to weigh the ingredients. The friction-material samples were produced in the conventional procedure for a dry formulation following dry mixing, pre-forming and hot pressing. These ingredients were mixed for 10 min using a commercial blender. The final mixture was loaded into a one-inch square (small samples) mold for pre-forming under a pressure of 9.8 MPa. The pre-formed samples were put

Table 2: Ingredients of the samples (*w*/%)
Tabela 2: Vsebnosti v vzorcih (*w*/%)

Sample code	UC-4 UCH-4	UC-8 UCH-8	UC-12 UCH-12	UC-16 UCH-16	UC-20 UCH-20
Phenolic resin	22	22	22	22	22
Steel fibers	15	15	15	15	15
Al_2O_3	3	3	3	3	3
Brass particles	5	5	5	5	5
Graphite	3	3	3	3	3
Barite	20	20	20	20	20
Cu particles	8	8	8	8	8
Cashew	4	8	12	16	20
Ulexite	20	16	12	8	4
Total	100	100	100	100	100

into a hot-pressing mold and pressed at a pressure of 14.7 MPa and at 180 °C for 15 min. During the hot--pressing process, pressure was released several times to release the gases that evolved from the cross-linking reaction (polycondensation) of the phenolic resin. Detailed conditions for each manufacturing step can be found in the author's other study.[23] The compositions of the friction materials studied in this work are shown in **Table 2**.

In order to define the friction coefficients of the automotive brake pad under different temperatures, a test device was designed and manufactured. **Figure 1** shows a schematic view of the brake tester used in this study.

Using a real brake-disc-type tester, the friction-coefficient characteristics of a pad next to the disc made of cast iron were investigated by changing the pad. The test sample was mounted on the hydraulic pressure and pressed against the flat surface of the rotating disc. Before performing the friction-coefficient tests, the surfaces of the test samples and the cast iron discs were ground with 320-grit sandpaper. The normal load was varied to achieve a constant friction force. The braking tests were carried out at a pressure of 1.05 MPa, a velocity of 6 ms^{-1} and at temperatures from 50 °C to 400 °C for 500 s. An electrical heater was used in order to achieve the friction-surface temperature of 400 °C. The temperature and friction-coefficient values were stored in the databank. The tests were repeated three times for each sample.

Friction coefficient/temperature/time graphs were obtained to identify the effects of these variables. The friction coefficient of the surface-material couple needs to be high and stable. The friction coefficient was calculated by measuring the normal and tangential pressures throughout the test 500 s. It was expressed as the mean value of the entire braking dependence during the friction-coefficient test. The specific wear rate was determined with the mass method following the Turkish Standard (TS 555) and British Standard (BS AU142) and calculated with the following Equation (1):

$$V = (m_1 - m_2)/(L\, f_m \rho) \quad (1)$$

where V is the specific wear (mm^3/MJ), m_1 is the mass of the brake pad before the testing (kg), m_2 is the mass of the brake pad after the testing (kg), L is the friction distance calculated using the number of revolutions and the radius of the disc (m), f_m is the average friction force (N) and ρ is the density of the brake pad (kg/mm^3).[24,25]

3 RESULTS AND DISCUSSION

3.1 Effect of the temperature on the friction performance

In the present study, 10 samples were used. These samples contained copper particles, phenolic resin, Al_2O_3, steel fibers, brass particles, graphite, barite, ulexite and cashew (**Table 2**). Only half of the samples (with the UCH indices) were heat treated for 4 h at a temperature of 180 °C. The remaining 5 samples were untreated (with the UC indices). These samples included 4–20 % ulexite and 20–4 % cashew, respectively, and the mean friction coefficient ranged from 0.394 to 0.454.

When the coefficient of friction (μ) was studied it varied significantly during the initial stage of the testing. This can be attributed to the fact that the size of the contact area increased and the friction layer was developed on the surface. In order to determine the variations in the friction coefficient and the temperature of the friction surface with the testing time of the samples, the tests were performed at applied temperatures from 50 °C to 400 °C (**Figures 2** to **6**). As seen from these figures, the friction coefficients show different features depending on the content.

Generally, the friction-coefficient value gradually increases for all the samples until the 100 s and then gradually decreases after the 400 s (**Figures 2** to **6**). The reason of the increasing friction coefficient is the contact of the metallic material with the disc surface. The wear of the ingredients of the metallic materials is tested.

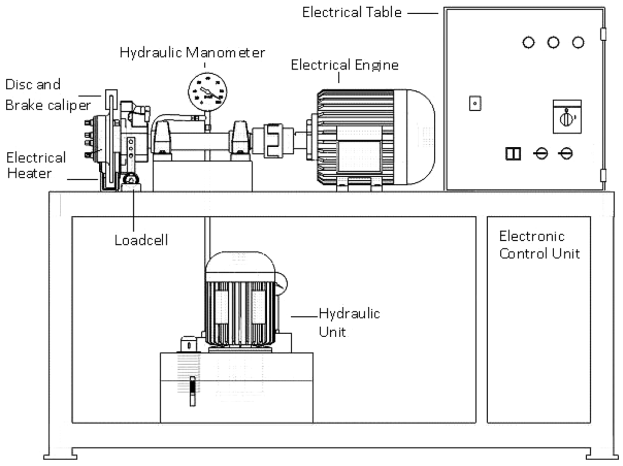

Figure 1: Schematic view of the brake tester
Slika 1: Shematski prikaz preizkuševalnika zavor

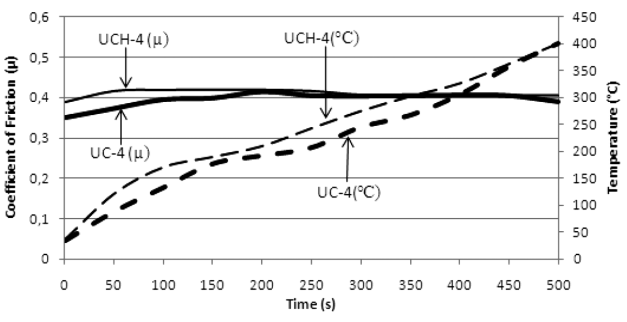

Figure 2: Change in the friction coefficient versus the temperature as a function of time for samples UC-4 and UCH-4
Slika 2: Spreminjanje koeficienta trenja v odvisnosti od temperature in časa pri vzorcih UC-4 in UCH-4

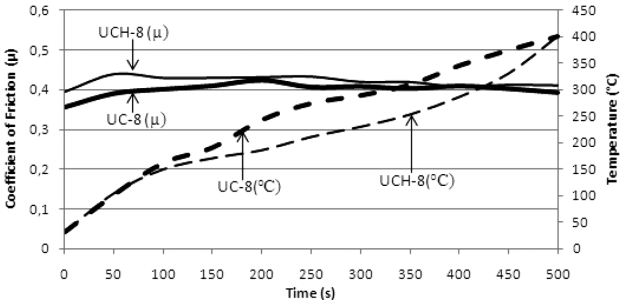

Figure 3: Change in the friction coefficient versus the temperature as a function of time for samples UC-8 and UCH-8

Slika 3: Spreminjanje koeficienta trenja v odvisnosti od temperature in časa pri vzorcih UC-8 in UCH-8

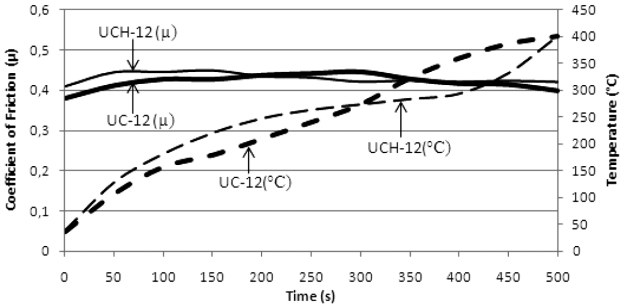

Figure 4: Change in the friction coefficient versus the temperature as a function of time for samples UC-12 and UCH-12

Slika 4: Spreminjanje koeficienta trenja v odvisnosti od temperature in časa pri vzorcih UC-12 in UCH-12

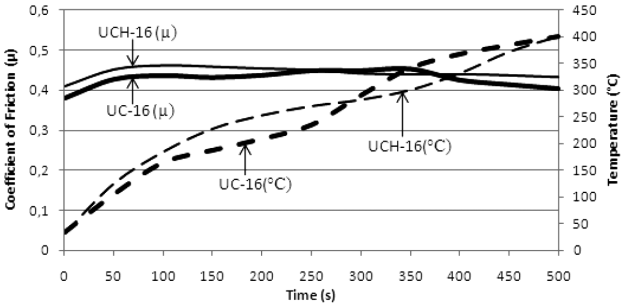

Figure 5: Change in the friction coefficient versus the temperature as a function of time for samples UC-16 and UCH-16

Slika 5: Spreminjanje koeficienta trenja v odvisnosti od temperature in časa pri vzorcih UC-16 in UCH-16

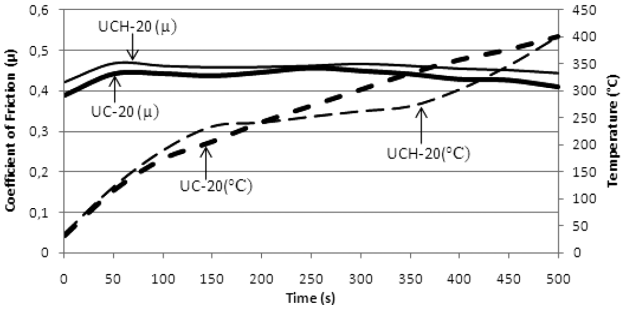

Figure 6: Change in the friction coefficient versus the temperature as a function of time for samples UC-20 and UCH-20

Slika 6: Spreminjanje koeficienta trenja v odvisnosti od temperature in časa pri vzorcih UC-20 in UCH-20

Therefore, these metallic materials detach from the surface of the brake pad and the friction coefficient decreases. This phenomenon continues until new friction surfaces appear. A rapid increase in the coefficient of friction may lead to a rapid increase in the temperature of the friction surface.

It was found that the friction coefficient decreases with the increasing testing temperature. Generally, the friction coefficient decreased between 350 °C and 400 °C due to the softening of the phenolic resin (**Figures 2** to **6**). As a result, fading occurred during the braking action. Furthermore, with the increasing temperatures, the ingredients in the brake pads affected each other due to a faster diffusion. This phenomenon is called the thermal fade.[4] Therefore, one can say that the samples remained unchanged only up to the temperature of 400 °C. There was an increase in μ before the 200 s, followed by a decrease just after the 350 s when μ was almost constant for the UCH-4, UCH-16 and UCH-20 samples (**Figures 2, 5** and **6**). This degradation is somewhat slow, having slight fluctuations. By the 300 s, as a result of the friction, a temperature of 300–350 °C was achieved on the friction surface.

As seen from these figures, it is understood that all the heat-treated samples (UCH) have higher friction-coefficient values and more stable friction coefficients than the others. The differences between the friction coefficients of the UC samples and the UCH samples are obvious especially at the beginning and after the 400 s. The difference at the initial state shows a good fit of the heat-treated samples to the surface. At the states after the 400 s the heat-treated samples have a lower temperature then the others at this time (**Figures 3** to **6**). Thus, the friction coefficients of the UC samples decreased due to the increase in the temperature.[26] It is observed that the friction-coefficient and temperature values of the non-heat-treated samples quickly change and fluctuate. As a result, it can be said that heat treatment makes the friction coefficients stable and increases the friction-coefficient values.

Nonetheless, it should be noted that a good stability of μ is achieved using the samples under the working condition considered. These results are consistent with the behavior of the friction coefficients of all the samples. Therefore, if a μ value of 0.39–0.45 is desired, additions of both ulexite and cashew can be used in the brake pads in the amounts of 4–20 %. Furthermore, if the stability of μ is desired and μ has higher values, the UCH-20 sample is suggested as the best material for the brake pads when compared to the others. Some middle vibrations and noise were observed during the testing with the friction assessment and screening test (FAST). This vibration was typically observed at the beginning of the test, before a stable friction layer was developed.

3.2 Microstructural characterization of friction surfaces

Apparently, friction layers are formed by the wear particles generated during the friction. The chemistry and structure of a friction layer depend on the bulk materials (lining and disc), the testing conditions and the environment. The role of the friction layer may vary depending on its characteristics.[27,28] The SEM micrographs of the braking-pad surfaces after the braking test are shown in **Figures 7** and **8**. The friction surfaces of the samples were characterized using SEM (LEO 1430 VP). The sample surfaces for the SEM observations were always coated with carbon. There are micro-voids on the surfaces of almost all the samples. Micro-voids consist of the metallic particles detached during the friction.

It is seen from **Figures 7** and **8** (UC-8 and UCH-4) that larger micro-voids occurred in the samples due to detached metallic particles. As seen in these figures, some particles are detached from the body causing micro-voids. The micro-voids on the surfaces of the samples can be classified as smaller or bigger in size. The bigger micro-voids were formed due to the pitting of the metallic particles during the friction. The worn metallic particles imply that they actively participated in the friction during the braking test. It is known that if the coherent surface of a metal component is bigger, the friction and wear will be increased. In addition to micro-voids, there are some micro-cracks on the surfaces. It is also observed that Al_2O_3 particles are distributed homogeneously, therefore, contributing to the effectiveness of the friction surfaces.

Several characteristic features can be observed on the friction surfaces of the pads. White spots are seen on **Figure 7** (UC-8 and UC-20). Dark areas can also be seen in **Figures 7** and **8** (UC-8 and UCH-4). A more loose contact on the trailing edge facilitates the access of air and an uneven wear related to a higher oxidation (a burn-off) of the phenolic resin. This is due to the distribution of the friction force over a pad surface.[28] When the pads heat up during the braking, the resin tends to expand at very high temperatures and turn into glassy carbon. Carbonized resins weaken the matrix and accelerate the pad wear (**Figure 7,** UC-8 and UC-16).[28,29] The glassy phase loses its support and is torn off from the surface by the shear force.[30] **Figures 7** and **8** relating to UC-12, UC-16, UC-20, UCH-8 and UCH-12 (from the SEM) show thick friction layers developed on the surfaces of the pads.

In this particular case, the friction layer covering a friction surface diminishes the abrasive effect of the glassy phase by eliminating the sharp edge of the glass and smoothing the friction surface. Hard glassy particles typically act as an abrasive element and scratch off the

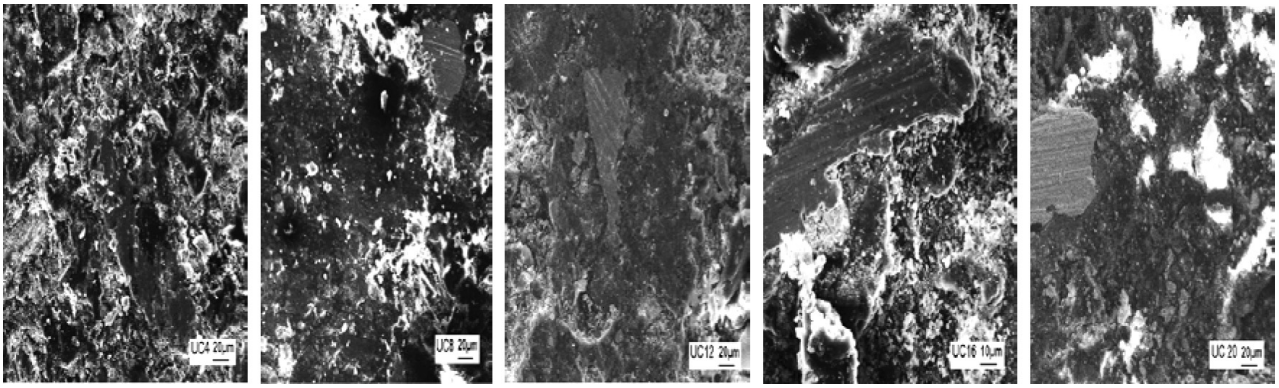

Figure 7: SEM micrographs of brake-pad samples with the UC code
Slika 7: SEM-posnetki vzorcev zavornih oblog z oznako UC

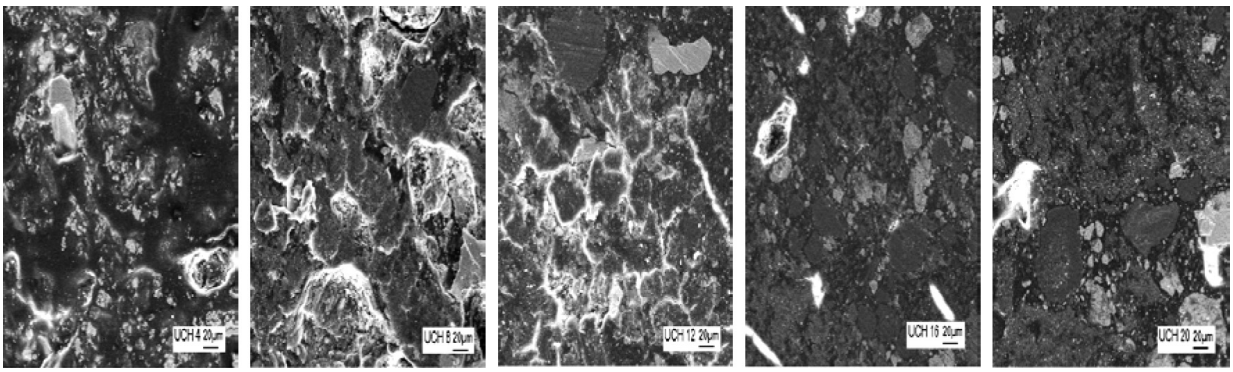

Figure 8: SEM micrographs of brake-pad samples with the UCH code
Slika 8: SEM-posnetki vzorcev zavornih oblog z oznako UCH

cast-iron-disc counter face and the material adhering to it.[28] Apparently, the carbonaceous matrix was formed of graphite, coke and degraded phenolic resin. The ingredient with the plastic-deformation capability developed a flake-like feature after the friction experiment (**Figures 7** and **8**; UC-16, UC-20, UCH-8 and UCH-12).

All matters were homogeneously distributed in the matrix and, therefore, very few micro-voids were observed in the structures (**Figures 7** and **8**; UC-4, UC-8, UC-12, UCH-8 and UCH-20). The friction process is characterized by the development of friction debris. Such debris adheres to the friction surface and forms a friction layer easily visible when examining a sample surface after the testing (FAST) (**Figures 7** and **8**; UC-16, UC-20, UCH-4 and UCH-8). A systematic analysis of the surfaces of the composite materials indicated that the friction process dominantly occurred on the friction layer, which eventually covered the top of the bulk. Well-developed friction layers on the friction surfaces as well as their morphologies are easily visible. Detailed views of the friction surfaces including the information about the friction layers are shown in **Figures 7** and **8**. Diffusion occurred in the Cu particles located in the friction layers. Brighter areas marked as Cu in **Figures 7** and **8** (UC-4, UC-8, UC-16 and UCH-12) represent the regions where Cu interacted with the friction layers.[31]

3.3 Wear behaviour

Table 3 gives the mean coefficients of friction, the standard deviations of coefficients of friction, densities, hardness values and the specific wear rates of the tested samples. As can be seen from **Table 3**, the friction coefficients are in the appropriate category according to the Turkish Standard TS 555 and British Standard BS AU142. Also, the standard deviations are very small, which means that the materials have stable friction characteristics.

Table 3: Typical characteristics of the brake pads used in this study
Tabela 3: Značilnosti zavornih oblog, uporabljenih v tej študiji

Sample code	Mean coefficient of friction	Standard deviation	Density (g cm^{-3})	Hardness (Brinell)	Specific wear (g mm^{-2})
UC–4	0.394	0.0182	1.935	18.2	0.26×10^{-6}
UC–8	0.401	0.0172	1.842	16.2	0.27×10^{-6}
UC–12	0.420	0.0192	1.765	15.9	0.34×10^{-6}
UC–16	0.427	0.0216	1.704	14.7	0.37×10^{-6}
UC–20	0.437	0.0223	1.680	13.9	0.38×10^{-6}
UCH–4	0.410	0.0091	1.834	23.2	0.21×10^{-6}
UCH–8	0.418	0.0127	1.782	20.3	0.22×10^{-6}
UCH–12	0.430	0.0127	1.717	18.9	0.29×10^{-6}
UCH–16	0.442	0.0140	1.652	18.2	0.33×10^{-6}
UCH–20	0.454	0.0134	1.588	15.3	0.35×10^{-6}

In the present study, no direct proportionality was found among the density, the hardness and the wear resistance due to the complexity of the composite structures. However, the highest friction coefficient was obtained for the UCH-20 sample. This sample includes 4 % of ulexite and 20 % of cashew and it was heat treated. The lowest friction coefficient was obtained for the UC-4 sample. This sample includes 20 % of ulexite and 4 % of cashew and it was heat untreated. In addition, less wear was observed on the heat-treated samples, which included 4–20 % of ulexite and 20–4 % of cashew, and their mean values of the friction coefficients ranged from 0.41–0.45 (**Table 3**). Besides, the minimum wear was obtained for the UC-4 and UCH-4 samples, including the heat-treated and untreated ones. It is seen from **Table 3** that the heat-treated samples generally have a better wear resistance than the untreated samples.

It is also seen from **Table 3** that heat treatment facilitated a more homogeneous braking-pad structure. In addition, a more stabilised friction coefficient was obtained due to heat treatment. It is assumed that some detached materials left the samples and then structural variations were obtained. Furthermore, with the increasing temperature the ingredients in the braking pad affected each other due to a faster diffusion. Therefore, it can be said that heat treatment is essential for braking pads. It is also known that the hardness of a sample increases and the density decreases due to heat treatment, while the specific wear ratio changes (**Table 3**). In the present work, heat treatment facilitated a better performance of all the samples compared with the untreated ones. These results are consistent with the earlier works.[32–35]

As can be seen from **Table 3**, the friction coefficients achieved for samples UCH-20 and UCH-16 are approximately 0.45, which is considered to be very good when compared to the coefficients of friction achieved with the current brake pads. The UC-4 sample has the highest density and hardness among the untreated samples. It includes 20 % of ulexite and 4 % of cashew; the specific gravity of ulexite is bigger than that of cashew. A higher amount of ulexite causes a higher density. But the heat-treated UCH-4 sample with the same ingredients has the highest hardness among the all samples.

It is well known that the friction coefficient is usually associated with an increase in the wear. In the present work, all the samples confirmed this assumption (**Table 3**). But the UCH-16 and UCH-20 samples have better values than the other samples. Therefore, one can say that only samples UCH-16 and UCH-20 are preferred for this kind of brake pads as they provide better mechanical and microstructural properties than the other samples.

It can be seen from the results that there is no direct correlation between the wear resistance and the hardness. However, this is an unavoidable reality of these features that affect each other. As can be seen from the table, a high-hardness pad has a high wear resistance and lower wear due to the amounts of the constituent components of the samples. The components made of the pad mate-

rials comprised of compounds of different contents can have a hard structure and, consequently, a higher hardness. But the amount of the resin component included in the materials is not sufficient as the particle adhesion surface is decreased and there is a quick separation of the particles that make up the main structure at low strains, while the friction can cause a wear that is higher than expected.

The heating process generally affects the microstructure of a brake pad and, accordingly, the hardness increases. It can be seen from **Table 3** that the friction coefficient of the UC-4 sample is 0.394 and its wear rate is $0.26 \cdot 10^{-6}$ and, after the heat treatment, these values are 0.410 and $0.21 \cdot 10^{-6}$, respectively. The situation is similar for the other samples. Thus, after the heat treatment, the coefficients of friction of the samples of the same ingredients increase and their wear rates decrease. Heat treatment has a positive impact on both the friction coefficient and specific wear.

The mean coefficient of friction, hardness, and wear rates of the heat-treated (UCH) and untreated (UC) samples showing parallelism to each other exhibit the characteristics of the material. The sample with a high mean coefficient of friction also has a high wear rate. In this case, the rubbing of the ruptures of large particles from the brake pad due to the strain has a significant impact. Also, since the pad's hardness is lower than the hardness of the disk, the wear naturally increases during the process of creating a high coefficient of friction. After the heat treatment, the densities of the samples decrease. During the heat treatment at a low evaporation temperature, volatile materials move away from the body and form micro-scale porosity in the body. This situation causes a decrease in the density, and the heat produced during the friction (rubbing) is removed from the body by the micro-pores, leading to a lower friction-surface temperature and a stable friction performance.[36]

4 CONCLUSIONS

In this study, the effect of ulexite and cashew amounts on the friction and wear behavior of a brake pad used in the automotive industry is experimentally analyzed. As a result of the experiments, the structure and chemical composition of the friction layer generated on the friction surface differ significantly from those of the bulk. It is apparent that no simple relationship exists between the composition of the friction layer and the bulk-material formulation. Heat treatment facilitated a more homogeneous structure and, hence, microstructural variations were minimized during the braking action. On the other hand, heat treatment increased the hardness of the samples and also decreased the density.

The highest friction coefficient was obtained for the heat-treated samples. Smaller values were obtained for the untreated samples. The UCH-4 sample had a more stable friction coefficient during the FAST than the other samples. As the UCH-4 and UCH-8 samples had lower friction coefficients, their wear ratios and standard deviations were also considerably lower. Out of 10 samples, UC-20, UCH-12, UCH-16 and UCH-20 exhibited better friction and wear properties. Therefore, these samples can be suggested as brake-pad materials.

In the present work, the standard deviation was within the acceptable range for all the samples. No direct proportionality among the mean coefficients of friction, the standard deviation and the wear resistance was found due to the complexity of the composite structures. Some micro-voids and micro-cracks were observed on the worn surfaces.

5 REFERENCES

[1] P. J. Blau (ed.), Friction, Lubrication, and Wear Technology, ASM Handbook, vol. 18, ASM International, 1992, 569–577

[2] M. Boz, A. Kurt, Relationship between density and friction coefficient in powder metal bronze brake lining, Proceedings of the second international conference on P/M, Cluj-Napoka, Romania, 2000, 181–187

[3] A. Kurt, M. Boz, Mater. Design, 26 (**2005**), 717–721, doi:10.1016/j.matdes.2004.09.006

[4] M. G. Jacko, S. K. Lee, Kirk–Othmer Encyclopedia of Chemical Technology, vol. 4, 4th ed., Wiley, 1992, 523–536

[5] E. W. Reinsch, Sintered Metal Brake Linings for Automotive Applications, chapter 2, In: H. H. Hausner et al. (eds.), Perspectives in Powder Metallurgy Fundamentals, Methods, and Applications, Plenum Press, New York 1970, 9–21, doi:10.1007/978-1-4684-3015-8_2

[6] J. W. Longley, R. Gardner, IMechE, 453 (**1988**), 31–38

[7] G. Drava, R. Leardi, A. Portesani, E. Sales, Chemometr. Intell. Lab., 32 (**1996**), 245–255, doi:10.1016/0169-7439(95)00085-2

[8] P. J. Blau, Compositions, functions, and testing of friction brake materials and their additives, Oak Ridge National Laboratory Technical Report ORNL/TM 2001/64, Oak Ridge, Tennessee, 2001, doi:10.2172/788356

[9] G. Nicholson, Facts about friction, Gedoran Publishing, Winchester, VA 1995

[10] H. Jang, S. J. Kim, Wear, 239 (**2000**), 229–236, doi:10.1016/S0043-1648(00)00314-8

[11] Y. Lu, Compos. Sci. Technol., 66 (**2006**), 591–598, doi:10.1016/j.compscitech.2005.05.032

[12] S. Ozcan, P. Filip, Wear, 259 (**2005**), 642–650, doi:10.1016/j.wear.2005.02.112

[13] I. Sugozu, I. Mutlu, J. Theor. Appl. Mech., 39 (**2009**) 1, 101–114

[14] I. Mutlu, J. Appl. Sci., 9 (**2009**) 2, 377–381

[15] F. Ficici, M. Durat, M. Kapsiz, J. Braz, Soc. Mech. Sci., 36 (**2014**) 3, 653–659, doi:10.1007/s40430-013-0115-x

[16] K. W. Liew, U. Nirmal, Mater. Design, 48 (**2013**), 25–33, doi:10.1016/j.matdes.2012.07.055

[17] M. A. Maleque, A. Atiqah, R. J. Talib, H. Zahurin, IJMME, 7 (**2012**) 2, 166–170

[18] A. Keskin, Sci. Res. Essays, 6 (**2011**) 23, 4893–4904, doi:10.5897/SRE10.1072

[19] http://www.boren.gov.tr, accessed 10 September 2013

[20] R. B. Kistler, C. Helvaci, Ind. Min. and Rocks, (**1994**), 171–186

[21] J. Bijwe, N. M. Nidhi, B. K. Satapathy, Wear, 259 (**2005**), 1068–1078, doi:10.1016/j.wear.2005.01.011

[22] A. Ganguly, R. George, Bull. Mater. Sci., 31 (**2008**) 1, 19–22, doi:10.1007/s12034-008-0004-6

[23] I. Mutlu, Investigation of some ceramic additive automotive brake pads, Dissertation, University of Sakarya, Turkey, 2002
[24] TS 555 (Turkish Standard), Highway vehicles, brake systems, brake pads for frictional brake, Turkey, 1992
[25] British Standards Specification: BS AU 142–1968, 1968
[26] G. P. Ostermeyer, Wear, 254 (**2003**), 852–858, doi:10.1016/S0043-1648(03)00235-7
[27] M. Eriksson, F. Bergman, S. Jacobson, Wear, 232 (**1999**), 163–167, doi:10.1016/S0043-1648(99)00141-6
[28] K. W. Hee, P. Filip, Wear, 259 (**2005**), 1088–1096, doi:10.1016/j.wear.2005.02.083
[29] A. Fischer, Wear, 194 (**1996**), 238–245, doi:10.1016/0043-1648(95)06738-8
[30] G. Straffelini, Wear, 245 (**2000**), 216–222, doi:10.1016/S0043-1648(00)00481-6
[31] I. Mutlu, I. Sugozu, C. Oner, Investigation of friction behavior of boric acid and black pine cone dust added brake pads, IATS'09, Turkey, 2009
[32] T. R. Champman, D. E. Niesz, R. T. Fox, T. Fawcett, Wear, 236 (**1999**), 81–87, doi:10.1016/S0043-1648(99)00259-8
[33] S. K. Rhee, M. G. Jacko, P. H. S. Tsang, Wear, 146 (**1991**), 89–97, doi:10.1016/0043-1648(91)90226-K
[34] J. R. Barber, T. W. Beamond, J. R. Waring, C. Pritchard, J. Tribol., 107 (**1985**) 2, 206–210, doi:10.1115/1.3261021
[35] T. Matsushima, H. Masumo, S. Ito, M. Nishiwaki, SAE Tech. Paper 982251, (**1998**), doi:10.4271/982251
[36] I. Sugozu, Production of non-asbestos automotive brake lining additional boron and investigation of its braking characteristic, Dissertation, Univ. of Fırat, Turkey, 2009

UDK 669.058:669.781:544.034
Original scientific article/Izvirni znanstveni članek

ISSN 1580-2949
MTAEC9, 49(5)759(2015)

DIFFUSION KINETICS AND CHARACTERIZATION OF BORIDED AISI H10 STEEL

KINETIKA DIFUZIJE IN KARAKTERIZACIJA BORIRANEGA JEKLA AISI H10

Ibrahim Gunes, Melih Ozcatal

Department of Metallurgical and Materials Engineering, Faculty of Technology, Afyon Kocatepe University, 03200 Afyonkarahisar, Turkey
igunes@aku.edu.tr

Prejem rokopisa – received: 2014-09-22; sprejem za objavo – accepted for publication: 2014-10-17

doi:10.17222/mit.2014.238

In this study, case properties and diffusion kinetics of the AISI H10 steel borided in Ekabor-II powder were investigated by conducting a series of experiments at temperatures of (1123, 1173 and 1223) K for (2, 4 and 6) h. The boride layer was characterized with light microscopy, X-ray diffraction technique and micro-Vickers hardness tester. The X-ray diffraction analysis of the boride layers on the surfaces of the steels revealed the existence of FeB, Fe_2B, CrB, Cr_2B and MoB compounds.
Depending on the chemical compositions of the substrates and boriding time, the boride-layer thickness on the surface of the steel ranged from 12.86 μm to 63.72 μm. The hardness of the boride compounds formed on the surfaces of the steels ranged from 1648 $HV_{0.05}$ to 1964 $HV_{0.05}$, whereas the Vickers-hardness value of the untreated steel was 306 $HV_{0.05}$. The activation energy (Q) of the borided steel was 160.594 kJ/mol. The growth kinetics of the boride layer formed on the AISI H10 steel and its thickness were also investigated.

Keywords: AISI H10, boride layer, microhardness, kinetics, activation energy

V tej študiji so bile preiskovane lastnosti in kinetika difuzije v jeklu AISI H10, boriranem v prahu Ekabor-II (2, 4 in 6) h na temperaturah (1123, 1173 in 1223) K. Boridni sloj je bil okarakteriziran s svetlobno mikroskopijo, z rentgensko difrakcijo in merjenjem mikrotrdote po Vickersu. Rentgenska difrakcija boridnega sloja je odkrila prisotnost naslednjih spojin: FeB, Fe_2B, CrB, Cr_2B in MoB.
Odvisno od kemijske sestave podlage in časa boriranja je bila debelina sloja borida na površini jekla med 12,86 μm in 63,72 μm. Trdota boridov, nastalih na površini jekla, je bila med 1648 $HV_{0,05}$ in 1964 $HV_{0,05}$, medtem ko je bila Vickersova trdota neobdelanega jekla 306 $HV_{0,05}$. Aktivacijska energija (Q) pri boriranju jekla je bila 160,594 kJ/mol. Preiskovana je bila tudi kinetika rasti in debelina boridnega sloja na jeklu AISI H10.

Ključne besede: AISI H10, sloj borida, mikrotrdota, kinetika, aktivacijska energija

1 INTRODUCTION

Boriding, or boronizing, is a thermochemical surface-hardening process that can be applied to a wide variety of ferrous, nonferrous and cermet materials. The process involves heating a well-cleaned material in the range of 973 K to 1373 K, preferably for 1 h to 12 h, in contact with a boronaceous solid powder (boronizing compound), paste, liquid, plasma, gaseous or electrochemical medium.[1–7]

Boron atoms, due to their relatively small size (an atomic radius of 0.09 nm) and very mobile nature can diffuse easily into ferrous alloys (an atomic radius of 0.124 nm) forming FeB and Fe_2B intermetallic, non-oxide, ceramic borides. The diffusion of B into steel results in the formation of iron borides (FeB and Fe_2B) and the thickness of the boride layer is determined by the temperature and time of the treatment.[8–12]

The basic advantage of boriding is that boride has a high melting point and high hardness at elevated temperatures and, consequently, researches of the boriding of transition metals have been accelerated in the recent decade, particularly for the applications in the production of cutting tools and heavy gears, and in the automotive, casting, textile, food-processing, packaging and ceramic industries where huge friction-dependent energy losses and intensive corrosion and wear occur.[13–15] In this study, the AISI H10 steel was borided considering these advantages of boriding. The characterization and growth diffusion of the obtained boride layers were calculated. The main objective of this study was to investigate the diffusion kinetics and the effects of the processing parameters such as the temperature, the time and the chemical composition on the boride layers formed on the AISI H10 steel after powder-pack boriding at different processing temperatures and times.

2 EXPERIMENTAL DETAILS

2.1 Boriding and characterization

The AISI H10 steel essentially contained mass fractions 0.32 % C, 3.15 % Cr, 2.90 % Mo, 0.65 % V and 0.40 % Mn. The test specimens were cut into dimensions of Ø 25 mm × 8 mm, ground up to 1200 G and polished using a diamond solution. The boriding heat treatment was carried out in a solid medium con-

taining an Ekabor-II powder mixture placed in an electrical-resistance furnace operating at temperatures of (1123, 1173 and 1223) K for (2, 4 and 6) h under atmospheric pressure. The microstructures of the polished and etched cross-sections of the specimens were observed under a Nikon MA100 light microscope. The presence of borides formed in the coating layer was confirmed with X-ray diffraction equipment (Shimadzu XRD 6000) using Cu-K_α radiation. The thickness of borides was measured with a digital thickness-measuring instrument attached to the light microscope (Nikon MA100). The hardness measurements of the boride layer on each steel and of the untreated steel substrate were made on the cross-sections using a Shimadzu HMV-2 Vickers indenter with a 50 g load.

2.2 Evaluation of the activation energy of boron diffusion

In order to study the diffusion mechanism, borided AISI H10 steel was used for this purpose. It is assumed that boride layers grow parabolically in the direction of the diffusion flux and perpendicular to the substrate surface. So, the time dependence of the boride-layer thickness can be described with Equation (1):

$$x^2 = Dt \tag{1}$$

where x is the depth of the boride layer (mm), t is the boriding time (s) and D is the boron diffusion coefficient through the boride layer. It is a well-known fact that the main factor limiting the growth of a layer is the diffusion of boron into the substrate. It is possible to argue that the relationship between the growth-rate constant D, the activation energy Q, and the temperature T in Kelvin, can be expressed as an Arrhenius equation (Equation (2)):

$$D = D_0 \exp\left(-\frac{Q}{RT}\right) \tag{2}$$

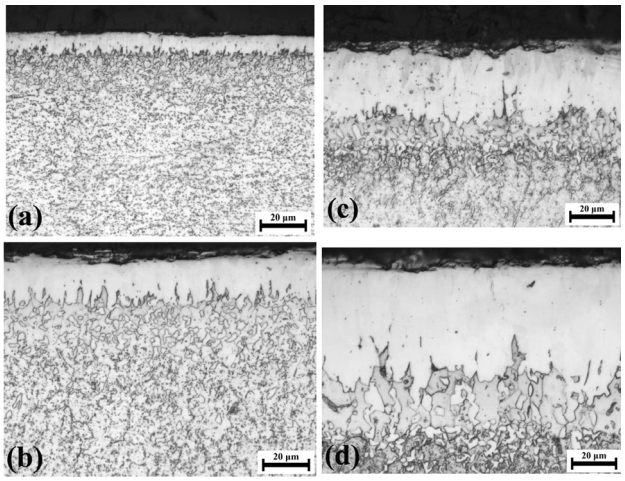

Figure 1: Cross-sections of borided AISI H10 steel: a) 1123 K – 2 h, b) 1123 K – 6 h, c) 1223 K – 2 h, d) 1223 K – 6 h

Slika 1: Prečni prerez boriranega jekla AISI H10: a) 1123 K – 2 h, b) 1123 K – 6 h, c) 1223 K – 2 h, d) 1223 K – 6 h

where D_0 is a pre-exponential constant, Q is the activation energy (J/mol), T is the absolute temperature in Kelvin and R is the ideal gas constant (J/(mol K)).

The activation energy for the boron diffusion in a boride layer is determined with the slope obtained in the plot of ln D vs. 1/T, using Equation (3):

$$\ln D = \ln D_0 - \frac{Q}{RT} \tag{3}$$

3 RESULTS AND DISCUSSION

3.1 Characterization of boride coatings

Light micrographs of the cross-sections of the borided AISI H10 steel at the temperatures of 1123 K and 1223 K for 2 h and 6 h are shown in **Figure 1**. As can be seen the borides formed on the AISI H10 substrate have a saw-tooth morphology. It was found that the coating/matrix interface and the matrix can be significantly distinguished and the boride layer has a columnar structure. Depending on the chemical compositions of the substrates, the boriding time and temperature, the boride-layer thickness on the surface of the AISI H10 steel ranged from 12.86 µm to 63.72 µm in **Figure 2.**

Figure 3 gives the XRD patterns obtained at the surface of the borided AISI H10 steel at 1123 K and 1223 K for the treatment times of 2 h and 6 h. The XRD patterns show that the boride layer consists of borides such as MB and M_2B (M = metal: Fe, Cr). The XRD results showed that the boride layers formed on the H10 steel contained FeB, Fe_2B, CrB, Cr_2B and MoB phases (**Figures 3a** to **3d.)**

Microhardness measurements were carried out along a line from the surface to the interior in order to see the variations in the hardness of the boride layer, the transition zone and the matrix, respectively. The microhardness of the boride layers was measured at 10 different locations at the same distance from the surface and the

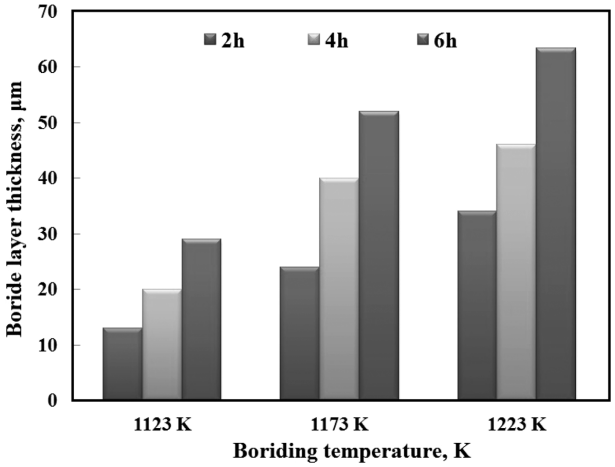

Figure 2: Thickness values of boride layers with respect to boriding time and temperature

Slika 2: Debelina borirane plasti glede na čas in temperaturo boriranja

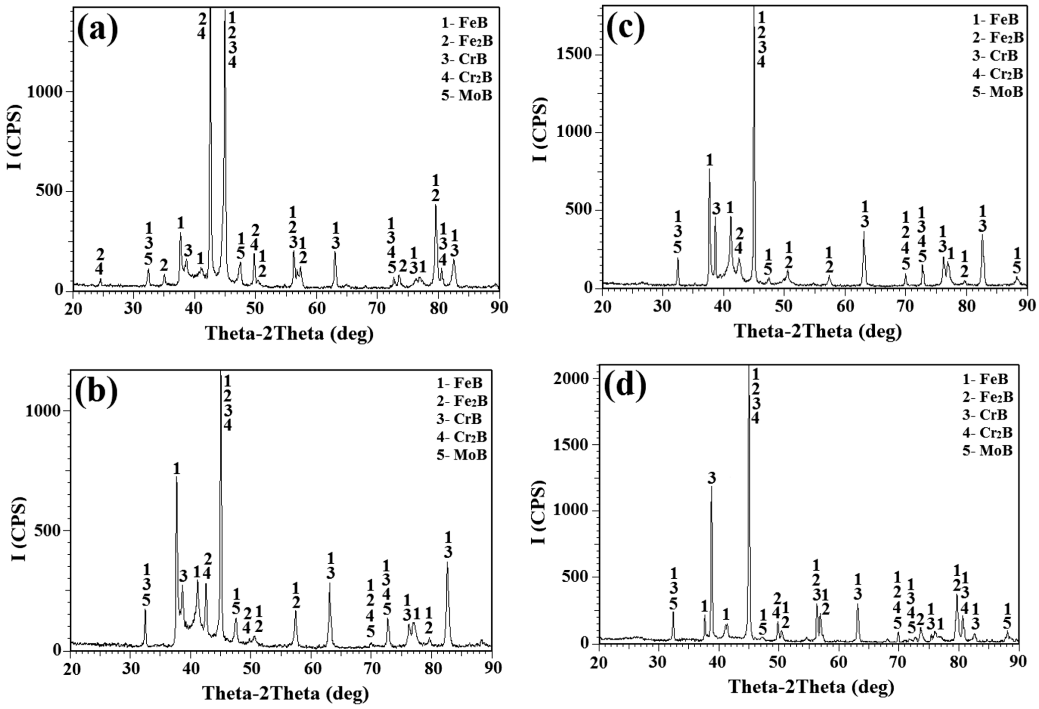

Figure 3: X-ray diffraction patterns of borided AISI H10 steel: a) 1123 K – 2 h, b) 1123 K – 6 h, c) 1223 K – 2 h, d) 1223 K – 6 h
Slika 3: Rentgenogrami boriranega jekla AISI H10: a) 1123 K – 2 h, b) 1123 K – 6 h, c) 1223 K – 2 h, d) 1223 K – 6 h

average value was taken as the hardness. The results of the microhardness measurements carried out on the cross-sections, along the line from the surface to the interior are presented in **Figure 4.** The hardness of the boride layer formed on the AISI H10 steel varied between 1648 $HV_{0.05}$ and 1964 $HV_{0.05}$. On the other hand, the Vickers hardness value for the untreated AISI H10 steel was 306 $HV_{0.05}$. When the hardness of the boride layer is compared with the matrix, the boride-layer hardness is approximately five times larger than that of the matrix.

3.2 Kinetics

In this study, the effects of the processing temperature and boriding time on the growth kinetics of a boride layer were also investigated. The kinetic parameters such as the processing temperature and time must be known for the control of the boriding treatment. **Figure 5** shows the time dependence of the squared value of the boride-layer thickness at increasing temperatures. This evolution followed the parabolic growth law where the diffusion of boron atoms is a thermally activated phenomenon. The growth-rate constant D at each boriding temperature can be easily calculated with Equation (1).

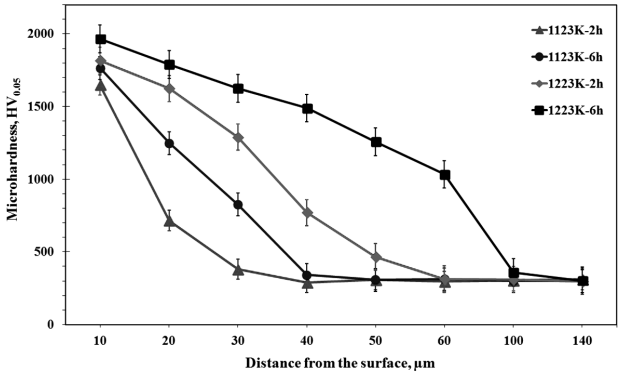

Figure 4: Hardness variation with the depth for the borided AISI H10 steel
Slika 4: Spreminjanje trdote po globini boriranega jekla AISI H10

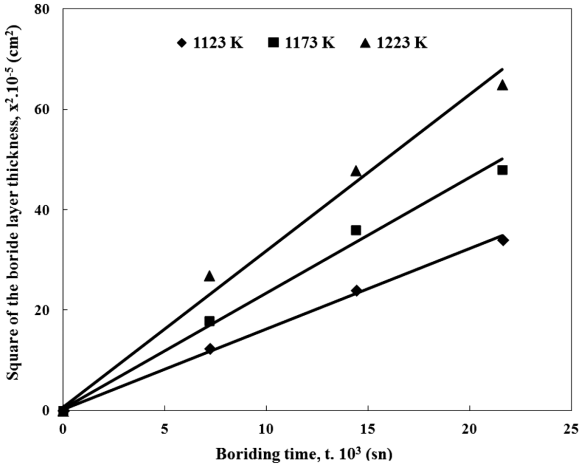

Figure 5: Time dependence of squared boride-layer thickness at increasing temperatures
Slika 5: Časovna odvisnost kvadrata debeline boridne plasti pri naraščajoči temperaturi

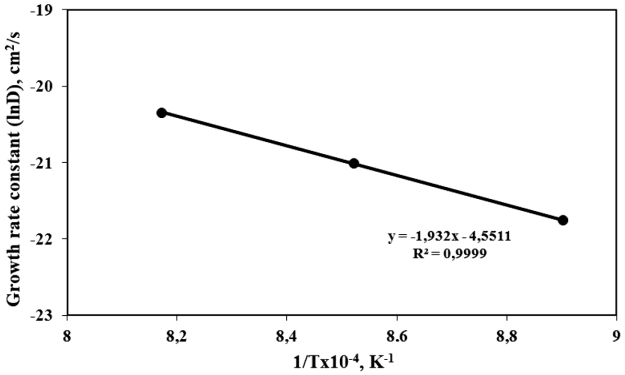

Figure 6: Temperature dependence of the growth-rate constant according to the Arrhenius equation
Slika 6: Temperaturna odvisnost konstante rasti, skladna z Arrheniusovo enačbo

Table 1: Growth-rate constant (*D*) as the function of boriding temperature
Tabela 1: Konstanta hitrosti rasti (*D*) v odvisnosti od temperature boriranja

Material	Growth-rate constant ($cm^2\ s^{-1}$)		
	Temperature		
	1123 K	1173 K	1223 K
AISI H10	5.58×10^{-10}	9.67×10^{-10}	1.18×10^{-9}

As a result, the calculated growth-rate constants at three temperatures, (1123, 1173 and 1223) K, are (5.58×10^{-10}, 9.67×10^{-10}, and 1.18×10^{-9}) $cm^2\ s^{-1}$ for the borided AISI H10 steel. **Table 1** lists the calculated values of the growth constant for each boriding temperature.

Figure 6 describes the temperature dependence of the growth-rate constant. The plot of ln *D* as a function of the reciprocal temperature exhibits a linear relationship according to the Arrhenius equation. The boron activation energy can be easily obtained from the slope of the straight line presented in **Figure 6.** The value of the boron activation energy was then determined as 160.594 kJ/mol for the borided AISI H10 steel.

Table 2 compares the obtained value of energy (160.594 kJ/mol) with the data found in the literature. It is seen that the reported values of the boron activation energy depended on the chemical composition of the substrate and the used boriding method. The calculated value in this study is comparable with the values reported in the literature as seen in **Table 2**.[16–21]

Table 2: Comparison of the activation-energy values for diffusion of boron with respect to different boriding media and substrates
Tabela 2: Primerjava aktivacijske energije za difuzijo bora glede na različne medije in snovi pri boriranju

Steel	Temperature range (K)	Boriding medium	Activation energy (kJ/mol)	References
AISI 8620	973–1073	Plasma paste	99.77	16
AISI W1	1123–1323	Pack	177.8	17
AISI 52100	1123–1223	Pack	269	18
AISI 1035	1073–1273	Salt bath	227.5	19
AISI H13	1073–1223	Powder	186.2	20
AISI H13	1073–1223	Salt bath	244	21
AISI H10	1123–1223	Pack	160.594	Present study

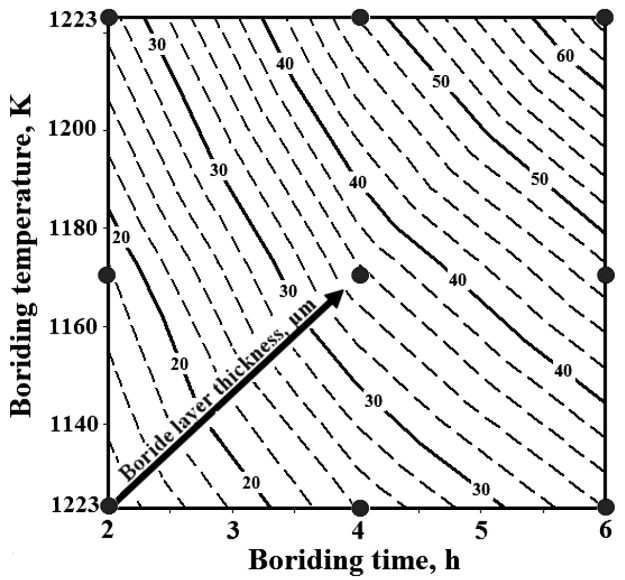

Figure 7: Contour diagram describing the evolution of boride-layer thickness as a function of boriding parameters
Slika 7: Konturni diagram, ki opisuje debelino plasti borida v odvisnosti od parametrov pri boriranju

A contour diagram describing the evolution of the boride-layer thickness as a function of the boriding parameters (the time and the temperature) is shown in **Figure 7**. This contour diagram can be used for two purposes: (1) to predict the coating-layer thickness with respect to the processing parameters, namely, the time and temperature; (2) to determine the value of the processing time and temperature for obtaining a predetermined coating-layer thickness.[22] The boride layer increased with an increase in the boriding time and temperature for the borided AISI H10 steel.

4 CONCLUSIONS

The following conclusions may be derived from the present study.

- The boride types formed on the surface of the hot-work tool steel have columnar structures.
- The boride-layer thickness obtained on the surface of the AISI H10 steel was 12.86–63.72 μm, depending on the chemical compositions of the substrates.
- The multiphase boride coatings that were thermochemically grown on the AISI H10 steel consisted of the FeB, Fe_2B, CrB, Cr_2B and MoB phases.
- The surface hardness of the borided steel was in the range of 1648–1964 $HV_{0.05}$, while for the untreated steel it was 306 $HV_{0.05}$.

- The boron activation energy was estimated to be 160.594 kJ/mol for the borided AISI H10 steel.
- A contour diagram relating the boride-layer thickness to the boriding parameters (the time and the temperature) was proposed. It can be used as a simple tool to select the optimum boride layer for a practical utilization of this kind of material.

5 REFERENCES

[1] A. K. Sinha, Boriding (Boronizing), ASM handbook, vol. 4, ASM International, OH, USA 1991, 437–447

[2] S. Taktak, Tribological behaviour of borided bearing steels at elevated temperatures, Surface and Coatings Technology, 201 (**2006**), 2230–2236, doi:10.1016/j.surfcoat.2006.03.032

[3] I. Gunes, Tribological behavior and characterization of borided cold-work tool steel, Mater. Tehnol., 48 (**2014**) 5, 765–769

[4] C. Bindal, A. H. Ucisik, Characterization of borides formed on impurity-controlled chromium-based low alloy steels, Surface and Coatings Technology, 122 (**1999**) 2–3, 208-213, doi:10.1016/S0257-8972(99)00294-7

[5] M. Erdogan, I. Gunes, A. Dalar, Investigation of Corrosion Behavior of Borided Gear Steels, Transactions of the Indian Institute of Metals, 67 (**2014**) 2, 291–297, doi:10.1007/s12666-013-0329-8

[6] G. Kartal, O. L. Eryilmaz, G. Krumdick, A. Erdemir, S. Timur, Kinetics of Electrochemical Boriding of Low Carbon Steel, Appl. Surf. Sci., 257 (**2011**) 15, 6928–6934, doi:10.1016/j.apsusc.2011.03.034

[7] M. Keddam, M. Kulka, N. Makuch, A. Pertek, L. Maldzinski, A kinetic model for estimating the boron activation energies in the FeB and Fe_2B layers during the gas-boriding of Armco iron: Effect of boride incubation times, Appl. Surf. Sci., 298 (**2014**), 155–163, doi:10.1016/j.apsusc.2014.01.151

[8] I. Gunes, Wear behaviour of plasma paste boronized of AISI 8620 steel with borax and B_2O_3 paste mixtures, Journal of Materials Science and Technology, 29 (**2013**) 7, 662–668, doi:10.1016/j.jmst.2013.04.005

[9] J. H. Yoon, Y. K. Jee, S. Y. Lee, Plasma paste boronizing treatment of the stainless steel AISI 304, Surface and Coatings Technology, 112 (**1999**), 71–75, doi:10.1016/S0257-8972(98)00743-9

[10] O. Ozdemir, M. A. Omar, M. Usta, S. Zeytin, C. Bindal, A. H. Ucisik, An investigation on boriding kinetics of AISI 316 stainless steel, Vacuum, 83 (**2008**), 175–179, doi:10.1016/j.vacuum.2008.03.026

[11] I. Ozbek, C. Bindal, Kinetics of borided AISI M2 high speed steel, Vacuum, 86 (**2011**) 4, 391–397, doi:10.1016/j.vacuum.2011.08.004

[12] I. Gunes, Kinetics of borided gear steels, Sadhana, 38 (**2013**) 3, 527–541, doi:10.1007/s12046-013-0138-0

[13] A. Kilic, G. Kartal, M. Urgen, S. Timur, Effects of electrochemical boriding process parameters on the formation of titanium borides, Surface Engineering and Applied Electrochemistry, 49 (**2013**) 2, 168–175, doi:10.3103/S1068375513020051

[14] C. Li, B. Shen, G. Li, C. Yang, Effect of boronizing temperature and time on microstructure and abrasion wear resistance of Cr12Mn2V2 high chromium cast iron, Surface and Coatings Technology, 202 (**2008**) 24, 5882–5886, doi:10.1016/j.surfcoat.2008.06.170

[15] M. Erdogan, I. Gunes, Corrosion Behavior and Microstructure of Borided Tool Steel, Revista Matéria, 20 (**2015**) 2, 523–529, doi:10.1590/S1517-707620150002.0052

[16] I. Gunes, S. Ulker, S. Taktak, Kinetics of plasma paste boronized AISI 8620 steel in borax paste mixtures, Protection of Metals and Physical Chemistry of Surfaces, 49 (**2013**) 5, 567–573, doi:10.1134/S2070205113050122

[17] K. Genel, I. Ozbek, C. Bindal, Kinetics of boriding of AISI W1 steel, Materials Science and Engineering A, 347 (**2003**) 1–2, 311–314, doi:10.1016/S0921-5093(02)00607-X

[18] Y. Kayali, I. Gunes, S. Ulu, Diffusion kinetics of borided AISI 52100 and AISI 440C steels, Vacuum, 86 (**2012**) 10, 1428–1434, doi:10.1016/j.vacuum.2012.03.030

[19] A. Kaouka, O. Allaoui, M. Keddam, Growth kinetics of the boride layers formed on SAE 1035 steel, Materiaux et Techniques, 101 (**2013**) 7, 705–713, doi:10.1051/mattech/2014003

[20] K. Genel, Boriding kinetics of H13 steel, Vacuum, 80 (**2006**) 5, 451–457, doi:10.1016/j.vacuum.2005.07.013

[21] S. Taktak, A study on the diffusion kinetics of borides on boronized Cr-based steels, Journal of Materials Science, 41 (**2006**) 22, 7590–7596, doi:10.1007/s10853-006-0847-4

[22] O. Kahvecioglu, V. Sista, O. L. Eryilmaz, A. Erdemir, S. Timur, Ultra-fast boriding of nickel aluminide, Thin Solid Films, 520 (**2011**) 5, 1575–1581, doi:10.1016/j.tsf.2011.08.077

UDK 621.941:519.233.4
Original scientific article/Izvirni znanstveni članek

ISSN 1580-2949
MTAEC9, 49(5)765(2015)

APPLICATION OF THE TAGUCHI METHOD TO OPTIMIZE THE CUTTING CONDITIONS IN HARD TURNING OF A RING BORE

UPORABA TAGUCHI-JEVE METODE ZA OPTIMIZACIJO TRDEGA STRUŽENJA ROBA IZVRTINE

Mehmet Boy[1], Ibrahim Ciftci[2], Mustafa Gunay[3], Feridun Ozhan[4]

[1]Karabuk Vocational College, Karabuk University, Karabuk, Turkey
[2]Department of Manufacturing Engineering, Karabuk University, Karabuk, Turkey
[3]Department of Mechanical Engineering, Karabuk University, Karabuk, Turkey
[4]ORS Bearing, Ankara, Turkey
mboy@karabuk.edu.tr

Prejem rokopisa – received: 2014-09-29; sprejem za objavo – accepted for publication: 2014-11-28

doi:10.17222/mit.2014.246

This paper is focused on optimizing the cutting conditions for the surface roughness, inner-diameter error and roundness obtained in hard turning of an inner ring bore. The hard-turning experiments were conducted on hardened and tempered AISI 52100 bearing rings using the L9 orthogonal array on a CNC lathe. The cutting speed, feed rate and number of the machined part were selected as control factors. The optimum cutting conditions were determined using the signal-to-noise (*S/N*) ratio. *S/N* ratios were calculated using the lower-the-better approach. An analysis of variance (ANOVA) was also employed to determine the level of the effect of the control factors for the surface roughness, inner-diameter error and roundness. The statistical analysis showed that the feed rate was the most significant factor for the surface roughness while the cutting speed was the most significant factor for the roundness and inner-diameter error. Finally, the optimum cutting conditions were further confirmed with confirmation tests.

Keywords: diameter error, hard turning, roundness, surface roughness, Taguchi method

Članek je osredinjen na optimiranje razmer pri rezanju glede na hrapavost površine, napake notranjega premera in okroglosti pri trdem struženju notranjega roba izvrtine. Preizkusi trdega struženja so bili izvršeni pri kaljenem in popuščenem AISI 52100 obroču ležaja z uporabo L9 ortogonalne matrike na CNC-stružnici. Hitrost rezanja, hitrost podajanja in število obdelanih kosov so bili izbrani kot kontrolni faktorji. Optimalne razmere rezanja so bile izbrane z uporabo razmerja signal-hrup (*S/N*). *S/N*-razmerja so bila izračunana s približkom čim manj tem boljše. Analiza variance (ANOVA) je bila tudi uporabljena za določitev vpliva kontrolnih faktorjev na hrapavost površine, napak notranjega premera in okroglosti. Končno so bili optimalni parametri potrjeni s potrditvenimi preizkusi.

Ključne besede: napaka premera, trdo struženje, okroglost, hrapavost površine, Taguchi-jeva metoda

1 INTRODUCTION

Bearings are the most important components of rotating mechanical systems. The highly precise surface finish, material properties, cleanliness, dimensions and tolerances of today's bearings contribute significantly to the product performance. Traditionally, bearing rings are manufactured from the soft AISI 52100 steel through forging, cold ring rolling and machining processes to their near-net shapes. Then, they are hardened and tempered to obtain the required hardness. The final geometry and surface quality are achieved through grinding and super-finishing processes. The hard-turning process has been increasingly used as an alternative to grinding operations. The hard-turning process has the capacity of machining the hardened components such as roller bearings, gears, shafts, cams, axles requiring a low surface roughness and close dimensional and form tolerances. Hard turning, compared to grinding operations, has many advantages such as a high material-removal rate, lower production costs, a shorter cycle time, an improved overall product quality, and a lower environmental impact. However, in the area of precision hard turning, due to the demands for a geometric accuracy of a few micrometers, its application is limited by the uncertainties with respect to the part quality and process reliability.[1–4]

For a turned part, the diameter error, the surface roughness and the roundness are the three most important quality characteristics.There are many causes for dimensional and geometric accuracy errors in hard turning. The roundness error is considered to be one of the important geometrical errors of cylindrical components because it has a negative effect on the accuracy and other important factors such as the mating mechanical components and wear of rotating elements.[5,6]

The machine-tool rigidity and clamping system influence the form accuracy and dimensional tolerance in precision hard turning. Possible machining errors may be caused due to different types of clamping, the number of clamping jaws, clamping forces, the hydraulic pressure of a clamping system, the clamping rigidity and accuracy. The effects of clamping techniques on the deformations of thin-walled rings have been investigated by many researchers.[7–13]

Geometric errors mostly result from the inaccuracy of tooling parts, such as inserts, tool holders and clamping devices.[12] An investigation suggested that after replacing an insert, the repeatability errors at the tip of the insert can reach up to several microns, and the displacement of a tool tip under a cutting load can also reach several microns. Precision hard turning requires highly precise machine tools to eliminate the form and dimensional errors induced by the moving components of a machine tool such as the spindle, the slide bed and the tail stock.[7–13]

The surface roughness is one of the most important requirements in a machining process, as it is considered to be an indicator of the product quality. It indicates the irregularities of a surface texture. Achieving a desired surface quality is critical for the functional behavior of a part. The surface roughness influences the performance of mechanical parts and their production costs because it affects the factors such as friction, ease of holding the lubricant, electrical and thermal conductivities. A relatively better surface finish may involve a higher cost of manufacturing. The surface roughness and the roundness error are affected by several factors including the cutting-tool geometry, the cutting speed, the feed rate, the microstructure of a workpiece and the rigidity of a machine tool.[14,15]

In recent years, much work has been performed using various statistical and experimental techniques. These studies were mostly based on the design and analysis of experimental methods to determine the effects of the cutting parameters on the diameter error, the roundness and the surface roughness of cylindrical parts. Islam[5] investigated the effects of the cooling method, the blank size and the work material on the dimensional accuracy and surface finish of various turning parts using the traditional analysis, Pareto ANOVA and the Taguchi method. The results showed that the work material had the greatest effect on the diameter error and surface roughness, while the major contributor to the circularity was the blank size. Rafai and Islam[6] experimentally and analytically investigated the effects of the cutting parameters on the dimensional accuracy and surface finish in dry turning. The Taguchi method and the Pareto ANOVA analysis were used to determine the effects of the major controllable machining parameters and, subsequently, to find their optimum combination. They reported that while the surface roughness could be optimized through a proper selection of the feed rate, optimization of the diameter error and circularity was difficult due to the complex interactions between the input parameters. Brinksmeier et al.[8] analyzed the basic mechanisms causing a ring distortion in soft machining in order to derive the strategies for its minimization. They concluded that distortion was significantly influenced by the turning before the heat treatment in the manufacture of bearing rings and that the elastic ring deformation under the clamping force led to variations in the depth of cut and polygonal form. Brinksmeier and Sölter[10] developed a new method to predict the shape deviation of machined workpieces with a complex geometry. This new method combined the experimental results for the machining workpieces with simple geometries using finite-element simulations. This was achieved by making use of the known source stresses in simple parts for which the approach was validated. Finally, the method was applied to predict the shape deviation of a ground linear rail guide. Zhou et al.[12] analyzed the possible error-driver factors and error sources in the precision hard turning and a strategy was proposed for an on-line compensation of dimensional errors, based on the tool-wear monitoring and a thermal-expansion prediction. They found that within a certain range of flank wear, the developed method could significantly improve the geometric accuracy. Sölter et al.[13] analyzed the strategies for reducing the roundness deviations of turned rings using a three-jaw chuck. The simulations and measurements agreed reasonably well and showed that the minimum out-of-roundness strongly depends on the interaction of the angular shift between the external and internal clamping with the deviation between the segment-jaw diameter and the inner-ring diameter.

The purpose of this study was to obtain the optimum cutting conditions (the cutting speed, the feed rate, the number of the machined part) for minimizing the surface roughness, diameter error and roundness when hard turning an inner-bearing ring bore. An L9 orthogonal array was used in the design of the experiment. The Taguchi method and an analysis of variance (ANOVA) were also used to achieve this purpose. Furthermore, ANOVA was used to determine the statistical significance of the cutting conditions. In addition, the optimum cutting conditions were aimed to be further confirmed by confirmation tests.

2 MATERIAL AND METHOD

2.1 Material

The hard turning tests were performed on the inner bearing ring bores of AISI 52100 steel, the composition of which is given in **Table 1**. The geometry of the inner-bearing ring is given in **Figure 1**. The rings were manufactured from soft AISI 52100 through forging, spheroidising, cold ring rolling, soft machining, hardening and, finally, tempering processes to their near-net shapes. The rings were hardened and tempered to 58–62 HRc.

Table 1: Chemical composition of AISI 52100 steel (*w*/%)
Tabela 1: Kemijska sestava jekla AISI 52100 (*w*/%)

C	Si	Mn	P	Ni	Cr	Mo	Cu	Al	Fe
0.99	0.24	0.36	0.016	0.06	1.43	0.02	0.10	0.017	Balance

2.2 Cutting inserts and the tool holder

The cutting tools used were commercial-grade TiN-coated low-content CBN inserts with the geometry of DCGW 11T304 produced by Sandvik Coromant.

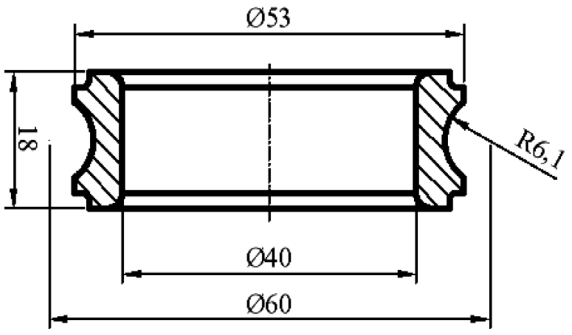

Figure 1: Geometry of the inner ring used for hard-turning tests
Slika 1: Geometrija notranjega obroča, uporabljenega pri preizkusih trdega struženja

These inserts were recommended for machining hardened steel by Sandvik and had the 7015 Sandvik designation. The inserts were rigidly mounted on a right-hand-style tool holder designated by ISO as A25T SDUCR 11 for hard turning inner ring bores.

2.3 Cutting conditions and measurements

The hard-turning tests were carried out on a twin-spindle CNC chucker equipped with a pair of highly precise collet chucks. Three cutting speeds (120, 140 and 160) m/min and three feed rates (0.04, 0.06 and 0.08) mm/r with a fixed depth of cut of 50 μm were tested. At each condition, a total of 12 rings were hard turned. Surface-roughness and roundness measurements were carried out on the hard-turned bore surfaces using a Taylor Hobson precision instrument. The inner diameter of an inner ring bore was measured with Diatest UD-1. The surface-roughness, roundness and diameter-error measurements were carried out on the 4th, 8th and 12th hard-turned rings and the readings were averaged.

2.4 Design and analysis of the experiments

Optimization of machining processes is essential for achieving a high responsiveness to production, which provides a preliminary basis for the survival in today's dynamic market conditions. The Taguchi method is widely used in engineering analyses and it is a powerful design tool. This method dramatically reduces the number of tests using orthogonal arrays and minimizes the effects of the factors that cannot be controlled. Furthermore, it provides a simple, efficient and systematic approach to specifying the optimum cutting parameters for a manufacturing process.[16,17]

The Taguchi method converts objective function values to the signal-to-noise (*S/N*) ratio to measure the performance characteristics at the levels of the control factors against these factors. The *S/N* ratio is defined as the desired signal ratio for an undesired random-noise value and shows the quality characteristics of the experimental data.[16,17] Usually, there are three categories of the performance characteristic in an analysis of the *S/N* ratio, i.e., the lower-the-better, the higher-the-better and the nominal-the-better characteristics. The goal of this study was to minimize the surface roughness, the inner-diameter error and the roundness. Therefore, the lower-the-better quality characteristic was used as shown in Equation (1):

$$\frac{S}{N(\eta)} = -10 \cdot lg\left[\frac{1}{n} \cdot \sum_{i=1}^{0} Y_i^2\right] \quad (1)$$

where Y_i is the observed data during the experiment and n is the number of experiments.[16,17]

In this study, the cutting speed (*V*), the feed rate (*f*) and the number of the machined part (*MP*) were selected as the control factors and their levels were determined as shown in **Table 2**. The L9 orthogonal array of the Taguchi method allowed us to determine the optimum cutting conditions and analyze the effects of the machining parameters.

Table 2: Control factors and their levels
Tabela 2: Kontrolni faktorji in njihovi nivoji

Control factors	Level 1	Level 2	Level 3
Cutting speed, *V*/(m/min)	100	120	140
Feed rate, *f*/(mm/r)	0.04	0.06	0.08
Machined part number, *MP*	4	8	12

ANOVA was used to find the relative contribution of the cutting conditions in controlling the response of a turning operation. The optimum combination of the

Table 3: Experimental results and corresponding *S/N* ratios
Tabela 3: Rezultati preizkusov in odgovarjajoča razmerja *S/N*

Run	Control factors			Experimental results			Signal-to-noise ratio (*S/N*)		
	V	*f*	*MP*	*IDe*	R_a	*R*	*R*	R_a	*IDe*
1	120	0.04	4	0.016	0.164	3.33	–10.448	15.703	35.917
2	120	0.06	8	0.012	0.293	3.04	–9.657	10.662	38.416
3	120	0.08	12	0.011	0.459	3.21	–10.130	6.763	39.172
4	140	0.04	12	0.010	0.176	2.63	–8.389	15.089	40.000
5	140	0.06	4	0.008	0.178	3.02	–9.600	14.991	41.938
6	140	0.08	8	0.005	0.363	2.35	–7.421	8.801	46.020
7	160	0.04	8	0.010	0.271	4.23	–12.526	11.340	40.000
8	160	0.06	12	0.013	0.342	4.6	-13.255	9.319	37.721
9	160	0.08	4	0.007	0.363	4.51	-13.083	8.801	43.098

control factors for the surface roughness, diameter error and roundness was determined with the ANOVA table and *S/N* ratios. Lastly, confirmation tests were done using the optimum cutting conditions found with the Taguchi optimization method and thereby the validity of the optimization was tested.

3 RESULTS AND DISCUSSION

The surface roughness, the inner-diameter error and the roundness achieved during the hard turning of inner-bearing rings were measured after the experiments performed according to the L9 orthogonal array. The lowest values of the surface roughness, the inner-diameter error and the roundness significantly improve the quality of the bearing assembly. For this reason, the lower-the-better quality characteristic was used for the calculation of the *S/N* ratio. The experimental results and *S/N* ratios are given in **Table 3**.

3.1 Evaluation of the surface roughness for an inner ring bore

The interaction plots for the surface-roughness parameters are given in **Figure 2**. The minimum value of the surface roughness (R_a) was obtained for V = 120 m/min, f = 0.04 mm/r and the 4th machined part. It can be seen from **Figure 2** that the R_a value increases as the feed rate is increased from 0.04 mm/r to 0.08 mm/r when hard turning the inner-bearing ring bores. With the raise in the feed-rate value from 0.04 mm/r to 0.08 mm/r, a significant increase is observed in the R_a value. No significant relation between the surface roughness and the number of the machined ring bore is seen.

The *S/N* ratios of the R_a data obtained from the experimental results, used to determine the optimum level of each variable, were calculated according to Equation (1). **Figure 3** illustrates the plots of the *S/N* ratios that were calculated for R_a in the hard turning of the inner ring bores. The *S/N* ratios of the factors for each level are shown in **Table 4**. Different values (Δ) of the *S/N* ratio between the maximum and the minimum

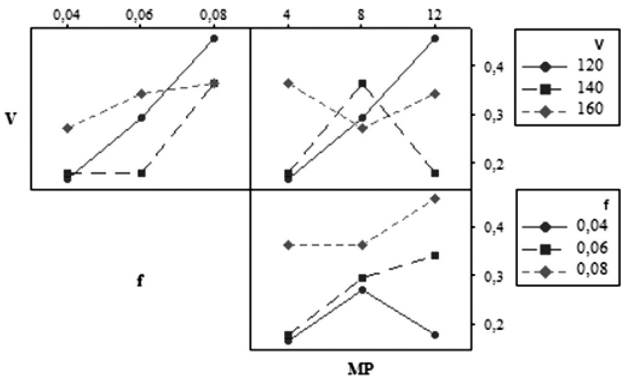

Figure 2: Interaction plots for surface roughness
Slika 2: Interakcijski diagrami za hrapavost površine

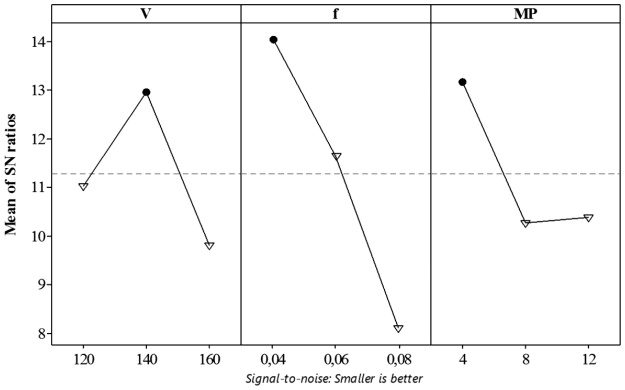

Figure 3: Main-effect plot for surface roughness
Slika 3: Diagram glavnega učinka na hrapavost površine

are also shown in **Table 4**. Therefore, by considering the *S/N* ratios in **Table 4** and **Figure 3**, the optimum cutting conditions for the surface roughness were $V2$ (V = 140 m/min), $f1$ (f = 0.04 mm/r) and $MP1$ (the 4th machined part). The smallest surface roughness and its *S/N* ratio that can be obtained with these levels were calculated using Equations (2) and (3). The R_a value and its *S/N* ratio were determined as 0.131 μm and 17.621 dB, respectively:

$$\eta_G = \overline{\eta}_G + (\overline{V}_0 - \overline{\eta}_G) + (\overline{f}_0 - \overline{\eta}_G) + (\overline{MP}_0 - \overline{\eta}_G) \quad (2)$$

$$R_{a_{cal}} = 10^{-\frac{\eta_G}{20}} \quad (3)$$

In these equations, η_G is the *S/N* ratio calculated at the optimum levels (dB), $\overline{\eta}_G$ is the average *S/N* ratio of all the variables (dB), $\overline{V}_0$, $\overline{f}_0$, $\overline{MP}_0$ are the mean *S/N* ratios when factors *V*, *f* and *MP* are at the optimum levels (dB), and $R_{a\ cal}$ is the calculated surface-roughness (R_a) value.

Table 4: Response table of *S/N* ratios for surface roughness
Tabela 4: Tabela odzivov razmerja *S/N* glede na hrapavost površine

Factor	*S/N* ratio				Rank
	Level 1	Level 2	Level 3	Δ	
V	11.043	12.961	9.821	3.14	2
f	14.044	11.658	8.122	5.922	1
MP	13.166	10.268	10.391	2.897	3

The analysis of variance (ANOVA) was used to find which design parameters significantly affect the surface roughness. This analysis was carried out at the 95 % confidence level. The ANOVA results for the surface roughness (R_a) are shown in **Table 5**. This table also shows the degree of freedom (*DF*), the sum of squares (*SS*), the mean square (*MS*), the *F*-values (*F*), the probability (*P*) and the percentage-contribution ratio (*PCR*) of each factor. A low *P*-value of 0.05 shows a statistically significant level of the source for the corresponding response. The *F*-ratios and their *PCR* were taken into consideration to identify the significance levels of the variables. **Table 5** indicates that the most effective variable for the R_a

value is the feed rate with the *PCR* of 62.84 %. It is well known that the theoretical geometrical-surface roughness is primarily a function of the feed for a given nose radius and that it changes with the square of the feed-rate value. It is once again shown that the feed rate has an important effect on the surface roughness in hard turning.The other variables having an effect on R_a are the number of the machined part with a *PCR* of 19.00 % and the cutting speed with a *PCR* of 17.74%.

Table 5: ANOVA for *S/N* ratios for surface roughness
Tabela 5: ANOVA za *S/N*-razmerje glede na hrapavost površine

Source	*DF*	*SS*	*MS*	*F*	*P*	*PCR*
V	2	15.0351	7.5176	42.42	0.023	17.74
f	2	53.265	26.6325	150.28	0.007	62.84
MP	2	16.1066	8.0533	45.44	0.022	19.00
Error	2	0.3544	0.1772			0.42
Total	8	84.7612				100

3.2 Evaluation of the roundness for an inner ring bore

The interaction plots for the roundness and the cutting conditions are given in **Figure 4**. The minimum value of the roundness was obtained at V = 140 m/min and f = 0.08 mm/r for the 8th machined part. The roundness is generally affected by the cutting parameters such as the cutting speed, the feed rate and the depth of cut. In **Figure 4** the roundness decreases for all the feed rates with the cutting speed increasing from 120 m/min to 140 m/min. This can be attributed to the cutting force decrease with the increasing cutting speed. This decrease is explained with a thermal softening of the machined material in the flow zone due to the increasing cutting temperature. The highest roundness values for all the feed rates were obtained at a cutting speed of 160 m/min. Although a moderate increase in the cutting speed decreases the cutting force, a further increase in the cutting speed was thought to increase the tool wear. This, in turn, increases the roundness. In addition to the cutting parameters, the roundness is also affected by other factors such as the clamping system and the machine-tool rigidity.

The experimental results and the calculated *S/N* ratios for the roundness are given **Table 3**. The *S/N* ratios of the factors for each level are shown in **Table 6**. The values in **Table 6** are given as the plots from **Figure 5**. It is seen from **Figure 5** and **Table 6** that the control factors can be used to reach the smallest roundness in the machining of inner ring bores. The smallest roundness is obtained in the following cutting conditions: *V*2, *f*3 and *MP*2. The optimum cutting conditions for the roundness were *V*2 (V = 140 m/min), *f*3 (f = 0.08 mm/r) and *MP*2 (the 8th machined part). The *S/N* ratios for the roundness of R_{cal} were calculated with Equation (3). Consequently, η_G and R_{cal} calculated for the optimum cutting conditions were found to be –7.5487 dB and 2.38 μm, respectively.

Table 6: Response table of *S/N* ratios for roundness
Tabela 6: Tabela odgovorov *S/N*-razmerje glede na okroglost

Symbol	*S/N* ratio				Rank
	Level 1	Level 2	Level 3	Δ	
V	–10.079	–8.474	–12.955	4.482	1
f	–10.458	–10.838	–10.212	0.626	3
MP	–11.044	–9.869	–10.595	1.176	2

Table 7: ANOVA for *S/N* ratios for roundness
Tabela 7: ANOVA za *S/N*-razmerje glede na okroglost

Source	*DF*	*SS*	*MS*	*F*	*P*	*PCR*
V	2	30.9353	15.4676	110.12	0.009	91.18
f	2	0.5965	0.2982	2.12	0.320	1.76
MP	2	2.1115	1.0558	7.52	0.117	6.23
Error	2	0.2809	0.1405			0.83
Total	8	33.9242				100

The ANOVA results for the inner-ring-bore roundness are given in **Table 7**. The *F*-ratios and their *PCR*s were taken into consideration to identify the significance level of the variables. **Table 7** shows that the most effective variable for the roundness is the cutting speed with a *PCR* of 91.18 %. The contributions of the number of the machined part and the feed rate were found to be 6.23 % and 1.76 %, respectively. Consequently, the feed rate and the number of the machined part do not have significant

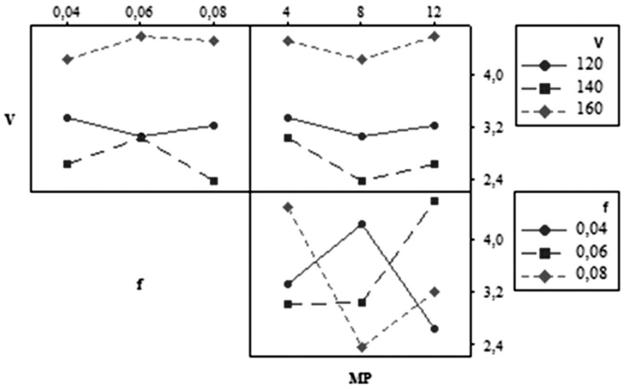

Figure 4: Interaction plots for roundness
Slika 4: Diagrami medsebojnih vplivov na okroglost

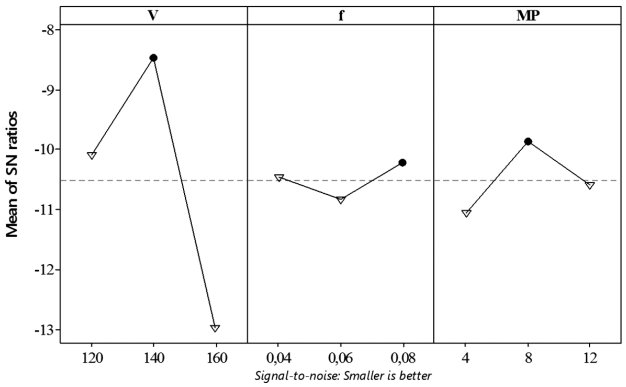

Figure 5: Main-effect plots for roundness
Slika 5: Diagrami glavnih vplivov na okroglost

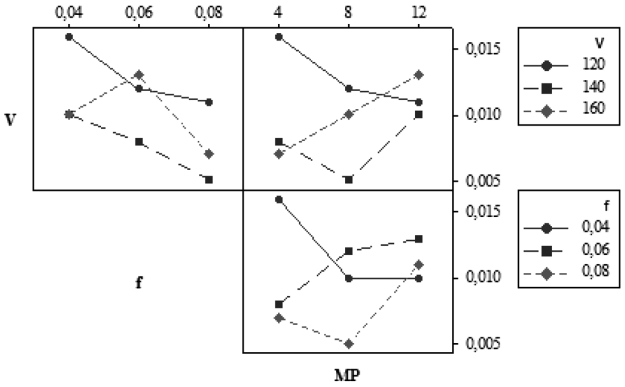

Figure 6: Interaction plots for inner-diameter error
Slika 6: Interakcijski diagrami za napako notranjega premera

effects on the roundness ($P < 0.05$). The error ratio was calculated as 0.83 % and it is the smallest ratio.

3.3 Evaluation of the inner-ring-bore-diameter error

The interaction plots for the inner-diameter error and the cutting conditions are given in **Figure 6**. The minimum value of the inner-diameter error was obtained at V = 140 m/min and f = 0.08 mm/r for the 8th machined part. The cutting speed might have influenced the resulting cutting forces and this interaction might have consequently influenced the diameter error in a number of ways, i.e., by changing the elastic deformation of the workpiece, by altering the tool wear, by increasing the thermal distortion, by forming a built-up edge (BUE) and by increasing the radial-spindle error. In this case, the most likely cause for the change in the diameter error is considered to be the change in the elastic deformation of the workpiece.

The experimental results and the calculated *S/N* ratios for the roundness are given **Table 3**. **Figure 7** shows the plots of the *S/N* ratios that were calculated for the inner-diameter error. The *S/N* ratios of the factors for each level are shown in **Table 8**. Hence, by considering the *S/N* ratios from **Table 8** and **Figure 7**, the optimum cutting conditions for the inner-diameter error were *V*2 (V = 140 m/min), *f*3 (f = 0.08 mm/r) and *MP*2 (the 8th machined part). The *S/N* ratios for the roundness of *IDe* (the inner diameter error) were calculated with Equation (3). Consequently, η_G and IDe_{cal} calculated for the optimum cutting conditions were found to be 46.388 dB and 0.0048 μm, respectively.

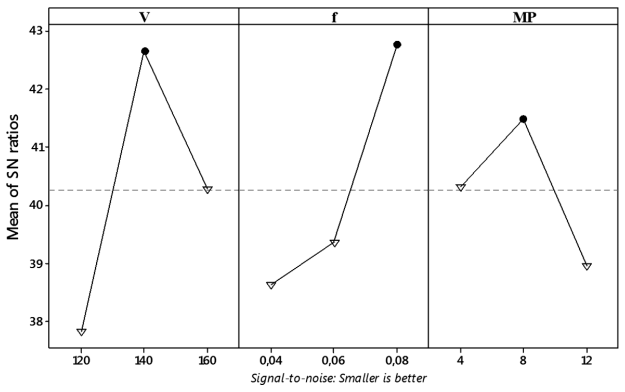

Figure 7: Main-effect plots for inner-diameter error
Slika 7: Diagrami glavnih učinkov na napako notranjega premera

Table 8: Response table of *S/N* ratios for inner-diameter error
Tabela 8: Tabela odgovorov razmerja *S/N* glede na napako notranjega premera

Symbol	Mean *S/N* ratio				Rank
	Level 1	Level 2	Level 3	Δ	
V	37.84	42.65	40.27	4.82	1
f	38.64	39.36	42.76	4.12	2
MP	40.32	41.48	38.96	2.51	3

Table 9: ANOVA for *S/N* ratios for inner-diameter error
Tabela 9: ANOVA za *S/N*-razmerje glede na napako notranjega premera

Source	*DF*	*SS*	*MS*	*F*	*P*	*PCR*
V	2	34.815	17.4075	54.87	0.018	46.99
f	2	29.1223	14.5612	45.9	0.021	39.32
MP	2	9.5031	4.7515	14.98	0.063	12.83
Error	2	0.6344	0.3172			0.86
Total	8	74.0748				100

The ANOVA results for the inner-diameter error are shown in **Table 9**. The *F*-ratios from **Table 9** and their *PCR* were taken into consideration to identify the significance levels of the variables. **Table 9** shows that the most effective variable for the inner-diameter error is the cutting speed with a *PCR* of 46.99 %. The feed rate and the number of the machined part also affect the inner-diameter error with their *PCR* being 39.32 and 12.83 %, respectively. Therefore, the number of the machined part does not have a significant effect on the inner-diameter error ($P < 0.05$). As the *P*-value of the number of the machined part is less than 0.05, it is not significant.

3.4 Confirmation tests

Confirmation tests of the control factors were made for the Taguchi method. The optimization was verified with the confirmation tests after the determination of the control factors that give the optimum results. The confirmation tests were conducted at the optimum factor levels for each surface roughness, roundness and diameter error. The confirmation tests performed at the optimum variable levels determined for the surface roughness, the roundness and the inner-diameter error were evaluated by taking into consideration the confidence interval (*CI*) calculated with Equations (4) and (5)[16,17]:

$$CI = \sqrt{F_{0.05}(1, \upsilon_e) V_e \left(\frac{1}{n_{\text{eff}}} + \frac{1}{r} \right)} \quad (4)$$

$$n_{\text{eff}} = \frac{N}{1 + \upsilon_T} \quad (5)$$

where v_e is the error degree of freedom, V_e is the error variance, n_{eff} is the repeating number of the experiments, N is the total number of the experiments, v_T is the variable's degree of freedom and r is the number of the confirmation tests.

Table 10 gives a comparison of the results of the confirmation tests conducted according to the optimum levels of the variables and the values calculated using Equations (2) and (3). Besides, confidence-interval values for R_a, R and *IDe* were calculated using Equations (4) and (5).

Table 10: Comparison between confirmatory test results and calculated values

Tabela 10: Primerjava med rezultati potrditvenih preizkusov in izračunanimi vrednostmi

Confirmatory experiment results		Calculated values		Differences	
$R_{a\ mea}$/μm	$_{mea}$/dB	$R_{a\ cal}$/μm	η_{cal}/dB	$R_{a\ mea} - R_{a\ cal}$	$\eta_{mea} - \eta_{cal}$
0.151	16.42	0.131	17.621	0.02	1.201
R_{mea}/μm	η_{mea}/dB	R_{cal}/μm	η_{cal}/dB	$R_{mea} - R_{cal}$	$\eta_{mea} - \eta_{cal}$
2.35	–7.4214	2.38	–7.5487	0.03	0.1273
IDe_{mea}/μm	η_{mea}/dB	IDe_{cal}/μm	η_{cal}/dB	$IDe_{mea} - IDe_{cal}$	$\eta_{mea} - \eta_{cal}$
0.005	46.020	0.0048	46.388	0.0002	0.368

Using Equation (5), confidence values of (2.56, 2.28 and 3.42) dB were obtained for the surface roughness (R_a), the roundness (R) and the inner-diameter error (*IDe*), respectively. **Table 10** shows differences between the values obtained with the confirmatory tests and the values of the *S/N* ratios calculated with Equations (2) and (3). It is seen that a difference of 1.201 dB is under the 5 % confidence interval for the surface roughness of 2.56 dB, a difference of 0.1273 dB is under the 5 % confidence interval of for the roundness of 2.28 dB and, similarly, a difference of 0.368 dB is under the 5 % confidence interval for the inner-diameter error of 3.42 dB. Therefore, the optimum-control-factor settings for all the cutting conditions were confirmed as confident.

4 CONCLUSIONS

In this study, the cutting conditions for the surface roughness, the inner-diameter error and the roundness during the hard turning of an inner ring bore were optimized with the Taguchi method. The results obtained from this study are presented below:

According to the results of the statistical analysis, it was found that the feed rate was the most significant factor for the surface roughness with a *PCR* of 62.84 %. The cutting speed was the most significant parameter for the roundness and the inner-diameter error with *PRC* of 91.18 and 46.99 %, respectively.

The optimum levels of the control factors for minimizing the surface roughness, the roundness and the inner-diameter error using *S/N* ratios were determined. The optimum conditions for the surface roughness were observed at *V*2-*f*1-*MP*1 (i.e., cutting speed V = 140 m/min, feed rate f = 0.04 mm/r and the 4th machined part). The optimum conditions for the roundness and the inner-diameter error were observed at the same levels, *V*2-*f*3-*MP*2 (i.e., cutting speed V = 140 m/min, feed rate f = 0.08 mm/r and the 8th machined part).

Confirmation tests were carried out at the optimum conditions. According to the confirmation-test results, the measured values were found to be within the 95 % confidence interval.

The outcomes for the roundness and the inner-diameter errors are very close to the predicted values. Thus, there is no need to carry out confirmation tests if the cutting conditions found with the optimization procedure are included in the cutting conditions within the Taguchi experimental design.

Acknowledgement

The authors would like to thank the Ministry of Science, Industry and Technology, Turkey (00980.STZ. 2011-2) and ORS Bearings, Turkey, for the financial support of this study.

5 REFERENCES

[1] H. K. Tönshoff, C. Arendt, R. B. Amor, Cutting of hardened steel, Annals of the CIRP, 49 (**2000**) 2, 547–566, doi:10.1016/S0007-8506(07)63455-6

[2] G. Byrne, D. Dornfeld, B. Denkena, Advancing cutting technology, Annals of the CIRP, 52 (**2003**) 2, 483–507, doi:10.1016/S0007-c8506(07)60200-5

[3] W. König, A. Berktold, K. F. Koch, Turning versus grinding – a comparison of surface integrity aspects and attainable accuracies, Annals of the CIRP, 42 (**1993**) 1, 39–43, doi:10.1016/S0007-8506(07) 62387-7

[4] F. Klocke, E. Brinksmeier, K. Weinert, Capability profile of hard cutting and grinding processes, Annals of the CIRP, 54 (**2005**) 2, 22–45, doi:10.1016/S0007-8506(07)60018-3

[5] M. N. Islam, Effect of additional factors on dimensional accuracy and surface finish of turned parts, Machining Science and Technology: An International Journal, 17 (**2013**) 1, 145–162, doi:10.1080/ 10910344.2012.747936

[6] N. H. Rafai, M. N. Islam, An investigation into dimensional accuracy and surface finish achievable in dry turning, Machining Science and Technology: An International Journal, 13 (**2009**) 4, 571–589, doi:10.1080/10910340903451456

[7] J. A. Malluck, S. N. Melkote, Modeling of deformation of ring shaped workpieces due to chucking and cutting forces, Journal of Manufacturing Science and Engineering, 126 (**2004**), 141–147, doi:10.1115/1.1643079

[8] E. Brinksmeier, J. Sölter, C. Grote, Distortion engineering – identification of causes for dimensional and form deviations of bearing rings, CIRP Annals – Manufacturing Technology, 56 (**2007**) 1, 109–112, doi:10.1016/j.cirp.2007.05.028

[9] L. Björn, T. Beekhuis, E. Brinksmeier, M. Garbrecht, J. Sölter, Improving the shape quality of bearing rings in soft turning by using a Fast Tool Servo, Prod. Eng. Res. Devel., 3 (**2009**), 469–474, doi:10.1007/s11740-009-0175-z

[10] E. Brinksmeier, J. Sölter, Prediction of shape deviations in machining, CIRP Annals – Manufacturing Technology, 58 (**2009**) 1, 507–510, doi:10.1016/j.cirp.2009.03.123

[11] D. Stöbener, B. Beekhuis, Application of an in situ measuring system for the compensation of wall thickness variations during turning of thin-walled rings, CIRP Annals – Manufacturing Technology, 62 (**2013**) 1, 511–514, doi:10.1016/j.cirp.2013.03.129

[12] J. M. Zhou, M. Andersson, J. E. Stahl, Identification of cutting errors in precision hard turning process, Journal of Materials Processing Technology, 153–154 (**2004**), 746–750, doi:10.1016/j.jmatprotec.2004.04.331

[13] J. Sölter, C. Grote, E. Brinksmeier, Influence of clamping strategies on roundness deviations of turned rings, Machining Science and Technology, 15 (**2011**), 338–355, doi:10.1080/10910344.2011.601207

[14] K. Bouacha, M. A. Yallese, T. Mabrouki, J. F. Rigal, Statistical analysis of surface roughness and cutting forces using response surface methodology in hard turning of AISI 52100 bearing steel with CBN tool, Int. J. Refract. Met. Hard., 28 (**2010**) 3, 349–361, doi:10.1016/j.ijrmhm.2009.11.011

[15] P. G. Benardos, G. C. Vosniakos, Predicting surface roughness in machining: A review, International Journal of Machine Tools & Manufacture, 43 (**2003**) 8, 833–844, doi:10.1016/S0890-6955(03)00059-2

[16] M. Gunay, E. Yucel, Application of Taguchi method for determining optimum surface roughness in turning of high-alloy white cast iron, Measurement, 46 (**2013**), 913–919, doi:10.1016/j.measurement.2012.10.013

[17] E. Yucel, M. Gunay, Modelling and optimization of the cutting conditions in hard turning of high-alloy white cast iron (Ni-Hard), Proc. IMechE, Part C: J. Mechanical Engineering Science, 227 (**2013**) 10, 2280–2290, doi:10.1177/0954406212471755

UDK 539.42:669.24:519.61/.64
Original scientific article/Izvirni znanstveni članek

ISSN 1580-2949
MTAEC9, 49(5)773(2015)

THERMAL FATIGUE OF SINGLE-CRYSTAL SUPERALLOYS: EXPERIMENTS, CRACK-INITIATION AND CRACK-PROPAGATION CRITERIA

TOPLOTNO UTRUJANJE MONOKRISTALNIH SUPERZLITIN: PREIZKUSI, MERILA ZA NASTANEK IN NAPREDOVANJE RAZPOKE

Leonid Getsov[1], Artem Semenov[2], Sergey Semenov[2], Alexander Rybnikov[1], Elena Tikhomirova[3]

[1]NPO CKTI, Saint-Petersburg, Russia
[2]Saint-Petersburg State Polytechnical University, Russia
[3]Klimov Company, Saint-Petersburg, Russia
guetsov@yahoo.com, semenov.artem@googlemail.com

Prejem rokopisa – received: 2014-10-03; sprejem za objavo – accepted for publication: 2014-11-06

doi:10.17222/mit.2014.251

Thermal-fatigue tests were performed on corset samples made from five single-crystal nickel-based superalloys with various crystallographic orientations (⟨001⟩,⟨011⟩,⟨111⟩) at different temperatures and cycle durations. The proposed criteria for the thermal-fatigue crack initiation and crack propagation are discussed and compared with experimental results. The sensitivity of durability to the crystallographic orientation and to thermal-cycle parameters is analyzed experimentally and by means of the corresponding finite-element simulations.

Keywords: nickel-based superalloy, single crystal, thermal fatigue, crack initiation, crack propagation

Preizkusi toplotnega utrujanja so bili izvršeni na vzorcih korzetne oblike. Vzorci so bili izdelani iz petih monokristalnih nikljevih superzlitin z različno kristalografsko orientacijo (⟨001⟩,⟨011⟩,⟨111⟩), preizkusi pa so bili narejeni pri različnih temperaturah trajanja ciklov. Predlagana merila za nastanek razpok in njihovo napredovanje pri toplotnem utrujanju so opisana in primerjana z eksperimentalnimi rezultati. Odvisnost zdržljivosti od kristalografske orientacije in parametrov toplotnih ciklov je eksperimentalno analizirana in ugotovljena z ustrezno simulacijo s končnimi elementi.

Ključne besede: superzlitina na osnovi niklja, monokristal, toplotno utrujanje, nastanek razpok, napredovanje razpoke

1 EXPERIMENTAL DATA

The durability of the single-crystal blades of modern gas turbines is mainly determined by their ability to resist the thermal-cycling stress. In Russia, the testing of the thermal fatigue of corset samples (**Figure 1**) in vacuum conditions, with and without lateral thermal-barrier coatings is widespread. During the test, the shear-band formation, the conditions of crack nucleation and the rate of crack propagation are investigated.

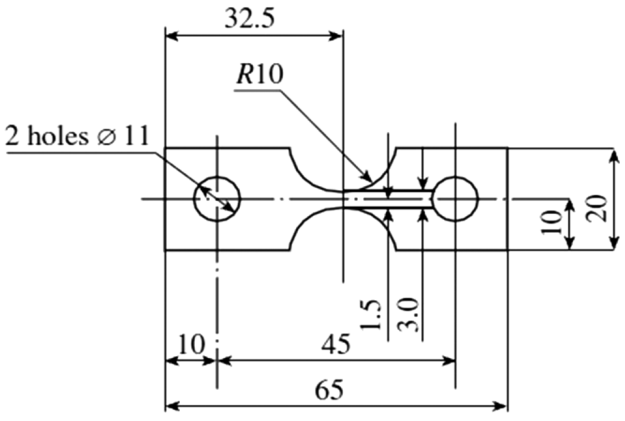

Figure 1: Specimen for thermal-fatigue tests
Slika 1: Vzorec za preizkus toplotnega utrujanja

Experimental studies were performed on five single-crystal alloys (ZhS32, ZhS36 and others) developed by the VIAM research centre, with different alloying and, most importantly, different carbon contents. The chemical compositions of the alloys are given in **Table 1**.

The tests of the thermal-fatigue resistance were carried out for different crystallographic orientations (CGOs) of the specimens, various minimum (T_{min}) and maximum temperatures (T_{max}) of the cycle, with and without a dwell time at T_{max}.[1,2] The test results were characterized with the number of cycles to the macrocrack initiation and to the failure of the samples and the in-plane and out-of-plane residual strains (ε_{in}, ε_{out}) in the central parts of the specimens. The changing of T_{max} and CGO has a significant influence on the thermal-cycling durability (**Table 2**).

The results of a comparative analysis of the thermal-fatigue durabilities of the five considered alloys are given in **Figure 2**, for a thermal cycle of 150⇔900 °C (**Figures 2a** and **2c**) and for a cycle of 500⇔1050 °C (**Figures 2b** and **2d**).

Table 1: Chemical compositions of Ni-based single-crystal alloys (*w*/%)
Tabela 1: Kemijska sestava monokristalnih zlitin na osnovi Ni (*w*/%)

	C	Cr	Co	Mo	W	Ta	Re	Al	Ti	Nb	Re	La	Ru	Ze	Si
Alloy 1	0.12–0.18	4.3–5.6	8.0–10.0	0.8–1.4	7.7–9.5	3.54–5	3.5–4.5	5.6–6.3	–	1.4–1.8	–	–	–	–	–
Alloy 2	0.05	4.5	9.0	1.5	12.0		2.0	5.9	1.0	1.0	2.0	–	–	–	–
Alloy 3	<0.02	2.85	6.20	4.0	3.8	4.5	6.2	6.0	–	–	–	–	3.9		<0.2
Alloy 4	<0.02	4.2	8.3	1.8	5.1	6.1	4.05	6.0	0.8	–	–	–	–	–	<0.2
Alloy 5	<0.02	3.2–3.8	4.6–5.4	4.2–4.8	2.2–2.8	5.7–6.3	0.25–0.55	8.1–8.6	–	–	–	0.01–0.2	–	<0.02	<0.2

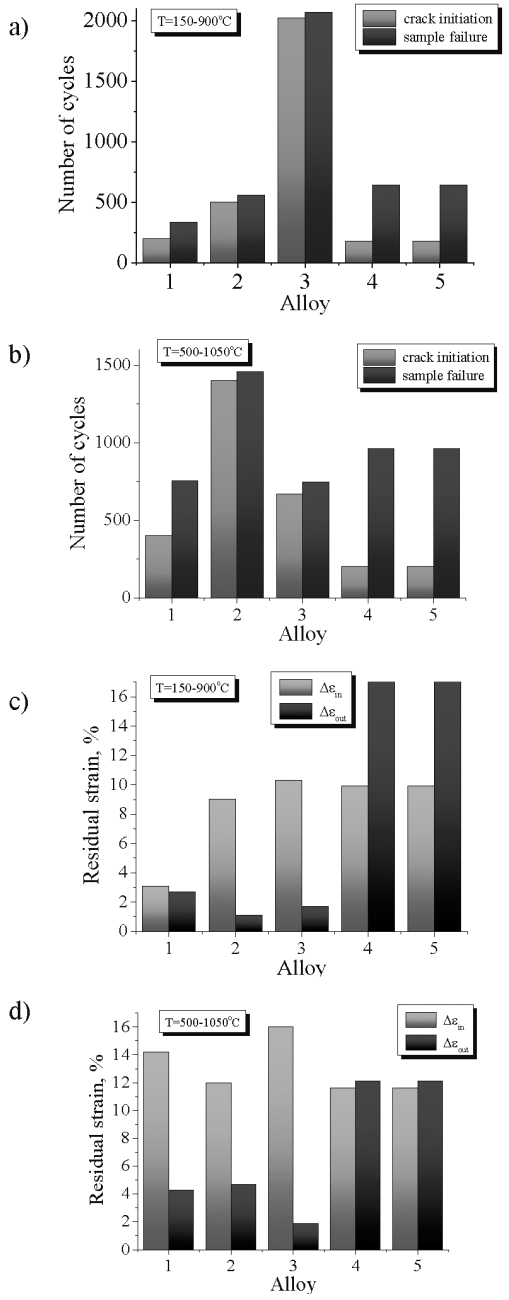

Figure 2: Comparison of thermal-fatigue resistance values for alloys 1–5 (number of cycles (a, b) and transversal residual strains at failure (c, d) for cycles of 150⇔900 °C (a, c) and 500⇔1050 °C (b, d)).
Slika 2: Primerjava odpornosti proti toplotnemu utrujanju zlitin 1–5 (število ciklov (a, b) in prečne preostale napetosti pri porušitvi (c, d) pri ciklih od 150⇔900 °C (a, c) in 500⇔1050 °C (b, d))

Table 2: Effects of cycle temperature and CGO (alloy 2)
Tabela 2: Vpliv temperature cikliranja in CGO (zlitina 2)

Orientation	ΔT/°C	T_{min}/°C	T_{max}/°C	Number of cycles to failure
[001]	750	150	900	951
		200	950	450
		250	1000	63
	500	450	950	2635
		500	1000	1220
		550	1050	356
[011]	750	150	900	560
		250	1000	95

Table 3: Effects of dwell time at T_{max} and of aging on the thermal-fatigue resistance for alloy 3 at thermal cycle of 500⇔1050 °C
Tabela 3: Vpliv zdržljivosti pri T_{max} in staranja na odpornost proti toplotnemu utrujanju zlitine 3 pri toplotnem cikliranju 500⇔1050 °C

Condition and test mode	Number of cycles to macrocrack	Number of cycles to failure	ε_{in}/%	ε_{out}/%
Without a dwell time at T_{max}	670	746	16	–1
Dwell time of 2 min at T_{max}	27	91	12	17
Aging at 850 °C, 500 h	85	242	13	4

ε_{in}, ε_{out} – residual strains in 2 directions transversal to the sample axis

The obtained results indicate a relatively weak influence of the chemical composition of the single-crystal alloys on the thermal-fatigue durability (the differences are less than 2–5 times). On the other hand, the long-term strengths and creep-resistance values of the single-crystal alloys with different compositions differ quite significantly.[3] None of the alloys among 1–5 demonstrates the maximum durability throughout the whole thermal-cycling-parameter range.

A significant decrease in the durability is observed after the dwell time at the maximum temperature of the cycle (**Table 3**). The preliminary aging at 850 °C also leads to a considerable decrease in the durability and residual strains.

2 CRITERION FOR THE TMF-CRACK INITIATION

The prediction of the thermo-mechanical-fatigue (TMF) failures of the single-crystal materials is per-

formed on the basis of the deformation criterion.[4–6] The macrocrack-initiation criterion is the condition for achieving the critical value of the total damage initiated by different mechanisms:

$$D_1(\Delta\varepsilon^{\mathrm{p}}_{\mathrm{eq}})+D_2(\Delta\varepsilon^{\mathrm{c}}_{\mathrm{eq}})+D_3(\varepsilon^{\mathrm{p}}_{\mathrm{eq}})+D_4(\varepsilon^{\mathrm{c}}_{\mathrm{eq}})=1 \quad (1)$$

Criterion (1) is based on the linear damage summation of the cyclic plastic strain:

$$D_1=\sum_{i=1}^{n}\frac{(\Delta\varepsilon^{\mathrm{p}}_{\mathrm{eq}_i})^{\mathrm{k}}}{\mathrm{C}_1(T_i)} \quad (2)$$

cyclic creep strain:

$$D_2=\sum_{i=1}^{n}\frac{(\Delta\varepsilon^{\mathrm{c}}_{\mathrm{eq}_i})^{\mathrm{m}}}{\mathrm{C}_2(T_i)} \quad (3)$$

one-sided accumulated plastic strain:

$$D_3=\max_{0\le t\le t_{\max}}\frac{\varepsilon^{\mathrm{p}}_{\mathrm{eq}}}{\varepsilon^{\mathrm{p}}_{\mathrm{r}}(T)} \quad (4)$$

and one-sided accumulated creep strain:

$$D_4=\max_{0\le t\le t_{\max}}\frac{\varepsilon^{\mathrm{c}}_{\mathrm{eq}}}{\varepsilon^{\mathrm{c}}_{\mathrm{r}}(T)} \quad (5)$$

where C_1, C_2, k, m, $\varepsilon^{\mathrm{p}}_{\mathrm{r}}$, $\varepsilon^{\mathrm{c}}_{\mathrm{r}}$ are the material parameters, depending on the temperature and crystallographic orientation. Usually the material parameters $k = 2$, $m = 5/4$, $C_1 = (\varepsilon_{\mathrm{r}}^{\mathrm{p}})^{\mathrm{k}}$, $C_2 = (3/4\varepsilon_{\mathrm{r}}^{\mathrm{c}})^{\mathrm{m}}$ are used.[4]

Different norms of the strain tensor are considered as the equivalent strains for (1)–(5), including the maximum shear strain in the slip system with normal $\mathbf{n}_{\{111\}}$ to the slip plane and slip direction $\mathbf{l}_{\langle 011\rangle}$:

$$\varepsilon_{\mathrm{eq}}=\mathbf{n}_{\{111\}}\cdot\boldsymbol{\varepsilon}\cdot\mathbf{l}_{\langle 011\rangle} \quad (6)$$

the maximum principal strain (the maximum eigenvalue of the strain tensor):

$$\varepsilon_{\mathrm{eq}}=\varepsilon_1=\max\arg\{\det(\boldsymbol{\varepsilon}-\lambda\mathbf{I})=0\} \quad (7)$$

the von Mises strain intensity:

$$\varepsilon_{\mathrm{eq}}=\sqrt{\frac{2}{9}\left[(\varepsilon_x-\varepsilon_y)^2+(\varepsilon_y-\varepsilon_z)^2+(\varepsilon_z-\varepsilon_x)^2\right]+\frac{1}{3}(\gamma_{xy}^2+\gamma_{yz}^2+\gamma_{zx}^2)} \quad (8)$$

the Hill strain intensity:

$$\varepsilon_{\mathrm{eq}}=\sqrt{\frac{2}{9}\left[(\varepsilon_x-\varepsilon_y)^2+(\varepsilon_y-\varepsilon_z)^2+(\varepsilon_z-\varepsilon_x)^2\right]+\frac{1}{K^*}(\gamma_{xy}^2+\gamma_{yz}^2+\gamma_{zx}^2)} \quad (9)$$

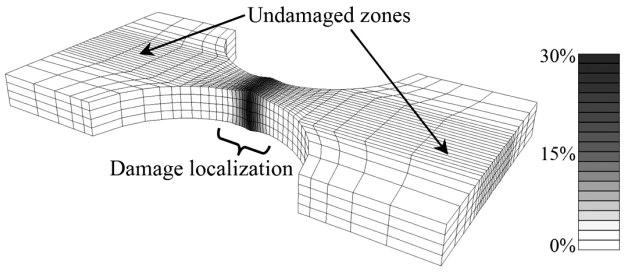

Figure 3: Damage-field distribution after the 10th cycle for sample 43 from alloy 3 with near to ⟨001⟩ orientation

Slika 3: Razporeditev polja poškodbe po 10. ciklu za vzorec 43 iz zlitine 3 z orientacijo blizu ⟨001⟩

and the maximum shear strain:

$$\varepsilon_{\mathrm{eq}}=\frac{1}{2}(\varepsilon_1-\varepsilon_3) \quad (10)$$

Equivalent strains (6) and (9) correspond to the crystallographic failure mode, while equivalent strains (7), (8) and (10) correspond to the non-crystallographic failure mode. In (9):

$$K^*=9\left[4\left(\frac{\varepsilon_{r\langle 001\rangle}}{\varepsilon_{r\langle 011\rangle}}\right)^2-1\right]^{-1}$$

3 RESULTS OF THE FINITE-ELEMENT SIMULATION

In order to verify criterion (1) a stress-strain analysis of the single-crystal corset samples (**Figure 1**) was carried out using the finite-element (FE) program PANTOCRATOR[7] with an application of physical models of elastoplasticity. These material models take into account the fact that inelastic deformation occurs in accordance with the crystal slip system due to a slip mechanism and, therefore, the deformation is strongly sensitive to the crystallographic orientation. The elasto-plastic and visco-elasto-plastic material models[8,9] with nonlinear kinematic and isotropic hardening, also including the self-hardening of each system and the latent hardening[10] between the slip systems, are used in the FE simulations. The application of the visco-elastic models leads to unrealistically overestimated levels of the stress.

The obtained results for the inhomogeneous stress, strain and damage fields allowed us to find the location of the crack initiation. The damage field is determined with criterion (1) on the basis of an analysis of the strain-field evolution using the experimental data on creep- and elastoplastic-deformation curves. The typical damage field distribution after the 10th cycle (20 °C→$T_{\max}$ = 900 °C⇔$T_{\min}$ = 150 °C) is presented in **Figure 3** for the sample from alloy 3 with the orientation near to ⟨001⟩. The best prediction (in comparison with

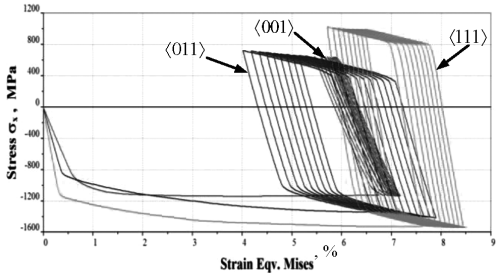

Figure 4: Influence of the crystal orientation on the cyclic stress-strain curve. Results of finite-element simulations of thermal cycles with $T_{\min}$ = 150 °C and $T_{\max}$ = 900 °C (the central point of a specimen).

Slika 4: Vpliv orientacije kristala na ciklično krivuljo napetost – raztezek. Rezultati simulacije s končnimi elementi za toplotne cikle s $T_{\min}$ = 150 °C in $T_{\max}$ = 900 °C (sredina vzorca).

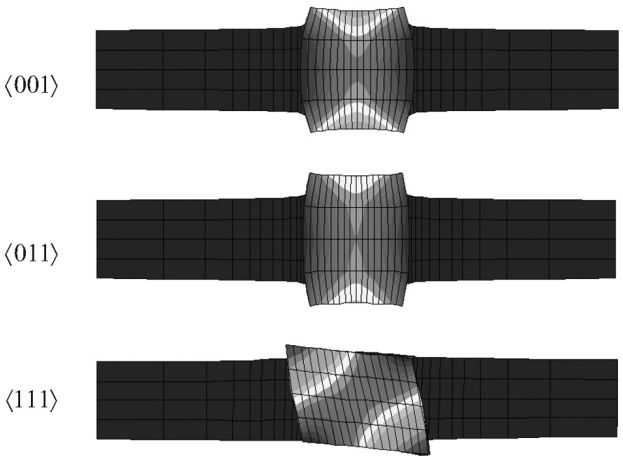

Figure 5: Comparison of deformed states (for clarity increased 10 times) of the central sections of the specimens with orientations ⟨001⟩, ⟨011⟩ and ⟨111⟩ for the cooling phase (T = 150 °C) after the 10th cycle. Colors show the damage-field distribution.

Slika 5: Primerjava deformacijskih stanj (za boljšo prepoznavnost povečano 10-krat) v srednjem prerezu vzorcev z orientacijo ⟨001⟩, ⟨011⟩ in ⟨111⟩ pri fazi ohlajanja (T = 150 °C) po 10. ciklu. Barve prikazujejo področje razporeditve poškodbe.

the experiment) of the number of cycles for the crack initiation is given for strain measure (6) in this loading case.

The results of the FE simulations show that the crystallographic orientation has a significant influence on the stress-strain state of the samples (**Figures 4** and **5**) which was also confirmed with the experiments.[10]

The results of the verification of criterion (1) for alloys 2 and 3 are given in **Figure 6**. The computed number of the cycles to crack initiation demonstrates a satisfactory accuracy.

The thermal-fatigue failure process for the corset specimens shows the presence of two distinct modes (crystallographic and non-crystallographic) of the failure. Their occurrence depends on the CGO and on temperatures T_{min} and T_{max} of the cycle. The experimental results and the Arrhenius approximation of the boundary between the failure modes are given in **Figure 7**. The difference in the failure mode is taken into consideration for the damage computation based on equation (1) by choosing the equivalent strain measure (6)–(10) and analysing the crack propagation by choosing the direction of the crack growth.

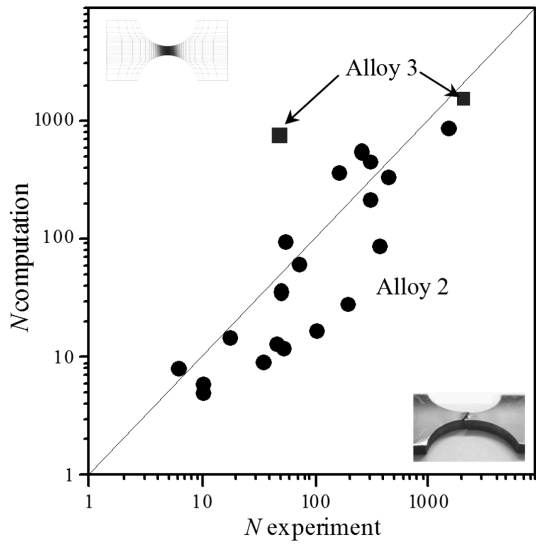

Figure 6: Comparison of experimental data with the results of computations of thermal-fatigue durability for alloys 2 and 3

Slika 6: Primerjava eksperimentalnih podatkov z rezultati izračunov odpornosti proti termičnemu utrujanju za zlitini 2 in 3

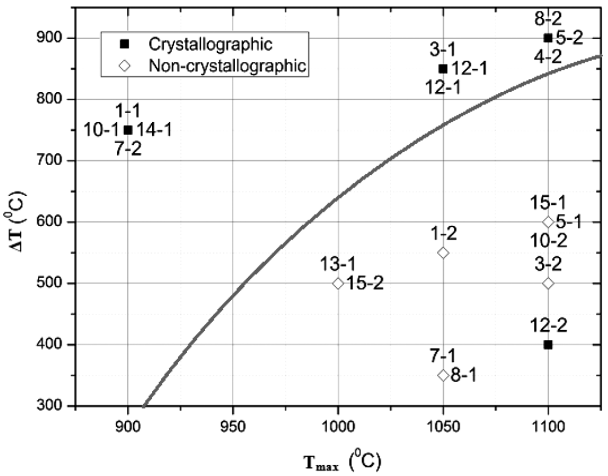

Figure 7: Diagram of thermal-fatigue failure modes (alloy 1)

Slika 7: Diagram vrste poškodb pri toplotnem utrujanju (zlitina 1)

The results of the experiments and computations showed that the dwell time has a significant effect on the thermal-fatigue durability. **Figure 8** shows the computed effect of the influence of the dwell time at T_{max} on the thermal-fatigue durability for the specimen from alloy 3 and for the thermal cycle of T_{min} = 500 °C ⇔ T_{max} = 1050 °C. A comparison of the numbers of the cycles to crack initiation computed with equation (1) and obtained with the experimental results is given in **Table 4**.

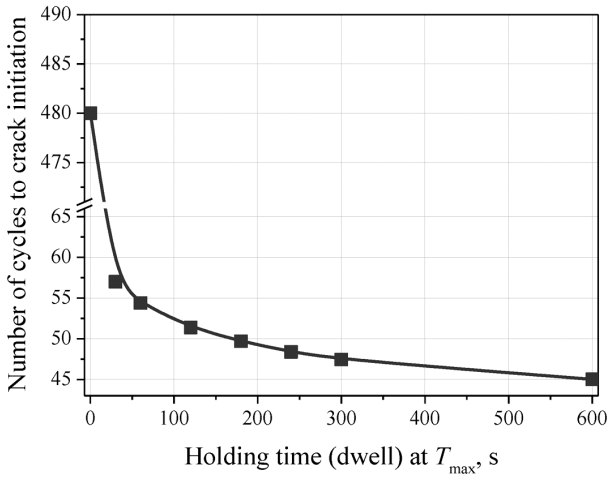

Figure 8: Influence of the dwell time at T_{max} on the thermal-fatigue durability (alloy 3)

Slika 8: Vpliv časa zadržanja pri T_{max} na zdržljivost pri toplotnem utrujanju (zlitina 3)

Table 4: Comparison of the numbers of the cycles to crack initiation obtained with the computation and with the experiment for various dwell times at T_{max} (alloy 3)
Tabela 4: Primerjava izračunanega števila ciklov do nastanka razpoke in eksperimentalnih rezultatov pri različnih časih zadržanja na T_{max} (zlitina 3)

	Dwell time	
	0 s	120 s
Computation with (1)	480	45
Experiment	670	27

Alloys 1–5 have significantly different creep characteristics and creep-rupture strengths, therefore it can be expected that the thermal-fatigue durability in the case of a dwell time at T_{max} varies significantly for different alloys, contrary to the cases of no dwell time at T_{max}.

4 CRITERION FOR THE TMF-CRACK PROPAGATION

The direction of a crack propagation in a single crystal is defined by the crystallographic structure (typically it is plane ⟨111⟩ for the considered alloys[11,12] in the crystallographic mode of failure) and, correspondingly, it is defined by the stress state during the non-crystallographic failure mode (a high temperature).

The criterion for the thermal-fatigue-crack propagation,[13] based on a linear sum of the contributions of the fatigue and creep, is used in order to determine the rate of crack propagation and the number of cycles to failure. The criterion is based on using stress-intensity factor ΔK_{eff} (for the description of the fatigue) and the C^*-integral (for the description of the creep during the dwell time at the maximum temperature of the cycle). The mathematical formulation of the criterion represents a generalization of the Paris power-type equation by taking into account two mechanisms of cracking:[13]

$$\frac{\mathrm{d}a}{\mathrm{d}N} = B(\Delta K_{\mathrm{eff}})^{\mathrm{m}} + \int_0^{t_y} A(C^*(\tau))^{\mathrm{q}}\,\mathrm{d}\tau \qquad (11)$$

where A, B, m, q are the material constants, defined separately from the fatigue experiments as $\mathrm{d}a/\mathrm{d}N(\Delta K_{\mathrm{eff}})$ and creep experiments as $\mathrm{d}a/\mathrm{d}t(C^*)$ crack-growth data.

The crack-propagation process in the corset sample (**Figure 1**) from alloy 2 is simulated cycle by cycle using

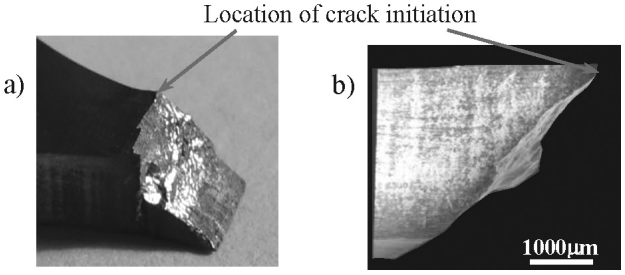

Figure 9: Views of the specimen from alloy 2 after the failure: a) left half, b) right half
Slika 9: Videz vzorca zlitine 2 po porušitvi: a) leva polovica, b) desna polovica

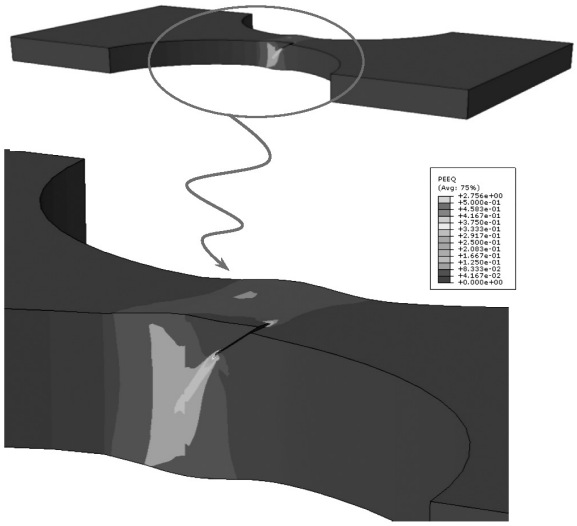

Figure 10: Plastic-strain-intensity-field distribution in the specimen from alloy 2 with a crack of a length of 0.5 mm
Slika 10: Razporeditev polja intenzitete plastične deformacije v vzorcu iz zlitine 2 z dolžino razpoke 0,5 mm

the FE program ABAQUS.[14] The specimen has its CGO near to ⟨001⟩. The deviation from the axial orientation is 5.47 ° and from the azimuthal orientation it is 41.97 ° (the Euler angles for rotations ZX'Z' are: φ = 354.7 °, θ = 41.7 °, ψ = 89.8 °). The CGO was determined with Laue diffraction patterns.

The location of the crack initiation is defined with an FE computation in section 3 and it corresponds with the experimentally obtained result. The crack propagates in plane ⟨111⟩ (**Figure 9**), except in the rupture stage. The crack-propagation process is simulated only in plane ⟨111⟩, without out-of-plane deviations, using a step-by-step technique with FE remeshing for the environment of the crack front at every step. The initial crack front has an elliptic form. The ΔJ_{eff} integral is used to calculate ΔK_{eff}. The fracture zone is established by comparing the calculated J integral with the J_{Ic} value. The details of the simulation are described in.[15]

In the experiment the sample failed after 560 thermal cycles (T_{min} = 150 °C T_{max} = 900 °C); the registered crack-initiation stage lasted for 435 cycles and the crack-propagation stage took 125 cycles. A comparison of the computed number of cycles for the crack-propagation stage based on the FE simulation (**Figure 10**) with the experimental results is given in **Table 5**.

A simulated crack-front evolution is shown in **Figure 11a**. It demonstrates a good correlation with the data of a fractography analysis (**Figure 11b**).

Table 5: Comparison of the estimated number of cycles for the crack-propagation stage with the experimental results (alloy 2)
Tabela 5: Primerjava določenega števila ciklov za fazo napredovanja razpok z eksperimentalnimi rezultati (zlitina 2)

	Number of cycles
FE computation with (11)	192
Experiment	125

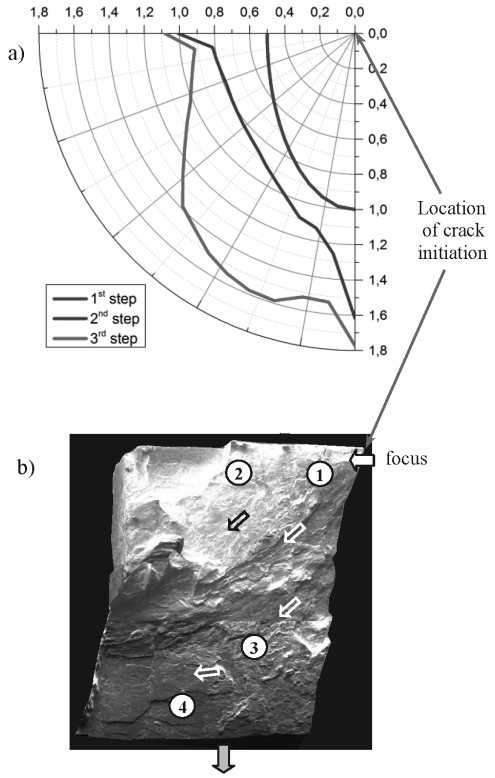

Figure 11: Evolution of the thermal-fatigue crack-front propagation on a fracture surface: a) results of finite-element simulations, b) data of a fractography analysis (specimen from alloy 2)

Slika 11: Razvoj napredovanja fronte toplotne utrujenostne razpoke na površini preloma: a) rezultati simulacije s končnimi elementi, b) podatki iz analize preloma (vzorec iz zlitine 2)

5 CONCLUSIONS

1. Thermal-fatigue tests were performed on corset samples from five Russian single-crystal nickel-based superalloys with various crystallographic orientations (⟨001⟩, ⟨011⟩, ⟨111⟩) under different temperatures and cycle durations with the aims to determine the characteristics of the thermal-fatigue resistance, compare the alloys and determine the thermal-fatigue-failure criterion.
2. The crack-initiation criterion for the single-crystal alloys under thermal cyclic loadings is proposed and discussed. A satisfactory correlation is observed between the proposed deformation criterion (1) and the obtained experimental results.
3. The finite-element simulations of the single-crystal corset specimens under the thermal cyclic loading were performed using different material models. The obtained results indicate an applicability of the proposed deformation criteria for failure for the five considered single-crystal alloys at temperatures of up to 1100 °C.
4. A high sensitivity of the thermal-fatigue durability to the crystallographic orientation and to the thermal-cycle parameters is observed experimentally and also in the corresponding finite-element simulations of the corset specimens.
5. The thermal-fatigue failures of the corset specimens show the presence of crystallographic and non-crystallographic modes of failure. The occurrence of these modes depends on the crystallographic orientation and the temperature parameters of the cycle.
6. The proposed crack-propagation criterion (11) under the thermal cyclic loadings demonstrates a satisfactory accuracy in comparison with the experimentally obtained number of cycles to failure and the crack-front evolution indicated by the data of a fractography analysis.
7. To obtain reliable analysis results for the thermal-fatigue strength and durability of the single-crystal blades of GTE, further detailed studies of the material characteristics, including the crack-resistance parameters, carried out over a wide temperature range, are required.

Acknowledgements

The present study is supported by Russian Science Foundation, grant No.15-19-00091.

6 REFERENCES

[1] L. B. Getsov, N. I. Dobina, A. I. Rybnikov, A. S. Semenov, A. A. Staroselsky, N. V. Tumanov, Strength of Materials, 40 (**2008**) 5, 538–551, doi:10.1007/s11223-008-9076-1

[2] L. B. Getsov, Materials and strength of gas turbine components 1-2, Publ. House, Rybinsk 2011

[3] N. V. Petrushin, I. L. Svetlov, O. G. Ospenkova, Heat-resistant casting nickel alloys, All materials, Encyclopedic Handbook 6, 2012, 15–19

[4] A. S. Semenov, L. B. Getsov, Strength of Materials, 46 (**2014**) 1, 38–48, doi:10.1007/s11223-014-9513-2

[5] L. B. Getsov, A. S. Semenov, E. A. Tikhomirova, A. I. Rybnikov, Mater. Tehnol., 48 (**2014**) 2, 101–106

[6] L. Getsov, A. Semenov, A. Staroselsky, Mater. Tehnol., 42 (**2008**) 1, 3–12

[7] A. S. Semenov, Proc. of V Int. Conf. Scientific and technical problems of forecasting the reliability and durability of the structures and methods for their solution, St. Petersburg, 2003, 466–480

[8] G. Cailletaud, International Journal of Plasticity, 8 (**1992**) 1, 55–73, doi:10.1016/0749-6419(92)90038-E

[9] J. Besson, G. Cailletaud, J. L. Chaboche, S. Forest, Non-linear mechanics of materials, 1st ed., Springer, Netherlands 2010, doi:10.1007/978-90-481-3356-7

[10] U. F. Kocks, T. J. Brown, Acta Metall., 14 (**1966**) 2, 87–98, doi:10.1016/0001-6160(66)90290-2

[11] P. A. S. Reed, I. Sinclair, X. D. Wu, Metallurgical and Materials Transactions A, 31 (**2000**) 1, 109–123, doi:10.1007/s11661-000-0058-6

[12] J. Telesman, L. J. Ghosn, Accelerated fatigue crack growth behavior of PWA 1480 single crystal alloy and its dependence on the deformation mode, In: S. Reichman, D. N. Duhl, G. Maurer, S. Antolovich, C. Lund (Eds.), Superalloys 1988, The Metallurgical Society, 1988, 615–624

[13] A. S. Semenov, S. G. Semenov, A. A. Nasarenko, L. B. Getsov, Mater. Tehnol., 46 (**2012**) 3, 197–203

[14] ABAQUS Analysis User's Manual, Version 6.10

[15] S. G. Semenov, A. S. Semenov, L. B. Getsov, B. E. Melnikov, Proc. Int. XLI Summer School – Conference Advanced Problems in Mechanics, St. Petersburg, 2013, 74–81

UDK 621.9:621.941:669.14.018.8
Original scientific article/Izvirni znanstveni članek

ISSN 1580-2949
MTAEC9, 49(5)779(2015)

INVESTIGATING THE EFFECTS OF CUTTING PARAMETERS ON THE BUILT-UP-LAYER AND BUILT-UP-EDGE FORMATION DURING THE MACHINING OF AISI 310 AUSTENITIC STAINLESS STEELS

PREISKAVA VPLIVOV PARAMETROV REZANJA NA NASTANEK NAKOPIČENE PLASTI IN NAKOPIČENEGA ROBA MED STRUŽENJEM AVSTENITNEGA NERJAVNEGA JEKLA AISI 310

Mehmet Burak Bilgin

Amasya University, Technology Faculty, Dept. of Mechanical Engineering, Amasya, Turkey
mehmetburak.bilgin@amasya.edu.tr

Prejem rokopisa – received: 2014-10-06; sprejem za objavo – accepted for publication: 2014-11-27

doi:10.17222/mit.2014.253

This study experimentally investigated the effects of machining parameters on the built-up-layer (BUL) and built-up-edge (BUE) formation and the wear behavior of cutting tools during the machining of the AISI 310 austenitic stainless steel with titanium-carbide cutting tools. Five different cutting speeds (50, 75, 100, 125 and 150) m/min, three feed rates (0.15, 0.20 and 0.25) mm/r and two cutting depths (1.5, 2) mm were used as the cutting parameters. The highest accumulation of the BUL and the BUE was observed at a cutting speed of 50 m/min, a feed rate of 0.15 mm/r and a cutting depth of 1.5 mm.

Keywords: built-up edge, built-up layer, machining, stainless steels

Ta študija eksperimentalno preučuje vpliv parametrov rezanja na nakopičeno plast (BUL) in nakopičen rob (BUE) ter na vedenje orodja za odrezovanje med struženjem AISI 310 avstenitnega nerjavnega jekla z orodjem iz titanovega karbida. Kot parametri odrezovanja je bilo uporabljeno pet različnih hitrosti (50, 75, 100, 125 in 150) m/min, tri hitrosti podajanja (0,15, 0,20 in 0,25) mm/r in dve globini rezanja 1,5 mm in 2 mm. Največja akumulacija BUL in BUE je bila opažena pri hitrosti rezanja 50 m/min, hitrosti podajanja 0,15 mm/r in globini rezanja 1,5 mm.

Ključne besede: nakopičen rob, nakopičena plast, strojna obdelava, nerjavna jekla

1 INTRODUCTION

In the machining process, workpiece materials may adhere to the cutting tool in two ways during the cutting. First, the workpiece becomes welded to the cutting edge, leading to the formation of what is known as a built-up edge (BUE). Second, workpiece materials may distribute and accumulate over a large portion of the cutting tool's rake face, leading to the formation of what is known as a built-up layer (BUL). These situations may arise separately on a cutting edge, or may occur simultaneously.

AISI 310 stainless steels are materials that are commonly used in the manufacturing industry despite their characteristically poor machinability. The most significant machinability problems of stainless steels are the tool smearing and the BUE formation.

Carrilero and Marcos[1] observed that the tool wear occurs due to a combination of load factors affecting the cutting edge (mechanical, thermal, chemical, abrasive factors). Individually, each load factor can be effective at a certain stage of the tool wear. Generally, the loads do not act separately and as the machining process continues the combined effect of the loads increases gradually.

Carrilero et al.[2] suggested that, in machining, the tool wear generally determines the tool life, along with the criteria such as the cutting strength or the surface roughness that vary in relation to the cutting parameters.

Korkut et al.[3] observed that the cutting-tool wear occurs at a faster rate during the machining of stainless steel. By increasing the wear of the cutting edges, a BUE leads to a poor surface finish on a workpiece. While warm chips are led away from the workpiece, they form a continuous wire that wears the cutter and adversely affects the surface of the workpiece. To prevent this, the operator must clean the chips from each machined workpiece, which, in turn, hampers the productivity.

Sanchez et al.[4] found that certain temperatures, depending on the cutting parameters, might be generated during the machining processes, increasing the occurrence of wear mechanisms (adhesion, oxidation, fatigue, abrasion, diffusion). They also suggested that facilitating the ability of tools to cut within a reasonable period of time is one of the most important topics that should be investigated in the studies conducted on the cutting tool wear.

List et al.[5] searched the wear behavior in the machining of an aluminum-copper alloy (2024). They suggested that under low cutting conditions, built-up edges form on the tool's rake face and take on the function of the cutting edge. They observed that the continuous sliding

of BUE fragments between the tool and chips increases the tool wear. They also suggest the use of a large rake angle and a polished tool surface at a low cutting speed as the adhesion mechanism is more mechanical than physical.

Rubio et al.[6] studied the surface roughness (R_a) of an AA7050 alloy. They observed that the R_a value of the AA7050 aluminum pieces obtained through the turning process had a certain tendency to decrease with the machined length. They also observed that R_a values slightly increase with the cutting speed. They suggested taking into account that parts of the machined material adhere to the tool on the edge (BUE) and on the rake face (BUL) during the cutting process.

In addition to the mechanical properties of a material, Özçatalbaş and Aydin[7] discovered that the machining parameters such as the cutting speed, the feed rate, the cutting depth and the cutting-edge geometry are also important to ensure a proper cut.

Gökkaya and Nalbant[8] investigated the effects of different cutting speeds, built-up layers and built-up edges on aluminum machining. They suggested that increasing the cutting speed decreased BUL and BUE formations, but did not eliminate them entirely.

Liew and Ding[9] investigated the wear progression in the low-speed end milling of stainless steel. They observed that a strong bonding between an adherent work material and a tool surface can result in the formation of a BUE. When the BUE and the adherent work material on the tool become unstable, they adhere to the underside of the work piece, resulting in a deterioration of the surface finish.

Katuku et al.[10] investigated the wear, cutting forces and chip characteristics of austempered ductile iron under finishing conditions. Using cutting speeds ranging from 50 m/min to 800 m/min, they observed that, at cutting speeds lower than 150 m/min, the abrasion wear was the main wear mechanism. They suggested that, at these cutting speeds, the fragmentation of chips and the instability of the BUE controlled the dynamic cutting forces.

Thakur et al.[11] studied the machinability of Inconel 718 during high-speed turning. They used cutting speeds within the range of 40–60 m/min; however, the BUE formation was not observed at the aforementioned machining parameters.

Chattopadhyay et al.[12] studied the wettability and machinability of pure aluminum for uncoated and coated carbide cutting-tool inserts. They observed that a large built-up edge was formed on the uncoated and all the coated carbide inserts, excluding diamond. They concluded that the flank-wear measurement confirms that the diamond-coated tool is superior.

Neugebauer et al.[13] investigated the velocity effects in metal forming and machining processes. They suggested that the adherent material may, assuming a low cutting velocity, form built-up edges, while at high speeds, a thin flow layer with extremely high shear deformations tends to develop.

Zhou et al.[14] investigated the surface damage in the high-speed turning of Inconel 718. They found that, at a low feed rate, the tendency to form built-up edges is also higher than at a higher feed rate, due to an increase in the size of the plastic-deformation area at the interface of the tool and the workpiece.

Khan et al.[15] investigated the tool wear/life in the finish turning of Inconel 718. They found that, at the lowest cutting speed (150 m/min), a severe grooving and a built-up-edge (BUE) formation were observed on the wear-scar micrographs in all the experiments. They observed that as the cutting speed increased to 300 m/min, the presence of the grooving and BUE diminished.

Gomez-Parra et al.[16] investigated the built-up-edge and built-up-layer formations in the turning of aluminum alloys. They suggested that the changes in the BUL and BUE took place and the formation mechanisms were related to the changes observed in the roughness profile of the machined pieces and evaluated through the average surface roughness, R_a. They confirmed that the BUE growth is responsible for a decrease in R_a; this is due to the fact that a higher BUE thickness can be related to a lower value of the tool-position angle and, thus, to a lower value of the maximum height of the cutting finger on the workpiece surface.

In this study, the machining of the AISI 310 austenitic stainless-steel material, i.e., the CNC turning machining under dry conditions was performed using a titanium-carbide cutting tool at five different cutting speeds, three different feed rates and two different cutting depths (1.5 mm, 2 mm) as the cutting parameters. The aim for this study was to establish the ideal cutting-condition parameters by determining the wear tendencies of the cutting edge and the effects of the cutting speed, the feed rate, and the cutting depth on the built-up-layer and built-up-edge formations with the aid of a scanning electron microscope (SEM).

2 MATERIALS AND METHODS

A spectral analysis of the AISI 310 stainless-steel material used in the experiments was performed using a 11814/00 optic emission spectrophotometer. The chemical composition of the test samples is indicated in **Table 1**.

All the test samples were extracted by cutting a single-sized part so that they all consisted of the same crucible material. Thus, it was ensured that the test samples had the same physical and chemical characteristics. The sample dimensions used in the tests are shown in **Figure 1**.

During the study, the cutting parameters indicated in **Table 2** were applied to the test samples listed in **Table 1**. Throughout the experiments, a TC 35 Johnford CNC turning machine with a Fanuc control unit was used according to the parameters indicated in **Table 2**. The

Table 1: Chemical composition of AISI 310 austenitic stainless steel (*w*/%)
Tabela 1: Kemijska sestava AISI 310 avstenitnega nerjavnega jekla (*w*/%)

C	Si	Mn	P	S	Cr	Mo	Ni
< 0.0050	0.3885	2.173	> 0.0960	0.0344	17.67	0.2983	14.71
Al	Cu	Nb	Ti	V	Fe		
0.0145	0.0806	< 0.0050	< 0.0010	0.0457	61.70		

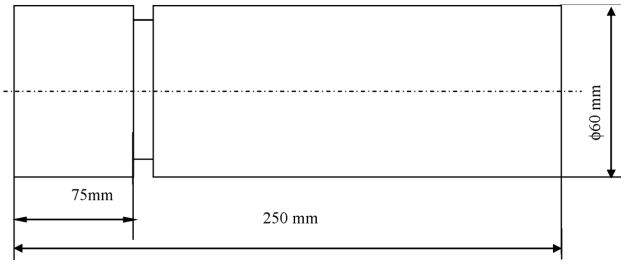

Figure 1: Dimensions of the samples used in the experiments
Slika 1: Dimenzije vzorcev, uporabljenih pri preizkusih

attachment of the test samples to the turning machine and their machining are schematically represented in **Figure 2**.

Due to dry cutting being recommended by a cutter's catalogue, the cutting fluid was not used during the machining of the test samples. A titanium-carbide-covered SNMG 120408-MS US735-shaped cutting edge, with an ISO M30 certification, recommended for austenitic stainless steel by the Mitsubishi company, a cutting-tool manufacturer, was used, along with its matching SSBCR112525 tool holder, for the machining of the test samples. The choice of the cutting parameters to be used during the tests was determined by taking into consideration the manufacturing company's data, prepared according to ISO 3685. These cutting parameters are listed in **Table 2**. Different machining parameters such as the cutting speed in addition to the feed rate and the cutting depth were used for each sample.

The optimum cutting speeds were 80–120 m/min for the chosen cutting edge. To observe the results obtained with the cutting speeds below and above the recommended cutting speed, cutting speeds of 50–150 m/min were also included in the tests. The feed rate and the cutting depth suitable for a radius 0.8 mm cutting-tool

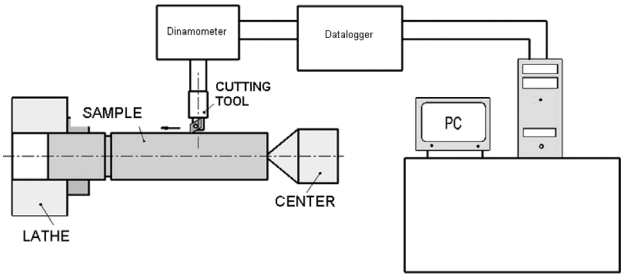

Figure 2: Attachment of the test samples and measurement of cutting forces
Slika 2: Namestitev preizkusnih vzorcev in merjenje sil pri rezanju

edge were determined based on the ISO 3685 reference values.

To determine the wear tendency of the cutting edge resulting from the machining performed with different cutting parameters, a different cutting edge was used for each test. Thus, an attempt was made to elucidate the contribution of each parameter to the built-up-layer and built-up-edge formations.

Table 2: Cutting parameters used in machining experiments
Tabela 2: Parametri rezanja pri preizkusih strojne obdelave

Experiment No.	*V*/ (m/min)	*f*/ (mm/r)	*a*/mm	Experiment No.	*V*/ (m/min)	*f*/ (mm/r)	*a*/mm
1	50	0.15	1.5	16	50	0.15	2
2	75			17	75		
3	100			18	100		
4	125			19	125		
5	150			20	150		
6	50	0.20	1.5	21	50	0.20	2
7	75			22	75		
8	100			23	100		
9	125			24	125		
10	150			25	150		
11	50	0.25	1.5	26	50	0.25	2
12	75			27	75		
13	100			28	100		
14	125			29	125		
15	150			30	150		

To determine the cutting forces involved in the chip formation during the machining performed with the CNC turning machine, a KISTLER 9257B piezoelectric-crystal-based dynamometer was used. To assess the wear rate, the wear and the smearing behavior of the cutting edges were examined using the JEOL JSM 6060 LV scanning electron microscope (SEM).

3 DISCUSSION

In this study, machining was performed at five different cutting speeds, three different feed rates and two different cutting depths using a titanium-carbide-covered tool. The analysis of the cutting edges with scanning microscopy revealed that the highest BUE formation occurred on the samples machined at lower cutting speeds. Hence, despite the use of different cutting parameters, the SEM images obtained for a cutting speed of 50 m/min and with the highest amounts of the built-up edge and built-up layer were evaluated. The scanning-electron-microscopy images of the BUE formed on the

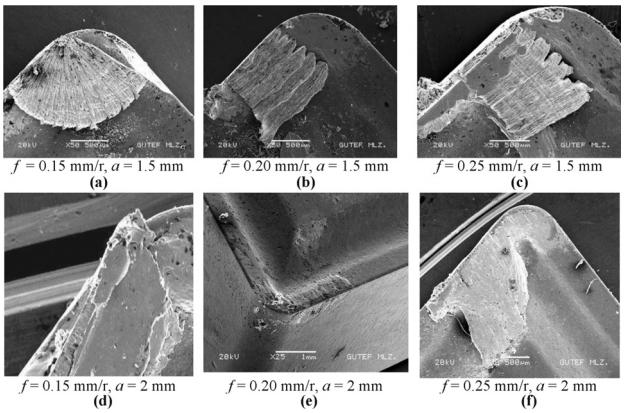

Figure 3: SEM images of BUE and BUL formed on the radius of the cutting tool used for the experimental sample at a cutting speed 50 m/min

Slika 3: SEM-posnetki BUE in BUL, ki nastajajo na radiusu rezilnega orodja, uporabljenega pri vzorcu, s hitrostjo rezanja 50 m/min

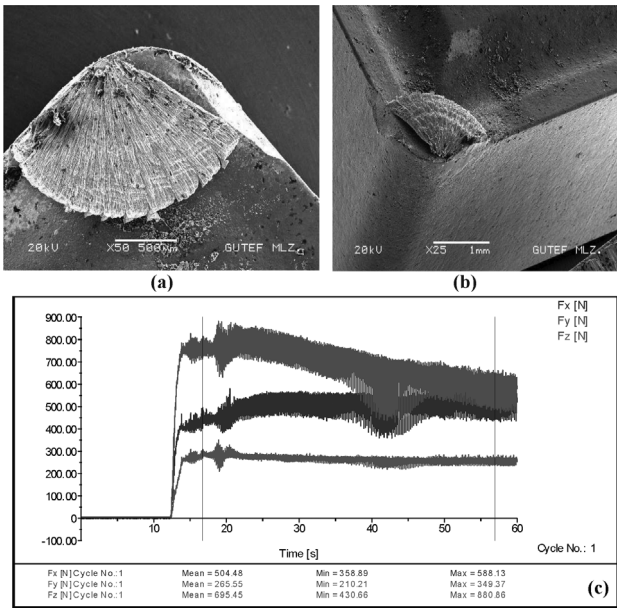

Figure 4: a), b) SEM images and c) a cutting-force diagram of the cutting tool under the machining conditions of 50 m/min cutting speed, 0.15 mm/r feed rate and 1.5 mm cut depth

Slika 4: a), b) SEM-posnetka in c) diagram sile rezanja rezalnega orodja pri strojni obdelavi: hitrost rezanja 50 m/min, hitrost podajanja 0,15 mm/r in globina rezanja 1,5 mm

cutting edge with the test samples machined at the cutting speed 50 m/min are provided in **Figure 3**. A uniformly distributed BUE can be seen in **Figure 3**, while a non-uniformly distributed BUE can be seen in other figures.

It is possible to claim that within the experimental ranges, the feed rate and cutting depth were not as signi-

Table 3: Wear of the cutting edges used in the experiments

Tabela 3: Obraba rezilnih robov pri preizkusih

Experiment No	*V*/ (m/min)	*f*/ (mm/r)	*a*/ mm	Evaluation	Experiment No	*V*/ (m/min)	*f*/ (mm/r)	*a*/ mm	Evaluation
1	50	0.15	1.5	There is a smooth BUE at the edge	16	50	0.15	2	There is a notch at the cutting edge because of the BUE
2	75			There is very little wear at the edge	17	75			The edge is clean
3	100			The edge is clean; there is very little accumulation at the far end	18	100			The edge is clean, there is a crush inside
4	125			The edge is clean	19	125			The edge is clean, there is a little accumulation inside
5	150			There is a little notch at the edge	20	150			The edge is clean
6	50	0.20	1.5	There is a BUE	21	50	0.20	2	There is crater erosion at the edge; there is a crush inside
7	75			There is a notch at the far end	22	75			There is notching at the side surface; there is a crush inside
8	100			There is very little BUE at the side surface	23	100			The edge is clean; there are residues
9	125			The edge is clean	24	125			There are notches at the edge and side surface
10	150			The edge is clean	25	150			The edge is clean
11	50	0.25	1.5	Plenty of BUE; there is a notch at the far end	26	50	0.25	2	There is an accumulation at the side surface
12	75			There is a little BUE at the side surface	27	75			The edge is clean; there is a crush inside
13	100			There is some BUE at the side surface	28	100			The edge is clean; there is a crush inside
14	125			There is a BUE line at the far end	29	125			The edge is clean; there is a crush inside
15	150			The edge is clean	30	150			The edge is clean; there is a crush inside

ficant as the cutting speed for the formation of the built-up edge and built-up layer. However, when the images in **Figure 3** are examined, it can be seen that the feed rate and the cutting depth also had a slight effect on the BUE and BUL, in addition to the cutting speed. It can be stated that increasing the cutting depth may slightly increase the BUE and BUL, while increasing the feed rate may lead to a slight decrease in the BUE and BUL.

The SEM images of the formations observed on the cutting tool under the machining conditions of the cutting speed 50 m/min, feed rate 0.15 mm/r, and cutting depth 1.5 mm are provided in **Figure 4**. As can be seen in **Figure 4**, if a built-up layer forms on the rake face of the cutting tool, the built-up edge forms uniformly along the main cutting edge and the tool-nose radius progresses towards the cutting tool's rake face. It was noted that the cutting forces increased when the BUE also increased. This is demonstrated in a two-dimensional image shown as **Figure 4a** and a three-dimensional image of **Figure 4b**. The cutting-force diagram is given in **Figure 4c**.

The images obtained with scanning electron microscopy for the other cutting edges used in the machining of the test samples are not provided. Instead, an evaluation of all the cutting parameters of the cutting edges is provided in **Table 3**. When the results obtained with the SEM for the cutting edges used during the test are examined, a decrease in the cutting-tool wear corresponding to a decrease in the smearing tendency is observed, as seen in **Figures 5** and **6**. In relation to the decrease in the smearing tendency, a decrease in the cutting-tool wear can also be observed when **Figures 5** and **6** are examined. In the tests conducted with the cutting speed of 50 m/min, the feed rate of 0.15 mm/r and the cutting depth of 1.5 mm, the wear of the cutting tool was observed to decrease as the cutting speed increased, despite the presence of a notch in the cutting edge.

In **Figure 5**, it is possible to see the traces of the built-up-layer and built-up-edge formations on the cutting tool after the machining at 75–100 m/min.

In **Figure 6**, the built-up layer can be observed once again on the rake face of the cutting tool. On the other hand, a built-up edge formed on the main cutting edge. At cutting speeds of 125 m/min and 150 m/min, smaller built-up layers and built-up edges formed. However, the built-up edge extended to the cutting tool's rake face due to an accumulation. A decrease in the BUE, corresponding to a decrease in the cutting strength, can be seen in **Figure 6c**.

It was observed that the cutting condition affected the formation of the built-up layer and built-up edge. The built-up-layer and built-up-edge thicknesses were observed to be on an increase up to the critical level as long as the machining was performed. Following this increase, the built-up edge was identified as being plastically deformed and extending towards the cutting-tool surface. For this reason, the previous built-up layer was covered and remained below the new layer. The built-up-layer and built-up-edge formations disrupt the geometry of the cutting tool. Disrupting the tool geometry and efficiency causes a workpiece to have a rough surface and reduced efficiency. The lowest surface quality was achieved with the cutting speed of 50 m/min, the 0.25 mm/d feed rate, and the cutting depth of 2 mm, which resulted in a surface-roughness value (R_a) of 5.75 µm. The formation of a BUE, particularly on the chip roots, contributed to the increase in the surface roughness.

In the assessments that were performed, the sizes of the built-up layer and built-up edge formed at the cutting speed of 50 m/min were observed as being larger than the built-up layer and built-up edge formed at the cutting speed of 150 m/min. At the 150 m/min cutting speed, no built-up edge was identified in the environs of the tool-nose radius that extended towards the rake face. This

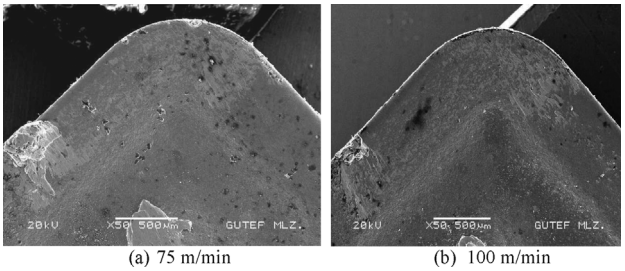

(a) 75 m/min (b) 100 m/min

Figure 5: Cutting-edge radius used for the test samples machined at cutting speeds of: a) 75 m/min and b) 100 m/min

Slika 5: Radius rezilnega roba pri vzorcu, obdelanem s hitrostjo rezanja: a) 75 m/min in b) 100 m/min

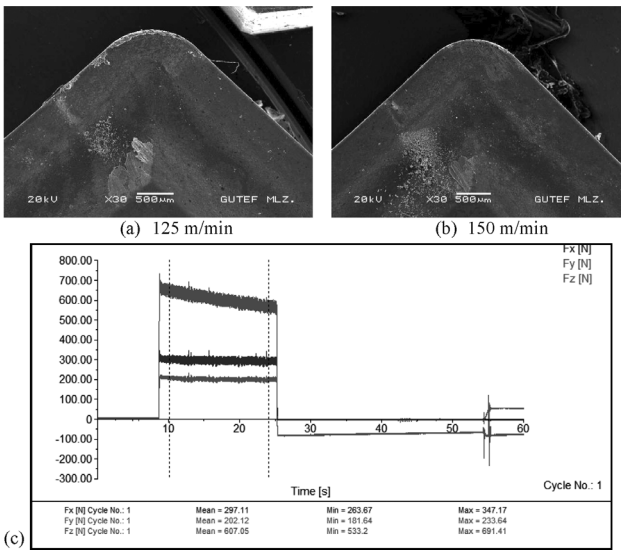

(a) 125 m/min (b) 150 m/min

(c)

Figure 6: Cutting-edge radius used for the test samples machined at cutting speeds of: a) 125 m/min, b) 150 m/min and c) cutting-force diagram

Slika 6: Uporabljeni radij rezilnega orodja pri obdelavi vzorca s hitrostjo rezanja: a) 125 m/min, b) 150 m/min in c) diagram sile rezanja

situation demonstrated that the cutting speed is an important parameter for the formation of a built-up edge.

The causes of this decrease can be explained with the effects of the factors such as the ease of deformation processes associated with the increasing temperatures at high cutting speeds, the ease of deformation of the workpiece material around the cutting edge and tool-nose radius, and the plastic flow formed at high temperatures.

The temperatures generated by the increase in the cutting speed result in soft layers that create a plastic flow. This, in turn, prevents the formation of built-up layers and built-up edges. Based on the observations from the experiments performed, it can be stated that cutting speeds above 100 m/min are necessary to prevent the formation of built-up layers and built-up edges.

4 CONCLUSIONS

Cutting tools were examined under a SEM to determine the effects of machining parameters on the formation of built-up layers and built-up edges on the cutting-tool surfaces during machining processes. The results obtained within the experimental ranges are provided below:

- The effects of the feed rate and cutting depth on the formation of built-up edges and built-up layers were not as significant as the effect of the cutting speed.
- built-up edge formed on the main cutting edge of the cutting tool.
- The built-up-edge formation along the main cutting edge of the cutting tool did not affect the characteristics of the main cutting edge.
- The wear of the cutting tools was observed mainly at low cutting speeds, particularly at 50 m/min. It is possible to claim that an increasing cutting speed leads to a decrease in the cutting wear.
- A built-up layer formed on the rake face of the cutting tool.
- A built-up edge formed at a low cutting speed of 50 m/min was observed to progress from the environs of the tool-nose radius towards the surface of the rake face.
- In the machining of the AISI 310 austenitic stainless steel, the built-up-layer and built-up-edge formations decreased as the tested cutting speeds increased. However, higher speeds could not entirely prevent the formations of built-up layers and built-up edges.
- It can be asserted that, during the machining of the AISI 310 austenitic stainless steel with titanium-carbide cutting tools, cutting speeds higher than 100 m/min are necessary to prevent the built-up-layer and built-up-edge formations, as well as the cutting-tool wear.

5 REFERENCES

[1] M. S. Carrilero, M. Marcos, On the Machinability of Aluminium and Aluminium Alloys, J of Mech Behav of Mater, 7 (**1996**) 3, 179–191, doi:10.1515/JMBM.1996.7.3.179

[2] M. S. Carrilero, R. Bienvenido, J. M. Sanchez, M. Alvarez, A. Gonzalez, M. Marcos, A SEM and EDS insight into the BUE and BUL difference in the turning processes of AA2024 Al-Cu Alloy, Int J of Mach Tool and Manuf, 42 (**2002**) 2, 215–220, doi:10.1016//S0890-6955(01)00112-2

[3] I. Korkut, M. Kasap, I. Çiftci, U. Şeker, Determination of optimum cutting parameters during machining of AISI 304 austenitic stainless steel, Mater Design, 25 (**2004**), 303–305, doi:10.1016/j.matdes.2003.10.011

[4] J. M. Sanchez, E. Rubio, M. Alvarez, M. A. Sebastian, M. Marcos, Microstructural characterization of material adhered over cutting tool in the dry machining of aerospace aluminium alloys, J of Mater Process Tech, 164–165 (**2005**), 911–918, doi:10.1016/j.matprotec.2005.02.058

[5] G. List, M. Nouari, D. Gehin, S. Gomez, J. P. Manaud, Y. Le Petitcorps, F. Girot, Wear behavior of cemented carbide tools in dry machining of aluminium alloy, Wear, 259 (**2005**), 1177–1189, doi:10.1016/j.wear.2005.02.056

[6] E. M. Rubio, A. M. Camacho, J. M. Sanchez-Sola, M. Marcos, Surface roughness of AA7050 alloy turned bars analysis of the influence of the length of machining, J of Mater Process Tech, 162–163 (**2005**), 682–689, doi:10.1016/j.matprotec.2005.02.096

[7] Y. Özçatalbaş, B. Aydin, Mekanik özellik ve kesme geometrisinin AA2014 alaşiminin işlenebilme özelliklerine etkileri, Gazi Üniversitesi Mühendislik Mimarlik Fakültesi Dergisi, 21 (**2006**), 21–27

[8] H. Gökkaya, M. Nalbant, Kesme hizinin yiğinti katmani ve yiğinti talaş oluşumu üzerindeki etkilerinin SEM ile incelenmesi, J of the Faculty of Eng and Arch of Gazi Uni, 22 (**2007**) 3, 481–488

[9] W. Y. H. Liew, X. Ding, Wear progression of carbide tool in low-speed end milling of stainless steel, Wear, 265 (**2008**), 155–166, doi:10.1016/j.wear.2007.09.003

[10] K. Katuku, A. Koursaris, I. Sigalas, Wear, cutting forces and chip characteristics when dry turning ASTM grade austempered ductile iron with PCBN cutting tools under finishing conditions, J of Mater Process Tech, 209 (**2009**), 2412–2420, doi:10.1016/j.matprotec.2008.05.042

[11] D. G. Thakur, B. Ramamoorthy, L. Vijayaraghavan, Study on the machinability characteristics of superalloy Inconel 718 during high speed turning, Mater Design, 30 (**2009**) 5, 1718–1725, doi:10.1016/j.matdes.2008.07.011

[12] A. K. Chattopadhyay, P. Roy, A. Ghosh, S. K. Sarangi, Wettability and machinability study of pure aluminium towards uncoated and coated carbide cutting tool inserts, Surf Coat Tech, 203 (**2009**), 941–951, doi:10.1016/j.surfcoat.2008.08.047

[13] R. Neugebauer, K. D. Bouzakis, B. Denkena, F. Klocke, A. Sterzing, A. E. Tekkaya, R. Wertheim, Velocity effects in metal forming and machining processes, CIRP Annals-Manuf Tech, 60 (**2011**), 627–650, doi:10.1016/j.cirp.2011.05.001

[14] J. M. Zhou, V. Bushlya, J. E. Stahl, An investigation of surface damage in the high speed turning of Inconel 718 with use of whisker reinforced ceramic tools, J of Mater Process Tech, 212 (**2012**), 372–384, doi:10.1016/j.matprotec.2011.09.022

[15] S. A. Khan, S. L. Soo, D. K. Aspinwall, C. Sage, P. Harden, M. Fleming, A. White, R. M'Saoubi, Tool wear/life evaluation when finish turning Inconel 718 using PCBN tooling, 5th CIRP Conference on High Performance Cutting, Procedia CIRP, 1 (**2012**), 283–288, doi:10.1016/j.procir.2012.04.051

[16] A. Gomez-Parra, M. Alvarez-Alcon, J. Salguero, M. Batista, M. Marcos, Analysis of the evolution of the Built-Up Edge and Built-Up Layer formation mechanisms in the dry turning of aeronautical aluminium alloys, Wear, 302 (**2013**), 1209–1218, doi:10.1016/j.wear.2012.12.001

UDK 75:693.611:555.2
Original scientific article/Izvirni znanstveni članek

ISSN 1580-2949
MTAEC9, 49(5)785(2015)

MORTAR-TYPE IDENTIFICATION FOR THE PURPOSE OF RECONSTRUCTING FRAGMENTED ROMAN WALL PAINTINGS (CELJE, SLOVENIA)

ANALIZA OMETOV ZA REKONSTRUKCIJO FRAGMENTOV RIMSKIH STENSKIH POSLIKAV (CELJE, SLOVENIJA)

Maja Gutman[1], Martina Lesar Kikelj[1], Jelka Kuret[1], Sabina Kramar[2]

[1]Institute for the Protection of Cultural Heritage of Slovenia, Restoration Centre, Poljanska 40, 1000 Ljubljana, Slovenia
[2]Slovenian National Building and Civil Engineering Institute, Dimičeva 12, 1000 Ljubljana, Slovenia
maja.gutman@rescen.si

Prejem rokopisa – received: 2014-10-08; sprejem za objavo – accepted for publication: 2014-11-07

doi:10.17222/mit.2014.256

Archaeological excavations of Roman Celeia (present-day Celje, Slovenia) carried out about 30 years ago revealed the remains of a Roman residential building where more than 9000 fragments of wall paintings were found. The past manual reassembling of fragments proved to be time consuming, limiting the amount of the material that can be examined and reconstructed. However, recently work has been resumed using a software application specifically developed for fragment reassembly. Information on mortar types can provide additional data about the fragments and thus help in the reconstruction process. Fragments of the wall paintings consist of up to three preserved mortar layers, differing in their thicknesses, aggregate compositions and binder colours. Based on the mineralogical/petrographic analyses of the mortars, the investigated fragments of the wall paintings were divided into several groups. The results revealed that the first-mortar-layer aggregates of all the fragments consist of carbonate grains, while the other-mortar-layer aggregates consist of carbonate, silicate/carbonate, silicate or silicate/ceramic grains.

Keywords: wall paintings, Roman mortars, petrography, reassembling, fragments

Arheološka izkopavanja rimske Celeie (današnje Celje) pred približno 30 leti so razkrila ostanke antičnega stanovanjskega objekta, v katerem je bilo najdenih več kot 9000 fragmentov stenskih poslikav. Sestavljanje takšnega števila fragmentov zahteva veliko časa. Nedavno je bila za sestavljanje fragmentov razvita posebna računalniška aplikacija. Informacije o sestavi malte se uporabljajo kot dodatni podatki pri sestavljanju fragmentov. Fragmente stenskih poslikav sestavljajo do tri ohranjene plasti ometov, ki se razlikujejo po debelini, sestavi agregata in barvi veziva. Analizirani fragmenti so bili na podlagi mineraloško-petrografskih preiskav razdeljeni v več skupin. Rezultati so pokazali, da pri vseh fragmentih zgornjo plast ometa sestavlja agregat iz karbonatnih zrn, medtem ko agregat spodnjih plasti sestavljajo bodisi karbonatna, silikatna/karbonatna, silikatna ali silikatna/keramična zrna.

Ključne besede: stenske poslikave, antični ometi, petrografija, sestavljanje, fragmenti

1 INTRODUCTION

The characterization of ancient wall paintings provides useful information about the painting technique and pigments used. Romans used lime of high purity, while aggregates most often contained siliceous sand, crushed marble and crushed ceramic.[1–3] A similar situation can be seen on the Roman wall paintings in Slovenia where, for instance, crushed carbonate grains are characteristic of the first mortar layer of the wall paintings from Roman Emona (today's Ljubljana), while in the lower mortar layers, besides silicate sand, grains of crushed ceramics also appear.[4] On the other hand, fluvial dolomite sand with an addition of crushed ceramic[5] or, in some cases, crushed marble prevails[6] in the wall-painting mortars of the Roman-villa rustica-bath complex near Mošnje.

Archaeological excavations in Celje in 1978 uncovered the remains of a Roman residential building from the first century A.D. where more than 9000 fragments of wall paintings were found. The elongated room of the residential building, measuring 4 m × 13 m, was heated with a hypocaust; the floors were decorated with a black-and-white mosaic with a simple rosette pattern, while the preserved walls were embellished with wall paintings.

Due to the large amount of fragments concentrated in the elongated room of the archaeological site, it is still unknown whether the fragments actually belonged to the Roman residential building or perhaps to a pit where the Romans deposited the material during a renovation process. The majority of the fragments are monochromatic (most often of white, red, green, blue, black or yellow colour), but on some of them various motifs such as animals, flowers and various patterns can be recognized. The pigments identified were Egyptian blue, vermilion, red ochre, yellow ochre and green earth,[7,8] which were all common pigments of the Roman period.[9,10] The excavated fragments were first transported to the Regional Museum in Celje and in 1989 to the Restoration Centre of the Institute for the Protection of Cultural Heritage of Slovenia. The manual reassembly process of the fragmented wall paintings performed 30 years ago proved to be time consuming and limiting the amount of the mate-

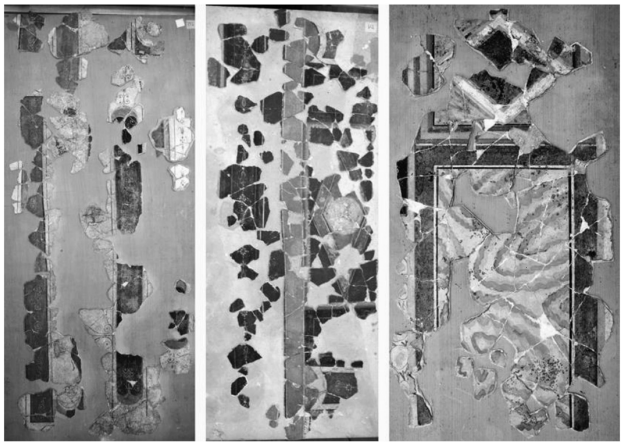

Figure 1: Wall paintings with various motifs reconstructed in 1989
Slika 1: Leta 1989 rekonstruirane stenske poslikave z različnimi motivi

rial that could be examined and reconstructed. **Figure 1** shows three wall paintings reconstructed in 1989, measuring about 200 cm in length and 30 cm to 90 cm in width.

A total of 9521 fragments thus still remained disassembled and are now documented and stored in 166 boxes. Given the large scale of the fragments and a high quality of the wall paintings, a decision for a reconstruction of the wall paintings and a presentation of the remaining fragments was made. In June 2010, a systematic cleaning and consolidation of the fragments began. The fragments were consolidated using nanoparticles of calcium hydroxide (nanolime) which is compatible with the lime-mortar layers of the wall paintings.

Due to the large number of fragments, it is difficult to have a comprehensive overview of the entity of the excavated wall paintings, but fortunately several systems for a virtual reconstruction of the wall-painting fragments, such as the computer-assisted reassembly of the wall paintings from the Akrotiri excavations in Thera (Santorini), Greece[11] or the 3D reassembling of the parts of the wall paintings belonging to the Mycenaean civilization (c. 1300 BC), enabled us to overcome this

Figure 2: Fragment with an identification number
Slika 2: Fragment z identifikacijsko številko

Figure 3: Scanning a wall-painting fragment
Slika 3: Skeniranje fragmenta stenske poslikave

problem.[12] Another advantage of a virtual reconstruction is also that it eliminates the physical contact with the fragments and thus prevents additional damage to the original pieces. Additionally, a system for a computer-assisted documentation and reassembling of the wall-painting fragments named Pedius[13] was developed especially for the Celje wall paintings.[14,15] Its online version, e-Pedius, is a newly developed computer program intended not only for restorers but also non-experts.

By means of the Pedius system, all the fragments were digitized (in 2D) and assigned a unique identification number (**Figure 2**). Capturing images of the fragments was carried out in two ways: with a scanner (**Figure 3**) or with a digital camera.

After the upload of the images in the database, a user can start an interactive assembling of the fragments (**Figure 4**). Since there is no need to manipulate the actual valuable fragments, the reassembling can also be performed by non-expert users. With the computer support, the assembling is much accelerated since the program provides some suggestions based on the colour of the surface, the lines, etc.

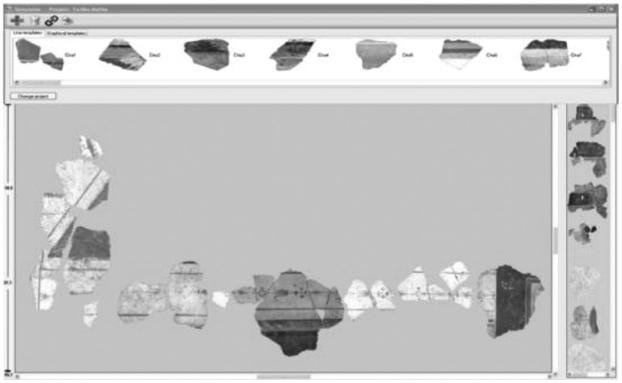

Figure 4: Example of interactive assembling of wall-painting fragments in Pedius
Slika 4: Zgled interaktivnega sestavljanja fragmentov stenskih poslikav v Pediusu

As the information on the mortar types can provide additional data about the fragments and help in the reconstruction process, the study deals with a mineralogical/petrographic characterization of the mortars of the Roman wall-painting fragments. The results obtained may not only help in the reconstruction of the fragmented wall paintings but also contribute new knowledge about Roman mortars and the technology of wall paintings in Slovenia and worldwide.

2 EXPERIMENTAL WORK

2.1 Materials

A total of thirty samples were selected among the fragments (**Table 1**). The fragments of the wall paintings consist of up to three preserved mortar layers that vary in their thicknesses, aggregates and binder colours.

2.2 Methods

In order to characterise the textures of the mortars and define the contents of particular aggregate components, the content of the binder and their ratios, our first approach was to examine thin sections of the fragments by means of optical microscopy. Polished thin sections of the mortar samples were studied with light microscopy using an Olympus BX-60 equipped with a digital camera (Olympus JVC3-CCD).

Raman spectra of the studied areas of the polished thin sections of the samples were obtained with a Horiba Jobin Yvon LabRAM HR800 Raman spectrometer equipped with an Olympus BXFM light microscope. Measurements were made using a laser-excitation line 785 nm, and a Leica 50× objective. The spectral resolution was about 1 cm^{-1}.

Table 1: Groups of analyzed samples
Tabela 1: Skupine analiziranih vzorcev

I. White binder of 1st layer			
Group	Subgroup	Composition	Sample
A – 1st layer thickness: 2–5 mm	A – 1	1st layer: Carbonate grains 2nd layer: Carbonate grains 3rd layer: Silicate grains	HTM 9, HTM 12, HTM 21
	A – 2	1st layer: Carbonate grains 2nd layer: Carbonate grains 3rd layer: Silicate grains (with ceramic grains)	HTM 16, HTM 47, HTM 48
	A – 3	1st layer: Carbonate grains 2nd layer: Silicate grains 3rd layer: Silicate grains	HTM 6, HTM 7, HTM 8, HTM 11, HTM 14, HTM 45, HTM 50, HTM 53
	A – 4	1st layer: Carbonate grains 2nd layer: Carbonate grains : Silicate grains = 2 : 1 3rd layer: Silicate grains (with ceramic grains)	HTM 17, HTM 20
	A – 5	1st layer: Carbonate grains 2nd layer: Carbonate grains : Silicate grains = 2 : 1 3rd layer: Silicate grains	HTM 49, HTM 52
	A – 6	1st layer: Carbonate grains 2nd layer: Silicate grains (with ceramic grains) 3rd layer: Silicate grains (with ceramic grains)	HTM 46
B – 1st layer thickness: 6–10 mm	B – 1	1st layer: Carbonate grains 2nd layer: Carbonate grains 3rd layer: Silicate grains	HTM 13
	B – 2	1st layer: Carbonate grains 2nd layer: Silicate grains	HTM 10, HTM 15
	B – 3	1st layer: Carbonate grains 2nd layer: Silicate grains 3rd layer: Silicate grains (with ceramic grains)	HTM 18
	B – 4	1st layer: Carbonate grains 2nd layer: Silicate grains (with ceramic grains)	HTM 19
II. Red binder of 1st layer			
C – 1st layer thickness: 2–5 mm	C – 1	1st layer: Carbonate grains 2nd layer: Carbonate grains 3rd layer: Silicate grains	HTM 51, HTM 54
	C – 2	1st layer: Carbonate grains 2nd layer: Carbonate grains 3rd layer: Carbonate grains	HTM 58
	C – 3	1st layer: Carbonate grains (calcite) 2nd layer: Silicate grains	HTM 55
	C – 4	1st layer: Carbonate grains (calcite) 2nd layer: Carbonate grains : Silicate grains = 2 : 1	HTM 56, HTM 57

3 RESULTS AND DISCUSSION

Each fragment has a multilayered structure typical for the wall paintings that consist of two or three separate mortar layers followed by the paint layer (**Figure 5**). As seen in **Table 1**, the first mortar layer (from the top outer layer) always contains a white carbonate aggregate but varies in the binder colour and layer thickness (the latter could vary between 2 mm and 10 mm). The aggregate of the second mortar layer, which is normally between 5 mm and 16 mm, most often consists of carbonate grains, followed by silicate grains or even a mixture of the two. Furthermore, the third mortar layer (the inner layer), with a thickness of up to 30 mm, mainly consists of silicate grains, sometimes with an addition of crushed ceramics. What binds them is the air lime or, in the cases of ceramic grains, the hydraulic binder and air lime. Lime lumps were present in all the samples from all the mortar layers, and they varied in size from 0.2 mm to 3 mm. Fissures were observed in most of the lower-layer samples with a silicate-sand aggregate, while the upper outer layers with carbonate grains were generally more compact.

The fragments were divided into two main groups based on the binder colour of the first mortar layer: (I) the fragments with white binder (most frequent – 24 fragments) and (II) the fragments with red binder (rare – 6 fragments). The samples of the first main group were, according to the thickness of the first layer, furthermore divided into two groups; (A) the samples with the thickness of the first mortar layer between 2 mm and 5 mm (19 fragments) and (B) the samples with the thickness of the first mortar layer between 6 mm and 10 mm (5 fragments). On the other hand, the second main group with the coloured binder consists of merely one subgroup, containing the samples whose first-layer thickness is between 2 mm and 5 mm. Considering the mineralogical/petrographic compositions of the mortar layers, the samples were grouped into 14 subgroups.

The common characteristic of the first mortar layers of all the samples is an exclusive presence of carbonate grains. Carbonate grains, determined by Raman miscrospectroscopy, are mostly represented by dolomite (**Figure 6a**), while calcite (**Figure 6b**) is observed only in a few samples (HTM 55, HTM 56, and HTM 57).

Most of the dolomite is represented by semi-angular grains (**Figure 7a**) with a small amount of subrounded grains. Crushed dolomitic rock was most probably used as an aggregate (cf. the wall paintings from the Roman site near Mošnje with round grains of dolomite indicating a fluvial deposit).[5] In addition, a coarse-grained sparry calcite (**Figure 7b**) may indicate the use of crushed marble.[1,6,16]

Furthermore, the grains in the aggregate are poorly sorted, between 0.02 mm and 3.0 mm in size. The binder is lime, mostly compact with rare fissures. In all three samples with the coarse-grained sparry calcite, the

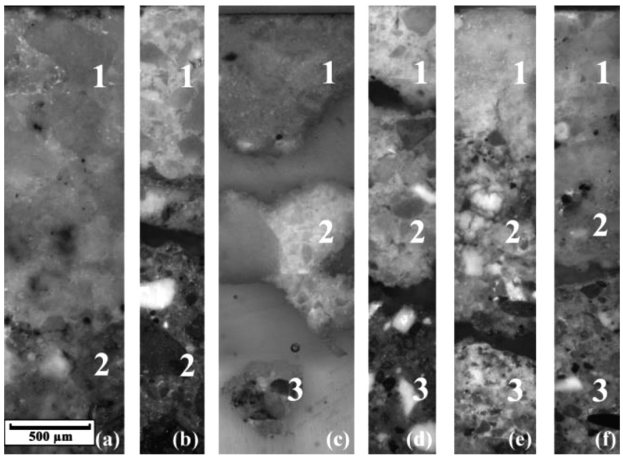

Figure 5: Wall-painting fragments representing various groups with different mortar layers: a) group B-2, sample HTM 10, b) group B-4, sample HTM 19, c) group C-1, sample HTM 54, d) group A-2, sample HTM 47, e) group A-3, sample HTM 7, and f) group B-1, sample HTM 13; Legend: 1: 1st mortar layer, 2: 2nd mortar layer, 3: 3rd mortar layer; light microscope, reflective light, crossed polars, 5-times magnifications

Slika 5: Fragmenti stenskih poslikav, razdeljeni v različne skupine glede na sestavo ometov: a) skupina B-2, vzorec HTM 10, b) skupina B-4, vzorec HTM 19, c) skupina C-1, vzorec HTM 54, d) skupina A-2, vzorec HTM 47, e) skupina A-3, vzorec HTM 7 in f) skupina B-1, vzorec HTM 13; legenda: 1: prva plast ometa, 2: druga plast ometa, 3: tretja plast ometa; svetlobni mikroskop, refleksijska svetloba, navzkrižni nikoli, 5-kratna povečava

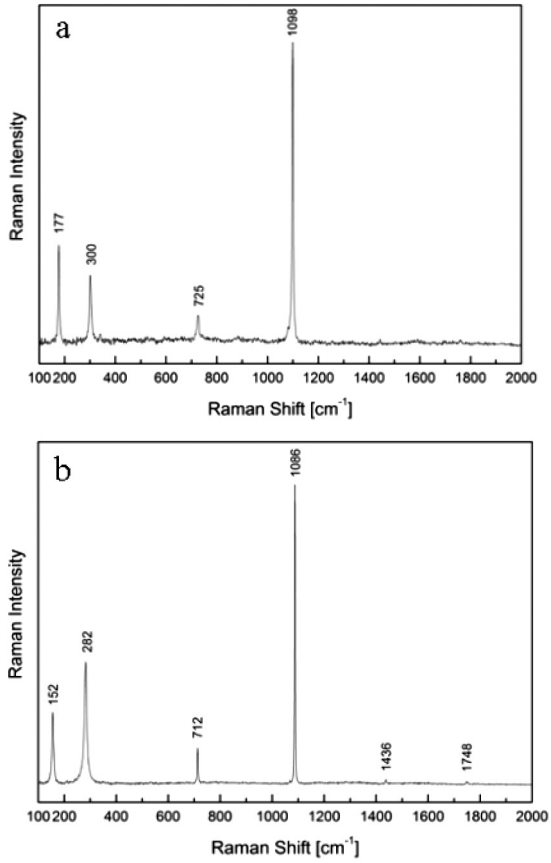

Figure 6: Raman spectra of: a) dolomite, sample HTM 54 and b) calcite, sample HTM 55

Slika 6: Ramanski spekter: a) dolomita, vzorec HTM 54 in b) kalcita, vzorec HTM 55

binder is red due to the addition of red ochre (hematite) pigment (**Figure 8**). A slightly red-coloured binder was also observed in some Emona samples, which was due to the addition of red ochre,[4] whereas Weber[16] reported additions of red ochre or cinnabar to the lime.

Regarding the second mortar layers, in general, three types of aggregate were observed: layers with predominant grains of carbonate, layers with carbonate grains and an addition of silicate grains or layers with prevailing silicate grains. Silicate aggregates such as quartz, chert and lithic grains of sedimentary and magmatic rocks were observed. Grains are rounded, subrounded and angular, measuring between 0.03 mm and 3.75 mm. In contrast to the wall paintings from some other archaeological sites in Slovenia where ceramic grains were observed exclusively in the first mortar layers,[4,5] ceramic grains measuring between 0.04 mm and 2.90 mm were present in the second layer of the two samples (**Figure 7c**).

In all the samples, the aggregate of the third mortar layer consists mostly of silicate grains, except for the HTM 58 sample where carbonate grains are present. The silicate aggregate is composed of subrounded quartz, rounded lithic grains of chert, quartz sandstone, magmatic rocks, some angular grains of feldspar and mica (**Figure 7d**). The grains measure between 0.06 mm and 3.50 mm in size. In some samples, significant amounts of ceramic grains in a size between 0.5 mm and 3 mm are present (for comparison: ceramic grains in the Emona samples are rare and observed only in a few samples.)[4]

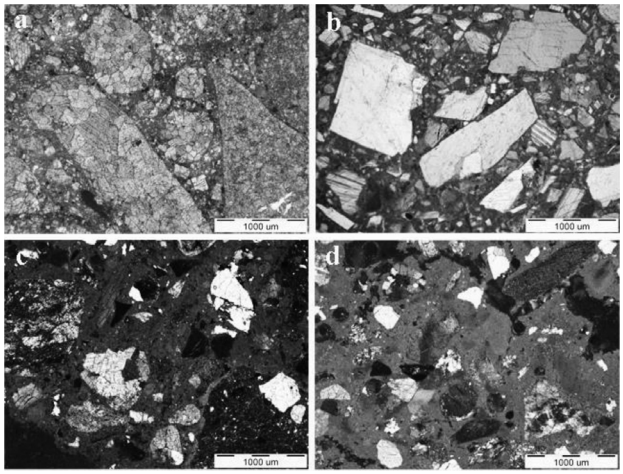

Figure 7: a) Dolomite aggregate in the first mortar layer, group B-2, sample HTM 10; light microscope, transmission light, parallel polars, b) coarse-grained calcite and slightly red-coloured binder in the first mortar layer, group C-4, sample HTM 56; light microscope, transmission light, parallel polars, c) ceramic particles in the second mortar layer, group B-4, sample HTM 19; light microscope, transmission light, crossed polars, d) silicate grains in the third mortar layer, group A-3, sample HTM 8; light microscope, transmission light, crossed polars

Slika 7: a) Zrna dolomita v zgornji plasti ometa, skupina B-2, vzorec HTM 10; svetlobni mikroskop, transmisijska svetloba, vzporedni nikoli, b) debelozrnat kalcit in rahlo rdeče obarvano vezivo v zgornji plasti ometa, skupina C-4, vzorec HTM 56; svetlobni mikroskop, transmisijska svetloba, vzporedni nikoli, c) zrna keramike v drugi plasti ometa, skupina B-4, vzorec HTM 19; svetlobni mikroskop, transmisijska svetloba, navzkrižni nikoli, d) silikatna zrna v tretji plasti ometa, skupina A-3, vzorec HTM 8; svetlobni mikroskop, transmisijska svetloba, navzkrižni nikoli

The results show that the wall-painting fragments with more sophisticated motifs or patterns, such as multiple colours (groups A-1, A-4, A-5, B-1, C-2, C-4), had two or even three mortar layers prepared with a carbonate aggregate or at least a mixture of carbonate and silicate, while those with monochromatic colours usually had only one carbonate layer followed by silicate sand. Vitruvius[17] wrote in his book about the correct method of plastering walls and ceilings and of making a quality base for wall paintings that plaster would not crack and would be without defects if the walls were covered with three layers of sand mortar and as many layers of marble mortar. The use of marble powder in the top layers improved the polishing effect and produced a mirror-like sheen on the surface. It is presumed that for the mortar layers with a mixture of carbonate and silicate grains (the second layer) crushed dolomite was mixed with fluvial sand. Dolomite was crushed most probably to obtain the so-called "polvere di marmo", but normally limestone was used.[18]

An addition of ceramic powder reduces the water permeability and increases the mechanical strength, which is attributed to the hydraulic reaction with lime in the presence of water at the edge of the ceramic particles.[19] This highly hydraulic lime has been used since the Roman times for rendering and plastering the buildings situated in the places with a high relative humidity, such as baths.[20]

The fragments of the same group display very similar micro-stratigraphic sequences and materials and therefore very probably belong to the same construction phase or room. Thus, such a large number of groups could indicate the existence of several different phases of the construction and different rooms.

The petrographic composition of the mortar aggregate could reflect local geological conditions. Since deposits of the upper and middle Triassic dolomite occur in the Celje area,[21] we could assume that the dolomite aggregate originated from the quarry in the vicinity. Fur-

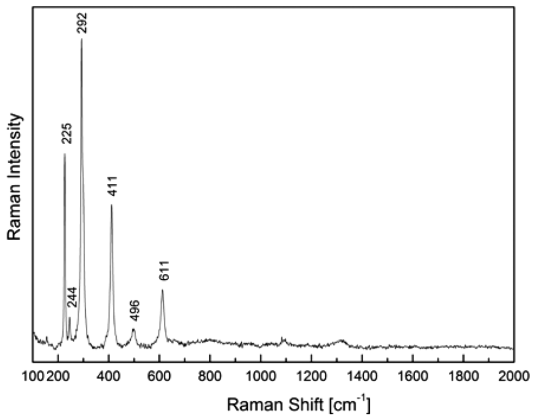

Figure 8: Raman spectra of red ochre (hematite), sample HTM 56

Slika 8: Ramanski spekter rdečega okra (hematit), vzorec HTM 56

thermore, the round-grain aggregate from the lower mortar layers suggests a fluvial origin from the rivers nearby the archaeological site, most probably the alluvial deposits of the Savinja River. A possible source of the coarse-grained calcite could be the abandoned marble quarry in Pohorje (40 km from the archaeological site) active in the Roman times.

4 CONCLUSIONS

The characterisation of the wall-painting mortars from the archaeological site in Celje revealed differences between the mortars employed and contributed to the knowledge of the Roman wall-painting technique. The samples were divided into two main groups based on the binder colour and three groups based on the thickness of the first mortar layer. According to the mineral/petrographic compositions of the layers, the fragments were further divided into 14 different subgroups. Such a large number of groups may indicate the existence of several different phases of the construction and different rooms, keeping in mind that the fragments did not necessarily belonged only to the room in which they were found.

The results revealed that the common characteristic of the first layers of all the samples was the exclusive presence of carbonate grains. In majority, carbonate grains were represented by dolomite, while coarse-grained calcite was found only in three samples that also indicated the use of crushed marble. The aggregates from the lower mortar layers consisted of only carbonate grains or silicate sand, or even of a mixture of both. An addition of ceramic grains was observed in some cases. Since crushed ceramic was commonly used in damp places such as hypocaust, baths and the lower parts of walls, we can say that some of the analyzed samples might have belong to such rooms, maybe also being part of the hypocoust where the fragments had been found.

A reassembly of wall-painting fragments requires that the fragments be put together in the right way to form the original artwork. Any knowledge of the compositions of the mortars (thickness, colour, mineral composition) not only gives us information about the technique, but also helps us reconstruct the object. A combination of an analysis and specific computer programs, such as Pedius, can help restorers reassemble the fragments faster and more effectively.

Acknowledgements

This research was financially supported by the Ministry of Culture of the Republic of Slovenia.

5 REFERENCES

[1] A. Wallert, M. Elston, Fragments of Roman wall painting in the J. Paul Getty Museum: a preliminary technical investigation, Proceedings of the International Workshop on Roman Wall Painting, Fribourg, 1996, 1–373

[2] P. Fermo, E. Delnevo, M. De Vos, M. Andreoli, Painting and mortars from villa Adriana Tivoli (Rome, Italy), The 8th international conference of the Infrared and Raman Users' Group (IRUG), Vienna, Austria, 6 (**2008**), 169

[3] A. Duran, L. A. Perez-Maqueda, J. Poyato, J. L. Perez-Rodriguez, Journal of Thermal Analysis and Calorimetry, 99 (**2010**) 3, 803–809, doi:10.1007/s10973-009-0667-2

[4] M. Gutman, B. Županek, J. Kuret, M. Kikel-Lesar, S. Kramar, Characterisation of wall painting mortars from the Roman Emona, AMMC, Conference on Ancient and Modern Mortars, Florence, 2013

[5] S. Kramar, V. Zalar, M. Urosevic, W. Körner, A. Mauko, B. Mirtič, J. Lux, A. Mladenović, Materials Characterization, 62 (**2011**) 11, 1042–1057, doi:10.1016/j.matchar.2011.07.019

[6] S. Kramar, J. Lux, B. Mirtič, Journal for the Protection of Monuments, 44 (**2008**), 190

[7] P. Ropret, Report on the pigment analysis, IPCHS, Restoration Centre, Ljubljana, 2008, 9 (in Slovene)

[8] P. Ropret, T. Spec, L. Legan, K. Retko, The report on the colour layer analysis of the "Turška mačka" fresco fragments, IPCHS, Restoration Centre, Ljubljana, 2010, 106 (in Slovene)

[9] G. A. Mazzocchin, F. Agnoli, M. Salvadori, Talanta, 64 (**2004**) 3, 732–741, doi:10.1016/j.talanta.2004.03.055

[10] R. Siddall, Not a day without a line drawn: pigments and painting techniques of Roman Artists, Proceedings of the Royal Microscopical Society, 2 (**2006**), 18

[11] B. Brown, C. Toler-Franklin, D. Nehab, M. Burns, D. Dobkin, A. Vlachopoulos, C. Doumas, S. Rusinkiewicz, T. Weyrich, A system for high-volume acquisition and matching of fresco fragments: Reassembling theran wall paintings, ACM Transactions on Graphics (Proc. of ACM SIGGRAPH 2008), 27 (**2008**) 3, Article No. 84, doi:10.1145/ 1360612.1360683

[12] C. Papaodysseus, D. Arabadjis, M. Exarhos, P. Rousopoulos, S. Zannos, M. Panagopoulos, L. Papazoglou-Manioudaki, Computers and Mathematics with Applications, 64 (**2012**) 8, 2712–2734, doi:10.1016/j.camwa.2012.08.003

[13] Pedius, A system for computer-assisted reconstruction of wall paintings, accessed on http://e-pedius.si/, 2012

[14] B. Filipič, M. Mlakar, E. Dovgan, T. Tušar, Developing a system for computer-assisted record keeping and reassembling of wall painting fragments, Proceedings of the 14th International Multiconference Information Society, A (**2011**), 45–48 (in Slovene)

[15] A. Mihalov, P. Benedik, B. Filipič, M. Mlakar, E. Fovgan, T. Tušar, Pedius, a system for computer-assisted documentation and reassembly of wall painting fragments, Konservator-restavrator, Summary Report of the Expert Meeting, Slovene Etnographic Musseum, 45 (**2012**)

[16] J. Weber, W. Prochaska, N. Zimmermann, Materials Characterization, 60 (**2009**) 7, 586–593, doi:10.1016/j.matchar.2008.12.008

[17] M. P. Vitruvius, Ten Books on Architecture (translated by M. Lopac and V. Bedenko), Zagreb 1999

[18] V. Meggiolaro, G. M. Molin, U. Pappalardo, P. P. Vergerio, Contribution to studies on Roma wall painting materials and techniques in Greece: Corinth, the southeast building, Proceedings of the International Workshop on Roman Wall Painting, Fribourg, 1996, 1–373

[19] A. Moropoulou, A. Bakolas, K. Bisbikou, Journal of Cultural Heritage, 1 (**2000**) 1, 45–58, doi:10.1016/S1296-2074(99)00118-1

[20] J. Elsen, Cemente and Concrete Research, 36 (**2006**) 8, 1416–1424, doi:10.1016/j.cemconres.2005.12.006

[21] S. Buser, Basic geological map of SFRJ, sheet Celje, 1:100000, 1979

UDK 669.21:620.3:537.533.35
Original scientific article/Izvirni znanstveni članek

ISSN 1580-2949
MTAEC9, 49(5)791(2015)

Au-NANOPARTICLE SYNTHESIS VIA ULTRASONIC SPRAY PYROLYSIS WITH A SEPARATE EVAPORATION ZONE

SINTEZA NANODELCEV ZLATA Z ULTRAZVOČNO RAZPRŠILNO PIROLIZO Z LOČENO CONO IZHLAPEVANJA

Peter Majerič[1], Bernd Friedrich[2], Rebeka Rudolf[1,3]

[1]University of Maribor, Faculty of Mechanical Engineering, Smetanova ulica 17, 2000 Maribor, Slovenia
[2]RWTH Aachen University, IME Process Metallurgy and Metal Recycling, Germany
[3]Zlatarna Celje d.d., Kersnikova ulica 19, 3000 Celje, Slovenia
peter.majeric@um.si

Prejem rokopisa – received: 2014-10-17; sprejem za objavo – accepted for publication: 2014-11-11

doi:10.17222/mit.2014.264

Some experiments were conducted in connection with the gold-nanoparticle production in an effort to produce a more accurate model for determining the gold-nanoparticle synthesis with a modified ultrasonic spray pyrolysis (USP). As previous experiments with gold nanoparticles yielded nanoparticles of various shapes (spherical, triangular, cylindrical, etc.), a focus on synthesizing only spherical nanoparticles is underway, as a mixture of different shapes is difficult to characterize and utilize. One of the factors for the particle formation is droplet evaporation. In an attempt to produce the optimum conditions for droplet evaporation with the solvent diffusion and precipitation, a separate furnace and a separate reaction-gas inlet were used. This modification separates the evaporation stage from the reaction stage, compared to the standard USP set-up. Using relatively low temperatures, from 60 °C up to 140 °C, for the evaporation stage provides for more time and better conditions for the diffusion of the solvent into the center of a droplet and a higher probability of forming a spherical particle.

Keywords: ultrasonic spray pyrolysis, gold nanoparticles, aerosol droplet evaporation, TEM microscopy

Prispevek opisuje sintezo nanodelcev zlata, ki smo jo izvedli z modificirano ultrazvočno razpršilno pirolizo (USP) s ciljem postavitve čim bolj realnega teoretičnega modela. Pri prejšnjih eksperimentih sinteze nanodelcev zlata smo dobili nanodelce različnih oblik (sferične, trikotne, cilindrične, itd.), zato smo se pri tej raziskavi osredinili na izdelavo sferičnih nanodelcev. Morfološko različni nanodelci so ovira ne samo pri karakterizaciji, ampak tudi kasneje pri sami uporabi. Pri sintezi nanodelcev ima velik vpliv na končno morfologijo izhlapevanje kapljic aerosola. Za zagotovitev razmer za izhlapevanje kapljic, ki omogočajo nastanek sferičnih nanodelcev, smo v procesu USP uporabili ločeno ogrevalno območje in ločen vnos reakcijskega plina. Ta modifikacija namreč ločuje stopnjo izhlapevanja od stopenj reakcij za nastanek nanodelcev. Nižja temperatura v fazi izhlapevanja (med 60 °C in 140 °C) omogoča boljše razmere za difuzijo topljenca do središča kapljice in večjo verjetnost nastanka sferičnih nanodelcev.

Ključne besede: ultrazvočna razpršilna piroliza, zlati nanodelci, izhlapevanje kapljic aerosola, TEM-mikroskopija

1 INTRODUCTION

Spray pyrolysis is a well-known method for obtaining nanoparticles of various shapes and sizes from a wide variety of materials. This is a process that creates powders or suspensions from droplets of a solution with a dissolved selected material[1,2]. There are variants of this process in terms of droplet generation, droplet-transportation orientation and final nanoparticle collection. However, the process is always the same and follows these steps: droplet generation, droplet transportation into the heating zone, particle formation from the droplet, particle collection.

Ultrasonic spray pyrolysis (USP) uses ultrasound to produce aerosol droplets from a precursor solution, a carrier gas for the transportation of the aerosol to the reactor furnace, a reaction gas for the formation of nanoparticles (if needed), a reactor furnace for the nanoparticle formation and a collection system for nanoparticles. The principle of nanoparticle production lies in the use of heavily diluted precursor solutions and the creation of small droplets. Ultrasound produces very small aerosol droplets in the range of a few micrometers in diameter (from 1 μm to 10 μm), or more, depending on the ultrasound frequency and the parameters of the used solution[3]. Using small solution concentrations the micron-sized droplets are evaporated and the quantity of the dried solute particles left behind is in the nano-range. By

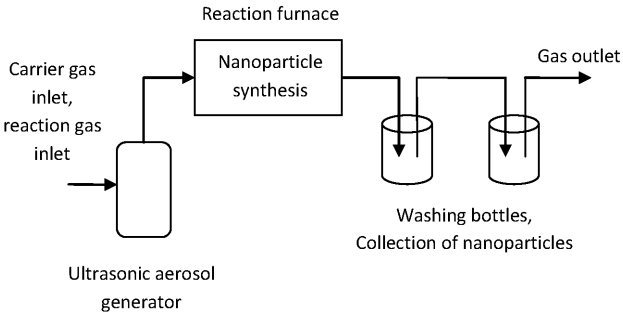

Figure 1: Schematic of the USP appliance previously used for the nanoparticle synthesis
Slika 1: Shema naprave USP, uporabljene za sintezo nanodelcev

increasing or decreasing the solute concentration inside the droplet, greater or smaller nanoparticles can be acquired. In theory, every aerosol droplet produces one nanoparticle. This is known as the one-particle-per-droplet mechanism[2].

For the gold-nanoparticle production with USP we used a solution of hydrogen tetrachloroaurate ($HAuCl_4$) with nitrogen as the carrier gas for the aerosol droplets and hydrogen for the reduction of dried gold-chloride particles into gold nanoparticles. In the previous publications we reported synthesizing gold nanoparticles of different sizes and differing shapes such as irregular, spherical, triangular and cylindrical size[4]. We also noticed some unexpected processes, such as the formation of nanoparticles inside the ultrasonic aerosol generator. This caused a change in the color of the initial precursor solution from a clear yellow to a dark brown solution after the synthesis.

The formation of gold nanoparticles occurs at relatively low temperatures during spray pyrolysis (theoretically, a decomposition of $HAuCl_4$ begins at 258 °C)[5]. This means that the conditions of the aerosol formation via ultrasound and the presence of the reduction hydrogen gas inside the generator may cause the nanoparticles to start forming inside the generator (**Figure 1**). A solution was proposed for this problem, where the reduction gas would be introduced at a later stage when the aerosol is already formed. This also provides for an opportunity to connect a separate evaporation stage to the current synthesis set-up.

The separate evaporation stage would ensure the formation of dried spherical particles of gold chloride before the reaction stage involving hydrogen. The separate heating zone (the evaporation stage) could accomplish this using the low temperatures required for a slow evaporation of the solvent. Theoretically, when the solvent (water) evaporation is slow enough, the solute (gold chloride) will diffuse into the center of a droplet, forming a dried spherical particle (**Figure 2**)[6] and, without the reaction gas present at this stage, the particles of gold chlorides cannot form on the surfaces of the droplets.

After the evaporation, hydrogen gas is introduced into the next heating zone (the reaction stage) and dried particles are reduced from gold chloride to gold. The particles are then collected for analysis. The dried-nanoparticle form can also be an indicator of the final nanoparticle form (**Figure 2**). For this reason, spray drying was utilized, with which we acquired dried particles only from $HAuCl_4$ solution droplets. These experiments are only discussed briefly in this article. There are descriptions of several models of the solute precipitation from a drying solution droplet[6], where the predicted dried-particle form depends largely on the solution concentration, the droplet size, the evaporation rate and the solubility of the solute, while other parameters, such as the relative humidity and the aerosol-droplet quantity, do not affect the dried-particle formation so much.

In our research for the application of the produced gold nanoparticles in medicine it was shown that the sizes of around 50 nm nominally lead to the best results regarding cytotoxicity and biocompatibility[7]. From a theoretical standpoint this means that low concentrations of gold should be used in the precursor solution. Low concentrations of the material in the precursor solution for the nanoparticle production also provide better conditions for a solid, spherical nanoparticle formation[8].

The separate evaporation zone with USP allows a better control of the particle formation during the first stages of the synthesis process. This, in turn, allows a production of more uniformly spherical nanoparticles, which are better suited for the applications in medicine compared to the mixture of nanoparticles of spherical, triangular and cylindrical shapes.

2 MATERIALS AND METHODS

For the aerosol-droplet generation we used an ultrasonic nebulizer Gapusol 9001 RBI (France), with an ultrasonic frequency of 2.5 MHz. The carrier gas, nitrogen, was passed through the nebulizer into the tubes leading towards the furnaces. Two tube furnaces were used; the first one was kept at the lower temperatures required for the evaporation, while the second one was kept at the higher temperatures, required for the nanoparticle-synthesis reactions. Hydrogen gas was released into the tubes between the furnaces to prevent a premature nanoparticle reduction before the droplets were completely evaporated (**Figure 3**). The washing bottles were filled with water for particle collection.

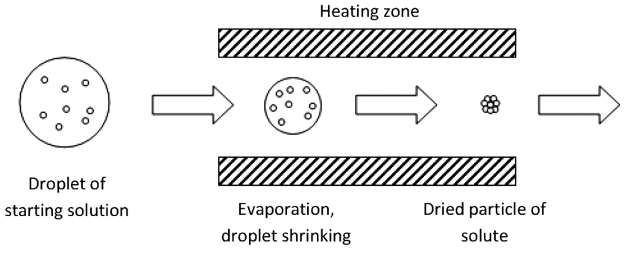

Figure 2: Simple presentation of the evaporation of an aerosol droplet with solute precipitation

Slika 2: Enostavna predstavitev izhlapevanja kapljice aerosola in izločanje topljenca

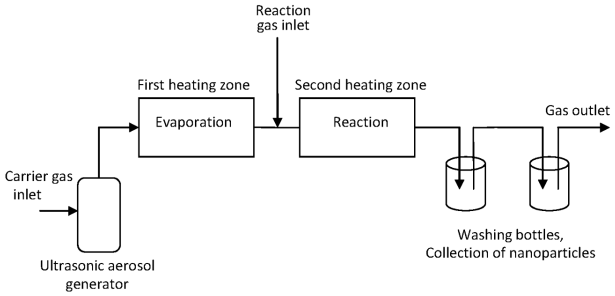

Figure 3: Schematic of the modified USP appliance used for experiments

Slika 3: Shema spremenjene naprave USP za izvedene eksperimente

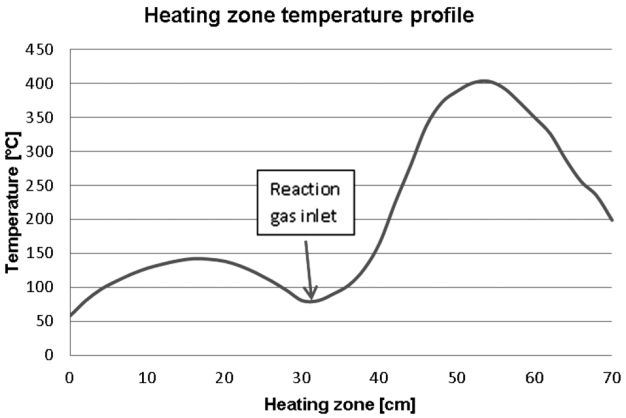

Figure 4: Temperature profile of the heating zone for aerosol-droplet evaporation (left side, before the gas inlet) and nanoparticle reactions (right side, after the gas inlet)

Slika 4: Temperaturni profil ogrevanega območja za izhlapevanje kapljic aerosola (leva stran grafa – pred vstopom plina) in reakcije nanodelcev (desna stran grafa – po vstopu plina)

The precursor solution in the aerosol generator was kept at 21 °C with a thermostat. The generated aerosol was carried into the evaporation heating zone via the quartz tubes with a diameter of 20 mm by nitrogen gas at a flow rate of 1.5 L/min. The residence time of the droplets/dried particles in the evaporation zone was 3.77 s. Both heating zones were 30 cm long, with a 5 cm gap between them for the reduction-gas inlet. The reduction gas, hydrogen, was passed into the tubes between the heating zones at a flow rate of 1 L/min. The residence time of the particles inside the second heating zone was 2.26 s.

The temperature profile of the two furnaces was measured prior to the nanoparticle synthesis using only water for the aerosol generation and nitrogen gas at both gas inlets (**Figure 4**).

In order to determine the feasibility of dried-nanoparticle collection a few experiments were performed with only the first furnace and without hydrogen gas (**Figure 5**). The aim of these experiments was to determine the morphology of dried particles from aerosol droplets before the final nanoparticle reactions. The particles were collected on a filter paper as they were assumed to be the particles of gold chloride. As gold chloride is highly soluble it would not be possible to collect it in wash bottles containing water, alcohol, or similar.

The experiments performed are presented in **Table 1**.

TEM images with an EDS analysis were used for the nanoparticle characterization.

3 RESULTS AND DISCUSSION

A number of thermal measurements were performed to ensure the best possible conditions for the particle formation. The temperatures measured were from 60 °C to 140 °C for the first furnace and from 250 °C to 400 °C for the second furnace. At the very low temperature settings (60–80 °C) for the first furnace, more condensation was observed in the tubes, resulting in an aerosol droplet loss with the synthesis. To avoid the needless condensation, the temperature at which no condensation was observed in the first furnace was selected. Condensation of aerosol droplets reduces the nanoparticle output.

A reasonable temperature was selected for the second furnace, where the temperature has to be high enough to allow for the gold-nanoparticle formation while ensuring a complete reaction so that no unreacted particles exit in the second furnace. The temperature profile of the heating zones is shown in **Figure 5**.

In the previous experiments of the nanoparticle synthesis with USP gold nanoparticles of different shapes were obtained without a separate evaporation stage. The collected nanoparticles were of spherical, irregular, triangular and cylindrical shapes[4]. In comparison, separating the evaporation stage from the reaction and densification stages yielded mostly non-ideally spherical nanoparticles and some irregularly shaped nanoparticles. Lower concentrations of gold in the precursor yielded less irregular shapes of the nanoparticles.

The average nanoparticle sizes were also reduced by separating the droplet evaporation from the rest of the process. Using a precursor solution with 2.5 g/L Au and an ultrasound frequency of 2.5 MHz, sizes ranging from 10–250 nm were obtained without a separate evaporation zone[4] (**Table 2**). With a separate evaporation zone, sizes ranging from 10–80 nm were obtained (**Figure 6** and **Table 2**). It seems there are less agglomeration and par-

Table 1: Experiments performed with the USP device

Tabela 1: Eksperimenti, izvedeni z USP-napravo

Experiment	Type	Au solution concentration (g/L)	Collection medium
1	Droplet evaporation	0.5	Filter paper
2	Droplet evaporation	1.25	Filter paper
3	Droplet evaporation	2.5	Filter paper
4	Nanoparticle synthesis	0.5	Water
5	Nanoparticle synthesis	1.25	Water
6	Nanoparticle synthesis	2.5	Water
7	Nanoparticle synthesis	5	Water

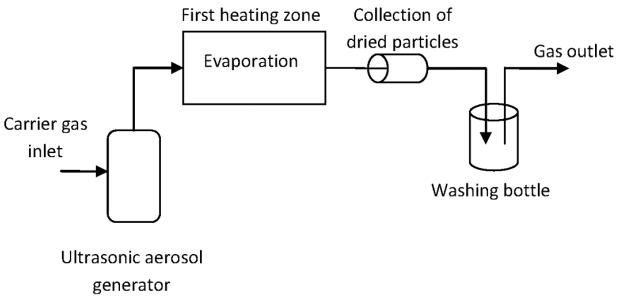

Figure 5: Schematic of the device for dried-nanoparticle-collection experiments

Slika 5: Shema naprave za preizkus zbiranja posušenih nanodelcev

ticle growth present when the nanoparticles are synthesized with a separate evaporation zone.

Table 2: Comparison of nanoparticle sizes after USP synthesis with and without a separate evaporation zone
Tabela 2: Primerjava velikosti nanodelcev pri sintezi z USP brez ločenega območja za izhlapevanje in z njim

USP	Gold concentration in precursor solution	Synthesized gold-nanoparticle size distribution
Without a separate evaporation zone	2.5 g/L	10–250 nm
With a separate evaporation zone	2.5 g/L	10–80 nm

The sizes of the nanoparticles are generally accepted to be mainly dependent upon the precursor concentration and droplet size. In our experiments, the droplet sizes are considered to be the same in each experiment, while the precursor concentration was changed for each experiment. With a gold concentration of 5 g/L in the precursor solution we obtained nanoparticles in the size range from around 50 nm up to 300 nm. While there are small nanoparticles present, the bulk of the nanoparticles have a diameter of about 200 nm. There are also a bigger number of irregularly shaped nanoparticles, with less spherical nanoparticles present. More agglomeration is also observed when using such a precursor solution concentration. The separate evaporation zone seems to be beneficial for the production of more uniformly shaped nanoparticles as the irregularly shaped nanoparticles have round edges even though they are not spherical. When not using the separate evaporation zone, nanoparticles have sharper edges in the form of triangles and discs and irregular shapes with sharp edges[4]. Such shapes did not appear in the case of the separate evaporation zone. The separate evaporation zone is, therefore, favorable in order to obtain only spherical shapes of the nanoparticles produced with USP.

With a gold concentration of 2.5 g/L in the precursor solution, we obtained sizes ranging from 10 nm to 80 nm. The average size of the nanoparticles with such a concentration is 55 nm. The shapes of the nanoparticles are still not ideally spherical as there are still particles with irregular shapes present. However, even though they are not ideally spherical, their shapes appear to have a high order of sphericity, with the smaller nanoparticles being more spherical than the bigger ones.

A gold concentration of 1.25 g/L in the precursor solution yielded nanoparticles in the range from 10 nm to 40 nm. The bulk of the nanoparticle sizes are about 20 nm. With a precursor concentration of 0.5 g/L of gold in the solution the nanoparticle sizes obtained were from 10 nm to 40 nm, with the average nanoparticle size being somewhat smaller, around 15 nm.

The shapes of the nanoparticles with gold concentrations of (2.5, 1.25 and 0.5) g/L in the precursor solution are very similar. With all three concentrations we obtained a mixture of spherical and irregularly shaped nanoparticles (**Figures 6** and **7**).

The separate evaporation zone yielded better results regarding the uniformity of the shapes and sizes with higher gold concentrations (2.5 g/L and 5 g/L) in the precursor. Even though the shapes are still not ideally uniform, less diverse shapes are produced while using the separate evaporation zone in the USP process. The sizes of the obtained nanoparticles are also less dispersed. In this regard, the separated evaporation zone is useful for producing gold nanoparticles of more similar shapes and sizes with USP. This is not apparent when using lower gold concentrations (0.5 g/L and 1.25 g/L). With lower concentrations, solid spherical shapes are formed more readily with USP, and the benefits of the separate evaporation zone are not seen so easily (**Figure 7**). From a theoretical standpoint, using a low concentration in the precursor solution is effective for producing solid and more uniform nanoparticles with the standard USP

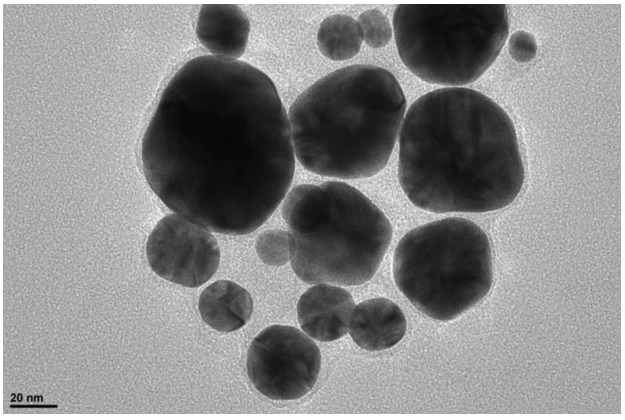

Figure 6: TEM image of gold nanoparticles obtained with USP with a separate evaporation zone; gold concentration in precursor solution: 2.5 g/L
Slika 6: TEM-posnetek nanodelcev zlata, pridobljenih z USP z ločenim območjem za izhlapevanje; koncentracija zlata v začetni raztopini: 2,5 g/L

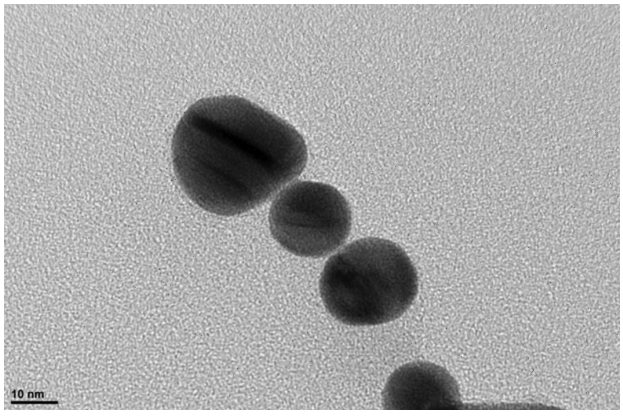

Figure 7: TEM image of gold nanoparticles obtained with USP with a separate evaporation zone, gold concentration in precursor solution: 0.5 g/L
Slika 7: TEM-posnetek nanodelcev zlata, pridobljenih z USP z ločenim območjem za izhlapevanje; koncentracija zlata v začetni raztopini: 0,5 g/L

process. Even though spherical shapes of the nanoparticles were formed in our experiments with the modified USP process, irregular shapes were also present.

As a result, it is difficult to determine the effectiveness of the separate evaporation zone when using lower concentrations of gold in the precursor solution. More work is needed with regard to the other synthesis parameters in order to determine the feasibility of using the separate evaporation zone when using lower gold concentrations in the precursor solution. However, from a technological point of view, the separate evaporation zone eliminates the reactions with hydrogen and the particle formation inside the ultrasound generator. The precursor solution remained the same before and after the nanoparticle synthesis, which is a good indicator of this technical issue being resolved, compared to the standard USP set-up where the precursor solution changes after the experiment.

The separate evaporation zone used in our experiments gave some favorable results with respect to reducing the nanoparticle-size distribution and producing more uniformly shaped nanoparticles. In order to advance the research in the direction of producing uniform shapes, other parameters, such as the gas flow, should be studied experimentally, or further modifications should be made to the USP process.

In the experiments with the droplet evaporation the produced particles were collected on a filter paper made from cellulose in order to prevent a re-dissolving of the gold chloride particles. This collection yielded two substances, or types of particles, visible on the filter paper after the collection. On the edges of the used filter paper a purple substance was collected, while at the center of the filter paper we collected a yellowish substance. This suggests that two chlorides of gold were collected: AuCl appeared in the form of yellow crystals, while $AuCl_3$ appeared in the form of red crystals[9].

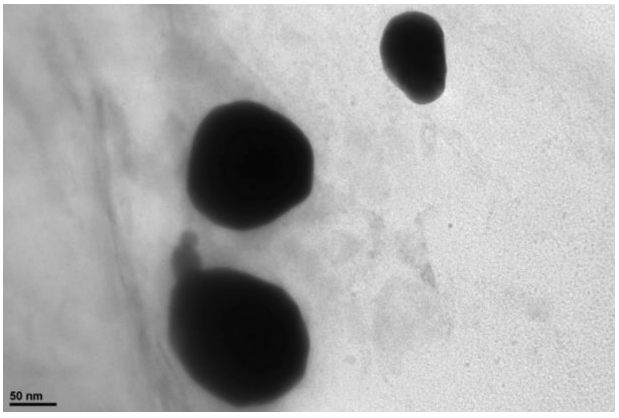

Figure 8: Nanoparticles collected on filter paper after evaporation, created with a gold concentration of 1.25 g/L in the precursor solution
Slika 8: Nanodelci, zbrani na filter papirju po izhlapevanju, narejeni s koncentracijo zlata 1,25 g/L v začetni raztopini

It is assumed that the nanoparticle morphology is dependent mainly upon the evaporation stage. The optimum drying of the aerosol droplets theoretically produces solid, spherical particles of the dried solute. In order to check the feasibility of dried-nanoparticle collection after the evaporation, the particles were first collected on filter paper (**Figure 8**). The particles collected in this way are difficult to characterize and an improved method for collecting dried nanoparticles will be utilized in future research for an easier particle characterization after the collection.

After the collection of dried particles, the correlation of dried particles with the final nanoparticles is examined. This insight into the separate synthesis stages provides a better understanding of the process and allows us to produce a more accurate model for determining the gold-nanoparticle synthesis with a separate evaporation zone.

4 CONCLUSION

Gold nanoparticles were synthesized using USP with a separate evaporation zone. The gold concentration in the precursor solution used for the aerosol generation was the primary variable parameter in order to determine the effects of the separate evaporation zone on the final nanoparticle sizes and shapes. When using higher concentrations of gold in the precursor solution, the experiments showed more uniformly shaped nanoparticles in the case of the separate evaporation zone compared to the standard USP set-up. A narrower size distribution of the gold nanoparticles was also obtained in comparison to the standard USP set-up. When using lower gold concentrations in the precursor solution, these advantages are not so obvious. As the separate evaporation zone does not entirely prevent the presence of irregularly shaped nanoparticles, similar nanoparticles can be obtained without a separate evaporation zone at low precursor-solution concentrations. However, it is apparent that separating the evaporation stage from the reaction and densification stages improved the process to some extent so that more nanoparticles of spherical shapes and more uniform sizes are produced. The produced nanoparticles are smaller in size (10–80 nm for 2.5 g/L Au in the precursor solution) compared to the nanoparticles produced without a separate evaporation zone (10–250 nm for 2.5 g/L Au in the precursor solution). Further work on the modifications and parameter optimization is now needed to improve the process in pursuit of gold nanoparticles with uniform shapes and as narrow a nanoparticle-size distribution as possible.

Acknowledgment

We would like to thank Dr. Darja Jenko for performing the TEM analysis on the Au nanoparticles. This research was made possible by the Slovenian Research Agency (ARRS), the Young Researcher Program and the

Slovenian Public Fund for the Development of Human Resources.

5 REFERENCES

[1] G. L. Messing, S. C. Zhang, G. V. Jayanthi, Ceramic Powder Synthesis by Spray Pyrolysis, J. Am. Ceram. Soc., 76 (**1993**) 11, 2707–2726, doi:10.1111/j.1151-2916.1993.tb04007.x

[2] S. C. Tsai, Y. L. Song, C. S. Tsai, C. C. Yang, W. Y. Chiu, H. M. Lin, Ultrasonic spray pyrolysis for nanoparticles synthesis, J. Mater. Sci., 39 (**2004**) 11, 3647–3657, doi:10.1023/B:JMSC.0000030718.76690.11

[3] J. Bogović, A. Schwinger, S. Stopic, J. Schröder, V. Gaukel, H. P. Schuchmann, B. Friedrich, Controlled droplet size distribution in ultrasonic spray pyrolysis, Metall, 65 (**2011**) 10, 455–459

[4] S. Stopic, R. Rudolf, J. Bogovic, P. Majeric, M. Colic, S. Tomic, M. Jenko, B. Friedrich, Synthesis of Au nanoparticles prepared by ultrasonic spray pyrolysis and hydrogen reduction, Mater. Tehnol., 47 (**2013**) 5, 577–583

[5] R. Dittrich, S. Stopic, B. Friedrich, Mechanism of nanogold formation by ultrasonic spray pyrolysis, Proceeding of the EMC Conference, Düsseldorf, Germany, 2011, 385

[6] G. V. Jayanthi, S. C. Zhang, G. L. Messing, Modeling of Solid Particle Formation During Solution Aerosol Thermolysis: The Evaporation Stage, Aerosol Sci. Technol., 19 (**1993**) 4, 478–490, doi:10.1080/02786829308959653

[7] S. Tomić, J. Đokić, S. Vasilijić, N. Ogrinc, R. Rudolf, P. Pelicon, D. Vučević, P. Milosavljević, S. Janković, I. Anžel, J. Rajković, M. S. Rupnik, B. Friedrich, M. Čolić, Size-Dependent Effects of Gold Nanoparticles Uptake on Maturation and Antitumor Functions of Human Dendritic Cells In Vitro, PLoS ONE, 9 (**2014**) 5, e96584, doi:10.1371/journal.pone.0096584

[8] T. T. Kodas, M. J. Hampden-Smith, Aerosol Processing of Materials, 1st edition, Wiley-VCH, New York 1998

[9] D. R. Lide (Ed.), CRC Handbook of Chemistry and Physics, 80th Edition, CRC Press, Boca Raton 1999

UDK 669.715:621.74:536.421.4
Original scientific article/Izvirni znanstveni članek

ISSN 1580-2949
MTAEC9, 49(5)797(2015)

DETERMINATION OF THE CRITICAL FRACTION OF SOLID DURING THE SOLIDIFICATION OF A PM-CAST ALUMINIUM ALLOY

DOLOČANJE KRITIČNEGA DELEŽA STRJENE FAZE MED STRJEVANJEM V PM ULITE ALUMINIJEVE ZLITINE

Ramazan Kayikci[1], Murat Colak[2], Selcuk Sirin[1], Engin Kocaman[1], Neset Akar[3]

[1]Sakarya University, Faculty of Technology, Dept. of Met. Mat. Eng., Sakarya, Turkey
[2]Bayburt University, Faculty of Eng., Dept. of Mat. Sci. and Nanotech. Eng., Bayburt, Turkey
[3]Gazi University, Faculty of Technology, Dept. of Met. Mat. Eng., Ankara, Turkey
rkayikci@sakarya.edu.tr

Prejem rokopisa – received: 2014-10-20; sprejem za objavo – accepted for publication: 2014-11-27

doi:10.17222/mit.2014.266

During the solidification of aluminium alloys, a flow of the interdendritic liquid through the mushy zone plays an important role in the feedability and shrinkage-driven porosity formation. Therefore, for almost all the studies about casting modelling, a good knowledge of the mushy-zone behaviour is necessary.
In this study, the limit of the mushy-zone permeability for permanent-mould (PM)-cast aluminium alloys was investigated. A novel experimental technique was developed to quantify the value of the critical fraction of solid (CFS) at which the interdendritic feeding stops. Grain-refined and non-grain-refined aluminium alloys were used to evaluate the effect of the grain size on the CFS limit of both the non-grain-refined and fully grain-refined alloys. Three different initial mould temperatures were used to find if the mould temperature has any effect on the feeding of a casting. Alloys of varying solidification intervals were also used to determine the critical fraction of solid (CFS) for the feeding limit of solidifying castings.
The results showed that the CFS values for solidifying aluminium alloys may vary from 34 % to 57 % depending on the casting conditions. The results also showed that for A356 aluminium-alloy castings the CFS value is not an alloy property, yet it significantly depends on the parameters such as the grain refinement and the modification of eutectic silicon.

Keywords: critical fraction of solid, mushy-zone permeability, PM casting

Med strjevanjem aluminijevih zlitin ima tok meddendritne taline skozi testasto področje pomembno vlogo pri napajanju in nastajanju poroznosti zaradi krčenja. Zato je skoraj v vseh modelih ulitkov potrebno dobro poznanje vedenja testastega področja.
V tej študiji je bila iskana meja prepustnosti testastega področja pri aluminijevih zlitinah, ulitih v stalne forme (PM). Razvita je bila nova eksperimentalna tehnika za oceno kritičnega deleža strjene faze (CFS), pri kateri se meddendritno napajanje ustavi. Uporabljene so bile aluminijeve zlitine z udrobnjenimi in neudrobnjenimi zrni za oceno vpliva velikosti zrn na mejno CFS pri obeh vrstah zlitin. Izmerjene so bile tri različne temperature kokil, da bi ugotovili, ali temperatura kokile vpliva na napajanje ulitka. Uporabljene so bile tudi zlitine z različnim intervalom strjevanja, da bi ugotovili kritičen delež trdne faze (CFS), ki pomeni mejo napajanja pri strjevanju ulitkov.
Rezultati so pokazali, da vrednosti CFS variirajo med 34 % in 57 %, odvisno od razmer pri ulivanju. Rezultati so tudi pokazali, da pri ulitkih iz aluminijeve zlitine A356 vrednost CFS ni odvisna samo od zlitine, temveč je zelo odvisna od parametrov, kot sta zmanjšanje zrn in modifikacija evtektičnega silicija.

Ključne besede: kritičen delež trdne faze, prepustnost testastega področja, ulivanje v stalne forme (PM)

1 INTRODUCTION

The solidification of aluminium alloys generally starts with dendrites of a aluminium and they continue to grow into a coherent network. With the progress of solidification, several intermetallics might precipitate and the solidification usually completes with one or more eutectic phases.[1] While the solidification continues, the viscosity of liquid aluminium alloys increase with a decrease in the fluidity. During the solidification, aluminium alloys pass through a long mushy region during which the liquid requirement for a contraction of solidifying dendrites can be compensated with a flow of the interdendritic liquid.[2] These mechanisms continue until a certain stage of the solidification in the mushy zone. Dendrite coherency is established in a later stage and the dendrite network gains some rigidity which becomes resistant against the flow of the interdendritic liquid.[3] This phenomenon continues until the liquid flow stops completely due to the blockage of the growing solid dendrites.[3] In the literature about casting solidification, this stage of the solidification is defined as either 'the critical fraction of solid' or 'the critical fraction of liquid'.[4]

At the critical fraction of the solid (CFS) stage, if there is still a need for the liquid flow for feeding the solidifying liquid, a pressure drop is created due to the resistance to the liquid flow. If this negative pressure in the mushy zone cannot be balanced by the flow of the liquid due to the dendrite blockage it may lead to some shrinkage porosity.[5] Shrinkage cavities that can often be seen in casting processes are typical examples of this porosity. Today high-performance technology requires

high-quality and light-section castings and therefore cannot even tolerate micro-porosity[6]. To avoid the formation of micro- and macro-porosities within the critical sections of cast parts, a variety of 3D casting-modelling software packages, often referred to as casting simulation packages, have been used during the design stages of casting processes. Since the CFS point is practically the end of the feeding action within a mushy region, it has been used as one of the most critical boundary conditions in all the commercial casting-simulation software packages. Therefore, to model aluminium casting processes with different alloys and cooling-solidification conditions, a good knowledge about the critical fraction of solid (CFS) is necessary.

In this study, using commercial A356 aluminium casting alloys, the CFS point of the mushy zone was investigated. Permanent mould castings with three different alloy conditions, namely, the as-cast, the grain-refined, and the grain-refined and modified conditions were used. Casting-simulation techniques, X-ray radiography, the Archimedes density measurement and metallographic techniques were also employed.

2 EXPERIMENTAL WORK

The experimental part of the present study is twofold. In the first part an A356 aluminium alloy was cast in a steel mould and the resulting shrinkage was examined for varying casting conditions. In the second part, the casting and mould geometries were modelled using the SOLIDCast 3D casting-simulation software. Finally, the amounts of the shrinkage porosity obtained from the actual castings were compared with the results from the computer modelling and the feeding threshold value (the critical fraction of solid) was determined for each casting condition.

The casting geometry and the solidified cast part within the mould are shown in **Figures 1a** and **1b**, respectively. The casting geometry was specially designed to obtain two thick sections connected to each other with a narrow feeding neck to create an insufficient feeding path so that it could produce a measurable amount of the shrinkage porosity at the bottom part of the casting, used for comparison and evaluation.

A chemical analysis of the A356 alloy was carried out with a Foundry-Master optical emission spectrometer before and after each addition to the master alloy as shown in **Table 1**. Primary ingots of 8 kg were melted in a SiC crucible in a bell-type electric-resistance-heated furnace. The alloy was degassed with dry nitrogen at 720 °C for 6 min before being cast into a steel mould which was preheated to 300 °C. The casting process was repeated and followed by an addition of an Al5Ti1B-type grain refiner or an Al-10Sr modification of the master alloy. The castings were radiographically tested on both sides to check whether any shrinkage porosity had occurred. Their upper and bottom parts were separated by cutting them apart from the top of the narrow neck and the cast density of the bottom parts was measured, using the Archimedes system of weighing the parts in air and in water. Finally, the castings were sectioned along the vertical axis to reveal any shrinkage in the central regions of the castings.

Table 1: Chemical composition of the A356 alloy used in the experiments (Al balance), *w*/%

Tabela 1: Kemijska sestava zlitine A356, uporabljene pri preizkusih (osnova je Al), *w*/%

Elements	Fe	Si	Cu	Mn	Mg	Ti	Sr
As-cast	0.35	6.9	0.1	0.35	0.38	0.03	0
TiB modified	0.35	6.8	0.1	0.34	0.36	0.12	0
Sr modified	0.35	6.82	0.1	0.3	0.3	0.1	0.08

A commercial 3D casting-simulation package, SOLIDCast, was used for modelling the castings. The system solves the Fourier heat-transfer equation with the finite-difference method and calculates the volume change within the casting with respect to the temperature. It assumes that the feeding takes place under the gravity effect and the volume of the total final shrinkage

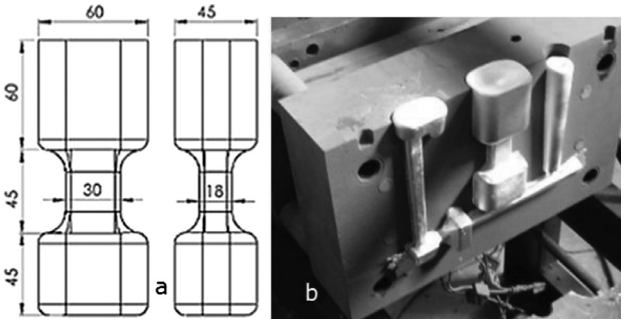

Figure 1: a) Casting geometry, b) solidified casting within a permanent mould

Slika 1: a) Geometrija ulitkov, b) strjen ulitek v stalni kokili

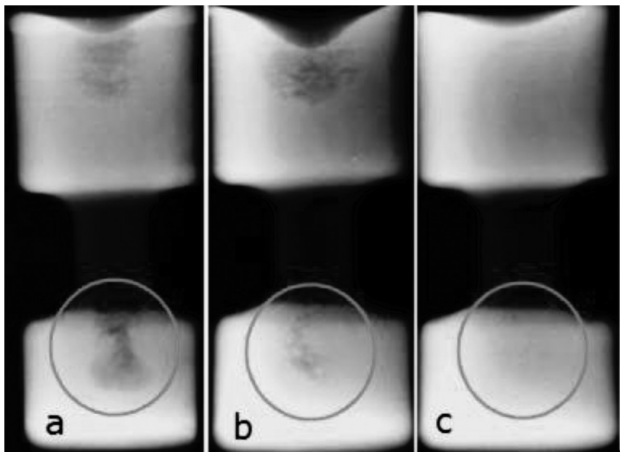

Figure 2: Scanned view of the radiographic test films of A356 castings: a) as cast, b) with added TiB, c) with added TiB + Sr

Slika 2: Skenirani posnetki filmov rentgenskih posnetkov ulitkov iz A356: a) lito stanje, b) dodan TiB, c) dodan TiB + Sr

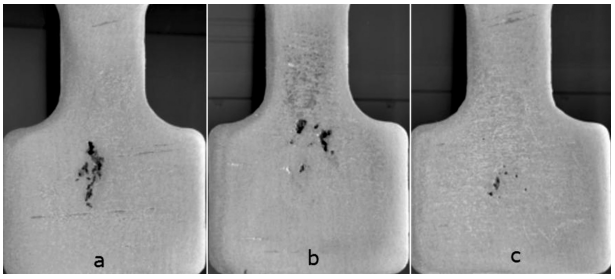

Figure 3: Cross-sections of A356 castings: a) as cast, b) with added TiB, c) with added TiB + Sr
Slika 3: Prerez ulitka iz A356: a) lito stanje, b) dodan TiB, c) dodan TiB + Sr

pores is equal to the volume of the unfed contracted liquid metal. The system can allow the feed-liquid movement as long as the feeding path is open, i.e., the fraction of solid (FS) is below the critical value in the mushy zone.

3 RESULTS AND DISCUSSION

A set of the radiographic test results representing the as-cast, TiB-modified and TiB + Sr-modified castings is shown in **Figure 2**. The potential shrinkage areas in the bottom sections of the castings are highlighted with circles. Dark smoky marks in the circled areas indicate the shrinkage porosity. The largest shrinkage occurred in the casting in the as-cast condition indicating the lowest feeding action of this particular casting. This was associated with a shorter CFS time due to an early blockage of coarser dendrites. On the other hand, the casting that was fully grain refined and modified with an addition of TiB + Sr revealed the smallest amount of the shrinkage porosity. This showed that the longest feeding action took place during the solidification. Only the grain-refined casting (TiB-modified only) showed an intermediate shrinkage porosity. These results are in good agreement with the report on the grain refinement of an aluminium alloy by Birol.[7]

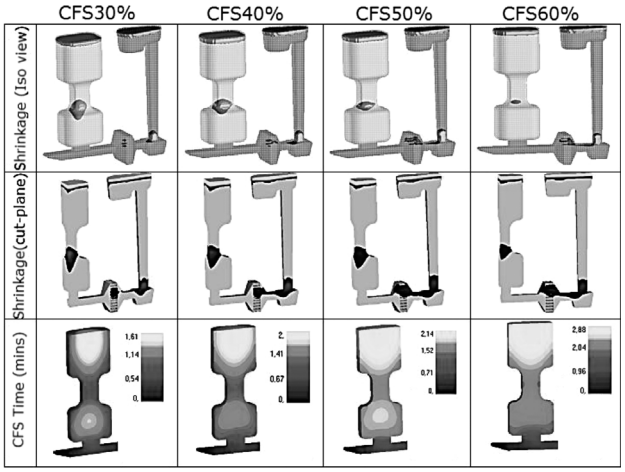

Figure 4: Representative results obtained with a casting simulation with four different CFS conditions
Slika 4: Značilni rezultati, dobljeni s simulacijo ulivanja pri štirih različnih CFS-razmerah

Figure 3 shows macrostructures of the cross-sections of the castings. The shrinkage patterns of the castings reveal characteristics similar to the X-ray radiography pattern shown in **Figure 2**. The percentages of the shrinkage porosity of the castings were determined by subtracting their measured Archimedes densities from the theoretical density of a well-fed PM cast of the A356 alloy. The results obtained from the simulations of the castings are shown in **Figure 4**. This figure shows that increasing the CFS values of the castings resulted in longer feeding times as the time required to reach a given CFS value of the mushy zone also increased. Modelled porosities were obtained directly from the simulation results. These values are given in **Table 2**. The corresponding CFS values for different casting conditions are also given in **Table 2**. A number of simulations were run to change the CFS point of a casting as a boundary condition from 30 % to 70 % and their resulting porosity values were compared with the measured porosity values of the actual castings. Determination of the actual CFS value of each casting was carried out by comparing the measured and modelled densities. When a close match was obtained between the two, the corresponding value of the CFS that was already used as an input boundary condition in that particular casting simulation was assumed to be the right value of the CFS. As seen in **Table 2**, the lowest CFS value of 34 % and the shorter feeding time were obtained for the PM-cast A356 alloy. The CFS value significantly increases with the grain refinement achieved with the TiB addition to the melt, reaching 52 %. The modification of the eutectic silicon with Sr provides further improvement, causing the CFS to rise to 57 %.

Table 2: Comparison of measured and modelled porosity fraction of the castings with their CFS values
Tabela 2: Primerjava izmerjenih in z modelom določenih deležev poroznosti ulitkov z vrednostmi CFS

Experimental castings	Modelling		
Alloy condition	Measured porosity (%)	Calculated porosity (%)	CFS value (%)
As-cast	2.25	2.22	34
TiB modified	1.83	1. 82	52
TiB + Sr modified	1.36	1.36	57

4 CONCLUSIONS

- An experimental casting technique coupled with a casting simulation was studied to determine the CFS values of the commercial A356 alloy in the as-cast, TiB-modified and TiB + Sr-modified conditions.
- The results showed that the CFS point of the mushy zone is not a constant value as it might vary significantly with different conditions of the cast alloy.

- The lowest CFS value of 34 % was obtained for the as-cast A356 alloy, while it increased up to 57 % with a grain refinement and modification of the eutectic silicon by adding TiB + Sr to the alloy.

Acknowledgement

The authors are grateful to The Scientific and Technological Research Council of Turkey (TÜBİTAK) for providing a research grant to the 112M422 project.

5 REFERENCES

[1] M. C. Flemings, Solidification Processing, McGraw-Hill, New York 1974

[2] B. O. Danylo, Ö. N. Doğan, An examination of effects of solidification parameters on permeability of a mushy zone in castings, Journal of Materials Science, 43 (**2008**), 1471–1479, doi:10.1007/s10853-007-2325-z

[3] Ø. Nielsen, S. O. Olsen, Experiment for Quantification of Feedability and Permeability in Industrial Aluminium Alloys, International Journal of Cast Metals Research, 19 (**2006**) 1, 32–37, doi:10.1179/136404606225023336

[4] D. Sun, S. V. Garimella, Numerical and Experimental Investigation of Solidification Shrinkage, Numerical Heat Transfer, Part A: Applications, 52 (**2007**) 2, 145–162, doi:10.1080/10407780601115079

[5] Ch. Pequet, M. Gremaud, M. Rappaz, Modelling of Microporosity, Macroporosity, and Pipe Shrinkage Formation during the Solidification of Alloys Using a Mushy-Zone Refinement Method: Applications to Aluminum Alloys, Metallurgical and Materials Transactions, 33A (**2002**) 7, 2095–2106, doi:10.1007/s11661-002-0041-5

[6] M. Tiryakioğlu, J. Campbell, Guidelines for Designing Metal Casting Research: Application to Aluminium Alloy Castings, International Journal of Cast Metals Research, 20 (**2007**) 1, 25–29, doi:10.1179/136404607X186509

[7] Y. Birol, Grain Refinement in Aluminium Shape Casting, Proc. of the 3rd Int. Aluminium Conference, Arak, Iran, 2012, 1–12

UDK 669.245:621.77:620.186
Original scientific article/Izvirni znanstveni članek

ISSN 1580-2949
MTAEC9, 49(5)801(2015)

MICROSTRUCTURAL EVOLUTION OF INCONEL 625 DURING HOT ROLLING

MIKROSTRUKTURNI RAZVOJ INCONELA 625 MED VROČIM VALJANJEM

Franc Tehovnik, Jaka Burja, Bojan Podgornik, Matjaž Godec, Franci Vode

Institute of Metals and Technology, Lepi pot 11, 1000 Ljubljana, Slovenia

Prejem rokopisa – received: 2015-08-25; sprejem za objavo – accepted for publication: 2015-09-09

doi:10.17222/mit.2015.274

This research provides an overview of the structural changes that occur during the hot rolling of the nickel superalloy Inconel 625. It is well known that microstructure control is of paramount importance concerning the mechanical properties of a material. The microstructure also plays an important role in processing materials at elevated temperature. In this work the hot-rolling behaviour of the Inconel 625 superalloy has been investigated. The specimens were hot rolled at a temperature of 1200 °C using different numbers of passes. During the hot rolling the loads were measured and recorded. A light microscope and an electron microscope, employing the electron-backscatter-diffraction (EBSD) technique, were employed to investigate the microstructure evolution, revealing a necklace dynamic-recrystallization mechanism.

Keywords: nickel superalloy, hot rolling, dynamic recrystallization, necklace mechanism

Raziskava obsega pregled strukturnih sprememb, ki se pojavijo med vročim valjanjem nikljeve superzlitine Inconel 625. Znano je, da je kontrola mikrostrukture odločilnega pomena za mehanske lastnosti materiala. Mikrostruktura ima pomemben vpliv na predelavo materiala pri povišanih temperaturah. Preučevali smo superzlitino Inconel 625 med vročim valjanjem. Vzorci so bili vroče valjani pri temperaturi 1200 °C z različnimi števili prevlekov, med poizkusi smo merili tudi sile valjanja. Vzorce smo preiskali s svetlobnim in elektronskim mikroskopom s tehniko difrakcije povratno sipanih elektronov (EBSD). Raziskali smo razvoj mikrostrukture in potrdili dinamično rekristalizacijo preko "mehanizma ogrlice".

Ključne besede: nikljeva superzlitina, vroče valjanje, dinamična rekristalizacija, mehanizem ogrlice

1 INTRODUCTION

The Inconel nickel-chromium superalloy 625 is well known for its high strength and outstanding corrosion resistance. The strength of the Inconel alloy is derived from the stiffening effect of the molybdenum and niobium on its nickel-chromium matrix. This combination of elements is also responsible for its superior resistance to a wide range of corrosive environments of high severity as well as the high-temperature effects such as oxidation and carburization. Because of these properties, as well as fatigue and creep resistance, nickel-based superalloys are widely used in modern aero engines and gas turbines[1,2].

During the hot deformation of metals and alloys, the material flow behaviour is often very complex. In order to optimize the final mechanical properties, control of the microstructure is of great importance[3]. Studies show that during hot deformation the work hardening, dynamic recovery (DRV) and dynamic recrystallization (DRX) often occur in the metals and alloys with a low stacking-fault energy[4–6]. Generally, DRX is not only an important softening mechanism, but also an effective method to refine the crystal grain size. Therefore, in the case of nickel-based alloys, which retain high strengths at high processing temperatures, causing high rolling loads, DRX plays a decisive role. The aim of the current work was to investigate the microstructure evolution and the nucleation mechanisms of the dynamic recrystallization of Inconel superalloy 625 during hot rolling.

2 EXPERIMENTAL

2.1 Material

Flat specimens of Inconel 625, with the chemical composition given in **Table 1**, were used for hot rolling tests. The specimens were cut from a thick hot-rolled plate; the specimens were 11 mm high, 145 mm long and 46 mm wide.

Table 1: Chemical composition of Inconel 625
Tabela 1: Kemijska sestava Inconela 625

w/%	C	N	Ni	Mo	Nb	Fe	Cr	Ti	Si
Inconel 625	0.012	0.018	63.4	8.7	3.5	0.15	21.8	0.29	0.24

2.2 Hot rolling

Before the hot-rolling experiment the specimens were heated to a temperature of 1200 °C and soaked for 30 min in order to obtain a homogeneous temperature field of 1200 °C before each rolling experiment, regardless of the number of passes used. Up to five rolling passes were employed in this study. The logarithmic deformation per

pass was 0.223. The logarithmic deformation rate during the rolling was calculated to be 7.12 s^{-1} for the first, 7.96 s^{-1} for the second, 8.90 s^{-1} for the third, 9.95 s^{-1} for the fourth and 11.12 s^{-1} for the fifth pass. During the hot rolling the rolling loads were monitored using a measurement system with 2000 recordings per second, and converted to stress by dividing the loads by the contact area. The specimen temperature was measured at the beginning and after each rolling pass. After the hot rolling the rolled specimens were air cooled and prepared for microscopic examination.

2.3 Microstructural analysis

Light microscopy, SEM and SEM-based electron-backscatter-diffraction (EBSD) analyses were performed on the metallographic samples to reveal the microstructure and microstructure evolution during the hot rolling. The microstructure was examined optically using a Nikon Microphot FXA, while the EBSD data were collected in a FE-SEM JEOL JSM 6500F field-emission scanning electron microscope using an HKL Nordlys II EBSD camera and Channel 5 software. The EBSD mapping analyses were performed with samples tilted by 70 ° using a 15 kV accelerating voltage and a 1.5 nA probe current. The EBSD map was generated in steps of 2 μm using 619 × 503 grids with 4 × 4 binning and minimum 5 and maximum 6 band detection and an indexing rate between 92 % and 97 %. The samples were prepared using a classic metallography preparation procedure, including grinding, polishing and etching, and colloidal silica polishing for the EBSD analysis.

3 RESULTS AND DISCUSSION

3.1 Hot rolling of Inconel superalloy

Although the degrees of deformation and the deformation rates used in this study were relatively high, no cracks or failures were observed at the edges of the hot-rolled specimens. The samples after hot rolling and air cooling are presented in **Figure 1**. However, the temperature drop after each rolling pass was found to be significant. The temperature at the end of first rolling pass was 1130 °C, and the dropped to only 840 °C at the end of the fifth pass.

The corresponding loads recorded during the five rolling regimes (number of passes) are given in **Figure 2**. As shown, the loads increase with the increasing number of passes. The values recorded during the first pass were found to be similar for all five regimes, which also applies to all the other sequences. Furthermore, the temperatures measured during each pass did not vary by more than 15 °C between consecutive tests and the five rolling regimes employed.

Nickel superalloys exhibit work hardening at high strains. When comparing the hot rolling of the nickel superalloy Inconel 625 to the superaustenitic steel 904L, done in previous work[7], the nickel superalloy shows a greater deformation resistance. For this reason the initial degree of deformation during the industrial processing of nickel superalloy slabs has to be small. The deformation degrees can be higher when the onset of recrystallization begins at sufficiently high temperatures. However, special care must be taken when processing as-cast microstructures. Otherwise, the ductility of nickel alloys is very good and does not represent any concern. In the present case the microstructure of the initial specimens was already wrought, eliminating any concern about defects occurring due to insufficient ductility.

Figure 3 shows the stress evolution during each rolling pass for up to five passes. The corresponding logarithmic strain rates and temperatures measured at the end of each rolling pass are provided in the figure caption.

Figure 1: Hot rolled and air cooled specimens of Inconel 625, subjected to different numbers of rolling passes
Slika 1: Vroče valjani in na zraku ohlajeni vzorci Inconela 625 z različnimi števili prevlekov

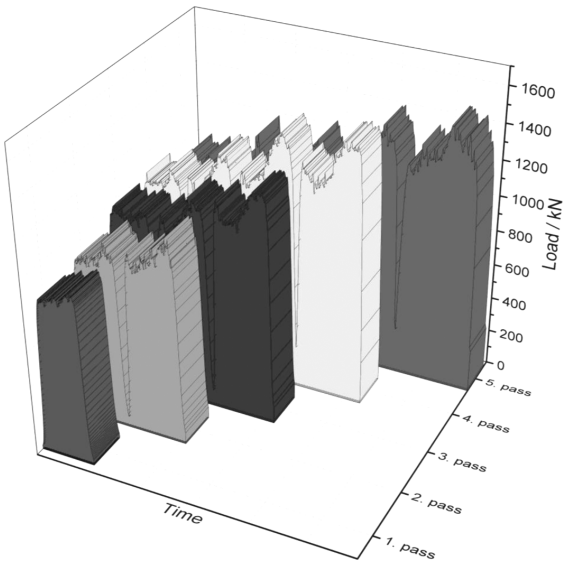

Figure 2: Rolling loads with different numbers of rolling passes
Slika 2: Sile valjanja z različnimi števili prevlekov valjanja

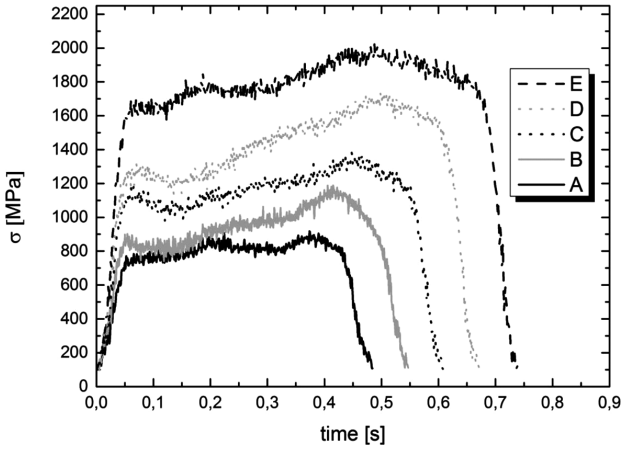

Figure 3: Calculated stress during rolling at different strain rates and the end of rolling temperatures, A first pass $\dot{\varphi} = 7.12\ s^{-1}$, $T = 1131$ °C, B second pass $\dot{\varphi} = 7.96\ s^{-1}$, $T = 1040$ °C, C third pass $\dot{\varphi} = 8.90\ s^{-1}$, $T = 983$ °C, D fourth pass $\dot{\varphi} = 9.95\ s^{-1}$, $T = 940$ °C, E fifth pass $\dot{\varphi} = 11.12\ s^{-1}$, $T = 840$ °C

Slika 3: Izračunane napetosti med valjanjem pri različnih hitrostih deformacije in končnih temperaturah valjanja, A prvi prevlek $\dot{\varphi} = 7{,}12\ s^{-1}$, $T = 1131$ °C, B drugi prevlek $\dot{\varphi} = 7{,}96\ s^{-1}$, $T = 1040$ °C, C tretji prevlek $\dot{\varphi} = 8{,}90\ s^{-1}$, $T = 983$ °C, D četrti prevlek $\dot{\varphi} = 9{,}95\ s^{-1}$, $T = 940$ °C, E peti prevlek $\dot{\varphi} = 11{,}12\ s^{-1}$, $T = 840$ °C

The stress during the first rolling pass reached values between 720 MPa and 900 MPa, while the specimen temperature dropped from 1200 °C to 1130 °C. During the second rolling pass the stress was between 790 MPa and 1180 MPa and the temperature was 1040 °C. For the third rolling pass the stress increased to 990 and 1360 MPa and final temperature dropped to 980 °C. During the fourth and fifth rolling passes the stress was between 1180 MPa and 1710 MPa, and between 1610 MPa and 2000 MPa, respectively. On the other hand, the specimen temperature decreased to 940 °C after the fourth, and even down to 840 °C after the last, rolling pass. Due to the elongation of the specimen the rolling time also increased from 0.48 s for the first pass to 0.74 s for the fifth pass.

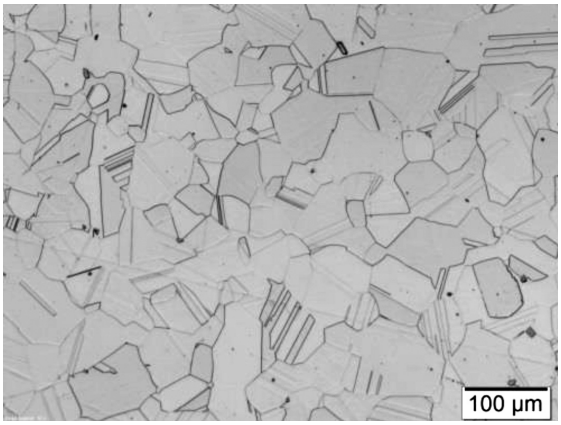

Figure 4: Light micrograph of the studied superalloy microstructure before hot deformation

Slika 4: Svetlobni posnetek mikrostrukture preiskovane superzlitine pred vročo deformacijo

The material's resistance to deformation increases for each rolling pass. This is the product of the decreased temperature, increased strain rate and the accumulation of strain. However, DRX did take place and partially softened the material, as was revealed by the microstructure analysis given in Section 3.2. The dispersion of the load data during rolling shown in **Figure 2** is attributed

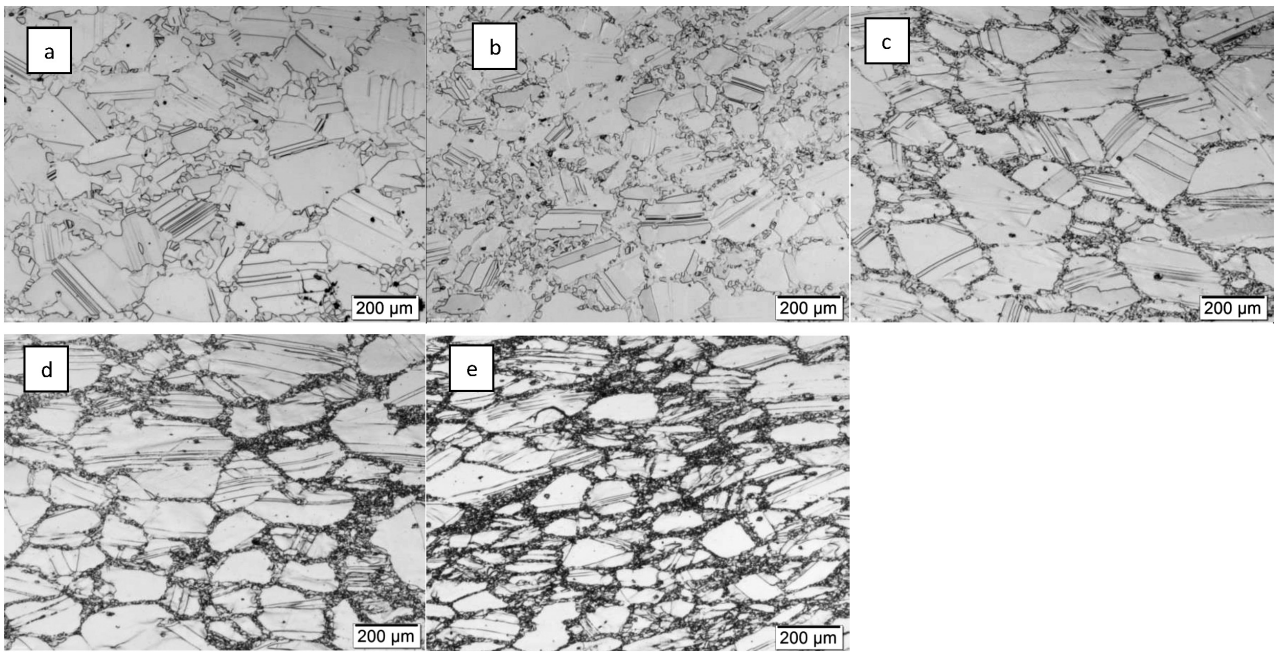

Figure 5: Microstructure of specimens after the hot rolling: a) after the first pass, b) after the second pass, c) after the third pass, d) after the fourth pass, e) after the fifth pass

Slika 5: Mikrostruktura vroče valjanih vzorcev: a) po prvem prevleku, b) po drugem prevleku, c) po tretjem prevleku, d) po četrtem prevleku in e) po petem prevleku

to the measurement error and DRX, while the gradual increase of the stress during a single pass is attributed to the sample cooling.

3.2 Microstructure

Figure 4 shows the initial microstructure of the Inconel 625 before hot deformation. The specimen was annealed at 1200 °C for 30 min, followed by water quenching, used to obtain a fine, homogeneous γ phase with carbides solute in the matrix. It is clear that the microstructure consists of equiaxed grains with a mean grain size of 80 μm and a large number of annealing twins in the austenite grains, typical for alloys with a low stacking-fault energy[6].

The microstructure of the hot-rolled and air-cooled specimens obtained for a different number of rolling passes is given in **Figure 5**.

The start of the recrystallization process is visible from **Figure 5a**, showing the microstructure of the Inconel 625 alloy subjected to a single rolling pass. The DRX occurs through the so-called necklace mechanism, forming at the grain boundaries. After starting at some individual boundaries, as seen in **Figure 5a**, the recrystallized grains start to appear along most of the grain boundaries as the number of rolling passes and the deformation rate increase (**Figure 5b**). The recrystallization proceeds by increasing in number and decreasing in size of the new grains (**Figure 5c**), forming along all the boundaries (**Figure 5d**) and finally representing a significant part of the microstructure and regularly appearing at the deformation twin boundaries (**Figure 5e**).

Figure 5 shows that newly formed twins exist in the original deformed grains. It has been reported that the formation of twinning plays an important role for the nucleation process during DRX in materials with a low stacking-fault energy[6]. Higher grain-boundary mobility results in the nucleation of the twins, which act as the main activate nucleation mechanism of DRX for nickel-based superalloys deformed at higher temperatures. This accelerates the bulging and the separation of bulged parts from the original grains[8]. The amount of twin boundaries increases with increased strain. **Figure 5e** clearly shows a large amount of recrystallized grains on the twin grain boundaries.

During the hot deformation of low-stacking-fault-energy metals, the plastic deformation leads to a serration of the grain boundaries. For the sufficient deformation level, the serrations can lead to the creation of new grains by bulging from the pre-existing grain boundaries[9]. Miura et al.[10] showed that the nucleation of new grains occurs preferentially at the triple junctions. The triple junctions acting as nucleation sites can either be constituted solely of three or more high-angle grain boundaries, or also include some twins among the intersecting boundaries. The initial stages of DRX appear on the grain boundaries. The new recrystallized grains nucleate on the deformed grain boundaries and form a necklace around it[7,11–13], as visible in **Figure 5c**.

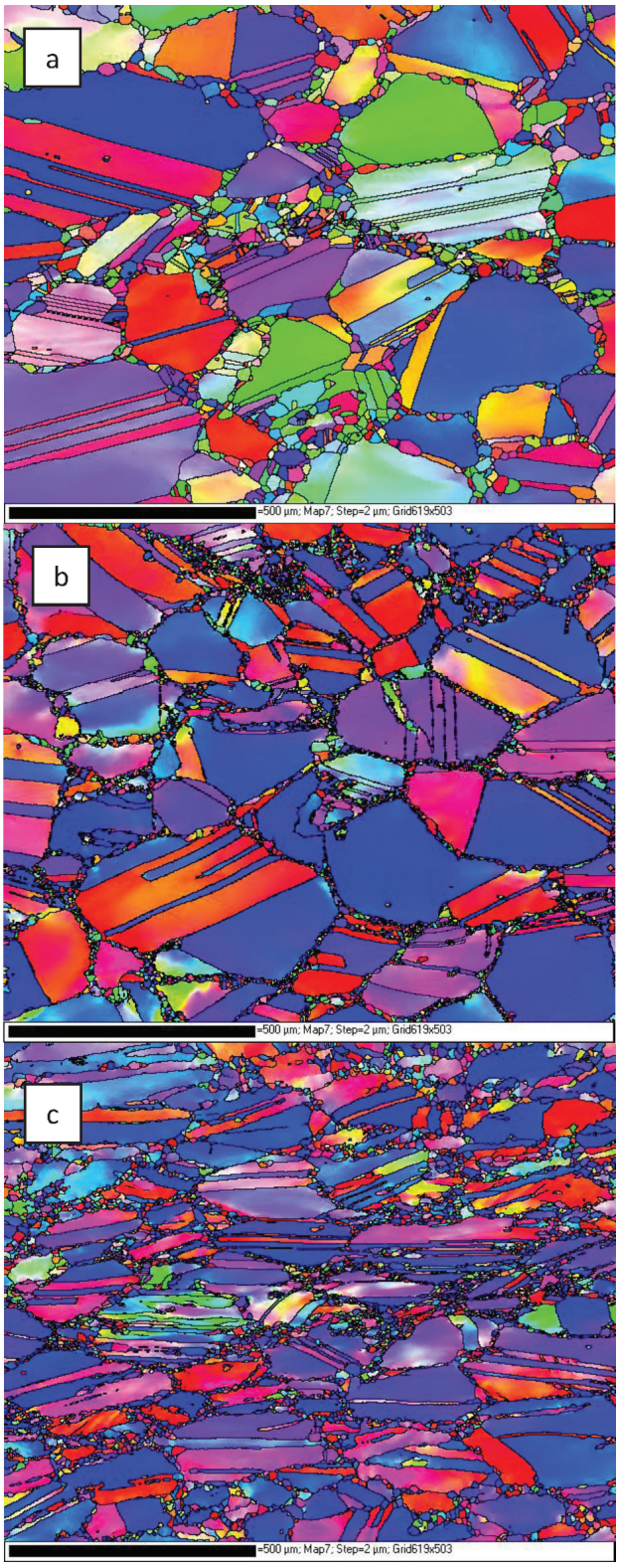

Figure 6: EBSD grain maps of samples: a) after one pass, b) after three passes and c) after five passes

Slika 6: EBSD ploskovna porazdelitev zrn: a) po prvem prevleku, b) po tretjem prevleku, c) po petem prevleku

It has been reported that during deformation the cooling is slower due to the conversion of deformation energy to heat by adiabatic heating[14]. It is well known that the temperature rise during hot deformation can not only induce the process of DRX, but also lead to a rapid reduction in the work-hardening rate[15]. A higher strain rate will result in increased dislocation density, which in turn will dramatically reduce the recrystallization temperature[16,17].

The deformation of the grains and the occurrence of new recrystallized grains were confirmed by the EBSD mapping shown in **Figure 6**. The microstructures presented correspond to the Inconel 625 superalloy at the end of hot deformation after: a) one pass, b) three passes and c) five rolling passes.

The analysis of the EBSD mapping images reveals large, non-recrystallized grains with twin grain boundaries and small recrystallized grains in the Inconel 625 alloy microstructure subjected to one rolling pass (**Figure 6a**). The evolution of the DRX structures clearly indicates that DRX starts predominantly at the boundaries of the deformed grains and not inside the grains[18]. Normal, large-angle grain boundaries are more susceptible to recrystallization than twin boundaries. In the case of a sample analysed after three rolling passes (**Figure 6b**) the non-recrystallized grains are slightly deformed, reflected in misorientation inside the grains and small recrystallized grains that are smaller compared to the sample after one rolling pass. This is due to the higher final deformation and the lower final temperature. The recrystallized grains do not remain isolated, but soon form closed networks, resulting in the well-known necklace structure[19]. For the most deformed sample obtained after five rolling passes (**Figure 6c**), large non-recrystallized grains are severely deformed, which is reflected in the misorientation inside the grains. Furthermore, small recrystallized grains are smaller than in the case of three rolling passes, caused by an even higher final deformation rate and a very low final temperature. The analysis of the EBSD data of the different passes clearly shows that the recrystallized fraction increases with strain.

4 CONCLUSIONS

This research provides an overview of the structural changes occurring during hot rolling of the superalloy Inconel 625. Specimens were hot rolled from a temperature of 1200 °C with different deformation rates, obtained by changing the number of rolling passes. A light microscope and an electron microscope, employing the electron-backscatter-diffraction technique, were employed to investigate the microstructure evolution and the nucleation mechanisms of dynamic recrystallization.

The necklace DRX mechanism was found to be the dominant material-softening mechanism. The recrystallization begins at the deformed grain boundaries, being consistent with the necklace mechanism. However, at high deformation rates, new recrystallized grains also appear at twin boundaries.

The misorientation in the deformed grains increases with the lower rolling temperature of the deformation and the increased strain rate. The fraction of recrystallized grains increases with a higher degree of deformation, while the size of the recrystallized grains is reduced with the higher deformation rate and the lower temperature.

5 REFERENCES

[1] L. B. Getsov, A. S. Semenov, E. A. Tikhomirova, A. I. Rybnikov, Thermocyclic- and Static-Failure Criteria for Single-Crystal Superalloys of Gas-Turbine Blades, Mater. Tehnol., 48 (**2014**) 1, 255–260

[2] M. Mohan, R. Subramanian, Z. Alam, P. C. Angelo, Evaluation of the Mechanical Properties OF A Hot Isostatically Pressed Yttria-Dispersed Nickel-Based Superalloy, Mater. Tehnol., 48 (**2014**) 6, 899–904

[3] Y. C. Lin, X. M. Chen, A critical review of experimental results and constitutive descriptions for metals and alloys in hot working, Mater. Des., 32 (**2011**), 1733–1759, doi:10.1016/j.matdes.2010.11.048

[4] Y. C. Lin, M. S. Chen, J. Zhong, Constitutive modeling for elevated temperature flow behavior of 42CrMo steel, Comput. Mater. Sci., 42 (**2008**), 470–477, doi:10.1016/j.commatsci.2007.08.011

[5] F. Chen, Z. Cui, D. Sui, B. Fu, Recrystallization of 30Cr2Ni4MoV ultra-super-critical rotor steel during hot deformation, Part III: Metadynamic recrystallization, Mater. Sci. Eng. A, 540 (**2012**), 46–54, doi:10.1016/j.msea.2012.01.061

[6] A. Hoseini Asli, A. Zarei-Hanzaki, Dynamic Recrystallization Behavior of a Fe-Cr-Ni Super-Austenitic Stainless Steel, J. Mater. Sci. Technol., 25 (**2009**), 603–606

[7] F. Tehovnik, B. Žužek, B. Arh, J. Burja, B. Podgornik, Hot Rolling of the Superaustenitic Stainless Steel AISI 904L, Mater. Tehnol., 48 (**2014**) 1, 137–140

[8] Y. Wang, W. Z. Shao, L. Zhen, X. M. Zhang, Microstructure evolution during dynamic recrystallization of hot deformed superalloy 718, Mater. Sci. Eng. A, 486 (**2008**) 1, 321–332, doi:10.1016/j.msea.2007.09.008

[9] T. Sakai, Dynamic recrystallization microstructures under hot working conditions, J. Mater. Process. Technol., 53 (**1995**), 349–361, doi:10.1016/0924-0136(95)01992-N

[10] H. Miura, T. Sakai, H. Hamaji, J. J. Jonas, Preferential nucleation of dynamic recrystallization at triple junctions, Scr. Mater., 50 (**2004**), 65–69, doi:10.1016/j.scriptamat.2003.09.035

[11] A. Momeni, K. Dehghani, Microstructural Evolution and Flow Analysis during Hot Working of a Fe-Ni-Cr Superaustenitic Stainless Steel, Metall. Mater. Trans. A, 42 (**2010**), 1925–1932, doi:10.1007/s11661-010-0565-z

[12] Y. Han, G. Liu, D. Zou, R. Liu, G. Qiao, Deformation behavior and microstructural evolution of as-cast 904L austenitic stainless steel during hot compression, Mater. Sci. Eng. A, 565 (**2013**), 342–350, doi:10.1016/j.msea.2012.12.043

[13] H. Mirzadeh, A. Najafizadeh, Hot Deformation and Dynamic Recrystallization of 17-4 PH Stainless Steel, ISIJ Int., 53 (**2013**), 680–689, doi:10.2355/isijinternational.53.680

[14] H. Monajati, A. K. Taheri, M. Jahazi, S. Yue, Deformation characteristics of isothermally forged UDIMET 720 nickel-base superalloy, Metall. Mater. Trans. A, 36 (**2005**), 895–905, doi:10.1007/s11661-005-0284-z

[15] W. S. Lee, C. F. Lin, High-temperature deformation behaviour of Ti6Al4V alloy evaluated by high strain-rate compression tests, J. Mater. Process. Technol., 75 (**1998**), 127–136, doi:10.1016/S0924-0136(97)00302-6

[16] H. Q. Sun, Y. N. Shi, M. X. Zhang, K. Lu, Plastic strain-induced grain refinement in the nanometer scale in a Mg alloy, Acta Mater., 55 (**2007**), 975–982, doi:10.1016/j.actamat.2006.09.018

[17] Y. Cao et al. An electron backscattered diffraction study on the dynamic recrystallization behavior of a nickel-chromium alloy (800H) during hot deformation, Mater. Sci. Eng. A, 585 (**2013**), 71–85, doi:10.1016/j.msea.2013.07.037

[18] S. Mitsche, P. Poelt, C. Sommitsch, Recrystallization behaviour of the nickel-based alloy 80 a during hot forming, J. Microsc., 227 (**2007**), 267–274, doi:10.1111/j.1365-2818.2007.01810.x

[19] Y. Wang, W. Z. Shao, L. Zhen, L. Yang, X. M. Zhang, Flow behavior and microstructures of superalloy 718 during high temperature deformation, Mater. Sci. Eng. A, 497 (**2008**), 479–486, doi:10.1016/j.msea.2008.07.046

UDK 669.721.5:621.74.043:620.186
Professional article/Strokovni članek

ISSN 1580-2949
MTAEC9, 49(5)807(2015)

THERMOPHYSICAL PROPERTIES AND MICROSTRUCTURE OF MAGNESIUM ALLOYS OF THE Mg-Al TYPE

TERMOFIZIKALNE LASTNOSTI IN MIKROSTRUKTURA MAGNEZIJEVIH ZLITIN TIPA Mg-Al

Petr Lichý[1], Jaroslav Beňo[1], Ivana Kroupová[1], Iveta Vasková[2]

[1]VŠB-Technical University of Ostrava, Faculty of Metallurgy and Materials Engineering, Department of Metallurgy and Foundry Engineering, 17. listopadu 15/2172, 708 33 Ostrava, Czech Republic
[2]Technical University of Košice, Faculty of Metallurgy, Department of Ferrous and Foundry Metallurgy, Letna 9, Košice, Slovak Republic
petr.lichy@vsb.cz

Prejem rokopisa – received: 2013-10-01; sprejem za objavo – accepted for publication: 2014-11-24

doi:10.17222/mit.2013.196

Generally speaking, magnesium alloys of the Mg-Al type are used as structural materials, but their disadvantage lies in their low heat resistance. The addition of suitable alloying elements can be positive, as it makes it possible to achieve good thermo-mechanical properties. For the application of a specific material for thermally stressed cast parts it is necessary to consider the extent of their linear and volumetric changes at elevated and high temperatures. The aim of this paper is to study the behaviour of selected magnesium alloys based on Mg-Al during heat stress conditions in order to simulate real conditions using dilatometric analyses. These properties were evaluated on samples of alloys prepared by gravity casting in metallic moulds. The effect of the metallurgical processing of the alloys on the studied parameters was also investigated.

Keywords: castings, magnesium alloys, thermophysical properties, microstructure

V splošnem se zlitine Mg-Al uporabljajo kot konstrukcijski materiali, toda njihova pomanjkljivost je, da imajo majhno toplotno odpornost. Dodatek ustreznih zlitinskih elementov pozitivno vpliva na izboljšanje njihove toplotne stabilnosti oz. odpornosti. Pri uporabi nekega materiala, ki bo toplotno obremenjen, moramo upoštevati njegove linearne in volumenske spremembe pri povišanih in visokih temperaturah. Namen tega prispevka je študij vedenja izbranih Mg-zlitin tipa Mg-Al med toplotnimi obremenitvami, da bi tako simulirali njihovo vedenje v realnih razmerah. Njihovo vedenje smo analizirali z dilatometričnimi analizami na vzorcih zlitin, ki so bili izdelani z gravitacijskim litjem v kovinskih modelih. Raziskovali smo tudi vpliv metalurških procesov na izbrane zlitine.

Ključne besede: ulitki, magnezijeve zlitine, termofizikalne lastnosti, mikrostruktura

1 INTRODUCTION

Aluminium is the main alloying element in magnesium alloys. Mg-Al based alloys belong to the most widely used group for the foundry industry and they are the oldest of the foundry magnesium alloys. Aluminium is one of the few metals that easily dissolves in magnesium. These alloys may also contain additional alloying elements (e.g., Si, Mn, Zr, Th, Ag, Ce). Their properties are the result of a relatively large area of the solid solution δ in the equilibrium diagram of a Mg-Al alloy and by the possibility of their alloying also with other elements. The most common alloys contain 7–10 % of Al.[1]

Alloys containing more than 7 % Al are hardenable, and during their hardening a discontinuous precipitate of the $Mg_{17}Al_{12}$ phase is formed, the alloys are usually alloyed with small quantities of zinc and manganese. An increasing aluminium content significantly increases the solidification interval and thus also the width of the two-phase zone. Such alloys have during gravity casting a strong tendency to form micro-shrinkages and shrinkage porosities. For this reason the content of Al in the alloys for gravity casting does not exceed 5 %. A brittle intermetallic $Mg_{17}Al_{12}$ phase is formed above the solubility limit. The limit of solubility of aluminium at the eutectic temperature is at the amount fraction x = 11.5 % (mass fraction, w = 12 %), and approximately 1 % at room temperature. As a result of this, the $Mg_{17}Al_{12}$ phase plays a dominant role and it decides what the properties will be.[2,3]

2 PROPERTIES OF MAGNESIUM ALLOYS AT ELEVATED TEMPERATURES

The use of magnesium alloys in the automotive industry is currently limited to several chosen applications (such as car dashboard, steering wheel, structure of seats, etc.).[4] The alloys used in these applications are based on the Mg-Al system, for example the series AM and AZ. The alloys based on the Mg-Al system are on an industrial scale the most acceptable from the perspective of economics. These alloys offer a good combination of strength and ductility at room temperature. Another advantage is their good corrosion resistance and excellent pourability. The main areas of the increasing use of Mg alloys for car manufacturers are such components as gear boxes and engine blocks. These applica-

Table 1: Chemical composition of the used magnesium alloys
Tabela 1: Kemijska sestava uporabljenih magnezijevih zlitin

alloy	Element, *w*/%									
	Zn	Al	Si	Cu	Mn	Fe	Ni	Ca	Be	Sr
AZ91	0.56	8.80	0.06	0.004	0.20	0.004	0.001	0.000	0.001	0.00
AM60	0.07	5.78	0.03	0.001	0.33	0.003	0.001	0.000	0.001	0.00
AMZ40	0.14	3.76	0.02	0.001	0.34	0.003	0.000	0.000	0.001	0.00
AJ62	0.01	5.78	0.04	0.001	0.35	0.003	0.001	0.008	0.001	2.92

tions require exploitation in operating conditions at a temperature of 150–200 °C. Commercial magnesium alloys of the type AM and AZ do not have these properties, this is related to their poor mechanical properties at elevated temperatures,[5] and the cause is the low structural stability, and thus the creep resistance. Developments in this area brought about the introduction of new alloys, i.e., Mg-Al-Sr (AJ) and Mg-Al-RE (AE). Magnesium alloys alloyed with rare-earth metals, which do not contain aluminium, are in the long term recognised as one of the most resistant to creep. From the viewpoint of the use of castings made from Mg-alloys at elevated temperatures the volumetric and linear changes of the material are also critical. Their magnitude is determined, among other things, by the chemical composition and by the microstructure of the material (e.g., by presence and share of individual phases, by grain size).

3 DESCRIPTION OF USED ALLOYS

For the experimental evaluation both commonly used alloys AZ91, AM60, AMZ40 and the AJ62 alloy were used. All the compared materials were supplied by a Czech manufacturer and **Table 1** shows their chemical composition according to the supplier's certificate.

4 PREPARATION OF THE TEST SAMPLES

Magnesium alloys were melted in an electric resistance furnace in a metal crucible made from low-alloyed steel. Magnesium alloys are highly reactive thanks to the high affinity of magnesium for oxygen. For this reason the material was treated during melting with an agent having the trade mark EMGESAL. This material in a form of covering and refining flux served for limiting the alloy oxidation and for cleaning the melt of possible inclusions. The castings were produced by gravity casting into the ingot mould made of cast iron, which was prior to pouring pre-heated to a temperature of 450 °C ± 30 °C in order to extend its service life and to achieve sufficient fluidity of the metal. Casting temperatures and operating temperatures were kept in a narrow range in order to achieve as high as possible limitation of the influence of different cooling effects. Part of the melt was treated metallurgically by an agent with the commercial designation MIKROSAL MG T 200, which was based on hexachloretane, and which introduced into the melt the nuclei for crystallisation to achieve the fine-grained structure. This was followed by the manufacture of samples from the castings for an evaluation of the microstructure, as well as samples for a determination of the thermo-physical properties, and test samples for the metallographic analyses.

5 MICROSTRUCTURE OF THE CAST SAMPLES

The microstructure of the AZ91 alloy is shown in **Figure 1**. It is a structure with a share of eutectics and with a significant share of the $Mg_{17}Al_{12}$ phase. The addition of the forced crystallisation nuclei did not have any significant effect on this material (**Figure 2**). A large share of plate-type precipitates is also evident. **Figure 3**

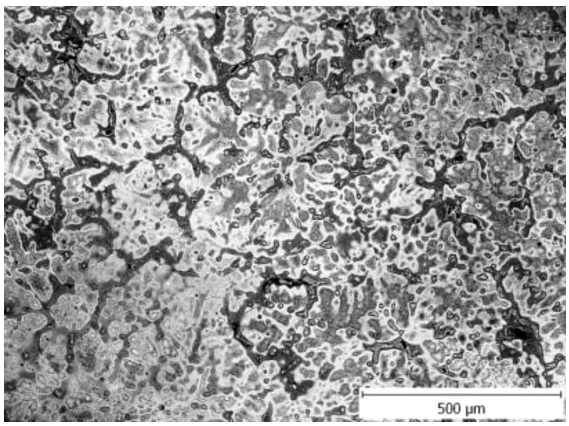

Figure 1: Non-inoculated material AZ91
Slika 1: Necepljena zlitina AZ91

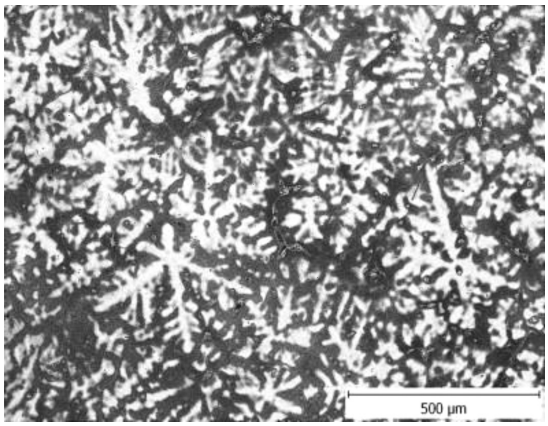

Figure 2: Inoculated material AZ91
Slika 2: Cepljena zlitina AZ91

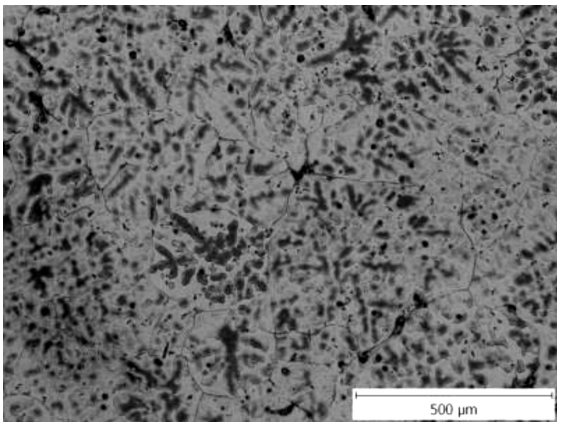

Figure 3: Non-inoculated material AM60
Slika 3: Necepljena zlitina AM60

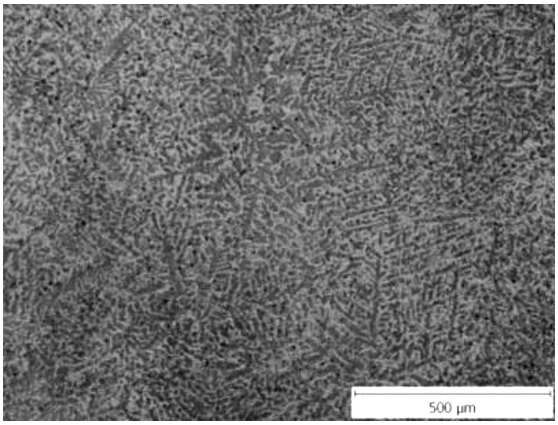

Figure 4: Inoculated material AM60
Slika 4: Cepljena zlitina AM60

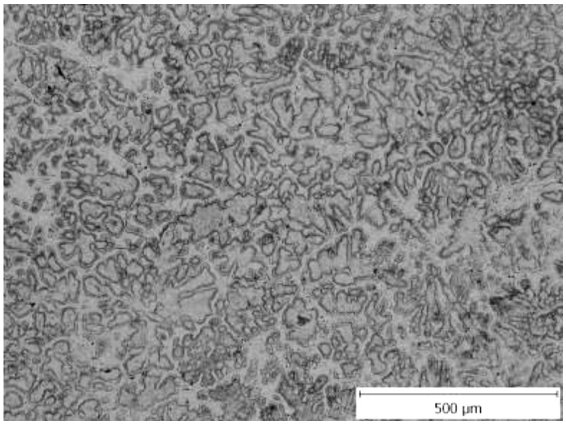

Figure 5: Non-inoculated material AMZ40
Slika 5: Necepljena zlitina AMZ40

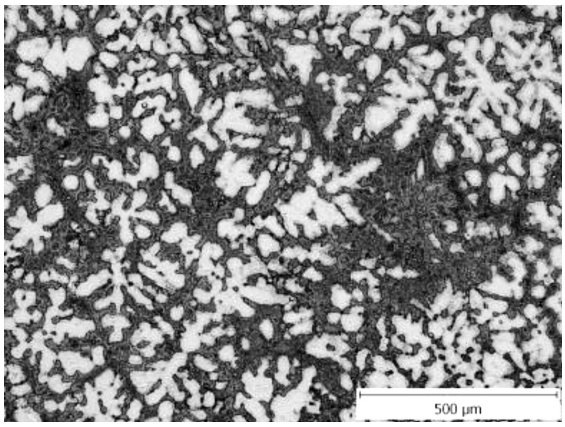

Figure 6: Inoculated material AMZ40
Slika 6: Cepljena zlitina AMZ40

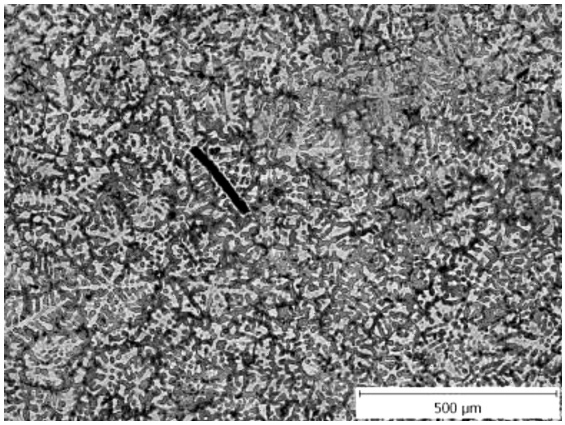

Figure 7: Non-inoculated material AJ62
Slika 7: Necepljena zlitina AJ62

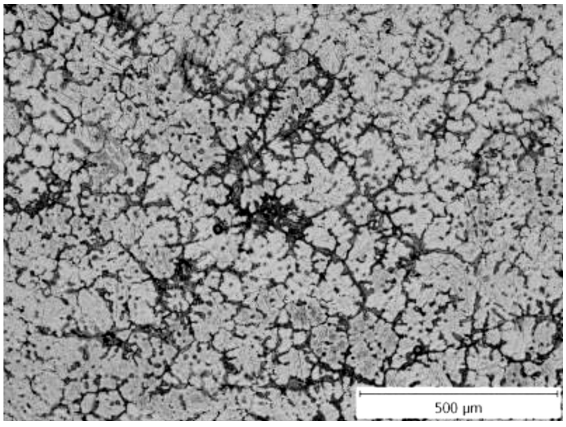

Figure 8: Inoculated material AJ62
Slika 8: Cepljena zlitina AJ62

shows the microstructure of the AM60 alloy, which consists of a matrix containing a solid solution of α-Mg, a secondary phase of Al-Mn compounds and eutectics. **Figure 4** illustrates the structure of the AM60 alloy after the metallurgical treatment (inoculation). The structure is much finer, and its homogeneity was generally improved, which means that it is possible to achieve better mechanical properties.

The effect of inoculation was not manifested in the achieved structure of the AMZ40 alloys (**Figures 5** and **6**). This alloy is characterised by the low content of alloying elements; its structure is formed by the primary α-Mg phase and by eutectics without the presence of precipitates.

Figures 7 and **8** show the microstructure of the alloy AJ62, consisting of the basic solid solution α, as well as

several types of intermetallic phases, i.e., $(Al, Mg)_4Sr$, $Al_3Mg_{13}Sr$ and very small quantity of Mn_5Al_8. In the case of the inoculated alloy (**Figure 8**) it is possible to find some differences; it is, however, impossible to identify unequivocally the finer structure.

6 MEASUREMENT OF THE PHYSICAL PROPERTIES

Dilatometric analyses were performed in order to verify the behaviour of the materials at elevated temperatures. Use of the given material for thermally stressed components is related, among others, to the dimensional stability of the cast part.

Heat expansion (Equation (1)) of the material is usually characterised by the mean temperature coefficient (coefficient of linear expansion):

$$\alpha_T = \frac{l_T - l_{T0}}{l_{T0}(T - T_0)} = \frac{1}{l_0}\left(\frac{dl}{dT}\right) \quad (1)$$

where:

α_T – coefficient of linear heat expansion

l_0 – sample length under reference (e.g. laboratory) temperature

dl – change of the sample length

dT – difference in temperatures.

The linear heat expansion was measured on the above-described samples with use of a Netzsch DIL 402C/7 dilatometer. The experiments ran in the temperature interval from (20 ± 5) °C up to 350 °C with heating and cooling rates of 15.0 K/min, with a holding time of 30 min at the maximum temperature (isotherm) in a protective argon atmosphere (99.9999 % Ar) with a constant gas flow of 20 mL/min. The size of the used samples was as follows: a mean length of 20 mm and a mean diameter of 6 mm. Samples of the non-inoculated (marked in the name of the sample – as "non") and inoculated materials (marked as "in") were divided into two groups. The first group was used in the as-cast state without previous heat stressing and the second one after their heat stressing (250 °C, 30 min) in the argon atmosphere for checking the influence of the increased temperature during the stressing of the castings in real conditions.

Table 2 contains the results of the measurements of the coefficient of linear heat expansion (α_T) for the chosen temperature interval ((20 ± 5) °C up to 350 °C). The table gives the values for the samples without heat stressing (T_{lab}) and after heat stressing (250 °C, 30 min) – T_{250}. **Figures 9** and **10** show the greatest change of length under a temperature of 350 °C (max $l_{350\,°C}$).

Table 2: Overview of thermophysical parameters of the Mg alloys
Tabela 2: Pregled toplotno-fizikalnih parametrov Mg-zlitin

Specimen	T_{lab}	T_{250}
	$\alpha_T \times 10^{-6}/K^{-1}$	$\alpha_T \times 10^{-6}/K^{-1}$
AZ91 non	29.6319	27.7702
AZ91 in	28.8887	27.3736
AM60 non	28.7385	26.2843
AM60 in	26.2465	26.0252
AMZ40 non	28.2639	18.1402
AMZ40 in	17.3364	17.1782
AJ62 non	28.8727	26.1917
AJ62 in	18.1686	17.5744

In the as-cast state, the highest absolute value of α_T (28.8727×10^{-6}) was achieved for the AZ91 alloy, and the lowest (17.3364×10^{-6} was achieved for the AMZ40 alloy after its metallurgical treatment. It is possible to find from the measured values a correlation between the measured value of the coefficient of linear thermal dilatation and the addition of the inoculant. The structure influenced by the inoculation shows substantially lower values of α_T.

A similar effect was observed in the thermally stressed samples of the magnesium alloys. In these cases the achieved values of the coefficient of linear thermal expansion were also the highest in the AZ91 alloy, followed by the AJ62 alloy, while the lowest values were achieved in the AMZ40 alloy.

The values of the maximum length change achieved at the temperature of 350 °C also correspond with these

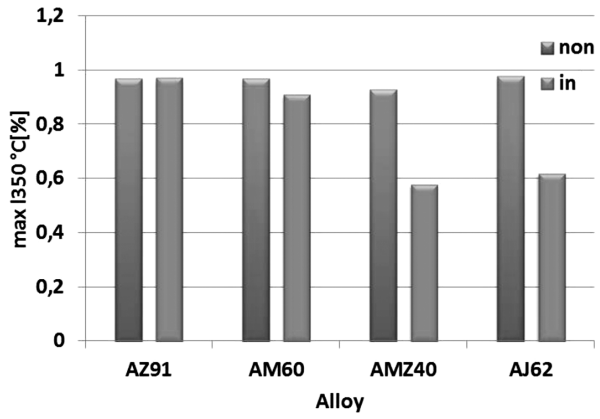

Figure 9: Thermal expansion of material without heat stress
Slika 9: Toplotni raztezek zlitin brez toplotne obremenitve

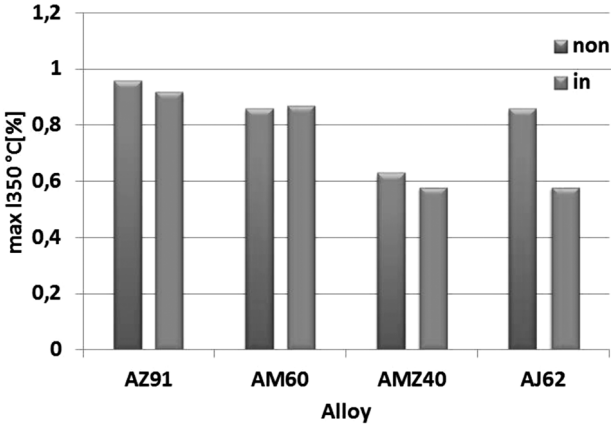

Figure 10: Thermal expansion of material after heat stress
Slika 10: Toplotni raztezek zlitin po toplotni obremenitvi

results. The positive impact of the inoculation was unequivocally demonstrated here, particularly in the case of the AMZ40 alloy. In case of the samples without thermal stressing (**Figure 9**) it was possible to note a considerable difference between the non-inoculated and inoculated materials. On the other hand, in the case of the thermally stressed samples (**Figure 10**), this difference is much smaller. It is therefore possible to assume a distinct influence of a possible heat treatment on these properties.

7 CONCLUSIONS

This study was focused on an evaluation of the thermophysical properties and microstructure of the magnesium alloys AZ91, AM60, AMZ40 and AJ62. On the basis of the realised experiments, it is possible to see a positive impact of the inoculation on the achievement of the smaller dilations of materials, which are important from the perspective of the use of casting for heat-stressed parts. The lowest values of the coefficient of linear thermal expansion and the maximum value of expansion at the temperature of 350 °C were achieved with samples of the alloys AJ62 and AMZ40, which were metallurgically processed. Despite the high cooling effect of the metallic mould, the positive effect of inoculation on the evaluated properties and microstructure of majority of the magnesium alloys were visible.

Acknowledgements

This work was conducted within the frame of the research project TA02011333 (Technology Agency of the CR).

8 REFERENCES

[1] M. J. F. Gándara, Mater. Tehnol., 45 (**2011**) 6, 633–637
[2] B. L. Mordike, T. Ebert, Materials Science and Engineering A, 302 (**2001**) 1, 37–45, doi:10.1016/S0921-5093(00)01351-4
[3] S. Roskosz, J. Adamiec, M. Blotnicki, Archives of Foundry Engineering, 7 (**2007**) 1, 143–146
[4] E. Adámková, P. Jelínek, S. Študentová, Manufacturing Technology, 13 (**2013**) 3, 255–262
[5] P. Lichý, M. Cagala, J. Beňo, Mater. Tehnol., 47 (**2013**) 4, 503–506

UDK 536.2:536.65:66.017
Professional article/Strokovni članek

ISSN 1580-2949
MTAEC9, 49(5)813(2015)

MICRO-ENCAPSULATED PHASE-CHANGE MATERIALS FOR LATENT-HEAT STORAGE: THERMAL CHARACTERISTICS

MIKROENKAPSULIRANI MATERIALI S FAZNO PREMENO ZA SHRANJEVANJE LATENTNE TOPLOTE: TOPLOTNE ZNAČILNOSTI

Milan Ostrý[1], Darina Dostálová[1], Tomáš Klubal[1], Radek Přikryl[2], Pavel Charvát[3]

[1]Brno University of Technology, Faculty of Civil Engineering, Institute of Building Structures, Veveří 95, 602 00 Brno, Czech Republic
[2]Brno University of Technology, Faculty of Chemistry, Purkyňova 464/188, 612 00 Brno, Czech Republic
[3]Brno University of Technology, Faculty of Mechanical Engineering, Technická 2, 616 69 Brno, Czech Republic
ostry.m@fce.vutbr.cz

Prejem rokopisa – received: 2013-10-01; sprejem za objavo – accepted for publication: 2014-11-24

doi:10.17222/mit.2013.210

A significant problem of the utilization of renewable energy is the mismatch between the demand and availability. From this point of view, heat storage contributes to the use of renewable energy for the heating and cooling of buildings. Heat can be stored using sensible- or latent-heat-storage techniques. Nowadays, activated concrete structures are used as an alternative cooling-and-heating system. Light-weight timber structures with an equivalent heat-storage capacity can be used instead of these heavy-weight structures. The latent-heat storage using micro-encapsulated phase-change materials (PCMs) represents a way to provide an adequate thermal mass within a small thickness of thermally activated structures. A series of experiments in a lab and test rooms were carried out to investigate the thermal behavior of micro-encapsulated PCMs for building applications. The Micronal®DS 5040 X microencapsulated PCM was used as the latent-heat-storage medium in combination with gypsum plaster. Differential scanning calorimetry (DSC) was used for a thermal analysis of the latent-heat storage medium. The storage medium underwent thermal cycling for an assessment of the heat-storage capacity changes during the proposed service life. The floor structure and the plasterboards fixed onto the ceiling and walls of an experimental room with an integrated PCM were thermally activated with capillary tubes. The performance of the system was continuously observed and evaluated.

Keywords: phase-change materials (PCMs), latent-heat storage (LHS), differential scanning calorimetry (DSC), thermal cycling, building, thermal capacity

Pomemben problem pri izkoriščanju obnovljive energije je neskladje med potrebo in razpoložljivostjo. S tega vidika shranjevanje toplote prispeva k uporabi obnovljive energije pri ogrevanju in hlajenju zgradb. Toplota se lahko smiselno shrani s tehniko shranjevanja latentne toplote. Danes se uporabljajo aktivirane betonske strukture kot alternativni ogrevni ali ohlajevalni sistemi. Lahke lesene strukture z enakovredno kapaciteto shranjevanja toplote se lahko uporabijo namesto teh težkih struktur. Shranjevanje latentne toplote z uporabo mikroenkapsuliranega materiala s fazno premeno (PCM) je način za zagotovitev ustrezne količine toplote kljub majhni debelini toplotno aktiviranih zgradb. Izvršena je bila serija preizkusov v laboratoriju in v preizkusnih sobah za ugotovitev toplotnega vedenja mikroenkapsuliranega PCM za uporabo pri zgradbah. Kot medij za shranjevanje latentne toplote je bil uporabljen mikroenkapsulirani PCM Micronal®DS 5040 X v kombinaciji z ometom iz mavca. Diferenčna vrstična kalorimetrija (DSC) je bila uporabljena za toplotno analizo medija za shranjevanje latentne toplote. Shranjevalni medij je bil izpostavljen toplotnim ciklom za ugotovitev sprememb kapacitete shranjene toplote med predlaganim delovanjem. Tla in mavčne plošče z vgrajenim PCM, pritrjene na strop in stene eksperimentalne sobe, so bile toplotno aktivirane s kapilarnimi cevkami. Vedenje sistema je bilo opazovano in ocenjeno.

Ključne besede: materiali s fazno premeno (PCM), latentno shranjevanje toplote (LHS), diferenčna vrstična kalorimetrija (DSC), toplotno cikliranje, zgradba, toplotna kapaciteta

1 INTRODUCTION

Heat storage can be in the forms of sensible heat in a liquid or solid medium, heat of fusion, chemical energy or products in a reversible chemical reaction.[1] Latent-heat storage represents a more efficient form of heat storage compared to sensible-heat storage due to a high storage capacity per volume or mass. Common storage media, e.g., brick walls or concrete structures, can store heat only through an increase in their temperature. This is a problem when the required change in ambient temperature is narrow. A typical example is indoor climate in buildings. The occupants require a stable indoor climate with very low changes in the temperature during the year. The heat-storage capacity of a building envelope helps to maintain the indoor air temperature in the required range without additional cooling and heating systems. This principle is strongly dependent on the potential of heat loses or heat gains. Building envelopes of modern office buildings are made of light-weight materials. Regarding the thermal comfort, the main disadvantages of light-weight structures are their low thermal mass, low thermal inertia and a potential comfort problem such as overheating.[2]

Therefore, light-weight building materials with a high heat-storage capacity represent a way of decreasing the energy consumption and operating cost.

Phase-change materials (PCMs) are latent-heat-storage media. The PCMs are able to store large amounts of heat during the melting process. The solidifying process

is accompanied by a release of the stored heat. The PCMs should have the melting and solidification temperature range in the practical range of an application and they need to have a high latent heat of fusion and a high thermal conductivity for the effective thermal storage[2].

There are some possible techniques to integrate PCMs directly into the building materials:[3]

- a simple immersion of a porous material in a liquid PCM;
- a vacuum impregnation of a PCM in the porous aggregates of a building material;
- a direct mixing of an encapsulated PCM into concrete or plaster during a concrete or plaster mixing.

Microcapsules are small containers encapsulating a PCM that can be mixed with many building materials. Micro-encapsulation is a process in which PCM particles are surrounded or coated with a continuous film of a polymeric material to produce capsules in a micrometer to millimeter range.[4] The PCM forms the core and the polymeric material creates the shell. The microcapsules are usually of a spherical shape though other shapes are also possible. The microcapsules allow for the volume changes of the PCM, reducing the reaction of the PCM with the outside environment.[5] This technology of encapsulation increases the heat-transfer area and allows for an easier handling of PCMs. There is no risk of a massive leakage of the PCMs since the PCM volume in a capsule is very small. The building structures with incorporated PCMs are similar to the commonly used building materials. The micro-encapsulation can be carried out with physical or chemical methods.[4] The physical methods are: pan coating, air-suspension coating, centrifugal extrusion, vibrational nozzle and spray drying. There are several chemical methods: interfacial polymerization, in-situ polymerization and matrix polymerization.

2 MATERIAL AND METHODS

There are several important aspects of a practical use of the latent-heat-storage technology:

- the kind of the phase-change material;
- the kind of encapsulation;
- the thermal characteristics and thermal stability of PCMs;
- the integration in building structures;
- the heat transfer.

Moreover, there is a requirement for a long-term stability of the storage medium and the PCM-container system. Other relevant aspects are the useful life of these systems and the number of cycles they can withstand without a degradation of their properties.[6]

The research and development at the Brno University of Technology dealing with thermal storage is focused on the integration of PCMs into building envelopes to provide a thermal comfort in the range required by the legislation. A micro-encapsulated paraffin-based PCM is used for this purpose. A team of investigators from the Brno University of Technology developed and patented heat-storage modules for a stabilization of the thermal environment in buildings. The composition of a module is shown in **Figure 1**.

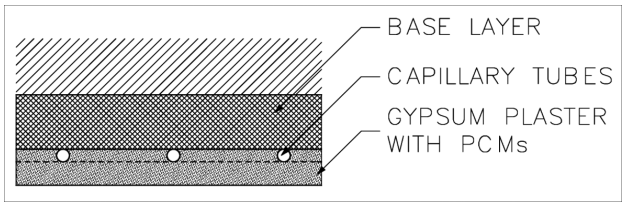

Figure 1: Detail of a heat-storage structure
Slika 1: Detajl strukture za shranjevanje toplote

The system can effectively stabilize the thermal microclimate in buildings with low operating costs. It allows not only a passive cooling of the rooms in summer, but it can also be used for a low-temperature heating in winter. The main technological components of the module are the basic slab, the heat-storage plaster and the capillary tubes for a thermal activation of the module. The system of the capillary tubes is placed in a layer of gypsum plaster with integrated micro-pellets containing a PCM for an advanced latent-heat/cold storage. Micronal®DS 5040 X was used as the latent-heat-storage medium (PCM). The capillary tubes integrated in the heat-storage plaster were connected to the distribution and return pipes. It is necessary to provide a direct exposure of the heat-storage layer to the indoor environment for a good heat transfer; therefore, the heat-storage structures containing PCMs cannot be obstructed by furniture or suspended ceilings.

Gypsum plaster with a special composition for the proposed use was modified with a mass fraction w = 30 % of Micronal®DS 5040 X.

Two important properties were tested in the experiments:

- the change in the thermal characteristics of the PCM after 100 melting-freezing cycles;
- the change in the thermal conductivity of the plaster with the microencapsulated PCM.

The thermal-energy-storage properties, the thermal reliability and the thermal durability of the composite with the PCM were determined with differential scanning calorimetry (DSC).[7]

DSC is a widely used method from the group of thermal-analysis methods. Nowadays, DSC is used for thermal analyses of new materials, e.g., in the study of the phase changes and testing quality of polymer materials. DSC compensation is a method whose principle consists of measuring the temperature and the heat flux during the heating or cooling of a tested material. The process is realized at a constant rate of heating or cooling and carried out in a closed chamber. The test result can be used to determine the melting temperature of a sample – the onset/offset of the phase-transition temperature – the

crystallization, or various types of crystallization, the heat capacity and the temperature degradation. The differential scanning calorimeter is a twin instrument, comprising a sample and a reference calorimeter within a common thermal enclosure, where the two calorimeters are usually assumed to be identical. A PYRIS1 Perkin Elmer calorimeter was used in the tests.

Micronal®DS 5040 X was tested before and after the thermal cycling. A sample of Micronal®DS 5040 X was placed in a glass laboratory test tube with a thermocouple sensor. The tube was immersed in liquid nitrogen until the temperature measured by the thermocouple dropped to –10 °C, then the tube was immersed in hot water (60 °C). The tube remained in nitrogen and warm water for about 1 min and 1.5 min. The whole procedure was repeated 100-times.

The heat transfer between the indoor environment and the heat storage depends mainly on the thermal conductivity of the plaster with the micro-encapsulated PCM. The thermal conductivity was determined with the guarded-hot-plate method. In this method a solid sample of a material is placed between two plates. One plate is heated and the other is cooled. The temperatures of the plates are monitored until they are constant. A constant heat flow flows through the test sample in the stationary-temperature state. The steady-state temperatures, the thickness of the sample and the heat input to the hot plate are used to calculate the thermal conductivity.

Several samples of gypsum plaster with various compositions were tested:

- referential sample (sample no. 0) – plain gypsum plaster;
- modified plaster (sample no. 1) – w = 68 % gypsum plaster and w = 32 % PCM;
- modified plaster (sample no. 2) – w = 65 % gypsum plaster, w = 30 % PCM and w = 5 % natural graphite;
- modified plaster (sample no. 3) – w = 61.5 % gypsum plaster, w = 29 % PCM and w = 9.5 % natural graphite;
- modified plaster (sample no. 4) – w = 67.9 % gypsum plaster, w = 31.8 % PCM and w = 0.3 % expanded graphite;
- modified plaster (sample no. 5) – w = 67.7 % gypsum plaster, w = 31.7 % PCM and w = 0.6 % expanded graphite.

3 RESULTS AND DISCUSSION

3.1 Thermal stability of the latent-heat-storage medium

The characteristics of all the samples were tested with DSC twice, before and after the cycling. The experiments were carried out at a temperature rate of 1.0 K/min. The onset and peak temperatures during the heating and cooling depend on the temperature rate. The melting temperatures rise with the temperature rate. The risk of supercooling rises with the heating rate.

The results are shown in **Tables 1** and **2**. Both tables show a minimum difference in the enthalpy of the phase change of the tested samples. The difference between the onset temperatures is 0.1 K.

The DSC curves in **Figure 2** show minimum differences between the characteristics of the samples.

Table 1: Characteristics of Micronal®DS 5040 X before thermal cycling
Tabela 1: Značilnosti Micronal®DS 5040 X pred toplotnim cikliranjem

	Heating	Cooling
Onset temperature, °C	18.8	21.8
Peak temperature, °C	24.5	Multi-peak
Enthalpy, J/g	96.2	92.6

Table 2: Characteristics of Micronal®DS 5040 X after thermal cycling
Tabela 2: Značilnosti Micronal®DS 5040 X po toplotnem cikliranju

	Heating	Cooling
Onset temperature, °C	18.9	21.9
Peak temperature, °C	24.5	Multi-peak
Enthalpy, J/g	96.5	93.4

3.2 Thermal conductivity of the plaster with PCM

Thermal conductivity is negatively influenced by the micro-encapsulated PCM. The increase in the thermal conductivity can be achieved with an addition of natural or expanded graphite. The influence of graphite on the thermal conductivity is shown in **Table 3**. As can be seen, the best material for the heat-conductivity improvement is natural graphite. A low amount of expanded graphite (w = 0.3 %) has no positive effect on the heat conductivity.

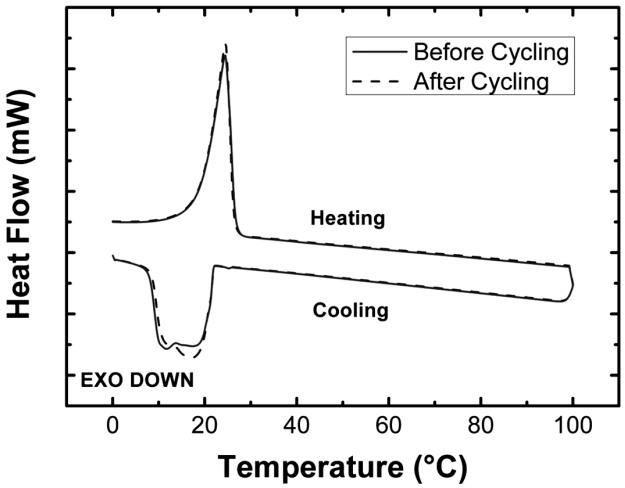

Figure 2: DSC results for Micronal®DS 5040 X before and after thermal cycling
Slika 2: Rezultati DSC za Micronal®DS 5040 X pred toplotnim cikliranjem in po njem

Table 3: Thermal conductivity of plaster with different compositions
Tabela 3: Toplotna prevodnost ometa pri različnih sestavah

Number of sample	Pour density of plaster kg/m^3	Thermal conductivity W/(m K)
Referential sample (no. 0)	1080	0.3866
Plaster with PCM (no. 1)	677	0.1760
w = 5 % natural graphite (no. 2)	676	0.1996
w = 9.5 % natural graphite (no. 3)	665	0.2336
w = 0.3 % expan. graphite (no. 4)	647	0.1598
w = 0.6 % expan. graphite (no. 5)	589	0.1766

4 CONCLUSION

The PCM used in the experiment did not significantly change its thermal properties even after 100 thermal cycles. From this point of view, the tested organic PCM is suitable for integration in building structures. The advantage of this kind of PCM is the possibility of integration in gypsum plaster that can be combined with capillary tubes for charging or discharging the heat. The modified plaster acting as a thermally activated layer can be used in radiant heating or cooling in residential buildings. However, the addition of a PCM causes a significant decrease in the thermal conductivity of the plaster. This problem can be overcome by adding natural graphite, e.g., w = 9.5 % of natural graphite increased the thermal conductivity of the plaster with the PCM from 0.1760 W/(m K) up to 0.2336 W/(m K).

Acknowledgement

This work paper has been worked out under project No. P104/12/1838 "Utilization of latent heat storage in phase change materials to reduce primary energy consumption in buildings", supported by Czech Science Foundation and under the project No. LO1408 "AdMaS UP – Advanced Materials, Structures and Technologies", supported by Ministry of Education, Youth and Sports under the "National Sustainability Programme I".

5 REFERENCES

[1] F. Agyenim, N. Hewitt, F. Eames, M. Smyth, A review of materials, heat transfer and phase change problem formulation for latent heat thermal energy storage systems (LHTESS), Renewable and Sustainable Energy Reviews, 14 (**2010**) 2, 615–628, doi:10.1016/j.rser.2009.10.015

[2] N. Soares, J. J. Costa, A. R. Gaspar, P. Santos, Review of passive PCM latent heat thermal energy storage systems towards buildings' energy efficiency, Energy and Buildings, 59 (**2013**), 82–103, doi:10.1016/j.enbuild.2012.12.042

[3] T. C. Ling, C. S. Poon, Use of phase change materials for thermal energy storage in concrete: An overview, Construction and Building Materials, 46 (**2013**), 55–62, doi:10.1016/j.conbuildmat.2013.04.031

[4] V. V. Tyagi, S. C. Kaushik, S. K. Tyagi, T. Akiyama, Development of phase change materials based microencapsulated technology for buildings: A review, Renewable and Sustainable Energy Reviews, 15 (**2011**) 2, 1373–1391, doi:10.1016/j.rser.2010.10.006

[5] L. Bayés-García, L. Ventola, R. Cordobilla, R. Benages, T. Calvet, M. A. Cuevas-Diarte, Phase Change Materials (PCM) microcapsules with different shell compositions: Preparation, characterization and thermal stability, Solar Energy Materials and Solar Cells, 94 (**2010**) 7, 1235–1240, doi:10.1016/j.solmat.2010.03.014

[6] B. Zalba, J. M. Marín, L. F. Cabeza, H. Mehling, Review on thermal energy storage with phase change: materials, heat transfer analysis and applications, Applied Thermal Engineering, 23 (**2003**) 3, 251–283, doi:10.1016/S1359-4311(02)00192-8

[7] A. Sari, A. Biçer, Preparation and thermal energy storage properties of building material-based composites as novel form-stable PCMs, Energy and Buildings, 51 (**2012**), 73–83, doi:10.1016/j.enbuild.2012.04.010

UDK 69:69.07:691.4:699.82
Professional article/Strokovni članek

ISSN 1580-2949
MTAEC9, 49(5)817(2015)

CERAMIC MASONRY UNITS INTENDED FOR THE MASONRY RESISTANT TO HIGH HUMIDITY

KERAMIČNI GRADBENI ELEMENTI, NAMENJENI ZA ZGRADBE, ODPORNE PROTI VISOKI VLAGI

Jiří Zach, Vítězslav Novák, Jitka Hroudová, Martin Sedlmajer

Brno University of Technology, Faculty of Civil Engineering, Veveří 331/95, 602 00 Brno, Czech Republic
zach.j@fce.vutbr.cz, novak.v@fce.vutbr.cz, hroudova.j@fce.vutbr.cz, sedlmajer.m@fce.vutbr.cz

Prejem rokopisa – received: 2014-08-01; sprejem za objavo – accepted for publication: 2014-10-14

doi:10.17222/mit.2014.170

The Faculty of Civil Engineering has been developing modern masonry blocks for several years. The aim is to develop masonry units that provide a good thermal insulation, mechanical and acoustic properties and a reduction in the energy consumption required for their production. Given the ever increasing frequency of natural disasters, which also affect landlocked countries, a part of this research also focuses on the development of ceramic blocks resistant to high humidity. High humidity is one of the most harmful effects occurring in a building construction. It causes an overall deterioration of the building construction and can lead to its degradation. Ceramic-brick constructions are already under stress due to a high humidity during the building period and also afterwards during their use. However, natural disasters such as floods, which have often occurred in the Czech Republic in recent years, cause the destruction of building constructions and their subsequent demolition. The paper deals with the possibility of a preventive use of hydrophobic ceramic masonry units intended for masonry plinths. This hydrophobisation serves as the prevention in the cases, in which the conventional waterproofing fails and also in the case of an extremely high humidity.

Keywords: ceramic masonry blocks, high humidity, hydrophobic, waterproofing, capillary absorption

Fakulteta za gradbeništvo že več let razvija moderne gradbene elemente. Namen je razviti moderno gradbeno enoto, ki bo imela dobro toplotno izolacijo, mehanske in akustične lastnosti ter zmanjšano porabo energije za njeno proizvodnjo. Zaradi vedno večje pogostosti naravnih katastrof, ki vplivajo tudi na otoške države, je del razvoja usmerjen tudi v razvoj keramičnih opek, odpornih proti visoki vlagi. Ta je med najbolj škodljivimi vplivi na gradbeno konstrukcijo. Povzroča splošno poslabšanje zgradbe in lahko povzroči celo njen razpad. Konstrukcije iz keramičnih opek so izpostavljene veliki vlagi že pri gradnji, kot tudi kasneje pri uporabi. Pri naravnih nesrečah, kot so poplave, ki so bile zadnja leta pogoste v Češki Republiki, so bile vzrok za uničenje gradbenih konstrukcij in posledično rušenje le-teh. Članek obravnava možnost preventivne uporabe hidrofobne keramične opeke za podlago zgradbe. Ta hidrofobizacija se uporablja kot zaščita v primeru, kjer navadna hidroizolacija odpove, in tudi v primerih ekstremno visoke vlažnosti.

Ključne besede: keramični gradbeni elementi, visoka vlažnost, hidrofoben, hidroizolacija, kapilarna absorpcija

1 INTRODUCTION

Two waterproofing principles can be applied to protect a building construction from the negative effects of water and moisture:[1,2]

The indirect waterproofing principle – following this principle, we minimise/reduce the moisture stress on a construction, e.g., by placing the building in an optimum environment, using the drainage of the adjacent building, increasing the surface temperature of the construction, etc.

The direct waterproofing principle – following this principle, we prevent water and moisture from penetrating into the structure. This is achieved by means of waterproof (or moisture-proof) materials, e.g., continuous-sheet waterproofing, waterproof concrete, injections, surface penetration and impregnation, surface hydrophobisation,[3–5] etc. It is also possible to prevent water or moisture penetration using active methods for reducing the moisture stress on a construction, e.g., electokinetic methods.

Masonry constructions, especially their lower parts, are under stress from increased moisture. Increased moisture has an effect both during the construction and during the use of a building. Building constructions are protected from increased moisture by horizontal, continuous, waterproof sheets and by the surface finish on the outside.[6]

In the case of increased moisture during the construction, the moisture mainly penetrates into the structure prior to the roof construction and surface finishing. A moisture increase during the construction does not necessarily mean that it has a decisive influence on the building. However, the building must not be sealed or used immediately after the finishing if it is completed in autumn or winter. If we fail to do so, a deterioration of the thermal properties often occurs due to the moisture in the lower parts of the building, often leading to hygrothermal failures such as damp areas and moulds.

The stress caused by increased moisture during the use of a building can have a number of causes. It may be a failure of the horizontal/vertical waterproofing as a

result of damage or a faulty application. Furthermore, waterproofing can be damaged during additional building operations, such as vents or wall repairs, etc. Waterproofing is also ineffective if the masonry reaches over the foundation plate, into the exterior. In the case of increased moisture during the use of the building, the problem is considerably more serious and the degree of masonry degradation is determined by the moisture stress.

To prevent hygric defects, hydrophobised masonry units can be used in the lower part of a masonry construction. This paper deals with the possibilities of additional hydrophobisation of ceramic bricks using chemical hydrophobic agents available in the EU market.

2 SPECIMENS

The specimens for testing the hydrophobisation of ceramic bricks were intended for the plinth masonry. They were wall bricks with a thickness of 250 mm. The bricks were chosen because of their low mass, small dimensions and the water absorption equal to that of the bricks used in thicker walls.

3 HYDROPHOBIC AGENTS

A total of five specimens from different producers and of different chemical compositions were chosen for the laboratory experiments. All the tested hydrophobic agents were silicon-based. They were organosilicate compounds exhibiting a high thermal resistance between –50 °C and 200 °C, the resistance to sudden temperature change, weather, sunlight and a high chemical resistance. A hydrophobic film was formed thanks to the intermolecular condensation of low-molecular-weight methylsiloxanes through the effect of atmospheric carbon dioxide. The main condition of the hydrophobising effect was the orientation of silicone molecules towards the surface of the masonry. There was a high amount of short-chain hydrocarbon residue, e.g., methyl, ethyl group (CH_{3-}, C_2H_{5-}) (**Figure 1**). This weak, often macromolecular, layer increases the contact angle to such an extent that the capillary elevation is reduced to zero or even that a capillary depression occurs. Thanks to this principle, the water-vapour and gas permeability of the building material is retained. These hydrophobic agents cannot be used in the cases where water under pressure acts upon the structure.[7]

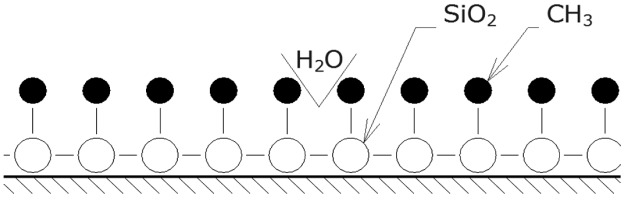

Figure 1: Orientation of silicone molecules[7]
Slika 1: Orientacija silikonskih molekul[7]

Some the most frequently used waterproofing preparations are silicone resin solutions formed in organic solvents, most often in white spirit or benzine. The resin content usually ranges from 3 % to 8 %. These are single-component solutions, mostly colourless or with a slight yellow hue and transparent; the hydrophobic effect occurs immediately after the solvent evaporates. These preparations cannot be used on wet surfaces; they can be used for hydrophobising previously hydrophobised materials. The presence of the solvent is disadvantageous in terms of fire, ecological and possible health hazard.

The other silicone hydrophobic agents are low-molecular-weight compounds – oligomers, which, due to air humidity, spontaneously polymerise upon application, producing the desired polymer. They are usually single-compound, translucent and colourless. Their advantage over the high-molecular-weight resins lies in their ability to chemically bond with the surfaces of quartz grains (if present) of the material being treated, thus increasing the abrasion resistance. They are sometimes supplied as a concentrate and the preparation is performed by mixing it with an appropriate solvent. Another advantage is their better ability to penetrate into a porous material.

Silicone microemulsions represent a special group. They are again silicone compounds with a relatively low molecular weight which, thanks to their molecular structure, are able to produce an emulsion with very small particles after being mixed with water. A slow reaction with water then produces the desired hydrophobic polymer. Their advantage lies in the possibility of mixing with water which facilitates the avoidance of organic solvents and a good penetration capability.

Methylsilanolates (methylsiliconates) – sodium or potassium – also belong to silicone hydrophobic agents. These substances are hydrophobising varieties of soluble glass. Similarly to soluble glass, when in contact with carbon dioxide, they are transformed into a modified gel of silicic acid that is hydrophobic in this case. Unfortunately, this chemical reaction also produces a hydroxide of the respective metal (sodium or potassium), later transformed into a carbonate. Thus, undesirable water-soluble efflorescent salts enter the structure of the material being treated. Their presence represents the risk of the formation of white efflorescence and even the degradation of the treated material due to the crystallisation pressure. The advantages of siliconates are their good water solubility (i.e., the possibility of application onto wet surfaces) and substantially lower prices in com-

Table 1: Used hydrophobic agents
Tabela 1: Uporabljena hidrofobna sredstva

No.	Description
1	Silane-siloxane microemulsion cream
2	Potassium methylsilanolate preparation
3	Hydrophobised siliconate solution
4	Solvent-free siloxane emulsion
5	Siloxane base with aromatic-free organic solvents

parison with the other silicone preparations. The resulting gel is non-soluble and thus effectively unremovable. Silanolates are recommended for the protection of historical buildings thanks to their good solubility and low price[8,9].

Table 1 contains an overview of the tested hydrophobic agents.

The soaking in hydrophobising solutions was always performed for (10, 20 and 30) s; only non-water-soluble preparations were applied by spraying them in a given amount. Next, the individual specimens were stored after the application of the hydrophobic agent in the laboratory environment for a week in order for the excess moisture to evaporate. The following tests were performed with the specimens thus prepared.

The bricks were put in a plastic box onto a wooden grid. Subsequently, they were flooded with water at a temperature of (20 ± 2) °C, always up to 50 mm of the height of the bricks. The bricks were weighed at regular intervals: after (1, 2, 3, 6, 24, 48, 72 and 96) h.

4 RESULTS

Hydrophobic preparations Nos. 1–4 were applied by soaking for (10, 20 and 30) s. Hydrophobic agent No. 5 was applied by being sprayed in the amount of approximately 250 g per brick. The measurement was also performed on the non-hydrophobised bricks. The testing was always carried out on two specimen bricks with a given hydrophobic-agent concentration and an immersion time. Hydrophobic agents Nos. 1, 2 and 4 were always prepared in two concentrations. The overview of the tested concentrations is summarized below:

- solution No. 1 was tested at concentrations of 1 : 20 and 1 : 30,
- solution No. 2 was tested at concentrations of 1 : 10 and 1 : 25,
- solution No. 3 was tested at a concentration of 1 : 2,
- solution No. 4 was tested at concentrations of 1 : 15 and 1 : 30.

The quantity being measured was the brick mass at the end of each interval (1, 2, 3, 6, 24, 48, 72 and 96) h. The amount of the absorbed water was calculated from the ratio of the measured mass to the brick surface area. Its capillary absorption was determined with the following formula:

$$A_w = \frac{m_w}{A} \quad (1)$$

A_w – capillary absorption in time (kg m^{-2})
m_w – mass of the brick soaked with water (kg)
A – area of the brick (m^2)

The values of the capillary absorption can be compared with each other despite the different methods of the application of the hydrophobic agents which is the validity of their efficiency. The results of the individual measurements are in **Table 2**:

Table 2: Overview of the obtained absorption values of the specimens
Tabela 2: Pregled dobljenih vrednosti absorpcije vzorcev

Hydrophobic agent number	Concentration	Dipping time (s)	Absorption (%)		Capillary absorption (kg m^{-2})	
			24 h	**96 h**	**24 h**	**96 h**
1	1 : 30	10	0.42	1.60	0.79	3.04
		20	0.41	1.39	0.77	2.64
		30	0.24	0.93	0.45	1.77
	1 : 20	10	0.35	0.76	0.65	1.44
		20	0.36	0.72	0.63	1.36
		30	0.38	0.67	0.60	1.27
2	1 : 25	10	16.38	22.05	32.98	42.31
		20	15.52	21.51	29.78	40.56
		30	11.08	20.14	20.65	40.07
	1 : 10	10	10.27	19.77	20.97	40.03
		20	8.47	19.61	17.26	38.19
		30	6.54	17.65	12.63	35.98
3	1 : 2	10	1.36	2.91	2.50	5.33
		20	1.26	2.15	2.44	4.16
		30	1.21	2.11	2.13	3.89
4	1 : 30	10	8.58	16.21	15.69	29.51
		20	7.51	15.42	11.74	28.19
		30	6.25	15.11	10.85	26.52
	1 : 15	10	6.01	12.65	12.35	24.64
		20	6.34	12.35	11.32	23.25
		30	5.52	11.01	6.28	19.97
5	–	–	9.42	17.26	18.39	33.70
Reference	–	–	25.70	27.22	47.65	50.47

The table shows that the effectiveness of individual hydrophobic agents varies significantly. The effectiveness of the hydrophobic agents is influenced by the concentration and the soaking time. The following chart compares the effectiveness values for the hydrophobic agents after 96 h of soaking in water by means of capillary absorption (**Figure 2**).

The values show that the most effective hydrophobisation was achieved by applying hydrophobic agent No. 1, specifically at a concentration of 1 : 20. The following chart on **Figure 3** shows the progression of the capillary

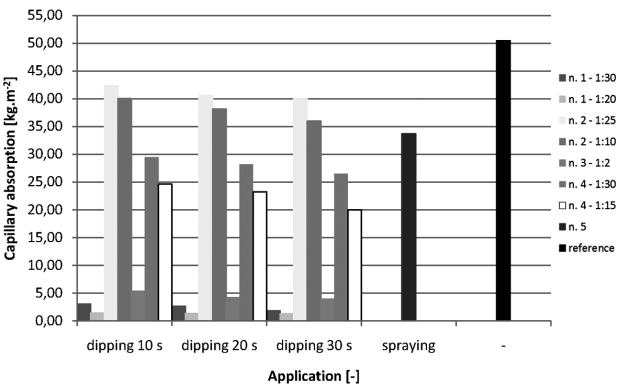

Figure 2: Capillary absorption of individual hydrophobic agents
Slika 2: Kapilarna absorpcija pri uporabi posameznih hidrofobnih snovi

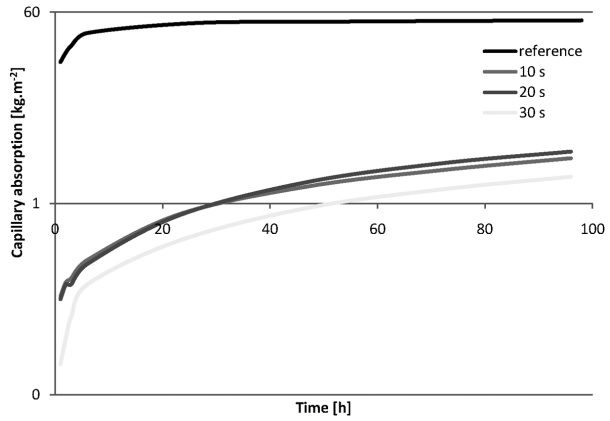

Figure 3: Process of capillary absorption over time for hydrophobic agent No. 1 (1 : 20)
Slika 3: Potek kapilarne absorpcije v odvisnosti od časa pri hidrofobni snovi št. 1 (1 : 20)

absorption over time of this hydrophobic agent applied by soaking for (10, 20 and 30) s, in comparison with the reference capillary absorption.

5 CONCLUSION

Table 2 lists all the experimentally obtained values, which show, when compared to the reference values, that the capillary absorption was reduced in all the instances by applying the tested hydrophobic agents. The effectiveness of the hydrophobic agents is influenced by the type of the preparation, its concentration and the time of the treatment with the agent.

The best results were reached using hydrophobic agent No. 1, i.e., the agent based on the silane-siloxane microemulsion cream with a concentration a 1 : 20. With this hydrophobic agent, as with as all the others, an increasing soaking time caused an increase in the effectiveness of the preparation at a reduced capillary absorption.

It is necessary to note that during a long-term exposure to moisture, capillarity is always at work. These tested hydrophobic agents cannot be considered as complete substitutes for sheet waterproofing; however, they can be used for masonry protection during construction. Also, in the case of an occasional moisture stress on the lower part of the masonry (spraying precipitation moisture), hydrophobic agents provide a sufficient protection.

Acknowledgements

This paper was elaborated with the financial support of the Technology Agency of the Czech Republic within the project under ref. n. TA04020920 and the project no. L01408 "ADMAS Up – Advanced Materials, Structures and Technologies".

6 REFERENCES

[1] Czech standard CSN P 73 0600, Waterproofing of buildings – Basic provisions, 2000
[2] Czech standard CSN P 73 0610, Waterproofing of buildings – The rehabilitation of damp masonry and additional protection of buildings against ground moisture and against atmospheric water – Basic provision, 2000
[3] D. Beben, Z. Manko, Influence of selected hydrophobic agents on some properties of autoclaving cellular concrete (ACC), Construction and Building Materials, 25 (**2011**), 282–287, doi:10.1016/j.conbuildmat.2010.06.028
[4] M. Medeiros, P. Helene, Efficacy of surface hydrophobic agents in reducing water and chloride ion penetration in concrete, Mater. Struct., 41 (**2008**), 59–71, doi:10.1617/S11527-006-9218-5
[5] L. Wolff, M. Raupach, Hydrophobieren von Stahlbetonoberflächen, Betonwerk und Fertigteil-Technik, 69 (**2003**) 10, 12–21
[6] Czech standard CSN P 73 0606, Waterproofing of buildings – Continuous sheet water proofing – Basic provisions, 2000
[7] R. Drochytka, Plastic substances, Study support, VUT Brno, Brno, 2007
[8] J. de Vries, R. B. Polder, Hydrophobic Treatment of Concrete, Construction and Building Materials, 11 (**1997**) 4, 259–265, doi:10.1016/S0950-0618(97)00046-9
[9] P. Kotlík, Stavební materiály historických objektů, 1. vydání, Praha 1999

UDK 678.7
Professional article/Strokovni članek

ISSN 1580-2949
MTAEC9, 49(5)821(2015)

FLAME RESISTANCE AND MECHANICAL PROPERTIES OF COMPOSITES BASED ON NEW ADVANCED RESIN SYSTEM FR4/12

NEGORLJIVOST IN MEHANSKE LASTNOSTI KOMPOZITOV NA OSNOVI NOVIH NAPREDNIH SISTEMOV SMOL FR4/12

Vladimír Rusnák[1], Soňa Rusnáková[2], Ladislav Fojtl[2], Milan Žaludek[2], Alexander Čapka[2]

[1]Faculty of Metallurgy and Materials Engineering, VŠB-Technical University of Ostrava, 17. listopadu 15, 708 33 Ostrava-Poruba, Czech Republic
[2]Faculty of Technology, TBU in Zlín, Nad Stranemi 4511, 760 05 Zlín, Czech Republic
vladimir.rusnak@form-composite.com

Prejem rokopisa – received: 2014-09-10; sprejem za objavo – accepted for publication: 2014-11-24

doi:10.17222/mit.2014.223

Composite materials used in the transport industry and also in other sectors must have a certain degree of flame resistance. For this purpose, commonly used flame retardants are based on halogen compounds in the liquid state or aluminum hydroxide in the solid state. Solid flame retardants have a negative effect on the processing and mechanical properties. Low viscosity and rapid wettability of fibers are very important, especially in an resin transfer molding (RTM) process.
Therefore, a new advanced matrix system based on phosphorus flame retardants was developed. The flame resistance and mechanical properties of the composite materials produced from the new resin system were tested. Furthermore, the processing parameters and tests are described in the article.

Keywords: flame-retardant composites, phosphorus, RTM, vacuum infusion

Kompozitni materiali, ki se uporabljajo v industriji transporta in tudi v drugih sektorjih, morajo ustrezati določeni stopnji negorljivosti. Za ta namen so splošno uporabljani zaviralci gorenja, ki temeljijo na osnovi spojin halogenov v tekočem stanju ali na aluminijevem hidroksidu v trdnem stanju. Zaviralci gorenja v trdnem stanju imajo negativen vpliv na izdelavo in mehanske lastnosti. Posebno majhna viskoznost in hitra omočljivost vlaken sta pomembni, posebno še pri RTM-procesu.
Zato je bila razvita nova napredna matrična zasnova na podlagi fosfornega zaviralca gorenja. Preizkušene so bile odpornost proti vžigu in mehanske lastnosti kompozitnega materiala, izdelanega iz novega sistema smol. V članku so opisani parametri izdelave in preizkusi.

Ključne besede: negorljivi kompoziti, fosfor, RTM, vakuumska infuzija

1 INTRODUCTION

Composite materials based on a polymer matrix and glass reinforcement are often used in transport vehicles. The main reasons for their utilization are their low mass, excellent formability and relatively low production costs for low and medium manufacturing series.

When composite and sandwich structures are used in train applications, they have to fulfill different requirements. The first (or the main) requirement is the fire safety.[1] In addition to the fire safety of these materials, relatively high mechanical properties, dimensional and thermal stabilities and health safety are required. For example the French standard NF F01-28: Fiber reinforced plastic in railway rolling stock requires a minimum bending strength of reinforced plastics of up to 150 MPa, while maintaining the self-extinguishing properties according to another French standard, NF F16-101.

Polyester matrices reinforced with fiber reinforcements in various forms are primarily used for these applications. In these composite systems self-extinguishing properties are primarily achieved with additions of flame retardants to the synthetic matrices.

Flame retardants are the materials that prevent or retard the burning of a material and are indispensable for plastic products, electrical applications, construction materials, textiles, etc. Generally, they can be divided into two main groups: the reactive organic and non-reactive inorganic compounds (additives). The reactive organic compounds include molecules of halogens (bromine and chlorine), melamine compounds, phosphate compounds and many others.[2] Their main advantage is that they do not change the physical properties of the resin. Generally, the amount of the flame retardant in a polymer matrix depends on the retarding effect. However, it is necessary to take into account the possibility of a negative effect influencing the mechanical and processing properties of the polymer.

The reactive inorganic compounds include aluminum hydroxide (ATH) and magnesium hydroxide, red phosphorus, ammonium compounds, antimony compounds of antimony or boron, graphite, etc.[3,4] These compounds are insoluble in a polymer matrix and need to be added in higher concentrations (30–150 %) to achieve the right fire-retardancy level. They have a very negative influence

on the viscosity of the resulting mixture, thus limiting their use in the preparation of a composite with the vacuum infusion or RTM technology. And, last but not least, they negatively influence the mechanical properties – the composites become less stiff and brittle.

They slow down the combustion process in different ways, physically or chemically. The physical processes include cooling the material, creating a protective layer (that continues to protect the remaining material, blocking the combustion by limiting the access of air) or diluting the gas flame with retardant components.

With respect to the chemical processes, flame retardancy is a reaction in the gaseous phase, leading to a release of significant amounts of water or carbon dioxide. Thus, a reaction at this stage limits and slows down a burning process. This group includes the flame retardants based on halogens. These compounds create carbon ash on the polymer surface or a swelling under the protective layer of the ash to provide a better thermal insulation.[5]

Some flame retardants based on halogens, such as polychlorinated biphenyls (PCB), or various brominated flame retardants (polybrominated diphenyl ethers, polybrominated biphenyls) may pose a health risk. The fire retardancy of a halogenated flame retardant is based on the formation of a volatile-combustion hydrobromic or hydrochloric acid in the presence of hydrocarbons (e.g., toxic dioxins) at a temperature of around 350 °C.

Flame retardants based on phosphorus are the compounds that are more environmentally friendly and their consumption is slowly growing. Phosphor flame retardants are already applied in matrices with phosphorus amounts of about 5–8 %. They work very well for the polymers containing oxygen in the chain.

2 EXPERIMENTAL WORK

2.1 Materials

2.1.1 Matrix

An unsaturated polyester resin diluted with styrene, containing a phosphorus flame retardant incorporated into the chain molecules was developed under the working title FR4/12 (**Table 1**). The goal was to prepare a resin, which enables, due to its viscosity, a preparation of the composite parts for rail vehicles using the RTM method or the vacuum infusion method. Pure resin would also meet the requirement for a flame resistance without the additives – the limited oxygen index (*LOI*) must be higher than 30. The requirement for the maximum viscosity was 600 mPa s.[6] The amount of phosphorus in the polyester chain is naturally limited since it greatly affects the mechanical properties. The resulting formulation is designed in such a way that the mechanical properties of pure resin match the mechanical properties of the halogenated resins, normally used for the production of the composite parts for rail vehicles.

Table 1: Mechanical and processing properties of FR4/12 matrix
Tabela 1: Mehanski in procesni parametri osnove FR4/12

Material description	Matrix FR4/12
Viscosity (Brookfield LV 2/12, 20 °C) (mPa s) [6]	475
T_g/°C	105
HDT/°C	68
Acid number, the KOH content (mg g^{-1})	2.5
Hydroxyl number, the KOH content (mg g^{-1})	50
Tensile strength (MPa)	63
Tensile modulus (MPa)	3400
Elongation (%)	2.2
Flexural strength (MPa)	3600
Flexural modulus (MPa)	130
Oxygen index	32–34

2.1.2 Reinforcements, coatings

A multiaxial nonwoven fabric (bidiagonal and triaxial fabric) was selected as the reinforcement. A nonwoven fabric guarantees a high proportion of glass in a composite (hence, better mechanical properties). It also has a suitable drapability. In line with the requirements of the process technology, mats with the trade name UNIFILLO ® were used for the RTM technology.

To determine the effect of the coating on the combustibility, two samples of the BÜFA gelcoat layer were provided.

2.2 Production methods and testing

The testing of the resin system was carried out at two levels. One level was the production of the test samples. These samples were produced on a simple plate or in a simple RTM mold. The second level of the matrix testing consisted of a production of real products (prototypes). Production methods were chosen with respect to the environmental, health and economic aspects (productivity), including two closed-production technologies – VIP (vacuum infusion process) and RTM (resin transfer molding).

In addition to the newly produced matrix, a total of five composite materials (**Table 2**) of various compositions as well as other polymer systems were produced (Sample D was made from a phenolic prepreg, Sample E was based on a commercial matrix). Samples B and E were provided with a gelcoat. Firstly, the flexural test was realized according to ISO 178.[7] With respect to the fire retardancy the oxygen index was recorded, and the tests of the flame spread and the (partial) heat release were performed using the cone calorimeter method.[8,9]

3 RESULTS AND DISCUSSION

The measured values of the mechanical properties and fire behavior are shown in **Figure 1**. As can be seen, the highest values for both flexural properties of the samples prepared with the wet technology were obtained

Table 2: Material characterization of composite materials
Tabela 2: Karakterizacija materialov v kompozitu

Material description	Sample A	Sample B	Sample C	Sample D	Sample E
Reinforcement lay-up	1 × BIDI glass fabric* 1 × CGM ** 1 × BIDI glass fabric*	1 × BIDI glass fabric* 1 × CGM** 1 × BIDI glass fabric*	1 × BIDl glass fabric* 1 × CGM** 1 × BIDI glass fabric*	10 × phenolic/glass* prepreg	1 × BIDI glass fabric* 1 × CGM** 1 × BIDI glass fabric*
Matrix	matrix FR4/12	matrix FR4/12	matrix FR4/12	phenolic matrix	Norester 880
Additive	–	–	–	–	ATH (100 % to matrix)
Coating	–	gelcoat BÜFA	–	–	gelcoat BÜFA
Production technology	RTM	RTM	VIP	prepreg	RTM

(*bidiagonal glass fabric, **continuous-filament glass mat)

for Sample C. Sample D prepared from prepregs showed excellent flexural performance and fire properties compared to the samples prepared with RTM and VIP; however, these materials are very expensive.

Moreover, comparing FR4/12 to the commercial matrix, it is obvious that the obtained mechanical properties are almost twice as high as for the samples prepared from FR4/12.

The tests of the fire properties (**Figure 2**) showed that the gelcoat layer also influences the flame spread and the heat release. Further, the oxygen index of Samples B (matrix FR4/12) and E (the commercial matrix) was the same for both samples. Sample C exhibited the lowest oxygen index of all the produced composites. Regarding the requirement for the oxygen index (higher than 30), all the samples passed the test. The heat-release parameter (**Figure 3**) was measured only for Samples A, B and C, where individual values were 211.6, 154.7 and 37.7. The curves in **Figure 3** show the heat release during the combustion of the samples. The flame spread (**Figure 4**) for Samples A and C is the same (due to the same material composition).

4 CONCLUSION

The main objective of the mechanical testing was to determine whether the strengths of the material combinations reached 150 MPa (this value is the requirement

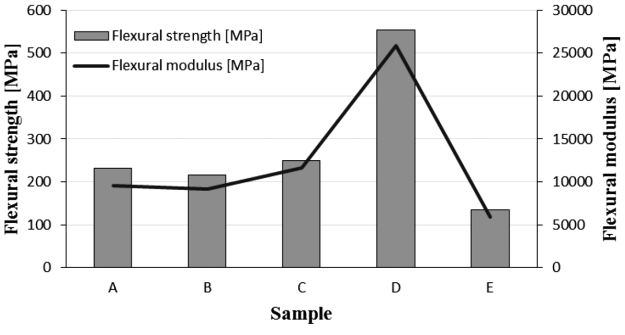

Figure 1: Flexural properties of prepared samples
Slika 1: Upogibne lastnosti pripravljenih vzorcev

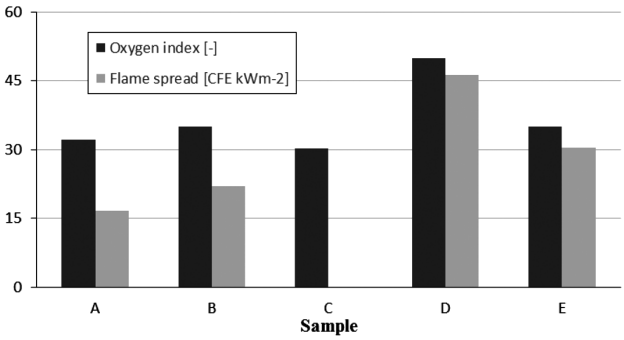

Figure 2: Fire properties of prepared samples
Slika 2: Požarne lastnosti pripravljenih vzorcev

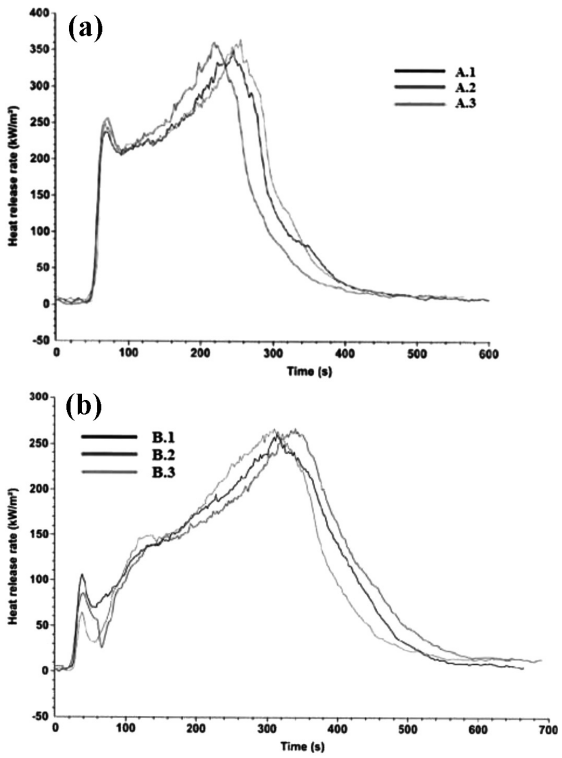

Figure 3: Heat release during the flame test of composite materials: a) sample A, b) sample B
Slika 3: Sproščanje toplote pri preizkusu kompozitnega materiala v plamenu: a) vzorec A, b) vzorec B

Table 3: Table guide to selecting the test classification[1]
Tabela 3: Tabelarni napotek za izbiro klasifikacije preizkusa[1]

ASTM 2863: LIMITED OXYGEN INDEX (*LOI*)	UK: BS 476 PART 6,7	GERMANY: 4102 5510		FRANCE: NF P 92-501		USA: ASTM E84 UL94		EUROCLASS: SINGLE BURNING ITEM (SBI)
41– 50	Class 0	Class A2	S4	M1	25	5V	0	B
34.5–41	Class 1	Class B1	S4	M2	50	0	1	B/C
28.5– 34.5	Class 2	Class B2	S3	M3	100	0	2	C/D
22–28.5	Class 3	Class B3	S2	M4	>100	1	3	D/E

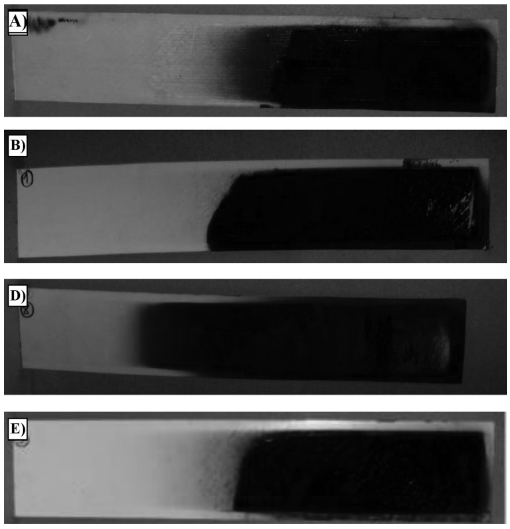

Figure 4: Composite samples after the flame-spread test
Slika 4: Kompozitni vzorci po preizkusu širjenja ognja

of French standard NF F01-281). All the material combinations met this requirement with a certain safety margin, except for Sample E. The result was expressed with a high amount of the filler in the resin (the ratio of 1 : 1). It is obvious that after adding the additives the value of the bending strength decreases.

The objective of testing the fire resistance of the materials was to determine the level of the flame retardancy of the composites made from the new matrix system. Using a simple test – determination of the oxygen index – the materials could be classified into the mid-level category of flame-retardant resins. It was assumed that with the addition of non-reactive additives the oxygen index, together with the overall resistance to fire, would increase. According to all the flame-retardancy tests, the flame-retardant gelcoat plays an important role in improving the fire resistance.

The oxygen index (**Table 3**) for various composites based on the new matrix is very similar to the oxygen index of pure resin. Increasing the glass amount has a minimum impact on the oxygen index. However, it is assumed that with the additions of non-reactive additives to a composite system, the oxygen index will increase. The values of the heat release for the phenolic systems are relatively large in comparison with the values for the composite systems based on the new matrix.

The developed matrix exhibits excellent processing properties, good and fast fiber wetting, adjustable reactivity and curing times. Another advantage is that the used promoter is based on iron compounds.

From the overview of the properties of all the systems, it is clear that the polyester systems do not reach the same fire-resistance values as the phenolic systems. On the other hand, due to other advantages (surface quality, price and processing methods) the development of the composite systems based on polyester systems will dominate.

Acknowledgement

This work and the project were realized with the financial support of the Ministry of Industry and Trade of the Czech Republic, project number FR-T13/433. Further, this study was also supported by an internal grant of TBU in Zlín, No. IGA/FT/2015/001, funded from the resources for specific university research.

5 REFERENCES

[1] Fire retardant polyester systems, Product guide of the Reichhold company

[2] N. Sain, S. H. Park, F. Suhara, S. Law, Flame retardant and mechanical properties of natural fibre-PP composites containing magnesium hydroxide, Polymer Degradation and Stability, 83 (**2004**), 363–367, doi:10.1016/S0141-3910(03)00280-5

[3] A. Genovese, R. A. Shanks, Structural and thermal interpretation of the synergy and interactions between the fire retardants magnesium hydroxide and zinc borate, Polymer Degradation and Stability, 92 (**2007**) 1, 2–13, doi:10.1016/j.polymdegradstab.2006.10.006

[4] A. P. Mouritz, A. G. Gibson, Fire properties of polymer composite materials, vol. 143, Springer, Netherlands 2006, 401, doi:10.1007/978-1-4020-5356-6

[5] G. E. Zaikov, S. M. Lomakin, S. V. Usachev, E. V. Koverzanova, N. G. Shilkina, L. V. Ruban, New Approaches to Reduce Plastic Combustibility, In: A. K. Kulshreshtha, C. Vasile (Eds.), Handbook of Polymer Blends and Composites, Volume 2, Smithers Rapra Technology, UK 2002, 165–199

[6] EN ISO 2555:1989, Plastics, Resins in the liquid state or as emulsions or dispersions, Determination of apparent viscosity by the Brookfield Test method, 1989

[7] ISO 178:2010, Plastics, Determination of flexural properties, 2010

[8] EN ISO 4589-2:1999, Plastics, Determination of burning behaviour by oxygen index, Ambient-temperature test, 1999

[9] ISO 5658-2:2006, Reaction to fire tests, Spread of flame – Part 2: Lateral spread on building and transport products in vertical configuration, 2006

UDK 621.791/.792:620.17:620.187:669.14
Professional article/Strokovni članek

ISSN 1580-2949
MTAEC9, 49(5)825(2015)

EFFECT OF PROCESS PARAMETERS ON THE MICROSTRUCTURE AND MECHANICAL PROPERTIES OF FRICTION-WELDED JOINTS OF AISI 1040/AISI 304L STEELS

VPLIV PROCESNIH PARAMETROV NA MIKROSTRUKTURO IN MEHANSKE LASTNOSTI TORNO VARJENIH SPOJEV JEKEL AISI 1040/AISI 304L

İhsan Kirik[1], Niyazi Özdemır[2]

[1]Batman University, Department of Metallurgy and Material Engineering, 72060 Batman, Turkey
[2]Fırat University, Department of Metallurgy and Materials Engineering, 23119 Elazığ, Turkey
alihsankirik@gmail.com

Prejem rokopisa – received: 2014-09-17; sprejem za objavo – accepted for publication: 2014-10-17

doi:10.17222/mit.2014.235

Couples of AISI 304L and AISI 1040 steels were welded using the continuous-drive friction-welding process. The welded joints were manufactured using three different rotational speeds ((1300, 1500 and 1700) r/min), three different frictional pressures and three different frictional times. To determine microstructural changes, the interface regions of the welded samples were examined by scanning electron microscopy (SEM), X-ray diffraction (XRD) and energy dispersive spectrometry (EDS). Microhardness and tensile tests of the welded samples were conducted. The results show that the properties of the microstructures are significantly changed and the interface temperature increased with the frictional time. An excellent tensile strength was observed for the joint made at a rotational speed of 1700 r/min and a frictional time of 4 s.

Keywords: friction welding, AISI 1040 steel, AISI 304L steel

Jekli AISI 304L in AISI 1040 sta bili zvarjeni z uporabo kontinuirnega tornega procesa varjenja. Zvarjeni spoji so bili izdelani pri treh različnih hitrostih vrtenja ((1300, 1500 in 1700) r/min), treh različnih tornih tlakih in treh različnih tornih časih. Za določitev mikrostrukturnih sprememb je bilo stično področje zvarjenega vzorca preiskano z vrstičnim elektronskim mikroskopom (SEM), z rentgensko difrakcijo (XRD) in z energijsko disperzijsko rentgensko spektrometrijo (EDS). Izvršeni so bili preizkusi mikrotrdote in natezni preizkusi varjenih vzorcev. Rezultati kažejo, da se mikrostruktura omembe vredno spremeni in da se temperatura stika povišuje s časom trenja. Odlična natezna trdnost stika je bila ugotovljena pri spoju s hitrostjo vrtenja 1700 r/min in pri tornem času 4 s.

Ključne besede: torno varjenje, jeklo AISI 1040, jeklo AISI 304L

1 INTRODUCTION

Stainless steels are iron-based alloys containing 8–25 % nickel and 12–30 % chromium, resisting both corrosion and high temperature. Generally, stainless steels can be classified as martensitic, ferritic and austenitic. Austenitic stainless steels represent the largest group of stainless steels and are produced in higher tonnages than any other group. They have a good corrosion resistance in most environments. Austenitic stainless steel can be strengthened significantly by cold working and are often used in the applications requiring a good atmospheric or elevated-temperature corrosion resistance.

In spite of a wide variety of austenitic stainless steel, the 300-series alloys, based on the 18Cr-8Ni system, are the oldest and most commonly used.[1–5] Type 304 is the foundation of this alloy series and, along with 304L, it represents the most commonly selected austenitic grade. Although austenitic alloys are generally considered to be very weldable, they are subjected to a number of weldability problems if proper precautions are not taken. Liquation cracking and weld solidification may occur depending on the composition of the base, the filler metal and the level of impurities, particularly S and P. In spite of the good general corrosion resistance of austenitic stainless steels, they may be subject to localized forms of corrosion at grain boundaries and in the heat-affected zone. For joining dissimilar materials, conventional fusion welding is used. However, this method has a lower efficiency when compared to the friction-welding method.[5–7]

The friction-welding process is a solid-state welding process producing welds due to a compressive-force contact of two workpieces: one is rotating and the other is stationary.[8,9] The heat is generated at the weld interface due to a continuous rubbing of the contact surfaces, while the temperature rises and softens the material. Eventually, the material at the interface starts to flow plastically and forms an upsetting. When a certain amount of upsetting occurs, the rotation is stopped and the compressive force is maintained or slightly increased to consolidate the joint. The fundamental parameters of the friction-welding (FW) process are the rotational speed, the frictional pressure and time, and the forging pressure and time. The advantages of friction welding are a high material saving, a short production time and the possi-

bility of joining different metals or alloys. This method can also be used to join the components that have circular or non-circular cross-sections.[10–17]

In this study, parts of the AISI 304L austenitic stainless steel and AISI 1040 carbon steel with equal diameters were welded using the friction-welding method. The strengths of the joints were determined with tensile tests and compared with those of the base materials. Then, the hardness variations and microstructures of the welding zones were obtained and investigated using macro- and microphotographs.

2 EXPERIMENTAL PROCEDURES

The workpieces used in this work were Ø 12 mm rods of AISI 1040 and AISI 304L austenitic stainless steels. The nominal chemical compositions and mechanical properties of the materials used are shown in **Tables 1** and **2**, respectively. The AISI 1040 medium-carbon steel and the AISI 304L austenitic stainless steel were joined with a PLC-controlled continuous-drive friction-welding machine using different rotational speeds, frictional times and frictional pressures, as indicated in **Table 3**. The temperature of the welded zone during the

Table 1: Chemical compositions of test materials in mass fractions
Tabela 1: Kemijska sestava materialov za preizkuse v masnih deležih

Materials	Alloying elements (*w*/%)							
	C	Mn	P	S	Cr	Mo	Ni	Fe
AISI 1040	0.37–0.44	0.60–0.90	0.040	0.050	–	–	–	Balance
AISI 304L	0.042	1.47	0.032	0.032	18.25	0.30	8.09	Balance

Table 2: Mechanical properties of parent materials
Tabela 2: Mehanske lastnosti izhodnih materialov

Material	Hardness (HV)	Yield strength (MPa)	Tensile strength (MPa)
AISI 1040	165	215	630
AISI 304L	210	380	700

Table 3: Process parameters used in friction welding
Tabela 3: Procesni parametri, uporabljeni pri tornem varjenju

Samp. No	Welding parameters								
	Rotational speed (r/min)	Frictional time (s)	Frictional pressure (MPa)	Forging pressure (MPa)	Forging time (s)	Axial short. (mm)	Max. temp. (°C)	Max. hardness (HV)	Max. tensile stren. (MPa)
S1	1300	8	30	60	4	6	1204	362	371.414
S2	1300	8	40	80	4	7	1189	311	412.431
S3	1300	8	50	100	4	8	1105	400	483.223
S4	1300	6	30	60	3	5	1176	348	387.026
S5	1300	6	40	80	3	6	1102	317	559.276
S6	1300	6	50	100	3	7	1152	312	600.061
S7	1300	4	30	60	2	4	1214	330	580.338
S8	1300	4	40	80	2	5	1124	277	599.821
S9	1300	4	50	100	2	6	1182	254	617.106
S10	1500	8	30	60	4	7	1175	320	473.096
S11	1500	8	40	80	4	8	1104	376	575.716
S12	1500	8	50	100	4	9	1123	329	596.613
S13	1500	6	40	60	3	6	1140	319	588.216
S14	1500	6	40	80	3	7	1164	337	599.296
S15	1500	6	50	100	3	8	1129	278	611.714
S16	1500	4	30	60	2	4.5	1104	356	586.311
S17	1500	4	40	80	2	5.5	1185	361	603.196
S18	1500	4	50	100	2	6	1075	256	588.807
S19	1700	8	30	60	4	8	1089	321	531.222
S20	1700	8	40	80	4	9	1067	342	563.691
S21	1700	8	50	100	4	10	1075	263	568.780
S22	1700	6	30	60	3	7	1125	349	573.808
S23	1700	6	40	80	3	7.5	1093	322	589.467
S24	1700	6	50	100	3	8.5	1143	245	571.993
S25	1700	4	30	60	2	4.5	1089	364	592.684
S26	1700	4	40	80	2	5.5	1092	300	612.923
S27	1700	4	50	100	2	6.5	1047	210	637.500

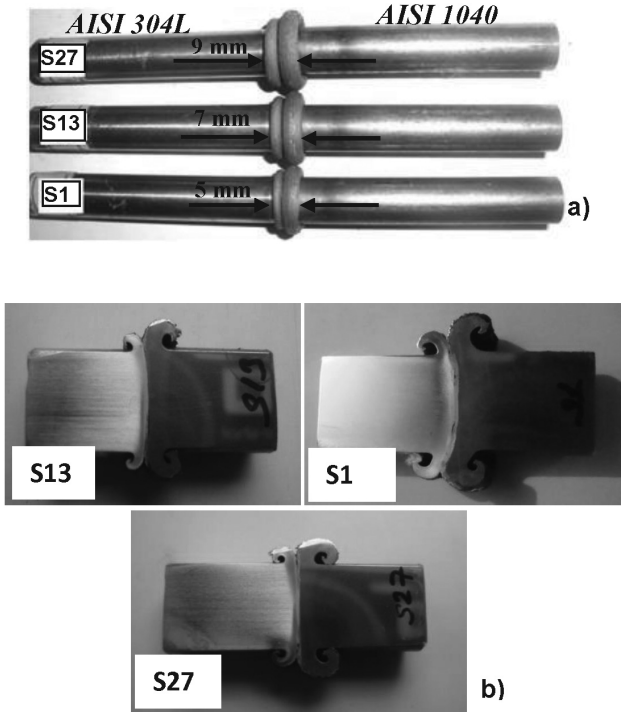

Figure 1: a) Surface and b) cross-sectional macro-images of FW joints of samples S1, S13 and S27
Slika 1: a) Površina in b) makrovidez prečnega prereza FW-spoja pri vzorcih S1, S13 in S27

welding process was measured with an IGA 15 PLUS device. After the friction welding, the microstructural changes in the interface regions of the joints were examined with scanning electron microscopy (SEM), X-ray diffraction (XRD) and energy dispersive spectrometry (EDS). Microhardness and tensile tests were conducted and the fracture surfaces of the tensile-test samples were investigated.

3 RESULTS AND DISCUSSIONS

3.1 Evaluation of macro- and microstructural properties

Figures 1a and **1b** show macro-images of the surfaces and interfaces of the friction-welded joints with three different frictional times, respectively. From the figures, the materials of the overflow out of the interfaces are seen to be clean-cut, and the widths of the flashes are measured to be (5, 7 and 9) mm for the frictional times of (4, 6 and 8) s, respectively. When joining dissimilar materials by friction welding flash is formed, depending on the mechanical properties of the materials. The extent of the flash increased with the increasing rotational speed, frictional time and frictional pressure. The flash diameter of the joints was larger for the AISI 1040 steel than for the AISI 304L steel. There are no cracks, cavities or disconnected regions seen on the samples joined at a rotational speed of 1700 r/min.

Table 3 shows the axial shortening of the friction-welded joints. As it can be seen from these results, the axial-shortening values for the materials are different owing to the plastic deformation of the materials. The axial shortening increases with the increasing rotational speed, frictional time and frictional pressure due to the increasing heat input and plastic deformation in the interface of the friction-welded joints. The maximum axial shortening is seen on S21 (10 mm) welded at the following process parameters: rotational speed is 1700

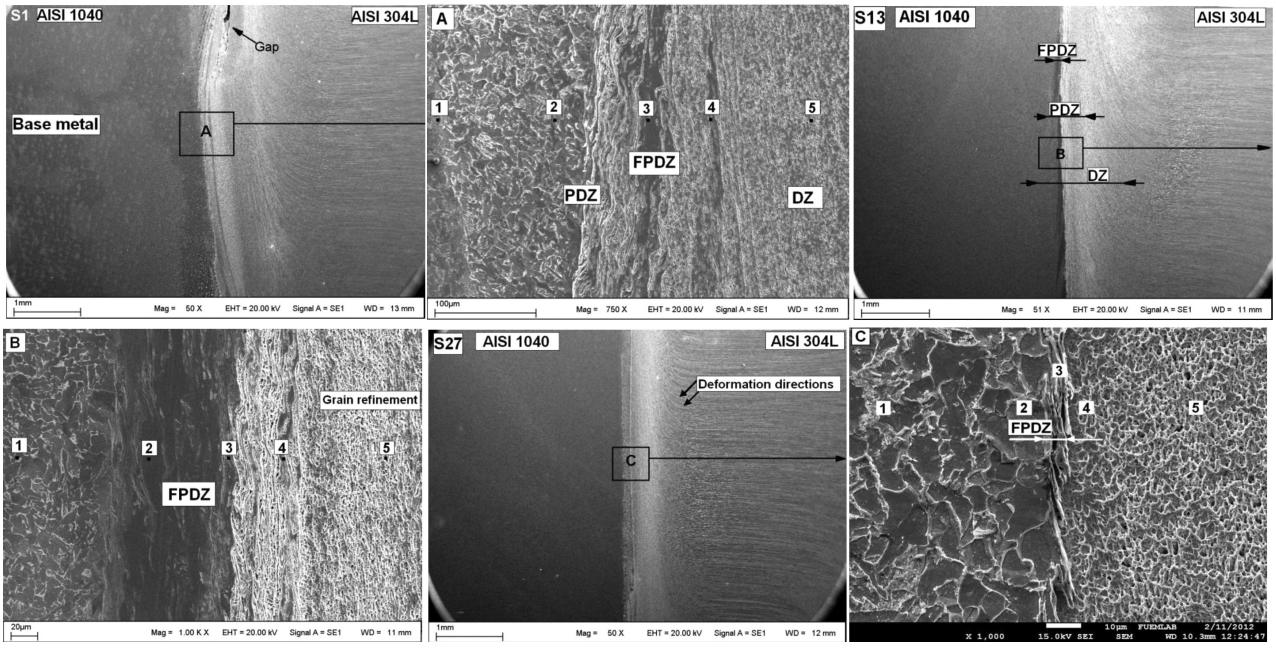

Figure 2: SEM micrographs of the weld zones of the S1, S13 and S27 samples
Slika 2: SEM-posnetki področja zvara pri vzorcih S1, S13 in S27

r/min, frictional pressure 50 MPa, forging pressure 100 MPa, frictional time 8 s, forging time 4 s.

Figure 2 shows the joint microstructures for samples S1, S13 and S27 obtained at three different rotational speeds. On **Figure 2** distinct regions are seen in the heat-affected zone and the interface of the S1 joint. As reported in the references, the evaluation of the microstructures of the joints revealed different zones in all the samples that were identified as the base metal (BM), the partially deformed zone (PDZ), the deformed zone (DZ) and the fully plasticized deformed zone (FPDZ)[13,15,17]. In S1, some disconnected regions and gaps were observed with SEM. In addition, the widths of the FPDZ and DZ expand, and the irregularities observed on all the samples were due to the decreasing frictional and forging pressure, and increasing frictional time. In the SEM micrographs of sample S1, the width of the deformed zone and the irregularity are increased due to a low frictional pressure and a high frictional time. The pressure caused a grain refinement in the central region of the S13 weld adjacent to the FPDZ and DZ. It was observed that the rotational speed and frictional time affected the weld-region geometry and the width.

In S27, a high rotational speed caused a rapid heating to high temperatures at the interface. A greater volume of the viscous material was pushed out of the interface due to the increased axial shortening and temperature gradient. In addition, in the areas adjacent to the PDZs on three SEM images of the samples, overflows and slip bands due to the effect of the heat and the axial pressure are clearly seen. Away from the region of deformation the density of the slip bands decreased due to the axial pressure.

3.2 Hardness-test results

The hardness tests of the welded samples were carried out in the lines perpendicular to the weld interfaces of the friction-welded joints (**Figure 3**). Similar microhardness profiles were observed for all the welds. The microhardness values for the weld zones were much higher than those for the parent steels. The microhardness was the highest at the interface for all the joints, decreasing toward the main material. A partial presence of martensite was the reason for an increase in the hardness of the weld zone[16] of the AISI 1040 steel, while a higher hardness of steel AISI 304L was due to the grain refinement.[9,10,17] Among the joints, the highest hardness value was measured for sample S1, due to a low rotational speed and a higher frictional time causing a more severe plastic deformation.

The temperatures of the weld zones, during the friction welding, were measured with the IGA 15 PLUS infrared temperature-measurement device (**Figure 4**) and they were between 1025 °C and 1214 °C. The temperature of a weld zone was directly affected and varied by the increasing frictional time. The increasing hardness of the interface of a friction-welded joint and the degree of deformation varied in dependence of the decreasing rotational speed. With a low rotational speed, the material of the interface was not sufficiently viscous. How-

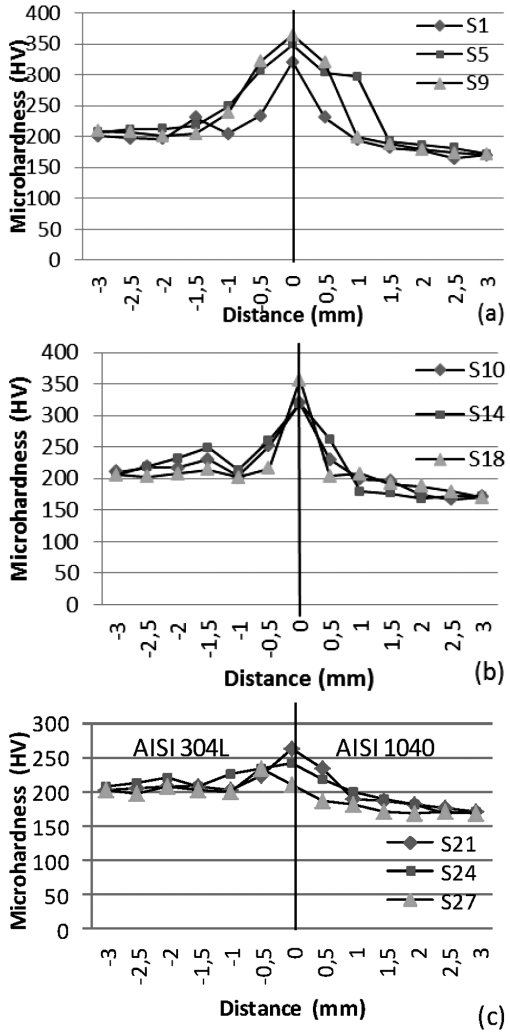

Figure 3: Typical microhardness distributions perpendicular to the interfaces of the joints: a) S1-S9, b) S10-S18 and c) S19-S27

Slika 3: Značilen potek trdote pravokotno na ravnino spoja vzorcev: a) S1-S9, b) S10-S18 in c) S19-S27

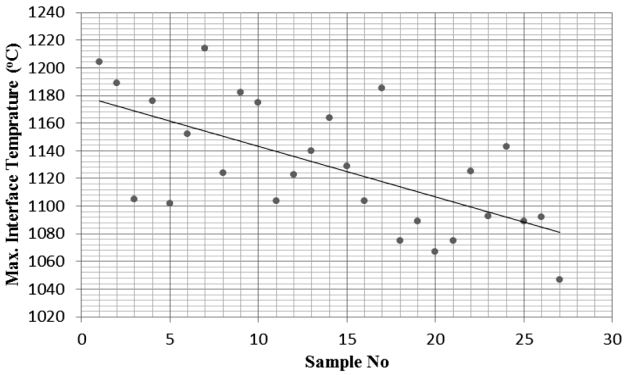

Figure 4: Temperatures of friction-welded joints

Slika 4: Temperature pri tornem varjenju spojev

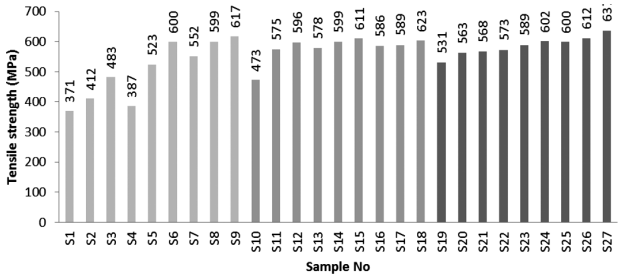

Figure 5: Tensile-test results for friction-welded joints of dissimilar materials

Slika 5: Rezultati nateznih preizkusov torno zvarjenih spojev različnih materialov

ever, looking at the hardness values for all the samples, the hardness values for the AISI 304L austenitic stainless steels were higher than for the AISI 1040 medium-carbon steels due to the deformation hardening. The main reasons for this difference are the heat-transfer capacity and the yield strength of the stainless steels that are 60 % higher than those of the medium-carbon steels.[18,19] The lowest hardness and the lowest temperature were obtained for specimen S27, at the rotational speed of 1700 r/min, frictional pressure of 50 MPa and frictional time of 4 s.

3.3 Tensile-test results

Figure 5 shows typical tensile strengths for the friction-welded joints consisting of dissimilar materials of AISI 304L and AISI 1040 tested at a strain rate of $1 \cdot 10^{-2}$ s^{-1}. The tensile fracture surfaces of the friction-welded joints are illustrated in **Figure 6**. All the samples failed in the area adjacent to the HAZ on the AISI 1040 side. The failure distance from the welding line increases depending on the higher rotational speed and frictional pressure (**Table 4**). The tensile strength of the welded joints depends markedly on the rotational speed and frictional time. The tensile-strength values for the FW joints were from 371 MPa to 637 MPa, and the highest tensile strength was exhibited by S27 welded at the rate of 1700 r/min and frictional time of 4 s. The increase in the tensile strength was due to the heat input and high plastic deformation that occurred at the interface of both

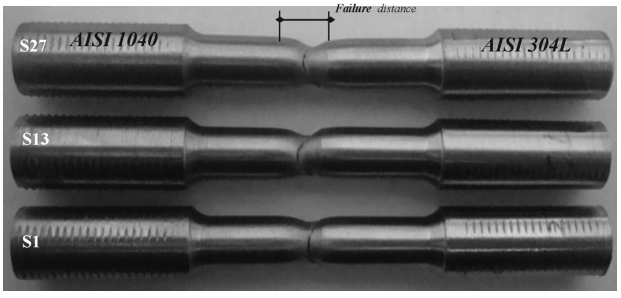

Figure 6: Typical failure locations on the tensile-test samples of friction-welded joints

Slika 6: Značilno področje porušitve pri nateznem preizkusu vzorcev s torno zvarjenim spojem

steels as a result of the rotational speed and frictional pressure.

The lowest tensile-strength value was obtained for sample S1 at 1300 r/min. This decrease in the tensile strength is associated with the width of the HAZ and the reactions in the AISI 1040 HAZ[17], causing a grain refinement of the microstructure, the σ-phase and the δ-ferrite[10,17,20] in the HAZ of AISI 304L. The occurrence of $Cr_{23}C_6$, Cr_7C_3 and Fe_7C_5 was confirmed with an X-ray analysis and an EDS analysis of the friction-welded joints and the occurrence of these phases in the HAZs has an important effect on the tensile strengths of the joints. Additionally, the formation of these phases could partly increase the hardness at the interface.[21] Due to a longer frictional time the volume of the viscous material

Table 4: Tensile results for AISI 304L/AISI 1040 friction welds

Tabela 4: Rezultati nateznih preizkusov torno zvarjenih spojev AISI 304L/AISI 1040

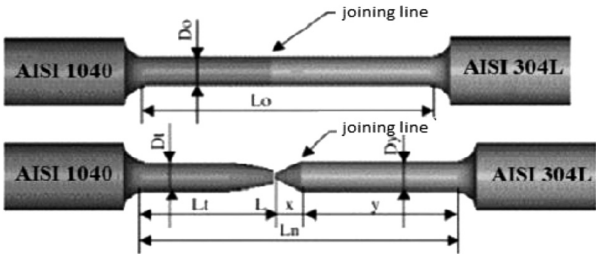

Sample No	L_o/ mm	L_n/ mm	D_o/ mm	AISI 304L		AISI 1040		Fracture distance x/mm
				L_y/ mm	D_y/ mm	L_t/ mm	D_t/ mm	
S1	40	42.1	8	22.6	7.80	20.5	7.30	1.60
S2	40	42.4	8	19.6	7.80	21.6	7.20	1,20
S3	40	43.6	8	22.6	7.49	20.8	7.20	1.60
S4	40	42.9	8	22.5	7.60	21.2	7.00	2.50
S5	40	43.8	8	19.6	7.30	24.1	6.20	3.20
S6	40	43.5	8	24.8	7.45	19.4	6.10	3.80
S7	40	43.9	8	24.0	7.33	19.6	6.00	3.55
S8	40	43.1	8	23.4	7.40	18.5	6.80	3.10
S9	40	43.7	8	23.3	7.30	20.3	6.30	3.00
S10	40	42.7	8	23.4	7.20	19.6	6.80	2.10
S11	40	43.4	8	23.9	7.20	19.8	6.30	3.20
S12	40	43.3	8	24.5	7.30	19.6	6.40	3.40
S13	40	43.7	8	24.4	7.20	19.7	6.20	3.00
S14	40	43.8	8	23.7	7.20	20.1	6.00	3.00
S15	40	43.6	8	24.5	7.30	19.4	6.50	2.60
S16	40	44.0	8	24.0	7.30	19.6	6.00	2.80
S17	40	43.0	8	23.9	7.20	19.3	6.20	3.60
S18	40	43.3	8	25.0	7.30	19.1	6.40	3.00
S19	40	43.7	8	24.0	7.30	19.8	6.50	3.50
S20	40	44.0	8	24.2	7.30	19.6	6.00	4.20
S21	40	44.0	8	24.8	7.20	20.6	6.40	3.00
S22	40	42.5	8	23.7	7.20	18.2	6.30	3.10
S23	40	43.6	8	25.2	7.20	20.1	6.00	4.00
S24	40	43.7	8	24.1	7.30	19.4	6.20	3.90
S25	40	43.9	8	23.5	7.30	19.9	6.40	3.40
S26	40	44.0	8	23.7	7.30	19.4	6.00	3.75
S27	40	44.1	8	23.6	7.20	20.4	5.80	3.50

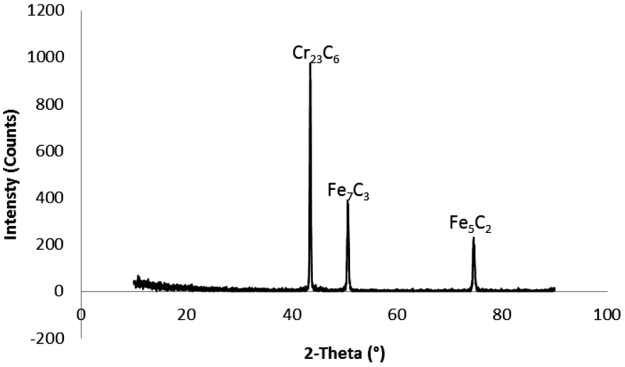

Figure 7: Result of XRD analysis for sample S13
Slika 7: Rentgenogram vzorca S13

Table 5: EDS analyses across the welding interfaces of friction-welded samples S1, S13 and S27
Tabela 5: EDS-analiza preko ravnine spoja torno varjenih vzorcev S1, S13 in S27

Sample No	EDS Points	Alloying elements (*w*/%)					
		C	Si	Cr	Mn	Fe	Ni
S1	point 1	0.62	0.22	0.54	2.54	92.7	0.68
	point 2	0.53	0.19	1.66	3.06	90	0.82
	point 3	0.55	0.33	10.06	3.64	79.4	4.89
	point 4	0.02	0.34	15.3	4.15	72.3	8.34
	point 5	0.37	0.49	16.45	3.74	65.43	8.03
S13	point 1	0.17	0.26	0.48	6.57	86.9	0.74
	point 2	0.59	0.31	6.07	6.86	81.17	2.98
	point 3	0.29	0.45	17.3	6.60	66.5	8.40
	point 4	0.24	0.50	17.46	6.58	62.38	9.61
	point 5	0.10	0.59	17.5	6.27	68.6	9.53
S27	point 1	0.04	0.21	0.53	6.38	88.3	0.69
	point 2	0.69	0.19	0.68	6.03	90.4	0.94
	point 3	0.03	0.45	10.7	6.21	74.3	4.23
	point 4	0.45	0.44	12.8	5.95	68.8	4.99
	point 5	0.39	0.44	18.1	6.90	62.3	8.72

transferred at the weld interface decreased and the tensile strength was lowered (**Figure 5**). On the other hand, the tensile strength increased with a higher rotational speed and a lower frictional time. This shows that the formation and the width of the FPDZ, which is a result of the heat input and plastic deformation at the interface, have detrimental effects on the mechanical strength and,

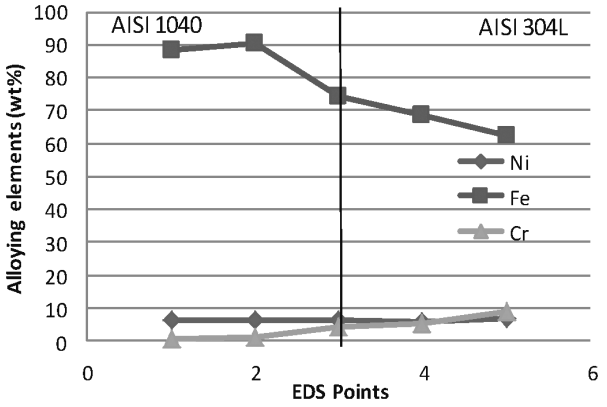

Figure 8: Concentration profiles of EDS analysis across the welding interface of friction-welded sample
Slika 8: Profil koncentracij pri EDS-analizi prereza stika pri torno zvarjenem vzorcu

consequently, on the process parameters of dissimilar friction-welded joints.

3.4 X-ray and EDS analyses

The results of the XRD analysis for friction-welded joint S13 are shown in **Figure 7**. The results confirm the presence of the $Cr_{23}C_6$, Cr_7C_3 and Fe_5C_2 compounds at the interface of the welded joints. SEM micrographs and EDS-analysis points of friction-welded joints S1, S13 and S27 are presented in **Figure 2**. In all the SEM images, the following EDS-analysis points are marked: point 1 (the AISI 1040 side), point 2 (the deformed zone), point 3 (the fully plasticized deformed zone), point 4 (the deformed zone of AISI 304L) and point 5 (on the AISI 304L side). The EDS-analysis results of samples of S1, S13 and S27 are also given in **Table 5**.

The results of the elemental analysis and microstructural examination in the interface regions of the friction-welded joints clearly demonstrated that different amounts of C, Fe, Cr, Si, Ni and Mn were obtained. Additionally, the EDS analysis of the interfaces of the friction-welded samples revealed that there was a transition of Cr and Ni from AISI 304L to AISI 1040. Furthermore, there was a Fe transition from AISI 1040 to

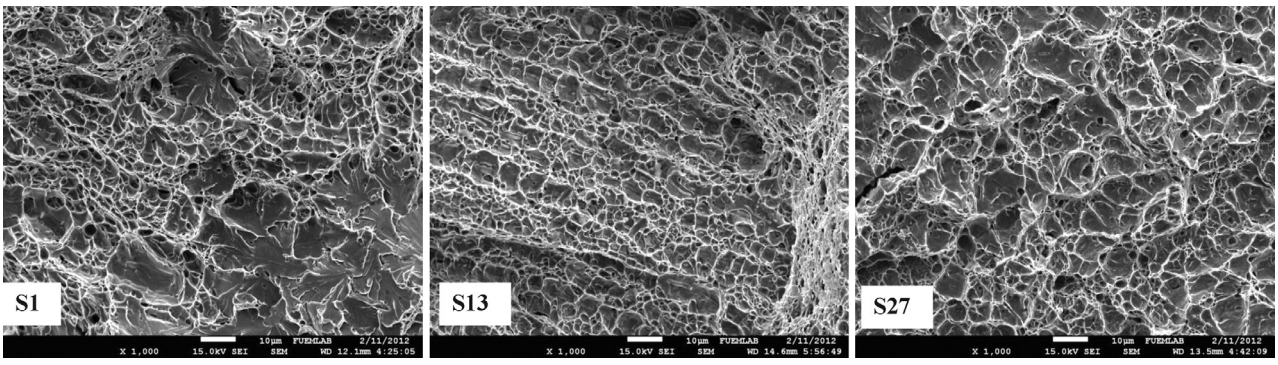

Figure 9: SEM micrographs of fracture surfaces after the tensile test of friction-welded samples S1, S13 and S27
Slika 9: SEM-posnetki površine preloma po nateznem preizkusu torno zvarjenih vzorcev S1, S13 in S27

the AISI 304L austenitic stainless steel, as seen in the concentration profiles of S13 in **Figure 8**.

3.5 Fractography

Figure 9 shows images of the fracture surfaces after the tensile test of friction-welded samples S1, S13 and S27. Examining the fracture-surface images, it was found that the fractures resulting from the tensile test mostly occurred on the AISI 1040 side, and especially ductile fractures in the form of quasi-cleavages were observed in the dimples. Moreover, all the samples showed a ductile fracture behavior; as seen on the SEM photographs of the fracture surfaces of the FW joints, these images resemble spider webs.

4 CONCLUSIONS

In this study, the following conclusions were made after a thorough investigation of the effects of the process parameters on the microstructure and mechanical properties of the friction-welded joints of the AISI 1040/AISI 304L steels:

1. The friction-welded AISI 1040 and AISI 304L steels were free of pores and cracks. A grain-size reduction occurred in the DZ of both materials. It was observed with SEM and EDS analyses that a transition of the materials occurred in the friction-weld zone.
2. Microstructural studies showed a presence of four different regions at the welding interface: a fully plasticized deformed zone, a partially deformed zone, a deformed zone and the base materials. The widths of the FPDZ and DZ of the joints were mainly affected by the frictional time and rotational speed. The use of a higher rotational speed and a lower frictional time increased the tensile strength of a friction-welded AISI 1040/AISI 304L steel couple. This shows that the formation of a FPDZ, which is a result of the heat input and plastic deformation at the interface, has a detrimental effect on the mechanical strength and, consequently, on the process parameters of dissimilar friction-welded joints, therefore, it needs to be controlled.
3. The highest tensile strength and a low microhardness were obtained very close to the AISI 1040 parent material of friction-welded sample S27 using a rotational speed of 1700 r/min, a frictional pressure of 50 MPa and a frictional time of 4 s. Depending on the formation of the FPDZ and DZ, a decrease in the tensile strength was detected because of the grain-refined microstructure, σ-phase, δ-ferrite and an increase in the frictional time.

Acknowledgements

The authors wish to thank the University of Fırat Research Fund for the support of this work under the FUBAP-2054 project.

5 REFERENCES

[1] A. Aran, Stainless steel production standards and using, STY, Istanbul, Turkey, 2003

[2] ASM, Metals handbook, vol.8, 1973, 424

[3] R. J. Castro, J. J. De Cadenet, Welding metallurgy of stainless steel and heat- resisting steels, Cambridge University Press, Cambridge 1974

[4] J. J. Demo, Structure, Constitution, and General Characteristics of Wrought Ferritic Stainless Steels, ASTM, Philadelphia 1977, doi:10.1520/STP619-EB

[5] J. C. Lippold, D. J. Kotecki, Welding metallurgy and weldability of stainless steels, 1st ed., Wiley-Interscience, 2005

[6] M. Erdoğan, Materials science and engineering materials 1, Ankara, Turkey, 2002, 326–331

[7] K. G. K. Murti, S. Sundaresan, Parameter optimization in friction welding dissimilar materials, Metal Construction, (**1983**), 331–335

[8] K. S. Mortensen, C. G. Jensen, L. C. Conrad, F. Losee, Mechanical properties and microstructures of intertia friction welded 416 stainless steel, Welding Journal, 80 (**2001**) 11, 268–273

[9] M. Sahin, H. E. Akata, An experimental study on friction welding of medium carbon and austenitic stainless steel components, Industrial Lubrication and Tribology, 56 (**2004**) 2, 122–129, doi:10.1108/00368790410524074

[10] N. Özdemir, Investigation of the mechanical properties of friction-welded joints between AISI 304L and AISI 4340 steel as a function rotational speed, Materials Letters, 59 (**2005**) 19–20, 2504–2509, doi:10.1016/j.matlet.2005.03.034

[11] V. V. Satyanarayana, G. Madhusudhan Reddy, T. Mohandas, Dissimilar metal friction welding of austenitic-ferritic stainless steels, Journal of Materials Processing Technology, 160 (**2005**) 2, 128–137, doi:10.1016/j.jmatprotec.2004.05.017

[12] S. Celik, I. Ersozlu, Investigation of the mechanical properties and microstructure of friction welded joints between AISI 4140 and 1050 steels, Materials & Design, 30 (**2009**) 4, 970–976, doi:10.1016/j.matdes.2008.06.070

[13] I. Kirik, N. Özdemir, Weldability and joining characteristics of AISI 420/AISI 1020 steels using friction welding, International Journal of Materials Research, 104 (**2013**) 8, 769–775, doi:10.3139/146.110917

[14] P. Sathiya, S. Aravindan, A. Noorul Haq, K. Paneerselvam, Optimization of friction welding parameters using evolutionary computational techniques, Journal of Materials Processing Technology, 209 (**2009**) 5, 2576-2584, doi:10.1016/j.jmatprotec.2008.06.030

[15] İ. Kırık, N. Özdemir, F. Sarsilmaz, Microstructure and Mechanical Behaviour of Friction Welded AISI 2205/AISI 1040 Steel Joints, Materials Testing, 54 (**2012**) 10, 683–687, doi:10.3139/120.110379

[16] O. Torun, I. Celikyürek, B. Baksan, Friction welding of Fe-28Al alloy, Intermetallics, 19 (**2011**) 7, 1076–1079, doi:10.1016/j.intermet.2011.02.009

[17] N. Özdemir, F. Sarsilmaz, A. Hasçalik, Effect of rotational speed on the interface properties of friction-welded AISI 304L to 4340 steel, Materials & Design, 28 (**2007**) 1, 301–307, doi:10.1016/j.matdes.2005.06.011

[18] C. R. G. Ellis, Friction Welding, Some Recent Applications of Friction Welding, Weld. and Metal Fab., (**1977**), 207–213

[19] H. Ates, M. Turker, A. Kurt, Effect of friction pressure on the properties of friction welded MA956 iron-based superalloy, Materials & Design, 28 (**2007**) 3, 948–953, doi:10.1016/j.matdes.2005.09.015

[20] F. D. Duffin, A. S. Bahrani, Frictional Behaviour of Mild Steel in Friction Welding, Wear, 26 (**1973**) 1, 53–74, doi:10.1016/0043-1648 (73)90150-6

[21] D. Ananthapadmanaban, V. Seshagiri Rao, N. Abraham, K. Prasad Rao, A study of mechanical properties of friction welded mild steel to stainless steel joints, Materials & Design, 30 (**2009**) 7, 2642–2646, doi:10.1016/j.matdes.2008.10.030

UDK 669.18:621.74
Professional article/Strokovni članek

ISSN 1580-2949
MTAEC9, 49(5)833(2015)

INFLUENCE OF INOCULATION METHODS AND THE AMOUNT OF AN ADDED INOCULANT ON THE MECHANICAL PROPERTIES OF DUCTILE IRON

VPLIV METOD MODIFIKACIJE IN KOLIČINE DODANEGA MODIFIKATORJA NA MEHANSKE LASTNOSTI DUKTILNEGA ŽELEZA

Hasan Avdušinović[1], Almaida Gigović-Gekić[1], Diana Ćubela[1], Raza Sunulahpašić[1], Nermin Mujezinović[2]

[1]University of Zenica, Faculty of Metallurgy and Materials Science, Travnička cesta 1, 72000 Zenica, Bosnia and Herzegovina
[2]CIMOS TMD CASTING, d. o. o., Zenica, Radna zona Zenica-1 bb, 72000 Zenica, Bosnia and Herzegovina
hasan.avdusinovic@famm.unze.ba

Prejem rokopisa – received: 2014-09-30; sprejem za objavo – accepted for publication: 2014-10-13

doi:10.17222/mit.2014.248

In most cases an addition of inoculants to molten cast iron is advisable and even necessary to produce good-quality castings. The mechanical properties and machinability of cast iron with nodular graphite greatly depend on the formation of graphite and the matrix microstructure and both are significantly influenced by the inoculation treatment. The mechanism of inoculation, the influence of the inoculation method and the amount of added inoculants are presented.

Keywords: ductile iron, inoculation, microstructure, graphite, metallic matrix

V večini primerov je dodatek modifikatorjev staljenemu livnemu železu priporočljiv in celo potreben za izdelavo dobrih ulitkov. Mehanske lastnosti in obdelovalnost litega železa z nodularnim grafitom so močno odvisne od oblike grafita in od mikrostrukture osnove, na oboje pa močno vpliva obdelava z modifikatorji. Predstavljen je mehanizem modifikacije, vpliv metode modifikacije in vpliv količine dodanega modifikatorja.

Ključne besede: duktilno železo, inokulacija, mikrostruktura, grafit, kovinska osnova

1 INTRODUCTION

Inoculants are the materials added to molten cast iron, modifying the microstructure and, thereby, changing the physical and mechanical properties to a degree not explained on the basis of the change in the composition. Inoculation is a phase of the technological process of producing ductile iron that controls and improves the microstructure and mechanical properties of castings. Through inoculation, graphite nucleation and eutectic undercooling of the melt can be controlled, which is crucial for achieving the required service properties of the castings.[1–3]

The inoculant most commonly used in foundries is a ferrosilicon alloy with precisely defined contents of Ca, Ba, Sr, Zr, Al and rare-earth elements. The benefits of inoculations are: an improved machinability, increased strength and ductility, reduced hardness and fracture sensitivity, a more homogenous microstructure, a reduced tendency for solidification shrinkage, etc.

During modularizing, numerous inclusions with a sulfide core and an outer shell containing complex magnesium silicates are formed. Such micro-inclusions do not provide an effective nucleation for graphite because the crystal lattice structure of magnesium silicates does not match sufficiently with the lattice structure of graphite. After the inoculation with a ferrosilicon alloy containing Ca, Ba or Sr, the surfaces of the micro-inclusions are modified and other complex Ca, Sr, or Ba silicate layers are obtained. Such silicates have the same hexagonal crystal lattice as graphite and act as effective nucleation sites for graphite nodules to grow during solidification.[4]

The required rate of adding inoculants to a liquid depends very much on the place and time of their inoculation.

2 EXPERIMENTAL PROCEDURE

In the investigations of the response of ductile-iron test melts to different amounts of added inoculants and different inoculation methods, three types of the inoculation method were applied: the ladle inoculation, the in-stream inoculation and the in-mold inoculation. The partner foundry in this research project was "Cimos TMD Casting" in Zenica.

In the first project step, 15 melts were prepared. Full lists of the chemical compositions, the amounts of added inoculants and the places of the inoculant introduction are included in **Table 1**. High-purity FeSi with additions of Al, Ca, and Sr was used for the inoculation. The test

Table 1: Chemical compositions of the experimental melts, places of the inoculation and added amounts of the inoculants (first step of the project)
Tabela 1: Kemijska sestava eksperimentalnih talin, mesto dodajanja modifikatorja in količina dodanega modifikatorja (prva stopnja projekta)

No.	Chemical composition (%)								Inoculant (%)			Temp.
	C	Si	Mn	P	S	Cr	Cu	Mg	stream	mold	ladle	°C
1	3.52	2.17	0.428	0.016	0.006	0.086	0.314	0.043	0	0	0	1388
2	3.51	2.20	0.433	0.016	0.006	0.090	0.314	0.040	0	0.05	0	1392
3	3.49	2.06	0.401	0.015	0.006	0.089	0.332	0.032	0	0.15	0	1402
4	3.58	2.15	0.403	0.014	0.005	0.076	0.346	0.043	0	0.20	0	1407
5	3.56	2.09	0.482	0.011	0.003	0.111	0.340	0.040	0.05	0.05	0	1395
6	3.44	2.11	0.485	0.012	0.003	0.095	0.356	0.047	0.05	0.10	0	1410
7	3.60	2.14	0.345	0.016	0.006	0.054	0.080	0.053	0.10	0	0	1380
8	3.54	2.10	0.337	0.017	0.009	0.071	0.090	0.055	0.05	0	0	1380
9	3.52	2.15	0.362	0.014	0.007	0.064	0.091	0.045	0.15	0	0	1390
10	3.56	2.11	0.398	0.017	0.008	0.068	0.316	0.047	0.10	0.05	0	1400
11	3.62	2.45	0.353	0.017	0.009	0.049	0.119	0.065	0.20	0	0	1387
12	3.65	2.11	0.392	0.019	0.012	0.054	0.149	0.079	0.15	0.05	0	1405
13	3.62	2.12	0.382	0.019	0.011	0.054	0.144	0.060	0	0.20	0	1390
14	3.61	2.11	0.357	0.018	0.009	0.037	0.187	0.048	0	0	0.05	1398
15	3.64	2.14	0.384	0.016	0.011	0.084	0.212	0.052	0	0	0.20	1402

Table 2: Range of the chemical compositions of the test melts (second step of the project)
Tabela 2: Obseg kemijskih sestav preizkusnih talin (druga stopnja projekta)

Composition	C	Si	Mn	S	P	Mg
w/%	3.4–3.6	2.1–2.3	0.2–0.4	0.003–0.012	0.01–0.02	0.003–0.055

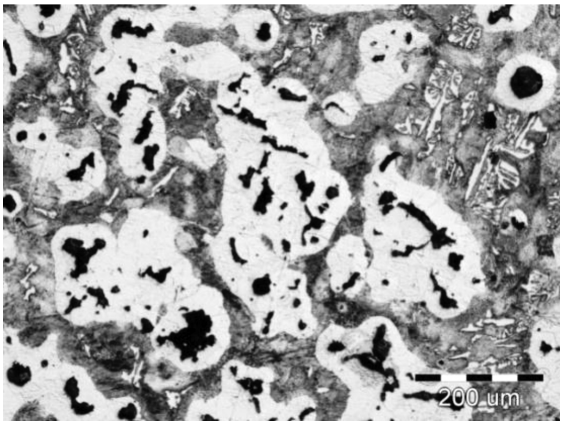

Figure 1: Ladle inoculation, Nital etched
Slika 1: Modifikacija v ponvi, jedkano v nitalu

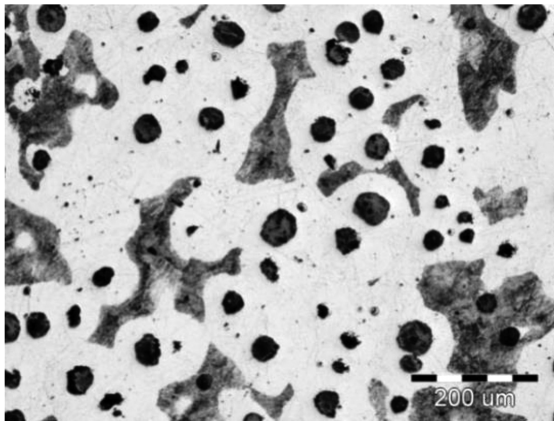

Figure 2: In-stream inoculation, Nital etched
Slika 2: Modifikacija v curek, jedkano v nitalu

iron melts were obtained using an induction furnace and casting iron into a green-sand mold. After the casts were cooled down and cleaned, samples for the mechanical-property examination were prepared.[1]

The testing of the mechanical properties was performed according to BAS EN 100002:2002 relating to tensile testing and BAS EN 6507-1/2007 relating to hardness testing of fractured tensile-test bars.

Based on the summary of the results of testing the casting properties, conclusions about the optimum amounts of the added inoculants needed for obtaining the required values of the mechanical properties, were drawn.

Casting procedures involving the exact amounts of the added inoculants required for three different methods

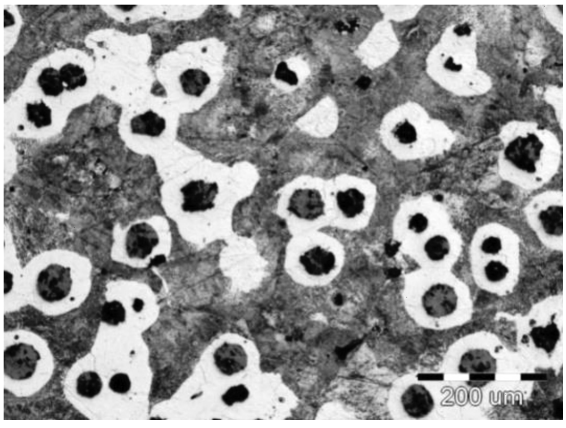

Figure 3: In-mold inoculation, Nital etched
Slika 3: Modifikacija v kokili, jedkano v nitalu

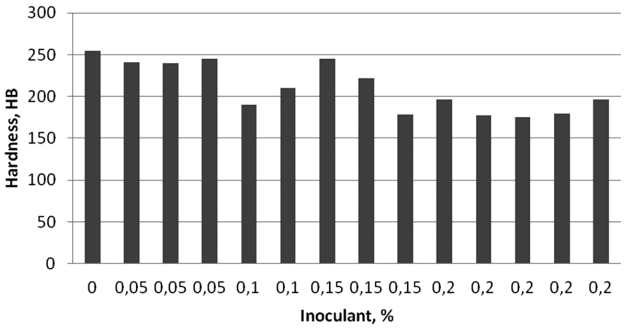

Figure 4: Hardness values of the tested samples (first step of the project)

Slika 4: Trdota preizkusnih vzorcev (prva stopnja projekta)

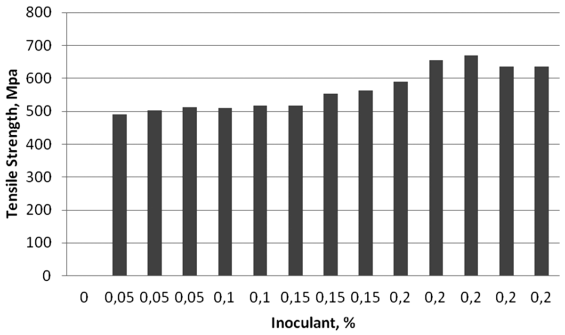

Figure 5: Tensile-strength values of the tested samples (first step of the project)

Slika 5: Natezna trdnost preizkusnih vzorcev (prva stopnja projekta)

Table 3: Average values and standard deviations of the hardness and tensile strength (second step of the project)

Tabela 3: Povprečne vrednosti in standardna deviacija trdote in natezne trdnosti (druga stopnja projekta)

	Hardness (HB)			Tensile strength (MPa)		
Inoculation method	In mold	In stream	Ladle	In mold	In stream	Ladle
Average	212.15	203.8	205.3	564.65	546.3	474.95
St. deviation	7.86	6.88	27.02	29.1	9.41	33.61

of inoculation were conducted in the second step to find the most suitable casting technology in the partner foundry. A total of 60 melts were prepared in the second step of the project and the average melt chemical composition is presented in **Table 2**.

3 RESULTS AND DISCUSSION

Figures 1 to **3** show the microstructures of the samples taken from the melts (castings) inoculated with different methods; the tensile strengths and hardness values are presented in **Figures 4** and **5**.

The required hardness was in the range of 180–220 HB and the tensile strength was in the range of 500–550 MPa. According to the results in **Figures 1** and **2**, the best result was observed with the samples with 0.1 % of the inoculants. In the second project step we used 20

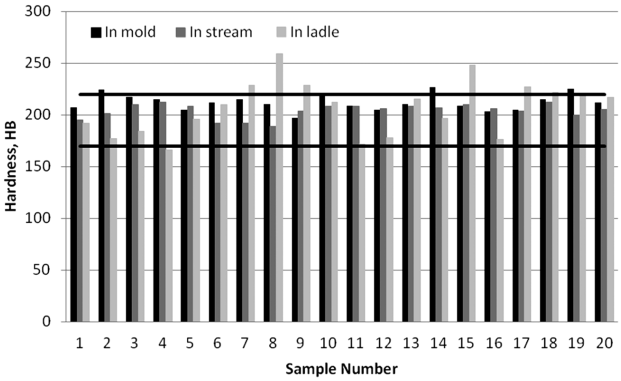

Figure 6: Hardnes values of the tested samples (second step of the project); black horizontal bars – targeted values

Slika 6: Trdota preizkusnih vzorcev (druga stopnja projekta); črne vodoravne črte – ciljne vrednosti

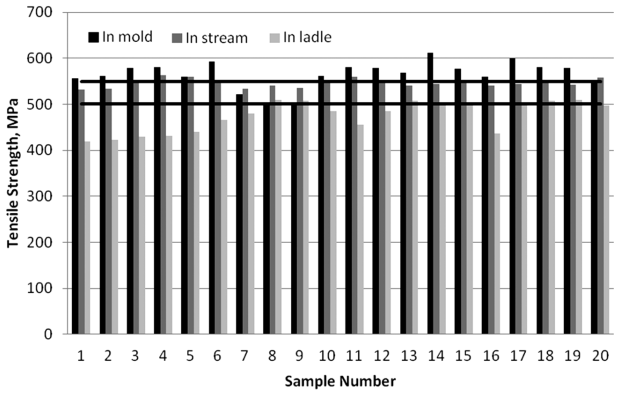

Figure 7: Tensile-strength values of the tested samples (second step of the project); black horizontal bars – targeted values

Slika 7: Natezna trdnost preizkusnih vzorcev (druga stopnja projekta); črne vodoravne črte – ciljne vrednosti

melts for each inoculation method, i.e., 60 melts were treated with 0.1 % of the added inoculants. The mechanical properties are shown in **Figures 6** and **7** and in **Table 3**.

4 CONCLUSIONS

Experimental materials with quite satisfactory characteristics were prepared with vacuum induction melting. The results obtained in the first project step showed that with 0.1 % of the inoculant the targeted hardness and tensile strength for the given ductile iron were achieved.

In the second project step it was found that the in-stream inoculation ensured the best result as almost 100 % of all the samples achieved the targeted values for the hardness and tensile strength and the standard deviation was the smallest.

Acknowledgment

The authors would like to thank the Federal Ministry of Education and Science of the Federation of Bosnia

and Herzegovina and Foundry "CIMOS TMD CASTING" in Zenica for their financial aid and cooperation during the implementation of the research project.

5 REFERENCES

[1] H. Bornstein et al., Cast Metals Handbook, American Foundrymen's Society, Des Plaines, Illinois, USA 1957, 31

[2] E. Fras, M. Gorny, Inoculation Effects of Cast Iron, Archives of Foundry Engineering, 12 (**2012**) 4, 39–46

[3] J. N. Harvey, G. A. Noble, Inoculation of Cast Irons – An Overview, 55th Indian Foundry Congress, India, 2007, 343–360

[4] T. Skaland, A New Approach to Ductile Iron Inoculation, American Foundry Society, Schaumburg, Illinois, USA 2001

UDK 620.3:66.017:544.6
Professional article/Strokovni članek

ISSN 1580-2949
MTAEC9, 49(5)837(2015)

ONE-STEP GREEN SYNTHESIS OF GRAPHENE/ZnO NANOCOMPOSITES FOR NON-ENZYMATIC HYDROGEN PEROXIDE SENSING

ENOSTOPENJSKA ZELENA SINTEZA NANOKOMPOZITA GRAFEN-ZnO ZA NEENCIMATSKO DETEKCIJO VODIKOVEGA PEROKSIDA

Sze Shin Low[1], Michelle T. T. Tan[1], Poi Sim Khiew[1], Hwei-San Loh[2], Wee Siong Chiu[3]

[1]Division of Materials, Mechanics and Structures, Center of Nanotechnology and Advanced Materials, Faculty of Engineering, University of Nottingham Malaysia Campus, Jalan Broga, 43500 Semenyih, Selangor, Malaysia
[2]School of Biosciences, Faculty of Science, University of Nottingham Malaysia Campus, Jalan Broga, 43500 Semenyih, Selangor, Malaysia
[3]Low Dimensional Materials Research Center, Department of Physics, Faculty of Science, University Malaya, 50603 Kuala Lumpur, Malaysia
michelle.tan@nottingham.edu.my

Prejem rokopisa – received: 2014-10-14; sprejem za objavo – accepted for publication: 2014-11-17

doi:10.17222/mit.2014.259

In the present study, a disposable electrochemical biosensor for hydrogen peroxide (H_2O_2) was fabricated using a graphene/ZnO nanocomposite-modified screen-printed carbon electrode (SPCE). The adopted method is simple, cost feasible and it avoids the usage of harsh oxidants/acids during the synthesis. Graphite material was subjected to liquid-phase exfoliation with the aid of ultrasonication, without going through the intermediate graphene-oxide phase that can disrupt the pristine structure of the yield. The as-prepared graphene/ZnO nanocomposite was then thoroughly characterized to evaluate its morphology, crystallinity, composition and product purity. All the results clearly indicate that pristine graphene was successfully produced with the graphite exfoliation and ZnO nanoparticles were homogeneously distributed on the graphene sheet, without any severe aggregation. The biosensing capability of the graphene/ZnO nanocomposite-modified SPCE was electrochemically evaluated with cyclic voltammetry (CV) and an amperometric analysis. The resulting electrode is found to exhibit an excellent electrocatalytic activity towards the reduction of H_2O_2. The graphene/ZnO-modified SPCE can detect H_2O_2 in a linear range of 1 mM to 15 mM with a correlation coefficient of 0.9859. The electrode is found to have a high sensitivity, selectivity and superior reproducibility for the non-enzymatic detection of an H_2O_2 compound.

Keywords: graphene/ZnO nanocomposite, sonochemical facile synthesis, electrochemical sensor, screen-printed carbon electrode, hydrogen peroxide

V predstavljeni študiji je bil izdelan elektrokemijski biosensor za enkratno uporabo za zaznavanje vodikovega peroksida (H_2O_2) z uporabo sitotiskane ogljikove elektrode (SPCE), modificirane z nanokompozitom grafen-ZnO. Ta prilagojena metoda je enostavna, stroškovno ugodna in omogoča, da se izognemo uporabi ostrih snovi, oksidanti-kislina, med sintezo. Grafitni material je bil izpostavljen ultrazvočni obdelavi, luščenju v tekoči fazi, ne da bi bil šel skozi vmesno fazo grafenovega oksida, ki lahko moti neokrnjeno zgradbo pridelka. Pripravljeni nanokompozit grafen-ZnO je bil nato skrbno karakteriziran, ocenjena je bila morfologija, kristaliničnost, sestava in tudi čistost proizvoda. Rezultati jasno kažejo, da je bil neokrnjen grafen izdelan z glajenjem grafita, ZnO nanodelci pa so bili homogeno razporejeni na ploščici iz grafena brez večjih segregacij. Biološka občutljivost ploščice SPCE, modificirane z nanokompozitom grafen-ZnO, je bila ugotovljena elektrokemijsko s ciklično voltametrijo (CV) in amperometrično analizo. Ugotovljeno je bilo, da ima dobljena elektroda odlično elektrokatalitičnost za redukcijo H_2O_2. SPCE, modificirana z grafen-ZnO, lahko zazna H_2O_2 v linearnem področju od 1 mM do 15 mM s korelacijskim koeficientom 0,9859. Ugotovljeno je bilo, da ima elektroda veliko občutljivost, selektivnost in boljšo ponovljivost pri neencimatski detekciji spojine H_2O_2.

Ključne besede: nanokompozit grafen-ZnO, sonokemijska sinteza, elektrokemijski senzor, sitotiskarsko natisnjena ogljikova elektroda, vodikov peroksid

1 INTRODUCTION

Graphene, a 2D one-atom-thick sheet of sp^2 carbon atoms arranged in a honeycomb lattice, was discovered by Novoselov et al.[1] in 2004. Ever since, it has intrigued enormous scientific activities due to its extraordinary properties. Graphene-based composites are anticipated to provide groundbreaking properties in new applications as they improve those of the host material.

Zinc oxide (ZnO), a II-VI compound semiconductor has been receiving considerable attention in the scientific community due to its unique properties. The wide-band-gap properties of ZnO have triggered tremendous research attention for its potential applications in electronic and optoelectronic devices. Besides, ZnO is also popular in the field of biosensing because it is biocompatible, biodegradable, biosafe as it can be dissolved into mineral ions within a few hours.[2]

For the purpose of hybridization of graphene with ZnO, researchers explored unique attractive properties like enhanced photocatalytic performance,[3] energy-storage property,[4] sensing property,[5] optoelectronic property[6] and ultrafast, nonlinear, optical switching property.[7] These intriguing properties of the composite are due to

the synergistic effect between graphene and ZnO, in which the carbon-based material acts as a good electron conductor and when coupled with a metal oxide, the charge transfer between the materials is improved.

There are many synthesis routes to combine graphene sheets and ZnO nanoparticles such as thermal decomposition,[8] electrochemical route,[9] ultrasonic spray pyrolysis,[10] electro-hydrodynamic atomization[11] and solvothermal process.[12] However, most of the attempts in the synthesis of a graphene/ZnO nanocomposite involve a reduction of the graphene oxide and an in-situ growth of ZnO which culminate in the presence of an oxygenated functional group on the graphene surface and impurities in the composite due to an incomplete reduction and purification process.

In this work, a graphene/ZnO nanocomposite was synthesised with one-step, low-cost, green approach, in which conductive graphene sheets serve as superior platforms for a deposition of flower-like ZnO nanoparticles. In comparison with the other work reporting on the synthesis of a graphene/ZnO composite, this synthesis method is novel and environmentally friendly because it omits the use of harsh chemicals for the exfoliation of graphite and growth of ZnO, resulting in a safer synthetic procedure and also preserving the pristine quality of both materials. From an economical perspective, the starting materials are inexpensive, while ultrasonication does not consume much power and can be conducted in a laboratory or scaled for a mass production. The as-synthesized graphene/ZnO nanocomposite was used to modify electrodes to demonstrate its viability for biosensing applications.

2 METHODOLOGY

2.1 Preparation of graphene and a graphene/ZnO nanocomposite

Graphite flakes (Bay Carbon, USA) were subjected to the one-step, green liquid-phase exfoliation method to synthesize graphene.[13] Graphite flakes were added into an optimized mixture of ethanol and deionized (DI) water (ratio 2 to 3) and sonicated for 3 h. The mixture was then centrifuged and washed with ethanol and DI water twice. The sediment was dried at 80 °C overnight and the graphene was collected.

The as-synthesized graphene was re-dispersed into ethanol via sonication. The graphene dispersion was then mixed with the zinc oxide (ZnO) dispersion and further sonicated to achieve an even mixing. The mixture was then subjected to mechanical stirring for 4 h for the synthesis of a graphene/ZnO nanocomposite. Next, the mixture was centrifuged and washed with ethanol and DI water twice. The graphene/ZnO nanocomposite was collected after drying at 80 °C overnight.

The as-synthesized graphene and graphene/ZnO nanocomposite were characterized via scanning electron microscopy (SEM), transmission electron microscopy (TEM) and X-ray diffractometry (XRD).

2.2 Electrochemical measurements

The electrochemical performances of the samples in connection with cyclic voltammetry (CV) and amperometry were analyzed with AUTOLAB PGSTAT302N. A planar screen-printed carbon electrode (SPCE) was fabricated (ScrintTechnology, Malaysia) based on the design described by Chan et al.[14] 2 μL of the as-prepared graphene/ZnO nanocomposite dispersion was dropped onto the surface of the working SPCE and dried at ambient temperature.

3 RESULTS AND DISCUSSIONS

3.1 Morphological analysis

A detailed morphology of the samples was studied with SEM and TEM, as shown in **Figure 1**. It can be observed in **Figure 1a** that graphene has a flat lamellar structure which provides graphene with a large surface to accommodate the hybridization with ZnO. The transparent nature of graphene shown in **Figure 1b** implies that graphite was fully exfoliated into a few layer sheets. **Figure 1c** shows that ZnO nanoparticles are dispersed on the graphene nanosheets. **Figure 1d** also demonstrates that the graphene sheets and ZnO nanoparticles are closely in contact with each other, which is beneficial for the electron transfer. Furthermore, no ZnO nanoparticles are observed outside the graphene sheets, suggesting a successful hybridization of the graphene/ZnO nanocomposite.

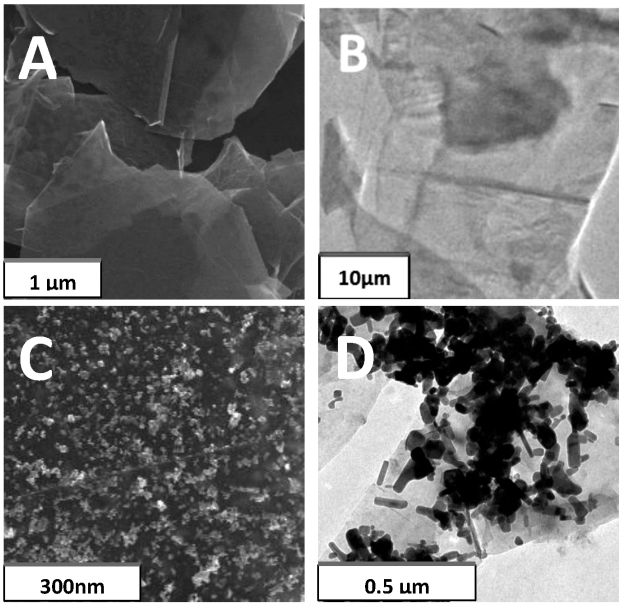

Figure 1: SEM and TEM images of the: a), b) as-produced graphene and c), d) as-synthesized graphene/ZnO nanocomposite

Slika 1: SEM- in TEM-posnetka: a), b) izdelanega grafena in c), d) sintetiziranega nanokompozita grafen-ZnO

3.2 Structural analysis

The crystalline structure of the as-synthesized graphene/ZnO nanocomposite was corroborated with an XRD measurement. The XRD pattern of the graphene/ZnO nanocomposite is shown in **Figure 2**, in comparison with graphite, graphene and ZnO as the references. **Figure 2** manifests diffraction peaks located at 2θ = (31.88°, 34.50°, 36.35°, 47.60°, 56.67°, 62.94°, 66.45°, 68.01° and 69.18°), which correspond to the crystal planes (002), (202), (501), (640), (660), (901), (931), (1000) and (941) of the hexagonal wurtzite structure of ZnO (ICSD no. 98-006-5172). Additional peaks at 2θ = 26.63° and 54.71° account for the graphitic reflection of the (002) plane, corresponding to a *d*-spacing of 0.334 nm. It is also illustrated that the XRD pattern of the graphene/ZnO nanocomposite is similar to those of graphite, graphene and ZnO, indicating that the synthesis method employed retained the pristine crystalline structures of the materials. This is crucial as lattice disruptions and crystalline-structure deformations can introduce defects that adversely affect the desired properties of the materials. The XRD data of the as-synthesized nanocomposite shows the absence of impurities, reflecting its high quality.

3.3 Electrochemical measurement

Cyclic voltammetry (CV) was recorded at room temperature for bare, graphene, ZnO and graphene/ZnO nanocomposite-modified SPCEs. The CV analyses were performed at a scan rate of 50 mV/s in the potential range of –0.4 V to 0.4 V. The redox reactions of H_2O_2 occur at very high switching potentials and therefore, for non-enzymatic H_2O_2 sensors, the maximum current is normally used for determining the sensing ability.[15] **Figure 3** shows that the graphene/ZnO nanocomposite-modified SPCE exhibits the greatest enhancement in terms of the electrochemical performance, with the highest peak currents (the maximum currents) being detected for both forward and reverse scans. There is a significant increase in the peak current by almost 2.5 times in the CV response of the composite-modified SPCE if compared to the bare electrode. On the other hand, the CV response of the graphene/ZnO nanocomposite-modified SPCE in different concentrations of H_2O_2 is also illustrated in **Figure 3**. The maximum current increased gradually upon increasing the concentration of H_2O_2 from (1 to 3, 5 and 7) μM (**Figure 3**

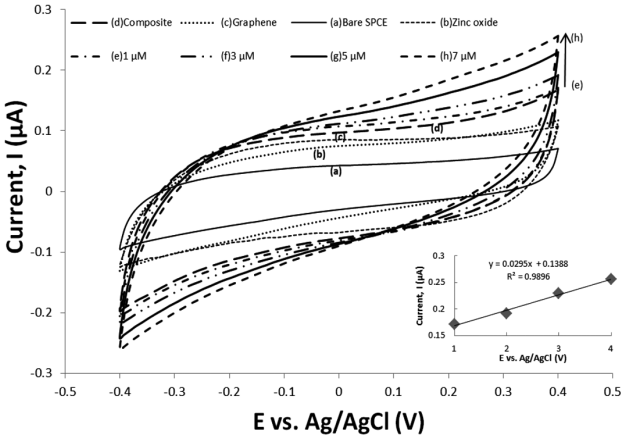

Figure 3: Cyclic voltammograms of: a) bare, b) ZnO, c) graphene, d) graphene/ZnO nanocomposite-modified SPCE in PBS buffer and cyclic voltammograms of graphene/ZnO nanocomposite-modified SPCE in the presence of: e) 1 μM, f) 3 μM, g) 5 μM, h) 7 μM H_2O_2. Inset shows the plot of the peak current against H_2O_2 concentration.

Slika 3: Ciklični voltamogrami: a) goli, b) ZnO, c) grafen, d) SPCE, modificiran z nanokompozitom grafen-ZnO v PBS-pufru. Ciklični voltamogrami modificiranega SPCE nanokompozita grafen-ZnO ob prisotnosti: e) 1 μM, f) 3 μM, g) 5 μM, h) 7 μM H_2O_2. Vstavek prikazuje diagram toka proti koncentraciji H_2O_2.

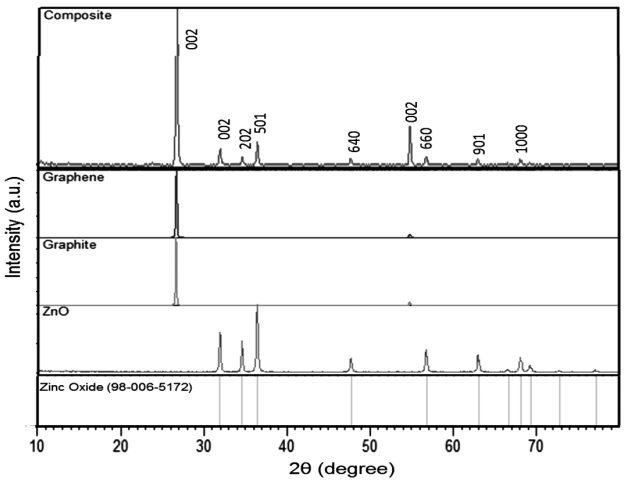

Figure 2: XRD patterns of graphite, graphene, ZnO and as-synthesized graphene/ZnO nanocomposite with the standard reference pattern

Slika 2: Rentgenski posnetki grafita, grafena, ZnO in sintetiziranega nanokompozita grafen-ZnO s standardnim referenčnim vzorcem

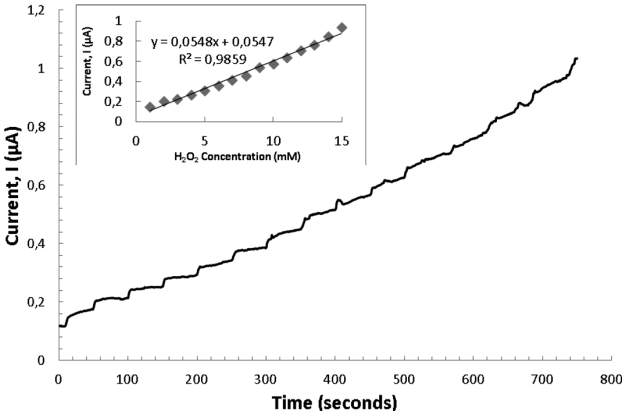

Figure 4: Amperometric *i–t* response of graphene/ZnO nanocomposite-modified SPCE to the additions of different H_2O_2 concentrations at an applied potential of 0.4 V. Inset shows a plot of concentration of H_2O_2 versus current in the linear range.

Slika 4: Amperometričen odgovor *i–t* SPCE, modificiranega z nanokompozitom grafen-ZnO, pri dodatku različnih koncentracij H_2O_2 pri uporabljenem potencialu 0,4 V. Vstavljeni diagram prikazuje koncentracijo H_2O_2 v odvisnosti od toka v linearnem področju.

inset). The high electrocatalytic activity of the graphene/ZnO nanocomposite can be ascribed to a large surface-area-to-volume ratio and the synergistic effect between graphene and ZnO.

The amperometric current – time ($i - t$) curve is the most often used method to evaluate the electrocatalytic activity of electrochemical sensors. The amperometric response of the graphene/ZnO nanocomposite-modified SPCE was investigated by successively adding hydrogen peroxide (H_2O_2) to a continuously stirred PBS solution. **Figure 4** clearly shows that the modified SPCE exhibits a rapid and steady response to each H_2O_2 addition, while the **Figure 4** inset displays the linear relationship between the current response and H_2O_2 concentration in the range of 1 mM to 15 mM with a sensitivity of 0.055 μA/mM. The linear regression equation is i/μA = 0.0548 C (mM) + 0.0547 with a correlation coefficient (R^2) of 0.9859, which permits a reliable quantification of the amount of H_2O_2 in a sample.

4 CONCLUSION

In summary, a facile green approach for the synthesis of a graphene/ZnO nanocomposite at room temperature was developed. The SEM and TEM images revealed that flower-like ZnO nanoparticles were homogenously distributed on the surface of the graphene sheets, while the XRD result affirms the structural integrity and purity of the as-synthesized graphene/ZnO nanocomposite. The graphene/ZnO nanocomposite-modified SPCE displayed excellent electrocatalytic activity towards H_2O_2 due to the synergistic effect between graphene and ZnO. The results herein suggest promising potentials of the graphene/ZnO nanocomposite for various sensing applications.

Acknowledgments

The Ministry of Science, Technology and Innovation research grant (E-Science code: 04-02-12-SF0198), the Early Career Research and Knowledge Transfer Scheme Award (ECKRT: A2RHM), HIR-Chancellory UM (UM.C/625/1/HIR/079), HIR-MOHE (UM.C/625/1/HIR/MOHE/SC/06) and the University of Nottingham are gratefully acknowledged. The authors also express heartfelt gratitude to Professor Dino Isa for access to the SAHZ pilot plant and its analytical equipment.

5 REFERENCES

[1] K. S. Novoselov, A. K. Geim, S. V. Morozov, D. Jiang, Y. Zhang, S. V. Dubonos, I. V. Grigorieva, A. A. Firsov, Science, 306 (**2004**), 666–669, doi:10.1126/science.1102896

[2] J. Zhou, N. S. Xu, Z. L. Wang, Adv. Mater., 18 (**2006**), 2432–2435, doi:10.1002/adma.200600200

[3] B. N. Joshi, H. Yoon, S. H. Na, J. Y. Choi, S. S. Yoon, Ceram. Int., 40 (**2014**), 3647–3654, doi:10.1016/j.ceramint.2013.09.060

[4] R. R. Salunkhe, Y. H. Lee, K. H. Chang, J. M. Li, P. Simon, J. Tang, N. L. Torad, C. C. Hu, Y. Yamauchi, Chemistry – A European Journal, 20 (**2014**), 13838–13852, doi:10.1002/chem.201403649

[5] K. Anand, O. Singh, M. P. Singh, J. Kaur, R. C. Singh, Sensors and Actuators B: Chem., 195 (**2014**), 409–415, doi:10.1016/j.snb.2014.01.029

[6] R. J. Chung, Z. C. Lin, P. K. Yang, K. Y. Lai, S. F. Jen, P. W. Chiu, Nanoscale Res. Lett., 8 (**2013**), 1–5, doi:10.1186/1556-276X-8-350

[7] Q. Ouyang, Z. Xu, Z. Lei, H. Dong, H. Yu, L. Qi, C. Li, Y. Chen, Carbon, 67 (**2014**), 214–220, doi:10.1016/j.carbon.2013.09.083

[8] Y. Zhu, H. I. Elim, Y. L. Foo, T. Yu, Y. Liu, W. Ji, J. Y. Lee, Z. Shen, A. T. S. Wee, J. T. L. Thong, C. H. Sow, Adv. Mater., 18 (**2006**), 587–592, doi:10.1002/adma.200501918

[9] S. Palanisamy, S. M. Chen, R. Sarawathi, Sensors and Actuators B: Chem., 166–167 (**2012**), 372–377, doi:10.1016/j.snb.2013.02.075

[10] T. Lu, Y. Zhang, H. Li, L. Pan, Y. Li, Z. Sun, Electrochim. Acta, 55 (**2010**), 4170–4173, doi:10.1016/j.electacta.2010.02.095

[11] A. Ali, K. Ali, K. R. Kwon, M. Hyun, K. Choi, J. Mater. Sci.: Mater. Electron., 25 (**2014**), 1097–1104, doi:10.1007/s10854-013-1693-1

[12] J. Wu, X. Shen, L. Jiang, K. Wang, K. Chen, Appl. Surf. Sci., 256 (**2010**), 2826–2830, doi:10.1016/j.apsusc.2009.11.034

[13] J. S. Y. Chia, M. T. T. Tan, P. S. Khiew, J. K. Chin, H. Lee, D. C. S. Bien, W. S. Chiu, Chem. Eng. J., 249 (**2014**), 270–278, doi:10.1016/j.cej.2014.03.081

[14] Y. Y. Chan, B. Kamarudin, D. A. Ozkan, S. Y. Lee, P. Lalitha, A. Ismail, M. Ozsoz, M. Ravichandran, Anal. Chem., 80 (**2008**), 2774–2779, doi:10.1021/ac702333x

[15] M. Florescu, C. M. A. Brett, Talanta, 65 (**2005**), 306–312, doi:10.1016/j.talanta.2004.07.003

UDK 519.61/.64:621.762.5:669.71
Professional article/Strokovni članek

ISSN 1580-2949
MTAEC9, 49(5)841(2015)

MATERIAL PARAMETERS FOR A NUMERICAL SIMULATION OF A COMPACTION PROCESS FOR SINTERED DOUBLE-HEIGHT GEARS

MATERIALNI PARAMETRI ZA NUMERIČNO SIMULACIJO POSTOPKA STISKANJA SINTRANIH DVOVIŠINSKIH ZOBNIKOV

Tomaž Verlak[1], Marko Šori[2], Srečko Glodež[1]

[1]University of Maribor, Faculty for Mechanical Engineering, Smetanova ulica 17, 2000 Maribor, Slovenia
[2]University of Maribor, Faculty of Natural Sciences and Mathematics, Koroška cesta 160, 2000 Maribor, Slovenia
tomaz.verlak@gmail.com

Prejem rokopisa – received: 2014-10-16; sprejem za objavo – accepted for publication: 2014-11-06

doi:10.17222/mit.2014.262

This paper presents the initial material parameters for the Ecka Alumix 231 aluminum-powdered metal required for a successful numerical simulation of a compaction process for sintered components with a proper software package. Experimental work was used to obtain Drucker-Prager-cap (DPC) model material parameters with the help of a Brazilian disc test and a uniaxial compression test for the linear part of the DPC model in the equivalent pressure stress/deviatoric stress (p-q) plane. The specimens used for this test were cylindrical probes (greens) that were compacted with a mechanical press and then compressed to the failure point in the axial and radial directions.

Keywords: aluminum-based powder, compaction process, Drucker-Prager cap model, numerical simulation, Ecka Alumix 231

V članku so predstavljeni začetni materialni parametri za aluminijev prah Ecka Alumix 231, ki so potrebni za uspešno izvedbo numerične simulacije stiskanja sintranih komponent s primerno programsko opremo. S porušitvenimi preizkusi in pridobljenimi eksperimentalnimi rezultati je bilo mogoče določiti potrebne parametre materiala z Drucker-Prager-jevim cap (DPC) modelom, ki določajo linearno območje DPC modela v grafu ekvivalentne tlačne obremenitve v odvisnosti od deviatorične obremenitve. Uporabljeni so bili cilindrični preizkušanci (zelenci), ki so bili stisnjeni z mehansko stiskalnico in kasneje obremenjeni do porušitve v osni in radialni smeri.

Ključne besede: aluminijev prah, stiskanje, Drucker-Prager-jev cap model, numerična simulacija, Ecka Alumix 231

1 INTRODUCTION

Sintering is a densification process of powder compacts based on the atomic diffusion of powder components. These mechanical compacts (products), especially gears (**Figure 1**), are widely used in numerous fields of mechanical engineering because they can be made into near-net- shaped objects with minimum or no machining after the sintering. The equipment for sintering is quite expensive and, for that reason, the sintering process required for manufacturing different, small, complex components is economical for larger production series.

The process of sintering can be divided into multiple steps, of which one of the most important is the compaction process. When a powder is being compacted with mechanically or hydraulically operated presses, the density distribution is changing.

The density magnitude and the density distribution within a component have large impacts on the mechanical properties of finished product[1,2] so it is crucial that the achieved density after the compaction process is as close as possible to 100 % of the theoretical density of the material and that the density distribution is uniform. To achieve a higher density and a uniform density distribution throughout the whole component after the compaction process, the press operator must have a great deal of experience to optimize the compaction parameters (the movement of the press components).

When optimizing compaction parameters based on experience, there is a great chance that damages occur to the press tools. To avoid high costs for repairing damaged tools and spending the time for optimizing the compaction parameters on a press, numerical simulations can be applied to resolve these situations. Using a numerical simulation in ABAQUS with a build-in Drucker-Prager cap model, it is possible to eliminate the trial-and-error process and numerically optimize press-compaction parameters, thus saving time and money.[2] The

Figure 1: Double-height gear
Slika 1: Dvovišinski zobnik

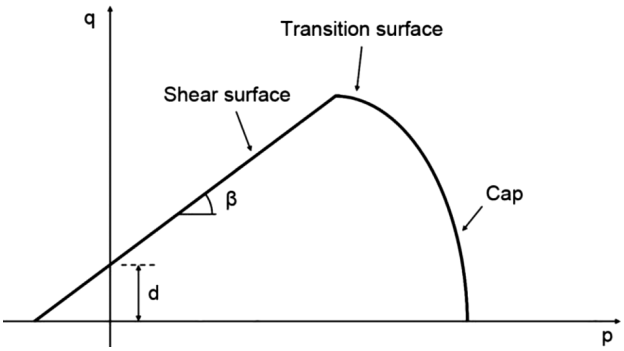

Figure 2: Drucker-Prager-cap-model chart
Slika 2: Graf Drucker-Pragerjevega cap modela

results of this kind of simulation show the local density distribution over the entire model. By optimizing the movement of the punches in a numerical simulation, the simulation can be restarted again and again with different compaction parameters and this way the results of the final density distributions can be compared. When the results of a numerical simulation are satisfactory, the compaction parameters can be transferred onto the press.

Before a numerical simulation can begin, the material parameters for the chosen metal powder must be known. These parameters are hard to come by or, in some cases, they do not even exist, which is specially the case with most aluminum powders.[3] To obtain the material parameters for a successful simulation, suitable tests must be done. These tests include a Brazilian disc test, a uniaxial compression test and a triaxial compression test. With these tests, it is possible to obtain the parameters that are needed for drawing a Drucker-Prager-cap-model chart and start a numerical simulation. The Drucker-Prager-cap-model chart, shown in **Figure 2**, is presented with the equivalent pressure stress/deviatoric stress (p-q) plane. It consists of three surfaces.[4,5] The first is the shear surface, the second is the transition surface and the third is the cap surface. This paper focuses on gathering the Drucker-Prager-cap-model parameters for the linear part, presented with the shear surface, and the tests required to gather proper information include a Brazilian disc test and a uniaxial compression test.

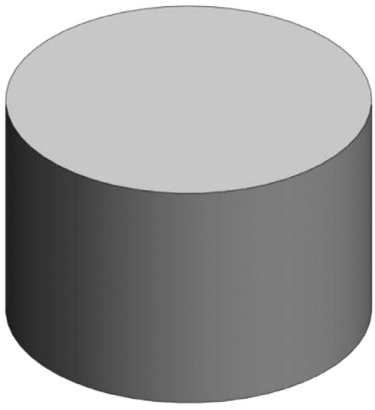

Figure 3: Specimen – a cylindrical disc
Slika 3: Vzorec – cilindrični ploščček

2 EXPERIMENTAL WORK

For the experimental work, the Ecka Alumix 231 aluminum powder was used. The basic powder specifications can be found in **Table 1** where ρ_A is the apparent density, ρ_G is the green density and σ_{CP} is the recommended compaction pressure. The testing can be divided into two parts. The first part involves the preparation of the samples and the second part involves the testing of the samples to the failure point and the reading of the failure-point load. The specimens used in this experimental work ware cylindrical discs (**Figure 3**) prepared with a DORST TPA 45 mechanical press (**Figure 4**) that is capable of a compaction force of 440 kN. A total of 24 samples were prepared. Each compacted specimen was measured and the values are presented in **Table 2** where D is the diameter of a specimen, L is the height of a specimen, m is the mass and ρ_G is the green density of a specimen.

Table 1: Basic properties of aluminum powder Ecka Alumix 231
Tabela 1: Osnovne lastnosti aluminijevega prahu Ecka Alumix 231

Physical characteristics			Chemical compositions, *w*/%		
ρ_A/(g/cm^3)	ρ_G/(g/cm^3)	σ_{CP}/MPa	Si	Cu	Mg
1.05 – 1.25	2.56	620	14–16	2.4–2.8	0.5–0.8

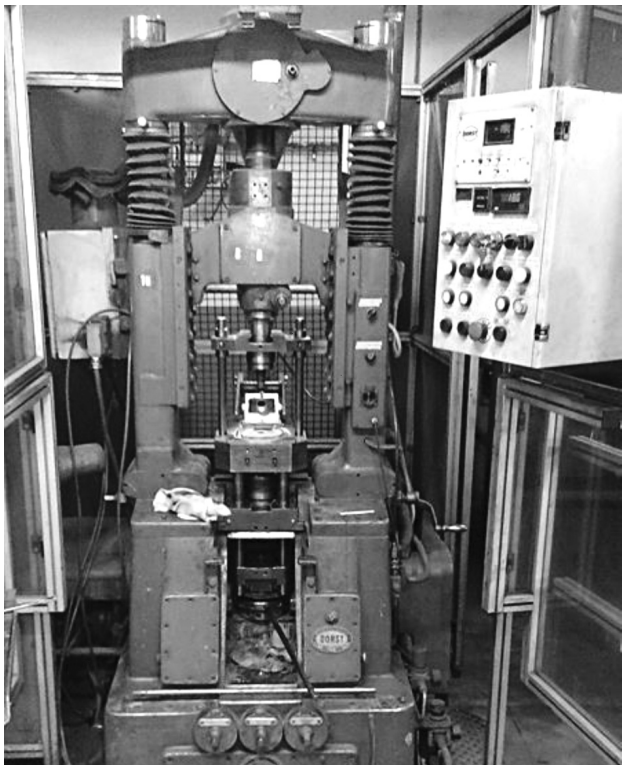

Figure 4: Dorst TPA 45 mechanical press
Slika 4: Mehanska stiskalnica Dorst TPA 45

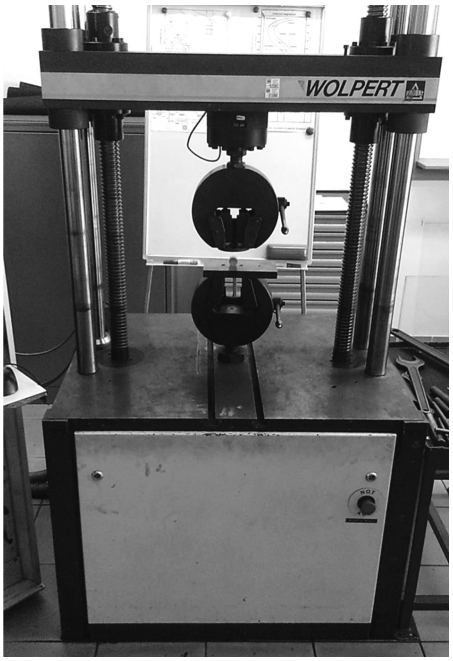

Figure 5: Wolpert TZZ 100 material-testing machine
Slika 5: Stroj za preizkušanje materialov Wolpert TZZ 100

Table 2: Average numerical values of specimens
Tabela 2: Povprečne numerične vrednosti vzorcev

Specimens	*D*/mm	*L*/mm	*m*/g	ρ_G/(g/cm^3)
1–6	24.15	16.19	18.73	2.53
7–12	24.15	16.21	18.79	2.53
13–18	24.14	16.27	17.28	2.32
19–24	24.15	16.28	17.30	2.32

For the second part of the experimental work, specimens were tested to the failure point with a WOLPERT TZZ 100 material-testing machine (**Figure 5**) that is capable of measuring compression and tension forces of up to 100 kN. The specimens were placed between two metal plates and then tested.[6] 12 cylindrical discs were tested to the failure point in the axial direction (**Figure 6a**) using a testing speed of 5 mm/min and another 12 in the radial direction (**Figure 6b**) using a testing speed of 2.5 mm/min.

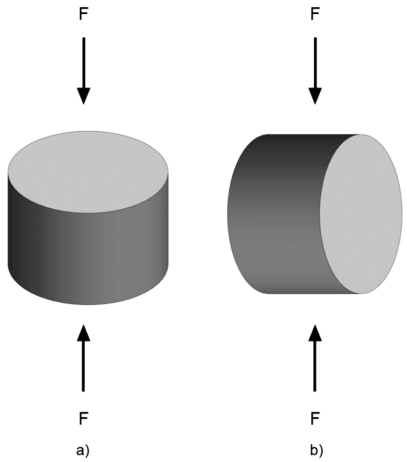

Figure 6: a) Axial and b) radial load directions
Slika 6: a) Osna in b) radialna obremenitev

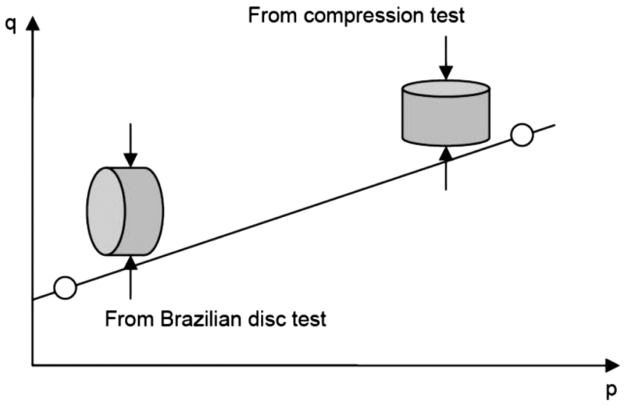

Figure 7: Linear part of the Drucker-Prager-cap model
Slika 7: Linearni del Drucker-Pragerjevega cap modela

3 RESULTS AND DISCUSSION

In order to obtain the linear part of the Drucker-Prager-cap model (**Figure 7**) parameters p and q for the compression test and Brazilian disc test must be calculated from the gathered data, where p is the hydrostatic-pressure stress and q is the deviatoric stress. For the compression test, parameter p can be calculated using Equation (1) and parameter q is calculated using Equation (2). For the Brazilian disc test, parameter p can be calculated using Equation (3), and parameter q is calculated using Equation (4):

$$p = \frac{\sigma_c}{3} \tag{1}$$

$$q = \sigma_c \tag{2}$$

$$p = \frac{2\sigma_t}{3} \tag{3}$$

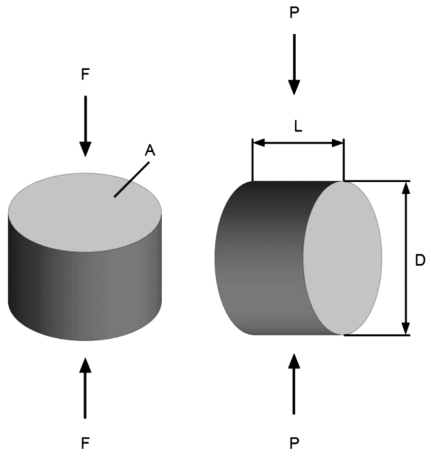

Figure 8: Parameters for calculation
Slika 8: Parametri za preračun

$$q = \sqrt{13}\sigma_t \quad (4)$$

where σ_c represents the compression strength expressed with Equation (5) and σ_t represents the splitting tensile strength expressed with Equation (6):

$$\sigma_c = \frac{F}{A} \quad (5)$$

$$\sigma_t = \frac{2P}{\pi LD} \quad (6)$$

where F is the maximum load applied during the uniaxial compression test, A is the surface area of a specimen, P is the maximum load applied during the Brazilian disc test, L is the thickness of a specimen and D is the diameter of a specimen. All the parameters mentioned above are presented in **Figure 8**. **Table 3** presents the average values gathered during the experimental work, where F is the maximum load applied in the axial direction and P is the maximum load applied in the radial direction. As expected, the values of the maximum load applied during the Brazilian disc test are smaller because of a grater notch factor and a smaller surface. With the help of Equations (1) to (6) and the added trend line, the linear part of the Drucker-Prager-cap model was plotted and it is presented in **Figure 9**.

Table 3: Average values of applied loads
Tabela 3: Povprečne vrednosti uporabljene sile

Specimens	Load direction	*F*/N	*P*/N
1–6	axial	77145	/
7–12	radial	/	8405
13–18	axial	64394	/
19–24	radial	/	4275

Using Microsoft Excel and its feature "display equation", the equation for the linear part of the Drucker-Prager-cap model of the Ecka Alumix 231 aluminum-powder metal can be displayed (Equation (7)):

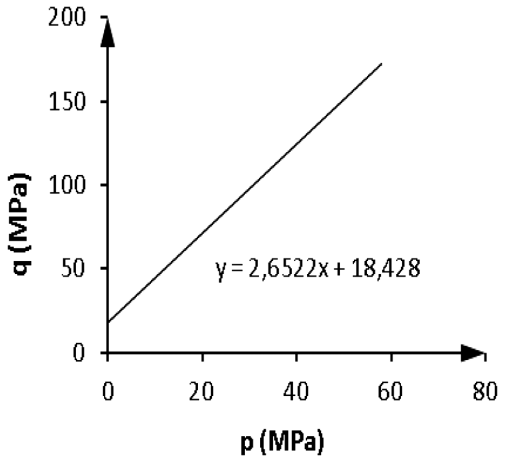

Figure 9: Linear part of the Drucker-Prager-cap model for powder Ecka Alumix 231
Slika 9: Linearni del Drucker-Prager-jevega cap modela za prah Ecka Alumix 231

$$y = 2.65x + 18.43 \quad (7)$$

In order to successfully complete the numerical simulation in ABAQUS, parameters d and β must be obtained.[2,7] Parameter d represents the material cohesion and parameter β represents the angle of friction. Both of these parameters can be obtained from Equation (7). Parameter d is the point on the p-q plane where the line intersects the y axis (**Figure 2**) and it has a value of 18.43 MPa. Parameter β represents the slope of the linear part (**Figure 2**) and can be calculated using Equation (8):

$$\beta = \tan^{-1} 2.65 \quad (8)$$

Using Equation (8), the angle of friction was calculated, having a value of 69 °.

4 CONCLUSIONS

Both the Brazilian disc test and the compression test are very popular testing methods for gathering material data for the linear part of a Drucker-Prager-cap model.[2] They are both inexpensive methods because individual specimens do not have to have exactly the same dimensions and the testing equipment is widely accessible. Dimensions are then taken into account with the use of appropriate equations. Lower-density specimens result in a lower applied failure load due to a lower diffusion of dust particles and a greater notch factor. On the other hand, higher-density specimens result in a higher applied failure load. The present study shows that there is a linear relationship for the specimens with different densities and that the specimens with higher densities are much more resistant to higher loads.

5 REFERENCES

[1] S. G. Selig, D. A. Doman, A Review of Finite Element Simulations of Metal Powder Die Compaction, Journal of Machinery Manufacturing and Automation, 3 (**2014**) 2, 32–40

[2] C. Lu, Determination of Cap Model Parameters Using Numerical Optimization Method for Powder Compaction, Dissertations, Marquette University, 2009

[3] L. H. Han, J. A. Elliott, A. C. Bentham, A. Mills, G. E. Amidon, B. C. Hancock, A modified Drucker-Prager Cap model for die compaction simulation of pharmaceutical powders, International Journal of Solids and Structures, 45 (**2008**), 3088–3106, doi:10.1016/j.ijsolstr.2008.01.024

[4] ABAQUS, ABAQUS 6.11 Theory Manual, Dessault Systems, 2011

[5] H. Diarra, V. Mazel, A. Boillon, L. Rehault, V. Busignies, S. Bureau, P. Tchoreloff, Finite Element Method (FEM) modeling of the powder compaction of cosmetic products: Comparison between simulated and experimental results, Powder Technology, 224 (**2012**), 233–240, doi:10.1016/j.powtec.2012.02.058

[6] Y. Yu, J. Yin, Z. Zhong, Shape effects in the Brazilian tensile strength test and 3D FEM correction, International Journal of Rock Mechanics & Mining Sciences, 43 (**2006**), 623–627, doi:10.1016/j.ijrmms.2005.09.005

[7] M. Šori, T. Verlak, S. Glodež, Numerical simulation of powder metal compaction with Drucker-Prager cap model in a multi height component, Euro PM2013 congress & exhibition, Vol. 2, Gothenburg, Sweden, 7–11